March 2015
Journal of Testing and Evaluation
Volume 43, Number 2

A MULTIDISCIPLINARY FORUM FOR APPLIED SCIENCES AND ENGINEERING

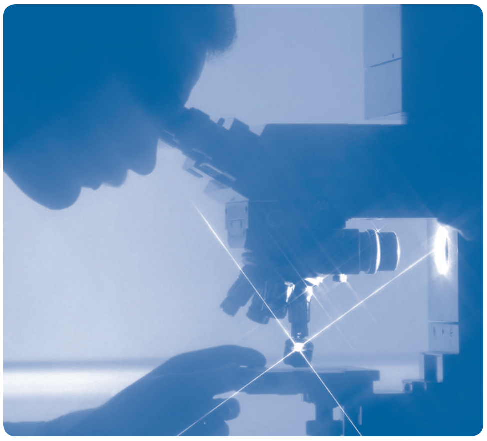

Journal of Testing and Evaluation

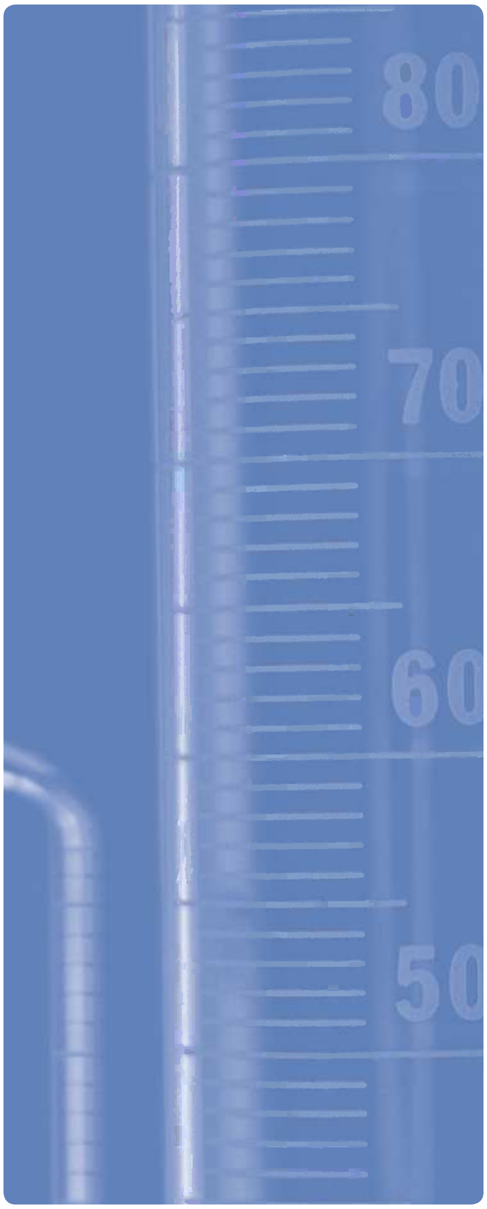

Contents:

SPECIAL ISSUE ON INNOVATIVE AND SUSTAINABLE TECHNOLOGIES AND MATERIALS IN CIVIL ENGINEERING INFRASTRUCTURES

Guest Editors: Mansour Solaimanian, Jia-Ruey Chang, Louis Ge, Dar Hao Chen

ASTM INTERNATIONAL

Volume 43, Number 2
March 2015
Coden: JTEVAB

(Contents continued on back cover)

Published bimonthly by ASTM International | 100 Barr Harbor Drive | PO Box C700 | W. Conshohocken, PA 19428-2959

EXECUTIVE COMMITTEE

DIRECTORS

INFORMATION FOR AUTHORS

For details regarding paper submission go to http://mc04.manuscriptcentral.com/astm-jote.

The subject matter must not be of a speculative nature and the contents must not include materials of an advertising nature. The paper must not be seriously defective as to literary form and structure, continuity of thought, and clarity of expression. The substance of the paper should not have been published previously in the open literature.

Authors preparing papers for submittal should observe the conventions of style explained in the ASTM Style Manual. Since the journal does not request page charges, the author is expected to conform to these standard conventions for style and the inclusion of complete references and high-quality figures. SI units are to be used throughout; if data were not measured in SI units, a note should appear to that effect and the original units should be included in parentheses after the SI units.

IN APPRECIATION OF THE REVIEWERS

The high quality of the papers that appear in this publication is a tribute not only to the obvious efforts of the authors represented but to the unheralded, though essential, efforts of their reviewers. It is to the reviewers dedication to upholding the high standards of their profession that this note pays tribute. On behalf of ASTM International and the authors as well, we acknowledge with appreciation their important contribution to the success of this journal.

COMMITTEE ON PUBLICATIONS

Journal of Testing and Evaluation (ISSN 0090-3973) is published in six issues per year by ASTM International. Some issues, in whole or in part, may be Special Issues forcused on a topic of interest to our readers. The views expressed in this journal are not those of ASTM International. The data and opinions appearing in the published material were prepared by and are the responsibility of the contributors, not of ASTM International.

Subscriptions include two formats-online access only or online access plus printed volumes. Individual subscriptions: $273.00 for 1 year online access and $338.00 for 1 year online access plus printed volumes. Institutional subscriptions (one geographic site via IP access): $422.00 for 1 year online access and $543.00 for 1 year online access plus printed volumes. Single copies are $55.00. For Multi-site subscription and pricing, please contact Sales or call 1-877-909-ASTM. To subscribe, please send prepaid order to ASTM International, Customer Service, 100 Barr Harbor Drive, P.O. Box C700, West Conshohocken, PA 19428-2959 or visit www.astm.org.

Periodicals postage paid at W. Conshohocken, Pa., and at additional mailing offices.

Note From The Editor

This Special Issue of the ASTM International's *Journal of Testing and Evaluation* (JTE) is a first in that it is dedicated entirely to the specific subject matter: Innovative and Sustainable Technologies and Materials in Civil Engineering Infrastructures.

This is a very timely topic since we hear on an almost daily basis of how the civil infrastructure in the United States and much of the world needs constant attention and upgrading. Certainly the economic impact will be huge, but employment opportunities would follow. Such improvements would obviously benefit from sustainable and innovative engineering materials and designs. These are the jobs of the engineers and scientists dedicated to this profession and on whom the burden is placed. The future holds many opportunities, not only in the near term for those presently in this challenging field, but for the engineering students in our universities about to embark on their careers in their chosen profession. This Special Issue of JTE is intended to piqué the reader's interest on this particular subject matter.

The Editorial Staff of JTE would appreciate comments on such special publications on specific topical interests for future editions. We welcome your responses.

Dr. M.R. Mitchell
Editor-in-Chief
ASTM International
Journal of Testing and Evaluation
e-mail: mrmitchell@illinoisalumni.org

Overview

More than any other time, engineers are facing the challenge of designing, constructing, and preserving the infrastructure system in a sustainable way. Economic prosperity and improved lifestyle are among the benefits of a resilient and sustainable infrastructure system. A resilient system is one that could withstand the extreme effects of a damaging factor and one that could be brought back to functionality in a timely manner. A sustainable system is one that is developed to last long with minimal adverse impact on social, economic, and environmental needs. In civil infrastructures, sustainable materials play a major role in this regard. These could be from renewable resources or materials that are abundantly available, durable, and recyclable.

This special publication of the ASTM's *Journal of Testing and Evaluation* (JTE) contains 26 papers that deal with materials used in sustainable civil infrastructure. The papers have been through rigorous peer review to be published in this special issue of JTE. The materials covered in this publication include asphalt, concrete, soils, and steel. The publication includes both numerical and experimental research and investigation of infrastructure materials. For asphalt, the papers tackle three dimensional discrete element modeling of crack development, intelligent compaction, oscillation testing, and characteristics of asphalt with recycled materials. The topics addressing sustainability in concrete deal with cracking and sustainability of fiber reinforced concrete, seismic behavior of reinforced concrete, cement fracturing, recycled concrete aggregate in drainage systems, polymer concrete, concrete pavements, and roller compacted concrete. In the areas of soils, foundations, and stabilization, there are innovative topics such as caisson behavior during sinking, use of reservoir siltation for backfill applications, bearing capacity application by seismic methods, lime stabilization of expansive soils, fly ash stabilization, properties of unsaturated soils, field versus laboratory stiffness of soils using surface waves, and ground vibration of clay soils. For steel, evaluation of long multi-span girders during incremental launching is presented in the publication. Other topics in the publication include tire-road interaction regarding skid resistance, and the role of infrastructure on emergency medical services.

There are seven papers dealing with material recycling and stabilization. Use of recycled materials in pavements has always been a hot topic. The work by Chen *et al.* was focused on how the volumetric properties and performance of asphalt concrete are influenced by complete replacement of coarse natural aggregates with basic oxygen furnace (BOF) slag, and reported this process as a feasible option. On another front, use of recycled concrete aggregate (RCA) in exfiltration drainage systems such as French drains was investigated by Nam *et al.* The authors concluded RCA No. 4 gradation does not restrict the flow of water, but the RCA fines being generated during aggregate handling process may cause clogging buildup over time. Using fly ash, blast-furnace slag, and silica fume in concrete has been around for many years. Lee *et al.* investigated the effects of steam and microwave curing on concrete containing these recycling materials. The microwave-cured concrete did not show an increase in permeability relative to the concrete that was steam-cured, but showed an increase in strength. The effect of lime and the curing period on the compressibility and durability characteristics of expansive semiarid soils was evaluated by Moghal *et al.* using a range of loading periods of time, concluding that lime significantly reduces the compressibility, and that increase in duration of loading time produces a moderate increase in the final void ratio values, and finally a considerable decrease in the concentration of calcium is observed with increasing the curing period. Factors limiting the application of some fly ash in stabilization of soils and roadbed materials are addressed by Mráz *et al.* Specifically, the researchers indicated that the limitations in usage in some cases are related to the relatively low resistance in repetitive contact with water, volumetric changes and the risk of partly unsatisfactory hygienic and environmental impact. Techniques to reduce these negative impacts are suggested by the authors. Treatment of fibrous peat, which is extremely soft with high moisture content, is studied by Kazemian *et al.* Experimental work with special type of binder indicated proper cementing and stabilization of peat. Finally, massive reservoir siltations (RS) have seriously disrupted the service of many reservoirs worldwide, with adverse effects on infrastructure sustainability. Wu and Lin propose a novel approach using RS to produce controlled low strength materials, reinforced with geobags, for storage and backfill applications.

Asphalt related topics are discussed in three papers. Cracking in epoxy asphalt concrete (EAC) used for steel bridge wearing course has always been a major cause of structural and functional deterioration of this material, particularly in cold climate. Qian *et al.* developed a three-dimensional (3-D) fracture model using a randomly generating algorithm to investigate the fracture behavior of EAC. Intelligent compaction of asphalt concrete has been gaining considerable momentum within the last decade. In the paper by Singh *et al.*, a procedure for estimation of effective modulus of a multilayered HMA pavement using Intelligent Compaction (IC) was investigated. Finally, in characterization of asphalt concrete behavior, assumptions are often made regarding the magnitude of material's Poisson's ratio disregarding the impact of loading time on this important property. Zak *et al.* used small amplitude sine load tests as well as relaxation tests to demonstrate how the Poisson's ratio changes as a function of time.

Concrete and cement are discussed in four papers. Highly flowable, strain-hardening fiber-reinforced concrete has good workability in the fresh state and high-performance in the hardened state. Through mechanical testing, Liao and Chao demonstrated that this type of concrete also presents a lower crack potential and excellent crack width control. Investigating fracture in roller compacted concrete (RCC) is the subject of investigation by Cui *et al.* The authors researched two groups of RCC specimens and determined double-K fracture parameters. It was indicated that the unstable fracture toughness increases and initial fracture toughness decreases when the crack depth ratio is increased. Yao *et al.* studied the mix proportion and mechanical properties of polyethylene terephthalate (PET) concrete using an orthogonal test. Influence of various factors was considered, and it was found that the ratio of PET/mineral aggregate had the largest impact on compressive strength. Finally, Ge *et al.* studied the behavior of concrete columns reinforced with high strength hot rolled bars of fine grains, and concluded satisfactory performance of such columns.

There are three papers regarding bearing capacity and soil characterization. Caisson is often used as the foundation of important structures, and its sinking process affects is performance. Zhao *et al.* carried numerical simulation as well as laboratory experiments to study the macro- and meso-scale mechanical behaviors of the caisson during sinking, providing tools for better understanding of the earth pressure on caissons. The challenge of determining the soil bearing capacity under a constructed building is tackled by Xu *et al.* using the Rayleigh wave method. Rayleigh wave velocity measurements and static load capacity were measured for several different kinds of soil, resulting in a fitting formula between shear wave velocity and soil bearing capacity under specific soil conditions. Finally, Wang *et al.* take advantage of several technologies including scanning electron microscope, energy dispersive spectrometer, digital image processing, and triaxial testing to characterize microstructure and unsaturated properties of special types of clay.

Construction challenges are topics of discussion in three papers. The challenge with construction of two bored tunnels passing underneath an existing high speed rail is presented by Ni and Cheng. The authors discuss the challenges associated with long distance horizontal wash boring through diaphragm walls, scattered with steel H-beams and accompanying grouting strategy. The experimental work undertaken by Busch *et al.* indicates the ground response of clay soils in confined conditions subjected to explosive airblast loading. Results of the study included surface crater geometry measurements, ground vibration data and air overpressure data. The experiment results provided a data set that could be used to predict the effects of airblast loads on clay soils. Finally, the structural performance of steel U-shaped girder during launching construction is the subject of investigation by Wang *et al.* The geometric configuration of the steel U-shaped girder was analyzed and a method was proposed to determine the girder behavior based on a comprehensive finite element analysis of local stress characteristics as well as experimental investigation.

Seismic response of materials is discussed in three papers. Vibration response of multilayered pavement system is studied by Yao *et al.* through a laboratory experimental exercise. The authors indicate how the use of geotextile interlayers reduced vibration displacement in the system. The interlayer has the effects of damping vibration and resisting water erosion of the pavement base. Dai *et al.* demonstrate the steps that one can take in conducting surface wave surveys for both small and large medium applications, and provide two specific examples at both ends of the size spectrum. The last paper of this group regards correlating the laboratory produced engineering properties of materials to the in-situ values, as it has always been a difficult task. Martins and Gomes present their approach in establishing a relationship between field and laboratory moduli based on spectral analysis of surface waves for clayey sand.

Three papers present some of the issues and concerns regarding pavements and transportation. A major factor in highway safety is the friction between the road surface and the trafficking tires. Chen exhibits a systematic framework to predict skid resistance of wet pavement with non-contact method in real time. Yang *et al.* discuss an emerging method, radio frequency identification (RFID) technology, for locating manholes beneath the pavements. Through the program developed by the authors, the time and costs of manhole identification can be significantly decreased. Finally, the effectiveness of emergency medical services (EMS) depends on the existing infrastructure and allocation of medical resources. Chen *et al.* assessed the effect of service area of EMS after a disaster on the transportation infrastructure, and proposed an approach for conducting such an assessment.

Dr. Mansour Solaimanian
Penn State University

Dr. Jia-Ruey Chang
National Ilan University

Dr. Louis Ge
National Taiwan University

Dr. Dar Hao Chen
TX Department of Transportation

Guest Editors

Journal of Testing and Evaluation

doi:10.1520/JTE20140079 / Vol. 43 / No. 2 / March 2015 / available online at www.astm.org

Shih-Huang Chen,[1] Jyh-Dong Lin,[2] Daud Huang,[3] and Ching-Tsung Hung[4]

Effect of Film Thickness and Voids in Mineral Aggregate in Basic Oxygen Furnace Slag Dense-Graded Asphalt Concrete

Reference

Chen, Shih-Huang, Lin, Jyh-Dong, Huang, Daud, and Hung, Ching-Tsung, "Effect of Film Thickness and Voids in Mineral Aggregate in Basic Oxygen Furnace Slag Dense-Graded Asphalt Concrete," *Journal of Testing and Evaluation*, Vol. 43, No. 2, 2015, pp. 229–236, doi:10.1520/JTE20140079. ISSN 0090-3973

Manuscript received February 27, 2014; accepted for publication July 24, 2014; published online October 10, 2014.

[1] Dept. of Civil Engineering, National Central Univ., No. 300, Jhongda Rd., Jhongli City, Taoyuan County 32001, Taiwan (Corresponding author), e-mail: hippo601204@gmail.com

[2] Dept. of Civil Engineering, National Central Univ., No. 300, Jhongda Rd., Jhongli City, Taoyuan County 32001, Taiwan, e-mail: jyhdongl@cc.ncu.edu.tw

[3] Dept. of Civil Engineering, National Central Univ., No. 300, Jhongda Rd., Jhongli City, Taoyuan County 32001, Taiwan, e-mail: huangtawi@hotmail.com

[4] Dept. of Transportation Technology and Management, Kainan Univ., No. 1 Kainan Rd., Luzhu Shiang, Taoyuan 33857, Taiwan, e-mail: hung.casper@gmail.com

ABSTRACT

This research is focused on how the volumetric properties and performance tests for asphalt concrete are influenced by the 100 % replacement of coarse natural aggregates with basic oxygen furnace (BOF) slag. A statistical analysis was conducted to explore whether the replacement of coarse natural aggregate with basic oxygen furnace slag would increase the moisture sensitivity and reduce the strength of asphalt concrete. According to the results of the mixture design, except for the basic oxygen furnace slag asphalt mixture with upper gradation curve, the film thicknesses are from 6 to 9 μm. However, performance tests, especially the moisture sensitivity and creep test, show that the lack of film thickness and void in mineral aggregate did not adversely affect the durability of asphalt concrete. Based on the results of the mixture design and the performance tests, complete replacement of coarse natural aggregates with basic oxygen furnace slag in asphalt concrete is considered feasible and worthy of further study.

Keywords

basic oxygen furnace slag, film thickness, asphalt concrete

Introduction

Basic oxygen furnace slag is a by-product commonly produced by steelmaking processes, and there are decades of research regarding the basic oxygen furnace slag materials [1]. Xie's study investigates basic oxygen furnace slag by various methods including X-ray diffraction, X-ray fluorescence, and scanning electron microscope. A basic oxygen furnace slag–prepared asphalt mixture is a hybrid mixture with basic oxygen furnace slag as coarse aggregate and limestone as fine aggregate. The resilient modulus and indirect tensile strength of the basic oxygen furnace

FIG. 1
Flow chart.

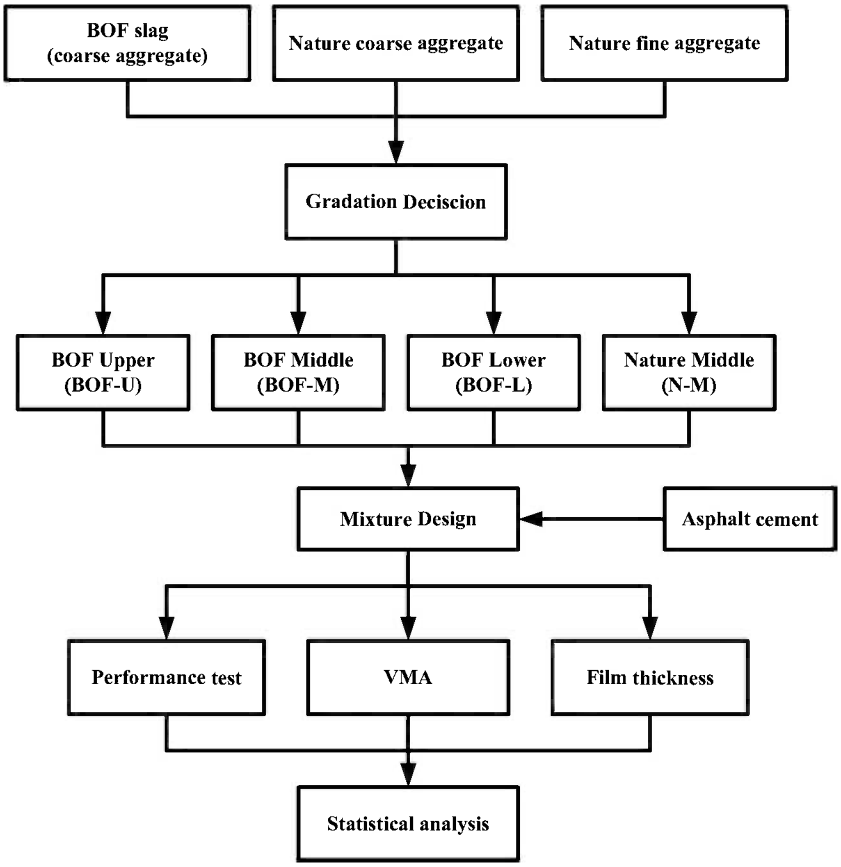

slag–prepared asphalt mixture show that it is superior to the basalt-prepared asphalt mixture with respect to moisture resistance [2]. Xie et al. found that basic oxygen furnace slag exhibits superior bonding strength to basalt and granite [3]. Mahieux et al. evaluated the mechanical properties and durability characteristics of steel slag aggregate concrete. Their results indicate that the durability characteristics of steel slag asphalt concretes are better than those of crushed limestone aggregate concrete [4]. Sengoz et al. proposed that asphalt concrete design and analysis should be standardized on a volumetric basis, rather than on a weight ratio concept. It was suggested that the voids in mineral aggregate (VMA) of dense-graded asphalt concrete (DGAC) should be no less than 15 % and that the air voids (Va) percentage should be between 3 % ~ 5 %. To ensure adequate durability of the asphalt concrete, the concrete should not be less than 4.5 % (weight ratio) or 10 % (volume ratio) [5]. Xiao et al. stated that the Superpave mix design method and volumetric analysis could be used for rubberized asphalt mixtures containing reclaimed asphalt pavement [6]. Chen claims that the film thickness is defined as the thin asphalt membrane adhering to the aggregate surfaces. Insufficient film thicknesses can result in a reduction of durability and stripping [7]. In 1965, Kandhal et al. stated that films of $6 \sim 8\,\mu$m are appropriate. However, others suggested that the film thickness of asphalt concrete should not be lower than $9 \sim 10\,\mu$m [8]. Anochie-Boateng et al. claimed that typical film thicknesses have been reported in the range of 5.8–8 μm in South Africa [9]. Chadbourn et al. proposed that Asphalt concrete in early stages does not need to consider the absorbed parts of asphalt by aggregates. This is because the absorbed parts do not cause the durability and strength of the asphalt concrete to decrease [10].

This study evaluates whether basic oxygen furnace slag can be regarded as a coarse aggregate in dense-graded asphalt concrete. In this study, the natural coarse aggregate in dense-graded asphalt concrete was replaced completely with basic oxygen furnace slag in the test sets. Conventional dense-graded asphalt concrete was used as the comparison set. The description of the mixture design results will be discussed, followed by the differences in the volumetric properties between the test and comparison sets. The performance tests are conducted in a laboratory setting to explore whether the influence of basic oxygen furnace slag is significant in dense-graded asphalt concrete. The relationship between film thickness and performance of dense-graded asphalt concrete is then further discussed.

Experimental Programs

The total framework of this study is shown in **Fig. 1**. Physical tests of all of the materials, following ASTM standards, were

FIG. 2 The gradation curve of different mixtures.

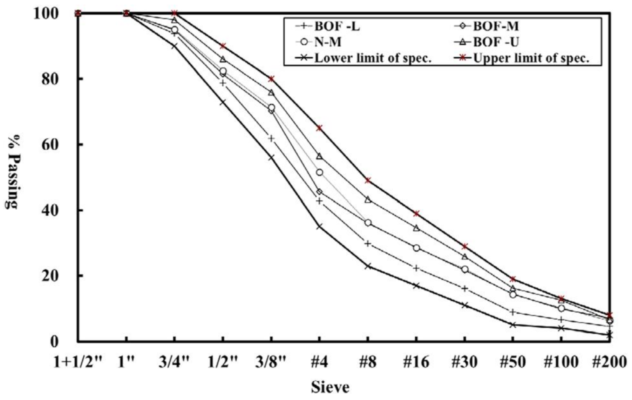

performed first. The gradation in this study complies with ASTM D3515 [11], and all mixture designs were according to the Asphalt Institute (AI) MS-2 standards. This study aims to explore whether the replacement of coarse aggregate with basic oxygen furnace slag would reduce the durability and strength of dense-graded asphalt concrete. This is done by using the mixture design to obtain the optimal asphalt content, and then conducting performance tests and a statistical analysis between the test set and the comparison set. The gradations of this study are shown in **Fig. 2**, and the details of the test and comparison sets are as follows:

1. Comparison set: applied natural aggregates that correspond with the middle curve of the standard, ASTM D3515, using mixture design. This study refers to the middle curve as the natural middle (N-M).
2. Test sets: replaced coarse aggregates with basic oxygen furnace slag and adjusted three different gradations, which are:
   (a) corresponds with upper curve of the standard to conduct mixture design, which is referred to as BOF-U in this study,
   (b) corresponds with the middle curve of the standard to conduct mixture design, which is referred to as BOF-M in this study, and
   (c) correspond with the low curve of the standard to conduct mixture design, which is referred to as BOF-L in this study.

CALCULATION OF FILM THICKNESS

At present, the average film thickness is calculated using one of the two following methods:

1. The Saskatchewan Department of Highway and Transportation in Canada calculates film thickness in accordance with the concept of aggregate surface area and percentage effective binder [12], as applied in the following six steps:
   (a) The aggregate's specific area is found by multiplying the sieving average of gradation by the area factor.
   (b) The percentage of absorbed asphalt is calculated as:

$$\text{Absorbed asphalt }(\%) = \frac{\text{ASP} \times \text{BSG} - \left[\frac{\text{BSG}(100 + \text{ASP})}{\text{TMSG}} - 100\right] \times \text{ASG}}{\text{BSG}} \tag{1}$$

   where:
   ASP = asphalt content of the mix by dry weight of aggregate,
   BSG = bulk specific gravity of the aggregates in the asphalt mix,
   TMSG = theoretical maximum specific gravity of the asphalt mixes, and
   ASG = specific gravity of the asphalt cement in the mix.

   (c) The absorbed asphalt by aggregates, Pba (%), is calculated as:

$$\text{Pba}(\%) = (\%\text{ absorbed asphalt}) \times \frac{100}{100 + \text{ASP}} \tag{2}$$

   (d) The percentage of asphalt content by total asphalt mixture, Pb (%), is given by:

$$\text{Pb}(\%) = (\text{ASP}) \times \frac{100}{100 + \text{ASP}} \times 100\% \tag{3}$$

   (e) The percentage of effective asphalt by total asphalt mixture (Pbe) (%) is given by the equation:

$$\text{Pbe}(\%) = \text{Pb} - \text{Pba} \tag{4}$$

   (f) Dust proportion (DP) is calculated as:

$$\text{DP} = \frac{\text{passing \#200}(\%)}{\text{Pbe}} \tag{5}$$

   (g) Effective film thickness (μm) is given by the formula:

$$\text{Fbe} = \frac{981 \times \text{Pbe}}{\text{SST} \times (100 - \text{Pb})} \tag{6}$$

   where:
   SST = denotes total surface area.
2. Aljassar and Haas developed a calculation for the aggregate total surface area [13]. Meanwhile, a formula was developed to obtain the average film thickness of the aggregate on behalf of the California Department of Transportation [12].

PERFORMANCE TESTS

The performance tests conducted in the laboratory include resilient modulus, indirect tensile strength, creep test, and the tensile strength ratio (TSR) (AASHTO T283 [14]). The indirect tensile strength for the resilient modulus method was used to measure the stiffness of the dense-graded asphalt concrete samples. Standard testing procedures from the ASTM D4123 were

TABLE 1 Physical properties of basic oxygen furnace slag and natural aggregate.

Item	Standard	Basic Oxygen Furnace Slag			NCA			NFA	Specimen
Aggregate size		1″	3/4″	3/8″	1″	3/4″	3/8″	Sand	
Bulk specific gravity	ASTM C127	3.42	3.44	3.34	2.58	2.45	2.43	2.43	–
Apparent specific gravity	ASTM C127	3.59	3.63	3.65	2.68	2.66	2.71	2.73	–
Water absorbed (%)	ASTM C128	1.4	1.6	2.5	1.5	1.1	1.3	1.5	–
Los Angeles abrasion (%)	ASTM C131	16	16	26	20	31	27	–	40
Percentage of flat and elongated (%)	ASTM D4791	5	5	1	10	13	9	–	15
Percentage of fractured particles (%)	ASTM D5821	100	100	100	100	95	96	–	90
Soundness (%)	ASTM C88	0.1	0.2	0.1	0.7	1.1	0.9	1.3	12

Note: NCA, nature coarse aggregate; NFA, nature fine aggregate.

performed. The test frequency used was 1.0 Hz. The creep test conditions were at an axial stress of 14.5 psi for 3600-sec loading and 1800-sec unloading times. The tests were conducted at 25°C and 40°C, respectively. The tensile strength was used to evaluate the asphalt concrete's ability to resist deformation. In this study, the Marshall method apparatus was used to apply loads. To uniformly distribute the load, the compressive load was applied through a 1/2-in.-wide metallic loading strip. These tests were performed using displacement control at a constant vertical displacement rate of 2 in./min [15]. The one-way analysis of variance was used to explore the significant differences among the N-M, BOF-L, BOF-M, and BOF-U, at a confidence level of 95 %. Analysis of variance results, however, can show only whether there are significant differences among the groups. For multiple comparisons of performance's results, it is necessary to distinguish the differences between two groups after analysis of variance. This study applies the Bonferroni correction approach to perform this test [16].

Results and Discussion

RESULTS OF PHYSICAL TEST AND MIXTURE DESIGN

The physical test of the natural aggregate is shown in **Table 1**. When compared to natural aggregate, basic oxygen furnace slag has a heavier specific gravity and is more resistant to abrasion. **Table 2** shows the results of various dense-graded asphalt concrete mixture designs. The BOF-M voids in mineral aggregate do not comply with the standards; therefore, this material's voids in mineral aggregate was not considered. **Table 2** indicates that the BOF-M and BOF-L dense-graded asphalt concrete have lower asphalt content than traditional asphalt concrete with natural aggregates. Because BOF-U has voids in mineral aggregate that do not correspond with the specified requirements, the asphalt content was slightly higher.

Basic oxygen furnace slag decreases the asphalt content of asphalt concrete because basic oxygen furnace slag has a high CaO content. Thus, basic oxygen furnace slag is categorized as a hydrophobic aggregate. Basic oxygen furnace slag also contains a large amount of iron. Its Gsb is greater than that of traditional aggregates. Therefore, the addition of basic oxygen furnace slag to an asphalt concrete mixture increases the unit weight of the concrete. High Gsb values naturally increase the bulk specific gravity of compacted specimens (Gmb). The VFA value of asphalt concrete equals the average volume of air voids (Va) occupied by asphalt. The specified VFA requirement is between 65 % ∼ 75 %. **Table 2** shows that all of the mixture curves, except BOF-U, meet the specified requirements.

Stability tests determine the strength or maximum load-bearing values of construction material specimens. The Marshall stiffness index (ASTM D1559) can be obtained by dividing the asphalt concrete's stability by its flow. In this study, the stability results of various specimens of dense-graded asphalt concrete show that the stability indices of all of the tested versions of asphalt concrete were higher than the specified requirement (818 kgf). The results are closely related in all cases, confirming that the presence of basic oxygen furnace slag material did not influence the stability or strength of asphalt concrete in our tests. The flow of an asphalt concrete specimen reflects the

TABLE 2 Results of mixture design.

Testing Item	N-M	BOF-U	BOF-M	BOF-L	Standard Requirements
VMA (%)	14.2	10.4	13.2	13.4	≧13
VFA (%)	72.4	62.0	72.0	72.0	65 ∼ 75
OAC (%)	5.7	6.1	5.3	5.1	–
Gmb at 25°C	2.236	2.630	2.725	2.768	–
Air voids (Va) (%)	4.0	4.0	4.0	4.0	3 ∼ 5
Stability (kgf)	2640	2200	2600	2200	≧818
Flow (0.25 mm)	12.0	12.5	11.6	13.0	8 ∼ 14

difference between the starting load-bearing capacity and the maximum load-bearing capacity of that particular asphalt concrete specimen. The specification requires that the flow must be measured from the vertical deformation in the specimen, and that the flow of dense-graded asphalt concrete must be between 8 ∼ 14 units (where each unit is 0.25 mm). Our experimental results show that the flow values for all of the sets were within this requirement. Furthermore, all specimens attained closely related results, meaning that the presence of the basic oxygen furnace slag material did not influence the vertical deformation-bearing capacity.

VOIDS IN MINERAL AGGREGATE

In reference to the report from the Minnesota Department of Transportation, the ranking of voids in mineral aggregate decreases of asphalt concrete are as follows [10]:

1. Large decrease: decrease range is approximately ≧2 %.
2. Moderate decrease: decrease range is approximately 0.5 % ∼ 1.0 %.
3. Small decrease: voids in mineral aggregate are larger than standard or decrease range is <0.5 %.

Figure 3 shows the different voids in mineral aggregate levels for the different dense-graded asphalt concrete materials with various (4.5 % ∼ 6.5 %) asphalt levels. The voids in mineral aggregate levels of the BOF-M and BOF-L meet the specified requirements, whereas the voids in the mineral aggregate level of the BOF-U is far below the requirements. **Table 2** shows the properties of four materials, all mixed to have 4 % voids of air. It can be seen from this table that the asphalt concrete materials made with basic oxygen furnace slag, instead of traditional aggregates, produced lower voids in mineral aggregate levels than materials made with traditional aggregates. Although BOF-M and BOF-L meet the voids in mineral aggregate specification requirements, both of their curves were at the borderline of the standard. The voids in mineral aggregate of BOF-M and BOF-L meet the minimal requirements, but they are just barely acceptable. The voids in mineral aggregate of the BOF-M is about 1 % lower than that of the N-M, which is not caused by gradation. This is categorized as a moderate decrease. BOF-U does not meet the minimum voids in mineral aggregate requirements. The voids in mineral aggregate of the BOF-U are about 4 % lower than that of the N-M, which is categorized as a large decrease. The large decrease in the BOF-U voids in mineral aggregate is not caused by the basic oxygen furnace slag material, but rather by the gradation process.

FIG. 3 VMA results.

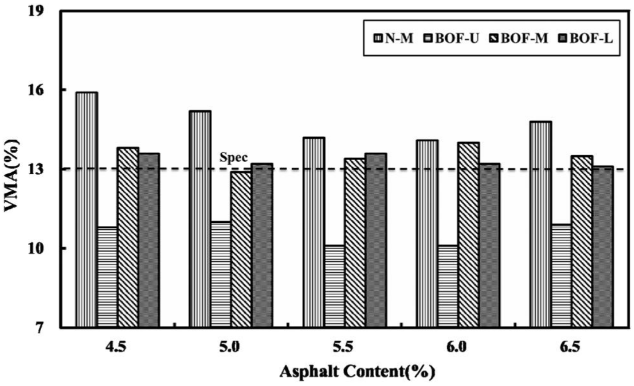

DUST PROPORTION

According to the relevant researches [7,8,13], the Marshall compaction will produce the densification, increasing total surface area of aggregate and influencing the dust proportion of mixtures. The voids in mineral aggregate are calculated with the Gmb of compacted specimens. Gmb is measured from a compacted specimen; the higher dust proportion will reduce voids in mineral aggregate and it is necessary to evaluate the dust proportion of original mixtures and compacted specimens. In addition, a higher dust proportion will decrease film thickness and percentage of effective asphalt by total asphalt mixture, and voids in mineral aggregate would also obviously be reduced. The dust proportion comparison of original mixture and compacted specimen is as shown in **Table 3**; it is easy to discover that the dust proportion in the mixtures will be significantly increased after compaction. Based on the above, the major reason for the voids in mineral aggregate moderate decrease between N-M and BOF-M should be the increasing of dust proportion after Marshall compaction.

FILM THICKNESS

It has been claimed that there are close relationships between film thickness and voids in mineral aggregate properties. For example, as voids in mineral aggregate decreases, the Pbe also decreases, causing reduced film thickness and reduced durability. By contrast, if the asphalt concrete has an appropriate void in mineral aggregate and sufficient percentage of effective asphalt by total asphalt mixture, it will have an appropriate film thickness and strong durability. Film thickness must be calculated precisely because it plays a vital role in the durability of asphalt concrete. Many professionals believe that the optimal film thickness is 6–8 μm. Kandhal claims that a film thickness of 9–10 μm will produce good durability. This study adopted the calculation methods of Superpave SP-2 from Canada's

TABLE 3 Dust proportion of original mixtures and compacted specimen.

Dust Proportion (DP)	N-M	BOF-U	BOF-M	BOF-L
Original mixture	1.07	2.77	1.43	1.15
Compacted specimen	2.15	5.11	2.81	2.07
Difference	1.08	2.34	1.38	0.92

TABLE 4 Calculation of film thickness.

Calculated Items	N-M	BOF-U	BOF-M	BOF-L
Asphalt content (to mixture, %)	5.7	6.1	5.3	5.1
ASP (%)	6.04	6.50	5.60	5.37
TMSG	2.327	2.741	2.836	2.881
BSG	2.455	2.760	2.972	3.031
ASG	1.026	1.026	1.026	1.026
SST (m^2/kg)	5.42	6.96	5.42	4.16
Absorbed asphalt (%)	1.08	3.81	1.92	1.70
Pba (%)	1.04	3.58	1.82	1.62
Pb (%)	5.70	6.10	5.30	5.10
Pbe (%)	4.68	2.53	3.49	3.49
DP	1.07	2.77	1.43	1.15
Average film thickness (μm)	**8.98**	**3.79**	**6.66**	**8.67**

Saskatchewan Department of Highways and Transportation. Three of the four film thickness values in **Table 4** range from 6 ~ 9 μm, and the film thickness of the BOF-U is noticeably lower. From the results of this study, it can be inferred that excessively fine aggregates were the primary cause of the BOF-U's low voids in mineral aggregate.

Performance and Discussion

Many scholars claim that voids in mineral aggregate should be based on film thickness rather than established by lowest asphalt content. The appropriate film thickness would maintain the durability of asphalt concrete, whereas adding basic oxygen furnace slag into asphalt concrete decreases the voids in mineral aggregate properties. The analysis of variance is used to estimate the difference between the comparison and testing set. The analysis of variance results of various performance tests, which include the resilient modulus, indirect tensile strength, creep test, and tensile strength ratio (AASHTO T283), are shown in **Table 5**. From **Table 4**, only the tensile strength ratio and creep (40°C) performance test results show significant differences. Therefore, this study proceeds to perform multiple comparisons in analysis of variance to analyze the influences of basic oxygen furnace slag toward tensile strength ratio results. The results are shown in **Table 5**. From the results in **Table 5** and **Fig. 4**, using tensile strength ratio results as an example, and by adding basic oxygen furnace slag into dense-graded asphalt concrete, the tensile strength ratio of the BOF-U shows significantly better results than the tensile strength ratio of asphalt mixture with the natural aggregates ($\text{Sig.} = 0.02 \leqq 0.05$). In addition, the tensile strength ratio of BOF-M and BOF-L are higher than the tensile strength ratio of asphalt mixture with the natural aggregates, but the differences are not significant. As can be seen from **Table 6**, the difference between BOF-L and BOF-U is only significant in the creep test ($\text{Sig.} = 0.04 \leqq 0.05$). Although natural aggregates have shown better results than the BOF-L and BOF-M in **Fig. 5**, the differences could not be defined. In other words, results of the creep test of the BOF-L and BOF-M are comparable to natural aggregates. Based on the above, the

FIG. 4 TSR results.

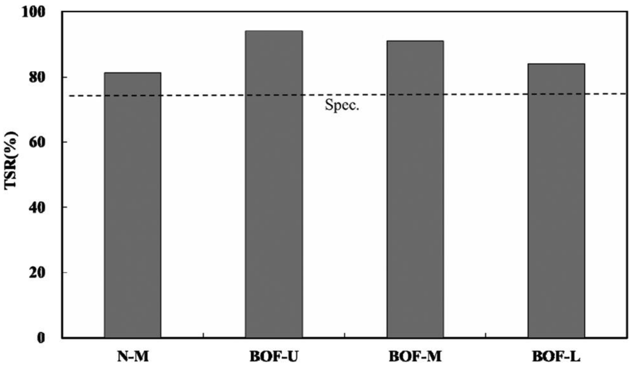

TABLE 5 Statistical analysis of performance tests.

Item		Unit	Test Sets				Significant Difference
			N-M	BOF-U	BOF-M	BOF-L	
Modulus resilient (ASTM D4123)	25°C	kgf/cm^2	24 970	23 541	22 968	23 113	[a]
	40°C		11 287	10 149	11 612	11 451	[a]
Creep test	25°C	kg sec/cm^2	14 434	15 796	16 432	13 488	[a]
	40°C		17 881	18 845	16 073	14 292	[b]
Indirect tensile strength	25°C	kgf/cm^2	11.9	12.5	12.3	11.9	[a]
	60°C		2.0	2.4	2.3	1.7	[a]
Indirect tensile strength-work	25°C	kgf cm	105.0	108.6	111.3	98.6	[a]
	60°C		14.5	15.9	13.7	11.0	[a]
Tensile strength ratio	–	%	81.3	94.1	91.0	84.0	[b]
Tensile strength ratio-work		kg cm	92.1	90.3	94.1	96.3	[a]

[a] No significant difference.
[b] Significant difference ($\alpha = 0.05$, analysis of variance).

TABLE 6 Results of multiple comparisons (Bonferroni approach).

	N-M		BOF-U		BOF-M	BOF-L
N-M			0.02	0.08	Creep	1.00
BOF-U	1.00		–	1.00		0.32
BOF-M	1.00	TSR	0.13	–		0.07
BOF-L	0.37		1.00	0.04		

Note: The mean difference is significant at the 0.05 level.

performance test and analysis of variance analysis concluded that an insufficient void in mineral aggregate and film thickness would not have an influence on the performance test results of the asphalt concrete. The key factor of success in paving quality of asphalt concrete is determined by the quality of aggregates; the aggregates have to possess high shear stress in resisting the repeated loading of vehicles that would cause permanent deformation. With good skeleton structure in the resistance of asphalt concrete, it decreases the producing of permanent deformation on pavements. The basic oxygen furnace slag possesses good properties of toughness surface, hydrophobic ability, high density, and durability, which are ideal to replace parts of natural aggregates in pavement engineering. In addition, the basic oxygen furnace slag is cheaper than nature aggregate; utilization of basic oxygen furnace slag in surface layers will significantly reduce the total cost of pavement engineering.

Conclusions

Under identical gradation conditions (N-M and BOF-M), the voids in mineral aggregate properties of BOF-M are lower than N-M by about 1 %, which is categorized as a moderate decrease of voids in mineral aggregate, and the major reasons should be the increasing of dust proportion after Marshall compaction. Although the voids in mineral aggregate of the BOF-M correspond to the specification requirement index (13 %), it falls at the borderline of the standard. Similar results are found with the BOF-L. As for BOF-U, the voids in mineral aggregate are about 5 % lower than the standard, which is categorized as a large decrease. Despite the fact that the basic oxygen furnace slag would cause the voids in mineral aggregate to decrease, the other main reason for voids in mineral aggregate decrease is related to the selected gradation. There are more fine aggregates on average in the BOF-U. This is discussed in literature reviews, which state that when the fine aggregates and dust proportion increase, surface area increases, and film thickness decreases, which is consistent with the results of obtaining decreased voids in mineral aggregate. With regard to adding basic oxygen furnace slag into dense-graded asphalt concrete, the optimum addition content shown by this study, based on three different gradations, which required their mixture designs to be processed and performances tested, is adopting the 100 % basic oxygen furnace slag replacement ratio over traditional aggregate in #8. From results of mixture design and laboratory performance tests, the 100 % basic oxygen furnace slag replacement of natural coarse aggregates is feasible in asphalt mixture, and field tests should be evaluated by the long-term performance of basic oxygen furnace slag asphalt mixture in the future. The BOF-M of this study has obtained the optimum asphalt content (OAC) result, and the optimum asphalt content is between 5.0 % ~ 5.5 %, which is lower than the optimum asphalt content of traditional aggregate by about 1 %. The primary reason for this is that the basic oxygen furnace slag is heavier than nature aggregate; therefore, the volume of the basic oxygen furnace slag is smaller than the volume of the natural aggregates. Under the same weight conditions, the absorbed ratio of the basic oxygen furnace slag is lower than the natural aggregates, because the Marshall compaction may produce gradation degradation. This study suggests that when applying the Marshall mixture design to produce a design, the design should consider the influences produced by degradation.

FIG. 5 Creep test results.

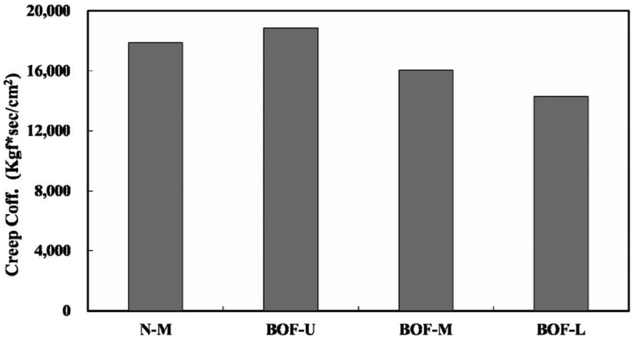

ACKNOWLEDGMENTS

The writers thank National Central University and China Hi-Ment Corporation for its financial support of this study.

References

[1] EUROSLAG, "Legal Status of Slags," The European Slag Association, Duisburg, Germany, 2006, pp. 16–17.

[2] Xie, J., Wu, S., Lin, J., Cai, J., Chen, Z., and Wei, W., "Recycling of Basic Oxygen Furnace Slag in Asphalt Mixture: Material Characterization and Moisture Damage Investigation," *Constr. Build. Mater.*, Vol. 36, 2012, pp. 467–474.

[3] Xie, J., Chen, Z., Pang, L., and Wu, S., "Implementation of Modified Pull-Off Test by UTM to Investigate Bonding Characteristics of Bitumen and Basic Oxygen Furnace Slag (BOF)," *Constr. Build. Mater.*, Vol. 57, 2014, pp. 61–68.

[4] Mahieux, P. Y., Aubert, J. E., and Escadeillas, G., "Utilization of Weathered Basic Oxygen Furnace Slag in the Production of Hydraulic Road Binder," *Constr. Build. Mater.*, Vol. 23, 2009, pp. 742–747.

[5] Sengoz, B. and Topal, A., "Minimum Voids in Mineral Aggregate in Hot-Mix Asphalt Based on Asphalt Film Thickness," *Build. Environ.*, Vol. 42, No. 10, 2006, pp. 3629–3632.

[6] Xiao, F., Amirkhanian, S. N., Putmana, B. J., and Juanga, H., "Feasibility of Superpave Gyratory Compaction of Rubberized Asphalt Concrete Mixtures Containing Reclaimed Asphalt Pavement," *Constr. Build. Mater.*, Vol. 27, 2012, pp. 432–438.

[7] Chen, S. H., 2002, "Taipave Mixture Design," Ph.D. dissertation, Department of Civil Engineering, National Central University, Taiwan, pp. 37–45 (in Chinese).

[8] Kandhal, P., Foo, K., and Mallick, R., "A Critical Review of VMA Requirements in Superpave," *NCAT Report*, National Center for Asphalt Technology, Auburn, AL, 1998, pp. 1–13.

[9] Anochie-Boateng, J. K., Komba, J., and Tutumluer, E., "Aggregate Surface Areas Quantified Through Laser Measurements for South African Asphalt Mixtures," *J. Transport. Eng.*, Vol. 138, No. 8, 2012, pp. 1006–1016.

[10] Chadbourn, B. A., Skok, E. L., Jr., Newcomb, D. E., Crow, B. L., and Spindler, S., "The Effect of Voids in Mineral Aggregate on Hot-Mix Asphalt Pavement," *Technical Report No. MN/RC–2000-13*, Department of Transportation, St. Paul, MN, 2000, pp. 1–23, 45–55.

[11] ASTM D3515-09: Standard Specification for Hot-Mixed, Hot-Laid Bituminous Paving Mixtures, *Annual Book of ASTM Standards*, ASTM International, West Conshohocken, PA, 2009.

[12] STP 204-19. 2001, "Asphalt Film Thickness Determination," *Standard Test Procedures Manual*, Saskatchewan Department of Highways and Transportation, Saskatchewan, Canada.

[13] Aljassar, A. and Haas, R., "Towards Automating Size-Gradation Analysis of Mineral Aggregate," *Transportation Research Record 1437*, Transportation Research Board, Washington, D.C., 1994, pp. 35–42.

[14] AASHTO T283:Standard Method of Test for Resistance of Compacted Asphalt Mixtures to Moisture-Induced Damage, Standard Specifications for Transportation Materials and Methods of Sampling and Testing, AASHTO, Washington, D.C., 2011.

[15] Asphalt Institute, "Mix Design Methods for Asphalt Concrete and Other Hot-Mix Types," Manual Series No. 2, Asphalt Institute, Lexington, KY, 1993.

[16] Sharma, S., *Applied Multivariate Techniques*, Wiley, Hoboken, NJ, 2003, pp. 7–8.

Journal of Testing and Evaluation

doi:10.1520/JTE20140066 / Vol. 43 / No. 2 / March 2015 / available online at www.astm.org

Boo Hyun Nam,[1] Zachary R. Behring,[2] Jinyoung Kim,[3]
Manoj Chopra,[4] John Shoucair[5] and Chul-Soo Park[6]

Evaluation of the Use of Recycled Concrete Aggregate in French Drain Systems

Manuscript received February 21, 2014; accepted for publication October 20, 2014; published online November 11, 2014.

[1] Assistant Professor, Department of Civil, Environmental, and Construction Engineering, Univ. of Central Florida, Orlando, FL 32825 (Corresponding author), e-mail: BooHyun.Nam@ucf.edu

[2] Structural Designer, Florida Department of Transportation, District 4, 3400 West Commercial Blvd., Ft. Lauderdale, FL 33309, USA, e-mail: Zachary.Behring@dot.state.fl.us

[3] Postdoctoral Researcher, Center for Advanced Infrastructure and Transportation (CAIT), Rutgers, Piscataway, NJ 08854, e-mail: longvingjue@gmail.com

[4] Associate Professor, Department of Civil, Environmental, and Construction Engineering, University of Central Florida, Orlando, FL 32825, e-mail: Manoj.Chopra@ucf.edu

[5] Geotechnical Engineer, Florida Department of Transportation State Material Office, 5007 Northeast 39th Avenue, Gainsville, FL 32609, e-mail: john.shoucair@dot.state.fl.us

[6] Senior Researcher, Geotechnical Engineering Research Division, Korea Institute of Civil Engineering and Building Technology, Daehwa-Dong 283, Goyangdae-Ro, Ilsanseo-Gu, Goyang-Si, Gyeonggi-Do, Korea, e-mail: cspark7707@gmail.com

Reference

Nam, Boo Hyun, Behring, Zachary R., Kim, Jinyoung, Chopra, Manoj, Shoucair, John and Park, Chul-Soo, "Evaluation of the Use of Recycled Concrete Aggregate in French Drain Systems," *Journal of Testing and Evaluation*, Vol. 43, No. 2, 2015, pp. 237–247, doi:10.1520/JTE20140066. ISSN 0090-3973

ABSTRACT

Recycled concrete aggregate (RCA) is often used as a replacement for virgin aggregate in road foundations (base course), embankments, hot-mix asphalt, and Portland cement concrete. However, the use of RCA in exfiltration drainage systems, such as French drains, is still uncommon. The primary concerns with using RCA as drainage media are excessive fines and calcite precipitation that can cause a reduction in permeability performance. This study investigates the potential benefits of RCA as drainage material. This paper presents and discusses: (1) the results of a nationwide survey on current practices and policies, (2) physical and chemical properties, (3) effective fine-removing methods, (4) re-cementation potential, (4) permeability (under varied fine content), and (5) long-term drainage performance of RCA as drainage material. Test results indicate that RCA No. 4 gradation does not restrict the flow of water, but the RCA fines being generated during aggregate handling process (e.g., stockpiling, placing and transporting) may cause clogging buildup over time.

Keywords

recycled concrete aggregate, permeability, clogging

Introduction

Recycled Concrete Aggregate (RCA) can be defined as a material that consists of about 60 to 75 % high quality, well-graded aggregate, bonded by a hardened cement paste [1]. RCA is a construction and demolition debris (C&D) material, and it can be obtained from various sources, such as buildings, roads, bridges, and highway or runway pavements. Other structures, such as Portland cement concrete curb, sidewalk, and driveway, are typically reinforced, and should go through a screening process that uses magnetic separators to extract the ferrous material. There are two main types of crushing devices utilized in recycling plants: compression crushers, and impact crushers. Compression crushers involve cone and jaw crushers, while impact crushers utilize impact and horizontal crushers. In North America, 61 % of recyclers use jaw crushers for the primary crushing, and 43 % of them use cone crushers for secondary crushing [2]. As a result of the crushing processes, the original concrete may yield about 75 % coarse aggregate, and 25 % fines [2].

In a national survey administered by Rutgers University [3], a research team gathered information on which state highway agencies (SHAs) use RCA in the base or sub-base layers of pavements. The survey result indicates that twelve SHAs use RCA for either base or sub-base layer, and five SHAs do not use RCA. 71 % of the respondents indicate that RCA alone is being used in the base/sub-base layer, while 29 % of them use RCA blended with other materials. Snyder and Bruinsma [4] investigated the effects of RCA in pavement drainage, and reported the potential of calcite precipitation, which can be related to the amount of exposed cement paste. In addition, it was found that washing the aggregate before use in the pavement can reduce the accumulation of fines that can cause clogging issues associated with filter fabric.

Minimal sources have reported on the use of RCA in exfiltration systems; however, Duval and Volusia counties in Florida allowed the use of RCA as media in waste-water treatment drainfields [5]. While neither county had evaluated the performance of the RCA, state environmental specialists conducted an evaluation of the RCA product and its reliability over the use of conventional aggregate (limestone) [5]. Sherman et al. [5] investigated 45 drainfields for signs of failure. The results show that only 2 of the 45 systems were classified as a "system failure." It is believed that the failed systems were due to the use of an unapproved No. 57 aggregate. This gradation, which is popular for use in concrete mix, is unsuitable for use in drainfields. The amount of fine particles from this aggregate are believed to be the cause of failure, as drainfields require aggregates with maximum porosity, and few particles smaller than 5 mm. The authors conclude that the RCA equals or exceeds the standards of other approved materials, as long as proper quality control is assured during the manufacturing process.

With proper quality control, the use of RCAs in exfiltration trench systems such as French Drains would be beneficial; however, minimal investigations on the drainage performance of RCAs have been conducted. French Drains collect water from the roadway and transfer the water into slotted pipes underground. The water then filters through coarse aggregate, and passes out through geotextile (or filter fabric). The presence of fine particles in the aggregate has the potential to clog the filter fabric, or to significantly reduce its drainage efficiency. The fines from RCA may pose additional clogging if they re-cement in the pores of the filter fabric. This study has focused on the use of RCA in French drain systems in the state of Florida; thus, the design of testing follows the specifications of the Florida Department of Transportation (FDOT).

This paper presents and discusses the practice on the use of RCA as drainage materials in the U.S. and the permeability performance of RCA. In particular, re-cementation, and the short- and long-term permeability of RCA were investigated. The re-cementation of RCA was evaluated by setting and compressive strength tests. The effect of fines was evaluated with 0, 2, and 4 % fines, and the long-term effects of these fines were monitored for 100 days, with a constant head throughout the test.

SURVEY ON PRACTICES AND POLICIES

A simple survey on the use of RCA was issued to all state highway agencies (SHAs) regarding their specifications and experiences with RCAs. The survey questions were as follows: (1) "Does your state Department of Transportation (DOT) use RCA in exfiltration trench systems?"; (2) "Does your state DOT have a specification for the RCA used in exfiltration trench?"; and (3) "Has your state DOT experienced any problem (i.e., poor drainage performance, environmental issue, etc.) by using RCA in drainage systems?". The survey responses are summarized in **Table 1**.

The survey result shows that none of the state DOTs currently use RCA specifically in exfiltration trench systems such as French drains. Most state DOTs currently allow the use of RCA in base and sub-base layers, embankment, borrow and backfill materials, but not for drainage purpose. The use of RCA in pavement base and sub-base layers is the most popular application; however, not many studies on the drainage performance of RCA have been conducted. Another popular use of RCAs is to replace fine aggregate in Portland cement concrete (PCC). Several state DOTs reported problems with RCA; thus, the specifications specifically do not allow the use of RCA as drainage filter materials. The Ohio DOT reported problems of RCA associated with re-cementation and calcite precipitation (or referred to as tufa). The Kansas DOT also reported a clogging problem, as well as killing vegetation because of high *p*H. The New Jersey DOT has the same concern about the *p*H of effluent and permeability concern, but no actual field experience. Some state DOTs (e.g., Texas and Oklahoma) do not prevent the use of RCA if it meets the same specification as virgin materials; however, their specifications indirectly discourage the RCA as drainage material. Most agencies showed strong interest in this research, and are working toward allowing RCA in drainage applications.

TABLE 1 Results from the nationwide survey.

State	Question 1	Question 2	Question 3	Note
Alabama	No	No	N/A	Allowed in embankments.
New Jersey	No	No	No	*p*H of effluent and permeability concerns.
Indiana	No	No	Yes, but not for drainage.	Used as sub-base material. Concerns with fines, un-hydrated cement, and leachate issues.
Oklahoma		No	No	No specification for RCA, but technically allowed, if meets the current specifications.
Georgia	No	No	No	
North Dakota	No	No	N/A	We have used it as a drainable base layer (cement stabilized), without any problems.
Connecticut	No	No	No	
Washington	No	N/A	N/A	We have used RCA for base and sub-base effectively, and have a study underway, to look at using it back in PCC.
Ontario	No	No	N/A	We use reclaimed concrete aggregate only in granular base/sub-base.
Arizona	No	No	No	
Montana	No	No	N/A	
Nebraska	No	No	N/A	We allow use of crushed concrete in our typical 4” foundation course below PCC pavements, but not for drainage.
Texas	No	No	No	Our specifications do not prevent the use of RCA, but there are no know uses of RCA for this purpose. The specifications are written that would indirectly discourage use of RCA.
New Hampshire	No	No	No	
Ohio	No	No	No	Not allowed in underdrains with filter fabric, had issues with pH of runoff, re-cementing, and tufa development.
Mississippi	No	No	N/A	Mississippi DOT uses and/or allows crushed concrete as a substitute for crushed stone base, and as a substitute for granular material used on shoulders.
Rohde Island	No	No	N/A	
South Carolina	No	No	N/A	
Maine	No	No	N/A	
Kansas	No	No		Not approved for drainage applications, has caused clogging issues with screens, and killed vegetation.
Utah	No	No	N/A	Allowed in Embankment, Borrow, and Backfill, if it meets the same specification as virgin materials.
Louisiana	No	No	N/A	
New York State	Not yet	Not yet		Current NYSDOT specifications do not allow RCA as a drainage filter material. We allow RCA as embankment, as sub-base gravel, and as select fill at this time.

Materials and Experiments

MATERIALS

RCA was obtained from a local construction and demolition waste recycling facility in Orlando, FL. Two 208-l drums of RCA were obtained, and the material was advertised as No. 4 gradation. A gradation analysis according to ASTM D422-63(2007)e2 [6] was performed, and the actual gradation failed to comply with the No. 4 gradation, as shown in **Fig. 1**. Thus, RCA “as is” specimens were recombined with smaller fractions, so that No.4 aggregates within the maximum and minimum limits were used in the permeability and clogging tests.

PHYSICAL PROPERTIES OF RCA

The specific gravity and absorption of RCA were determined in accordance with ASTM C127-12 [7]. The specific gravity and absorption for No. 4 minimum limit, maximum limit, and average were calculated by measuring the submerged weight, saturated surface dry weight, and oven dry weight of the RCA. The unit weight and % voids were measured as specified in ASTM C29/C29M [8]. The bulk unit weight was determined by filling a rigid wall container in three layers with RCA. Each layer was rodded with 25 strokes, using a tamping rod. With the unit weight and specific gravity, the % voids for each gradation were then calculated. The abrasion resistance of RCA was measured with the use of the

FIG. 1

Gradation analysis of RCA.

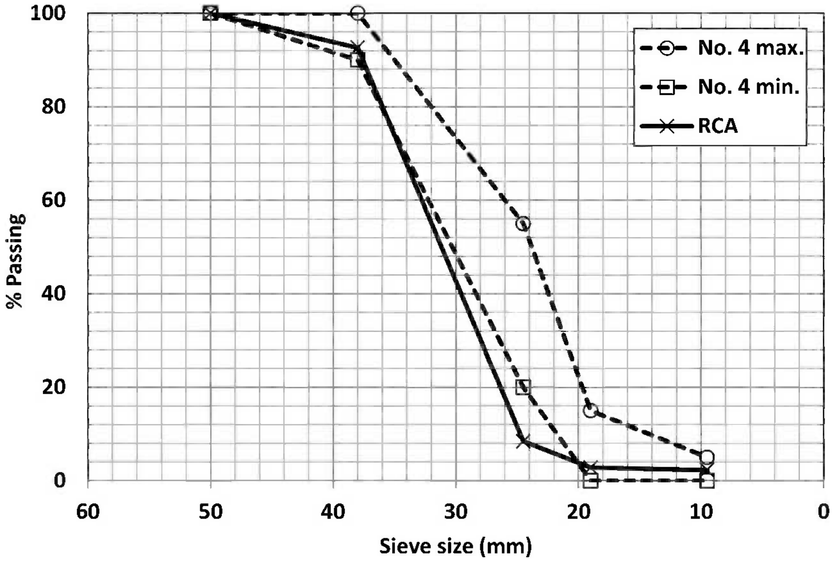

HM-70 A Los Angeles Abrasion Machine, in accordance with ASTM C535-12 [9].

CHEMICAL PROPERTIES OF RCA FINES

RCA was ground to fine particles (passing the No. 200 sieve), by using a ball mill. The powder samples were then chemically characterized using Energy dispersive X-ray (EDX) and X-ray diffraction (XRD) analyses according to ASTM C295/C295M-12 [10]. The EDX and XRD were used to characterize the chemical compositions and crystallographic structure of RCA fines, respectively. In the grinding process, unhydrated cement grains can be exposed, and these can be detected in the XRD analysis.

AGGREGATE WASHING

The effectiveness of multiple aggregate cleaning/washing methods was evaluated in order to identify the best fine-removing method. Testing methods were designed to simulate aggregate suspension, agitation, and pressure washing. All samples were approximately 5 kg, and the mass lost was determined by measuring the weight of each sample before and after the washing. The testing setup for each washing method is shown in **Fig. 2**. The detailed plan for each method is shown in **Table 2**. The suspension test was performed using a wire mesh basket suspended in water. This setup was necessary to allow suspended particles to settle to the bottom of the water container, and also to completely separate fines from the bulk aggregate sample. The agitation and pressure-washing test was conducted using an automated barrel mixer. Samples of RCA were placed in the mixer with approximately 10 kg of water. The agitation test involved tumbling of the RCA for 5, 10, and 15 min under water, in a concrete mixer. The pressure-washing test was conducted in a similar manner to the agitation test; however, the excess water was allowed to drain during the test, and a water nozzle was mounted and directed at the aggregate. The

FIG. 2

Testing setup for automated aggregate washing.

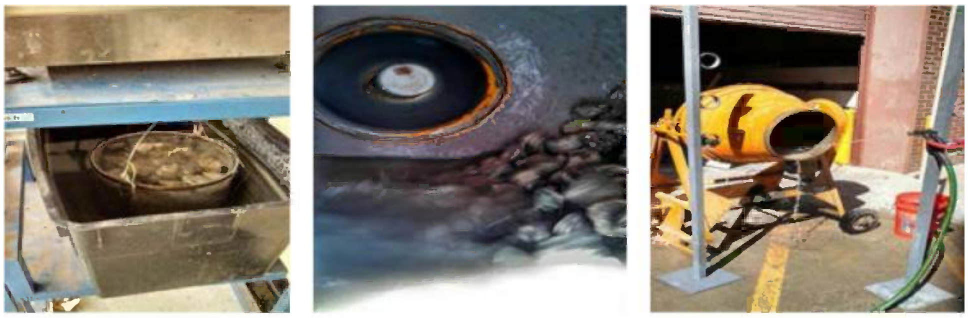

(a) suspension (b) suspension + agitation (c) pressure washing

TABLE 2 Aggregate washing methods.

Suspension	Suspension + Agitation	Pressure Washing
5 min	5 min	5 min
10 min	10 min	10 min
15 min	15 min	15 min

mounted water nozzle ensured that the treatment received by the RCA was consistent between each test.

RE-CEMENTATION OF RCA FINES

In order to evaluate the re-cementation of RCA fines, setting and compressive strength tests were conducted. RCA fine samples were prepared by grinding bulk RCAs, and sieving with a No. 200 sieve (75 μm). The material passing the sieve was then mixed with water in the water-to-solid ratio of 0.5. The purpose of this re-cementation evaluation was to determine whether RCAs produce cement hydration; thus, the typical water-to-cement ratio of 0.5 was chosen. Control samples of virgin cement were also mixed with the same water-to-cement ratio of 0.5. The setting time test was performed according to ASTM C191-13 [11] and using a Vicat needle. The initial set time is defined by the time required to achieve a penetration reading of less than 25 mm. The final set time is defined as the time required such that a 1-mm diameter needle does not make a fully circular indentation on the sample surface. Compressive strength testing was conducted following the ASTM C39/C39M-12 a [12] procedure for cement-paste and RCA-paste specimens. The compressive strength of each sample was measured at days 7 and 28. **Table 3** summarizes the compressive strength test information of the sample. Samples were cast into 50-mm diameter and 100-mm length cylinders. All cast samples were cured in an environmental chamber that controlled the constant temperature and humidity at 35°C and 99 %, respectively.

PERMEABILITY

The coefficient of permeability was measured using Darcy's Law:

$$k = \frac{Q \cdot L}{A \cdot h \cdot t} \tag{1}$$

where:

k = coefficient of permeability (cm/s),

Q = volume of discharge collected in time (t) (cm^3),

L = length of the specimen (cm),

A = cross-sectional area of the specimen (cm^2),

h = head, difference in elevation of head tank and tailwater tank (cm), and

t = time to collect discharge, Q (s).

TABLE 3 Compressive strength sample identification.

Sample ID	Material	W/C Ratio	Tested at Day
A7	RCA fine	0.5	7
A28	RCA fine	0.5	28
C7	Cement	0.5	7
C28	Cement	0.5	28

FIG. 3 Constant head permeability test setup.

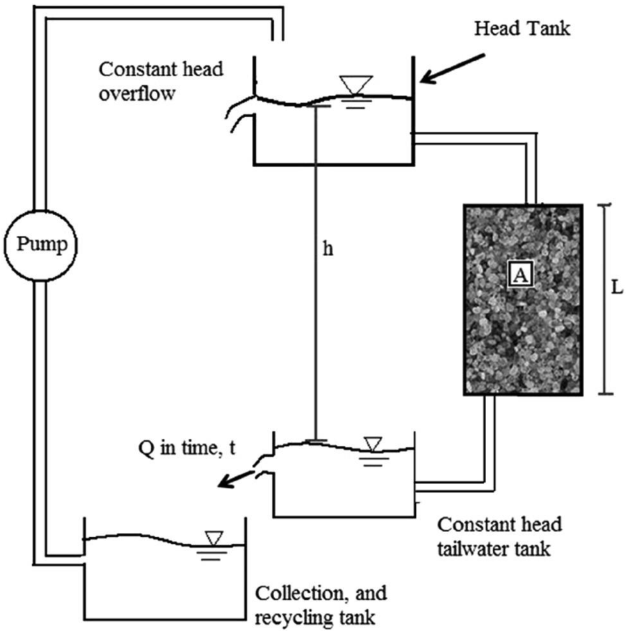

Figure 3 is a schematic diagram that shows the testing setup. The testing setup consists of a 23-cm diameter permeameter, constant-head tank, constant-head tailwater tank, collection (or recycling) tank, and testing specimen. Since large voids in RCA No. 4 aggregate allow for much faster flows than traditional soil specimens, such as sand or clay, a falling-head permeability testing setup should not be recommended. As a result of the high flow rates, it is necessary to collect and recycle the water; thus, water flow through the RCA No.4 aggregate was re-circulated. This circulation system better simulates the in situ condition of French drain systems, where post construction fines can enter the filtration systems, and surrounding soils can continuously supply fines.

The effect of a hydraulic system (e.g., permeameter size, tube size, and head) had to be evaluated because the No. 4 gradation has large void space; thus, the flow of water through the media is fast enough for a turbulent flow regime. In such a case, the limiting factor on the flow can be the permeameter, and/or tube sizes that determine the conditions of the hydraulic system. That is, if the flow rate through the aggregate is measured as close enough to the flow rates of the empty hydraulic system, then that material can have a higher flow capacity than what is measureable with the current hydraulic systems that are available. Therefore, several tests were conducted without any RCA material in the permeameter. **Table 4** lists the different sizes of

TABLE 4 Hydraulic system designs.

System ID	Permeameter Size (mm)	Tube Size (mm)
H150-6	150	6
H150-12	150	12
H150-20	150	20
H230-6	230	6
H230-12	230	12

permeameter and tube that were used. All testing setups included geotextile.

Figure 4 shows the results of permeability tests with the five different hydraulic systems listed in **Table 4**. It is clear that the tube size has a substantial impact on the flow of water. The highest permeability coefficient was obtained with the 20-mm tube, while the slowest permeability coefficient resulted from the 6-mm tube. For the permeability test setup with RCA specimens, therefore, H230-6 and H230-12 hydraulic systems were chosen due to less variability being expected between the ranges of applied heads.

RCA with the No. 4 average, minimum, and maximum gradations, as well as “as is” gradation, were used for permeability testing. **Table 5** lists the samples prepared for the permeability test. The permeability was also measured with the fine additions of 2 and 4 %, and compared with the test result of the control sample with 0 % fine addition (sample ID P4A6). The percentages of fines addition are based on the FDOT standard specification section 901–1.2 [13], which states that coarse aggregate may not have more than 1.75 % fines at source, or 3.75 % at a point of the jobsite, for L.A. abrasion values of 30 or greater.

For further investigation, long-term permeability tests (or referred to as clogging tests) were conducted using the same setup, in order to determine the long-term effects of the flow of water through RCA. The effect of excess RCA fines (referred to as physical clogging) was evaluated by performing the clogging tests on the RCA specimens with 0, 2, and 4 % fines addition. The flow rate of each sample was monitored over 100 days. In this long-term permeability test, P4A6 seen in **Table 5** was selected as the control sample (0 % fine addition). For all samples, the head was kept constant at about 35 cm, with the re-circulation of water.

FIG. 4 Effect of permeameter and tube size on permeability.

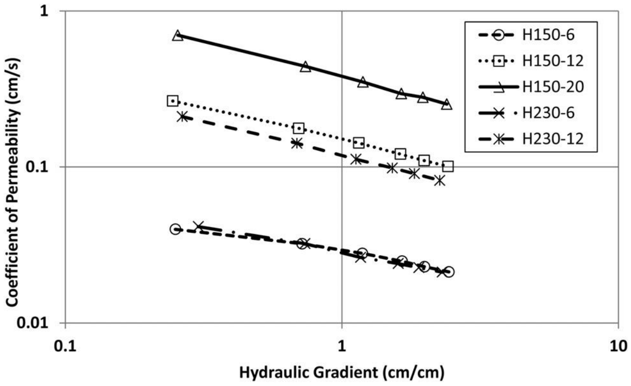

TABLE 5 Sample information for permeability test.

Sample ID	RCA	Permeameter Size (mm)	Tube Size (mm)
PE6	Empty	230	6
PE12	Empty	230	12
PA6	As is	230	6
PA12	As is	230	12
P4M6	No. 4, min.	230	6
P4M12	No. 4, min.	230	12
P4A6	No. 4, avg.	230	6
P4A12	No. 4, avg.	230	12
P4Mx6	No. 4, max.	230	6
P4Mx12	No. 4, max.	230	12

Results and Discussion

PHYSICAL PROPERTIES OF RCA

Table 6 summarizes the measured specific gravity, unit weight, voids, L.A. abrasion, and absorption of the sampled RCA. There are slight variations in the physical properties between the No. 4 gradations. The specific gravity also varies slightly. Considering the RCA as C&D debris, it includes deleterious materials, with different properties than crushed concrete. It is important to note that the physical properties of RCAs may vary, depending on the source location and material. For example, concrete products made from different raw materials (e.g., cement, aggregate, supplementary cementitious materials, etc.) and different mix proportions significantly affect the cement hydration products, resulting in different chemical and physical behaviors of the final concrete products.

Percent void space is related to particle size; the void % slightly decreases with an increase in particle size; that is, the more open No. 4 gradation (minimum limit) has the highest measured voids, while the closed grade No. 4 (maximum limit) has the least measured voids. The large void content may also allow for smaller overall dimensions for drain construction. The L.A. abrasion value measured 43.70, which is under the FDOT limit of 45 % [13]. This abrasion value indicates that RCAs are very susceptible to degradation and the generation of fines

TABLE 6 Physical properties of RCA (No. 4 gradation).

Measured Property	Minimum	Average	Maximum
Specific gravity	2.19	2.16	2.18
Unit weight (g/cm^3)	1.22	1.21	1.25
Voids (%)	44.3	43.9	42.6
L.A. abrasion (%)	43.70	43.70	43.70
Absorption (%)	6.43	6.43	6.43

TABLE 7 EDX data: chemical compositions of RCA fines.

Element	Measured Value (% by Weight)
C	20.98
O	37.43
Al	3.67
Si	3.68
Ca	34.24
Total	100.00

during the aggregate handling procedure, such as transporting, stockpiling, or placing. In a study performed by Kuo [1], RCA samples collected from seven Districts in the state of Florida exhibited similar results. Kahraman and Toraman [15] reported the L.A. abrasion values for virgin limestone aggregates at 28.9 % mass loss. The measured absorption values of RCA were relatively high, compared to the typical absorption value of normal aggregates used in concrete, ranging from 0.5 to 4 % [16]. The higher absorption of RCA could decrease the water-to-cement ratio for concrete mixture; thus, the workability will decrease.

CHEMICAL PROPERTIES OF RCA FINES

Table 7 presents the chemical compositions of RCA fines obtained from EDX. The major elements present within RCA fines are Ca, Si, and Al, as the main chemical compositions of concrete [17].

The mineral components of RCA determined using XRD analysis are shown in **Fig. 5**. This shows that the main components of RCA are calcite ($CaCO_3$) and quartz (SiO_2). This indicates that RCA fines are mainly composed of hydrated cement, sand, and limestone. These results are consistent with the EDX results (see **Table 7**). There is no evidence for the existence of portlandite ($Ca(OH)_2$), which is the byproduct of cement hydration. This is likely due to the carbonation process over time [17–19], in which portlandite reacts with carbon dioxide (CO_2), and transforms into calcite. Additionally, the leaching of portlandite during its storage time in outdoor stockpiles likely occurs due to its high solubility [19,20]. This leaching process of portlandite may be maximized in the state of Florida due to the relatively high temperatures and humidity of the Florida climate; this lack of portlandite in RCA has also been observed in other research works [18,21–25].

FIG. 5 XRD spectrum of the ground RCA sample.

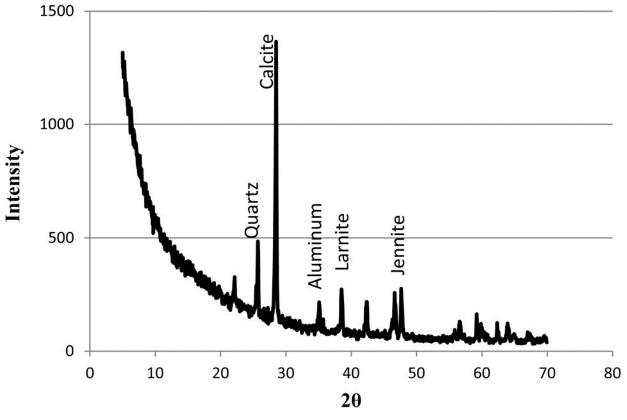

AGGREGATE WASHING

Figure 6 shows the results for the series of fine-removing methods. As expected, pressure washing was the most effective means of removing fine material, and suspension plus agitation, and suspension follow, in that order. Longer washing times result in more fines removal. Pressure washing with 15 min of treatment exhibits 10.4 % of mass lost, while suspension alone shows 6.3 % of mass lost. Pressure washing is almost twice as effective in removing the fines, compared to suspension alone.

RE-CEMENTATION

Table 8 shows the results of setting tests for the cement- and RCA-paste samples. The results indicate that RCA involves no measurement of an initial and final set. It is apparent that the RCA does not develop sufficient strength gain during the hydration process. The setting time test on the RCA sample was terminated after 24 h, since no initial set was detected. Additionally, at the final measurement of RCA at 24 h, the Vicat needle was able to still penetrate the full depth of the sample.

The results of the compressive strength tests are shown in **Table 9**. The cement-paste samples (C7 and C28) exhibited an increase of strength from about 10 to 28 MPa; however, the RCA samples (A7 and A28) resulted in considerably lower strengths of 0.1 and 0.4 MPa at 7 and 28 days, respectively. Comparatively, the RCA possesses only 1.6 % the strength of virgin cement at 28 days. It was observed that the RCA samples were very brittle and soft, and needed to be handled carefully, because the samples could be broken apart by hand, or fall apart, if submerged in water for several minutes. Clearly, very little or no strength gain was developed in the RCA sample. The apparent strength of RCA is more likely due to cohesion after a decrease in water content [22,23]. It can be concluded that re-cementation (or rehydration) of RCA is hardly expected under the typical condition of road pavement system.

PERMEABILITY

Figure 7 presents the results of the RCA permeability tests listed in **Table 5**. This clearly shows that none of the gradations impose or restrict the flow of water by any means. It is assumed that the flow rate of water for the RCA and the empty permeameter are the same. As the hydraulic gradient increases, the flow rate increases due to the higher velocity of water; however, the coefficient of permeability decreases. These results support that No. 4 RCA does not follow Darcy's Law (Eq 1), because the

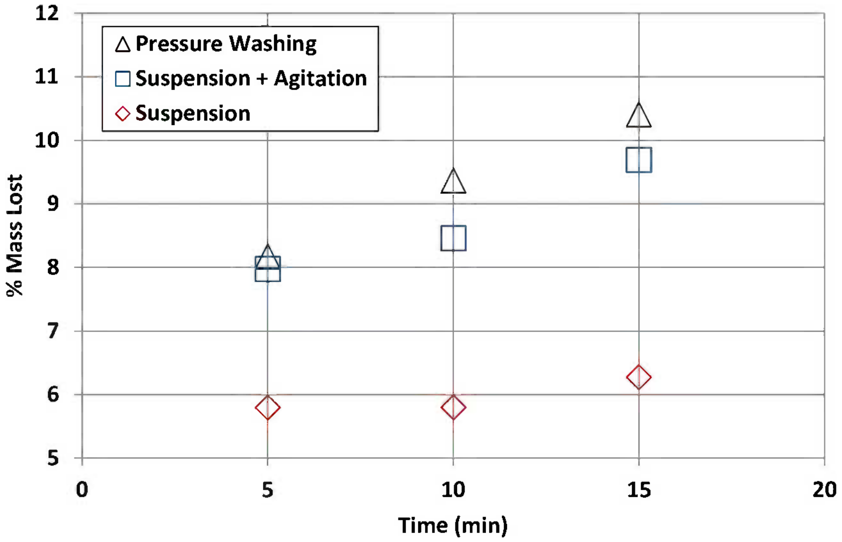

FIG. 6

Aggregate washing results.

TABLE 8 Results for time of setting test.

Material	W/C Ratio	Initial Set	Final Set
RCA Fine	0.5	Not detected	Not detected
Cement	0.5	5 h, 23 min	9 h, 10 min

TABLE 9 Compressive strength test results.

Sample	Compressive Strength (MPa)
A7	0.1
C7	9.9
A28	0.4
C28	28

measured permeability is not constant, with respect to the change in head.

The permeability was also measured with the addition of 0, 2, and 4 % RCA fines. These percentages of fine addition were selected based on the FDOT Standard Specification Section 901–1.2. **Figure 8** shows the results of this permeability test with fine addition. As expected, an increasing amount of fines leads to a reduction in flow rate. In the plot of hydraulic gradients versus permeability coefficients, the permeability coefficient decreases with increase of the hydraulic gradient. The fines additions ranging from 0 to 2 % exhibit a small difference in permeability, but the 4 % fines results in a significant reduction in the permeability. Considering the brittleness of RCAs, the amount of fines generated by aggregate handling activities

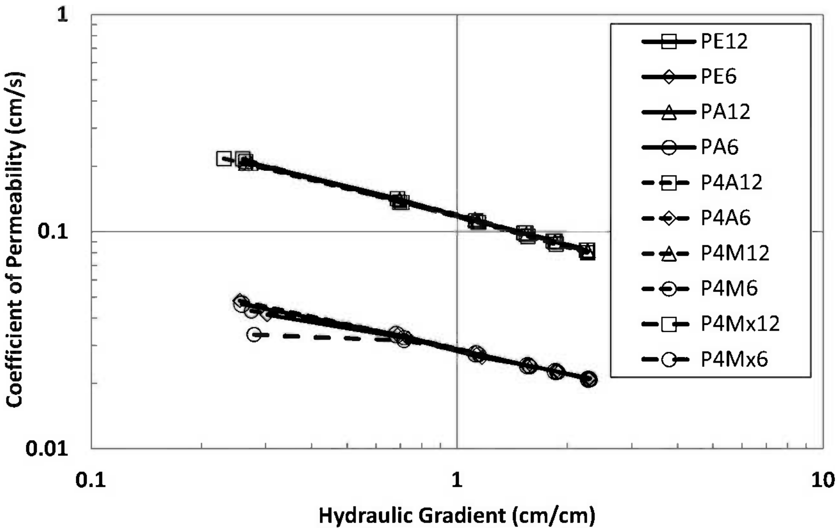

FIG. 7

Permeability measurements of the specimens (as shown in **Table 5**) under varied hydraulic gradients.

FIG. 8 Effect of fines on permeability test under varied hydraulic gradients.

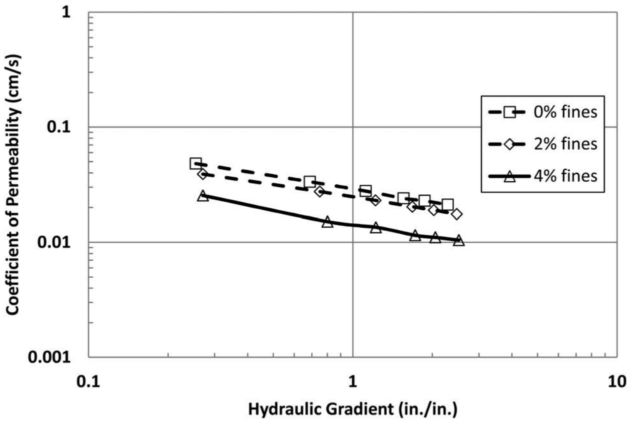

should be specified in construction sites at the moment of usage.

GEOTEXTILE CLOGGING

Clogging tests (long-term permeability test) were conducted, by monitoring the flow rate of RCA over 100 days. **Figure 9** presents the results of the clogging tests; the clogging buildup over time is presented in the form of flow rate. In the field, the cause of clogging can be either accumulation of excess fines, or calcite precipitation over time. The maximum flow rate expected (plotted as the dashed line in **Fig. 9**) was determined based on a separate test performed with the washed RCA No. 4 aggregate and 0 % fines. The flow rate was monitored for one day, until a steady-state flow rate was observed. With the sample with 0 % fine, water leakage occurred between days 60 and 72; thus, no measurement of flow rate was made during that period.

The initial flow rates measured with the 0, 2, and 4 % fines were 12.6, 11.9, and 11.1 cm^3/sec, respectively. Over time, the flow rates for all samples were reduced through the process of clogging, which included the deposition of fines and/or calcite on the geotextile, through the re-circulation of water and fines. The 4 % fines sample exhibits faster reduction in flow rate. Increase of fines addition will accelerate the rate of clogging buildup. The re-circulation system was designed to better simulate an in situ drainage system, where a continuous source of fines from surrounding soils is available (the so-called "worst" environment). The specimens with 0 and 2 % fines show slower reduction in flow rate, than the specimen with 4 % fines. Around 100 days, a relatively flat trend of flow rate was observed for the 0 and 2 % fine samples. Observed initial reduction in flow rate may be due to the immediate deposition of fines on the geotextile; however, once the fines settle, the flow reduction becomes minimal. On the other hand, the 4 % fine sample shows a continuous reduction in flow rate, and about 82 % reduction in flow rate at 100 days.

FIG. 9 Results of long-term permeability tests on the RCA specimens with 0, 2, and 4 % fines.

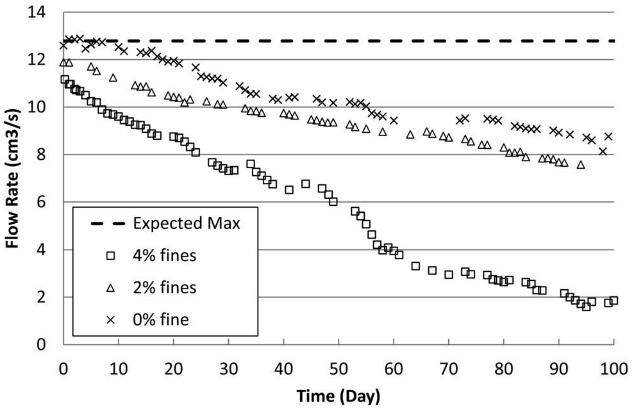

LIMITATIONS AND RECOMMENDATIONS

The limitations of this study and future studies are discussed herein. The scope of this study was to characterize the physical and chemical properties of RCAs, and also to evaluate the performance of RCA materials as potential drainage media in French drain systems. However, in order to promote the beneficial use of RCA in drainage systems, a future study that evaluates the long-term performance of in situ systems needs to be carried out. The future research will focus on the following areas:

- The effect of varied material source of RCAs
- Long-term performance evaluation with in situ drainage systems with RCAs

RCA can be obtained from any source; for example, sidewalks, building structure elements, highway bridges, pavements, retaining walls, and so on. Concrete products made from different raw materials and different mix proportion will significantly affect the products of cement hydration; thus, the physical and chemical properties and behaviors of RCA will be different. In particular, the chemical composition of RCAs will significantly influence re-cementation and calcite precipitation. Thus, the drainage performance of RCAs can vary, depending on the source of RCA materials. As one means of addressing the material variation issue, this paper discusses the importance of material characterization prior to the use of RCAs. A meaningful alternative is to use petrographic analyses (e.g. EDX and XRD) that are capable of characterizing and quantifying the chemical components in RCAs.

Another recommendation is to conduct in situ study with full-scale RCA drainage systems. One of the challenges that the authors have faced is to relate the findings of the laboratory permeability tests to the in situ performance of the RCA exfiltration trench. Laboratory environments are apparently different from in situ environments. The laboratory setup cannot match the same level (e.g. quantity and frequency) of fine supplies from surrounding soils, and CO_2 level for calcination. Temperature and water saturation conditions will also differ between the laboratory setup and in situ systems.

The authors clearly understand the limitations of the current study. Thus, a Phase II project that can address the two limitations of the current study is under development; construction of in situ/full-scale RCA French drain systems and long-term performance monitoring will be included.

Summary and Conclusions

Some states have reported that RCAs have shown performance concerns due to re-cementation or calcite precipitation of RCAs; however, not many studies on the drainage performance of RCAs have been performed, and even fewer studies are well documented. Due to a lack of information on RCA's drainage performance and its field problems, many states have prevented the use of RCA in exfiltration trench systems. This paper evaluated the potential use of RCAs as pipe backfill materials in French drain systems, and investigated the current practices and policies for the use of RCA in drainage media. Subsequently, multiple laboratory testing methods were employed, not only to determine the physical and chemical properties of RCAs, but also to evaluate the short- and long-term drainage performance. Based on the findings, the conclusions drawn and recommendations are summarized below:

- RCA involves aggregate handling procedures, such as stockpiling, transporting, and placing, which can generate a significant amount of fines. RCA has the potential to generate a large amount of fines, based on the measured value of L.A. abrasion of 43 %. Thus, the amount of fines at construction sites should be checked.
- Based on laboratory methods, such as compressive strength test, setting measurement, and XRD analyses, RCA shows no tendency to re-cementate (or rehydrate) over a short period of time. RCA re-cementation on stockpiles have been reported; thus, further investigations on long-term RCA re-cementation will be necessary.
- Based on the measurements, RCA No. 4 gradation does not restrict the flow of water through the permeameters. This is concluded based on the flow rates measured from samples with RCA being identical with the flow rates through empty permeameters. The flow of water is predominantly controlled by the size and gradation of aggregate; thus, RCA would have the same drainage performance as other standard aggregates, such as granite, dolomite, and limestone. On the other hand, aggregate type controls the chemical composition of aggregate, and thus will affect chemical reaction (e.g., calcite precipitation) over a long period of time.
- The effect of RCA fines on the permeability was found to be significant, based on the results with 0, 2, and 4 % fines measured over time. Considering the recirculation of water ("worst" in situ environment), the RCAs with 0 and 2 % did not exhibit significant difference; however, the 4 % fines apparently reduced the flow of water by more than 80 % reduction. Thus, it is recommended to limit the fine content at job sites to no more than 2 %. Alternatives are to utilize aggregate washing methods to remove fines, prior to placing the aggregates in drainage systems.
- RCA appears to have preferable qualities to serve as a drainage media in French drain systems. The tendency to produce RCA fines should be carefully considered, and it is recommended that before its use, the RCA should be properly treated, and should abide by the state standards.

ACKNOWLEDGMENTS

The authors thank the financial support of Florida Department of Transportation. The authors also thank the technical support of Mr. Juan Cruz in the Department of Civil, Environmental, and Construction Engineering at University of Central Florida.

References

[1] Kuo, S. S., "Use of Recycled Concrete Made with Florida Limestone Aggregate for a Base Course in Flexible Pavement," *Final Report BC-409*, Florida Department of Transportation, Orlando, FL, 2001.
[2] ECCO, "Recycling Concrete and Masonry," *Information Bulletin EV 22*, Environmental Council of Concrete Organizations, Skokie, IL, 1999.
[3] Bennert, T. and Maher, A., "The Use of Recycled Concrete Aggregate in a Dense Graded Aggregate Base Course," *NJDOT Research Final Report*, NJDOT, Trenton, NJ, 2008.
[4] Snyder, M. and Bruinsma, J., "A Review of Studies Concerning the Effects of Unbound Concrete Bases on PCC Pavements Drainage," *J. Transp. Res. Board*, Vol. 1519, 1996, pp. 51–58.
[5] Sherman, K. M., Hextell, P., and Massicotte, J. L., "An Evaluation of Drainfields in Florida Using Recycled Crushed Concrete Aggregate," *Proceedings of the Seventh International Symposium on Individual and Small Community Sewage Systems*, Atlanta, GA, Dec 11–13, 1994, ASAE, Washington, D.C., pp. 436–443.
[6] ASTM D422-63(2007)e2: Standard Test Method for Particle-Size Analysis of Soils, *Annual Book of Standards*, ASTM International, West Conshohocken, PA, 2007, www.astm.org.
[7] ASTM C127-12, Standard Test Method for Density, Relative Density (Specific Gravity), and Absorption of Coarse Aggregate, *Annual Book of Standards*, ASTM International, West Conshohocken, PA, 2012, www.astm.org.
[8] ASTM C29/C29M-09: Standard Test Method for Bulk Density ("Unit Weight") and Voids in Aggregate, *Annual Book of Standards*, ASTM International, West Conshohocken, PA, 2009, www.astm.org.
[9] ASTM C535-12: Standard Test Method for Resistance to Degradation of Large-Size Coarse Aggregate by Abrasion and Impact in the Los Angeles Machine, *Annual Book of*

Standards, ASTM International, West Conshohocken, PA, 2012, www.astm.org.

[10] ASTM C295/C295-12: Standard Test Method for Petrographic Examination of Aggregates for Concrete, *Annual Book of Standards*, ASTM International, West Conshohocken, PA, 2012, www.astm.org.

[11] ASTM C191-08: Standard Test Methods for Time of Setting of Hydraulic Cement by Vicat Needle, *Annual Book of Standards*, ASTM International, West Conshohocken, PA, 2008, www.astm.org.

[12] ASTM C39/C39M-12a: Standard Test Method for Compressive Strength of Cylindrical Concrete Specimens, *Annual Book of Standards*, ASTM International, West Conshohocken, PA, 2012, www.astm.org.

[13] Standard Specifications for Road and Bridge Construction 2010, State of Florida Department of Transportation, Tallahasse, FL, 2010.

[14] Haung, Y. H., *Pavement Analysis and Design*, Prentice Hall, Upper Saddle River, NJ, 2004.

[15] Kahraman, S. and Toraman, O. Y., "Predicting Los Angeles Abrasion Loss of Rock Aggregates From Crushability Index," *Bull. Mater. Sci.*, Vol. 31, No. 2, 2007, pp. 173–177.

[16] American Concrete Institute, "Aggregates for Concrete," *ACI Education Bulletin E1-07*, ACI, Farmington Hills, MI, 2007.

[17] Mindess, S., Young, F., and Darwin, D., *Concrete*, Prentice Hall, Upper Saddle River, NJ, 2003.

[18] Song, Y., Phillip, S. K., Hellebrand, E., and Muenow, D. W., "Potential for Tufa Precipitation from Crushed Concrete Containing Coarse Basaltic and Fine Coralline Sand Aggregates," *Environ. Eng. Geosci.*, Vol. 17, No. 1, 2011, pp. 53–66.

[19] Mehta, P. K., *Concrete: Structure, Properties, and Materials*, McGraw-Hill, New York, 1993.

[20] Hewlett, P. C., *Lea's Chemistry of Cement and Concrete*, Butterworth–Heinmann, London, 2004.

[21] Poon, C. S., Qiao, X. C., and Chan, D., "The Cause and Influence of Self-Cementing Properties of Fine Recycled Concrete Aggregates on the Properties of Unbound Sub-Base," *Waste Manage.*, Vol. 26, No. 10, 2006, pp. 1166–1172.

[22] Dafalla, M. A., "Effects of Clay and Moisture Content on Direct Shear Tests for Clay–Sand Mixtures," *Adv. Mater. Sci. Eng.*, Vol. 2013, 2013, 562726.

[23] Kim, J., Nam, B. H., Behring, Z. and Al Muhit, B., "Evaluation of Re-Cementation Reactivity of Recycled Concrete Aggregate Fines," *Transportation Research Record 2401*, pp. 44–51.

[24] Behring, Z., Kim, J. Y., Nam, B. H., Chopra, M., and Shoucair, J., "Drainage Performance Evaluation of Reclaimed Concrete Aggregate," *ASCE Geotechnical Special Publication 245, Innovative and Sustainable Use of Geomaterials and Geosystems*, Yichang, Hubei, China, July 20–22, 2014, pp. 33–40.

[25] Behring, Z., Nam, B. H., Kim, J., Chopra, M., and Shoucair, J., "Clogging Potential of Recycled Concrete in Road Drainage," *T&DI Congress 2014*, 2014, pp. 153–162.

Journal of Testing and Evaluation

doi:10.1520/JTE20140107 / Vol. 43 / No. 2 / March 2015 / available online at www.astm.org

Ming-Ju Lee,[1] Ming-Gin Lee,[2] Yung-Chih Wang,[3] Yishuo Huang,[4]
and Wei-Chien Wang[5]

Study of Steam and Microwave Curing of Concretes Containing Slag, Fly Ash, or Silica Fume

Reference

Lee, Ming-Ju, Lee, Ming-Gin, Wang, Yung-Chih, Huang, Yishuo, and Wang, Wei-Chien, "Study of Steam and Microwave Curing of Concretes Containing Slag, Fly Ash, or Silica Fume," *Journal of Testing and Evaluation*, Vol. 43, No. 2, 2015, pp. 248–254, doi:10.1520/JTE20140107. ISSN 0090-3973

Manuscript received March 11, 2014; accepted for publication May 23, 2014; published online August 11, 2014.

[1] Associate Professor, Nursing and Management Department of Jen-Teh Junior College of Medicine, Miaoli, Taiwan,
e-mail: mingju6099@yahoo.com.tw

[2] Professor, Department of Construction Engineering, Chaoyang Univ. of Technology, Taichung County, 413, Taiwan, e-mail: mglee@cyut.edu.tw

[3] Professor, Department of Civil Engineering, National Central Univ., Chungli, Taoyuan 320, Taiwan,
e-mail: wangyc@ncu.edu.tw

[4] Assistant Professor, Department of Construction Engineering, Chaoyang Univ. of Technology, Taichung County, 41349, Taiwan,
e-mail: yishuo@cyut.edu.tw

[5] Assistant Professor, Department of Civil Engineering, Chung Yuan Christian Univ., Chungli, Taoyuan 320, Taiwan,
e-mail: a654.joy@ msa.hinet.net

ABSTRACT

This study investigates the effects of steam and microwave curing on concretes containing fly ash, blast-furnace slag, or silica fume. Two steam curing treatments, four microwave curing times, and four types of concrete mix were used in this study. The test results indicated that microwave heating could further increase the compressive strength of mortar and concrete. Pozzolanic reaction of silica fume, fly ash, and blast-furnace slag was observed to be further promoted by steam-microwave curing. Mortar and concrete samples with 10 % silica fume added responded well to microwave curing. The strength gain development of mortar and concrete appeared to level off after 40 min of microwave curing. Thus, a 40-min microwave heating time appeared to be the optimal time for energy saving consideration. The microwave-cured concrete did not show an increase in permeability relative to the concrete that was steam-cured, but showed an increase in strength. Thus, the microwave techniques could provide the advantage of quick and uniform heating for curing of cement mortar and concrete.

Keywords

microwave heating, steam curing, compressive strength, chloride electrical penetrability

Introduction

Thermal acceleration method in concrete can benefit several operations in the construction industry such as precast concrete fabrication. The quality of a steam cured precast concrete is affected by curing time and temperature variables [1]. Steam curing might cause micro-cracks along the interface of aggregate and cement paste. It has been reported that the strength of concrete by steam curing could decrease in later stages such as 28 or 90 days while compared with concrete cured in air or in water [2]. Additionally, it requires a relatively long period for curing since heat must diffuse inward from the surface and the inherently non-uniform temperature can generate thermal cracking. Thus, microwave heating may be a potentially attractive method for accelerating cement hydration [3].

The pioneering study of Watson [4] shows that 28-day compressive strength of microwave cured concretes displayed only half the strength of the normally cured concretes. However, his results were uncertain because the temperature of the specimens might have fluctuated due to the pulsed microwave energy which he used. Moreover, an internal temperature of 90 °C was reached at which cracks could be generated, resulting from the escape of steam from the interior side [5]. However, Wu et al. reported that microwave heating improved the 28-day compressive strength of mortar as much as 3 %–7 % as well as enhancing short-term strength [6]. They emphasized optimization of the internal temperature and the final water cement ratio of the specimen, controlling processing time and microwave power. Too much microwave energy could cause a decrease in strength due to overvaporation and overheating [7]. The results from Pheeraphan and Leung [8,9] indicated that microwave curing could impair the freeze-thaw durability of high w/c concrete but not for low w/c concrete. In addition, under microwave curing, the decrease in strength due to air entrainment becomes more significant. Based on these observations, it is recommended that for microwave cured air-entrained concrete, a low w/c ratio, should be employed.

The main aim of the work presented here is to assess the acceleration of strength development in steam curing and/or microwave heating and to evaluate the strength and permeability of concretes containing fly ash, blast-furnace slag, or silica fume.

Experiments

Preparation of material is first described, followed by the specimen preparation, curing method, and the chloride electrical penetration test [3].

MATERIALS

Both mortar and concrete specimens are made with a Type I Portland cement but with different mineral admixtures. A Type I cement, a class F fly ash, a ground blast furnace slag, and a silica fume were used. The chemical compositions of the cement and admixtures used are shown in **Table 1** [10].

An Ottawa sand was used to make the mortar samples, while local construction sand and crushed gravel were used to make the concrete samples.

TABLE 1 Chemical compositions of cement and mineral admixtures.

Compositions	Cement	Fly Ash	Slag	Silica Fume
CaO	64.05	3.26	40.82	0.52
SiO_2	21.02	56.14	33.68	95.00
Al_2O_3	5.78	22.26	14.32	0.10
Fe_2O_3	3.20	7.48	3.23	0.03
MgO	1.65	1.36	7.88	1.10
SO_3	2.35	0.58	0.73	0.50
Na_2O	0.21	0.50	0.29	0.02
K_2O	0.63	3.10	0.23	0.20
Free Lime	0.96	–	–	–
C_3S	55	–	–	–
C_2S	19	–	–	–
C_3A	10	–	–	–
C_4AF	7	–	–	–
Loss on Ignition	1.13	3.55	0.22	2.45
Fineness (m^2/g)	0.33	0.30	0.36	25.00
Specific Gravity	3.15	2.22	2.95	2.20

SPECIMEN PREPARATION

Mortar Samples

50-mm mortar cubes with or without different mineral admixtures, were prepared according to ASTM C109-13 [11] and used to investigate the effects of microwave and steam curing on the compressive strength development. For mortar samples, the cement/sand ratio was fixed at 1:2.75 and the mix proportion of mortars used was shown in **Table 2**. The factors considered and the combinations of mortar samples used are shown in **Table 3**.

Concrete Samples

Concrete cylinders, 50 mm in diameter and 100 mm in height, were used for the compressive strength test. The other concrete cylinders, 100 mm in diameter and 200 mm in height, were used for the rapid chloride permeability test. For concrete samples, the water/binder ratio was fixed at 0.55 and the mix proportion of concretes used was shown in **Table 2**. The factors considered and the combinations of concrete samples used are also shown in **Table 3**.

CURING METHOD

This study was conducted to assess the acceleration of strength development by steam curing and/or microwave heating and to evaluate the strength and permeability of these concretes. Two steam-curing temperatures (65 and 75 °C) and one curing time (7 h) were used in this investigation. Two combinations of steam-curing cycle were chosen as (a) 65 °C and 7 h and (b) 75 °C and 7 h. After the steam-curing cycle and demolding, the

TABLE 2 Mix proportions of mortar and concrete.

		Batch Weight			
Mix	W/C	C	W	A	F
Mortar	0.45	500 g	225 g	0	1375 g
Concrete	0.55	360 kg/m^3	198 kg/m^3	1082 kg/m^3	700 kg/m^3

Note: C = cement, W = water, A = coarse aggregate, F = fine aggregate.

TABLE 3 Test combinations of mortar and concrete samples.

Mixture	Binder Replacement	Steam Curing Temperature	Steam Curing Time	Microwave Curing Time
(1) Mortar	(1) 100 % Cement	(1) 65 °C	7 hours steam curing + 17 hours water curing	(1) 0 min
	(2) 10 % Fume Ash			(2) 20 min
(2) Concrete	(3) 20 % Fly Ash	(2) 75 °C		(3) 40 min
	(4) 40 % Slag			(4) 60 min

mortar or concrete samples were cured in water for 17 h. The microwave curing method for accelerating cement hydration was then applied at this stage. A Tatung Electronics Model TMO-2071M microwave oven with 700 watts power was employed [12]. Four microwave heating treatments (0, 20, 40, and 60 min) were used. The specimens were placed in a glass container with 1000 ml of water in it, and the glass container was placed in the microwave oven for the specified amount of time (see **Fig. 1**). After microwave heating treatments (20, 40, and 60 min), the samples were heated and water in the glass container was vaporized so its temperature could reach 100 °C. The curing factors considered and the combinations of mortar and concrete samples used are shown in **Table 3** and **4**, respectively. After microwave heating, the samples were cooled to room temperature and immediately placed in lime-saturated water until testing was begun.

CHLORIDE ELECTRICAL PENETRATION TEST

The chloride electrical penetration test, designated as ASTM C1202-12 [13], was the test proposed for rapid qualitative assessment of chloride permeability of concrete. This method has been used previously to investigate mineral admixture effects on resistance to chloride ion penetration, the influence of aggregate fractions, and curing conditions and pore sizes related to the penetration of chloride ions [12]. This test is not a true measure of concrete permeability. The test measures the electrical conductance of the concrete, which can be correlated to concrete permeability. The test measures the amount of electrical charge (in coulombs) which passes through a 50 mm thick by 100 mm diameter saturated concrete specimen during a 6-h period. A potential difference of 60 V is maintained across the ends of the specimen. A concrete with a high permeability will allow a high amount of current to pass through the concrete and, therefore, have a high coulomb value. A concrete with a low permeability will result in a low amount of current passing through the concrete and therefore have a low coulomb value. A concrete having a total charge passed of less than 2000 C and more than 4000 C is considered to have a low permeability and a high permeability, respectively.

FIG. 1 Specimen in microwave oven.

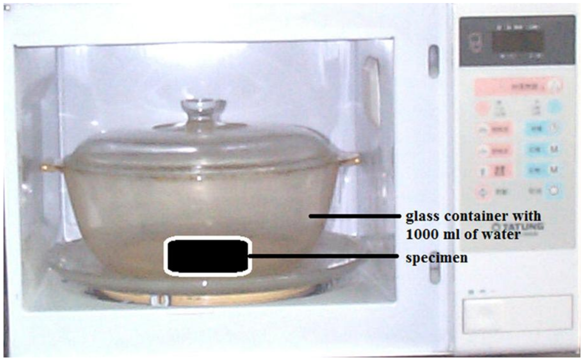

The chloride electrical penetration testing of steam and microwave cured concrete was performed on the laboratory cured 100 by 200 mm concrete cylinders at the ages of 2 and 28 days.

Experimental Results and Discussion

MORTAR

The results of 1-day compressive strength tests on the mortar samples for the eight combinations of steam and microwave curing methods are displayed in **Table 4**. The results show that the higher curing temperature or longer curing time produced higher early strength for all four mortar mixes. The results also indicate that the strength of cement mortars increases as a result of microwave heating. The amount of the strength gain was about 10 MPa by using a 20-min microwave heating. The amount of the strength gain was from 15 to 25 MPa by using 40 or 60 min of microwave heating. The % strength development due to microwave curing, which is the ratio of the strength of the microwave-cured sample minus that of the steam-cured sample to the 28-day strength of the normally cured sample, was computed for the different steam-cured temperature and mix. The results of % strength development are shown using line graphs in **Figs. 2(*a*)** and **2(*b*)**. These graphs give a good indication of the % strength development of the various mortar mixes. The mortar incorporating 20 % fly ash or 40 % slag developed strength at a relatively slower rate than the control mortar. The samples with 10 % silica fume added responded to microwave curing very well and had a high % strength development.

CONCRETE

Compressive Strength Testing

The results of 1-day and 28-day compressive strength tests on the concrete samples for the eight combinations of steam and

TABLE 4 Result of 1-day compressive strength of cement mortars with steam and microwave curing (MPa).

Mortar Curing		Microwave Curing (minute) 0	20	40	60	28-day Water Curing
100 % Cement	7 hr 65°C steam curing	26.61	35.71	43.16	45.89	51.96
	7 hr 75°C steam curing	30.79	37.79	49.26	50.43	
10 % Fume Ash	7 hr 65°C steam curing	32.96	48.25	57.18	57.11	66.11
	7 hr 75°C steam curing	37.12	48.56	62.98	63.40	
20 % Fly Ash	7 hr 65°C steam curing	19.83	27.14	32.90	33.77	47.93
	7 hr 75°C steam curing	24.12	32.14	37.27	38.33	
40 % Slag	7 hr 65°C steam curing	19.71	27.14	31.69	31.89	43.27
	7 hr 75°C steam curing	21.15	29.44	33.88	35.07	

Note: Each value is the average of 3 test specimens.

microwave curing methods are displayed in **Tables 5** and **6**, respectively. The results show that the higher curing temperature or longer curing time produced higher early strength for all four concrete mixes. The results also indicate that the strength of concrete was increased by microwave heating. The amount of the strength gain was close to 5 MPa by using 20 min microwave heating. The amount of the strength gain was from 10 to 15 MPa by using 40 or 60 min of microwave heating. The difference of the strength gain between mortar and concrete by using 40 or 60 min of microwave heating could be cement content or size effect. High early compressive strength of steam and microwave cured concrete was obtained while its 28-day strength was slightly lower than the 28-day strength of normally water-cured ones. Percent strength development due to microwave curing, which is the ratio of the strength of the microwave-cured sample minus that of the steam-cured sample to the 28-day strength of the normal cured sample, was computed for the different steam-cured temperatures and mixes [10]. The results of % strength development are shown using line graphs in **Figs. 3(*a*)** and **3(*b*)**. These graphs give a good indication of the % strength development of the various concrete mixes. The concrete incorporating 20 % fly ash or 40 % slag developed strength at a relatively slower rate than the control concrete. At 28-day curing, the strength of the fly ash concrete or the slag concrete was still generally slightly lower than that of the control concrete. The strength development due to microwave heating appears to level off after 40 min of microwave heating. Thus, a 40-min microwave heating may be the optimum length of time for energy saving consideration [12].

FIG. 2 (*a*) Comparison of 1-day compressive strength of mortar with 65 °C steam and microwave curing (MPa). (*b*) Comparison of 1-day compressive strength of mortar with 75 °C steam and microwave curing (MPa).

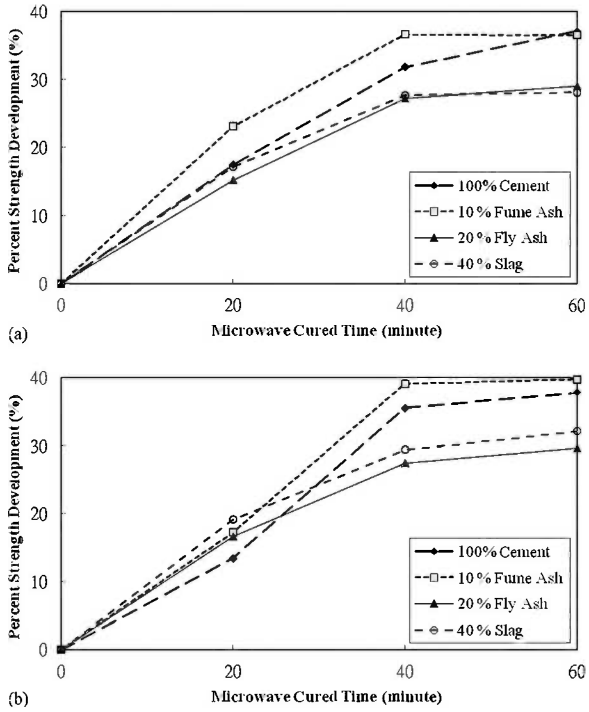

Chloride Electrical Penetration Test

The results of the chloride electrical penetration test are summarized in **Table 7** for the samples after 2-day curing and **Table 8** for the samples after 28-day curing. It can be seen from these tables that the test values for one of the curing methods (20-min microwave curing) are significantly higher than the values of the other curing methods. Among the four types of concrete evaluated, the silica–fume concrete shows the lowest permeability at all curing methods and ages. It can be seen that the concrete permeability drastically decreases with the silica fume addition. At 2-day curing, the fly ash concrete showed substantially higher permeability value than the control concrete, while the silica–fume concrete and the slag concrete had a lower permeability than the control one in **Fig. 4**. At 28-day curing, the fly ash concrete was very close to the control concrete in the chloride electrical penetration test, while the silica–fume concrete and the slag concrete had lower permeability than the control one in **Fig. 5**.

TABLE 5 Result of 1-day compressive strength of concretes with steam and microwave curing (MPa).

		Microwave Curing (minute)				
Concrete Curing		0	20	40	60	7-Day Water Curing
100 % Cement	7 h 65 °C steam curing	20.10	24.82	31.50	32.45	31.82
	7 h 75 °C steam curing	21.81	28.50	37.67	37.24	
10 % Fume Ash	7 h 65 °C steam curing	17.05	23.29	32.18	32.63	33.35
	7 h 75 °C steam curing	18.35	24.28	33.53	33.54	
20 % Fly Ash	7 h 65 °C steam curing	14.26	18.91	24.09	24.29	24.79
	7 h 75 °C steam curing	15.53	20.72	27.80	28.43	
40 % Slag	7 h 65 °C steam curing	10.51	13.00	19.55	19.98	21.20
	7 h 75 °C steam curing	13.63	17.53	22.06	22.02	

TABLE 6 Result of 28-day compressive strength of concretes with steam and microwave curing (MPa).

		Microwave Curing (minute)				
Concrete Curing		0	20	40	60	28-Day Water Curing
0	20	40	60			
100 % Cement	7 h 65 °C steam curing	35.28	37.23	39.38	35.70	39.20
	7 h 75 °C steam curing	33.52	35.37	37.84	37.12	
10 % Fume Ash	7 h 65 °C steam curing	41.25	37.26	43.44	37.12	45.83
	7 h 75 °C steam curing	39.18	35.40	39.10	35.27	
20 % Fly Ash	7 h 65 °C steam curing	32.07	28.37	30.11	26.72	35.63
	7 h 75 °C steam curing	30.46	26.94	28.60	26.38	
40 % Slag	7 h 65 °C steam curing	29.10	24.73	26.39	24.98	32.33
	7 h 75 °C steam curing	27.64	23.50	25.07	24.48	

FIG. 3 (*a*) Comparison of 1-day compressive strength of concrete with 65 °C steam and microwave curing (MPa). (*b*) Comparison of 1-day compressive strength of concrete with 75 °C steam and microwave curing (MPa).

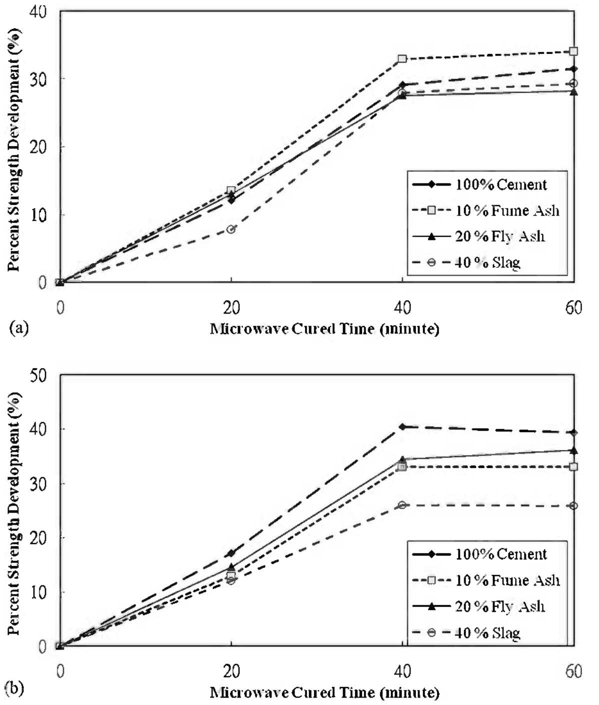

One objective of this study was to determine if the steam-microwave curing of the specimens increases the permeability of the concrete. The test results show that the steam-microwave cured tests had slightly higher permeability values as compared with the concrete that was water cured for 28 days. Therefore, for the conditions used in this study, the steam-microwave curing of the concrete had little effect on the concrete permeability. The microwave-cured concrete did not show an increase in permeability relative to the concrete that was steam-cured, but did show an increase in strength development. As can be seen in **Tables 7** and **8**, the average permeability of the 28-day cured concrete was significantly lower than that of the 2-day cured concrete.

TABLE 7 Result of 2-day chloride ion penetration of concretes with steam and microwave curing (coulombs).

		Microwave Curing (minute)			
Concrete Curing		0	20	40	60
100 % Cement	7 h 65 °C steam curing	8984	9203	6839	6986
10 % Fume Ash		4558	5335	3954	4848
20 % Fly Ash		8992	9613	7160	8825
40 % Slag		5698	6669	4943	6060

Note: Each value is the average of 2 test specimens.

TABLE 8 Result of 28-day chloride ion penetration of concretes with steam and microwave curing (coulombs).

		Microwave Curing (minute)				
Concrete Curing		0	20	40	60	28-Day Water Curing
100 % Cement	7 hr 65°C steam curing	3851	4147	3217	4268	2972
10 % Fume Ash		1641	2115	1456	2177	1373
20 % Fly Ash		3650	4300	3502	4012	3102
40 % Slag		2284	2944	2224	3030	2001

Note: Each value is the average of 2 test specimens.

FIG. 4 Comparison of 2-day chloride ion penetration of concretes with microwave curing.

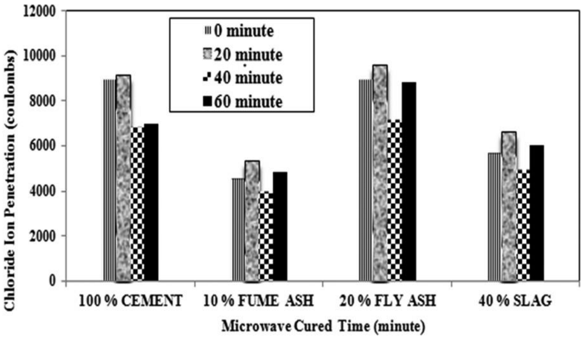

FIG. 5 Comparison of 28-day chloride ion penetration of concretes with microwave curing.

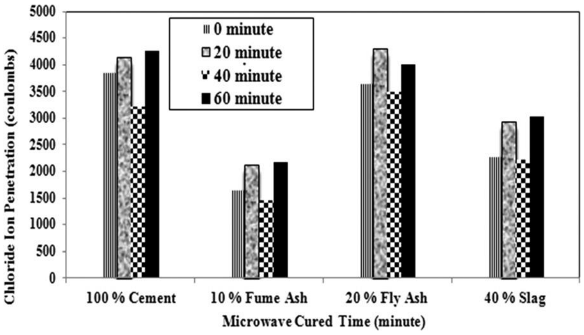

Conclusions

The main findings from this study are summarized as follows:

(1) The 1-day strength results show that the higher curing temperature and longer curing time produced higher early strength for all mortar mixes.
(2) The mortar test results indicated that microwave heating could further increase the compressive strength of the mortar. The mortar samples which combine 7-h steam curing at 75 °C plus 40-min microwave heating had a high % strength development.
(3) High early compressive strength of the steam and microwave cured mortar or concrete was obtained while its 28-day strength was slightly lower than the 28-day strength of normally water-cured ones.
(4) The strength gain development of mortar or concrete appeared to level off after 40 min of microwave curing. Thus, a 40-min microwave heating time appeared to be the optimal length of time for energy saving consideration.
(5) The mortar test results indicated that microwave heating could further increase the compressive strength of the mortar. The amount of strength gain was about 10 MPa by using 20 min microwave heating, and was from 15 to 25 MPa by using 40 or 60 min microwave heating.
(6) Pozzolanic reaction of silica fume, fly ash, and slag could be further promoted by steam-microwave curing. Mortar samples with 10 % silica fume added responded well to microwave curing. The addition of silica fume resulted in a reduction in the permeability of concrete.
(7) The 28-day chloride electrical penetrability of the accelerated curing samples reduces greatly when curing them in water after the accelerated curing. To produce concrete with low permeability, pozzolanic materials (i.e., silica fume, furnace slag) should be used.
(8) The microwave-cured concrete did not show an increase in permeability relative to the concrete that was steam-cured, but showed an increase in strength. Thus, microwave heating may be a potentially attractive method for accelerating cement hydration.

ACKNOWLEDGMENTS

This research was supported by the National Science Council, Taiwan, under contract No. NSC 99-2622-E-324-034.

References

[1] Lee, M. G. and Chern, J. C., "Effect of Steam-Curing Cycle and Proportion Mix on the Strength of Precast Concrete," *Proceedings of the Seventh East Asia-Pacific Conference on Structural Engineering & Construction*, JSCE, Kochi, Japan, July 25–27, 1999, pp. 1390–1395.
[2] Lee, M. G., "Effect of Steam-Curing on the Strength of Precast Concrete," *Proceedings of the Seventh International Conference on Composites Engineering*, ICCE, Denver, CO, July 2–8, 2000, pp. 513–514.
[3] Lee, M. G., Huang, Y., and Kan, Y., "The Strength and Rapid Chloride Permeability of Microwave Cured Concrete," *Int. J. Appl. Sci. Eng.*, Vol. 5, No. 1, 2007, pp. 53–63.
[4] Watson, A., "Curing of Concrete," *Microw. Power Eng.*, Vol. 2, 1968, pp. 108–118.

[5] Leung, C. K. Y. and Pheeraphan, T., "Very High Early Strength of Microwave Cured Concrete," *Cem. Concr. Res.*, Vol. 25, No. 1, 1995, pp. 136–146.

[6] Wu, X., Dong, J., and Tang, M., "Microwave Curing Technique in Concrete Manufactures," *Cem. Concr. Res.*, Vol. 17, No. 2, 1987, pp. 205–210.

[7] Hutchison, R. G., Chang, J. T., Jennings, H. M., and Brodwin, M. E., "Thermal Acceleration of Portland Cement Mortars With Microwave Energy," *Cem. Concr. Res.*, Vol. 21, No. 8, 1991, pp. 795–799.

[8] Leung, C. K. Y. and Pheeraphan, T., "Microwave Curing of Portland Cement Concretes: Experimental Results and Feasibility for Practical Applications," *Constr. Build. Mater.*, Vol. 9, No. 2, 1995, pp. 67–73.

[9] Pheeraphan, T. and Leung, C. K. Y., "Freeze-Thaw Durability of Microwave Cured Air-Entrained Concrete," *Cem. Concr. Res.*, Vol. 27, No. 4, 1997, pp. 427–435.

[10] Lee, M. G., "A Preliminary Study for Strength and Durability of Microwave and Steam Cured Concrete," *ASCE J. Mater. Civ. Eng.*, Vol. 19, No. 11, 2007, pp. 972–976.

[11] ASTM C109-13: Standard Test Method for Compressive Strength of Hydraulic Cement Mortars, *Annual Book of ASTM Standards*, ASTM International, West Conshohocken, PA, 2013.

[12] Lee, M. J., Lee, M. G., Su, Y. M., and Hsu, W.-K., "Experimental Study of Applying Steam Curing and Microwave Heating Technology for Fresh Concrete," *ASCE Geotechnical Special Publications* ID107, ASCE, Reston, VA, 2014.

[13] ASTM C1202-12: Standard Test Method for Electrical Indication of Concrete's Ability to Resist Chloride Ion Penetration, *Annual Book of ASTM Standards*, ASTM International, West Conshohocken, PA, 2012.

Journal of Testing and Evaluation

doi:10.1520/JTE20140060 / Vol. 43 / No. 2 / March 2015 / available online at www.astm.org

Arif Ali Baig Moghal,[1] Ali Abdul Kareem Obaid,[2] Talal O. Al-Refeai,[3]
and Mosleh Ali Al-Shamrani[4]

Compressibility and Durability Characteristics of Lime Treated Expansive Semiarid Soils

Reference

Moghal, Arif Ali Baig, Kareem Obaid, Ali Abdul, Al-Refeai, Talal O., and Al-Shamrani, Mosleh Ali, "Compressibility and Durability Characteristics of Lime Treated Expansive Semiarid Soils," *Journal of Testing and Evaluation*, Vol. 43, No. 2, 2015, pp. 255–263, doi:10.1520/JTE20140060. ISSN 0090-3973

Manuscript received February 18, 2014; accepted for publication October 22, 2014; published online November 11, 2014.

ABSTRACT

The current study evaluates the role of lime and the curing period on the compressibility and durability characteristics of two expansive semiarid soils samples originating from Saudi Arabia. The compressibility behavior of these soil samples was evaluated using a range of loading periods of time. Starting with a minimum practicable loading period of 0.5 h, the loading periods were progressively increased to 1, 2, 4, 8, and 24 h. It has been observed that the addition of lime significantly reduces the compressibility behavior of both the selected soils. The study shows that, for a given consolidation pressure increment, an increase in the duration of loading time produces a moderate increase in the final equilibrium void ratio values. In order to evaluate the durability characteristics, lime leachability tests (amount of lime that is converted into soluble form by dissociation into calcium and hydroxyl ions) were conducted on compacted specimens at varying lime contents on samples cured for 1, 7, 14, and 28 days. Analysis of the soil samples subject to increasing periods of curing time show a considerable decrease in the concentration of calcium. This is due to the transformation of amorphous lime into a stable crystalline form, which leads to the formation of pozzolanic compounds.

Keywords

compressibility, durability, lime leachability, curing period, cementation, pozzolanic compounds

Nomenclature

Cc = Coefficient of Compressibility
e = Void ratio (%)
P = Consolidation Pressure (kPa)

[1] Assistant Professor, Department of Civil Engineering, College of Engineering, King Saud Univ., Riyadh, 11421 Saudi Arabia (Corresponding author), e-mail: reach2arif@gmail.com

[2] Master Student, Department of Civil Engineering, College of Engineering, King Saud Univ., Riyadh, 11421 Saudi Arabia, e-mail: aliobaid@ksu.edu.sa

[3] Professor, Department of Civil Engineering, College of Engineering, King Saud Univ., Riyadh, 11421 Saudi Arabia, e-mail: trefeai@ksu.edu.sa

[4] Professor, Department of Civil Engineering, College of Engineering, King Saud Univ., Riyadh, 11421 Saudi Arabia, e-mail: shamrani@ksu.edu.sa

Introduction

The compressibility characteristics of soil are of prime importance in the context of designing civil engineering applications. The compressibility characteristics of natural clays are influenced by a range of factors, which include sample disturbance, water content, dry density, strain rate, type and amount of clay mineral, type of exchangeable cation, duration of pressure increment, stress path, and stress history [1,2]. Expansive soils expand on absorbing water, and shrink on drying out. Owing to these characteristics of expansive soils, suitable treatment techniques are often employed to improve the engineering properties of these soils. Lime is an excellent choice for modifying the properties of soil on a short-term basis. Lime is used extensively in civil engineering applications to stabilize expansive soils [3], as well as in treating distress in pavements [4]. Addition of lime to expansive soils causes clay particles in these soils to flocculate, which aids in the formation of inter-particle cementation bonds [4,5].

Earlier studies relied on consolidation tests which were carried out in accordance with either ASTM D2435-04 [6] or BS 1377-Part 5-1990 [7]. These consolidation tests require that each load increment, applied to the soil sample under test, be held constant for a particular duration (usually 24 h), providing sufficient time to allow the 100 % completion of primary consolidation. A typical test on plastic soils normally comprises six increments of loading, each loading held constant for a period of 24 h. It takes more than a week for the tests to complete since plastic soils undergo both primary and secondary consolidations at a very slow pace. During this period, if the material is pozzolanic (ability to form cementitious compounds with water), the results will affect the compressibility nature of the material after the soil has undergone considerable changes in particle surface characteristics due to cementation reactions [8]. Furthermore, geo-materials with stabilizing agents undergo primary consolidation very quickly and require a shorter time period for each load increment [8,9]. In order to understand the effect of loading duration on the compressibility characteristics of lime treated soil, a series of laboratory fixed ring one dimensional oedometer consolidation tests have been undertaken, using a range of loading interval time periods. In view of the fact that duration of a loading increment less than 30 min is not practicable, the loading increment time periods have been varied as 0.5, 1, 2, 4, 8, and 24 h.

Furthermore, in most of the applications such as structural fills, liners and landfill covers, road bases, embankments etc., lime treated soils are often prone to the leaching of lime [10,11], which reduces the lime content in the stabilized clay matrix, affecting their performance [12,13]. This lime leaching from the clay matrix severely hampers the rate at which pozzolanic reactions proceed. The slower pace of pozzolanic reactions increase the material porosity as well as its hydraulic conductivity. In addition, these reactions reduce the mechanical and engineering properties of the material. Hence, the durability of lime treated soils is dependent on the leachability of lime from the matrix. This study incorporates lime leachability tests on both the sample expansive soils stabilized with lime. The effects of important parameters such as the proportion of lime content, duration of the curing period, and the flow period on the leaching of lime have been studied. The process used for the retention of lime, and mechanism used to achieve the effect, are integral to this study.

Materials

SOILS

The expansive soil samples used in this study were sourced from two sites in the towns of Al-Ghat and Al-Qatif in the Kingdom of Saudi Arabia. Al-Qatif is a historic, coastal oasis region located on the western shore of the Persian Gulf in the Eastern Province of Saudi Arabia (26° 56′ 0″ N, 50° 1′ 0″ E). Al-Ghat is a town located 270 km to the Northwest of Riyadh (26° 32′ 42″ N, 43° 45′ 42″ E). While soil from both the sample sites is expansive in nature, the soils differ in their degree of expansivity and mineralogy. Sampling from both the terrain sites was carried out at a depth of 3 m. The physical properties and chemical composition of these soils are presented in **Tables 1** and **2**, respectively. The two sample soils used in this study are classified as clays with high plasticity, as per the Unified Soil Classification System (USCS).

LIME

Analytical grade Calcium Hydroxide, sourced from Winlab Chemicals, UK, has been used in the present study.

EXPERIMENTAL METHODS

The presence of predominant minerals in both the sample soils were determined by carrying out X-ray diffraction (XRD), using the Bruker D8 Advance system. The soil samples were scanned from 2° to 60° (2θ) using a 2.2 kW Cu anode long fine focus ceramic X-ray tube at a scanning rate of 1° per minute. **Figure 1** depicts a comprehensive XRD analysis. Basically, the Al-Ghat soil sample predominantly consists of kaolinite mineral, whereas Al-Qatif soil sample consists montmorillonite, a typical

TABLE 1 Physical properties of the soils.

Physical Property	Al-Ghat	Al-Qatif
Liquid limit (%)	62	137
Plastic limit (%)	30	60
Shrinkage limit (%)	17	22
Plasticity index (%)	32	77
Linear shrinkage (%)	31	77
% Finer than 200 μm	87.3	99.1
USCS classification	CH[a]	CH

[a] CH refers to clay with high plasticity.

TABLE 2 Chemical composition of the soils.

Chemical Composition (%)	Al-Ghat	Al-Qatif
K^+	1.1	1.8
K_2O	1.3	2.2
Al	7	3.3
Al_2O_3	13.3	6.3
Si	9.8	8.1
SiO_2	21	17.3
Ca^{+2}	1.4	0.7
CaO	2	0.9

swelling mineral. The target lime content percentages of 2 and 4 were added to the sample soils, on dry weight basis. The maximum proctor density values corresponding to each percentage of lime addition is shown in **Fig. 2**, and were determined by employing the mini compaction test procedure [14]. In case of the soil sample from Al-Ghat, it has been observed that an increase in the lime content of the soil decreases its maximum dry density. In case of the soil sample from Al-Qatif, no such consistent result was observed (**Fig. 2**). The maximum dry density and the corresponding optimum moisture content values at different lime contents are provided in **Table 3**.

The representative soil, after dry mixing with lime, was mixed with the amounts of water corresponding to the respective Proctor maximum dry densities, for each percentage of lime. The wet mixed material was then compacted using a static compaction technique, with the aid of a cylindrical consolidation metal ring of 75 mm diameter and 16 mm height, corresponding to the ASTM D2435-04 [6] specification. The entire assembly was then mounted in the consolidation cell and positioned in the loading frame. At the commencement of the test, an initial seating load of 6.25 kPa was applied, and the dial gauge reading was allowed to stabilize. Next, the sample was inundated with water and this point marks the start of the test. The duration of each load increment was varied as 0.5, 1, 2, 4, 8, and 24 h. Starting from the initial seating load of 6.25 kPa, all the soil samples were loaded to 800 kPa, while maintaining a standard load increment ratio of unity for each specified duration of load increment. For each pressure increment, the Void ratio–log consolidation pressure curves were plotted and the coefficient of compressibility values (Cc) were calculated. A minimum of three tests were carried out in each case, in order to validate the results for repeatability and reproducibility.

FIG. 2 Compaction curves of selected soils.

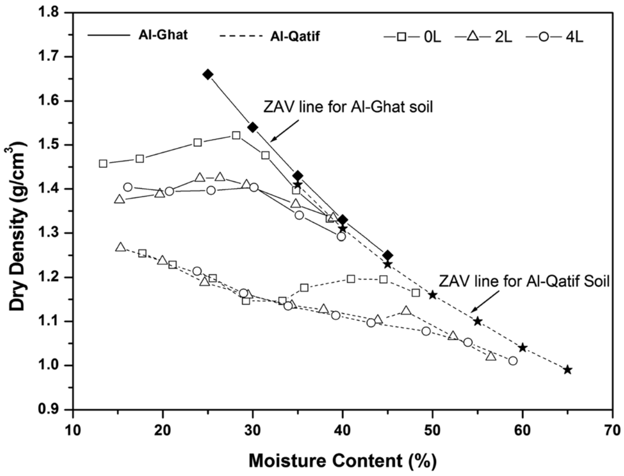

FIG. 1

X-ray diffractographs of selected soils.

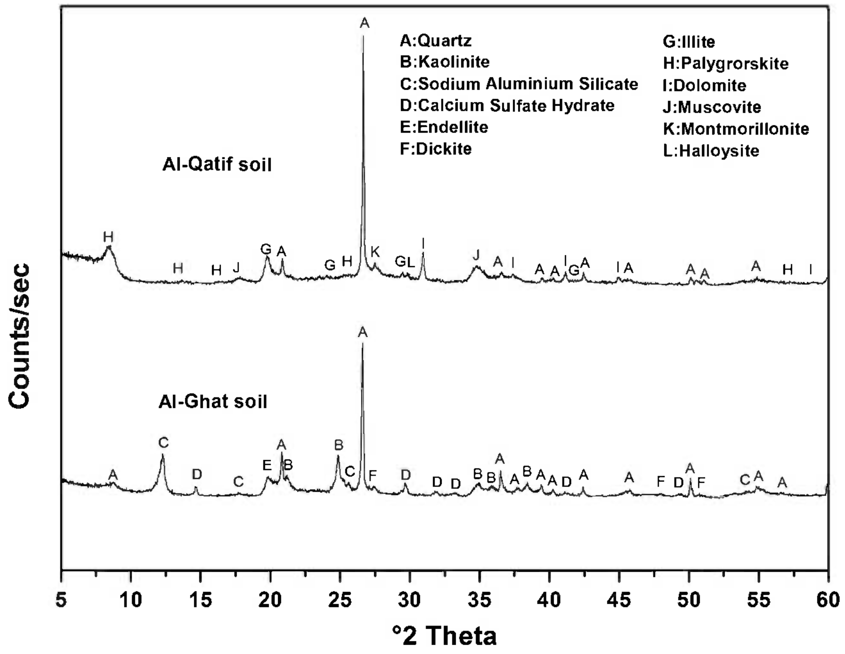

TABLE 3 Variation of maximum dry density and the corresponding optimum moisture content values at different lime contents.

	Al-Ghat		Al-Qatif	
Lime (%)	Maximum Dry Density (g/cm^3)	Optimum Moisture Content (%)	Maximum Dry Density (g/cm^3)	Optimum Moisture Content (%)
0	1.52	24	1.2	43
2	1.43	27	1.12	47
4	1.41	29	1.08	49

Durability studies were carried out using specially fabricated Perspex molds. The inner sides of the perspex molds were coated with a thin layer of silicon grease in order to ensure a good contact between the compacted material and the inner surface of the mold. All test samples were compacted to their maximum dry density and corresponding optimum moisture content values (**Table 3**), as per ASTM D5856-07 [15]. Poly Tetra-Fluoro Ethylene (PTFE) screens were fixed to the top and bottom of the perspex molds. Chemically inert glass beads, each measuring 0.5 cm diameter, were sandwiched between the two PTFE screens at both ends of the perspex molds in order to ensure uniform flow of water throughout the cross section of the compacted specimen. The perspex molds with the compacted specimen were kept in a desiccator maintained at a relative humidity greater than 95 %, and cured for periods of 7, 14, and 28 days. After curing the specimen, the perspex mold was fitted into the position and connected to the flexible tube. Then, water of a millipore grade was allowed to flow through the specimen and the pressure for the water was derived from an overhead water tank maintaining a hydraulic gradient of 10 at any given point of time. An air vent, attached to the top of the perspex mold, was used to remove entrapped air, if any. Leachate was collected in sampling bottles. The concentration of the calcium in the leachate was analyzed on the spot, using the Jenway calcium ion electrode. In each case, these tests were repeated at least thrice, in order to validate the results for repeatability and reproducibility.

Results and Discussions

EFFECT OF DURATION OF LOADING INCREMENT ON THE COMPRESSIBILITY BEHAVIOR OF UNTREATED SOILS

Figure 3 shows the void ratio–log pressure curves for Al-Ghat sample soil, at different durations of load increments, and with different levels of lime contents. In case of the soil sample without any added lime content, it has been observed that, the final equilibrium void ratio increases with the increase in duration of loading. It has been observed that as the duration of the of load increment increases, the difference in change in void ratio becomes smaller (**Fig. 3**). This is due to the fact that, for a soil mass under compression, at any given surcharge load, the volume change is predominantly due to the slipping of grains, one relative to another. The grains that have slipped do not spring back to their original positions upon removal of the stress. However, there is a small elastic rebound under low pressures, and this is attributed to the elastic compression of the adsorbed water surrounding the grains. This is particularly true in case of kaolinite mineral rich clays [8]. In case of the Al-Ghat soil sample without any added lime content, the void ratio–log consolidation pressure curves are nearly parallel (**Fig. 3**). The data here indicate that duration of loading does not affect the compressibility characteristics of the sample soil.

The Al-Qatif soil is rich in montmorillonite mineral content. The compressibility behavior of Al-Qatif soil sample without any added lime content is presented in **Fig. 4**. The compressibility behavior of this untreated soil sample is primarily governed by the long range electrical repulsive forces (forces originating from tightly adsorbed ions, dissociated surface groups, or substituted ions within the crystal lattice). The swelling phenomenon observed during the initial seating load of 6.25 kPa, as seen in **Fig. 4**, is relatively more in the Al-Qatif clay sample than in the Al-Ghat clay sample (**Fig. 3**). This swelling phenomenon is due to the presence of montmorillonite and palygorskite mineral (**Fig. 1**) in the sample soil. These minerals induce considerable swelling upon interaction with water. Similar observations were also reported for black cotton expansive soils, rich in montmorillonite mineral [16]. In case of the Al-Ghat soil sample, the resultant compressibility is predominantly contributed by two factors. One dominant contributor to

FIG. 3 Effect of lime content and duration of loading increment on the compressibility behavior of Al-Ghat soil.

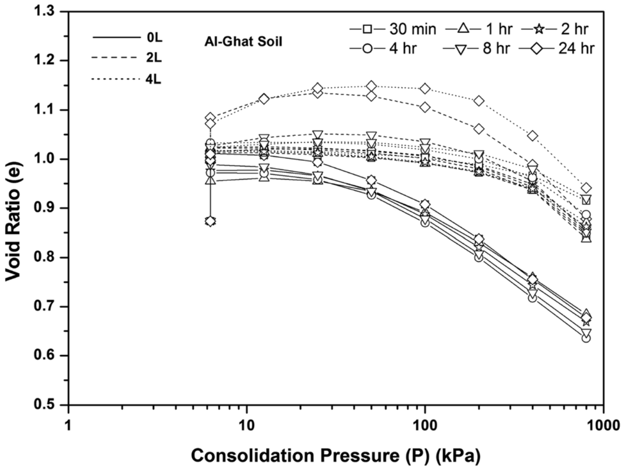

FIG. 4 Effect of lime content and duration of loading increment on the compressibility behavior of Al-Qatif soil.

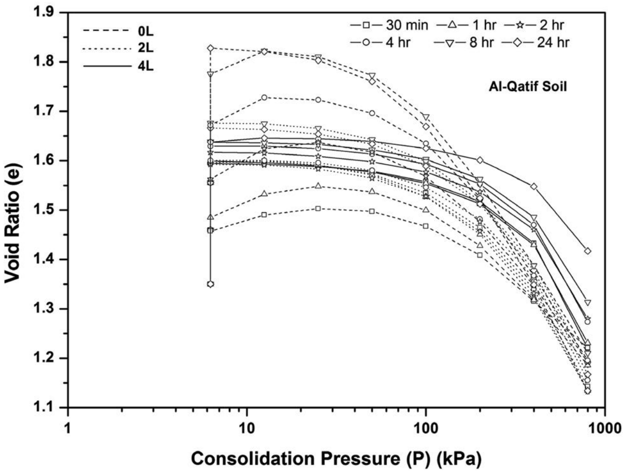

the resultant compressibility is the shearing resistance at the near contact points. The other prime contributor is the change in volume of the sample soil owing to shear displacement and/or sliding between particles.

Hence, at higher durations of loading increments exceeding 2 h, relatively higher swelling has been observed in case of the Al-Qatif soil sample (**Fig. 4**) than in case of the Al-Ghat soil sample (**Fig. 3**). In case of the Al-Ghat soil sample, the Cc increases with increase in consolidation pressure, when the load increment duration is maintained at 30 min (**Fig. 5**). When the loading increment duration is increased in the range 100–800 kPa, the Cc values remain unaffected (**Fig. 5**). Similar observations were noted in case of Al-Qatif soil sample (**Fig. 6**). It is noteworthy that the Cc values increase with increase in consolidation pressure, irrespective of the duration of loading increment adopted. However, the % increase in the values of Cc is higher in case of a loading increment of a duration 24 h, than in case of a loading duration of 30 min, in case of Al-Qatif soil sample (**Fig. 6**), when compared to Al-Ghat soil sample (**Fig. 5**). The higher values of Cc are predominantly due to higher specific surface area available in case of Al-Qatif clay 124.25 (m^2/g) (**Table 1**), which allows it to have both exposed extensive internal and external lamellae surfaces available for swelling, a virtue of clays characteristically opulent in montmorillonite and smectite minerals [17].

FIG. 5 Effect of lime content and duration of loading increment on the coefficient of compressibility values for Al-Ghat soil.

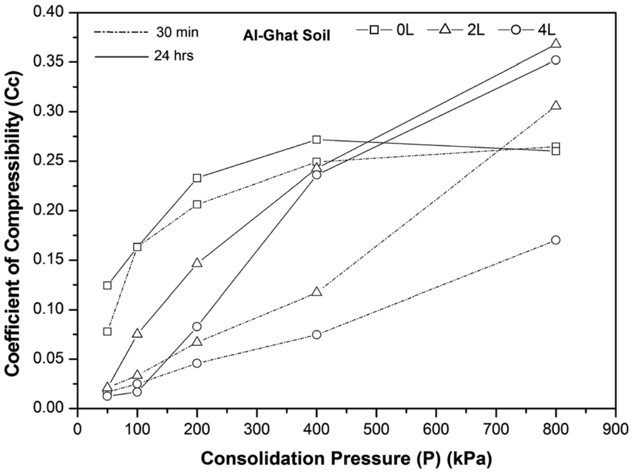

FIG. 6 Effect of lime content and duration of loading increment on the coefficient of compressibility values for Al-Qatif soil.

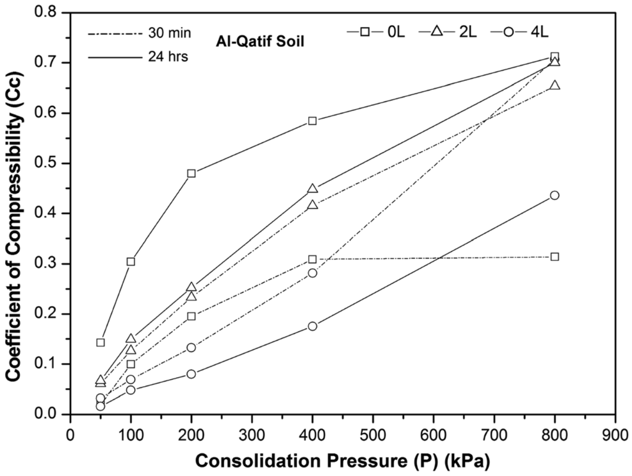

EFFECT OF DURATION OF LOADING INCREMENT ON THE COMPRESSIBILITY BEHAVIOR OF LIME TREATED SOILS

Figures 3 and **4** depict the effect of the addition of lime in different proportions to the soil samples, and the range of loading increment durations have on the void ratio–consolidation pressure relationship curves, of both Al-Ghat and Al-Qatif soil samples. From **Fig. 3**, it can be observed that at any pressure, the final equilibrium void ratio increases with increases in the duration of loading, as in the case of soil samples not treated with lime. However, the difference in the change in void ratio is further reduced with the increase in duration of loading increment, at 2 % lime addition to each of the two soil samples (**Figs. 3** and **4**). With the increase in lime content to 4 % in both the soil samples, the flocculation reactions are more pronounced as more number of cations are displaced from the clay matrix by calcium ions. The net result is a dense flocculated structure with relatively higher concentration of crystallized calcium ions. With increase in lime content (4 %), the release of silica and alumina phases from the clay particle surfaces aid in bridging the individual clay particles due to the formation of relatively strong pozzolanic bonds. The cementitious gel formed around the individual clay particles due to pozzolanic reactions holds them intact and resists any further compression.

Furthermore, with an increase in lime content from 2 to 4 %, there is a net increase in effective porosity, which aids in better release of built up pore water pressures upon application of surcharge loads. In case of lime treated soils, if the duration of loading increment is increased from 30 min to 24 h, the soil sample has relatively more curing time during which pozzolanic reactions occur between the clay matrix and calcium ions, leading to the formation of cementitious compounds. These pozzolanic cementitious compounds bind clay particles and improve the strength and stiffness, resulting in an increased resistance to compression [8], as seen in **Figs. 3** and **4**.

Typical swelling phenomenon upon addition of lime, at an initial seating load of 6.25 kPa, as seen in **Figs. 3** and **4**, is relatively more pronounced in Al-Qatif soil sample compared to the Al-Ghat soil sample. The typical swelling phenomenon is attributed to the fact that, with increase in lime content, the *p*H of the soil–lime system increases, which in turn increases the charge on the clay particles [10,11,18]. The increase in the charge on the clay particles results in a net increase in the thickness of a diffused double layer, owing to increased repulsion between individual particles of clay. As a result, a relatively higher swelling is noticed in the Al-Ghat soil sample (**Fig. 3**), which is otherwise relatively non-swelling compared to the Al-Qatif soil sample. Moroever, at any given level of consolidation pressure, for an increase in lime content, the coefficient of compressibility values reduce at higher duration of loading increments (24 h), in case of both Al-Ghat and Al-Qatif sample soils, as seen in **Figs. 5** and **6**, respectively. The practical applicability of both Al-Ghat and Al-Qatif lime treated soils is in construction of embankments, as well as structural fills. Since the coefficient of compression values of these lime treated soils is practically marginal after 30 min, these lime treated soils help in reducing the time required for laying successive lifts, in the construction of embankments and structural fills.

DURABILITY STUDIES

When clayey soils are chemically treated with lime, to enhance their desirable properties, the durability of such treatment technique assumes prime importance. The presence of sulfate in any additive severely affects the performance of treated soil by decreasing the unconfined compressive strength as well as its moisture susceptibility [18]. Apart from sulfate content, durability of any treatment technique is directly controlled by the prevalent freeze-thaw/wet-dry phenomena [19]. One of the important factors affecting the durability of any soil treatment technique is the leaching of the stabilizer from the stabilized matrix. In case of lime treatment, the leaching of calcium ions from pore solution forces the dissolution of calcium hydroxide, which severely hampers the rate at which pozzolanic reactions take place. Hence, in order to study the rate at which calcium ions leach out from the lime treated clay matrix, water was allowed to flow through the compacted specimen continuously for seven days. The effects of various parameters, such as lime content and curing period, on the lime leachability values have been studied in detail.

The improvement in the engineering properties of clays due to the addition of lime is attributed to cation exchange, flocculation, agglomeration, and pozzolanic activity. The pozzolanic reaction is a time and temperature dependent process. During a pozzolanic reaction, alumina and silica dissolve out of the clay mineral and combine with the calcium to produce cementitious compounds, calcium silicate hydrate (CSH), and calcium aluminate hydrate (CAH) [20,21]. These cementitious compounds contribute to the long term increase in shear strength of lime treated soils.

In the present study, remolded samples with different levels of lime dosages were tested for lime leachability behavior, in specially fabricated Perspex molds, the details of which are as shown in **Fig. 7**, and were briefly explained in earlier section. **Figure 8** shows the variation of calcium concentration with flow period for soil samples stabilized with 2 % lime content, and at different curing periods. It is observed that the duration of flow (of Millipore grade water) does not affect the lime leachability values. The lime leachability values remain consistently the same from the third day onwards (from the start of flow period). With an increase in curing period, the leachability values of 2 % lime treated soil samples (both Al-Ghat and Al-Qatif) are drastically reduced, as lime is converted from a

FIG. 7

Perspex column used to carry out lime leachability test.

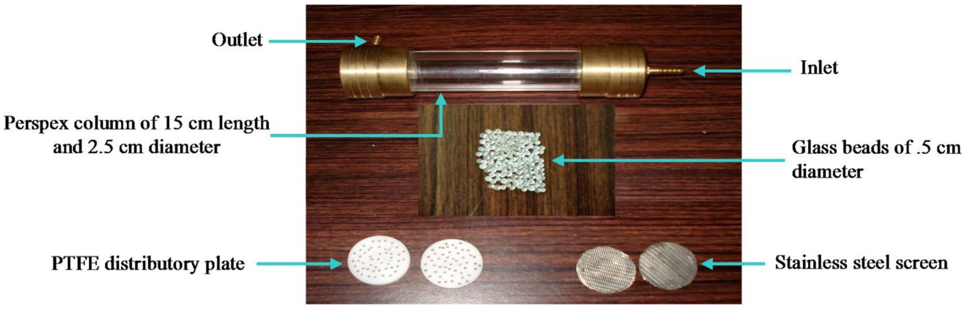

FIG. 8 Effect of curing period on the variation of calcium concentration with flow period at 2 % lime content.

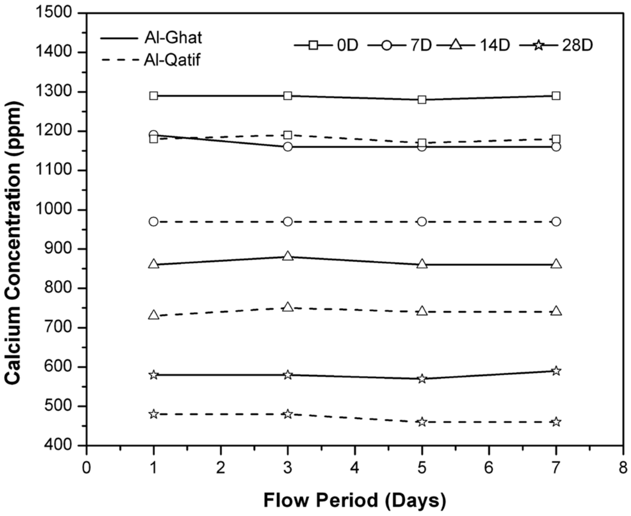

FIG. 9 Effect of curing period on the variation of calcium concentration with flow period at 4 % lime content.

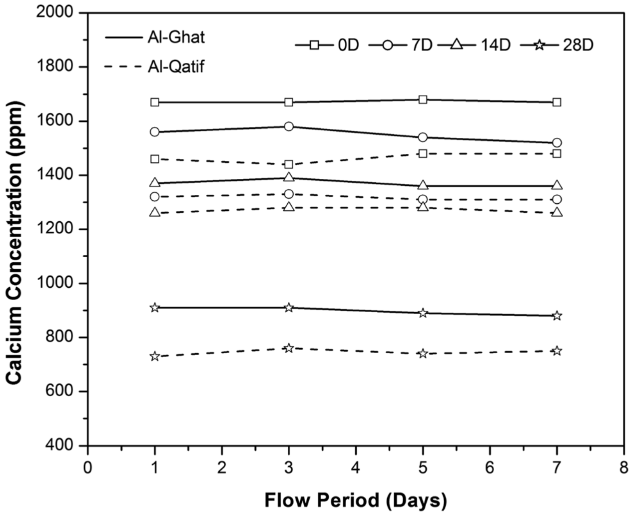

more soluble form to the less soluble form of calcium silicate hydrates. The cementation products formed at higher curing periods harden the clay matrix, thereby reducing the lime leachability values. With the increase in lime content to 4 %, the calcium ion concentration in the leaching fluid increases, particularly at lower curing periods, as seen in **Fig. 9**. However, with an increase in curing periods, the solubility of silica from the clay is enhanced, as the excess lime breaks the Si–O bonds in the silica rich phases of clay particles (particularly that of Quartz, as seen from **Fig. 1**). This dissolution of silica is better in the soil sample with 4 % of lime content than in the soil sample with 2 % of lime content, as 4 % is nearer to the optimum lime content [21,22]. Apart from silica, alumina is also released from the mineral phase, which triggers a significant reduction in the lime leachability values at 4 % addition compared to that at 2 % lime addition at any given curing period. As such, the difference in lime leachability values of both the soils can be attributed to their differences in mineralogical composition, as seen from their X-ray diffractographs (**Fig. 1**).

Figures 10 and **11** represent X-ray diffractographs for Al-Ghat and Al-Qatif soil samples with different levels of lime content and at different curing periods, respectively. The

FIG. 10

X-ray diffractographs of Al-Ghat soil at different lime contents and at different curing periods (L and D refer to lime content and curing periods, respectively).

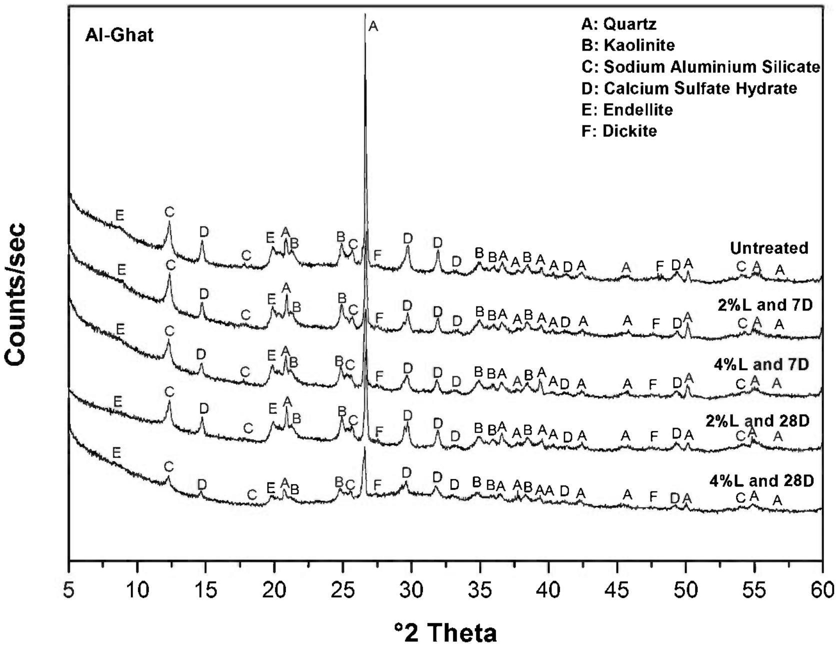

FIG. 11

X -ray diffractographs of Al-Qatif soil at different lime contents and at different curing periods (L and D refer to lime content and curing periods, respectively).

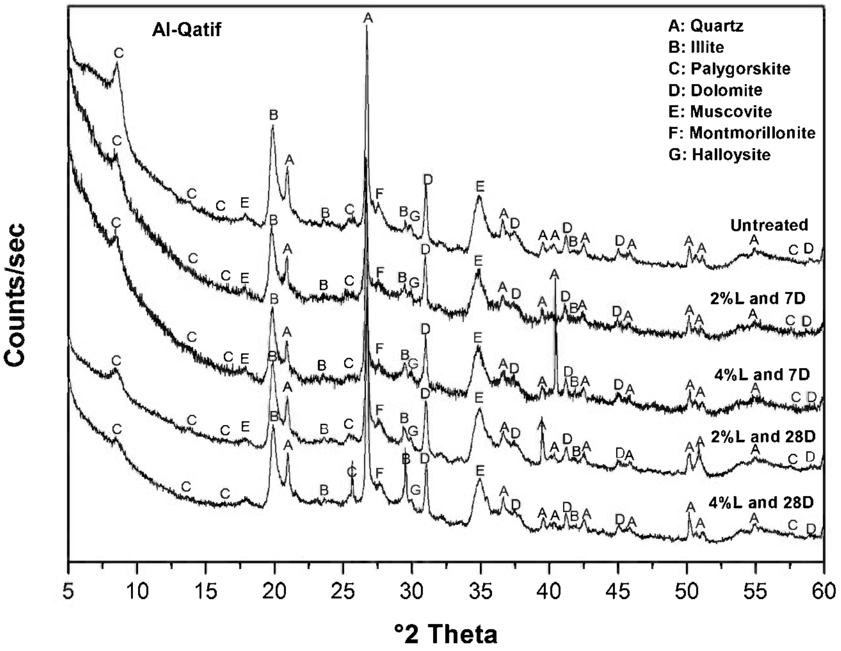

samples were taken prior to conducting the lime leachability tests from identical Perspex column molds. At the end of fixed curing periods, the samples were removed from the molds and powdered before conducting the XRD testing. It has been observed that when the sample soils were treated with different dosages of lime, and at different curing periods, the intensities of the characteristic mineral peaks are found to decrease (**Figs. 10** and **11**). The decreased intensities suggest an attack by lime on the soil particles, where the dominant minerals (montmorillonite, illite, and kaolinite) are present [23]. These minerals are the primary source of silica and alumina, which are necessary for the formation of cementitious agents. However, the results do not reveal new peaks corresponding to CSH, CAH, and calcium aluminate silicate hydrated (CASH). This is due to the fact that the new peaks formed have weak reflections due to their poor crystalline nature and also due to the overlap between the reflections of new minerals with those of existing primary minerals (Quartz and Illite) especially in 20°–40° 2θ field [24]. From **Figs. 10** and **11**, in the best case, even if 5 % new minerals are formed, it is highly unlikely that they would be detected by the XRD technique, taking account of their variability. These inherent weaknesses in the XRD technique make it difficult to identify the new peaks formed in the present study. Nevertheless, this does not mean that new cementitious compounds are not formed. The net resultant decrease in lime leachability values, particularly at higher curing periods, validates the formation of these pozzolanic compounds. Similar results were obtained for low lime non-plastic fly ashes, when they were treated with lime and gypsum as additives [25].

Conclusions

The present study evaluates the compressibility behavior of two soil samples having different mineralogy. The soil samples were subjected to accelerated loading conditions and at varying levels of lime content. In order to evaluate the durability characteristics of these soil samples, the role of lime and curing period on the lime leachability behavior has also been studied. The lime leachability behavior was evaluated by simulating a sustained leaching condition, equivalent to the prevailing hydrological field conditions the treated samples experience, due to continuous exposure of water flow. The following conclusions are drawn from the study:

1. With an increase in duration of loading increment, there is an increase in the final equilibrium void ratio.
2. Upon lime treatment, the difference in final equilibrium void ratio is reduced when compared with untreated soil samples. These values further reduce when the lime dosage is increased from 2 %–4 %. This is due to the fact that, flocculation reactions are more rapid at 4 % of lime content, resulting in the formation of dense crystallized pozzolanic compounds, which resist compression even at higher surcharge loads, and as a result, the resultant differences in void ratio further reduces. The difference in the final equilibrium void ratio values for both the soils is attributed to their difference in particle size characteristics and their primary mineral composition.
3. At a given level of lime content, the lime leachability values were found to reduce with increase in curing periods. The dosage of lime has a direct bearing on the lime

leachability values. With an increase in the initial level of lime content, higher amounts of calcium ions are leached. The duration of flow does not affect the lime leachability pattern.

4. The formation of new minerals could not be validated from the XRD technique due to nature of pozzolanic compounds formed. The amorphous nature of the cementitious compounds make it difficult to determine their respective characteristic mineral peaks.

ACKNOWLEDGMENTS

This project was supported by NSTIP strategic technologies programs, Project No. 11-BUI1489-02, in the Kingdom of Saudi Arabia. The writers would like to thank the Bugshan Research Chair in Expansive Soils, King Saud University, for providing the experimental facilities to carry out the research work. The writers are grateful to Mr. Bipin Rajivar, for his assistance in revising the manuscript. The writers would also like to thank the reviewers for their constructive comments which have been of immense help for the cause of the manuscript.

References

[1] Sridharan, A., Sivapullaiah, P. V., and Stalin, V. K., "Effect of Short Duration of Load Increment on the Compressibility of Soils," *Geotech. Test. J.*, Vol. 17, No. 4, 1994, pp. 488–496.

[2] Sridharan, A., Nagaraj, H. B., and Srinivas, N., "Rapid Method of Consolidation Testing," *Can. Geotech. J.*, Vol. 36, No. 2, 1999, pp. 392–400.

[3] Al-Mhaidib, A. I. and Al-Shamrani, M. A., "Swelling Characteristics of Lime-Treated Expansive Soils," *Geotech. Eng. J.*, Vol. 27, No. 2, 1996, pp. 37–53.

[4] Mallela, J., Quintus, H. V., and Smith, K., *Consideration of Lime–Stabilized Layers in Mechanistic-Empirical Pavement Design*, The National Lime Association, Arlington, Virginia, 2004.

[5] Bell, F. G., "Lime Stabilization of Clay Minerals and Soils," *Eng. Geol.*, Vol. 42, No. 4, 1996, pp. 223–237.

[6] ASTM D2435-04: Standard Test Methods for One-Dimensional Consolidation Properties of Soils Using Incremental Loading, *Annual Book of ASTM Standards*, ASTM International, West Conshohocken, PA, 2004, www.astm.org.

[7] BS 1377 Part 5: Determination of Consolidation Characteristics, British Standard Methods of Test for Civil Engineering Purposes, British Standard Designation, British Standard Institution, London, 1990.

[8] Moghal, A. A. B., Obaid, A., and Al-Refeai, T., "Effect of Accelerated Loading on the Compressibility Characteristics of Lime Treated Semiarid Soils," *J. Mater. Civ. Eng.*, Vol. 26, No. 5, 2014, pp. 1009–1016.

[9] Moghal, A. A. B. and Sivapullaiah, P. V., "Effect of Pozzolanic Reactivity on Compressibility Characteristics of Stabilised Low Lime Fly Ashes," *Geotech. Geol. Eng.*, Vol. 29, No. 5, 2011, pp. 665–673.

[10] Chittoori, B. S., Puppala, A. J., Wejrengsikul, T., and Hoyos, L. R., "Experimental Studies on Stabilized Clays at Various Leaching Cycles," *J. Geotech. Geoenviron. Eng.*, Vol. 139, No. 10, 2013, pp. 1665–1675.

[11] Chittoori, C. S., Pedarla, A., Puppala, A. J., Hoyos, L. R., Nazarian, S., and Saride, S., "Leachate Studies on Lime and Portland Cement Treated Expansive Clays," *Geotechnical Special Publication No. 211*, GeoFrontiers, Rowlett, TX, 2011, pp. 4479–4488.

[12] Moghal, A. A. B. and Sivapullaiah, P. V., "Role of Lime Leachability on the Geotechnical Behaviour of Fly Ashes," *Int. J. Geotech. Eng.*, Vol. 6, No. 1, 2012, pp. 43–51.

[13] Moghal, A. A. B. and Elkady, T. Y., "Durability Studies on Expansive Soils Treated With Lime," *Proceedings of the International Conference on Ground Improvement and Ground Control*, Wollongong, Australia, Oct 30–Nov. 2, 2012, pp. 1187–1192.

[14] Sridharan, A. and Sivapullaiah, P. V., "Mini Compaction Test Apparatus for Fine Grained Soils," *ASTM Geotech. Test. J.*, Vol. 28, No. 3, 2005, pp. 240–246.

[15] ASTM D5856-07: Standard Test Method for Measurement of Hydraulic Conductivity of Porous Material Using a Rigid-Wall, Compaction–Mold Permeameter, *Annual Book of ASTM Standards*, ASTM International, West Conshohocken, PA, 2007, www.astm.org .

[16] Sridharan, A. and Rao, G. V., "Mechanisms Controlling Volume Change Behaviour of Saturated Clays and the Role of Effective Stress Concept," *Geotechnique*, Vol. 23, No. 3, 1973, pp. 359–382.

[17] Brady, N. C., *The Nature and Properties of Soils*, 10th ed., Prentice Hall of India Private Limited, New Delhi, 1995.

[18] Solanki, P. and Zaman, M. M., "Laboratory Performance Evaluation of Subgrade Soils Stabilized With Sulfate-Bearing Cementitious Additives," *ASTM J. Test. Eval.*, Vol. 38, No. 1, 2010, pp. 1–12.

[19] Khalife, R., Solanki, P., and Zaman, M., "Evaluation of Durability of Stabilized Clay Specimens Using Different Laboratory Procedures," *ASTM J. Test. Eval.*, Vol. 40, No. 3, 2012, pp. 363–375.

[20] Nalbantoglu, Z. and Tuncer, E., "Compressibility and Hydraulic Conductivity of Chemically Treated Expansive Clay," *Can. Geotech. J.*, Vol. 38, No. 1, 2001, pp. 154–160.

[21] Al Mukhtar, M., Lasledj, A., and Alcover, J. F., "Behavior and Mineralogy Changes in Lime–Treated Expansive Soils at 50°C," *Appl. Clay Sci.*, Vol. 50, No. 2, 2010, pp. 199–203.

[22] Sivapullaiah, P. V., Sridharan, A., and Bhaskar Raju, K. V., "Role of Amount and Type of Clay in the Lime Stabilization of Soils," *Ground Improv.*, Vol. 4, No. 1, 2000, pp. 37–45.

[23] Pedarla, A., Chittoori, S., Puppala, A., Hoyos, L., and Saride, S., "Influence of Lime Dosage on Stabilization Effectiveness of Montmorillonite Dominant Clays," *Geotechnical Special Publication No. 199, GeoFlorida 2010*, West Palm Beach, FL, 2010, pp. 767–776.

[24] Choquette, M., Andribirubi, M., and Locat, J., "Mineralogical and Microtextural Changes Associated With Lime Stabilization of Marine Clays From Eastern Canada," *Appl. Clay Sci.*, Vol. 2, No. 3, 1987, pp. 215–232.

[25] Sivapullaiah, P. V. and Moghal, A. A. B., "Role of Gypsum in the Strength Development of Fly Ashes With Lime," *J. Mater. Civ. Eng.*, Vol. 23, No. 2, 2011, pp. 197–206.

Journal of Testing and Evaluation

doi:10.1520/JTE20140097 / Vol. 43 / No. 2 / March 2015 / available online at www.astm.org

Václav Mráz,[1] Jan Valentin,[2] Jan Suda,[3] and Lubomír Kopecký[4]

Experimental Assessment of Fly-Ash Stabilized and Recycled Mixes

Reference

Mráz, Václav, Valentin, Jan, Suda, Jan, and Kopecký, Lubomír, "Experimental Assessment of Fly-Ash Stabilized and Recycled Mixes," *Journal of Testing and Evaluation*, Vol. 43, No. 2, 2015, pp. 264–278, doi:10.1520/JTE20140097. ISSN 0090-3973

ABSTRACT

The use of fly-ash stabilizers, materials from fluidized combustion fly-ash, and other solid coal-burning residues, which are called coal combustion by-products (CCB), have good potential for application in subgrade structures and roadbed materials of roads as well as in the structural pavement layers. One of the many factors limiting the application of some CCB sorts is the relatively low resistance in repetitive contact with water, volumetric changes, and the risk of partly unsatisfactory hygienic and environmental parameters. With respect to the aforementioned negative characteristics of CCB, which occurred primarily under the repetitive impact of water and freezing, the experimental examination focused on improving CCB resistance to frost and water, verification of volumetric changes, and improvement of pozzolana characteristics of CCB by increasing the percentage of fine particles in the original material (e.g., by means of mechanical and/or chemical activation, including combination of both types). At the same time, the road construction industry strives to find a suitable substitute for the traditionally applied hydraulic binders as well as expand the existing base of the binders applied. The experience with using CCB as a binder or binder component has not been as extensive so far as to allow any generalisation of conclusions. Therefore, the possibilities of applying alternative additives as a replacement for the binders traditionally applied have been researched. Another application of the coal combustion by-products tested was in cold recycling mixes. In this case, the fly-ash from fluidized combustion is used as a substitute for the hydraulic binder. The fly-ash tested was subjected to mechanical activation, while the parameters of the mix under scrutiny reflected the impact on the strength and deformation parameters of the mix; last but not least, the water susceptibility indicator was also monitored. From the environmental perspective of practical applicability of the mixes a chemical analysis and leaching tests have been done.

Keywords

fly-ash, fluidized-bed fly-ash, mechanical and chemical activation, high energy milling, cold recycling mixes, roadbed structures, fly-ash stabilized material, chemical analysis, leaching tests, compressive strength

Manuscript received March 4, 2014; accepted for publication November 6, 2014; published online December 5, 2014.

[1] Ph.D. Candidate, Faculty of Civil Engineering, Deptartment of Geotechnics, CTU in Prague, Thakurova 7, Prague, 166 29, Czech Republic, e-mail: vaclav.mraz@fsv.cvut.cz

[2] Deputy Head, Faculty of Civil Engineering, Department of Road Structures, CTU in Prague, Thakurova 7, Prague, 166 29, Czech Republic, e-mail: jan.valentin@fsv.cvut.cz

[3] Ph.D. Candidate, Faculty of Civil Engineering, Department of Road Structures, CTU in Prague, Thakurova 7, Prague, 166 29, Czech Republic, e-mail: jan.suda@fsv.cvut.cz

[4] Researcher, Faculty of Civil Engineering, Department of Mechanics, CTU in Prague, Thakurova 7, Prague, 166 29, Czech Republic, e-mail: lubomir.kopecky@fsv.cvut.cz

Introduction

All technically advanced countries have intensified their research and development of various types of waste as secondary material sources in recent years. This trend also applies to the brown coal combustion residuals, great quantities of which are a waste in the power industry since they occur as solid residues from coal combustion and residue purification in power plants, heating plants, or heat stations. The materials are called coal combustion by-products (CCB) and include, e.g., fly-ash, slag, cinder, bottom ash, and flue gas desulfurization (FGD) gypsum.

Those countries that support their power policy primarily by generating power in thermal power stations research the options of processing and subsequently effectively utilising CCB. Practical applications have focused primarily on the construction industry so far. One of the paths seems to be applying CCB in roadbed structures of roads, railroads, or airfield structures as there is an assumption of processing larger quantities of CCB.

Another possible application of CCB gained after coal combustion, according to Refs. [1,2], is use of such material for soil modification or improvements in the roadbed structure. Such modifications of soil usually lead to higher strength properties, improved workability, and increased resistance to climatic effects. Other mechanical or physical characteristics of the original soil can be improved as well.

A limiting factor for the use of some CCB types is their relatively low resistance in repetitive contact with water and freezing [3,4], volumetric changes, and in some cases, the risk of partly unsatisfactory health and environmental parameters [5,6]. Particularly for fly-ashes from fluidized combustion, ettringite (high-calcium sulfo-aluminate mineral) might be formed in case of long-term contact with water [7,8]. Extensive analyses of CCB chemical characterization have been collected and done, e.g., during the planning and preparation of embankment structure for a motorway project in the UK. CCB samples were taken from three different power plants. Leaching analyses have shown increased contents of arsenic, cadmium, chromium, mercury, selenium, and sulphates. At the same time, the *p*H value was increased as well as the concentration of polycyclic aromatic hydrocarbons [9].

With respect to the aforementioned negative CCB characteristics, which occurred primarily under repetitive influence of water and freezing, the experimental research focused on improvement of CCB resistance to frost and water, verification of volumetric changes, and improvement of pozzolana properties of CCB by increasing the percentage of fine particles in the original material (e.g., by means of mechanically and chemically activated fly-ash).

At the same time, the road construction industry strives to find a suitable replacement for the hydraulic binders traditionally used as well as extend the existing base of the binders applied. The experience with application of CCB as a binder or binder component is not as extensive so far as to allow generalisation of its conclusions. Therefore, the possibilities of alternative additive application as a substitute of the binders traditionally used were examined.

Materials

COAL COMBUSTION BY-PRODUCTS

The samples chosen for the purposes of experimental research of stabilised fly-ash mixes were the so-called fly-ash from electrostatic separators (filters) of the Melnik power plant (hereinafter "EME"), often called high-temperature fly-ash, and bed ash from fluidized combustion from the Ledvice power plant (hereinafter "ELE") (see **Fig. 1**). The aforementioned power plants represent the two basic types of desulphurisation; each of them produces CCB of differing technical parameters. EME

FIG. 1 (*a*) filter fly-ash EME, (*b*) bed ash from fluidized combustion ELE.

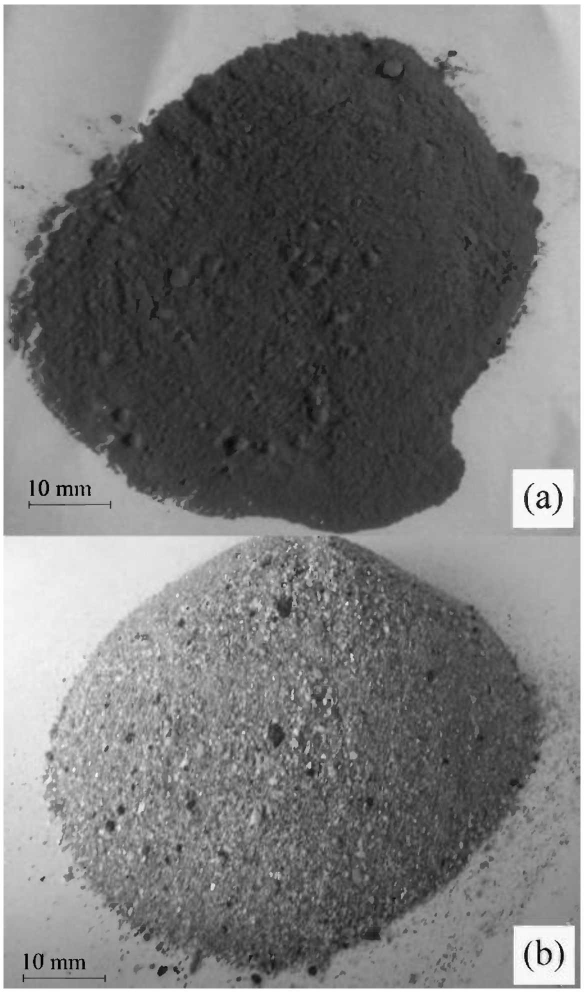

desulphurisation follows the route of the wet scrubbers. In ELE, CCB from furnace FK4 were used; this is desulphurised by the fluidized combustion method.

With respect to the combustion technology applied, the chemical and mineralogical composition of fly-ashes from fluidized combustion fundamentally differs from the composition of classic high-temperature fly-ashes. The main phases of high-temperature fly-ashes consist of amorphorous silicon dioxide, silica, and both high temperature modifications of silicon dioxide—cristobalite, as well as tridymite and mullite. Fly-ashes from fluidized combustion contain aluminosilicate phase, silica, insoluble anhydride II, free calcium oxide, and possibly calcium hydrate and calcium carbonate. As ensues from the above, high-temperature fly-ashes demonstrate the pozzolana properties exclusively, while fly-ashes from fluidized combustion, thanks to the presence of calcium ions, have hydraulic properties even on their own [10].

Within the structural analysis of two selected types of energetic by-products, assessment of internal material structure has been carried out by application of electron microscopy. Microscopy and microanalyses have been processed by the environmental scanning electron microscope (ESEM FEI PHILIPS), equipped by the set of electron detectors—the scattered electron diffraction (SED) for morphology on the micro level and BSED for phase contrast, both in high vacuum mode and the environmental mode. The electron diffractions (ED) analysis of secondary X-ray spectra provides the quantitative chemical composition of the selected objects. The quantitative phase mineral composition both on the micro and nano level is facilitated by orientational imaging microscopy based on back scattered electron diffraction (OIM-BSED). This equipment gives the information about the quantitative phase mineral composition and structural orientation maps.

In the **Fig. 2**, it is possible to observe the received internal structures. In particular, the general structure was analyzed for different zoom in, with stress on anomalies in the fractural structure (failures, bubbles) and fundamental structural elements of the material structure (crystals).

Sample Preparation Used for Electron Microscopy Analysis

Before the electron microscopy analysis, a representative quantity of fly-ash sample (10 ccm) was mixed with low viscose epoxy resin. After hardening (at 25°C), the sample was brushed (emery papers) and polished (diamond paste) in dry mode. The obtained surface was cleaned by pure methanol. This method of sample preparation prevents eventual reaction of water-sensitive fly-ash particles.

Methods of electron microscope assessment were based on phase contrast taken by back-scattered electrons detection (BSE) and energy dispersed X-ray analysis (EDS).

FIG. 2 (*a*) bed ash from fluidized combustion ELE in electron microscope, (*b*) filter fly-ash EME in electron microscope.

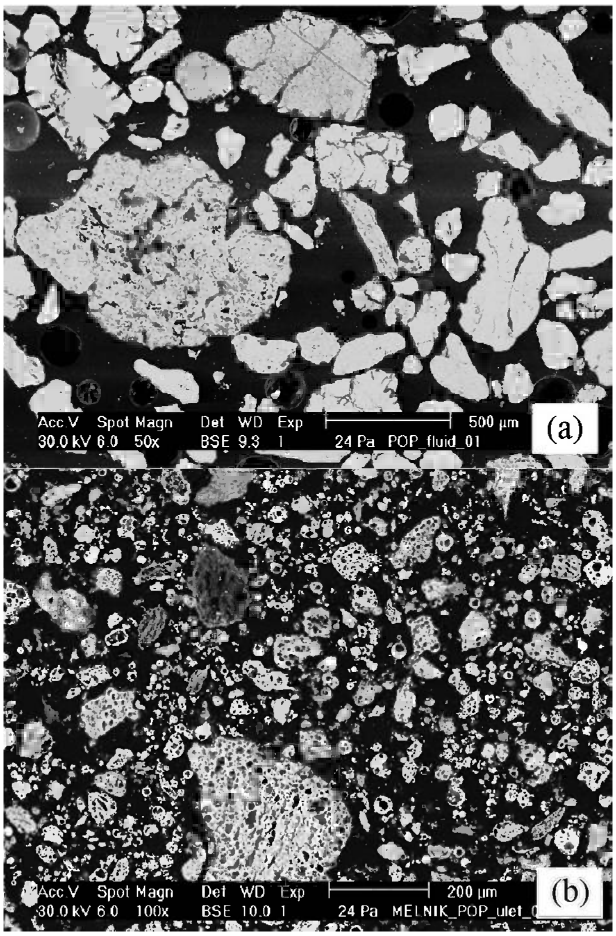

Analyses of Fly-Ash from Melnik Coal Power Plant

Fly-ash particles (FAP) are represented by the very porous slaggy debris, whereas some of the larger particles are almost foamy. The character of FAP is very monotonous; nearly all particles have the same character: porous and foamy. The size of FAP varies from first micrometers up to several tenths of a milimeter. The compact-like glassy balls of FAP or iron oxides particles do not occur in this type of fly-ash from EME power station.

Analyses of Fly-Ash from Ledvice Coal Power Station

FAP are mostly represented by calcium sulphates (gypsum, hemihydrate, anhydrite etc). Some grains are alumosilicates (mullite, quartz). Only a small portion of FAP is porous (in comparison with FAP from Melnik).

The examination of the second type of mixes used fly-ashes from fluidized combustion from the thermal power plants CEZ Tisova, CEZ Hodonin, and the Plzen generation (heating) plant, which are equipped with the fluid furnace technology that is

TABLE 1 Chemical composition of activated fly-ash from fluidized combustion.

Fly-Ash From Fluid Combustion	SiO_2	Al_2O_3	CaO_{Total}	MgO	TiO_2	Fe_2O_3	SO_3	Na_2O	K_2O	P_2O_5	MnO	Cl^-	F^-	Annealing Loss
							(%)							
Tisova	39.50	24.70	15.45	0.70	5.47	7.63	3.06	<1.0	0.49	0.35	0.058	—	—	2.05
Hodonin	43.16	16.27	16.83	1.86	1.28	3.62	5.08	0.7	3.58	1.53	—	0.71	0.34	4.85
Plzen	Not defined													

installed in a number of power-generating operations in the Czech Republic. The types of fly-ash obtained are formed primarily during fluidized combustion of brown coal and powder limestone which, from the perspective of potential for further application in the construction industry, are rather significant. The ash material was driven between the rotors of a twin-rotor contra-rotating high speed mill– disintegrator under mutual peripheral speed of the rotors of approximately 204 $m \cdot s^{-1}$ and power consumption at the level of approximately 20 W per kg of pulverized ash.

X-ray diffraction and chemical analysis was performed for the material obtained. The chemical analysis is indicated in **Table 1**.

Fly-ashes from fluidized combustion from the Tisova power plant have a standard composition in comparison to other ashes. The only unusual feature is the higher content of non-decomposed limestone and anhydrite. The fly-ashes from the Hodonin power plant and the Plzen heating plant contain unusually small quantities of free lime; such ash loses its self-binding ability and an addition of a certain quantity of lime or cement would be recommended in a certain stage of compacted mix production. The contents of the amorphous phase are rather high in such type of fly-ashes. The results of XRD analysis for mechanically activated fly-ashes are indicated in **Table 2** and **Fig. 3**.

MECHANICAL ACTIVATION

The mechanical process or interference with the structure of a substance that increases its chemical reactivity can be called mechanical activation. Such an intervention in the substance structure can consist of grinding/pulverization. According to the classic interpretation, grinding is defined as mechanical dispersion of solid substances, which results in reduced particle size and a simultaneous increase of specific surface and surface

TABLE 2 Evaluation of phase composition of mechanical chemically activated fly-ashes from fluidized combustion based on XRD data record.

Reference Code	Compound Name	Score	Total Lines	Scale Factor	SemiQuant (%)
Fly-Ash From Fluidized Combustion—Power Plant Tisova					
01-086-2334	Calcite	66	9	0.801	26
01-085-0796	Quartz	48	7	0.492	3
01-074-2421	Anhydrite	53	16	0.974	57
01-079-0007	Hematite	37	7	0.130	4
01-078-0315	Portlandite, syn	53	5	0.239	7
01-078-0649	Lime	42	2	0.152	3
Fly-Ash From Fluidized Combustion—Power Plant Hodonin					
01-089-8935	Quartz $-alpha	72	7	1.002	46
01-072-0503	Anhydrite	69	16	0.294	23
01-079-1741	Hematite, syn	47	7	0.104	4
01-082-1691	Lime	47	2	0.084	3
00-005-0586	Calcite, syn	34	9	0.052	4
00-009-0478	Anorthoclase, disordered	30	28	0.042	9
00-046-1311	Muscovite-2\ITM\RG#1, ammonian	36	20	0.204	11
Fly-Ash From Fluidized Combustion—Generation Plant Plzen					
01-085-0794	Quartz	69	7	0.994	24
01-074-2421	Anhydrite	63	16	0.722	31
01-079-0007	Hematite	46	7	0.136	3
01-078-0649	Lime	49	2	0.800	13
01-083-0578	Calcite	43	9	0.071	2
01-089-6423	Albite	26	83	0.076	9
00-026-0911	Illite-2\ITM\RG#1 (NR)	36	17	0.427	18

FIG. 3 XRD data record of mechanically activated fly-ash from fluidized combustion: (*a*) Tisova, (*b*) Hodonin, and (*c*) Plzen.

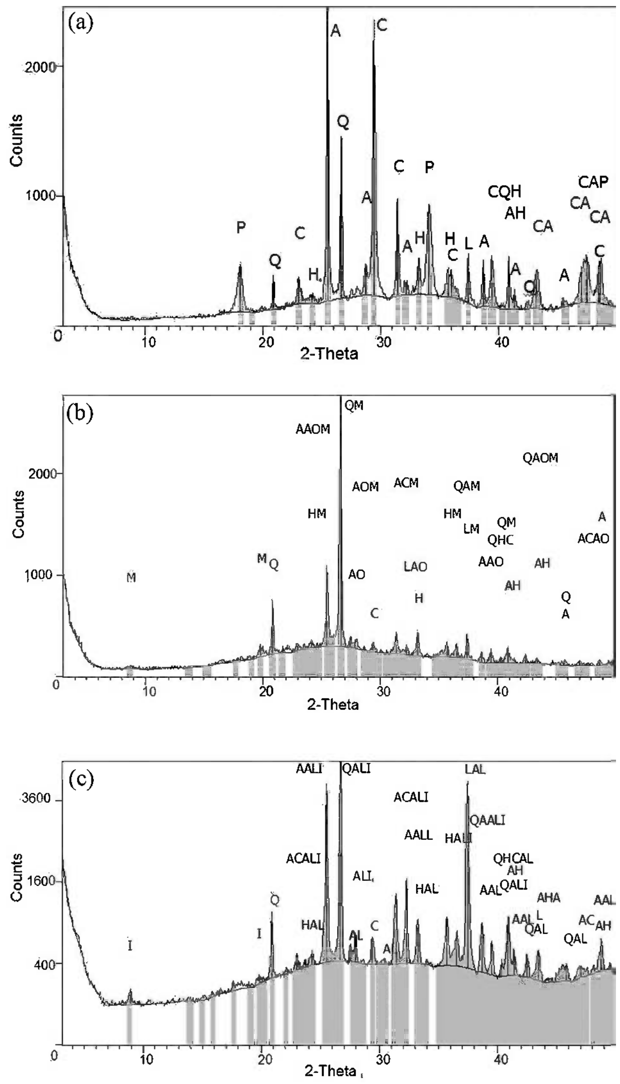

energy within the system; nevertheless, mechanical effects occurring in the course of dry grinding of solid particles might cause significant structural changes and chemical reactions in the material ground. The character of the surface, or morphology thereof, distribution of charges, and chemical nature of the thin grain surface film have a very distinctive impact on reactivity as well [11–14].

Grinding might be a possible solution for rough fluid combustion separation process residuals. The grinding process causes large plerospheres (porous particles) to disintegrate and reduces particle roughness. Such reduction, together with the increased reactivity of the fly-ash, improves strength. The grinding of cenospheres increases density and fineness, which results in higher pozzolana reactivity of the fly-ash. The grinding time affects the particle size, shape, and, consequently, the need for water [15].

STABILIZED FLY-ASH MIX

The so-called fly-ash stabilizate was chosen as the first type of compacted mix for experimental verification. Fly-ash stabilizate is a solid mass which usually arises by wetting a mix of fly-ashes or ashes with a binder (e.g., lime or cement) or by wetting a mix of fly-ashes from fluidized combustion that demonstrate self-setting properties. Ettringite might form during this process, which causes volumetric changes. Ettringite forms in fly-ash stabilizate from soluble compounds of calcium, aluminium, and sulphur in wet, alkali environments. In some cases, its expansion ability might damage the solidified stabilizate. According to the composition of the mix and mutual component proportions, the quantity of added water and the processing method, a mass whose strength and other physical properties (permeability, weight, and thermal conductivity), are similar to those of lightweight concrete.

A deponate is understood as non-solidifying mass (with no additional additives), which is only strengthened by dehydration, drying or thixotropy.

The following additives were applied to prepare the fly-ash stabilizates:

- Cement CEM II/B-M 32,5R
- Lime CL90S
- Mechanically activated or combined mechanically and chemically activated fluid ashes (from the Plzen heating plant)
- Mechanically activated dolomitic limestone (from the Krty u Strakonic quarry)
- Mechanically activated or combined mechanically and chemically activated recycled mix from concrete (recycled aggregate generated by crushing and sorting of reclaimed concrete from the airport Ruzyne)
- Chemical additives Iterstab, Zycosoil

COLD RECYCLING MIXES

The second type of selected fly-ash application was a compacted mix formed by cold recycling of asphalt pavements. This technology involves the milling of the original structural pavement layers (mainly asphalt layers or combination with granular base layers, but applicable also to, e.g., cement stabilized material), mixing thereof with bituminous or hydraulic binders followed by levelling and compacting. Sorted reclaimed asphalt material (asphalt mix obtained by milling the asphalt layers or crushing plates knocked from asphalt pavements or large pieces of asphalt mix and asphalt mix from non-identical or excess production, RAP) of grading 0/11 from the Porr Bechovice mixing plant, for which bitumen content of 7.3 wt. % was detected, was used to prepare the cold recycled bitumen based mix. Cationic bituminous emulsion C60B7 was applied as the bituminous binder for cold recycled mixes. This is a standard emulsion used for this type of cold recycling applications. Similarly, the commonly used Portland slag cement CEM II/B–S 32.5 was used in the reference mix.

TABLE 3 Cold recycled mix designs.

Component/Mix	REF	MCAT 1a	MCAT 1b	MCAH 2a (%)	MCAH 2b	MCAP 1	MCAP 2
Bituminous emulsion - Katebit C60B6	3.5	3.5	3.5	3.5	3.5	3.5	3.5
Cement CEM II/ B-S 32,5	3.0						
Mechanically activated fly-ash; fluidized combustion—power plant Tisova		3.0	10.0				
Mechanically activated fly-ash; fluidized combustion—power plant Hodonin				3.0	10.0		
Mechanically activated fly-ash; fluidized combustion—generation plant Plzen						3.0	10.0

A set of various cold recycled mixes with a variable representation of fly-ashes from fluidized combustion modified by mechanical activation were designed for the laboratory testing; the fly-ashes from fluidized combustion play the role of hydraulic binder substitute or reactive filling admixture in this case. At the same time, a set of laboratory tests was defined to verify the impact of the material on mix properties. The compositions of the mixes researched are indicated in **Table 3**. The optimum water content of the cold recycling mix for the composition as indicated was determined according to the standard CSN EN 13286-2 [16].

Evaluation Methodology for Compacted Fly-Ash Mixes

The Department of Road Structures, CTU, Faculty of Civil Engineering, determined the workability, strength characteristics, and, with respect to the negative results in case of repetitive exposure to water, a test of resistance to frost and water immersion including the verification of volumetric changes of the mixes examined.

Mixes from both desulphurisation technologies and mixes with various binder proportions were tested. For CCB, the binders used as a standard were replaced by inorganic loose binders obtained by means of mechanical activation of fly-ashes from fluidized combustion, dolomitic limestone and reclaimed concrete materials. Besides such binders, the Iterstab (an additive used primarily in soil improvement and stabilization) and Zycosoil (an additive on a nanotechnology basis using silane groups) chemical additives were verified; the main benefit is preventing water from entering the mix. The objective was observing the same principles in CCB property modification as well.

One of the objectives of applying mechanically activated materials in CCB was eliminating ettringite formation, which is generally one of the limiting factors of CCB application in embedding in roadbed structures of roads.

COMPACTION ASSESSMENT

The workability of fly-ash mixes was tested by the Proctor standard tests which simulate the compaction achieved by construction rollers very well. The laboratory test of CCB compaction quality is an important test for the assessment of applicability in road construction. CCB compaction effort is related to particle shapes and sizes. The mix compaction quality was examined by the standard Proctor test under CSN EN 13286-2 [16]. Compaction was started after a certain time elapsed from the wetting of the mix. This models the delays caused by transportation, spreading, and other handling during real-life paving of the mix. Cement, lime, or other additives were added to the dry CCB in samples with additives. The mix was dry-homogenised and wetted only afterwards.

COMPRESSIVE STRENGTH TESTING

The laboratory test of compressive strength was performed according to the CSN EN 13286-41 [17] standard, where a test specimen shaped like a right circular cylinder was loaded by the growing axial stress σ until its failure. The test principle consists in loading the test specimen of hardened energetic by-products with uniaxial compression with a simultaneous measurement of deformation. Strength characteristics after different curing times were studied in detail.

EME fly-ash and ELE bed ash were used to make test specimens by compaction in the laboratory with dimensions of $R = 100$ mm and the height of 120 mm. The test specimens were cured for 7, 14, 21, 28, 60, and 90 days (for some mixes even for 1 year) in a laboratory environment in an airtight cover. The test specimen was also tested for immediate strength after compaction where the prepared specimen was cured at a laboratory temperature of 20°C –23°C for approximately 2–3 h.

RESISTANCE TO FROST AND WATER IMMERSION

The preparation and curing of test specimens followed the same process as in the case of compressive strength test. Once the 28-day curing was completed, the test samples were placed on a felt pad partly sunk in water and left to saturate through capillaries until the set weight so that the weight increment for at least 1 h would not exceed 1 %. All test specimens were saturated in the course of 20 min from putting on the felt pad.

Subsequently, the test specimens were placed in a freezer box for 6 h from under −20°C to −22°C. After freezing, the test specimens were taken out of the freezer box and stored on a felt pad partly sunk in water for 18 h to allow further capillary saturation. Simultaneously, de-frosting under +20°C to +25°C occurred. The test continued by another round of freezing and repeated 10 cycles according to the method stipulated in the National Annex NB CSN EN 14227-5 [18]. Once the last cycle was completed, a strength test was carried out according to the standard CSN EN 13286-41 [17].

SWELLING SUSCEPTIBILITY OF FLY-ASH STABILIZATES

Monitoring of CCB volumetric changes is of crucial importance from the perspective of pavement structure durability. Volumetric changes might be demonstrated by shrinking or expansion and, subsequently, result in deterioration of the technical and environmental parameters or, often, complete destruction of the pavement structure.

Further factors affecting volumetric changes of CCB include:

- Chemical and physical properties of the input materials
- Risk component content and variability
- Mix design
- Production technology
- Environment in which the CCB is placed (e.g., humidity and thermal parameters, pressure, and combination of these factors);
- Other specific factors [19]

In relation to the risk of undesired volumetric changes, this test must be viewed with more emphasis. The experimental research examined the impact of the mix on volumetric changes.

The subject matter of swelling measurements for fly-ash stabilizate was determining the linear and volumetric coefficient of swelling. Volumetric changes are understood as increasing of the fly-ash stabilizate volume caused by physical and mechanical processes ongoing in the material, or by additional water absorption.

A CBR bin and other equipment used for the preparation and facilitation of CBR testing under CSN EN 13286-47 [20] were used for the purposes of this test.

The mix saturated to w_{opt} according to the Proctor Standard test was compacted in the CBR cylinder by means of Proctor Standard (PS) energy.

Fly-ash stabilisers were cured from 7 and 28 days in moulds under (20 ± 2)°C in impermeable wraps and, subsequently, saturated by water until all deformations ceased to occur. Within the time intervals as mentioned, the changes of surface level of the compacted, saturated samples loaded by a weight were measured.

Cold Recycled Mix Assessment Methodology

TEST SPECIMEN PREPARATION METHODOLOGY

Optimum water content of the mixes was determined according to CSN EN 13286-2 [16]. The valid Czech technical conditions for cold recycled mixes TP 208 [21] stipulate test specimen preparation by means of cylindrical moulds of 150.0 ± 1.0 mm diameter and 200–300 mm height. For the purposes of experimental assessment, cylindrical test specimens of 101.60 ± 0.1 mm diameter and 63.5 ± 2.5 mm heights were chosen as more appropriate. During the processing, the mix was compressed in the moulds by means of static pressure of 5.0 MPa. The test specimens were left in the mould under the temperature of (20 ± 2)°C for (24 ± 6) h; subsequently, the specimens are stored under 90 %–100 % humidity and at a temperature of (20 ± 2)°C for another two days. Then, the test specimens are stored under 40 %–70 % humidity and at a temperature of (20 ± 2)°C. The mixes examined were left to cure under the aforementioned conditions for 7 and 14 days. From the point of view of water susceptibility detection, the set of samples was soaked in water for another 7 days after seven days' curing under 40 %–70 % humidity and a temperature of (20 ± 2)°C.

INDIRECT TENSILE STRENGTH, STIFFNESS MODULUS, AND WATER SUSCEPTIBILITY

Determination of indirect tensile strength is done on test specimens that have been prepared according to the procedure described in the section Test Specimen Preparation Methodology. Testing is proceeded according to TP 208 [21], whereas the test specimens are air conditioned for at least 4 h to prescribed temperature (15 ± 1)°C. Specimens are then tested at constant speed of the laboratory press jaws (50 ± 1) mm/min until the total specimen failure.

Stiffness modulus of cold recycled mixes has been done according to CSN EN 12697-26 [22], applying the method of non-destructive cyclic indirect tensile stress on the Nottingham Asphalt Tester apparatus. Stiffness is an important strain characteristic and is used together with Poisson's ratio in multilayer pavement structure design. The principle of the stiffness modulus determination is to apply direct compressive stress, which is transferred in the plane of the vertical cut of test specimen to deduce indirect tensile stress perpendicular to the loading direction. The stress applied is causing horizontal deformation of the specimen. The stiffness modulus is therefore defined as a ratio between stress and strain at a given temperature, for which a particular value of Poisson's ratio can be defined.

Water susceptibility according to TP 208 [21] normally reflects coefficient of indirect tensile strength decrease. Generally this is defined as a ratio of indirect tensile strength of specimens cured 7 days versus indirect tensile strength of test specimens after seven days curing at 40 %–70 % moisture at temperature of (20 ± 2)°C and seven days water immersion. In this article, the water susceptibility evaluated only as a strength characteristic of combined curing.

CHEMICAL ANALYSIS

Chemical analysis have been carried out in cooperation with the Geological Institute of the Academy of Sciences of the Czech Republic (AV CR) for fundamental analysis of elements represented in the used materials and partly as a basis for description of leaching effects. Particularly selected samples of waste granular material, by-products, and reclaimed materials the use of which is being considered or expected in pavement structures, or where such construction applications already exist, has been selected for the analyses done. The set of tested materials involves waste filler from aggregate production, fly-ashes, and reclaimed asphalt material.

In connection to the list of technical standards governing the leaching methods for various types of mineral materials, different analytical procedures are used [23]. None of the methods governed by any standard concerned have been used; a modified procedure was preferred and applied based on analytical spectroscopy method. For this test procedure, samples were analysed with IRIS Intrepid II XPS spectrometer (ICP-EOS) manufactured by Thermo Electron Corporation, using axial plasma view and cyclone type nebulizer. The standard operational conditions were used (plasma power 1150 W, nebulizer pressure 25.0 psi, auxiliary gas flux 1.0 ml/min, sample uptake 2.40 ml/min). For the analytical purposes, wavelengths recommended by the manufacturer for each element were used, as is published in the instrument manual as well. The calibration curves were constructed using four points (blank and multi-element standards in 1 % supra-pure nitric acid) covering full range of the concentrations measured. Concentration of macroelements and microelements were calibrated and measured in separate experiments. Each sample was analysed three times. Quality control was ensured inserting QC sample into analytical run after each ten unknown sample.

For analytical purposes and as a basis for future leaching tests, the total element contents in the solid samples were measured, after total decomposition of the solid samples in nitric acid/hydrofluoric acid/perchloric acid mixture. In this way, the solid samples went into acidic solutions, in which elements concentrations were measured by ICP EOS. The concentrations of basic elements (macroelements) were estimated as well as the trace elements (microelements) by ICP EOS technique. ICP EOS stands for the spectroscopic analytical technique optical emission spectroscopy with inductively coupled plasma. Among others, the macroelements aluminium, calcium, ferrum, kalium, magnesium, manganese, natrium, phosphor, sulphur, silicium, and the microelements arsen, borum, barium, beryllium, cadmium, cobalt, chromium, cuprum, lithium, molybdenum, nickel, strontium, titanium, and zinc were analysed.

For the future alternative leaching tests, distilled water (pH value ~6.5) and aqueous solution of acetic acid (pH value ~4.5) will be used as leaching agents. Acetic acid was chosen to approximate the effect of leaching by acidic rain water. A similar testing procedure and environment can be found, e.g., in Ref. [24]. Analytical experiments were performed on samples of the materials pulverised and homogenised, and afraction of grain size <0.1 mm was used. Even if such testing sample preparation is not usual in the standardised leaching test methods for granular materials, the pulverisation has been decided for the total inorganic analysis. Sample weight 1–5 g and 100 ml of the leaching solution was used. Weighted samples were covered with the leaching solution and agitated on an overhead shaker for 2 h at room temperature. Leachates were then filtered over 0.45 μm filter and analysed. No leaching solution exchange was performed in the course of the test. Thus, the test can be characterised as a short-time procedure without dynamic character, i.e., without leaching solution exchange.

DIFFUSIVE TEST

Within the framework of possible utilisation of cold recycling mix using coal combustion by-products in pavement base courses, it is necessary to take into consideration the environmental aspects of such applications too; the necessity of determining the leaching of potentially hazardous substances in the surrounding environment arises. In a laboratory environment, the leaching can be simulated by a diffusion test. The essence of a diffusion test according to EA NEN 7375:2004 [25] is monitoring the long-term effect of water on the product from the chemical (contents of analytes in the leach) and mechanical perspective (content of the solid part separated). The diffusion test is carried out statically to avoid influencing the natural diffusion and, at the same time, to avoid disturbing the sample surface. The nature and properties of the basic material with the entire sample (monolithic cylindrical specimen) placed in the leaching liquid (demineralised water of neutral pH), additions of the leaching liquid at certain time intervals for the period of 64 days, and the quantity of the leach per surface unit is determined. The qualitative evaluation of the leach observed the limits stipulated in the regulation concerning construction materials of the Dutch Ministry of Housing, Spatial Planning and the Environment issued in 1999, as amended. The leaches were compared to the limits for pavement base courses (Building Materials Decree BMD, 64 days). Then, the results were compared to the Landfill Regulation Amendment for

TABLE 4 Compactability parameters of fly-ash stabilizates.

Mix	Fluidized-Bed Fly-Ash From ELE Without Additive	Fluidized-Bed Fly-Ash From ELE With 3 wt. % of Cement CEM II/B-M 23,5R	Fluidized-Bed Fly-Ash From ELE With 6 wt. % of Pulverized Dolomitic Limestone	Fluidized-Bed Fly-Ash From ELE With 10 wt. % of Pulverized Fluidized-Bed Ash	Fly-Ash From EME Without Additive	Fly-Ash From EME With 6 wt. % Cao
Maximum density (kg/m^3)	1122	961	996	1084	1080	1060
Optimal moisture (%)	36.7	34.7	36.2	35.3	21.0	20.0

England and Wales No. 1640 of 2005 for waste deposited at landfills–leach after 64 days).

Results and Discussion

FLY-ASH STABILIZED MIXES

Compaction

From the results of optimum compaction assessment done on fly-ash form EME implies, that optimal moisture content of fly-ash mixes with 6 % of CaO addition are only slightly dependent on the content of hydraulic binder in the mix and reach for guidance around 20 %.

Filter fly-ash without any additives showed optimum moisture content for compaction at 21 %, whereas filter fly-ash from EME with 6 % CaO reached optimum moisture content at 20 %.

Compaction quality of fluidized-bed ash from ELE was reached with optimum moisture content about 35 %; if 6 % of pulverized dolomitic lime was added, the optimum moisture content increased slightly to 36 %. In case of 10 % activated fly-ash from fluidized combustion, the value went up to 38 %. Overall results of mix compactability are given in the **Table 4**.

Indirect Tensile Strength Results

From **Figs. 4** and **5**, it is apparent that the best values of compressive strength are reached for mixes where mechanically activated fly-ash, dolomitic lime, and cement are represented. These mixes fulfilled required threshold limits for compressive strength according to the technical specifications TP 93 [26]. By applying mechanically activated fly-ash form fluidized combustion, as well as dolomitic lime or pulverized recycled concrete, the possibility of substituting traditional hydraulic binders by these alternative materials was proven.

Resistance to Frost and Water Immersion

Resistance to freezing and water depends to a great degree on the composition of the original mix. Stabilizates (deponates) prepared with material from the wet scrubber process mixes disintegrated after the first freezing cycle already, or even during the saturation stage. Stabilizates prepared with material from fluidized combustion technology disintegrated after 2 to 3

FIG. 4 Compressive strength results of compacted energetic by-products with different additives.

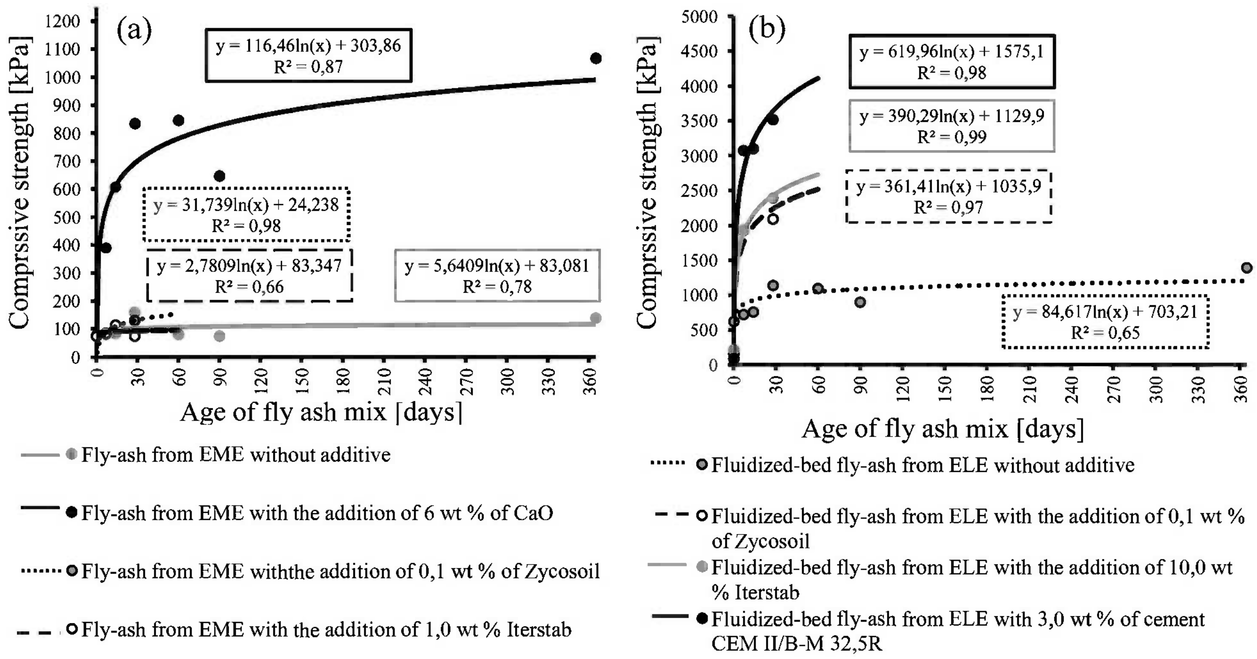

FIG. 5 Compressive strength results of compacted energetic by-products with added mechanically and chemically activated materials.

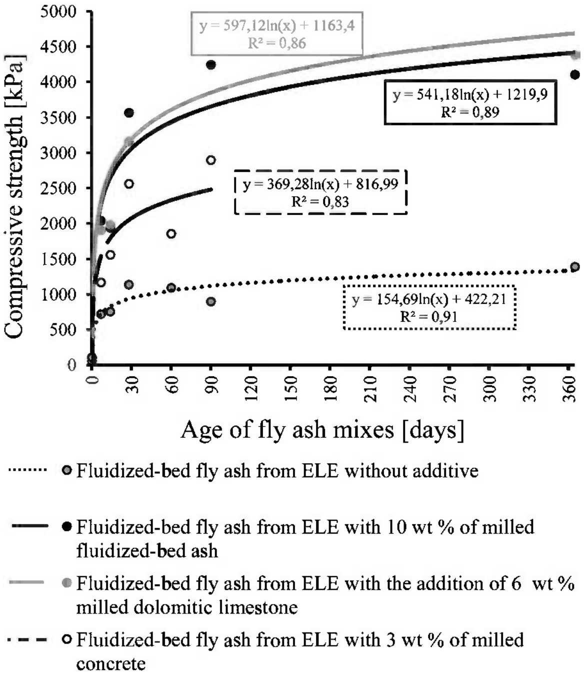

freezing cycles. Stabilizates made of compacted hydrated mix with an addition of mechanically activated fly-ashes from fluidized combustion, dolomitic lime, reclaimed concrete, or chemical additives improve the resistance feature of fly-ash mixes against the effects of water and freezing better than stabilizates with no additives. The drop in strength after freezing ranged from 20 to 30 %. For the stabilizate from fluidized-bed ash with the addition of 6 wt. % mechanically activated dolomitic lime, the original compression strength even increased by 11 % after defrosting. The values must be confirmed again with more test specimen sets.

For the deponate prepared with fly-ashes from EME with no additives, the specimen collapsed in 50 min from placement on the felt pad partly soaked in water (see **Fig. 6(*a*)**). Specimens collapsed after the first cycle also in the case of application of chemical additives with 0.1 wt. % Zycosoil and with 1 wt. % Iterstab in fly-ashes from EME.

The stabilizate prepared from the EME fly-ashes with 6 wt. % calcium oxide resisted 10 cycles; however, it demonstrated minor longitudinal and alligator cracks (see **Fig. 6(*b*)**). Compression strength after the last cycle fell to 0.41 MPa, i.e., approxiamtely half of the strength detected in the design stage.

FIG. 6

(*a*) Filter fly-ash mix, EME, (*b*) stabilizate EME +6 wt. %. CaO, (*c*) stabilizate from bed ash ELE without additives, (*d*) stabilizate from bed ash ELE +10 wt. % of pulverized fly-ash from fluidized combustion–generation plant Plzen, and (*e*) stabilizate from bed ash ELE +6 wt. % pulverized dolomitic limestone.

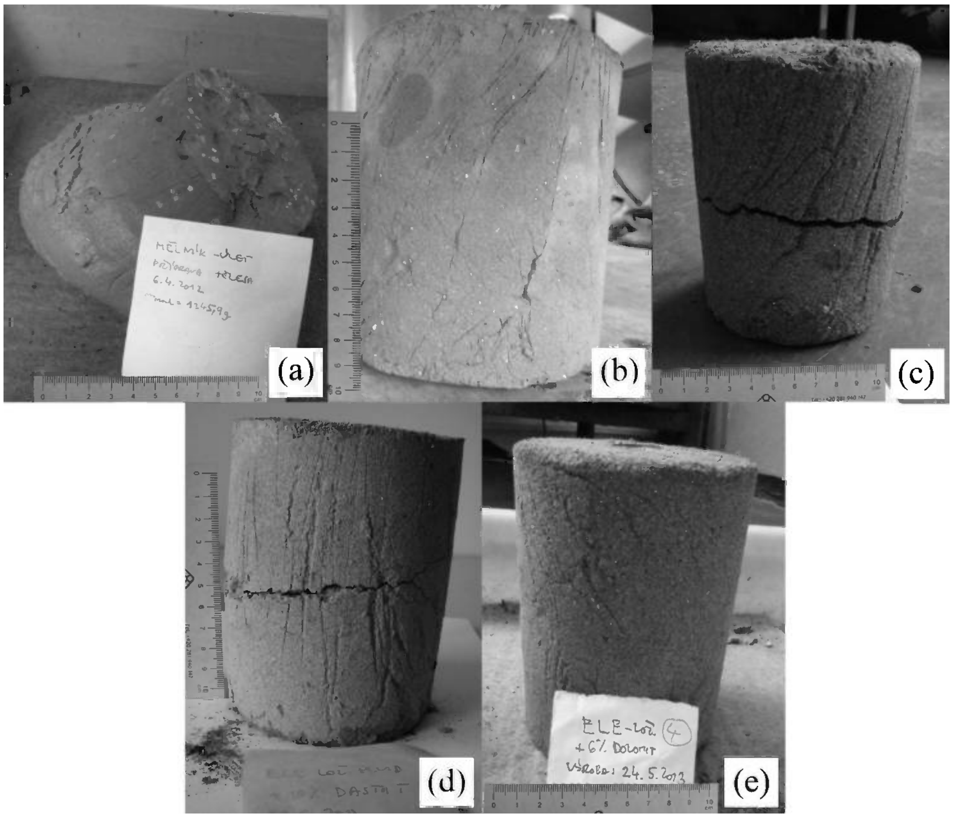

The stabilizate from fluidized-bed ash from ELE showed a transverse crack; the specimen broke after approximately 4 h freezing in the second cycle (see **Fig. 6(*c*)**).

In the case of the test specimen from fluidized-bed ash with the addition of 3.0 wt. % cement CEM II/B-M 32.5R, compression strength fell by 26.5 % after freezing.

Stabilizates from fluidized-bed ash from ELE with the addition of 1 wt. % Iterstab and 0.1 wt. % Zycosoil survived 10 cycles and demonstrated the greatest resistance; nevertheless, the strength indicators fell by 19 % for Zycosoil and by 38 % for Iterstab. The stabilisers failed to meet the requirements of CSN EN 14227-14 [27] and, therefore, frost susceptibility according to CSN 72 1191 [28] must always be determined.

For the stabilizates from fluidized-bed ash with the addition of 10 wt. % mechanically activated fly-ashes from fluidized combustion, a transverse crack formed after the tenth cycle (see **Fig. 6(*d*)**).

The stabilizate from fluidized-bed ash with the addition of 6 wt. % mechanically activated dolomitic lime (see **Fig. 6(*e*)**), which was stressed by a graded number of freezing, and defrosting cycles demonstrated a value of strength even higher than the initial compression strength. These values must be reconfirmed with more specimen sets.

FIG. 7 Time dependent progression of fly-ash stabilizate swelling.

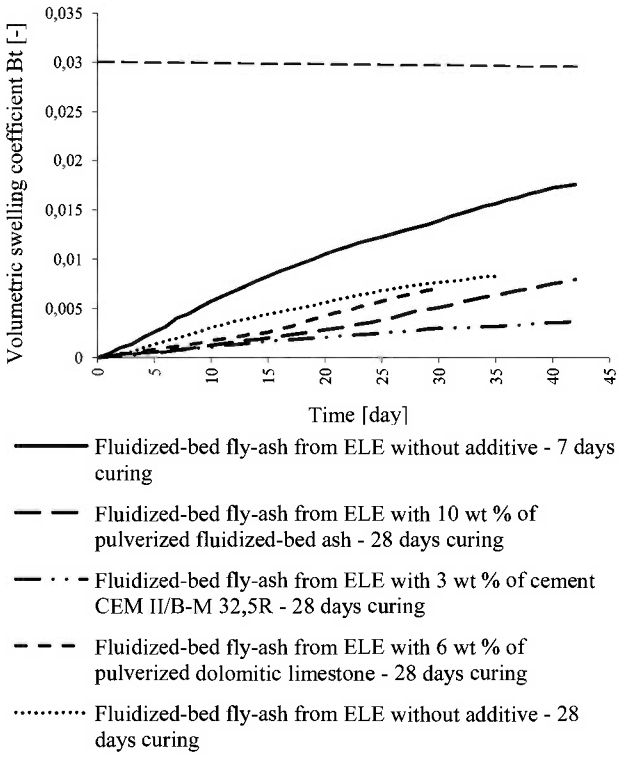

FIG. 8 Strength characteristics of cold recycled mixes.

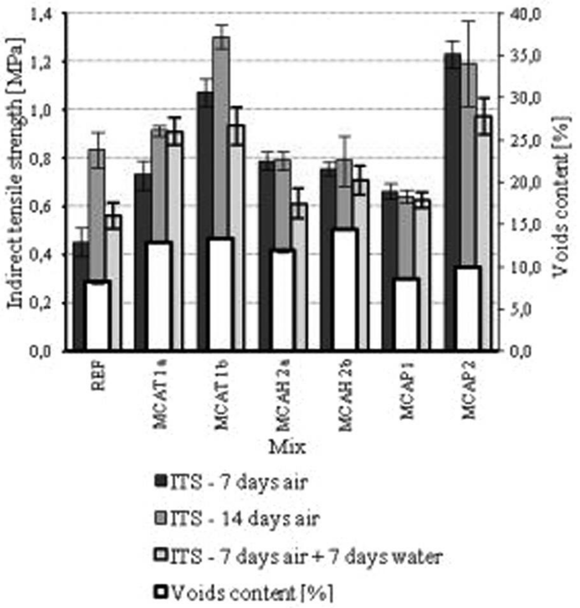

Swelling of Fly-Ash Stabilizate

Based on the results of measurements of swelling during hardening and setting of the fly-ash stabilizates indicated in **Fig. 7**, it can be noted that the volumetric changes of the stabilizate amount to rather low values. The greatest volume increase (by approximately 1.5 %) was demonstrated by stabilizate from ELE with no additives after 7 days of curing. It shows no signs of setting even after 40 days. The remaining mixes show a slower

FIG. 9 Strain characteristics of cold recycled mixes.

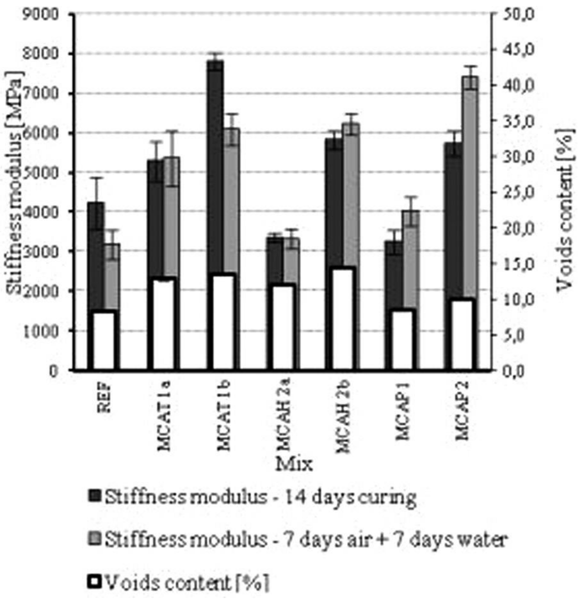

TABLE 5 Total sample analysis—macro-elements.

	Al	As	Ca	Fe	K	Mg	Mn	Na	P	S	Si
Element Sample	Total Content (mg) of Element per 1 g of Sample										
sorted RAP material 0/11	55.01	0.10	56.06	31.02	17.61	12.6	0.66	21.84	0.35	2.82	72.47
Fly-ash Plzen (fluid combustion)	105.95	—	166.36	40.39	1.55	9.88	0.96	8.20	1.58	32.29	0.51
Fly-ash Hodonin (fluid combustion)	108.33	—	141.67	36.11	1.80	9.44	0.43	5.11	0.54	29.64	0.35

"<" stays for below the detection limit, generally <0.020 ppm.

volume increase, roughly linear with the hardening time. It can be assumed that the limit value <3 % of swelling in CBR cylinder under TP 93 [26] will not be reached by all fly-ash stabilizates tested even after a longer examination period. It is likely that a hydration reaction occurs once the stabilizate components are mixed with water and compressed; ettringite forms during the reaction. In contrast to other materials with hydraulic bonds (e.g., concrete, cement-stabilized soil), ettringite's slight tendency to swell is a prevention against shrinking during hydration.

COLD RECYCLED MIXES

Strength and Strain Characteristics of Recycled Mixes

As is obvious from the results obtained and indicated in **Figs. 8** and **9**, substitution of cement by activated fly-ashes from fluidized combustion improves mix strength; the strength is reached already in the first 7 days of curing and does not increase significantly afterwards. The mixes assessed with 3.0 % fly-ash meet the strength parameters set by technical specifications TP 208 [21], namely minimum 0.3 and maximum 0.7 MPa, mixes with 10 % fail to meet the upper limit of the strength criterion, or the fast increase of strength demonstrates a potential risk of huge hydration heat generation and, potentially, shrinkage microcracks during the curing time. From the point of view of deformation parameters, the increase of the stiffness modulus is insignificant in relation to the reference mix. The indirect tensile strength and stiffness modulus values of water-soaked specimens show a positive trend with activated fly-ash application, namely no significant drop in water susceptibility of the mixes was observed as is the case of the reference mix. From the point of view of the parameters observed, it has to be mentioned that, for the sake of improved resistance of the mixes, the fly-ashes from fluidized combustion should be dosed for cold recycling mixes within the range of 2.0 %–5.0 % of the weight of the mix.

Results of Chemical Analysis

The results of performed measurements are summarized in the tables presented below. The concentrations of particular elements are normalized by the unit mg/g per sample. Due to this normalization, easy and well understandable comparison of particular macro- and microelements is possible. It is possible to transform the normalized amounts into a relative expression showing that besides the analyzed elements, the material usually also contains some other elements.

The macro-elements aluminum, calcium, and partly silicon seem to have the highest concentration (see **Table 5**). The elements are represented in the chemical compounds in crystalline or amorphous phases. Aluminum represented in both fly-ash samples is a puzzle because the source material burnt was soft coal and lime-stone used as catalyst. However, in the case of the fly-ash Hodonin sample, the energy producer is trying to modify the burn process by including municipal waste. The content of calcium can be easily explained by the burning process as already stated previously. This explanation might be used for sulphur as well. Silicon is represented in the RAP materials. This can be explained by the source of mineral materials.

From the micro-elements analysis, the following conclusions can be made. Increased content of hazardous/toxic microelements (observed) was found in total sample analyses as part of the analyzed material:

- Both fly-ashes: cadmium
- Reclaimed asphalt material 0/11: barium

In this context, it should be emphasized that in the case of beryllium (Be) and cadmium (Cd), the elements in question are highly poisonous and toxic and are distributed mainly in dust.

TABLE 6 Total sample analysis—micro-elements.

	B	Ba	Be	Cd	Co	Cr	Cu	Li	Mo	Ni	Sr	Ti	Zn
Element Sample	Total Content (mg) of Element per 1 g of Sample												
sorted RAP 0/11	1.89	0.30	0.0004	0.006	<	0.03	0.02	0.03	0.002	0.05	0.11	1.73	0.06
Fly-ash Plzen (fluid combustion)	—	0.41	0	0.01	0.07	0.11	0.19	0.24	0.008	0.05	0.54	18.4	0.10
Fly-ash Hodonin (fluid combustion)	—	0.31	0	0.01	0.02	0.13	0.13	0.12	0.01	0.07	0.29	5.42	0.30

TABLE 7 Values from leaching tests for cold recycled mixes.

Determined Leach of Monitored Elements		REF	MCAP 2	MCAH 2b	BMD 64 Days; U1a	Land Filled Waste (Leach After 64 Days)
Chloride	(mg/m^{2})	2 809.80	2552.90	2 516.10	—	10 000
Sulfate	(mg/m^{2})	2 390	71 397	126 308	27 000	10 000
Arsenic	(mg/m^{2})	0.45	8.712	2.48	41	1.3
Cadmium	(mg/m^{2})	0.09	0.086	0.085	1.1	0.2
Chromium	(mg/m^{2})	0.6	0.6	0.6	140	5
Copper	(mg/m^{2})	4.3	4	3.6	51	45
Mercury	(mg/m^{2})	0.03	0.03	0.02	0.4	0.1
Nickel	(mg/m^{2})	0.9	0.9	0.8	50	6
Lead	(mg/m^{2})	0.2	0.31	0.3	120	6
Zinc	(mg/m^{2})	8.3	5.2	6.1	200	30

Significantly different content of titanium in fly-ash from generation and cogeneration plant in Plzen cannot be explained easily. There might be an important amorphous compound rich on this element. The reason for that might probably be in the source material of soft coal.

In terms of total analysis reclaimed, asphalt material can be described as a material rich in arsenic. During the respective leaching test of RAP samples, it was found that arsenic is released from the brown coal multi-dust sample. In this connection, it is necessary to emphasize that in terms of the total extracted content of particular elements, the type of bond between such element and the analyzed material will play an important role.

FIG. 10 Test specimens immersed in distilled water (*a*) REF, (*b*) MCAP 2.

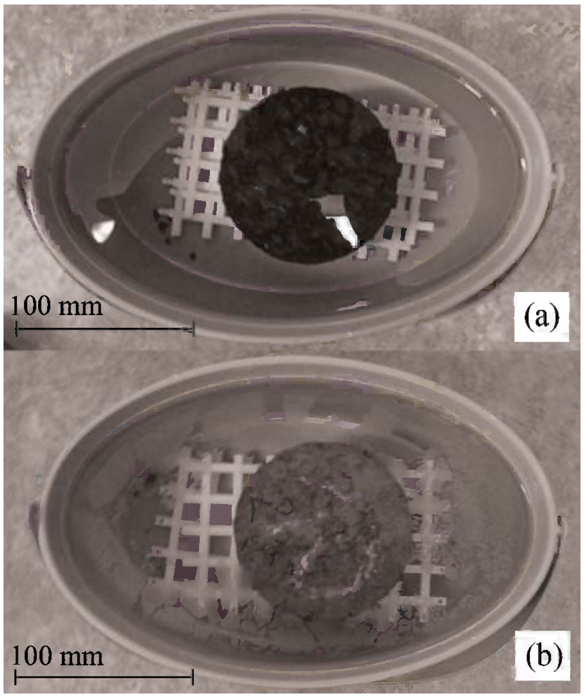

Besides the elements shown in **Table 6**, for both fly-ash samples, zirconium has also been detected in the amount of 0.08–0.34 mg/g.

Diffusive Test Results

As ensues from the results indicated in **Table 7**, higher sulphates and arsenic values were detected in mixes where fly-ash from fluidized combustion was applied. The highest sulphate quantity is seen in the mix with fly-ash from the Hodonin power plant (the higher value is probably caused by burning brown coal together with unsorted municipal waste). The highest arsenic content in the leach was shown by the mix with fly-ash from fluidized combustion from the Plzen heating plant. The leach water from all mixes examined demonstrated alkaline *p*H within the range of 8.0–11.0; the *p*H values increased within the 14 days of the test's duration; subsequently, slight decreases were recorded.

Test specimens of mixes REF and MCAP 2 demonstrated matt sediment on the water surface at the end of each leaching period (mostly in the ultimate periods) (see **Fig. 10**).

Conclusions

The present article focused on the possibility of using CCB by-products directly or applying them after certain modifications (through improvement of the properties required) in roadbed structures of roads, or even as structural layers of the pavements.

Laboratory research of CCB has emphasised the dominant influence of the technology applied to desulphurisation on the resulting CCB characteristics. The results of long-term CCB testing have proven that besides the deposit from EME, mechanical properties of fly ash stabilisers improve significantly in time. The results obtained confirmed that the highest values of simple compressive strength are achieved by mixes with a representation of ground (mechanically and chemically activated) fluidized fly-ash, pulverized dolomite limestone, or recycled concrete and, therefore, such mixes meet the minimum values required for simple compressive strength according to technical specifications TP 93 [26].

Based on the results yielded by the measurement of fly-ash swelling capacity, it can be concluded that the volumetric changes of the stabiliser amount to relatively small levels.

Frost and water susceptibility testing has indicated that the deposits and stabilisers tested are not resistant to frost and water. The majority of the samples tested disintegrated in the course of ten freezing and thawing cycles or, subsequently, compressive strength fell considerably after the last cycle.

A stabiliser made of compacted, slightly wet mix with the addition of mechanically and/or chemically activated mineral materials or chemical additives partly improves the characteristics of fly-ash mix resistance to water and frost when compared to a stabiliser alone (no additives). The application of mechanically and chemically activated materials or used additives facilitates elimination of some CCB problems, while indicating a possibility of substitution for lime, or cement.

Experimental results of the assessment of cold recycled mixes with application of combined binder formed by bituminous emulsion and mechanically activated fly-ash showed a benefit that can be delivered by materials otherwise rather difficult to use (often classified as waste or by-products) if mechanical and chemical activation process is employed. The refinement achieved during the process and, primarily, the structural changes caused by high-energy grinding allow both applications of the materials examined as a partial substituent of traditional binders, particularly in the case of fluid ashes. In the case of cold recycled mixes, they potentially eliminate even the much more fundamental problem of water susceptibility and, therefore, poor durability of such mixes. However, with respect to the reclaimed material fraction used, we can assume that with more coarse-grained reclaimed material, the effect should be greater. Based on these findings, further assessments are being carried out to evaluate the stability of the strengths or stiffness characteristics over time. From the environmental perspective, the application of the binder concerned in cold recycled mixes is associated with certain problems; further risk identification in relation to the contamination of the surrounding environment, primarily ground and surface waters, is necessary.

The experimental results of the cold recycling mixes bound by mechanically activated fly-ashes as presented demonstrate a contribution that materials, otherwise difficult to apply and often qualified as waste or residuals, can make if the mechanical activation process is employed. The fineness achieved by the process and, primarily, the structural changes caused by high-energy grinding result both in the possibility of utilising the materials observed as a partial substitute for traditional binders, particularly in the case of fly-ashes from fluidized combustion. In the case of cold recycling mixes, they potentially eliminate even the much more fundamental problem of water susceptibility and, therefore, poor durability of such mixes. However, with respect to the fractions of reclaimed materials used, we can assume that a greater effect should be visible in the case of reclaimed materials with coarse grains. Based on these findings, further assessments are in progress, which should evaluate the permanence of the strength or stiffness characteristics in time. From the environmental point of view, utilisation of this binder in cold recycling mixes is partly a problem; further identification of risks associated with contamination of the surrounding environment, particularly underground and surface waters, is necessary.

ACKNOWLEDGMENTS

The Presented results have been gained with the financial support of Student Grant Competition of CTU Prague within the project SGS12/039/OHK1/1T/11 “Design parameters and selected performance characteristics of cold asphalt mixes” and the project SGS13/125/OHK1/2T/11 “Experimental Assessment of Selected Performance Parameters of Cold Recycling Mixes.”

References

[1] Athanasopoulou, A., “Addition of Lime and Fly Ash to Improve Highway Subgrade Soils,” *J. Mater. Civ. Eng.*, Vol. 26, No. 4, 2013, pp. 773–775.

[2] Nalbantoğlu, Z., “Effectiveness of Class C Fly Ash as an Expansive Soil Stabilizer,” *Constr. Build. Mater.*, Vol. 18, No. 6, 2004, pp. 377–381.

[3] Chen, Z., Wang, Z., Wang, X., and Zhao, Y., “Study on the Frost Resistance Test Method of Lime-Fly Ash Stabilized Material Base Course,” *Proceedings of the ICCTP 2009*, Harbin, China, Aug 5–9, 2009.

[4] Sear, L. K. A., *Properties and Use of Coal Fly Ash: A Valuable Industrial By-Product*, Thomas Telford Ltd., London, 2001.

[5] Bin-Shafique, S., Benson, C. H., Edil, T. B., and Hwang, K., “Leachate Concentrations From Water Leach and Column Leach Tests on Fly Ash-Stabilized Soils,” *Environ. Eng. Sci.*, Vol. 23, No. 1, 2006, pp. 53–67.

[6] Aydilek, A. H. and Cetin, B., “Geoenvironmental Impacts of Using High Carbon Fly Ash in Structural Fill Applications,” *MD-13-SP909B4P*, MD State Highway Administration, Baltimore, MD, 2013.

[7] Rezník, B., *The Effect of Aggressive Conditions on Mechanical Properties of Alkali-Activated of Fly Ash*, Juniorstav, Brno, Czech Republic, 2011, pp. 312.

[8] Chindaprasirt, P., Thaiwitcharoen, S., Kaewpirom, S., and Rattanasak, U., “Controlling Ettringite Formation in FBC Fly Ash Geopolymer Concrete,” *Cem. Concr. Compos.*, Vol. 41, 2013, pp. 24–28.

[9] Vaníček, I. and Vaníček, M., *Earth Structures—In Transport, Water and Environmental Engineering*, Springer, New York, 2008.

[10] Vehovská, L., *FBC-Ash for Preparation of Blended Cement*, Juniorstav, Brno, Czech Republic, 2007.

[11] Faltus, M., “New Types of Hydraulic Binders Based on Waste Materials,” *Ecology and New Building Materials and Products: Proceedings of the 18th Conference of Research Institute for Building Materials Ecology and New Building*

Materials and Products (ICEBMP 2014), June 3–5, 2014, Cerná Hora, Czech Republic, 2009.

[12] Sekulić, Z., Popov, S., Duričić, M., and Rosić, A., "Mechanical Activation of Cement With Addition of Fly Ash," *Mater. Lett.*, Vol. 39, No. 2, 1999, pp. 115–121.

[13] Blanco, F., Garcia, M. P., Ayala, M. J., Mayoral, G., and Ángeles, F. G. M., "The Effect of Mechanically and Chemically Activated Fly Ashes on Mortar Properties," *Fuel*, Vol. 85, Nos. 14–15, 2006, pp. 2018–2026.

[14] Baláž, P., "High Energy Milling," *Mechanochemistry in Nanoscience and Minerals Engineering*, Springer, New York, 2008, pp. 103–132.

[15] Hela, R. and Orsáková, D., "The Mechanical Activation of Fly Ash," *Proc. Eng.*, Vol. 65, 2013, pp. 87–93.

[16] CSN EN 13286-2: Unbound and Hydraulically Bound Mixtures—Part 2: Test Methods for Laboratory Reference Density and Water Content—Proctor Compaction, ÚNMZ, Nové Město, Czech Republic, 2011.

[17] CSN EN 13286-41: Unbound and Hydraulically Bound Mixtures—Part 41: Test Method for Determination of the Compressive Strength of Hydraulically Bound Mixtures, CNI, Prague, Czech Republic, 2004.

[18] CSN EN 14227-5: Hydraulically Bound Mixtures—Specifications—Part 5: Hydraulic Road Binder Bound Mixtures, CNI, Prague, Czech Republic, 2008.

[19] Opravilová, L., Všianský, D., and Kubátová, D., "Impact Testing of Risk Components on Volume Changes of Cement Composites," *Proceedings of the 14th International Conference on Ecology and New Buildings Materials and Products*, Telč, Czech Republic, June 8–10, 2010.

[20] CSN EN 13286-47: Unbound and Hydraulically Bound Mixtures—Part 47: Test Method for the Determination of California Bearing Ratio, Immediate Bearing Index and Linear Swelling, ÚNMZ, Nové Město, Czech Republic, 2012.

[21] TP 208: Technical Specifications—Cold Recycling of Structural Layers of Flexible Pavements, Technical Requirements, Czech Ministry of Transportation, Prague, Czech Republic, 2009.

[22] CSN EN 12697-26: Bituminous Mixtures—Test Methods for Hot Mix Asphalt—Part 26: Stiffness, ÚNMZ, Nové Město, Czech Republic, 2012.

[23] Valentin, J. and Rohovec, J., "Alternative Leaching Test for Selected Secondary Materials Used in Road Construction," *ENVIROAD* (CD-ROM), Warszawa: Road and Bridge Research Institute, Warsaw, Poland, 2009.

[24] Townsend, T. G., "Leaching Characteristics of Asphalt Road Waste," *Final Report No. 98-2*, State University System of Florida, Florida Center for Solid and Hazardous Waste Management, Gainesville, FL, 1999.

[25] EA NEN 7375:2004: Leaching Characteristics of Moulded or Monolithic Building and Waste Materials—Determination of Leasing of Inorganic Components With the Diffusion Test, Netherlands Normalisation Institute Standard, Delft, the Netherlands, 2005.

[26] TP 93: Technical Specifications—Design and Construction of Road Structures With Utilization of Fly-Ashes, Ashes, Czech Ministry of Transportation, Prague, Czech Republic, 2011.

[27] CSN EN 14227-14: Hydraulically Bound Mixtures—Specifications—Part 14: Soil Treated by Fly Ash, CNI, Prague, Czech Republic, 2008.

[28] CSN 72 1191: Determination of the Frost Heave Testing Method of Soils, ÚNMZ, Nové Město, Czech Republic, 2013.

Journal of Testing and Evaluation

doi:10.1520/JTE20140082 / Vol. 43 / No. 2 / March 2015 / available online at www.astm.org

Sina Kazemian,[1] Hossein Moayedi,[2] and Mansour Mosallanezhad[3]

The Effect of Cement–Sodium Silicate Grout Compounds on Void Ratio and the Coefficient of Secondary Compression of Treated Fibrous Peat

Reference

Kazemian, Sina, Moayedi, Hossein, and Mosallanezhad, Mansour, "The Effect of Cement–Sodium Silicate Grout Compounds on Void Ratio and the Coefficient of Secondary Compression of Treated Fibrous Peat," *Journal of Testing and Evaluation*, Vol. 43, No. 2, 2015, pp. 279–285, doi:10.1520/JTE20140082. ISSN 0090-3973

ABSTRACT

Peats have low shear strength and high deformation characteristics. Peat is a naturally occurring material that is extremely soft with a high moisture content and exists in an unconsolidated state. The conventional binders used are cementitious materials, and the introduction of a new binder, sodium silicate, with other additives gives a better output than the conventional peat treatment. This article describes a laboratory study on the effect of different compounds of cement–sodium silicate grout on void ratio and the coefficient of secondary compression of fibrous peat. It is shown that by increasing the amount of sodium silicate (within 2.5 %), cement, and kaolinite in treated peat, we were able to decrease the mentioned properties of treated peat.

Keywords

fibrous peat, coefficient of secondary compression, void ratio, cement, sodium silicate, kaolinite

Introduction

The stabilization of highly organic soils such as peat is much more demanding than the stabilization of clay. The traditionally used cement, lime, and lime–cement mixtures are not necessarily the most suitable for these soils. Instead, mixtures of cement and granulated blast furnace slag are often used. These new binders have been extensively researched and tested both in the laboratory and in the field [1–3]. In addition, in most countries, the need for the consolidation of soft soil

Manuscript received February 28, 2014; accepted for publication July 8, 2014; published online October 7, 2014.

[1] M. ASCE, Assistant Professor, Civil Engineering Dept., Faculty of Engineering, Payame Noor of I.R. Iran, 9187995759, e-mail: kazemian.s@pnum.ac.ir

[2] M. ASCE, Postdoctorate Scholar, Geotechnics & Transportation Dept., Faculty of Civil Engineering, Universiti Teknologi Malaysia, Skudai, Johor 81310, Malaysia, e-mail: hossein.moayedi@gmail.com

[3] Assistant Professor, Dept. of Civil and Environmental Engineering, Shiraz Univ., Shiraz, Iran, 7188834399, e-mail: mosalla578@yahoo.com

deposits and the use of different improvement materials or techniques is extensively high [4,5]. One of the problems with applying this technology to organic soils is that organic matter inhibits cementitious reactions. In fact, for all soils, inorganic and organic, the properties of the stabilized product are extremely difficult to predict, in part because of the lack of understanding of the reactions of the soil, water, and binding agent [6]. Therefore, construction on peat soils has proven to be a challenging task, as this soil is highly compressible, has a low strength, and retains neither its form nor its strength after oxidation.

Huge numbers of poor foundation conditions are reported in all areas of Malaysia where clay, mud, and peat deposits appear. Accordingly, intensive geotechnical research work on soil-improvement techniques in Malaysia is performed at three universities: Universiti Putra Malaysia [7–10], Universiti Teknologi Malaysia [11–13], and Universiti of Malaya [14–16]. Peat or peaty soil normally having a high organic matter content is generally associated with high compressibility and a high magnitude and rate of creep [17]. It may also be associated with poor strength characteristics and a risk of large deformation [5,18]. Thus, peat soil is often viewed as a problematic soil because its engineering properties are inferior to those of other soft soils. It poses serious problems in the construction industry because of its long-term consolidation settlement even when subjected to a moderate load [7,19].

Anderssonl [1] investigated hydraulic cement-based binders for the mass stabilization of organic soils. He describes mass stabilization as a new, environmentally friendly soil improvement method in which stabilizer is mixed into peat, mud, or soft clay. The results have been encouraging, showing that it is possible to provide environmentally friendly solutions and stabilize organic soils cost-effectively. Edil and Fox [20] studied a field test of thermal precompression on peat. They presented a new concept for the improvement of soft ground using moderate heating to control post-construction settlement. Accordingly, they provided the long-term creep behavior of a peat based on laboratory oedometer tests involving step-stress and step-temperature changes. Finally, the feasibility of thermal precompression as a method of controlling or accelerating in situ settlement has been discussed. Hampton and Edil [6] investigated the strength gain of organic ground with cement-type binders. They presented a synthesis of mixture tests conducted in Delft, The Netherlands, and Madison, WI, on several peats and an organic clay showing that the current experimental techniques are not sufficient to create a comprehensive model of strength gain in stabilized organic soil. Research is needed on the fundamental chemical reactions contributing to changes in the geotechnical properties of stabilized organic ground [6]. DenHamer et al. [21] investigated the stabilization of peat by silica-based solidification. They developed a novel soil stabilization concept (called peat silicification) in which soil properties are modified in situ through encapsulation of the peat fibers with a layer of silicate. The results could increase strength and offer some resistance to biological and chemical oxidation. The silicification process involves the addition of three components: a cationic surfactant, a binding agent (a sodium metasilicate solution), and molasses to stimulate microbial fermentation, leading to the production of organic acids that will harden the geopolymer gel formed by the surfactant and binding agent. They achieved strengths of up to 1 MPa (UCS) in the laboratory using this process.

The main aim of this study was to determine the effect of cement–sodium silicate grout compounds on the void ratio (e) and the coefficient of secondary compression (C_α) of fibrous peats. Different ratios of grouts were tested in order to find the effect of each compound on the mentioned properties of fibrous peat.

Materials and Methods

Fibrous peat was collected from different locations in Kampung Jawa, Kelang, southwest of Kuala Lumpur, Malaysia. The physicochemical properties of fibrous peat are presented in **Table 1**. Ordinary Portland cement, kaolinite [$Al_2Si_2O_5(OH)_4$], sodium silicate, and calcium chloride were used to mitigate settlement problems in fibrous peat.

In order to determine the effects of different compounds on the compressibility parameters of fibrous peat, samples were prepared by mixing a specified amount (as a percentage) of cement, kaolinite, sodium silicate, and calcium chloride by weight of wet peat. The dosages of the various compounds used

TABLE 1 Physico-chemical characteristics of untreated fibrous peats.

Parameters	Method	Fibrous Peat
Fiber content, %	ASTM D1997-91 [22]	79.1
Moisture content, %	BS 1377: Part 2: 1990, Clause 3 [23]	506.5
Specific gravity	BS 1377: Part 2: 1990, Clause 8.4 [23]	1.26
Organic content, %	BS 1377: Part 3: 1990, Clause 4 [23]	94.23
Bulk unit weight, kN/m^3	BS 1377: Part 2: 1990, Clause 7 [23]	9.86
Degree of humification, %	von Post [24]	H_3

FIG. 1 Rowe cell apparatus.

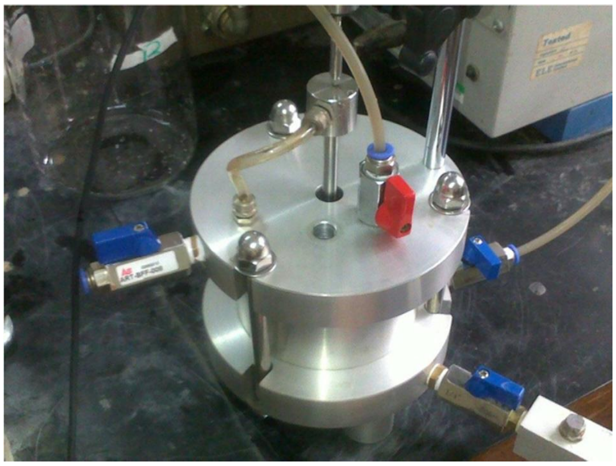

were as follows: cement, 5 %, 10 %, 20 %, and 30 %; kaolinite, 0 %, 10 %, 20 %, and 30 %; sodium silicate, 0 %, 1 %, 2.5 %, 3 %, and 5 %; and calcium chloride, 1 %. The samples were prepared by first mixing thoroughly homogenized peat at its natural water content with a household mixer and then adding the desired amounts of kaolinite, calcium chloride, cement, and sodium silicate. Three samples were prepared according to the percent weight of wet peat, as per the ratio of additives, and the average values of the results are reported. The samples were transferred to cylindrical containers and kept in a tray containing water. The compressibility parameters of fibrous peats, in vertical and horizontal directions, were evaluated with a Rowe cell according to BS 1377 Part 6: 1990 [23]. The Rowe cell apparatus is shown in **Fig. 1**.

Results and Discussion

INFLUENCE OF ORDINARY PORTLAND CEMENT ON FIBROUS PEAT

The variation in secondary compression for 20 % and 30 % cement and effective pressures ranging from 25 to 200 kPa is shown in **Fig. 2**. It was observed that the coefficient of secondary compression C_α decreased with the increase in cement. The C_α of untreated peat was 0.122 at a pressure of 25 kPa. It decreased to 0.00023 and 0.00008 with 20 % cement, and it decreased to 0.00008 with 30 % cement at the same pressure. Further, C_α was observed to increase with an increase in effective pressure. For untreated peat, it increased from 0.122 to 0.187 when the pressure was increased from 25 to 200 kPa. Similarly, it increased from 0.00023 to 0.00052 when the effective pressure increased from 25 to 200 kPa for samples with 20 % cement and from 0.00008 to 0.0002 for the same increase in effective pressure for samples with 30 % cement.

The variation in void ratio *e* with an increase in cement content is shown in **Fig. 3**. The void ratio was observed to decrease with an increase in cement content. The void ratio, at an effective pressure of 10 kPa, was observed to decrease from 0.805 to 0.62 when the cement content increased from 20 % to 30 %. For samples with 20 % cement, it decreased from 0.805 to 0.79 when the effective pressure increased from 10 to 200 kPa. Similarly, for samples with 30 % cement, it decreased from 0.62 to 0.61 when the effective pressure increased from 10 to 200 kPa. The void ratio was also observed to decrease with an increase in effective pressure for all samples.

Pozzolanic reaction is responsible for the long-term strength gain of stabilized soil, so in this case the pozzolanic reaction might not be the main factor, because the samples were

FIG. 2
Influence of cement concentration on coefficient of secondary compression of fibrous peat.

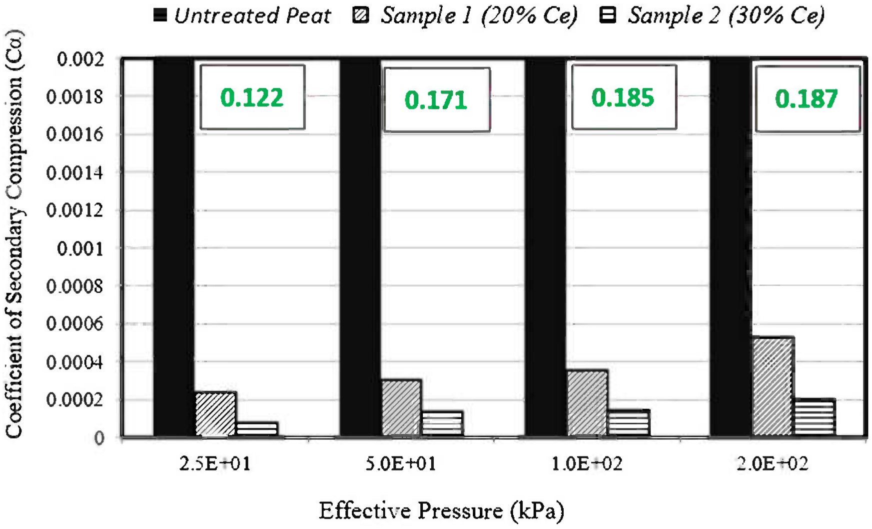

FIG. 3

Influence of cement concentration on void ratio of fibrous peat.

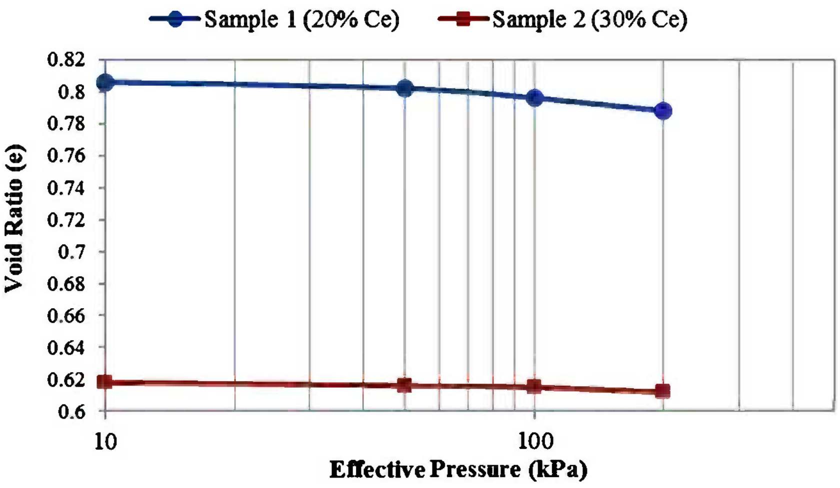

treated for less than a week. The ion exchange between calcium ions from cement and calcium chloride from kaolinite also would have decreased the mentioned parameters of the samples.

INFLUENCE OF KAOLINITE ON FIBROUS PEAT

The variation of C_α with effective pressure for samples with 10 %, 20 %, and 30 % kaolinite is shown in **Fig. 4** C_α was observed to gradually decrease as the percentage of kaolinite increased.

The C_α of untreated peat was 0.123 at an effective pressure of 25 kPa. With the addition of 0 %, 20 %, and 30 % kaolinite, it decreased to 0.0009, 0.00022, and 0.00007, respectively. Similarly, the C_α of untreated peat increased with an increase in effective pressure from 0.123 at 25 kPa to 0.187 at 200 kPa. Similar variation in C_α was observed for samples with 0 %, 20 %, and 30 % kaolinite when the pressure was increased from 25 to 200 kPa.

The variation in void ratio with an increase in kaolinite is shown in **Fig. 5**. The void ratio was observed to decrease with an increase in kaolinite and with an increase in effective pressure from 10 kPa to 200 kPa.

The void ratio was found to be 1.1, 0.69, and 0.62 for samples with 10 %, 20 %, and 30 % kaolinite at an effective pressure of 10 kPa. The void ratio decreased with an increase in effective pressure for all samples. For samples with 10 % kaolinite, the void ratio decreased from 1.1 to 1.04 when the effective pressure increased from 10 to 200 kPa. However, for samples with more kaolinite, the void ratio showed a very small reduction, from 0.69 to 0.68 and from 0.62 to 0.61 for samples with 20 % and

FIG. 4

Influence of kaolinite concentration on coefficient of secondary compression of fibrous peat.

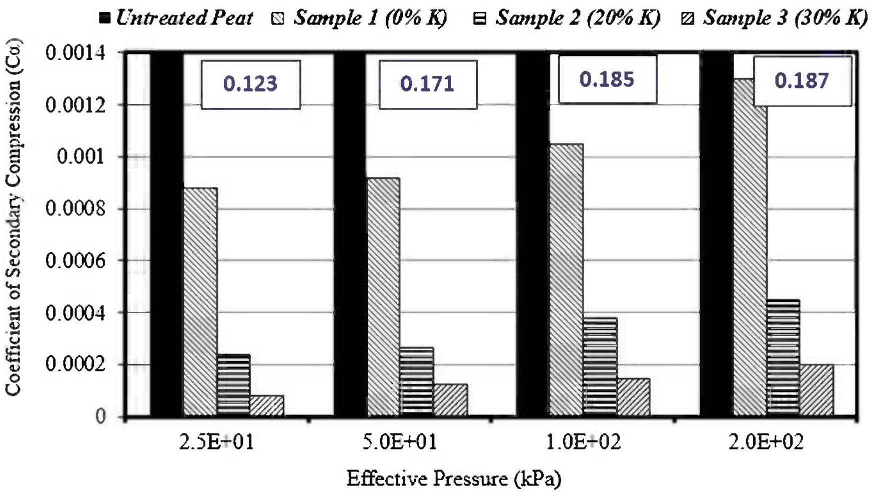

FIG. 5

Influence of kaolinite concentration on void ratio of fibrous peat.

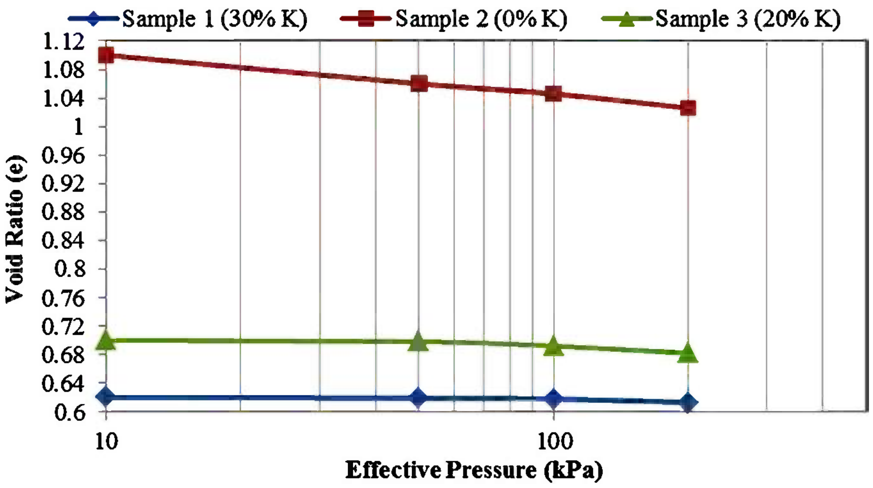

30 % kaolinite, respectively. The effect of kaolinite on the compressibility behavior is considered small relative to the effect of cement.

These results agree well with the published results; with the addition of kaolinite and calcium chloride, the adsorption of organic compounds will increase and calcium may create a bridge or connection (mentioned above) between the organic compound and the mineral part of fibrous peat and kaolinite [9,10].

INFLUENCE OF SODIUM SILICATE ON FIBROUS PEAT

The variation in C_α with changes in sodium silicate content and effective pressure is shown in **Fig. 6**.

As observed from **Fig. 6**, the C_α decreased from 0.0008 to 0.0001 when the sodium silicate content increased from 0 to 2.5 % at an effective pressure of 25 kPa. With an increase in sodium silicate content from 2.5 % to 5 %, a reversal in C_α was observed. It increased from 0.0001 to 0.0003 at the same pressure.

The void ratio, as shown in **Fig. 7**, decreased from 1.04 to 0.62 when sodium silicate was increased from 0 to 2.5 %. With a further increase in sodium silicate content, the void ratio increased, instead of decreasing, from 0.62 to 0.91, indicating that the optimum dose of sodium silicate is 2.5 %.

This behavior could be due to the fact that the mixture of cement and sodium silicate in the presence of calcium chloride causes intensive hydration, and the OH^- ions passing into the solution are consumed in the reaction of depolymerization and hydrolysis of silicate anions of the additives. When the concentration of calcium and hydroxide ions reaches a certain value,

FIG. 6

Influence of sodium silicate concentration on coefficient of secondary compression of fibrous peat.

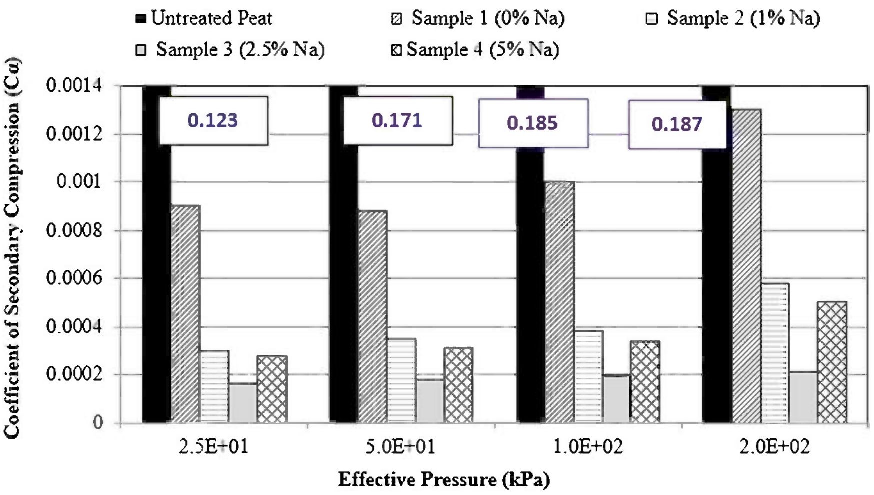

FIG. 7

Influence of sodium silicate concentration on void ratio of fibrous peat.

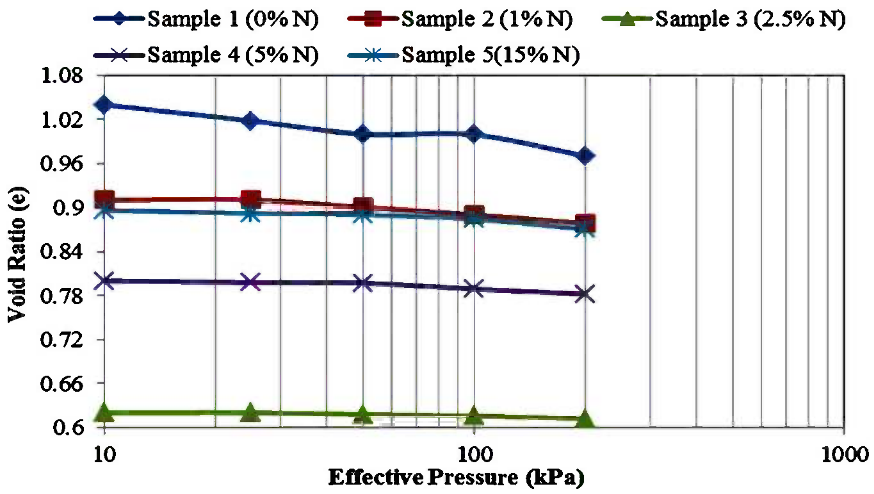

calcium hydroxides crystallize out of solution and finally lead to the production of calcium silicate hydrate (C–S–H), which improves the compressibility parameters of fibrous peat [14,15].

A polymerization process takes place to form a gel when sodium silicate is mixed with soil. This gel makes the binder behave as a glue to bond the soil particles together and as a filler to reduce the void ratio of the soil.

Conclusions

Based on the results, the following conclusions can be drawn:

- Settlement, C_α, and *e* decreased gradually with an increase in cement and kaolinite content. The effect of increased cement content was more significant than the effect of increased kaolinite content.
- All the parameters measured also decreased with an increasing percentage of sodium silicate binder until an optimum value was achieved. After the optimum percentage, an increase in the sodium silicate content increased the compressibility parameters.
- Regarding the effects of cement and sodium silicate (within 3 %) on the samples, the research showed that when the percentages of these compounds were increased, the compressibility parameters of fibrous peat improved. This happens because the hydration of cement and the fast reaction between cement and sodium silicate causes hydrated calcium silicates to be formed, both via precipitation of silicate ions of the additive and via release of silicate and aluminate ions from the clinker.

ACKNOWLEDGMENTS

The writers express their gratitude to the Ministry of Science, Technology Innovation, Malaysia (Project No. 03-01-04-SF0889) for the financial support for this study.

References

[1] Anderssonl, R., "Hydraulic Cement Based Binders for Mass Stabilization of Organic Soils," J. L. Hanson and R. J. Termaat, Eds., *Geotechnical Special Publication No. 112*, *Soft Ground Technology Conference*, Noordwijkerhout, the Netherlands, ASCE, Reston, VA, 2001, pp. 158–169.

[2] Edil, T. B., "Improvement of Peat: a Case History," *Proceedings of the Eighth European Conference on Soil Mechanics and Foundation Engineering*, Helsinki, Finland, 1983, pp. 739–744.

[3] Jones, A., "Ground Improvement: For Peat's Sake," *Ground Eng*., Vol. 39, No. 7, 2006, pp. 22–23.

[4] Jarvis, M. G., Allen, R. H., Fordham, S. J., Hazelden, J., Moffat, A. J., and Sturdy, R. G., "Soils and Their use in South East England," *Bulletin of the Soil Survey of Great Britain No. 15*, Harpenden, England, 1984.

[5] Haan, E. J. D. and Kruse, G. A. M., "Characterization and Engineering Properties of Dutch Peats. Characterization and Engineering Properties of Natural Soils," *Proceedings of 2nd International Workshop*, Singapore, Taylor & Francis, London, 2006, pp. 2101–2133.

[6] Hampton, M. B. and Edil, T. B., "Strength Gain of Organic Ground with Cement-type Binders," *Geotechnical Special Publication No. 81*, Sessions of ASCE Annual Convention, Boston, Massachusetts, Oct 18–21, Geo-Institute of ASCE, ASCE, Reston, 1998, pp. 135–148.

[7] Kazemian, S., Asadi, A., Huat, B. B., Prasad, A., and Rahim, I. B., "Settlement Problems in Peat Due to Their High Compressibility and Possible Solution Using Cement Columns," C. Shen-en, A. D. de Leon, A. M. Dolhon, M. J. Drerup, and K. Parfitt, Eds., *Forensic Engineering*, ASCE, Reston, VA, 2009.

[8] Kazemian, S., Huat, B., Prasad, A., and Barghchi, M., "A State of Art Review of Peat from General Perspective," *Int. J. Phys. Sci*., Vol. 6, No. 8, 2011, pp. 1988–1996.

[9] Kazemian, S., Prasad, A., Huat, B., Bazaz, J. B., Mohammed, T., and Aziz, F. A., "Effect of Aggressive pH Media on Peat Treated by Cement and Sodium Silicate

Grout," *J. Central South Univ. Technol.*, Vol. 18, No. 3, 2011, pp. 840–847.

[10] Kazemian, S., Prasad, A., Huat, B. B. K., and Barghchi, M., "A State of Art Review of Peat from Engineering Perspective," *Int. J. Phys. Sci.*, Vol. 6, No. 8, 2011, pp. 1974–1981.

[11] Eisazadeh, A., Kassim, K. A., and Nur, H., "Characterization of Phosphoric Acid- and Lime-stabilized Tropical Lateritic Clay," *Environ. Earth Sci.*, Vol. 63, No. 5, 2011, pp. 1057–1066.

[12] Kassim, K. A., "Lime Stabilized Malaysian Cohesive Soils," *Jurnal Kejuruteraan Awam*, Vol. 16, No. 1, 2004, pp. 13–23.

[13] Eisazadeh, A., Kassim, K. A., and Nur, H., "Stabilization of Tropical Kaolin Soil with Phosphoric Acid and Lime," *Nat. Hazards*, Vol. 61, No. 3, 2012, pp. 931–942.

[14] Ali, F. H., "The Flow Behaviour of Deformed Prefabricated Vertical Drains," *Geotext. Geomembranes*, Vol. 10, No. 3, 1991, pp. 235–248.

[15] Ali, F. H., Adnan, A., and Choy, C. K., "Use of Rice Husk Ash to Enhance Lime Treatment of Soil," *Can. Geotech. J.*, Vol. 29, No. 5, 1992, pp. 843–852.

[16] Sing, W. L., Hashim, R., and Ali, F. H., "Unconfined Compressive Strength of Cemented Peat," *Aus. J. Basic Appl. Sci.*, Vol. 3, No. 4, 2009, pp. 3850–3856.

[17] Huat, B. B. K., Prasad, A., Asadi, A., and Kazemian, S., *Geotechnics of Organic Soils and Peat*, Taylor & Francis, London, 2014.

[18] Huat, B. B., Kazemian, S., and Kuang, W. L., "Effect of Cement-Sodium Silicate Grout and Kaolinite on Undrained Shear Strength of Reinforced Peat," *Electron. J. Geotech. Eng.*, Vol. 16, 2011, pp. 1221–1228.

[19] Jarrett, P., "Geoguide 6. Site Investigation for Organic Soils and Peat," *JKR Document No. 20709-0341-95*, Public Works Department, Kuala Lumpur, Malaysia, 1995.

[20] Edil, T. B. and Fox, P. J., "Field Test of Thermal Precompression," *Geotechnical Special Publication (GSP) No. 40*, Geo-Institute (G-I) College Station, Texas, 1994, pp. 1274–1286.

[21] DenHamer, D. A., Venmans, A. A. M., Van Der Zon, W. H., and Olie, J. J., "Stabilization of Peat by Silica Based Solidification," M. Hamza, M. Shahien, and Y. El-Mossallamy, Eds., *Proceedings of the 17th International Conference on Soil Mechanics and Geotechnical Engineering*, The Academia and Practice of Geotechnical Engineering, Alexandria, Egypt, Oct 5–9, IOS Press, Amsterdam, the Netherlands, 2009, pp. 2224–2227.

[22] ASTM D1997-13: Standard Test Method for Laboratory Determination of the Fiber Content of Peat Samples by Dry Mass, *Annual Book of ASTM Standards*, ASTM International, West Conshohocken, PA, 2013.

[23] BS 1377 Part 6: *British Standard Institution Code of Practice for Foundation*, British Standard Institution, London, 1990.

[24] von Post, L., *Sveriges Geologiska Undersvknings torvinventering och negra av dess hittills vunna resultat*, "Sveriges Geologiska Undersvknings torvinven-tering och negra av dess hittills vunna resultat [Geological survey of sweden peat inventory and some of its hitherto missing results]," 1922 (in Swedish).

Journal of Testing and Evaluation

doi:10.1520/JTE20140126 / Vol. 43 / No. 2 / March 2015 / available online at www.astm.org

Jason Y. Wu[1] and Yijian Lin[2]

Experimental Study of Geobagged Reservoir Siltations for Backfill Applications

Reference

Wu, Jason Y. and Lin, Yijian, “Experimental Study of Geobagged Reservoir Siltations for Backfill Applications,” *Journal of Testing and Evaluation*, Vol. 43, No. 2, 2015, pp. 286–294, doi:10.1520/JTE20140126. ISSN 0090-3973

ABSTRACT

Infrastructure sustainability has become a major global concern. Massive reservoir siltations (RS) have seriously disrupted the service of many reservoirs worldwide. The dredged siltations are difficult to stockpile, or dispose of, because of their high water content and soft nature. This study explores a novel approach using RS to produce controlled low-strength materials (CLSM), reinforced with geobags that are used for storage and backfill applications. Test results have shown that, initially, geobags provided a significant contribution to the strength improvement of an RS-based CLSM. However, effective reinforcement appears to be highly dependent upon the type of geotextile and the original strength of the RS-CLSM. The results show a promising solution for reusing reservoir siltations and ensuring a sustainable approach for the mitigation of a silted reservoir.

Manuscript received March 21, 2014; accepted for publication June 24, 2014; published online October 7, 2014.

[1] Dept. of Civil Engineering, Chung Hua Univ., 707 Wufu Rd., Sec. 2, Hsinchu, 30012 Taiwan, e-mail: jasonwu@chu.edu.tw

[2] Zhao-Feng Engineering Co., Ltd., 481 Guangfu Rd., Sec. 2, Hsinchu, 30012 Taiwan, e-mail: lin0407@shie-ho.tw

Keywords

reservoir siltation, controlled low-strength material, CLSM, geobag

Introduction

Since the United Nations World Summit 2005, environmental protection and infrastructure sustainability have become major concerns for global social and economic development. Reservoirs are an important resource for water supplies, irrigation, and flood control. Reservoir siltation (RS) is caused by the flow of water and sediment into the reservoir. In general, all sediment transported to a reservoir by a river is derived from erosion of the land surface. Chanson [1] and White [2] reported that around 40 000 large reservoirs suffer from sedimentation; it is estimated that each year, between 0.5 % and 1 % of the world’s storage capacity is lost. Over the past few decades in Taiwan, total annual average reservoir siltations have reached about 1.36×10^7 m^3 as a result of unfavorable environmental conditions and poor watershed management [3–6]. That is about 20 %

FIG. 1

Dredged reservoir siltations have been sluiced to the retention ponds for temporarily storage.

of the reservoirs' total effective storage volume, and it seriously threatens the efficiency of all reservoir operations [4,5]. As a result, the expeditious removal of the RS and finding an innovative resource recovery for these materials have become priority issues for national security, economic development, and environmental protection. However, dredged RS materials contain appreciable amounts of fines and water; therefore, only a small portion of such material is reusable. They are neither easy to dispose of, nor to stockpile because of their extremely soft elements. For example, over the past decade, a total of 3.78 × 10^6 m^3 dredged reservoir siltations have been sluiced to 13 retention ponds in the proximity of the Shihmen reservoir, one of the most important water resources in northern Taiwan (**Fig. 1**). It has been difficult locating final dumpsites for these materials, and the end result has been pond spaces incapable of accommodating any more dredged materials (**Fig. 2**).

Recently, experts have proposed several technical solutions to develop various trial applications for reusing dredged RS material in areas such as construction fill, lightweight aggregates, as a raw material in brick and cement manufacturing, paving blocks for pedestrian walkways, chemical stabilization, agricultural soil, etc. However, for economic reasons, none has been a marketable success [3–5].

Controlled low-strength material (CLSM) or flowable fill is a self-compacting, flowable, durable strength, cementitious material used primarily as a backfill, void fill, or utility bedding in lieu of a conventional compacted fill [7–10]. It consists of water, cement, fly ash, or other similar byproducts, and fine or coarse aggregates, or both [7,11]. During the past decades, many researchers have well documented the performance and criteria of CLSM for pipeline construction and other infrastructure projects [3,7]. In comparison with conventional granular backfill, CLSM exhibits many advantages such as easy construction, low cost, high strength, and low compressibility. In many cases, it facilitates the backfill operation and ensures construction quality [7,8,10,12–14].

For the production of CLSM, concrete sand and coal fly ash are the most commonly used fine aggregates. However, the ACI [11] has also recommended that any available recycled granulated material may be considered as an alternative aggregate for CLSM, as long as it has been tested prior to use. Non-standard materials, such as boiler slag, recycled glass, cement kiln dust, crumb rubber, incinerator ash, flue gas desulfurization materials, and other similar granulated industrial byproducts have been used in the past to replace fine aggregates in CLSM [7,13,15–20]. Wu and Lin [3] successfully used RS as an aggregate to produce RS-based CLSM (RS-CLSM), a flowable material consisting only of cement, RS, and water. However, before engineers use it for construction, there remains the unresolved difficulty of an effective interim storage for the dredged RS.

FIG. 2 Retention pond has been fully filled with dredged reservoir siltation.

Geobags, made of polymer geosynthetics, are commonly used as an innovative technology for reinforced soil structures. In situ studies have demonstrated that piled geobags performed well for bearing capacity and are suitable as backfill materials for many infrastructure applications [21–23]. In practice, geobags filled with natural soils have been successfully used as reinforced backfill in soft ground treatments. This is primarily attributed to the mobilization of the tensile forces of the bags. It is concluded that the use of geobags for earth reinforcement could substantially improve the bearing capacity of soft material by minimizing its deformation under working loads [21,23]. Therefore, it is reasonable to use them as a temporary storage of RS-CLSM before it can be used in other backfill applications. The procedure for using geobags with RS-based CLSM consists of three steps. First, geobags are used as flexible forms to serve as an interim measure to facilitate the stockpiling of RS-CLSM in a fluid state. Second, the RS-CLSM contained in geobags gradually hardens because of hydration and cementation of the cement. Finally, the stone-like geobagged RS-CLSMs are readily available as a structural backfill component for the construction of future infrastructures.

This research is a feasibility study on using geobags filled with flowable RS-CLSM for the improvement of RS storage and future construction projects. The study focuses on exploring the effects of geotextile reinforcement on improving the strength of hardened RS-CLSM in geobags. This paper reports the findings of laboratory investigations and demonstrates the beneficial use of surplus dredged waste material to alleviate stringent, global environmental challenges.

Experimental Program

The aim of this study's experimental program is to investigate the effect of geotextile's reinforcement on the strength of RS-CLSM. The results can then become the basis of future research to explore the feasibility of using geobags to facilitate the RS-CLSM storage issue. This study used representative RS samples from the No. 7 retention pond near Shihmen reservoir (**Fig. 3**). The particle-size distribution in the tested RS material is given in **Fig. 4**. Based on Wu and Lin [3] the gray silty, clayey RS sample can be classified as CL in a unified soil classification system with an averaged plasticity index of about 11 and a liquid limit of 35. The observed specific gravity was 2.67. There were variations in the natural water content at different depths of the dredged RS. Starting at 36.6 % on the surface, it gradually increased to 48.7 % at a depth of 2.5 m where sampling was terminated. Although the dredged RS materials have been dehydrated for quite a long time, all tested values are higher than the liquid limit, which further substantiates the difficulty of managing these materials.

FIG. 3 Sampling of dehydrated dredged reservoir siltation.

FIG. 4 Particle size distribution of dredged reservoir siltation.

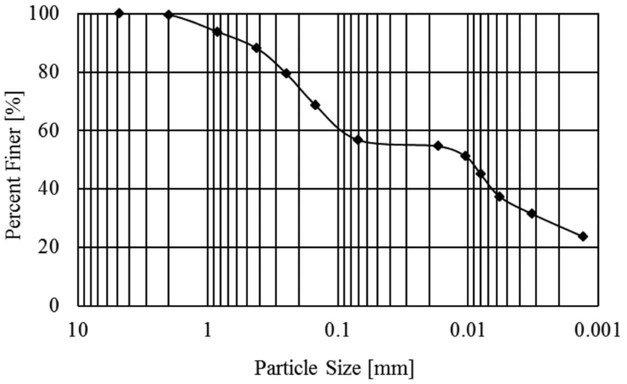

Compositions of the RS material are dependent upon geological conditions in each watershed of the reservoir. The chemical characteristics of the target RS have been investigated by many researchers. Although tests have been conducted at different locations, the RS is mainly composed of smectite clays containing SiO_2, Al_2O_3 and FeO_3. Other trace minerals are CaO, MgO, Na_2O, K_2O, and organics [3]. **Table 1** summarizes the chemical properties of the reservoir siltation collected by others [3]. **Table 2** shows the heavy metal results examined for RS materials. As shown in **Table 3**, samples have been taken at different depths of the retention pond to investigate possible trace elements of various anions in the dredged reservoir siltation [3]. Because reservoirs are important water resource facilities, their surrounding environments are well protected from contamination. It is much less hazardous when compared to municipal

TABLE 1 Summary of chemical properties of the reservoir siltation [3].

Minerals	SiO_2 (%)	Al_2O_3 (%)	Fe_2O_3 (%)	Others (%)[a]
Contents	58.2 ∼ 69.3	17.2 ∼ 24.1	6.10 ∼ 8.50	6.10 ∼ 15.87

[a] Other minerals include CaO, MgO, Na_2O, K_2O, and trace organics.

TABLE 2 The analysis of heavy metal for reservoir siltation [3].

Tested Item (mg/kg)	Sample A	Sample B	Sample C	Sample D	Sample E	EPA Safety Limit
Cadmium	ND	ND	ND	ND	ND	20
Lead	28.22	28.72	29.07	28.29	26.83	20 000
Copper	30.20	26.74	26.61	26.34	25.31	400
Zinc	138.62	146.57	124.17	127.8	123.03	2000
Chromium	17.82	14.36	15.77	17.01	16.71	250

sewage or riverbed sludge that contains various amounts of heavy metals or toxic substances [3,5]. The chemical analysis indicates that the RS presents compositions similar to those of natural clean earth materials; therefore, it can certainly be used as a construction material, if properly treated.

Type I Portland cement, the most widely used cementitious material, was selected for the proposed RS-CLSM. Based on other studies, flowability and strength are the two most important CLSM properties, and highly dependent upon the amount of water within the composite [7,9,11,24]. Therefore, the weight ratios of cement-to-water (C/W) and water-to-solid (W/S) were selected as control parameters for the mix design [3]. The W/S is, essentially, the CLSM's water content; therefore, it is a perfect indication of the amount of water within the material. With the target RS, the optimal mix ratios ($C/W = 0.3 \sim 0.5$, $W/S = 0.6 \sim 0.8$), developed in previous research, were selected. These corresponded to the most appropriate flowability (10 ~ 20 cm) and the 28-day unconfined compressive strength (400 ~ 1500 kPa), to produce this study's RS-CLSM [3].

The best practice for the production of the RS-CLSM is on-site preparation, directly using dredged RS materials. For this type of construction, field-batching facilities with appropriate weighing and mixing apparatus should be established [18]. However, in this research, a dry RS was used to better control the experimental results. Based on the design mix ratio, oven-dried RS and cement were first blended dry, following a designated mix formula. Tap water was then introduced and the sample was mixed using a Hobart mechanical mixer. Once the mixing was completed, a representative slurry sample was immediately extracted to test flowability and bleeding. The remaining material was cast into cylindrical samples using 10 cm × 20 cm cylinder molds in accordance with ASTM D4832-10 [25] for unconfined compressive strength tests. They were numbered, sealed with plastic wrap, and stored in a 100 % relative humidity curing room at a temperature of 25°C. They were tested at ages of 1, 7, and 28 days for compressive strength.

TABLE 3 The analysis of trace anions for reservoir siltation [3].

Tested Item (mg/kg)	Upper Zone (1.0 ~ 1.6 m Below Grade)	Middle Zone (2.5 ~ 3.1 m Below Grade)	Lower Zone (4.4 ~ 5.0 Below Grade)
Sulfate	73.32	20.42	31.47
Chloride	0.32	0.02	0
Nitrate nitrogen	1.023	0	0
Phosphate	0.02	0.048	0.056

Two types of materials, polyester (PET) non-woven and polypropylene (PP) woven geotextiles, were used for the geobags in this study (**Table 4**). They are the most common materials available on the market. The materials were cut into pieces with appropriate size and then stitched to wrap around the hardened RS-CLSM samples to simulate the effect of geobag containment. Reinforced and unreinforced RS-CLSM samples were then examined for deformation and strength based on geotechnical engineering aspects. Each ratio mix was replicated in three samples for cross verification, and all tests were performed in accordance with the procedures outlined in ASTM D4832-10 [25].

Results and Discussion

FLOWABILITY AND BLEEDING

Flowability is the most important attribute that makes the CLSM attractive for backfill construction. It is primarily controlled by the amount of water contained in the composite. The larger the amount of water used, the higher the flowability. However, greater water content may cause aggregate segregation, bleeding increase, and strength reduction. Therefore, the main priority of the designed mix was selecting suitable water content for the material to exhibit the best engineering performance [3]. Under such conditions, the RS-CLSM should not only be flowable for easy construction, but also durable for structural support.

Flowability was measured by procedures recommended by ASTM D6103-04 [26]. For most applications, specifications require an average flowability ranging from 20 to 30 cm [11]. A minimum flowability of 18 cm is required to ensure fill placement [17]. However, research also indicates that a maximum flowability of slightly less than 40 cm may be acceptable as long as the material provides suitable strength and there is no visible segregation [13]. The flowability used for construction should consider site condition variables and determine its most appropriate value based on each particular case. To simplify the mixing design, this research used dredged RS as the only aggregate to produce the RS-CLSM. For this type of mixture, Wu and Lin [3] reported that a flowability of 15 to 20 cm has shown acceptable performance for subgrade construction. For conventional backfill applications, the RS-CLSM should be produced with higher flowability to accommodate tight or restricted-access areas where placing and compacting the fill is difficult. However, in this study, the RS-CLSM will not be used directly for backfill; instead, it will be contained in geobags. Higher flowability is not mandatory as long as the material maintains an essential flowable condition. Excess water also leads to the risk

TABLE 4 Properties of geotextile materials for geobags.

Properties	PET Non-Woven Geotextile	PP Woven Geotextile
Nominal thickness (mm)	2.278	0.6
Apparent opening size (O_{95}) (mm)	$\leq$0.425	$<$0.075
Tensile strength (MD/CD) (kN/m)[a]	14.7/10.36	$\geq$40/40
Tearing strength (MD/CD) (N)[a]	309/263	$\geq$400/400
Puncture strength (N)	486	$\geq$400
Elongation (MD/CD) (%)[a]	52.81/63.15	20 ± 3/15 ± 3

[a] MD, machine direction; CD, cross machine direction.

of extreme consolidation and deformation when geobags are stockpiled. Therefore, this research proposed a flowability of 15 to 20 cm for the geobagged RS-CLSM.

Bleeding is another important issue for quality control of the CLSM in a fluid state. Mixtures with excessive bleeding are highly likely to induce an unacceptable, weak formation in the pavement, and a significant post-placement settlement. Therefore, bleeding measurements, as per ASTM C940-10a [27], were taken immediately after the mixing was completed, by directly placing 800 mL of each flowable sample into a 1000 mL graduated cylinder and measuring the volume of bleed water that accumulated on the surface.

Table 5 shows the observed bleeding and flowability for the RS-CLSM in its fluid state. All of the flowability values tested within the design range of 15 ~ 20 cm. The results clearly indicate that flowability increased with an increase in the W/S ratio. Increasing the amount of water tends to reduce the viscosity of the flowable material, and therefore causes the flowability to increase. The mixtures show a greater capacity of water retention because of the presence of clayey fines. In addition, a substantial increase in flowability is observed when the W/S ratio reaches a value of 0.8, indicating a threshold amount of water for the mixture's viscosity. Further increase in the amount of water only shows a slight improvement in flowability and tends to cause unacceptable segregation.

The flowability also increases with the increase in C/W ratios because the sample is prepared in such a manner that the amounts of water and solids are fixed for a specific sample. Increasing the amount of cement causes the clay to reduce by an equal amount, and therefore causes an increase in flowability. Although the W/S and C/W appear to be interactive with each other, because both include the effect of the water, evidence has shown that W/S ratios give direct indications for flowability. The C/W ratios are more specific to representing the potential of the cementation effects as those reported for other cementitious composites.

TABLE 5 Properties of RS-CLSM in fluid state.

Sample No.	Mix Ratio	Bleeding (%)	Flowability (cm)
1-1	W/S = 0.6 C/W = 0.3	0.67	15.1
1-2		0.67	15.1
1-3		0.67	15.7
2-1	W/S = 0.7 C/W = 0.4	1.33	16.1
2-2		0.67	16.6
2-3		0.67	16.8
3-1	W/S = 0.8 C/W = 0.5	1.33	18.3
3-2		1.33	18.5
3-3		1.33	18.1

The observed bleeding values ranged from 0.67 % to 1.33 %. Bleeding generally increased when the W/S ratio was increased. Apparently, the amount of water used in the mixture is the most notable factor that controls determined bleedings. Other researches have also reported similar results and suggested using 2 % to 3 % bleeding as the tolerable limit for the production of the CLSM [15]. Based on this criterion, bleedings for all of the RS-CLSM test samples are acceptable for construction. The RS material presents great potential of water absorption because of its smectite clay mineral composition [3]. The results in **Table 5** show that all of the given mix ratios conform to the flowability and bleeding requirements.

UNCONFINED COMPRESSIVE STRENGTH

The RS-CLSM gradually hardened and achieved strength through hydration of the cement. The composites were examined for strength after curing for 1, 7, and 28 days. **Figure 5** shows selected test data for the observed unconfined compression strength (q_u). Test results indicate that the q_u value of each mix varied as a function of W/S, C/W, and curing time. The q_u values increase when the C/W, W/S, and curing time are increased.

For a given C/W ratio, an increase in W/S ratio causes the amount of cement to increase, and therefore causes a higher strength. Most specifications require the CLSM to have a minimum strength for acceptable bearing capacity, and a maximum strength to allow for future excavation [15]. The target

FIG. 5 Unconfined compressive strength of different RS-CLSM mixes and curing time.

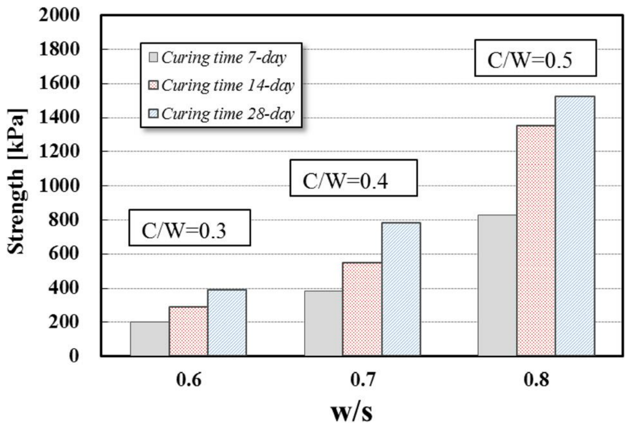

unconfined compressive strength is often required to be at least 345 kPa, whereas the maximum strength is often limited to 1380 kPa [11,13,15,28]. The observed values for the 28-day strength were approximately between 400 and 1500 kPa, and therefore generally satisfied the design considerations for construction backfill. Because the maximum strength recommended in the literature is 1380 kPa, using mix ratios of 0.8 for the W/S and 0.5 for the C/W is considered unacceptable for a higher strength. In addition, the proposed RS-CLSM herein will be reinforced later with geobags. A mix ratio of W/S = 0.6 ~ 0.7 and C/W = 0.3 ~ 0.4 for a lower strength would be sufficient for the final design. In conclusion, the RS-CLSM samples with these mix ratios conform to flowability, bleeding, and strength requirements.

EFFECT OF GEOTEXTILE REINFORCEMENT

The hardened RS-CLSM samples were wrapped with PET non-woven or PP woven geotextile materials to simulate the effect of a geobag reinforcement on strength development. Strength tests were then conducted to observe the differences between both the unreinforced and reinforced samples of the different types of geobags, with different cure times (**Figs. 6** and **7**).

Representative results are given in Figs. **8–11** to show the comparisons of such an effect. Although the stress–strain relationships vary, test results indicate that both geotextiles show significant contributions to the strength increase. For group A (W/S = 0.6, C/W = 0.3), the ultimate improvement ratio (UIR = $q_{u\text{-reinforced}}/q_{u\text{-unreinforced}}$) is about 1.7 for the PP woven material and about 3.98 for the PET non-woven material. The measured axial strains at failure for the reinforced samples also extend up to 28 to 65 times higher than that of an unreinforced sample and causes their deformation to become more plastic. For group B (W/S = 0.7, C/W = 0.4) with a higher unreinforced strength, a similar tendency was observed, but with substantially lower improvement ratios ranging from 1.24 to 1.64.

FIG. 6 Hardened RS-CLSM sample reinforced with PET non-woven geotextile.

FIG. 7 Unconfined compressive strength test for hardened RS-CLSM sample reinforced with PP woven geotextile.

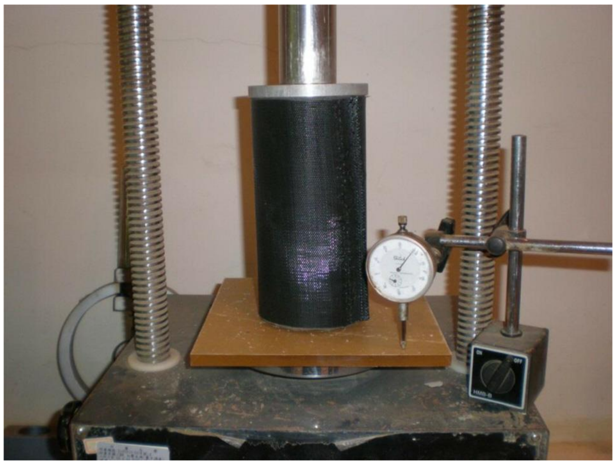

The effects of geotextiles on the stress–strain behavior of reinforced RS-CLSM are readily seen by comparing the results in Figs. **8–11**. For the ultimate condition, the use of the PET non-woven geotextile presented a higher confinement than the PP woven geotextile did. However, the original strength of the confined RS-CLSM material again exhibited a noticeable effect on the reinforcement. The effect of the reinforcement appears to be highly dependent upon the original strength of the RS-CLSM and the types of geotextile.

As the test results from Figs. **8–11** indicate, the fundamental reinforcement mechanism when using geotextiles occurs when an axial loading is acting on the contained RS-CLSM; the geotextile's tensile strength will then be mobilized. The reinforcement effectiveness appears to be affected by the tensile strength and the maximum extension strain of the geotextile. Different types of geotextiles have a considerably distinctive stress–strain relationship. Generally, woven fabrics exhibit high tensile

FIG. 8 Comparisons of unreinforced and reinforced strength (group A: curing time, 7 days; W/S = 0.6; C/W = 0.3).

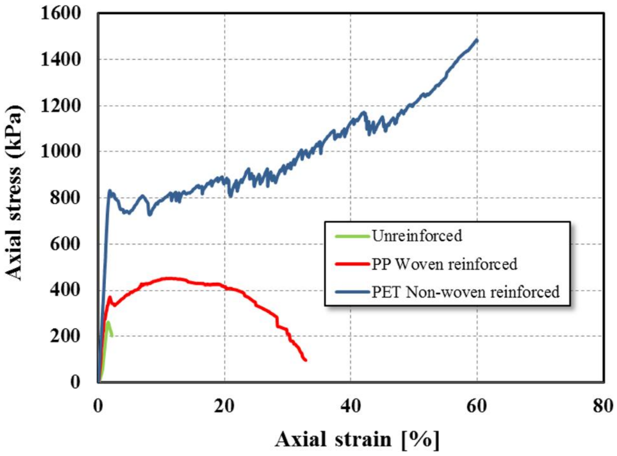

FIG. 9 Comparisons of unreinforced and reinforced strength (group A: curing time, 28 days; W/S = 0.6; C/W = 0.3).

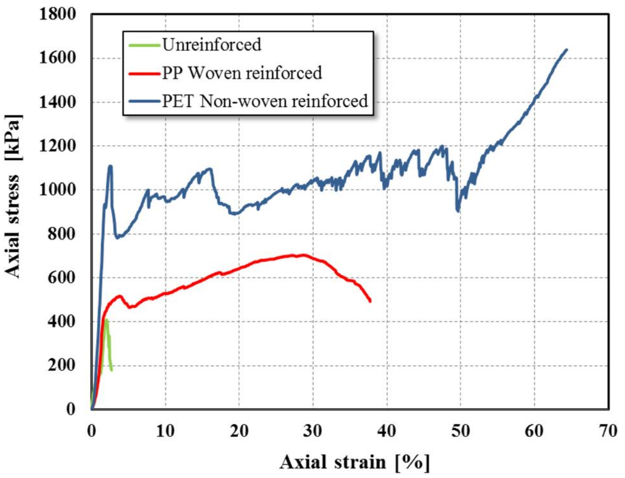

strength and low elongation. Non-woven fabrics present relatively lower strength, but with higher elongation and conformability (**Table 4**).

FIG. 10 Comparisons of unreinforced and reinforced strength (group B: curing time, 7 days; W/S = 0.7; C/W = 0.4).

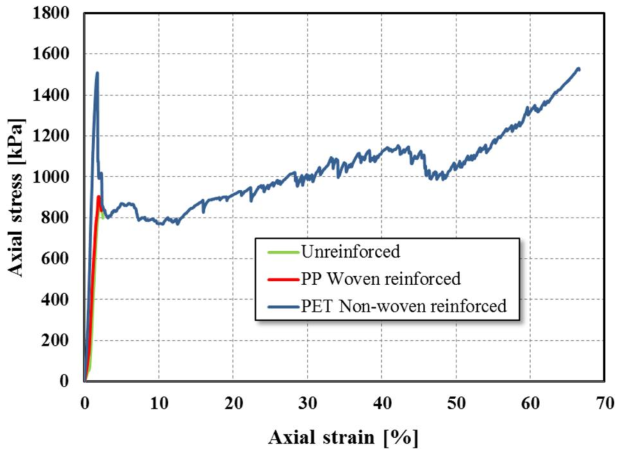

FIG. 11 Comparisons of unreinforced and reinforced strength. (group B: curing time, 28 days; W/S = 0.7; C/W = 0.4).

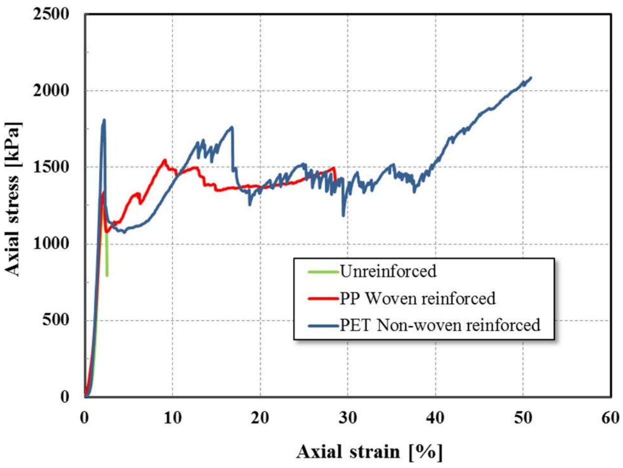

As can be seen in Figs. **8–11**, test results have shown that samples with the PET non-woven geotextiles present significant influences on the increase of strength development. The axial stress values are continually developing an axial strain of about 60 %. Although the PET non-woven geotextile exhibits a lesser tensile strength, it shows a more prominent effect on the reinforcement than that of the PP woven geotextile because of its high-elongation characteristics. **Figures 12** and **13** show the appearance of both geotextiles upon the ultimate compressive strength. The PP woven geotextile presents numerous tensile ruptures within the fabric, whereas the PET non-woven material only shows tearing failure along the stitched seam. Although reinforced with geobags, substantial deformations are likely for stockpiled RS-CLSM because of compression of the unconsolidated material. Use of a non-woven geotextile for geobag reinforcement appears to warrant a better performance because of its higher conformability. The contained backfill material also shows great influence on the stress–strain behavior. Such findings concur with other researches [21,23]. Further studies are underway to explore the feasibility of using full-sized geobagged RS-CLSM for construction backfill.

BENEFICIAL EVALUATIONS

The disposal of dredged reservoir siltations is troublesome and costly. The geobagged RS-CLSM developed in this study presents a viable scheme for the potential use of extremely soft dredged materials. The test results gathered in this research indicate that the use of native RS for the production of RS-CLSM results in comparable engineering properties of a conventional CLSM. Furthermore, the use of geobags to reinforce the RS-CLSM essentially alleviates the difficulty of piling up

FIG. 12 The rupture of PP woven geotextile upon ultimate compressive strength.

FIG. 13 The rupture of PET non-woven geotextile upon ultimate compressive strength.

massive amounts of soft dredged material. The stone-like geobags will be useful as a structural component for many infrastructural backfill applications and helpful in eliminating the consumption of limited standard aggregates. Considering the increasing environmental challenges and critically silted reservoirs in many countries, this paper offers a different solution for the development and building of a more sustainable environment.

Based on this study's findings, the proposed alternatives used for the improvement of reservoir maintenance are acceptable. However, it should be noted that the derived results in this research are site specific. The findings can only ensure the validity of the mixtures with the materials used in this study. It is highly recommended that those interested in this type of material perform site-specific experimental studies using local materials to generate specific mix designs.

Conclusions

The storage and disposal of dredged soft reservoir siltation is difficult and costly in a congested area such as Taiwan. This study's proposed use of geobags to contain RS-based CLSM presents an attractive alternative for the potential use of dredged soft clayey materials. The results presented in this paper indicate that the W/S and C/W ratios are the main control parameters for the physical and engineering properties of the proposed material. The observed values for the 28-day unconfined compressive strength have shown good correlations with C/W, W/S ratios, and curing times. Considering the criteria of flowability and strength for geobagged RS-CLSM applications, the recommended C/W and W/S ratios are 0.3 ~ 0.4 and 0.6 ~ 0.7, respectively. The use of both geotextiles for the reinforcement of the RS-CLSM presented significant contribution to their increased strength. Improvement ratios between 1.24 and 3.98 were found, with the PET non-woven geotextile showing the better strength increase. In addition, the reinforcement effect appears to be highly dependent upon the original strength of the RS-CLSM and the type of geotextile. The study confirms that a geobagged RS-CLSM with acceptable properties can be developed to alleviate the difficulty of depleting imperfect dredged reservoir siltations. The proposed novel solution not only can be used as a guideline for the development of such a beneficial alternative, but also for other similar clay-based CLSMs.

ACKNOWLEDGMENTS

This research is partially funded by the Ministry of Science and Technology, ROC, Project No. NSC 95-2211-E-216-004, whose support is greatly appreciated.

References

[1] Chanson, H., "Extreme Reservoir Sedimentation in Australia: A Review," *Int. J. Sediment Res.*, Vol. 13, No. 3, 1998, pp. 55–63.

[2] White, R., *Evacuation of Sediments from Reservoirs*, Thomas Telford, London, 2001.

[3] Wu, J. Y. and Lin, Y., "Use of Reservoir Siltation as CLSM for Subgrade Constructions," *Adv. Mater. Res.*, Vol. 723, 2013, pp. 535–542.

[4] Kuo, W. Y., Huang, J. S., and Tan, T. E., "Organo-Modified Reservoir Sludge as Fine Aggregates in Cement Mortars," *J. Constr. Build. Mater.*, Vol. 21, No. 3, 2007, pp. 609–615.

[5] WRA, "Comprehensive Report, Assessment and Planning for Multi-treatment of Shihmen Reservoir's Sludge," Water Resource Agency, Taiwan, 2008.

[6] Shihmen Reservoir, http://www.wranb.gov.tw/mp.asp?mp=4 (Last accessed 2 July 2014).

[7] Hitch, J. L., "Test Methods for Controlled Low-Strength Material (CLSM): Past, Present, and Future," *The Design and Application of Controlled Low-Strength Materials (Flowable Fill)*, *ASTM STP 1331*, A. K. Howard and J. L. Hitch, Eds., ASTM International, West Conshohocken, PA, 1998, pp. 3–10.

[8] Kaneshiro, J., Navin, S., Wendel, L., and Snowden, H., "Controlled Low Strength Material for Pipeline Backfill—Specifications, Case Histories and Lessons Learned," Joseph P. Castronovo, Ed., *Pipeline 2001: Advances in Pipelines Engineering and Construction, Proceedings of the ASCE Pipeline Division Specialty Conference*, San Diego, CA, July 15–18, ASCE, Reston, VA, 2001, pp. 1–13.

[9] Du, L., Folliard, K. J., and Trejo, D., "Effects of Constituent Materials and Quantities on Water Demand and Compressive Strength of Controlled Low-Strength Material," *J. Mater. Civil Eng.*, Vol. 14, No. 6, 2002, pp. 485–495.

[10] Khalifa, A.-J.,Taha, R., Al-Harthy, A., Al-Oraimi, S., and Al-Nuaimi, A., "Use of Cement By-Pass Dust in Flowable Fill Mixtures," *J. Cement, Concrete, Aggregates*, Vol. 24, 2002, pp. 1–5.

[11] ACI Committee 229, "Controlled Low Strength Materials," ACI-229R-99, American Concrete Institute, Farmington Hills, MI, 1997.

[12] Masada, T. and Sargand, M., "Field Demonstration Test on Construction and Strength of Flexible Pipe Drainage System Using Flowable Fill," *J. ASTM Int.*, Vol. 1, No. 6, 2004, JAI11880.

[13] Wu, J. Y., "Soil-Based Flowable Fill for Pipeline Construction," C. Vipulanandan and R. Ortega, Eds., *Pipeline 2005: Optimizing Pipeline Design, Operations, and Maintenance in Today's Economy, Proceedings of the ASCE Pipeline Division Specialty Conference*, ASCE, Houston, TX, Aug 21–24, ASCE, Reston, VA, 2005, pp. 925–938.

[14] Lin, D. F., Luo, H. L., Wang, H. Y., and Hung, M. J., "Successful Application of CLSM on a Weak Pavement Base/Subgrade for Heavy Truck Traffic," *J. Perform. Constr. Facil.*, Vol. 21, No. 1, 2007, pp. 70–77.

[15] Pierce, C. E. and Blackwell, M. C., "Potential of Scrap Tire Rubber as Lightweight Aggregate in Flowable Fill," *J. Waste Manage.*, Vol. 23, No. 3, 2003, pp. 197–208.

[16] Katz, A. and Kovler, K., "Utilization of Industrial By-Products for the Production of Controlled Low Strength Materials (CLSM)," *J. Waste Manage.*, Vol. 24, No. 5, 2004, pp. 501–512.

[17] Butalia, T. S., Wolfe, W. E., Zand, B., and Lee, J. W., "Flowable Fill Using Flue Gas Desulfurization Material," *J. ASTM Int.*, Vol. 1, No. 6, 2004, pp. 1–12.

[18] Chang, C. F. and Chen, J. W., "Development and Production of Ready-Mixed Soil Material," *J. Mater. Civil Eng.*, Vol. 18, No. 6, 2006, pp. 792–799.

[19] Lachemi, M., Hossain, K. M. A., Shehata, M., and Thaha, W., "Characteristics of Controlled Low-Strength Materials Incorporating Cement Kiln Dust," *Can. J. Civil Eng.*, Vol. 34, No. 4, 2007, pp. 485–495.

[20] Taha, R. A., Alnuaimi, A. S., Al-Jabri, K. S., and Al-Harthy, A. S., "Evaluation of Controlled Low Strength Materials Containing Industrial By-Products," *J. Build. Environ.*, Vol. 42, No. 9, 2007, pp. 3366–3372.

[21] Lohani, T. N., Matsushima, K., Aquil, U., Mohri, Y., and Tatsuoka, F., "Evaluating the Strength and Deformation Characteristics of a Soil Bag Pile from Full-Scale Laboratory Tests," *Geosynth. Int.*, Vol. 13, No. 6, 2006, pp. 246–263.

[22] Matsuoka, H. and Liu, S., *A New Earthy Reinforcement Method Using Soilbags*, Taylor & Francis, London, 2006.

[23] Xu, Y., Huang, J., Du, Y., and Sun, D., "Earth Reinforcement Using Soilbags," *J. Geotextiles Geomembr.*, Vol. 26, No. 3, 2008, pp. 279–289.

[24] Tripathi, H., Pierce, C. E., Gassman, S. L., and Brown, T. W., "Methods for Field and Laboratory Measurement of Flowability and Setting Time of Controlled Low-Strength Materials," *J. ASTM Int.*, Vol. 1, No. 6, 2004, JAI 11875.

[25] ASTM D4832-10: Standard Test Method for Preparation and Testing of Controlled Low Strength Material (CLSM) Test Cylinders, *Annual Book of ASTM Standards*, ASTM International, West Conshohocken, PA, 2014.

[26] ASTM D6103-04: Standard Test Method for Flow Consistency of Controlled Low Strength Material (CLSM), *Annual Book of ASTM Standards*, ASTM International, West Conshohocken, PA, 2014.

[27] ASTM C940-10a: Standard Test Method for Expansion and Bleeding of Freshly Mixed Grouts for Preplaced-Aggregate Concrete in the Laboratory, *Annual Book of ASTM Standards*, ASTM International, West Conshohocken, PA, 2014.

[28] Dingrando, J. S., Edil, T. B., and Benson, C. H., "Beneficial Reuse of Foundry Sands in Controlled Low Strength Material." *J. ASTM Int.*, Vol. 1, No. 6, 2004, pp. 1–16.

Journal of Testing and Evaluation

doi:10.1520/JTE20140086 / Vol. 43 / No. 2 / March 2015 / available online at www.astm.org

Zhen-Dong Qian,[1] Jiang-Yang Wang,[2] Lei-Lei Chen,[3] and Lin-Bing Wang[4]

Three-Dimensional Discrete Element Modeling of Crack Development in Epoxy Asphalt Concrete

Reference

Qian, Zhen-Dong, Wang, Jiang-Yang, Chen, Lei-Lei, and Wang, Lin-Bing, "Three-Dimensional Discrete Element Modeling of Crack Development in Epoxy Asphalt Concrete," *Journal of Testing and Evaluation*, Vol. 43, No. 2, 2015, pp. 295–307, doi:10.1520/JTE20140086. ISSN 0090-3973

ABSTRACT

Cracking in epoxy asphalt concrete (EAC) used for a steel bridge wearing course has always been a major cause of structural and functional deterioration of this material, particularly in cold climate. Therefore, it is important to understand the complex fracture behavior of this heterogeneous mixture, which is composed of irregularly shaped and randomly distributed aggregates surrounded by asphalt mastics. A three-dimensional (3D) fracture model independent of laboratory, based on the discrete element method (DEM), is reconstructed using a randomly generating algorithm to investigate the fracture behavior. A bilinear cohesive-softening model is implemented into the DEM framework to simulate the crack initiation and propagation in EAC. Several experimental tests are performed to obtain input parameters of materials for numerical models. The simulation results of a single-edge notched beam test agree well with experimental results and accurately capture the stress distribution and development of fracture zone. The modeling technique herein provides insight into the progressive cracking process; 3D visualization of crack trajectories also demonstrates the influence of heterogeneity on crack path. The 3D user-defined microstructural DEM fracture model is capable of giving a realistic cracking process of quasi-brittle materials such as EAC and can help us better understand various fracture mechanisms through numerical simulations.

Keywords

epoxy asphalt concrete, three-dimensional discrete element method, single-edge notched beam test, digital image correlation system, fracture, crack development

Manuscript received March 1, 2014; accepted for publication September 8, 2014; published online October 10, 2014.

[1] Professor, Intelligent Transport System Research Center, Southeast Univ., Number 35 Jinxianghe Road, Nanjing, 210018, People's Republic of China, e-mail: qianzd@seu.edu.cn

[2] Engineer, Suzhou Highway Bureau, Number 300 Tongjing South Road, Suzhou, 215007, People's Republic of China, e-mail: wjy0804@163.com

[3] Lecturer, Intelligent Transport System Research Center, Southeast Univ., Number 35 Jinxianghe Road, Nanjing, 210018, People's Republic of China, e-mail: Chenleilei@seu.edu.cn

[4] Professor, Charles E. Via, Jr. Department of Civil and Environmental Engineering, Virginia Polytechnic Institute and State Univ., 200 Patton Hall, MC 0105, Blacksburg, VA 24061, e-mail: wangl@vt.edu

Introduction

The epoxy asphalt has been successfully used in the wearing course on top of steel decks in China in recent years, and there have been many research projects on the performances of epoxy asphalt concrete (EAC) consisting of thermosetting epoxy asphalt binder and high quality aggregates. The thermosetting nature of epoxy asphalt binder has significantly contributed to the excellent field performanace of EAC, such as great resistance to fatigue and permanent deformation [1]. This is because the curing reactions can transform the epoxy resin contained in the epoxy asphalt binder into plastic or rubber by a cross-linking process, subsequently forming into a three dimensional rigid molecular structure. However, cracking has been shown to be the major distress in the epoxy asphalt layer of the wearing course [2].

It is well known that many different fracture toughening mechanisms occur in heterogeneous solid mediums such as asphalt concrete (AC), including crack branching and bridging, crack deflection, crack face sliding, and crack tip blunting. Thus, material microstructure (including composition, distribution, and configuration) should be considered, since crack growth is mainly influenced by these three factors. Additionally, the quality of results obtained from simulating fracture in heterogeneous materials is directly related to the appropriateness of selected constitutive models. For quasi-brittle materials such as portland cement concrete and AC, softening-type separation models such as cohesive zone model (CZM) can be successfully employed to capture the postpeak softening response noted in Mode I (pure tension) fracture tests.

In the past decade, more realistic fracture modeling with the consideration of heterogeneous material microstructure in asphalt concrete has been studied using the finite element method (FEM) [3,4] and discrete element method (DEM) [5–10] with the implementation of CZM. DEM is an ideal method which can simulate not only continuum but also granular properties, especially the fracture mechanism of asphalt concrete due to the following advantages: (1) changing contact and moving boundary conditions does not pose convergence problems; and (2) larger deformations and frictional sliding between particles or clustered assemblies can be handled routinely. Kim and Buttlar [5,6] successfully developed a heterogeneous fracture model using DEM and CZM to investigate various fracture toughening mechanisms of AC and to simulate the initiation and propagation of crack. This model was also used to predict the size-dependent [7] and rate-dependent [8] nature of fracture behavior, and to simulate mixed-model crack propagation [9]. The simulation results were also compared with the test results of a disk-shaped compact tension test and a single-edge notched beam test, respectively. However, the above model is 2D and based on a high-resolution image processing technique. Obviously, the actual crack path is a 3D trajectory tunneling through the specimen thickness rather than in 2D. Consequently, it is necessary to investigate mechanical performances and crack failure mechanisms of AC using 3D models.

Recently, 3D visualization and simulation of the microstructure of AC has been performed [10,11], where the X-ray computed tomography technique or random particles generation was used. These 3D models can accurately depict the internal structures of asphalt mixtures and give more reliable results, but they are time consuming.

The aim of this study is to demonstrate the potential benefits of numerical prediction of fracture behavior and 3D crack trajectories of EAC. In this work, a 3D heterogeneous fracture model is reconstructed based on a randomly-truncating algorithm, involving the cohesive-softening model (CSM), to model the progressive fracture process and to simulate crack initiation and propagation of the thermosetting EAC. The simulation of a fracture test is performed using the model based on particle flow code in 3 dimensions (PFC3D), with comparison to experimental results to validate DEM simulation results. Selected results are used to illustrate progressive fracture process and show 3D crack trajectories in epoxy asphalt concrete.

Discrete Element Fracture Model

DIGITAL SAMPLE: A RANDOMLY GENERATED MODEL

In the last decade, micromechanics models have been developed using DEM to simulate granular properties of AC [12–15]. To rebuild the microstructure of AC (including 2D and 3D), two methods were typically utilized: image-based models [14] and user-defined models [15].

The major advantage of the image-based models is that they are able to represent relatively accurate AC microstructure; the disadvantage is that they are laboratory dependent. Thus, Liu and You [11] developed a methodology for visualization and simulation of AC with DEM; the gradation, shape, and distribution of aggregates were considered. Aggregates in their study are randomly generated rather than from generated from digital images.

In this study, virtual polyhedron aggregate particles were generated using a randomly-truncating algorithm presented in an earlier study [16]. A cube was selected as the original shape and a polyhedron was formed by truncating the cube with several reference planes. The internal zone of the polyhedron was filled with uniformly sized balls, and all the balls fallen in the polyhedron were bonded together to represent an aggregate. Some of the randomly created polyhedron particles with irregular shapes are shown in **Fig. 1**, as example. The shapes, distribution, and sizes of aggregates can be controlled by user-defined statistical parameters. Virtual aggregates also could be crushable because the aggregate particles were simulated with clusters of discrete elements.

The microstructure of a beam specimen was rebuilt with a randomly created model presented in an earlier study [16]. The

FIG. 1 Examples of randomly created polyhedrons.

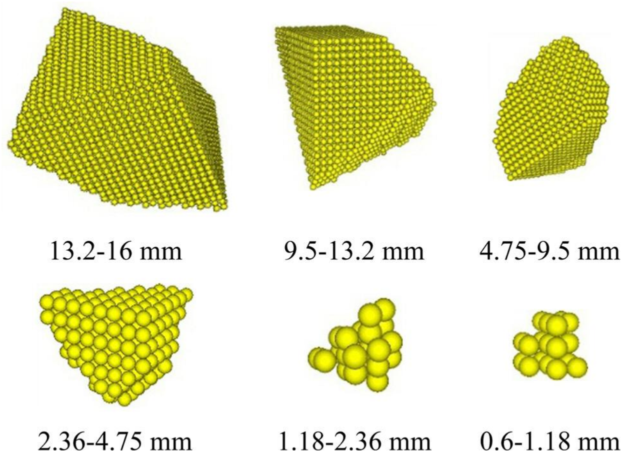

EAC mixture is considered as a three-phase composite: asphalt mastic, air voids, and mineral aggregates with the size larger than 2.36 mm. A simple example of the procedure for the randomly generated model is shown as **Fig.** 2.

Even though the asphalt mastic is actually a composite aggregates finer than 2.36 mm, as well as asphalt binder, it is considered as a homogeneous medium and then simulated using a cluster of discrete elements. Air voids were created in the 3D digital sample by randomly deleting some mastic discrete elements until the void volume percentage reached the target. A total of ten digital samples with single-sized discrete elements (1.0 mm in radius) were created.

FIG. 3 Concept of cohesive-softening model.

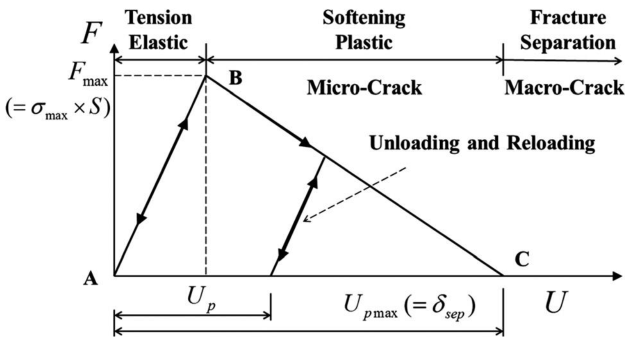

COHESIVE SOFTENING MODEL

An intrinsic bilinear cohesive softening model (CSM) [17], as shown in **Fig.** 3, has been implemented as a user-defined model in the DEM for numerical fracture simulations. Cohesive softening models are described by three parameters (two of them are independent): cohesive fracture energy (φ_c), cohesive strength (σ_{max}), and separation/critical displacement (δ_{sep}). F_{max} is the contact force in maximum. $U_{p\max}(=\delta_{sep})$ is the accumulated plastic displacement for which the bond strength softens to zero.

In general, cohesive energy is obtained from experiments and can be represented as simply:

FIG. 2

Sketch for a randomly generated model: (*a*) graded balls, (*b*) uniformly sized balls, (*c*) two-phase system, (*d*) air voids distribution, (*e*) finalized digital sample.

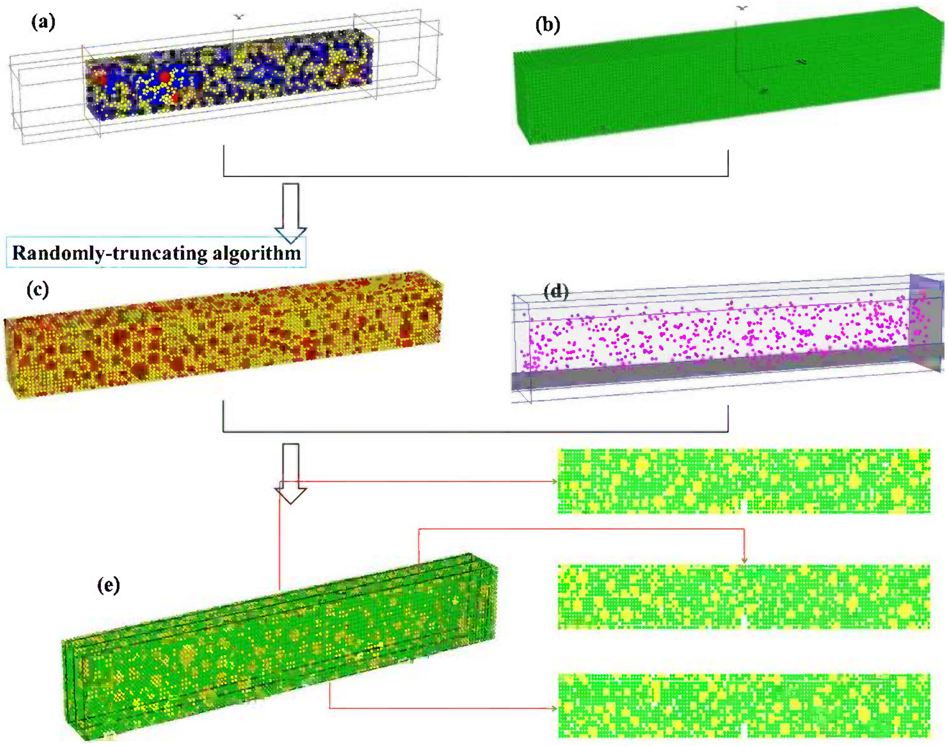

$$\varphi_c = \int_0^{\delta_{sep}} \sigma_c(\delta)d\delta \qquad (1)$$

The cohesive energy, assumed to be equivalent to the work of fracture, is usually obtained from experiments, whereas the separation displacement is a parameter that is difficult to measure. The verification of cohesive fracture had been established using a double cantilever beam by Kim et al. [5].

Experimental Tests and Material Parameters

SINGLE-EDGE NOTCHED BEAM TEST

For this study, a single-edge notched beam (SE[B]) was selected as the laboratory test tool for the aforementioned modeling approach. The SE[B] geometry can be readily fabricated from laboratory compacted beams or slabs. The loading configuration (three-point bend) allows for simple stress and ease of test control with closed-loop servo-hydraulic equipment. Constant velocity (or displacement) boundary conditions are imposed at the center of the top edge of the model in order to predict stable fracture behavior. Further details of the notched beam fracture test for asphalt concrete can be found in Ref. [18].

The EAC currently used is a typical steel deck bridge wearing course mixture that consists of a 9.5 mm nominal maximum aggregate size (NMAS) and a 6.5 % epoxy asphalt binder by weight of dry aggregates produced by Chemco System Company. The aimed air-void content is 1.68 %. **Figure 4(*a*)** plots the aggregate gradation, **Fig. 4(*b*)** describes a simply-supported, SE(B), 250 mm in length, 35 mm in height, and 30 mm in thickness. A mechanical notch was then inserted with a length of 7 mm, giving a notch (a/H) ratio of 0.2. A closed-loop servo-hydraulic load frame (MTS 810) was used to perform the fracture test, and the fixture span is 200 mm. A total of ten specimens were fabricated using rolling wheel compaction, cured for 4 h at 120°C, and then cut to the final dimensions.

The test was performed at −10°C and the beam loading was performed with a constant load-line displacement (LLD) rate of 1 mm/min. The material fracture energy was computed as the area under the load-LLD curve normalized by the initial ligament length and beam width, and the self-weight of the beam was neglected.

FIG. 4 Illustration of SE(B) test for EAC (−10°C): (*a*) aggregate gradation of EAC, (*b*) single-edge notched beam test fixture.

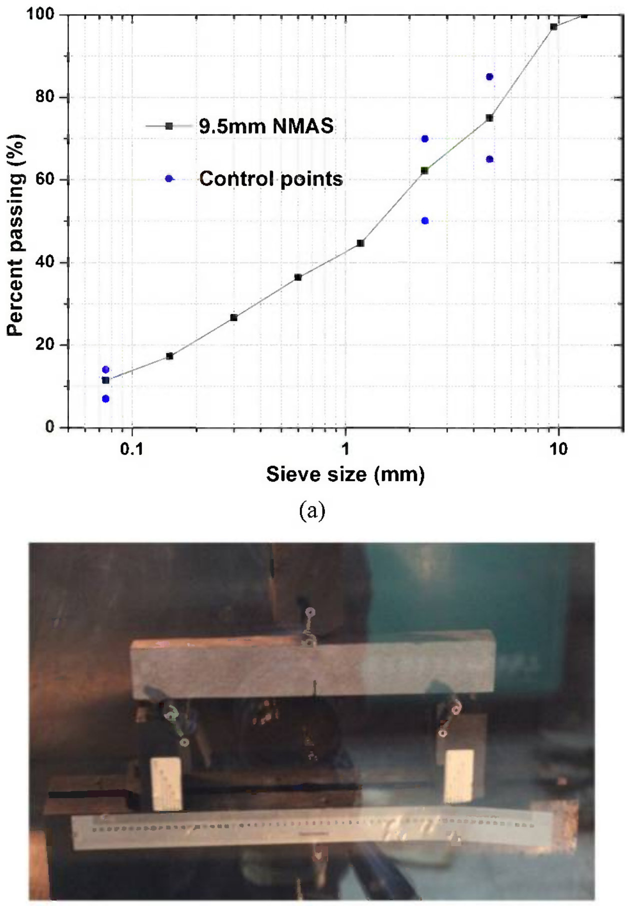

(a)

(b)

DIGITAL IMAGE CORRELATION SYSTEM

Recent work conducted by Birgisson et al. [19,20] has led to the development of a digital image correlation (DIC) system to describe plain displacement/strain fields in AC mixture testing. Image correlation analysis involves measurement of the grey scale values at each pixel location in the grabbed area. By comparing the grey scale values of images of a specimen during its deformation with those of the initial image of the specimen, the movement and deformation and, consequently, the displacement of the central pixel of images can be determined. The image sequence of a specimen is acquired with a digital camera during fracture testing. The specimen surface is properly treated to generate a set of features (speckle pattern) tracked by the algorithm along the sequence. From the image coordinates, displacements and deformations can be evaluated in image space and, with an appropriate scale factor, in object space.

The system is made up of three elements: the hardware (i.e., the digital camera and the illumination devices), the specimen set-up, and the software (image acquisition and processing). A complementary metal oxide semiconductor-based digital camera is currently used, which is located on a support before a climatic material testing system chamber, as shown in **Fig. 5(*a*)**. A lighting system, created for the purpose of providing adequate illumination of the specimen, and a laptop directly connected with the camera are also used, as shown in **Fig. 5(*b*)**. A specimen requires a preliminary surface treatment to ensure a successful image acquisition and the subsequent application of the image correlation. The camera is set up at a distance away

FIG. 5 Image correlation-based system: (*a*) digital camera, (*b*) computer and illumination, and (*c*) finite area for obtaining strain/displacement field.

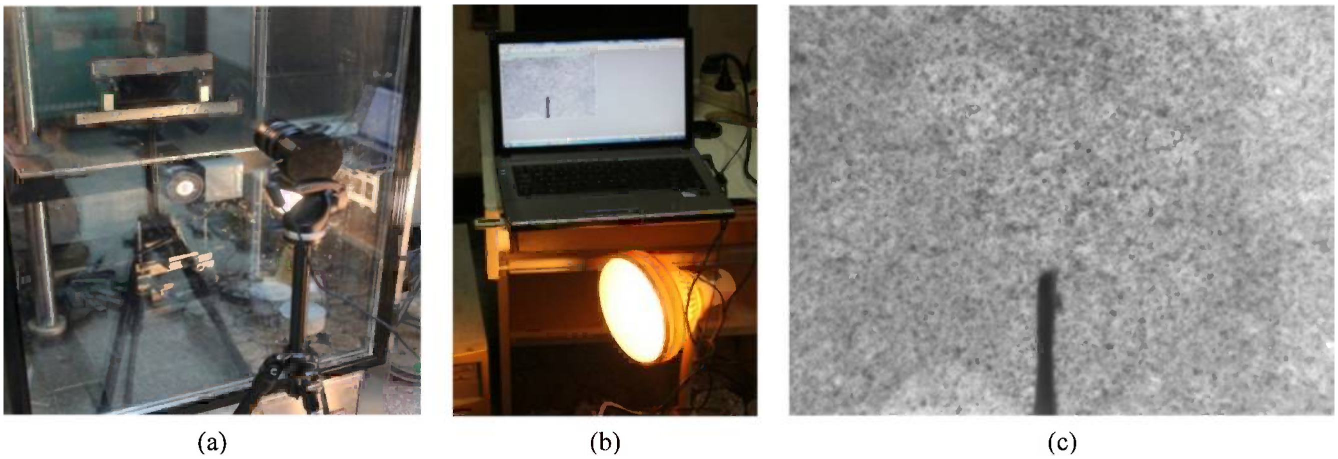
(a) (b) (c)

from the specimen so that the resulting imaging window is focused on a proper region of interest at around the location of maximum stress, as shown in **Fig. 5(*c*)**. The camera is set to acquire 1/8 fps, which was determined by processing time and data storage capacity.

DETERMINATION OF MATERIAL PARAMETERS

The overall material property of discrete element model could be simulated through assigning a constitutive model at a certain contact. A homogeneous material can be simulated using a single constitutive model for all contacts of discrete elements, whereas a heterogeneous material needs more than one constitutive model for different contacting interaction behaviors.

There are four contact interactions in the EAC microstructure, including between adjacent aggregates (i.e., agg-agg), within a single aggregate (i.e., agg-in), between an aggregate and mastic (i.e., agg-mas), and within the mastic (i.e., mas-in). Four different constitutive models are built for these four types of contacts and each of them consists of three sections: stiffness model, slip model, and bonding model. As shown in **Fig. 6**, at contacts within mastic, the constitutive model was built by employing CSM [17] as the stiffness model, as well as setting the bonding strength and friction as the bonding model and slip model [17]. At contacts between aggregates and mastic, the constitutive model was built by employing CSM connected with a spring element in series as the stiffness model as well as setting the bonding strength and friction as the bonding model and slip model. At contacts between aggregates, the constitutive model was built by employing the contact-stiffness model [17] as the stiffness model as well as the slip model. In this case, no bonding model is available. Different from the contacts between aggregates, the constitutive model at contacts within aggregates is built with the contact-stiffness model, slip model, and a bonding model. The detailed information about cohesive-softening model, slip model, contact-stiffness model, and bonding model is included in the PFC2D/3D manual [17,21].

The constitutive models within discrete element model are micro-scale mechanical models built by synthesizing macro-scale material behaviors from the interaction of micro-scale components (balls or contacts to represent different material properties). In order to determine the model parameters, macro-scale properties which can be measured directly from laboratory specimens are needed. Liu et al. [15] developed and illustrated the conversion from macro-scale properties to micro-scale model parameters As shown in **Fig. 6**, Young's modulus (*E*) and flexural strength (σ_t) of basalt aggregates for the linear contact and contact-bond parameters, were obtained using the flexural beam test. Young's modulus (*E*) of mastic was obtained at $-10°C$ using a uniaxial compressive modulus test. The CSM parameters were determined using two experiments. Tensile strength (σ_t, 13.2 MPa) of mastic was obtained with the indirect tension (IDT) test following the AASHTO T322-03. The fracture energy (G_f) of mastic was determined to be 465.5 J/m^2 using a SE(B) test. The cohesive parameters obtained through laboratory tests may not represent the real intrinsic properties required for the CSM. Thus, calibration via test results is required to arrive at more appropriate local material parameters.

Heterogeneous Fracture Analysis

Current experiments limit the ability to measure all required parameters, especially the interface parameters. The modulus of the interface is assumed as the same value of mastic. The remaining parameters are estimated from the inverse analysis and calibrated based on the experimental test data of mixture.

The material parameters for each phase are shown in **Table 1**, and the calibrated cohesive energy was 250.9 J/m^2, which is less than the test result. The reason is that the laboratory fracture energy was measured using the area under the load-LLD curve, which overestimates the energy required to fully separate the material. The calibrated parameter was used for the remainder of this study.

FIG. 6

Determination of DEM model parameters.

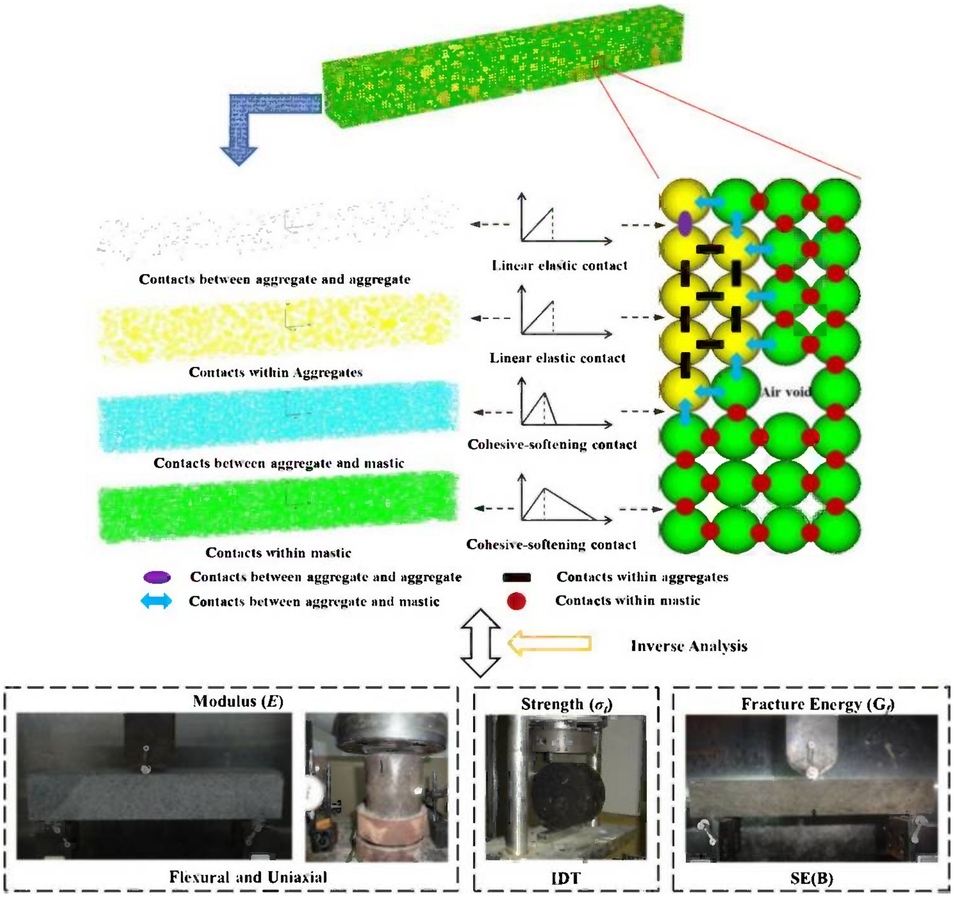

For the DEM simulations, constant velocity boundary conditions are imposed at the center of the top edge of the model in order to induce the desired Mode I fracture loading.

PROGRESSIVE FRACTURE PROCESS ZONE

As shown in **Fig.** *7(a)*, three DEM models give similar responses of force versus LLD. In particular, three numerical results have very good agreement on the peak load. The slight differentiation in softening response may be attributed to the cracks traversing through aggregates in the simulation, resulting in some fluctuations in the softening curves. However, **Fig.** *7(b)* shows that there are significant differences in both the initial loading and softening response on the force-displacement relationships from laboratory experimental results. Generally, the overall repeatability of the simulation appears to be totally satisfactory, with the discrete coefficients (the ratio of variance to average) being 1.7 and 2.6 % (peak load and fracture energy), while those of laboratory are 4.2 and 10.2 %, respectively. The significant variability of the experimental results can be attributed to the instability of equipment and manpower. Instead, digital samples being essentially computer-generated models have the potential for reproducing exact symmetric loading conditions so that it can provide better stabilized global response.

The 1# virtual specimen and 2# experimental specimen were selected as example. **Figure** *8(a)* provides the experimental and numerical macro results as described in terms of force versus LLD curve. The peak load and softening curve is quite reasonable as compared to experimental results. However, the most

TABLE 1 Parameters for heterogeneous DEM fracture model (9.5 NMAS at −10°C).

	Material Properties			DEM Contacts Input Parameters			
Phases	E (GPa)	σ_t (MPa)	Contacts Interactions	Normal Stiffness (GN/m)	Shear Stiffness (GN/m)	Bond Force (N)	δ_{sep} (m)
Aggregate	56.1	24.1	agg-agg	0.224	0.0911	–	–
			agg-in	0.224	0.0911	110	–
Mastic	6.5	13.2	mas-in	0.026	0.0093	53	3.8×10^{-5}
Interface	6.5	10.5	agg-mas	0.026	0.0093	42	3.2×10^{-5}

FIG. 7 Heterogeneous SE(B) numerical and experimental results at −10°C: (*a*) virtual test results, (*b*) experimental test results.

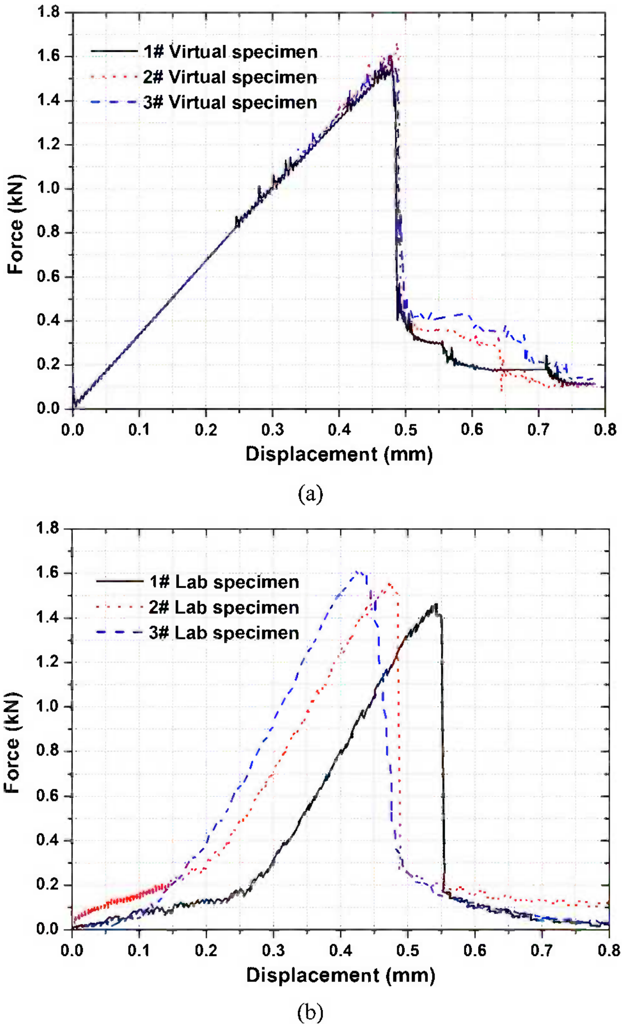

(a)

(b)

noticeable deviation is the initial loading portion of the curves due to the characteristic of the bilinear CSM. The macro fracture responses show generally good agreement with experimental results, although better results could be obtained with a further calibration procedure, and with a more sophisticated softening model, which is beyond the scope of current work. Furthermore, the force verses LLD curve also denotes that the brittleness of the thermosetting EAC is more significant than the conventional thermoplastic AC, especially at a low temperature.

Since a larger amount of energy supplied by the applied load is consumed within the fracture process zone (FPZ), the existence of the FPZ is significant for the fracture response after the peak load is reached. To illustrate this phenomenon in detail, the boundary of the zones of compression, tension, softening, and fracture in the SE(B) model as the force versus LLD curve varying are captured from the DEM simulation. It is noted that boundaries of several phenomena are used to illustrate the progressive fracture process, but not the real sizes.

FIG. 8 Progress fracture process of the heterogeneous DEM model with stress distribution: (*a*) load versus LLD curves, (*b*) numerical progressive fracture process.

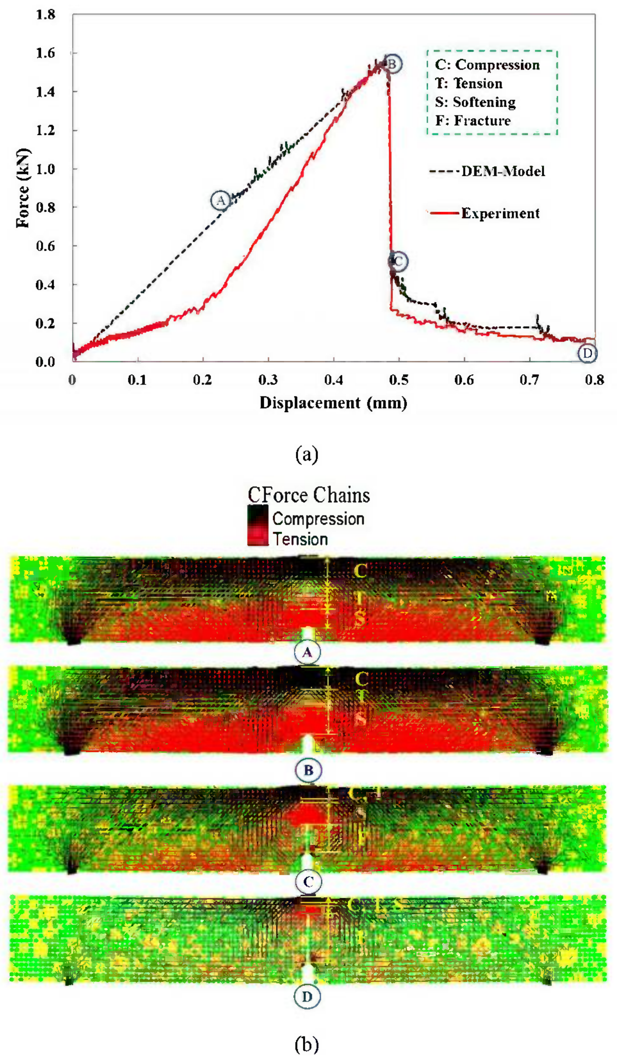

(a)

(b)

As shown in **Fig. 8(*b*)**, during the fracture simulation of a PFC3D synthetic material, the softening starts just at the time of the initiation of the first crack (A). The boundary of the softening zone increases until passing the peak load (B). It then gradually decreases as the post-peak fracture (C, i.e., crack propagation) and a macrocrack occurs. Finally, a substantial number of cracks traverse through a vertical path from the notch tip and the fracture occurs (D). Therefore, the current heterogeneous DEM model can capture the stress distributions of development of fracture zone during trial modeling.

PROGRESSIVE MICRO CRACK GROWTH PROCESS

Microcracks in a PFC3D synthetic specimen may only form between bonded particles. Thus, the number and location of potential microcracks are limited by the number and location of the bonds in the initial model. **Figure 9(*a*)** depicts the total number of normal- and shear-type microcracks (N_{fn} and N_{fs}, respectively) versus load-line displacement, and force versus LLD curve is also presented for comparison.

During a fracture test performed upon a PFC3D synthetic material, it is considered that the load where the first crack appears corresponds to the initial cracking measured in typical experiments. Although the thresholds depend on the literature reference and simulation level, it is quite reasonable as compared to test results based on the digital image correlation technology.

The potential crack path might traverse through aggregates, mastics and the interfaces. **Figure 9(*b*)** illustrates the development of microcracks within different contact interactions as the LLD increases. As the temperature decreases, the difference in the strength between epoxy asphalt mastic and aggregates decreases, resulting in some cracks traversing through the aggregates, although most cracks travel around the aggregates.

3D MICRO CRACK TRAJECTORIES

In a PFC3D synthetic specimen, the geometry and location of each microcrack are determined by the sizes and current locations of the two parent particles from which the microcrack originated. Each microcrack is assumed to be an 8-sided polygon whose axis lies along the line joining the two parent particles.

FIG. 9 Number of microcracks versus load-line displacement: (*a*) number of tensile and shear microcracks versus displacement, (*b*) number of microcracks within different contact interactions versus displacement.

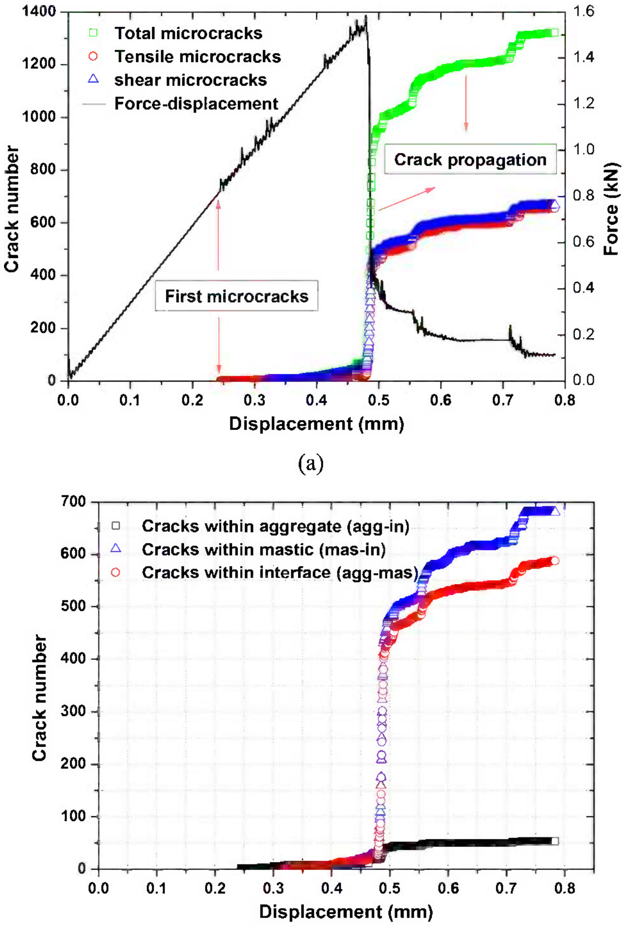

(a)

(b)

The center coordinate of the model is (0,0,0) and *x*, *y*, *z* axes represent the directions of length, height, thickness, respectively. As illustrated in **Fig. 10(*b*)**, the red tensile cracks tend to be oriented parallel with the direction of load application, and the black shear cracks tend to be oriented at approximately 45° to the direction of load application. The current 3D model provides a more realistic visualization of the progressive cracking process, where the microcracks initiate from the notch and propagate with tunneling through the model thickness in a vertical path from the notch tip.

As stated above, the initial cracking load is 0.846 kN, which corresponds to the point A as shown in **Fig. 8(*a*)**. As the applied force increases, the number of microcracks increases whereas the growth rate decreases. It can be assumed that the point B (peak load), as shown in **Fig. 8(*a*)**, approximately corresponds to the critical situation of the unstable crack propagation. As shown in **Fig. 9(*a*)** in conjunction with **Figs. 10(*c*)** and **10(*d*)**, it is noted that a huge substantial amount of microcracks ($N_f = N_{fn} + N_{fs}$, changes from 75 to 880) observed after the peak force has been reached, following with a sharp decrease of force (F, changes from 1.586 to 0.528 kN), which can be recognized as the process of the unstable crack propagation. As shown in the softening curve from **Fig. 10(*d*)**, a substantial amount of microcracks are clearly visible within the center area of the virtual specimen, followed by fracture occurred with the final 1322 microcracks including 655 normal- and 667 shear-type microcracks.

As shown in Figs. **11–13**, the internal material of a beam may be more likely to crack than the beam surface, resulting in an inside crack appeared earlier than a surface crack. Thus, the appearance of one thin surface crack cannot be absolutely considered as the starting point of initial cracking. This means that one should use laser speckle interferometry, photoelastic coating, and the strain gauges to determine the real fracture process in the laboratory. However, it can be seen from Figs. **8–13** that the discrete element modeling is able to visualize the crack development and to determine the critical points during the fracture process. As previously mentioned, the DIC system introduced here is capable of providing a dense and accurate displacement/strain field of asphalt mixture at the microstructural level and is therefore suitable for detecting both crack initiation and crack propagation.

According to the image correlation approach, a nephogram of the crack can be drawn using the relative displacement differential between the two sides of a crack, as shown in **Fig. 14(*a*)**. **Figure 14(*a*)** shows the 2D nephogram of the in-plane transverse displacement of the specimen. The in-plane displacement is discontinued and the discontinued value is exactly the size of the

FIG. 10 Numerical progressive cracks propagating process: (*a*) first microcrack at an applied force of 0.846 kN (crack initiation), (*b*) 14 microcracks at an applied force of 1.250 kN (stable crack propagation), (*c*) 75 microcracks at an applied force of 1.586 kN (peak load), (*d*) 880 microcracks at an applied force of 0.528 kN (unstable crack propagation), (*e*) 1322 microcracks in the specimen at fracture.

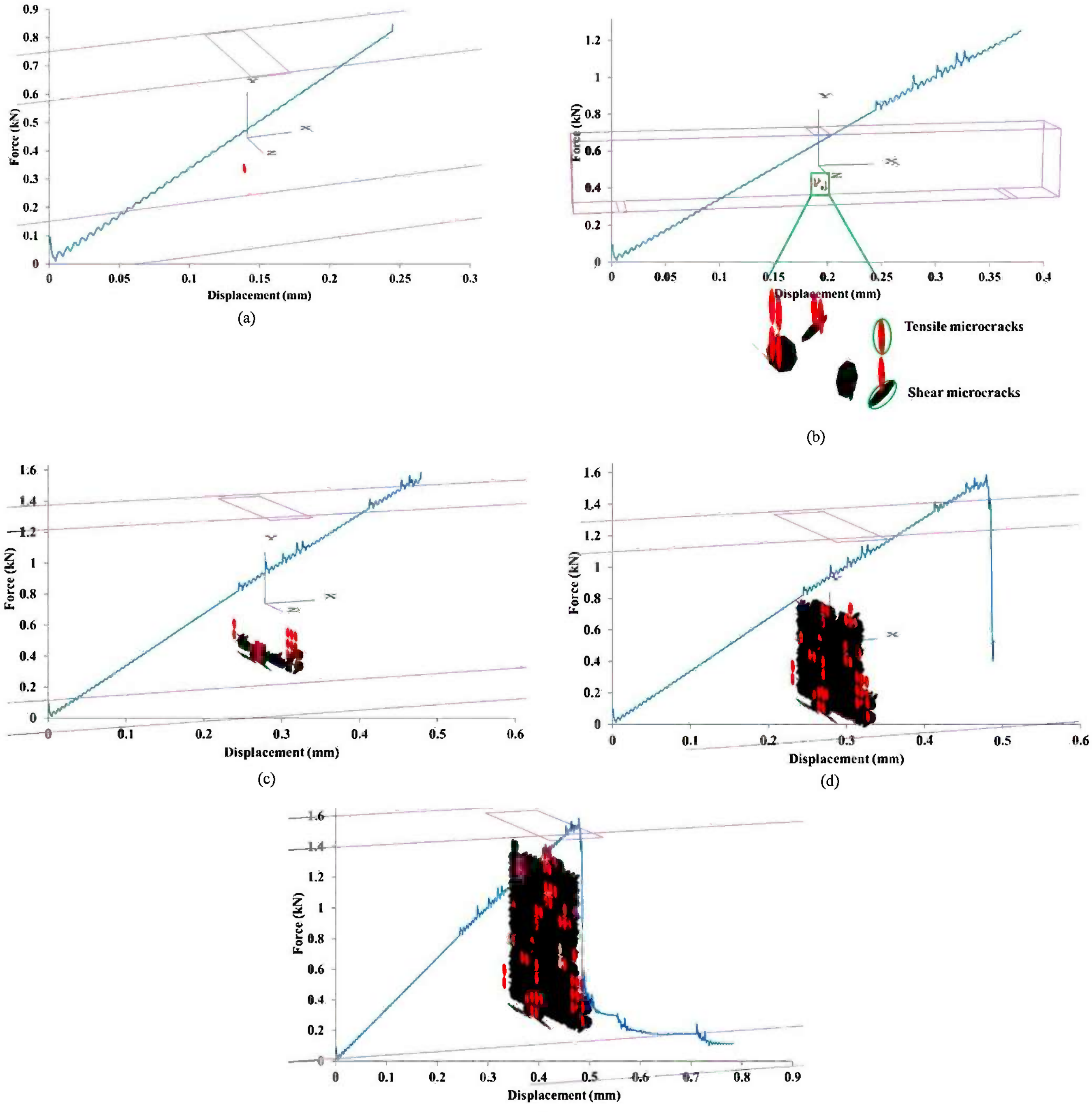

(a)
(b)
(c)
(d)
(e)

crack. Cracking can be easily observed from the 2D nephogram. The 3D nephgrams are also described as shown in **Fig. 14(*b*)** through **Fig. 14(*d*)** so as to accurately measure the size of the crack. The nephograms show that the *x*-axis represents the length direction of the beam, the *y*-axis, the height direction of the beam in accordance with the FE direction in **Fig. 14(*a*)** and the *z*-axis, the cracking size. The unit in the figure is pixel. According to the calibration results before the test, the relationship between length and pixel is about 14.3 μm per pixel. It can be seen from **Figs. 14(*b*)** to **14(*d*)** that the crack width at point F is measured to be 0.091, 0.14, and 0.19 mm, respectively.

As shown in **Table 2**, it is noted that the virtual test results using DEM models have a good agreement with those of DIC. Since the DIC system appears to be a successful technology in

FIG. 11 Positive surface of crack progressive development (x-0°,y-0°,z-0°): (*a*) first crack, (*b*) 14 cracks, (*c*) 75 cracks, (*d*) 880 cracks, (*e*) 1322 cracks.

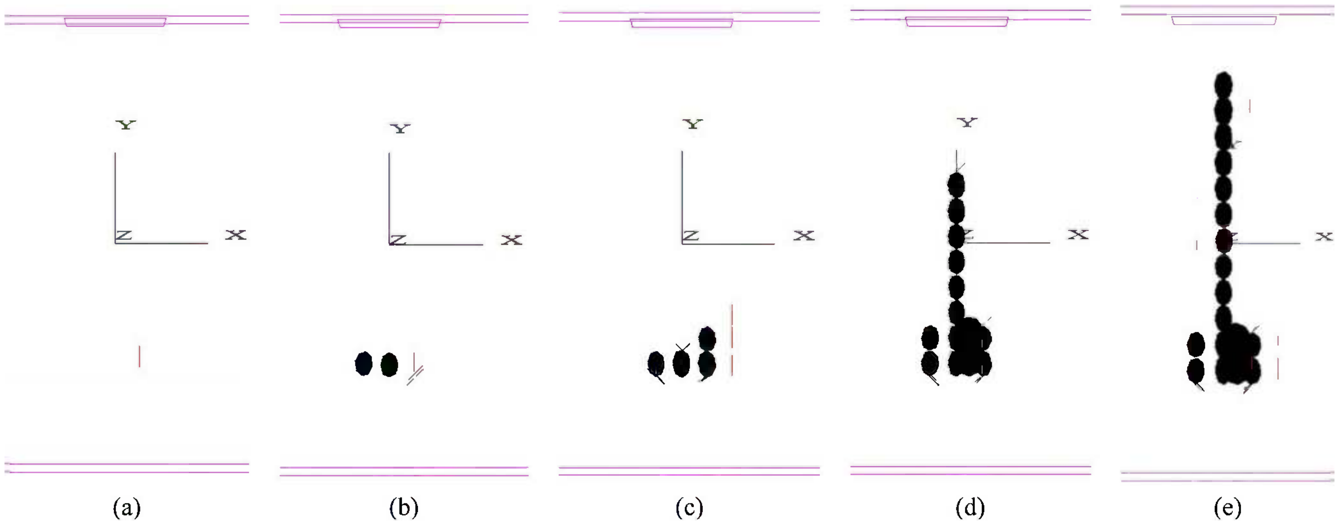

FIG. 12 Top surface of crack progressive development (x-90°,y-0°,z-0°): (*a*) first crack, (*b*) 14 cracks, (*c*) 75 cracks, (*d*) 880 cracks, (*e*) 1322 cracks.

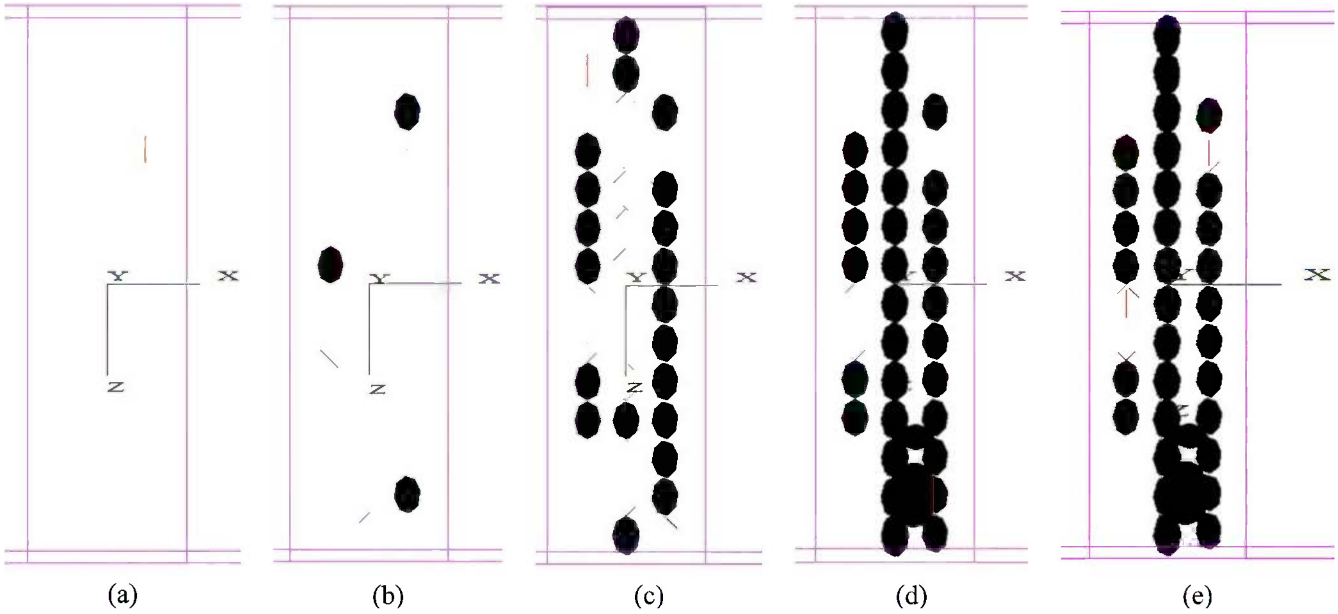

FIG. 13 Side surface of crack progressive development (x-0°,y-90°,z-0°): (*a*) first crack, (*b*) 14 cracks, (*c*) 75 cracks, (*d*) 880 cracks, (*e*) 1322 cracks.

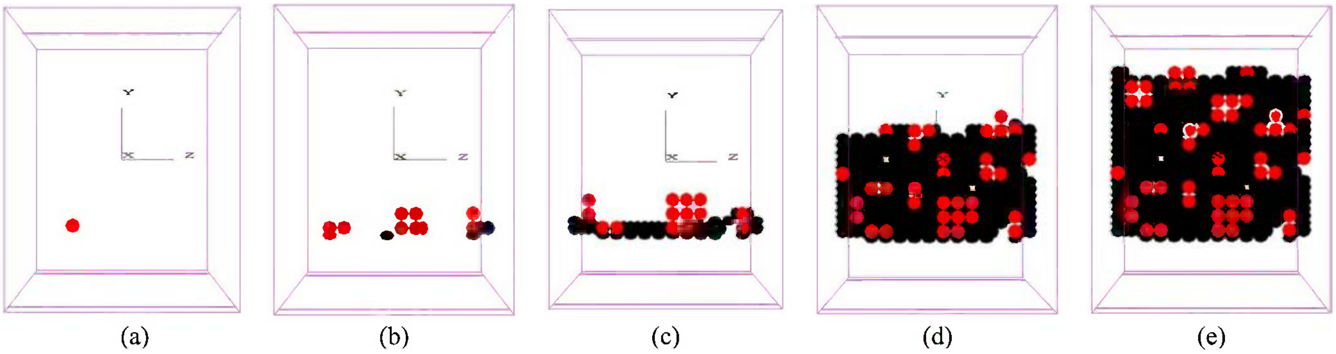

FIG. 14 Nephpograms of the crack during the fracture test: (*a*) 2-D horizontal displacement field at crack initiation, (*b*) nephogram at crack initiation, (*c*) nephogram at crack propagation, (*d*) nephogram at fracture.

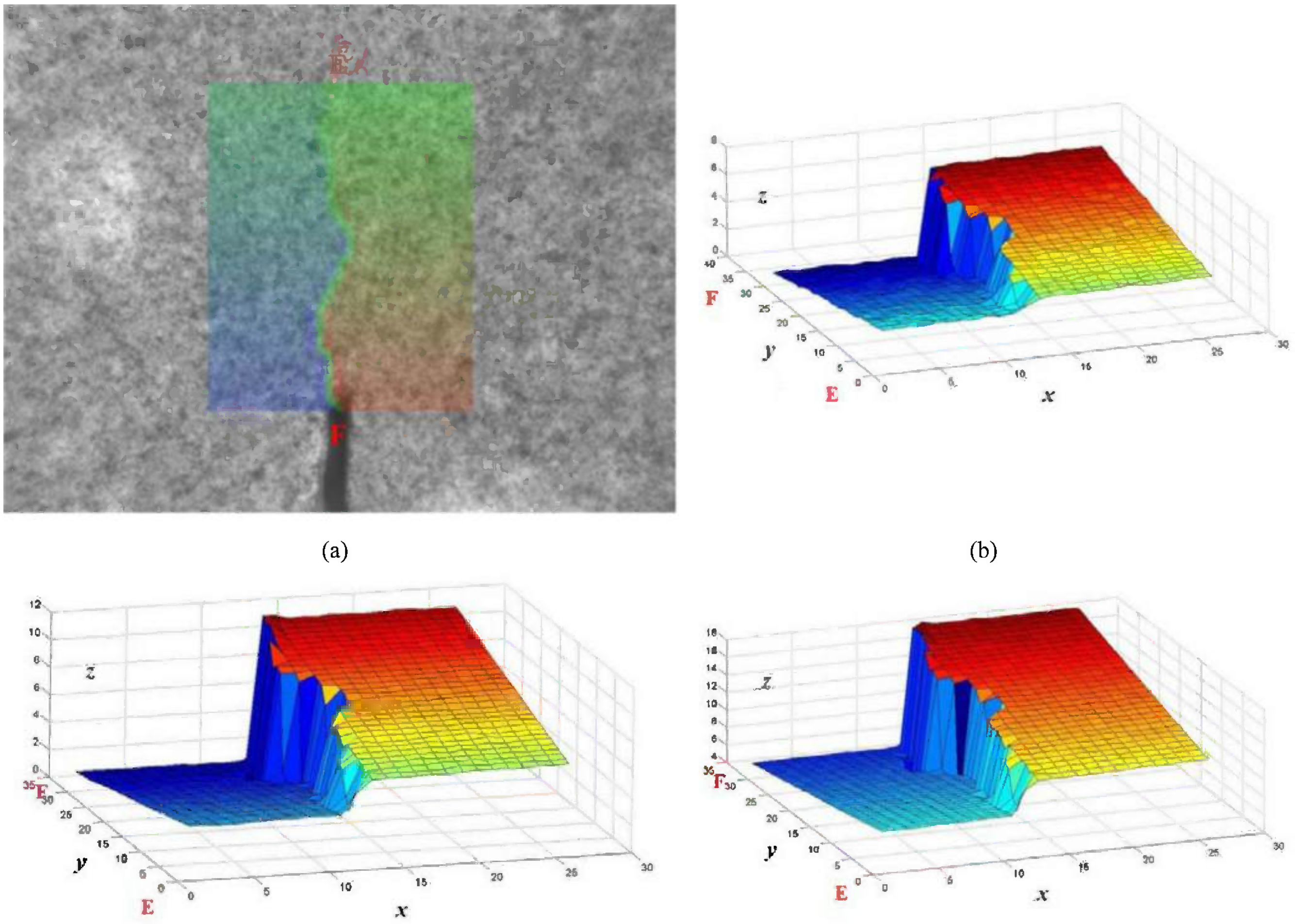

(a) (b)

(c) (d)

TABLE 2 Parts of numerical and experimental test results.

	DEM					DIC				
Index	1#	2#	3#	5#	Average	2#	4#	5#	7#	Average
Crack width at initial cracking	0.088	0.089	0.086	0.090	0.088	0.091	0.085	0.093	0.092	0.090
Crack width at peak load	0.16	0.14	0.15	0.15	0.15	0.14	0.11	0.13	0.14	0.13
Crack width at fracture	0.22	0.23	0.21	0.22	0.22	0.19	0.18	0.22	0.20	0.20
Initial cracking load	0.848	1.347	1.155	1.084	1.109	0.984	1.124	1.283	1.012	1.101
Peak load	1.586	1.670	1.607	1.582	1.611	1.564	1.530	1.593	1.614	1.575

the analysis of a 2D displacement full-field during asphalt concrete fracture testing [18,19], the 3D discrete element modeling is also demonstrated to be a powerful tool to investigate tcrack development in asphalt concrete material.

Conclusions

This study presents a user-defined microstructural DEM model, which combines laboratory experiments and numerical simulations to predict the fracture behavior and crack growth of heterogeneous epoxy asphalt concrete. Based on the results, the following conclusions can be drawn:

- A 3D heterogeneous DEM model for EAC is reconstructed using a randomly generating algorithm, to successfully achieve visualization and simulation. Although the user-defined model only partially represents real geometry of aggregate particles, it is a lab-independent approach.

- The calibrated cohesive-softening fracture model successfully simulates single-edge notched beam test. The overall repeatability of the simulation appears to be very satisfactory. Computer-generated models are equipped to reproduce exact symmetric loading conditions so that it can provide better stabilized global response. The trends in peak load and corresponding load-line displacement matched favorably with experimental results. Simulation results also demonstrate the ability to accurately capture the fracture zone evolution and stress distribution within the specimen.
- Crack initiation condition is determined as long as the first crack appears. The segment from initial cracking to peak load can be taken as the stage of the stable crack propagation, with peak load representing the critical unstable point of crack propagation; the segment crossing peak load describes the unstable fracture. The development of microcracks within different contact interactions is also captured, and it is demonstrated that due to the high strength of epoxy asphalt mastic at low temperature, some cracks traverse through aggregates, although most of them travel around the aggregates. The current 3D heterogeneous model provides a more realistic representation of the progressive cracking process, where the microcracks initiate from the notch and propagate with tunneling through the model thickness in a vertical path from the notch tip. The results performed using DEM method have good agreements with those of DIC system.
- The results shown in this work indicate that 3D heterogeneous microstructure models have the potential to use as an efficient design and analysis tool to reduce the amount of expensive and time-consuming experimental tests. Complex fracture behavior of EAC can be predicted when properties of mixture constituents and geometric features of aggregate particles are obtained and considered.
- The methods developed have potential applications in mix design and performance predictions for EAC.

ACKNOWLEDGMENTS

Authors would like to acknowledge the financial support provided by National Natural Science Foundation of China (NSFC, 51178114 and 51308116) and US National Science Foundation (NSF, Award number 1000172). NSF (1000172) and NSFC (51178114) supported the developed micromechanical modeling presented in this study. Meanwhile, NSFC (51308116) supported the application of the digital image correlation system presented in this study.

References

[1] Cubuk, M., Guru, M., and Cubuk, M. K., "Improvement of Bitumen Performance with Epoxy Resin," *Fuel.*, Vol. 8, No. 7, 2009, pp. 1324–1328.

[2] Huang, W., Qian, Z. D., Chen, G., and Yang, J., "Epoxy Asphalt Concrete Paving on the Deck of Long-Span Steel Bridges," *Chinese Sci Bull.*, Vol. 48, No. 21, 2003, pp. 2391–2394.

[3] Soares, J. B., Freitas, F. A., and Allen, D. H., "Crack Modeling of Asphaltic Mixtures Considering Heterogeneity of the Material," *Transp. Res. Rec.*, Vol. 1832, 2003, pp. 113–120.

[4] Aragão, F. T. S., Kim, Y. R., Lee, J. H., and Allen, D. H., "Micromechanical Model for Heterogeneous Asphalt Concrete Mixture Subject to Fracture Failure," *J. Mater. Civil Eng.*, Vol. 23, No. 1, 2011, pp. 30–38.

[5] Kim, H., Wagoner, M. P., and Buttlar, W. G., Simulation of Fracture Behavior in Asphalt Concrete Using a Heterogeneous Cohesive Zone Discrete Element Model," *J. Mater. Civil Eng.*, Vol. 20, No. 8, 2008, pp. 552–563.

[6] Kim, H. and Buttlar, W. G., "Discrete Fracture Modeling of Asphalt Concrete," *Int. J. Solids. Struct.*, Vol. 46, No. 13, 2009, pp. 2593–2604.

[7] Kim, H., Wagoner, M. P., and Buttlar, W. G., "Numerical Fracture Analysis on the Specimen Size Dependency of Asphalt Concrete Using a Cohesive Softening Model," *Constr. Build. Mater.*, Vol. 23, No. 5, 2009, pp. 2112–2120.

[8] Kim, H., Wagoner, M. P., and Buttlar, W. G., "Rate-Dependent Fracture Modeling of Asphalt Concrete Using the Discrete Element Method," *Can. J. Civil Engi.*, Vol. 36, No. 2, 2009, pp. 320–330.

[9] Kim, H., Wagoner, M. P., and Buttlar, W. G., "Micromechanical Fracture Modeling of Asphalt Concrete Using a Single-Edge Notched Beam Test," *Mater. Struct*, Vol. 42, No. 5, 2009, pp. 677–689.

[10] Wang, L. B., Park, J. Y., and Fu, Y. R., "Representation of Real Particles for DEM Simulation Using X–Ray Tomography," *Constr. Build. Mater.*, Vol. 21, No. 2, 2007, pp. 338–346.

[11] Liu, Y. and You, Z. P., "Visualization and Simulation of Asphalt Concrete With Randomly Generated Three-Dimensional Models," *J. Comput. Civil Eng.*, Vol. 23, No. 6, 2009, pp. 340–347.

[12] Buttlar, W. G. and You, Z. P., "Discrete Element Modeling of Asphalt Concrete: Microfabric Approach," *Transp. Res. Rec.*, Vol. 1757, 2001, pp. 111–118.

[13] You, Z. P. and Buttlar, W. G., "Micromechanical Modeling Approach to Predict Compressive Dynamic Moduli of Asphalt Mixture Using the Distinct Element Method," *Transp. Res. Rec.*, Vol. 1970, 2006, pp. 73–83.

[14] You, Z. P., Adhikari, S., and Dai, Q. L., "Three-Dimensional Discrete Element Models for Asphalt Mixtures. *J. Eng. Mech.*, Vol. 134, No. 12, 2008, pp. 1053–1063.

[15] Liu, Y. and You, Z. P., "Accelerated Discrete–Element Modeling of Asphalt-Based Materials with the Frequency-Temperature Superposition Principle," *J. Eng. Mech.*, Vol. 137, No. 5, 2011, pp. 355–365.

[16] Wang, J. Y., Qian, Z. D., and Wang, L. B., "Three-Dimensional Fracture Modeling of Epoxy Asphalt Concrete Using a Heterogeneous Discrete Element Model," *Proceedings of the 92nd Annual Meeting of the Transportation Research Board*, Washington, D.C., Jan 13–17, 2013.

[17] *PFC 2D Version 3.1.* (2004a). Itasca Consulting Group, Minneapolis, MN.

[18] Wagoner, M. P., Buttlar, W. G., and Paulino, H. G., "Development of a Single-Edge Notched Beam Test for

Asphalt Concrete Mixtures," *J. Test. Eval.*, Vol. 33, No. 6, 2005, pp. 452–460.

[19] Birgisson, B., Montepara, A., Napier, J., Romeo, E., Roncella, R., and Tebaldi, G., "Micromechanical Analyses for Measurement and Prediction of Hot–Mix Asphalt Fracture Energy," *Transp. Res. Rec.*, Vol. 1970, 2006, pp. 186–195.

[20] Birgisson, B., Montepara, A., Romeoa, E., Roncella, R., Napier, J. A. L., and Tebaldi, G., "Determination and Prediction of Crack Patterns in Hot Mix Asphalt (HMA) Mixtures," *Eng. Fract. Mech.*, Vol. 75, Nos. 3–4, 2008, pp. 664–673.

[21] *PFC 2D Version 3.1*. (2004b). Itasca Consulting Group, Minneapolis, MN.

Journal of Testing and Evaluation

doi:10.1520/JTE20130305 / Vol. 43 / No. 2 / March 2015 / available online at www.astm.org

Dharamveer Singh,[1] Fares Beainy,[2] Sesh Commuri,[3] and Musharraf Zaman[4]

Application of Intelligent Compaction Technology for Estimation of Effective Modulus for a Multilayered Asphalt Pavement

Reference

Singh, Dharamveer, Beainy, Fares, Commuri, Sesh, and Zaman, Musharraf, "Application of Intelligent Compaction Technology for Estimation of Effective Modulus for a Multilayered Asphalt Pavement," *Journal of Testing and Evaluation*, Vol. 43, No. 2, 2015, pp. 308–318, doi:10.1520/JTE20130305. ISSN 0090-3973

ABSTRACT

In this paper, a procedure for estimation of effective modulus of a multilayered hot mix asphalt (HMA) pavement using intelligent compaction (IC) is investigated. The study is conducted during the construction of an interstate highway (I-35) in Norman, OK. A complete coverage of the level of compaction of each of the asphalt pavement layers was recorded using the intelligent asphalt compaction analyzer (IACA). The collected IACA data allow determination of the level of compaction (density) at any selected location, for each layer, and provided a set of global positioning system (GPS) coordinates. Calibration procedures have previously been tested and validated by the authors to estimate the density of different types of pavements from IACA data. In this paper, a different calibration procedure is used to measure the dynamic modulus instead of the density of a pavement using IACA. Considering the IACA estimated density, the dynamic modulus of each of the selected locations for an individual pavement layer was measured from laboratory developed master curves. Thereafter, an effective modulus of the three-layer pavement system was calculated for all of the selected locations using Odemark's method. The proposed technique was verified by conducting falling-weight deflectometer (FWD) tests at these selected locations. Analyses of the results show that the proposed intelligent compaction technique may be promising in estimating the effective modulus of the pavement layers in a non-destructive manner. In addition, the Witczak model was used to estimate moduli of each of the pavement layers. The comparison of the Witczak model with FWD revealed that the model over-predicted the modulus significantly.

Keywords

intelligent compaction, stiffness, FWD, Witczak model

Manuscript received November 23, 2013; accepted for publication July 8, 2014; published online October 7, 2014.

[1] Assistant Professor, Dept. of Civil Engineering, Indian Institute of Technology, Mumbai, India,
e-mail: dvsingh@civil.iitb.ac.in

[2] Senior Research Engineer, Emerging Technologies, Advanced Engineering, Volvo Construction Equipment, Shippensburg, PA, United States of America,
e-mail: fares.beainy@volvo.com

[3] Professor, School of Electrical and Computer Engineering, Univ. of Oklahoma, Norman, OK, United States of America,
e-mail: scommuri@ou.edu

[4] Fellow of the ASCE, David Ross Boyd Professor and Aaron Alexander Professor, Associate Dean for Research and Graduate Programs, College of Engineering, Univ. of Oklahoma, Norman, OK, United States of America,
e-mail: zaman@ou.edu

Introduction

Quality assurance (QA) and quality control (QC) programs provide agencies and contractors the means to ensure that the desired results are obtained to produce high-quality and long-life pavements. Verification of the level of compaction is an essential component of QA and QC functions during the construction of hot mix asphalt (HMA) pavements [1–6]. Traditional QA and QC procedures include a variety of laboratory and field test methods that measure volumetric and surface properties of pavement materials [1]. Accurate real-time determination of stiffness and density of pavements during construction allows quality control of mix parameters to match as close as possible with the design values.

QA procedures that are commonly used during the construction of asphalt pavements require extraction of roadway cores from the finished pavement and may additionally require several measurements using a point-wise density measurement tool, such as a nuclear density gauge [7]. Whereas the density measured from the cores provide an accurate indication of quality, these tests are destructive in nature and a source of some of the performance issues, such as potholes that reduce the useful life of pavement [3,5,8]. In addition, any quality issues that are identified during this process cannot be easily rectified after the pavement has cooled down. Spot tests using nuclear or non-nuclear density gauges provide a quick measurement of the level of compaction, but have inherent limitations that reduce their effectiveness as QA methods. Furthermore, the above QA methods are time consuming to perform and are only helpful in determining the density of pavement layer at a discrete number of points [3,5].

Although the measurement of finished pavement density is a widely accepted method for acceptance, such measurements are only an indirect way of assessing the desired pavement property, namely, stiffness. Because pavement is designed to have adequate strength and stiffness to withstand traffic loads, the property of interest is stiffness of the finished pavement layers and not their densities. As a result, there is an emerging consensus that the stiffness (modulus) of the asphalt pavement is a better indicator of its performance [1,9].

The falling-weight deflectometer (FWD) is currently one of the most accepted techniques for measuring the modulus of different layers in an asphalt pavement [10,11]. The FWD measures road surface deflections resulting from an applied impulse loading. The measured surface deflections are used to backcalculate pavement layer moduli. However, the FWD testing method has several limitations that prevent its use as a QC method. Mainly, the FWD test has to be performed on pavements after they cool down, usually after 24 h of the completion of construction. As a result, any quality issues that are identified cannot be easily rectified. In addition, the backcalculation techniques that have been used so far have been cumbersome and time consuming [12].

The complexity of asphalt pavement compaction and the limitations of the spot tests have led researchers to develop advanced compaction technologies for improving the as-built quality of the pavements [7]. Intelligent compaction (IC) is a promising technology that can improve the quality of the road being constructed while reducing the associated cost and adverse environmental impacts. It provides a real-time complete coverage of the compaction area, and also reduces compaction costs resulting in significant overall construction cost saving [2,3,5,7,13–19]. As a result, several agencies in the United States have launched programs to evaluate different technologies and determine the maturity of such technologies for implementation [13].

The current research in intelligent compaction of HMA pavements demonstrates the application of continuous compaction control to achieve uniform compaction. Development of techniques to measure dynamic modulus of asphalt mixes over a wide range of temperatures and frequencies would be helpful in determining the quality of asphalt pavements during construction. The estimation of modulus in real time will alleviate the quality control issues during the construction of HMA pavements. Further, mapping of the modulus of the finished pavement will facilitate the acceptance testing of the constructed roadway.

In this paper, a procedure to estimate effective modulus of pavements during construction is demonstrated. Given a location on the pavement, the estimated modulus of each layer is used to determine the effective modulus of the combined pavement layers. The estimated modulus at the selected location is then verified through FWD measurements. The proposed method is non-destructive in nature and will help prevent under/over compaction of an asphalt pavement and achieve uniform compaction.

Intelligent Asphalt Compaction Analyzer (IACA)

The IACA functions on the hypothesis that the vibratory roller and the underlying pavement layers form a coupled system [14–16,20]. The response of the roller is determined by the frequency of its vibratory motors and the natural vibratory modes of the coupled system. Compaction of a pavement increases its stiffness and as a consequence, the vibrations of the compactor are altered. The knowledge of the properties of the mat and the vibration spectra of the compactor can, therefore, be used to estimate compacted modulus of the mat. That can be seen from the constitutive equation of the visco-elastic-plastic (VEP) model that was developed by Beainy et al. [8,21].

$$\begin{aligned}(m_d + m_a)\ddot{z}_d = (m_d + m_a)\ddot{z}_a = m_{ec} r_{ec} \omega_{ec}^2 \sin(\omega_{ec} t) \\ + m_d g + m_a g - k_{df}\left(z_d - z_f\right) - \eta_{df}\left(\dot{z}_d - \dot{z}_f\right) \\ - K_{ae}\left[z_a - \left(\frac{1}{\eta_{av}} \int_a^F e^{\frac{K_{av}}{\eta_{av}} t} dt + C_1 \right) e^{-\frac{K_{av}}{\eta_{av}} t} - \frac{\int_a^F dt + C_2}{\eta_{ap}} \right]\end{aligned} \tag{1}$$

where:

m_d = the mass of the roller drum (kg),

m_a = the mass of the asphalt mat under the roller drum (kg),

$m_{ec}r_{ec}$ = the moment of the eccentric mass,

ω_{ec} = the angular frequency of rotation,

z_a = the displacement of the asphalt layer,

F_a = the reaction force of the asphalt layer,

z_d = the displacement of the drum,

z_f = the displacement of the frame,

k_{df} = the drum-frame stiffness coefficient,

$\dot{z}_d$ = the velocity of the drum,

$\dot{z}_f$ = the velocity of the frame,

η_{df} = the drum-frame damping coefficient,

m_a = the asphalt weight,

$\ddot{z}_d$ = the vertical acceleration of the drum,

$\ddot{z}_a$ = the vertical acceleration of the asphalt pavement, and

$\ddot{z}_f$ = the acceleration of the frame.

The functional modules of the IACA system are schematically shown in **Fig. 1**. The sensor module (SM) consists of accelerometers for measuring the vibrations of the compactor drum during operation, infrared temperature sensors for measuring the surface temperature of the asphalt mat being compacted, and a user interface for specifying mix type and lift thickness. The feature extraction (FE) module computes the fast Fourier transform (FFT) of the input signal and extracts the features corresponding to vibrations at different salient frequencies. The artificial neural network (ANN) classifier is a multi-layer ANN that is trained to classify the extracted features into different classes where each class represents a vibration pattern specific to a pre-specified level of compaction. The calibrated compaction analyzer (CA) maps the output of the ANN into a density or modulus (depending on the used calibration procedure) value in real time [20].

Training IACA to Estimate the Level of Compaction

The IACA has to be trained and calibrated prior to its use to determine the compaction levels achieved. For that purpose, a 10-m-long control strip is constructed first. The vibrations of the roller are measured using an accelerometer mounted on the axle of the drum. The power content in the vibration signals during each roller pass is then calculated, and the lowest and the highest power levels are determined [14–16]. Five equally spaced power levels between the lowest and the highest power levels are identified and the features corresponding to these five power levels are used to train the ANN. During compaction, the ANN observes the features of the roller vibration and classifies them into one of the five reference levels. **Figure 2** shows typical features corresponding to the five different compaction levels extracted from the spectrogram of the vibration signals. In this figure, the lowest level corresponds to the case where the roller is operating with the vibration motors turned off, and the highest level corresponds to the case where the maximum vibrations are observed. It is assumed that the characteristics of the underlying pavement layers do not vary extensively over the project extent. Therefore, any changes in the spectra of the vibrations are a result of the compaction achieved in the topmost asphalt layer. Large variations in the properties of the underlying pavement layers are usually a result of pavement failure or insufficient site preparation. These effects result in low compaction, even after several roller passes and can easily be detected [21].

Calibrating IACA to Measure Modulus

After the IACA is trained to classify the vibrations into different levels of compaction, it is calibrated to reflect the modulus of pavement layer after construction. To accomplish this, dynamic modulus tests for the mix used in the construction of the asphalt mat are performed according to the AASHTO TP62-03 test method [22]. From the master curves, the modulus value (M_T) at the target density (i.e., 94 % of theoretical maximum specific gravity, equivalent to 6 % air voids) of the compacted mix (from the mix design sheet) is noted at selected temperature and frequency. This modulus value is assumed to be the highest modulus that can be achieved during the compaction of pavement. Likewise, the lowest modulus value observed, (M_{ld}), is assumed to correspond to the lay down density (i.e., 88 % of theoretical maximum specific gravity, equivalent to 12 % air voids) of the asphalt mat at same temperature and frequency. The modulus estimated by the ANN model (M_{NN}^i) at location $P_i(i = 1, \ldots, n)$, is then approximated as a linear relationship

FIG. 1

Functional schematic of the IACA.

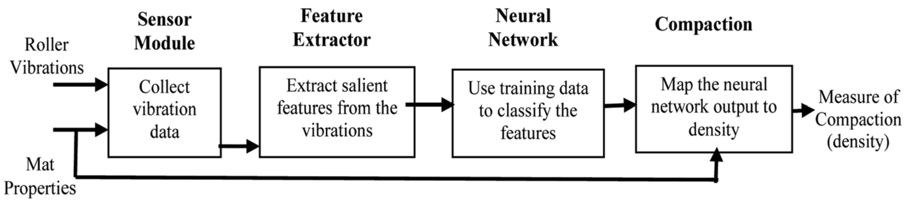

FIG. 2

Spectral features corresponding to five levels of compaction.

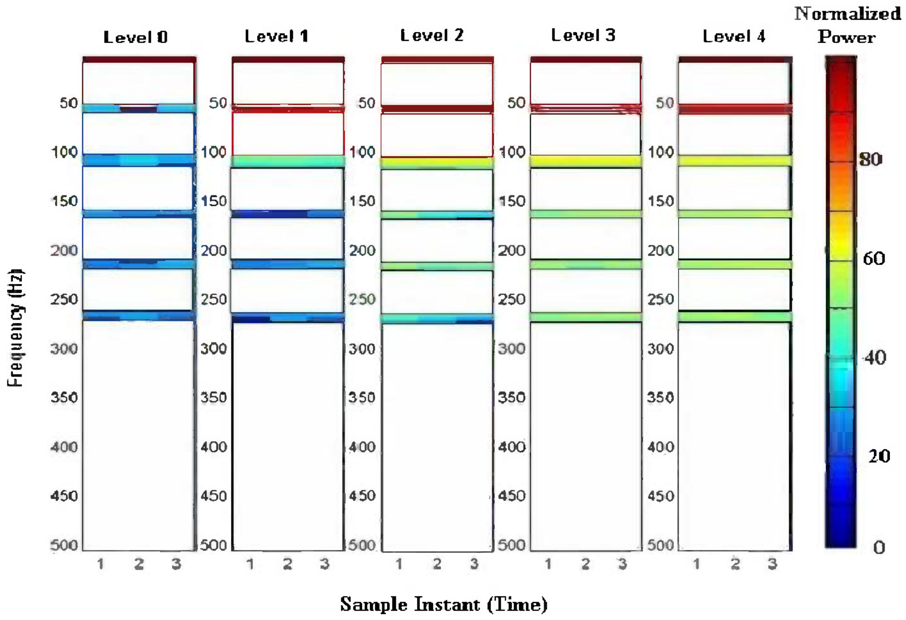

between the stiffness of the pavement and the observed levels of vibration:

$$M^{i}_{NN} = M_{ld} + k \times l^{i}_{NN} + \text{off} \tag{2}$$

where:

M^{i}_{NN} = modulus estimated by the neural network,

k = slope,

off = offset, and

l^{i}_{NN} = compaction level estimated by the neural network.

The initial slope is assumed to be equal to $(M_T - M_{ld})/$(number of compaction levels), and the initial offset is set to 0.

All of the modulus values that are used during calibration (M_T and M_{ld}) correspond to the standard temperature and frequency at which FWD measurements are provided (21°C and 5 Hz). Therefore, M^{i}_{NN} or the IACA estimated modulus value is at 21°C and 5 Hz.

It should be noted that the determination of the highest and lowest modulus values that can be achieved during the compaction of pavement for calibration purposes can be done through alternative methods. For example, empirical or ANN prediction models can be used to determine these values for a particular mix design. Several predictive models have been developed and evaluated, such as the original and modified Witczak equation, Hirsch model, etc. [23].

The modulus estimated by the IACA after the initial calibration is based on the assumption that the target modulus for the specified mix is indeed achieved during the compaction in the field. However, several factors, such as the compaction equipment, rolling pattern, lay-down temperature of the mix, lift thickness, etc., influence the actual modulus of pavement at any given location. To account for these deviations, the effective modulus of the compacted pavement were measured using a FWD, and the slope and offset in Eq 2 were recalculated to minimize the error between the IACA estimated and measured values. If the modulus measured at location P_i is represented by M^{i}_{FWD}, then the measurement error is given by e_i and can be calculated as

$$e_i = M^{i}_{NN} - M^{i}_{\text{FWD}} = M_{ld} + k \times l^{i}_{NN} + \text{off} - M^{i}_{\text{FWD}} \tag{3}$$

Minimizing the mean-square error (MSE), one obtains the desired slope, k:

$$k = \frac{\sum_{i=1}^{n} \left[\left(M^{i}_{\text{FWD}} - M^{i}_{ld} - \text{off} \right) \times l^{i}_{NN} \right]}{\sum_{i=1}^{n} \left(M^{i}_{NN} \right)^{2}} \tag{4}$$

The new offset is calculated as the mean error between the IACA estimated and the measured stiffness, that is

$$\text{off} = \frac{1}{n} \sum_{i=1}^{n} \left(M^{i}_{\text{FWD}} - M^{i}_{NN} \right) \tag{5}$$

It should be noted that the M^{i}_{FWD} (effective modulus) values were obtained from the calibration stretch. Therefore, the performance analysis by comparing the IACA estimated modulus to the FWD effective modulus in the validation stretch is still valid (**Fig. 3**).

FIG. 3 Illustrations of the lay-out of the calibration and validation stretches.

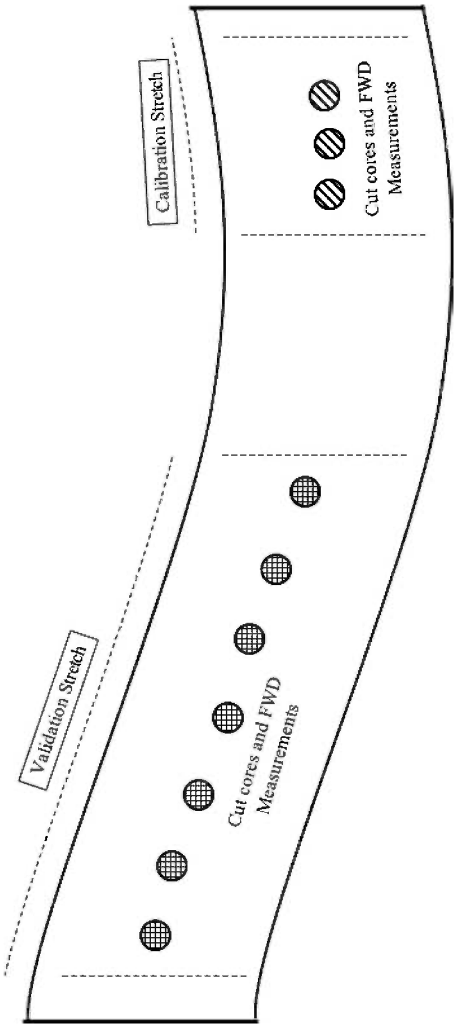

Field Testing and Validation

The ability of the IACA in estimating the dynamic modulus of a multi-layer HMA pavement was investigated during the construction of Interstate I-35 in Norman, OK. This project involved the expansion of the existing highway, stabilizing the subgrade to a depth of 200 mm using 10 % cement kiln dust (CKD), followed by a 200-mm-thick aggregate base. The base layer consisted of 100-mm-thick asphalt layers of 19-mm nominal maximum aggregate size (NMAS) S3 (64-22 OK), whereas second and third layers were constructed with 19-mm NMAS S3 (76-28 OK) consisting of 100-mm and 75-mm thicknesses, respectively.

Calibration of IACA System

MATERIAL COLLECTION AND SAMPLE PREPARATION

Loose HMA mixes of type S3 (PG 64-22 OK) and S3 (PG 76-28 OK) were collected from the construction site during the time of pavement construction. The S3 (PG 64-22 OK) type of mix was used in base layer, whereas S3 (PG 76-28 OK) mix was used in second and third layers of pavement. The nominal maximum aggregate (primarily limestone) size for all mixes was 19 mm. The base mix contained approximately 20 % 25-mm rock, 44 % manufactured sand, 11 % sand, 25 % recycled asphalt pavement (RAP), and 4.1 % PG 64-22 OK binder. The second and third layer mixes contained approximately 22 % 25-mm rock, 50 % manufactured sand, 13 % sand, 15 % recycled asphalt pavement (RAP), and 4.1 % PG 76-28 OK binder. The gradations and other volumetric properties of all HMA mixes are given in **Table 1** and **Table 2**, respectively. Loose HMA mixes were preheated in an oven, and specimens were compacted using a Superpave gyratory compactor (SGC). Three replicates of specimens were compacted at 6 %, 8 %, 10 %, and 12 % ± 1 % target air voids levels. Initially, samples having 150-mm diameters by 167.5-mm heights were prepared. Then, the test specimens of 100-mm-diameter samples were cored from the center of the gyratory compacted specimens, and sawed from each end of the specimen to get final sample of size 100-mm diameter by 150-mm height. The volumetric analysis was conducted to obtain effective binder content (V_{beff}), the voids in mineral aggregates (VMA), the voids filled with asphalt (VFA), and the air voids (V_a) for all of the mixes (**Table 3**).

DYNAMIC MODULUS TESTING

Dynamic modulus was measured for all collected mixes at four different air voids: 6 %, 8 %, 10 %, and 12 %. The wide range of air voids were selected to capture variation in the compaction quality during the construction of a pavement in the field.

TABLE 1 Aggregate gradations.

Material (%)	Base Layer	Second and Third layer
25 mm rock	20	22
Manufactured sand	44	50
Sand	11	13
RAP[a]	25	15
Sieve size (mm)	Gradation (% passing)	
25	100	100
19	98	98
12.5	87	87
9.5	80	80
4.75	58	62
2.36	37	40
1.18	25	27
0.6	19	20
0.3	12	12
0.15	4	5
0.075	2.9	2.8

[a] RAP, reclaimed asphalt pavement.

TABLE 2 Volumetric property of mixes.

Volumetric Properties	Base Layer	Second and Third Layer
G_{mm}	2.505	2.523
G_{se}	2.671	2.677
G_{sb}	2.645	2.657
G_b	1.01	1.01
Binder type	PG 64-22	PG 76-28
P_b (%)	4.1	4.1
VMA (%)		
Minimum	14.1	14.81
Maximum	20.4	20
VFA (%)		
Minimum	39.9	41.9
Maximum	62.2	60.8
Va (%)	6, 8, 10, 12	
Aggregate type	Limestone	Limestone
Mix type	Recycled	Recycled

Note: G_{mm} = maximum theoretical specific gravity mixture, G_{sb} = bulk specific gravity of aggregate, G_{se} = effective specific gravity of aggregate, G_b = specific gravity of binder, P_b = asphalt content, VMA = voids in mineral aggregates, VFA = voids filled with asphalt, and V_a = air voids.

Dynamic modulus tests were performed using a MTS servo-hydraulic testing system. The test specimen was placed in an environmental chamber and allowed to attain equilibrium to the specified testing temperature ±0.5°C. The temperature of the specimen was monitored using a dummy specimen with a thermocouple mounted at the center. Two linear variable differential transducer (LVDTs) were mounted on the specimen. Two friction-reducing end treatment or teflon papers were placed between the specimen ends and loading plates. To begin testing, a minimal contact load was applied to the specimen. A sinusoidal axial compressive load was applied in a cyclic manner to the specimen without causing any impact. The test was run on each test specimen at four different temperatures, namely, 4°C, 21°C, 40°C, and 55°C, starting from the lowest temperature to the highest temperature. For each temperature level, the test was run at different frequencies from the highest to the lowest, namely, 25, 10, 5, 1, 0.5, and 0.1 Hz. Prior to testing, the sample was conditioned by applying 200 cycles of load at a frequency of 25 Hz. The load magnitude was adjusted based on the material stiffness, air void content, temperature, and frequency to keep the strain response within 50–150 micro-strains. The data was recorded for the last five cycles of each sequence. Dynamic modulus tests were performed according to the AASHTO TP62-03 [22].

DEVELOPMENT OF THE MASTER CURVES

Dynamic modulus of asphalt mixes can be shifted along the frequency axis to form single characteristic master curves at a desired reference temperature or frequency. The master curve is generated at a reference temperature of 21°C using the procedure outlined in Bonaquist and Christensen [24]. Equations 6 and 7 show the sigmoidal function and shift factor used for

TABLE 3 Volumetric properties of compacted samples.

		Base Layer (mix-S3 64-22)			Second and Third Layer (mix-S3 76-28)		
		Sample					
Target Air Voids (%)	(%)	1	2	3	1	2	3
6	V_a	5.4	5.6	5.6	6.5	6.4	6.4
	VMA	14.1	14.3	14.3	14.9	14.8	14.7
	VFA	62.2	61.4	61.5	60.1	60.4	60.8
	V_{beff}	8.8	8.8	8.8	8.9	8.9	9.0
8	V_a	7.3	7.2	7.2	8.3	8.1	7.9
	VMA	15.8	15.7	15.7	16.5	16.3	16.1
	VFA	54.5	54.7	54.9	53.3	53.9	54.6
	V_{beff}	8.6	8.6	8.6	8.8	8.8	8.8
10	V_a	9.3	9.6	9.1	9.6	10.2	9.8
	VMA	17.7	17.9	17.5	17.7	18.3	17.9
	VFA	47.7	46.9	48.3	48.9	47.0	48.3
	V_{beff}	8.4	8.4	8.4	8.6	8.6	8.6
12	V_a	11.5	12.4	12.4	12.2	11.7	12.0
	VMA	19.7	20.4	20.4	20.0	19.6	19.9
	VFA	41.8	39.9	39.9	41.9	43.2	42.3
	V_{beff}	8.2	8.1	8.1	8.4	8.4	8.4

Note: V_a = air voids, VMA = voids in mineral aggregates, VFA = voids filled with asphalt, and V_{beff} = effective asphalt content by volume.

fitting the master curve. A nonlinear optimization program was used for simultaneously solving these unknown parameters:

$$\log|E^*| = \delta + \frac{(\max - \delta)}{1 + e^{\beta+\gamma\left[\log(f)+c\left(10^{(A+\mathrm{VTS}\log T_R)} - \log \eta t = r\right)\right]}} \tag{6}$$

The shift factor used here was of the following form:

$$a(T) = \frac{f_r}{f} \tag{7}$$

where:

max = the maximum $|E^*|$ for a particular mix,

f_r = the reduced frequency at reference temperature,

f = the frequency at a particular temperature,

$\eta t = r$ = the viscosity of binder at reference temperature,

A = the regression intercept of viscosity-temperature curve,

VTS = the regression slope of viscosity-temperature susceptibility,

$a(T)$ = the shift factor as a function of temperature and age, and

δ, β, γ, c = fitting parameters.

The A and VTS parameters for PG 64-22 OK (10.98, −3.680), and PG 76-28 OK (9.2, −3.024) were taken from the MEPDG guide [25]. The constructed master curves for base, second, and third layers mixes are shown in **Fig. 4** and **Fig. 5**, respectively. It can be seen from **Figs. 4** and **5** that dynamic modulus decreases as air voids increases. Developed master curves were then used to estimate dynamic modulus of each layers at given air voids, temperature, and frequency.

The "goodness-of-fit" statistic, S_e/S_y (standard error of the estimated/standard deviation), and correlation coefficient (R^2) were used to assess the validity of the correlation between laboratory measured modulus and master curve fit equation [26]. Based on these criteria, the developed master curve equations in this study were found to be in excellent correlation with laboratory measured data. The coefficients and the fitting statistics of the master curves are summarized in **Table 4**.

FIG. 4 Master curves for base layer mixes (S3 64-22).

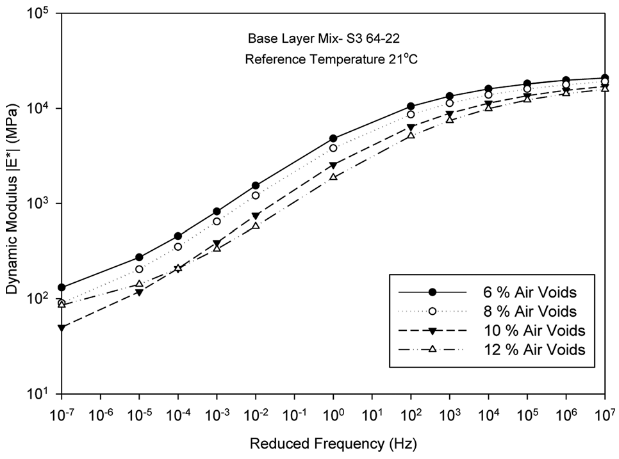

FIG. 5 Master curves for second and third layers mixes (S3 76-28).

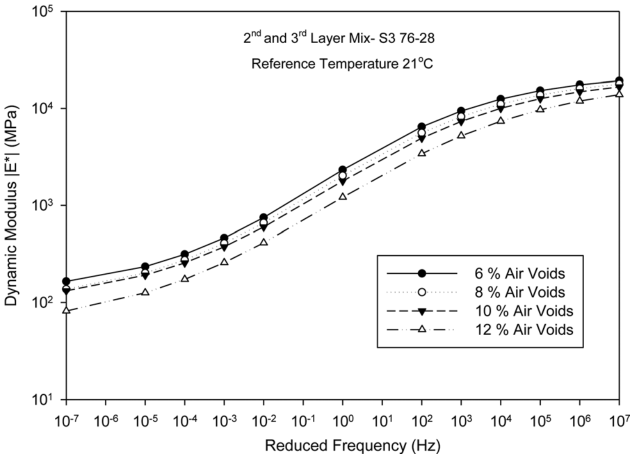

Results and Discussion

ESTIMATING DYNAMIC MODULUS OF EACH PAVEMENT LAYER

A validation section, approximately 150 m in length, was selected and seven test locations, approximately 20 m apart, were marked in the middle of the lane for verification analysis. The IACA was used to estimate the modulus of each of the layers during the construction. The IACA records the global positioning system (GPS) coordinates of the roller in real time and the modulus estimated at this location during each roller pass.

The IACA was used to collect the GPS data and the modulus readings during the compaction of the all three layers (base, second, and third layers). First, the test points were marked on base layer, and the IACA data was collected. The GPS location of these points was recorded to locate these test locations on each pavement layer. Similar points were marked on second and third layers and the IACA data was collected during the compaction of each of these layers. The IACA estimated values of each layer and at every location are shown in **Table 5**.

The dynamic modulus was also estimated using the Witczak predictive model for comparison purposes with IACA. The estimated values using the Witczak equation for each layer and at every location are presented in **Table 6**.

ESTIMATING EFFECTIVE MODULUS OF PAVEMENT LAYERS

The Odemark method was used to transform a system consisting of layers with different moduli into an equivalent system where the thicknesses of the layers are altered but all layers have the same modulus. The transformation assumes that the stiffness of the layer remains the same, i.e., $I \times E/(1-\mu^2)$ remains

TABLE 4 Master curve parameters

Air Voids (%)	max E^* (MPa)	δ	β	γ	c	$R2$	S_e/S_y	Fit
Base layer (mix-S3 64-22)								
6	23084	1.81	−1.02	−0.43	1.20	0.99	0.07	Excellent
8	22256	1.54	−0.98	−0.39	1.20	0.99	0.05	Excellent
10	21232	1.23	−0.86	−0.37	1.04	0.99	0.06	Excellent
12	19942	1.72	−0.41	−0.40	1.05	0.99	0.08	Excellent
Second and third layer (mix-S3 76-28)								
6	22826	2.10	−0.25	−0.45	1.24	0.99	0.04	Excellent
8	22027	1.99	−0.24	−0.42	1.18	0.99	0.05	Excellent
10	21157	1.98	−0.17	−0.42	1.12	0.99	0.04	Excellent
12	20182	1.71	−0.12	−0.37	1.13	0.99	0.05	Excellent

Shift factors log(aT)	Base layer (mix-S3 64-22)				Second and third layer (mix-S3 76-28)			
	4°C	21°C	40°C	55°C	4°C	21°C	40°C	55°C
6	2.66	0.00	−2.23	−3.60	2.24	0.00	−1.96	−3.20
8	2.65	0.00	−2.22	−3.58	2.13	0.00	−1.86	−3.04
10	2.30	0.00	−1.93	−3.11	2.02	0.00	−1.77	−2.89
12	2.32	0.00	−1.95	−3.14	2.04	0.00	−1.78	−2.91

constant, where I = moment of inertia, E = layer modulus, and μ = Poisson's ratio [27–30].

This approach is used in the present paper to calculate the effective modulus of the three layers that constitute the pavement on I-35. The IACA data collected during the compaction of each of the pavement layers was first used to determine density at selected location. The estimated density (air voids) was then used to determine dynamic modulus at each of the each test locations. The effective modulus (E_{eff}) of three layers of pavement was calculated using Eq 8. The effective moduli were calculated at 21°C and 5-Hz frequency (**Table 6**). A similar approach was used by several other researchers to find the effective modulus for layered system of pavement [31–33].

$$E_{\text{eff}} = \left[\frac{C_2\left(C_1 h_1 \sqrt[3]{E_1} + h_2 \sqrt[3]{E_2}\right) + h_3 \sqrt[3]{E_3}}{h_1 + h_2 + h_3}\right]^3 \quad (8)$$

where:

E_1, E_2, and E_3 = dynamic modulus of third (top layer), second, and base layer,

h_1, h_2, and h_3 = the thickness of respective layers, and

C_1 and C_2 = the correction factors to obtain better agreement with exact theory of elasticity [29,34].

The value of correction factors depend on the layer thicknesses, modular ratios, Poisson ratios, and the number of layers in pavement structure. In the present study, correction factors were taken as $C_1 = 1$, whereas $C_2 = 0.8$.

Verification of Effective Modulus

A verification of the IACA measured modulus (effective modulus using the Odemark method) was done by conducting FWD testing on seven test locations that were marked before for

TABLE 5 IACA and FWD measured effective moduli for different layers.

Laboratory measured base and surface layer: 21°C at 5 Hz

	Measured Dynamic Modulus (MPa)			IACA Effective	FWD Effective	Ratio Effective Modulus
Point	Base Layer	Second Layer	Third Layer	Modulus (MPa)	Modulus (MPa)	(FWD/IACA)
T1	5406	2190	3049	2365	3062	1.29
T2	5070	2659	3456	2502	2482	0.99
T3	4910	3227	3576	2637	2353	0.89
T4	5889	2751	3227	2667	2696	1.01
T5	4963	3155	3155	2554	2878	1.13
T6	4556	3227	3191	2482	2657	1.07
T7	3880	2345	3617	2161	2760	1.28

TABLE 6 Witczak and FWD effective moduli for different layers.

Witczak predicted base and surface layer: 21 Hz at 5 Hz

	Predicted Dynamic Modulus (MPa)			Witczak Effective	FWD Effective	Ratio Effective Modulus
Points	Base Layer	Second Layer	Third Layer	Modulus (MPa)	Modulus (MPa)	FWD/Witczak
T1	4669	3954	4997	2991	3062	1.02
T2	4478	4560	5388	3139	2482	0.79
T3	4381	5177	5492	3263	2353	0.72
T4	4915	4669	5177	3255	2696	0.83
T5	4413	5105	5105	3196	2878	0.90
T6	4154	5177	5141	3140	2657	0.85
T7	3673	4164	5526	2832	2760	0.97

estimating density using the IACA. In FWD test, a transient load is dropped from a specified height on a 300 mm diameter circular plate with a thin rubber pad mounted underneath. The load and deflection is measured using load cell and sensors set on the ground. Seven sensors were placed at 0, 200, 300, 450, 600, 900, and 1500 mm away from the center of the loading plate. In the present study, the FWD test was conducted on a third layer of pavement using a Dynatest FWD test system. A numerical backcalculation software program, MODULUS 6.0, was used to process the FWD raw data so as to determine the modulus value [35]. The backcalculated modulus is often called the effective modulus because the value represents the effect of the layer within the whole pavement structure. The effective modulus was calculated at 21°C to compare this modulus with laboratory measured effective dynamic modulus. Because the FWD loading induces a pulse of duration of 0.03 s [36], which is equivalent to a test frequency of 5.3 Hz ($1/0.03/2\pi$), hence, the comparisons in this paper are performed using modulus values calculated at 21°C and 5 Hz frequency. **Table 5** shows the results of the FWD test as well as the IACA effective modulus. **Table 6** shows the results of the FWD test as well as the Witczak effective modulus.

FIG. 6 Comparison of IACA, Witczak, and FWD effective modulus.

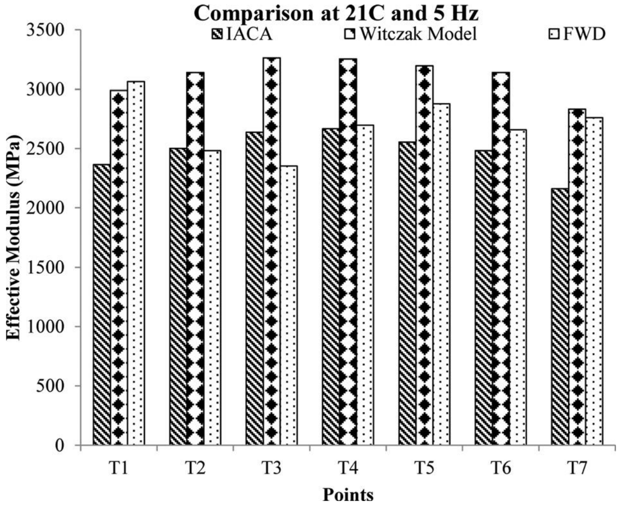

It is evident from **Fig. 6** that the modulus estimated by the proposed IACA method is in good agreement with the FWD effective modulus measurements. The ratio of FWD to IACA effective modulus is shown in **Table 1**. It can be seen that the ratio between FWD to IACA effective modulus is close to 1, indicating that the proposed approach is capable of measuring effective modulus of a multi-layer pavement system. However, the FWD effective modulus readings show about 30 % variation in the measured modulus for locations with identical density. Such reduction in the modulus values at certain locations might be because of variation in the subgrade, thickness of each layer, and inconsistency in the mix [37,38]. Therefore, the error between the measured and estimated modulus is within the range of the measurement accuracy of the FWD device. As evident from **Table 6** and **Fig. 6**, the Witczak model over-predicts the dynamic modulus. Ratio between effective modulus value calculated from FWD and Witczak falls within range of 0.72 to 1.02, indicating that the Witczak model over-predicted the modulus approximately 40 %. Likewise, a comparison of the Witczak model and IACA estimated modulus reveals that the Witczak over-estimated the modulus close to 21 %. Overall, results indicate that the proposed approach shows a better agreement with the currently adopted FWD technique. However, future validation must be done to further validate this approach by doing testing on different types of pavement (considering different thickness and mix type).

Concluding Remarks

An artificial neural network-based Intelligent Asphalt Compaction Analyzer (IACA) to determine the effective stiffness of a pavement layer during construction was demonstrated in this paper. The following conclusions can be drawn based on the results and discussion presented in the paper.

- Laboratory measured dynamic modulus values for different levels of air voids indicate that compaction has a significant effect on the quality (stiffness) of a pavement.
- The master curves can be used to estimate dynamic modulus values for a wide range of temperature and frequency encountered during and after construction of a pavement.
- IACA estimated real-time density can be converted into the stiffness using master curves, and IACA can provide the stiffness values over the entire pavement in a non-destructive manner. The proposed approach was validated using FWD.
- Comparison of IACA effective modulus with FWD effective modulus indicates that the proposed technique can estimate the effective modulus of the pavement layers in real time during the construction process.
- Comparison of Witczak model effective modulus with FWD effective modulus shows that the Witczak model over-predicted the stiffness, therefore, may not be used as confidently as compared to the proposed IACA method.

Overall, the proposed method is non-destructive in nature and will help prevent under-/over-compaction of the asphalt pavement and achieve uniform compaction of the pavement. Research is currently underway to validate the performance of the IACA during the compaction of warm mix asphalt pavements and during the compaction of stabilized soil subgrades. It is recommended that a future study be conducted considering the latest predictive models and approaches to compare estimation of effective modulus and to evaluate visco-elastic behavior of a pavement system.

ACKNOWLEDGMENTS

This work is funded through grants from the Highways for Life Program, FHWA, Washington, D.C.; Volvo Construction Equipment Company, Shippensburg, PA; and Oklahoma Transportation Center (OTC), Oklahoma City, OK.

The writers thank Mr. Eric Weaver, Research Highway Engineer, FHWA Office of Infrastructure R&D, McLean, Virginia, and Mr. Victor Gallivan, Asphalt Pavement Engineer, FHWA Office of Pavement Technology, Indianapolis, IN, for their numerous suggestions and assistance during this project. The writers also express their sincere gratitude to Haskell Lemon Construction Company, Oklahoma City, OK, and Imran Asif (Graduate student at the University of Oklahoma) for their assistance during every phase of this project.

References

[1] Von Quintus, H. L., Rao, C., Ninchin, R. E., Nazarian, S., and Prowell, B., "NDT Technology for Quality Assurance of HMA Pavement Construction," *Report No. 626*, National Cooperative Highway Research Program, Washington, D.C., 2009.

[2] White, D. J. and Thompson, M. J., "Relationships Between In Situ and Roller-Integrated Compaction Measurements for Granular Soils," *J. Geotech. Geoenviron. Eng.*, Vol. 134, No. 12, 2008, pp. 1763–1770.

[3] Maupin, G. W., "Preliminary Field Investigation of Intelligent Compaction of Hot-Mix Asphalt," Virginia Transportation Research Council, Charlottesville, VA, 2007.

[4] Akkinepally, R., 2006, "Quality Control and Quality Assurance of Hot Mix Asphalt Construction in Delaware," Master's thesis, University of Delaware, Newark, DE.

[5] Briaud, J. L. and Seo, J., "Intelligent Compaction: Overview and Research Needs," Texas A&M University, College Station, TX, 2004.

[6] Beainy, F., 2011, "Non-Contact Sensor for the Real-Time Measurement of Quality of Asphalt Pavements during Compaction," Ph.D. dissertation, University of Oklahoma, Norman, OK.

[7] Zambrano, C., Drnevich, V., and Bourdeau, P., "Advanced Compaction Quality Control," Indiana Department of Transportation, Indianapolis, IN, 2006.

[8] Beainy, F., Commuri, S., Zaman, M., and Syed, I., "Visco-Elastic-Plastic Model of Asphalt-Roller Interaction," *Int. J. Geomech.*, Vol. 13, No. 5, 2013, pp. 581–594.

[9] National Research Council, "Simple Performance Tests: Summary of Recommended Methods and Database," *NCHRP Report 547*, The National Academies Press, Washington, D.C., 2006.

[10] Abdallah, I., Yuan, D., and Nazarian, S., "Integrating Seismic and Deflection Methods to Estimate Pavement Moduli," *J. Transport. Res. Rec.*, No. 1755, 2001, pp. 43–50.

[11] Scullion, T., "Perpetual Pavements in Texas: The State of the Practice," *Technical Report FHWA/TX-05/0-4822-1*, Texas Transportation Institute, College Station, TX, 2007.

[12] Ceylan, H., Gopalakrishnan, K., and Kim, S., "Improving the Accuracy and Usability of Iowa Falling Weight Deflectometer Data," *Final Report, InTrans Project 11-415*, Iowa Department of Transportation, Federal Highway Administration, Ames, IA, 2013.

[13] CTC and Associates LLC and WisDOT Research and Communication Services, "Intelligent Compaction of Soils," Wisconsin Highway Research Program, Madison, WI, 2006.

[14] Singh, D. V., Mai, A. T., Beainy, A. F., Commuri, S., and Zaman, M. M., "In-Situ Assessment of Stiffness during the Construction of HMA Pavements," *Int. J. Pavement Res. Technol.*, Vol. 4, No. 3, 2011, pp. 131–139.

[15] Commuri, S., Mai, A., and Zaman, M., "Calibration Procedures for the Intelligent Asphalt Compaction Analyzer," *ASTM J. Test. Eval.*, Vol. 37, No. 5, 2009, pp. 454–462.

[16] Commuri, S., Mai, A., and Zaman, M., "Neural Network-Based Intelligent Compaction Analyzer for Estimating Compaction Quality of Hot Asphalt Mixes," *J. Constr. Eng. Manage.*, 137, No. 9, 2009, pp. 634–644.

[17] Camargo, F., Larsen, B., Chadbourn, B., Roberson, R., and Siekmeier, J., "Intelligent Compaction: A Minnesota Case History," *54th Annual University of Minnesota Geotechnical Conference*, Feb 17, Continuing Education and Conference Center, St. Paul Campus, University of Minnesota, MN, 2006.

[18] Peterson, L. and Peterson, R., "Compaction and In-Situ Testing at Mn/DOT TH53," Minnesota Department of Transportation, St. Paul, MN, 2006.

[19] Petersen, D. L., "Continuous Compaction Control MnROAD Demonstration," Minnesota Department of Transportation, Maplewood, MN, 2005.

[20] Beainy, F., Commuri, S., and Zaman, M., "Asphalt Compaction Quality Control Using Artificial Neural Network," *49th IEEE Conference on Decision and Control (CDC)*, Dec 15–17, 2010, Hilton Atlanta Hotel, Atlanta, Georgia, pp. 4643–4648.

[21] Beainy, F., Commuri, S., and Zaman, M., "Quality Assurance of Hot Mix Asphalt Pavements Using the Intelligent Asphalt Compaction Analyzer," *J. Constr. Eng. Manage.*, Vol. 138, No. 2, 2011, pp. 178–187.

[22] AASHTO TP62-03, 2006, "Standard Method of Test for Determining Dynamic Modulus of Hot-Mix Asphalt Concrete Mixess," *AASHTO Provisional Standards*, American Association of State Highway and Transportation Officials, Washington, D.C.

[23] Kim, R., Underwood, B., Sakhaei, M., Jackson, F., and Puccinelli, J., "LTPP Computed Parameter: Dynamic Modulus," *Final Report, FHWA-HRT-10-035*, Nichols Consulting Engineers, Federal Highway Administration, Reno, NV, 2011.

[24] Bonaquist, R. and Christensen, D. W., "Practical Procedure for Developing Dynamic Modulus Master Curves for Pavement Structural Design," *J. Transport. Res. Board*, No. 1929, 2005, pp. 208–217.

[25] AASHTO, "Guide to the Mechanistic-Empirical Design of New and Rehabilitated Pavement Structures," *NCHRP-1-37A*, American Association of State Highway and Transportation Officials, Washington, D.C., 2002.

[26] Pellinen, T. K. and Witczak, M. W., "Use of Stiffness of Hot-Mix Asphalt as a Simple Performance Test," *J. Transport. Res. Board*, No. 1789, 2002, pp. 80–90.

[27] Odemark, N., "Investigations as to the Elastic Properties of Soils Design of Pavement According to the Theory of Elasticity," Staten Vaeginstitut, Stockholm, Sweden, 1949.

[28] Huang, Y., *Pavement Analysis and Design*, Pearson, Prentice Hall, NJ, 2004, pp. 124–125.

[29] Ullidtz, P., *Modeling Flexible Pavement Response and Performance*, Narayana, Odder, Denmark, 1998, pp. 38–43.

[30] Lytton, R., "Backcalculation of Pavement Layer Properties," *STP 1026*, ASTM International, West Conshohocken, PA, 1989, pp. 14–15.

[31] Lu, Q., Ullidtz, P., Basheer, I., Ghuzlan, K., and Signore, J. M., "CalBack: Enhancing Caltrans Mechanistic-Empirical Pavement Design Process with New Back-Calculation Software," *J. Transport. Eng.*, Vol. 135, No. 7, 2009, pp. 479–488.

[32] Loulizi, A., Flintsch, G. W., and McGhee, K., "Determination of In-Place Hot-Mix Asphalt Layer Modulus for Rehabilitation Projects by a Mechanistic-Empirical Procedure," *J. Transport. Res. Board*, No. 2037, 2007, pp. 53–62.

[33] Shalaby, A., Liske, T., and Kavussi, A., "Comparing Back-Calculated and Laboratory Resilient Moduli of Bituminous Paving Mixes," *Can. J. Civil Eng.*, Vol. 31, 2004, pp. 988–996.

[34] Ullidtz, P. and Peattie, K. R., "Pavement Analysis by Programmable Calculators," *J. Transport. Eng.*, Vol. 106, No. TE5, 1980, pp. 581–597.

[35] Scullion, T. and Liu, W., *MODULUS 6.0 for Windows; User's Manual.* (2003). *Technical Report 0-1869-2*, Texas Transportation Institute, College Station, TX.

[36] Loulizi, A., Al-Qadi, I. L., Lahouar, S., and Freeman, T., "Measurement of Vertical Compressive Stress Pulse in Flexible Pavements and Its Representation for Dynamic Loading," *Paper #02-2376*, *Transportation Research Board 81st Annual Meeting*, Washington, D.C., Jan 13–17, 2002, pp. 1–21.

[37] Gedafa, D. S., Hossain, M., Romanoschi, S. A., and Gisi, A. J., "Comparison of Moduli of Kansas Superpave Asphalt Mixes," *89th Annual Transportation Research Board Meeting*, Washington, D.C., Jan 10–14, 2010.

[38] Hossain, M. and Scofield, L., "Correlation between Back-calculated and Laboratory-Determined Asphalt Concrete Moduli," *J. Transport. Res. Rec.*, No. 1377, 1992, pp. 67–76.

Journal of Testing and Evaluation

doi:10.1520/JTE20130325 / Vol. 43 / No. 2 / March 2015 / available online at www.astm.org

Josef Zak,[1] Jiri Stastna,[2] Jiri Vavricka,[3] Kristyna Milackova,[4] Lukas Kasek,[5] and Ludo Zanzotto[6]

Poisson's Ratio of Hot Asphalt Mixtures Determined by Relaxation and Small Amplitude Oscillation Test

Manuscript received December 16, 2013; accepted for publication June 24, 2014; published online October 7, 2014.

[1] Faculty of Civil Engineering, Department of Road Structures, CTU in Prague, Thakurova 7, Prague, 166 29, Czech Republic (Corresponding author), e-mail: josef.zak@fsv.cvut.cz

[2] Department of Civil Engineering, Schulich School of Engineering, Univ. of Calgary, 2500 Univ. Drive Northwest, Calgary, T2N 1N4, Alberta, Canada.

[3] Faculty of Civil Engineering, Department of Road Structures, CTU in Prague, Thakurova 7, Prague, 166 29, Czech Republic.

[4] Faculty of Civil Engineering, Department of Road Structures, CTU in Prague, Thakurova 7, Prague, 166 29, Czech Republic.

[5] Faculty of Civil Engineering, Department of Road Structures, CTU in Prague, Thakurova 7, Prague, 166 29, Czech Republic.

[6] Department of Civil Engineering, Schulich School of Engineering, Univ. of Calgary, 2500 Univ. Drive Northwest, Calgary, T2N 1N4, Alberta, Canada.

Reference

Zak, Josef, Stastna, Jiri, Vavricka, Jiri, Milackova, Kristyna, Kasek, Lukas, and Zanzotto, Ludo, "Poisson's Ratio of Hot Asphalt Mixtures Determined by Relaxation and Small Amplitude Oscillation Test," *Journal of Testing and Evaluation*, Vol. 43, No. 2, 2015, pp. 319–325, doi:10.1520/JTE20130325. ISSN 0090-3973

ABSTRACT

One of the basic material characteristics of solids is Poisson's ratio. Its exact knowledge, including its dependence on time, allows us to model the effect of load, with given boundary conditions, on the behavior of material under consideration. Poisson's ratio, or rather the relationship between the longitudinal and transverse strain, has an important implication in engineering mechanical applications (assessment of pavement structure performance). Nowadays, Poisson's ratio is usually used as a constant, based on an incorrect assumption that a hot asphalt mix is a linear elastic material. This paper reports Poisson's ratio as a function of time determined from the relaxation and small amplitude oscillation tests on cylindrical specimens. A hot asphalt mix is considered homogeneous isotropic material and linear theory of viscoelasticity is applied for the experimental determination of the lateral contraction ratio.

Keywords

asphalt mixture, Poisson's ratio, relaxation, small amplitude oscillation

Introduction

The amount of testing methods based on empirically established assumptions used in the HMA design and the pavement performance assessment is enormous. The reason for the use of these test methods is likely in part the complexity of the hot mix asphalt (HMA) structure and its properties and it is also caused by the history of the development of measurement techniques and test equipment.

Poisson's ratio, or rather the relationship between the longitudinal and transverse deformation is an important characteristic that enters into the pavement design process in two phases. Firstly, it enters into the design process in the course of laboratory determination of material characteristics. An HMA is a three component system consisting of stone aggregates, pores filled by air, and asphalt binder. Nowadays, the system is characterized as elastic in pavement design practice. The elastic characterization is based on the stiffness measurement of asphalt mixtures in accordance with CSN EN 12697-26 [1], in Czech Republic.

The conventionally used test method from CSN EN 12697-26 [1] is the indirect tension test on cylindrical specimens (IT–CY). The determination of stiffness modulus by IT–CY is based on the application of the stress pulse in a vertical plane and the measurement of the strain response in a horizontal plane. The stress has a haversine shape and its target rise time is 150 ms, so the length of the stress pulse is 300 ms. This test method does not reflect the phase shift between the stress and the strain response and also the recovery of a specimen.

The resilient modulus testing procedure is currently used to determine the Poisson's ratio of asphalt mixtures [2]. Some of the topics for criticism, related to the measurement of Poisson's ratio measurement with the resilient modulus test, are the biaxial stress pattern, the impossibility of performing the test in the controlled strain mode, and the accumulation of permanent deformation during the test [3–5]. Such a methodology is capable of meausring the Poisson's ratio as a constant at the changing boundary conditions (temperature, loading stress, loading time). The procedures to calculate Poisson's ratio from the known asphalt mixture tensile modulus at specific temperature can be found in Ref. [6]. The review of Poisson's ratio determination with the change of temperature is summarized in the following paragraph.

The presented approach utilizes uniaxial relaxation and a small amplitude oscillation test to measure the so-called lateral contraction ratio as a function of time and frequency rather than Poisson's ratio as a material constant. The loading is uniaxial and the resulting tensile stress is constant over the specimen cross section. The testing methodology allows to test the cylindrical and prismatic specimens.

Furthermore, Poisson's ratio enters into the calculation of the pavement stress and strain conditions by multi-layer systems implemented in currently used software [7,8]. The assessment of such a pavement system principally overestimates the HMA performance in the case of a low velocity traffic speed and underestimates the HMA performance in the case of high velocity traffic. In addition, it does not reflect the permanent deformation effects of HMA. Researchers attempt to capture the majority of these effects in pavement designs with the inclusion of calibrated coefficients [9–11].

The critical role is generally played by the choice of Poisson's ratio in the numerical modeling of asphalt mixtures. Oftentimes, a Poisson's ratio of 0.5 is used to simplify the issue of the relationship between shear and normal deformations. This error is then introduced into the calculation inaccuracies resulting from the unavailability of the measuring device or indirect methods to calculate Poisson's ratio from already identified characteristics.

The Poisson's ratio can be calculated from two other linear viscoelastic properties of the material like moduli, in theory, e.g., tensile moduli, shear moduli, and bulk moduli. Each of the properties must be determined by a separate test and the techniques used to determine the moduli of hot mix asphalts have several inaccuracies from an ideal highly accurate test method. If we consider the most used property of the HMA mechanical properties, in CEN countries, it is tensile modulus (stretch modulus). Several methodologies to determine the tensile moduli are known (4PBB–PR, 2PBB–PR, 2PBB–TR, 3PBB–PR, IT–CY, DT–CY). Although the determined moduli have positive correlations, they do not overlap. Poisson's ratio determination by calculation from any other two viscoelastic functions appears to be even more exacting. More information can be found in Ref. [12].

Review of Currently Used Values of Poisson's Ratio

Based on a literature review that was conducted in order to find the specific value of Poisson's ratio, the asphalt mixture Poisson's ratio cannot be firmly defined from the temperature and loading time. The sources presented below provide a range from which Poisson's ratio can be found. The broad range of experimental values is a logical consequence of the number of factors that can influence the value of Poisson's ratio. **Table 1** shows the approximate ranges of Poisson's ratio for asphalt concrete in relation to temperature.

Other values of Poisson's ratio, which can be found in the literature, are reported particularly in relation to the IT–CY test, which is among the most popular tests in the countries of the CEN for the determination of the modulus of a compacted asphalt mixture. Most sources indicate that the value 0.35 for Poisson's ratio is acceptable for calculating the stiffness at test temperature of 77°F (25°C). This value is also specified in the EN 12697-26 [1] specification where it is also noted that this value, in the case of unknown Poisson's ratio and its dependency on temperature, can be used for all temperatures.

Another distinct value of Poisson's ratio used for the indirect tensile test can be obtained by using the following equation, which was derived by Witczak and Mirza [13]:

$$\nu = 0.15 + \frac{0.35}{1 + \exp[3.1849 - 0.04233 * Temp(^{\circ}F)]} \quad (1)$$

The values of Poisson's ratio from targeted specification for roads in former Czechoslovakia "Katalog tuhých a netuhých

TABLE 1 Poisson's ratios from literature review.

[15]		[14]		[16]		[13]		[6]	
Temperature (°C)	Poisson's Ratio	Temperature (°C)	Poisson's Ratio	Temperature (°C)	Poisson's Ratio	Temperature (°C)	Poisson's Ratio	Temperature (°C)	Poisson's Ratio
4	0.18 ÷ 0.35	0	0.21	10	0.25	4	0.21	<−18	<0.15
13	0.28 ÷ 0.43	11	0.33	20	0.35	13	0.25	−18 ÷ 4	0.15 ÷ 0.20
21	0.32 ÷ 0.44	27	0.44	30	0.45	21	0.31	4 ÷ 21	0.20 ÷ 0.30
38	0.40 ÷ 0.50					38	0.41	21 ÷ 38	0.30 ÷ 0.40
60	0.40 ÷ 0.50					60	0.48	38 ÷ 54	0.40 ÷ 0.48
								>54	0.45 ÷ 0.48

vozoviek pozemných komunikácií, Typizačná smernica" [14] are also listed in **Table 1**.

Laboratory Measurements

Asphalt mixture is a multiphase system with many components, some of which have complicated internal structures with high-temperature susceptibility (conventional or polymer modified asphalt binder) [17]. Notwithstanding its complicated structure, the thermo-mechanical behavior of asphalt paving mix can be modeled with the help of the theory of viscoelasticity [18]. The testing device is periodically calibrated within the laboratories accreditation system. The suitability of selected testing procedures was checked with specimens made from two elastic materials with the known Poisson's ratio. To check the suitability of the test method, the homogenous elastic material with both higher and lower tensile modulus than the studied asphalt mixtures was selected. In **Fig. 1**, one can see examples of "dummy" samples made from polyethylene-measured tensile modulus 63.1 MPa, polycaprolactam-measured tensile modulus 1.32 GPa, and asphalt mixture sample–measured tensile modulus ranging from 7 GPa to 380 MPa with the loading time at 15°C.

Three asphalt mixtures were used to conduct the measurements. All mixtures were designed in accordance with a specification [19]. Conventionally used unmodified asphalt binder designated as 50/70 (Pen grade) in accordance with Ref. [20] was used in all asphalt mixtures. The used aggregate was of spilite type and limestone mineral filler was added into the mixtures. The asphalt mixture's grading curves are given in the **Fig. 2**.

FIG. 1 Specimens made from polyethylene, polycaprolactam, and asphalt mixture (from left to right).

The first asphalt mixture, labeled ACO 11+, belongs to surface courses by its application. The binder content was 5.2 % by weight and the air void content was 4 %.

The second and third asphalt mixtures were designed for the application in base course. Their designation is ACL16+ and ACL 22+. All bituminous mixtures had different sizes of the nominal maximum aggregate, as indicated by the number in the designation after three letters.

The ACL 16+ mixture had 4.7 % of the binder content and the air void content of 4.25 %, while the ACL 22+ mixture had 4.8 % of the binder content and the air void content of 3.6 %.

A universal testing machine with a hydraulic power unit was used for the measurements. The averaged vertical and horizontal deformations were always obtained with pairs of LVDTs, the result were then calculated as the average.

The ratio of uniaxial extension, caused by applying the step strain (step function), to the transverse deformation in the time domain is hereafter called the lateral contraction ratio.

UNIAXIAL RELAXATION

Relaxation of uniaxial extension caused by strain loading defined as a step function of time was selected as the simplest test method to determine the time-dependent lateral

FIG. 2 Asphalt mixtures grading curves.

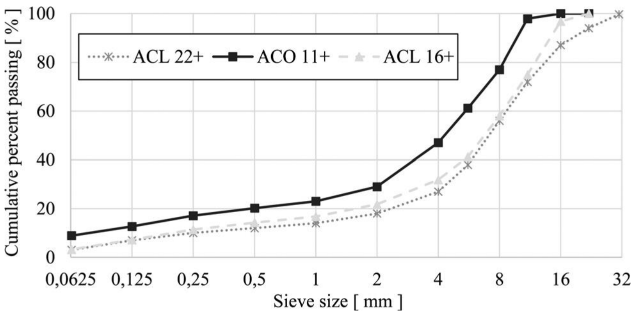

contraction ratio. The test specimen was loaded by the strain ε_0 and its transverse deformation was measured.

The lateral contraction ratio, μ, was then computed from the equation [21]:

$$-\bar{\varepsilon}_2(s) = \bar{\mu}(s)\varepsilon_0 \tag{2}$$

where $\bar{\varepsilon}_2(s)$, $\bar{\mu}(s)$ are Laplace transforms of transverse strain, or lateral contraction, respectively, and $\varepsilon_0$is uniaxial strain. Then, by applying the inverse Laplace transform (L^{-1}), we obtain [21]:

$$\mu(t) = L^{-1}\left[\frac{-\bar{\varepsilon}_2(s)}{\varepsilon_0}\right] \tag{3}$$

where ε_0 is the applied strain.

If we consider ε_0 as a unit step function and $L^{-1}[-\bar{\varepsilon}_2(s)] = \varepsilon_2(t)$, then the isotropic time dependent lateral contraction $\mu(t)$ can be computed from the equation [21]:

$$\mu(t) = \frac{-\varepsilon_2(t)}{\varepsilon_0} \tag{4}$$

LABORATORY MEASURED DATA

From each asphalt mixture, 20 specimens were prepared and tested at four temperatures (30, 45, 50, 60°C). Thus, each presented lateral contraction ratio at a given temperature is the average from five tested samples. The measured data in a time window from 4 to 40 s are presented in **Figs. 3** and **4**. The first 4 s of the measured lateral contraction ratio are not presented as this time was needed to increase the loading stress to the required value of strain. From the records of strain and stress conditions, it was obvious that during this time period, the measured vertical strain response does not match the assumption that vertical strain is a monotonic function of time. After 40 s, it was found that the lateral contraction ratio had reached its steady state.

The measured lateral contraction ratio is in the range of 0.15 to 0.45, which is in the range of the values measured by previous authors. The lateral contraction ratio is presented as a function of time (in order to capture the effect of relaxation) and temperature. If we focus on the effect of the maximum nominal aggregate size, it seems that asphalt mixtures with a higher nominal aggregate size have smaller values of the lateral contraction ratio. Asphalt mixtures with smaller nominal aggregate size seem to show initial lateral contraction ratios in the majority of tested specimens by 0.07 smaller than the steady state value. However, this effect should be further examined to find out to what extent this effect is due to the nominal maximum aggregate size and the extent to which the overall aggregate composition in mixtures can influence this phenomenon.

FIG. 3 Lateral contraction ratio as function of time (left ACO 11+, right ACL 16+).

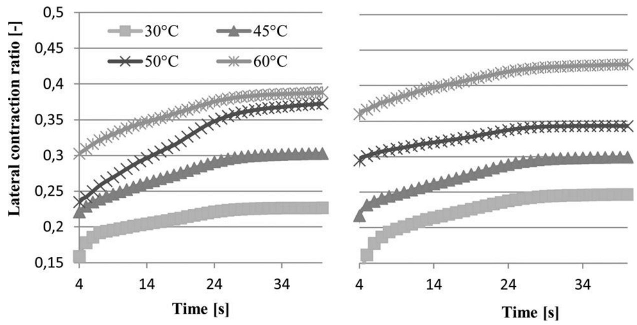

FIG. 4 ACL 22+ lateral contraction ratio as function of time (left); average lateral contraction ratio of studied asphalt mixtures as function of time (right).

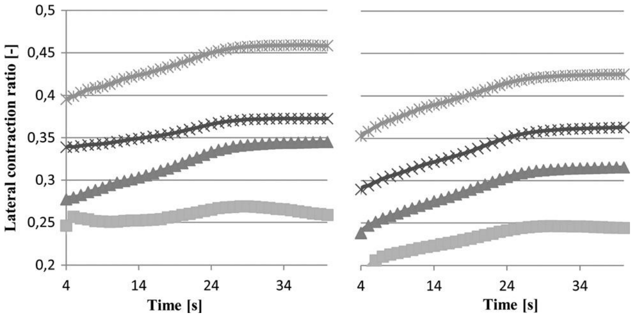

The lateral contraction ratio's dependency on time seems to have a similar effect at each temperature in the tested range. The lateral contraction ratio tends to reach a plateau 11 s after the achievement of the constant strain excitation at all temperatures.

From **Fig. 5**, it is evident that the lateral contraction ratio's depend on temperature. To express this variability with the inclusion of the time effect, three different time periods were used. First, as the "initial" lateral contraction ratio, the value at 4 s is plotted, followed by the value of the lateral contraction ratio at 11 s where the lateral contraction ratio seems to reach the plateau and then at 40 s where the steady state value was reached. From the correlation coefficients higher than 0.95 for all the values of lateral contraction ratios, it can be concluded that the temperature dependence in the range from 30 to 60°C

FIG. 5 Average lateral contraction ratio of studied asphalt mixtures as a function of temperature (30°C–60°C).

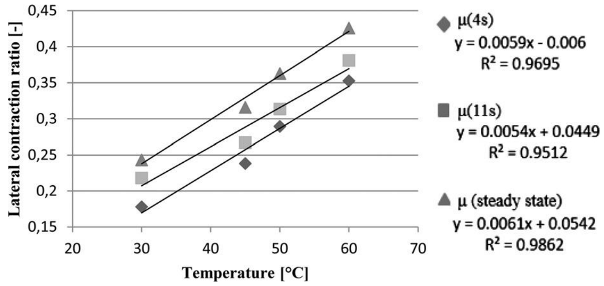

can be approximated as a linear one. This effect was also observed by others [22] for asphalt binder.

The statistical variance of the lateral contraction ratio as a function of time was studied at specific loading times. The variance of measured results is presented in the **Fig. 6**. The variance of each lateral contraction ratio measurements at selected temperature was up to 2.73e-3. The variance increased with the increase of temperature as can be seen from the trend of linear regression of each temperature average variance with correlation coefficient equal to 0.8014.

SMALL AMPLITUDE TENSILE OSCILLATIONS

The sinusoidal contraction strain (in compression) was applied to the specimens with the amplitudeε_0. To follow up the specification for the measurement of tensile dynamic modulus measurements [1,23] and to stay in the linear-viscoelastic domain [24,25], the amplitude of the applied strain was set at 100 micro strains.

Simultaneously, lateral and transverse strains were measured until the steady-state was reached. The tests were done at a temperature range from 0 to 45°C. The recorded data were then fitted with the harmonic functions (Eqs 5, 6, and 7). The fitting was done using the two solvers aiming at the regression coefficient equal to 1 and minimum total least squares simultaneously.

$$\sigma(t) = \sigma_0 * \sin(\omega t + \delta_\sigma) + A \tag{5}$$

$$\varepsilon_1(t) = \varepsilon_{10} * \sin\left(\omega t + \frac{2}{\pi} + \delta_{\varepsilon_1}\right) + B \tag{6}$$

$$\varepsilon_2(t) = \varepsilon_{20} * \sin\left(\omega t + \frac{2}{\pi} + \delta_{\varepsilon_2}\right) + C \tag{7}$$

where:

σ_0 = the amplitude of stress,

ε_{10} = the amplitude of vertical strain (in the compression direction),

ε_{20} = the amplitude of horizontal strain (in the lateral direction),

ω = the frequency, and

δ_{yi} = phase angles.

FIG. 6 Variance of asphalt mixtures lateral contraction ratio at different temperatures and specific loading times.

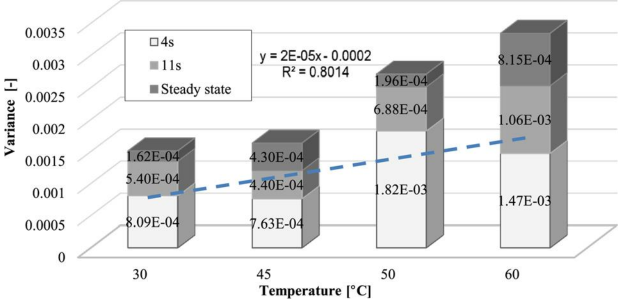

Then, the dynamic modulus phase θ can be computed from the shift between the peaks of the vertical strain equation as:

$$\theta = \delta_\sigma - \delta_{\varepsilon_1} \tag{8}$$

The shift between the peaks of the applied strain and the transverse strain response can be determined from the measured data. This shift represents the lateral contraction phase (or loss) angle. Thus, the lateral contraction phase angle is:

$$\delta_\mu = \delta_{\varepsilon_2} - \delta_{\varepsilon_1} \tag{9}$$

Successively, the complex lateral contraction ratio was computed from the measured results as [12,21]:

$$\mu^*(\omega) = \frac{-\varepsilon_2(\omega)}{\varepsilon_{10}} \tag{10}$$

Then, the real and imaginary parts are obtained as [12]:

$$\mu'(\omega) = \mu^*(\omega) \cos \delta_\mu(\omega) \tag{11}$$

$$\mu''(\omega) = \mu^*(\omega) \sin \delta_\mu(\omega) \tag{12}$$

where:

δ_μ = the lateral contraction phase angle,

$\mu'(\omega)$ = the real part of the complex lateral contraction ratio, and

$\mu''(\omega)$ = the imaginary part of the complex lateral contraction ratio.

The data of the measured, frequency-dependent, components of lateral contraction and its phase angle taken at several temperatures were plotted into one chart and with the help of the time–temperature–superposition principle (TTS) shifted into one master curve.

The Williams–Landell–Ferry (WLF) [25] equation was used to fit the shift factors of each HMA.

LABORATORY MEASURED DATA

All three studied asphalt mixtures tend to have the same value of the complex lateral contraction ratio and the phase angle; thus they are presented in one figure (**Fig. 7**). Each value presented in **Fig. 7** was taken as the average value from three last

FIG. 7 Real and imaginary part of lateral contraction ratio.

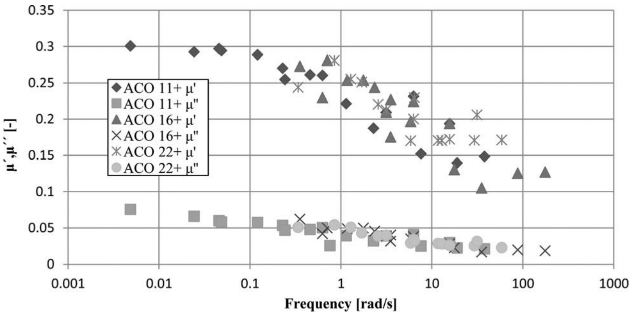

cycles of the frequency stage and three specimens. For every regression of the measured horizontal and vertical strain, the regression coefficient was computed using Eqs 6 and 7. The regression coefficient was then used as the weight, and the final presented data point is the weighted average from these nine values.

The WLF coefficients for each asphalt mixture were: C1 = 100, C2 = 1919 for ACO 11+, C1 = 5, C2 = 125 for ACO 16+, C1 = 100, C2 = 2948 for ACO 22+. The TTS shift factors were computed using the IRIS RheoHub software [26,27].

The complex lateral contraction ratio decreases with the frequency and increases with the measured temperature. The decrease is largely caused by the decrease of the real part of the lateral contraction ratio, which can be seen from **Fig. 7** and the difference between the real part and the imaginary part of the lateral contraction ratio. The lateral contraction phase angle, and the components of the complex lateral contraction ratio decreases with the frequency and increases with temperature.

Conclusions

The contribution presents data of the measured lateral contraction ratio by the application of the small amplitude oscillation test method and the relaxation test. The findings by other authors discussing the lateral contraction ratio's dependency on temperature were proven. Over and above, the article provides exact data of the measured asphalt mixture lateral contraction ratio as a function of time and the frequency.

Both test methods show the time and temperature dependence of the lateral contraction ratio. The relaxation test provides data for a longer time period than the small amplitude oscillation, but due to mechanical constrains, it is not capable of exciting the vertical strain as the step function of time; thus it does not provide the values of the lateral contraction ratio at the beginning of the stage. With the small amplitude oscillation at high frequencies or low temperatures and the application of TTS, the values of the lateral contraction ratio at a smaller time period can be captured. Thus, the lack of one test can be overlapped by another test method as was shown in Ref. [17]; the connection between the two presented test methods will be part of our future study.

It should be mentioned that the difficulties related to the measurement of the lateral contraction ratio by the application of tensile compression were significant. Special effort should be taken to prepare a sample with a "perfect" parallel base and perpendicular sides. This paper presents results from 69 specimens. The variation of the lateral contraction ratio is compressed between the values of about 0.1 and less than 0.5. Some of the specimens showed the measured lateral contraction ratio out of these boundaries. The specimens excluded from further analysis had measured values between 2 and 8; such extreme, unrealistic values obviously determined the test error. None of the statistical detection methods were used to find outliers. Our personal opinion is that the error results from bending of the sample caused by axial loading on non-parallel bases. As part of the study was also taken to attempt to measure the lateral contraction ratio from constant rate of strain and creep test. These test methods have proved to be impractical due to the limit of accuracy between programed stress or strain function and measured excitation.

The lateral contraction ratio can also be expressed from two other response functions. The test methods used for measuring $E(t)$ or complex $E(\omega)$ and $G(t)$ or complex $G(\omega)$, respectively, are known [12]. These response functions must be measured separately; thus, this procedure can bring errors in the calculation arising from the differences between the test samples and the test methods.

ACKNOWLEDGMENTS

This paper has been supported by the research project SGS13/050/OHK1/1T/11 granted by the Czech Technical University in Prague.

The writers would like to express their thanks for cooperation with the Experimental Centre of the Faculty of Civil Engineering, CTU in Prague, especially to Prof. Petr Konvalinka CSc., without whom we would not be able to continue in the project.

References

[1] CSN EN 12697-26: Bituminous Mixtures—Test Methods for Hot Mix Asphalt—Part 26: Stiffness, Czech Office for Standards, Metrology and Testing, Prague, Czech Republic, 2012.

[2] Zhang, W., Drescher, A., and Newcomb, D., "Viscoelastic Analysis of Diametral Compression of Asphalt Concrete," *J. Eng. Mech.*, Vol. 123, No. 6, 1997, pp. 596–603.

[3] SHRP-A-404: Fatigue Response of Asphalt-Aggregate Mixes, Strategic Highway Research Program, National Research Council, 1994.

[4] Benedetto, H., Roche, C., Baaj, H., Pronk, A. C., and Lundström, R., "Fatigue of Bituminous Mixtures," *Mater. Struct.*, Vol. 37, No. 3, 2004, pp. 202–216.

[5] Hudson, W. R. and Kennedy, T. W., "An Indirect Tensile Test for Stabilized Materials. Research Report 9801," Center for Highway Research, The University of Texas, Austin, TX, 1968.

[6] Hallin, J. P., "Guide for Mechanistic-Empirical Design," NCHRP 1-37A, National Cooperative Highway Research Program, Washington, D.C., 2004.

[7] Burmister, D. M., "The General Theory of Stresses and Displacements in Layered Soil Systems," *J. Appl. Phys.*, Vol. 16, No. 3, 1944, pp. 296–302.

[8] Huang, Y. H., "Stresses and Displacements in Visco-Elastic Layered Systems Under Circular Loaded," *Proceedings of the 2nd International Conference on Asphalt Pavements*, Ann Arbor, MI, 1967.

[9] Tsai, B. W., Wu, R., Harvey, J., and Monismith, C. L., "Development of Fatigue Performance Specification and

its Relation to Mechanistic-Empirical Pavement Design Using Four-Point Bending Beams Test Results," *Four Point Bending*, CRC Press, Boca Raton, FL, 2012, pp. 59–71.

[10] TP 170, "Navrhování Vozovek Pozemních Komunikací," Ministerstvo dopravy České Republiky, Czech Republic, 2004.

[11] SETRA and LCPC, *Conception et Dimensionnement des Structures de Chaussée-Guide Technique*, Ministére de l'Équipement des Transports et du Tourisme, Paris, 1994.

[12] Tschoegl, N. W., Knauss, W. G., and Emri, I., "Poisson's Ratio in Linear Viscoelasticity—A Critical Review," *Mech. Time-Depend. Mater.*, Vol. 6, No. 1, 2002, pp. 3–51.

[13] Witczak, M. W. and Mirza, M. W., "Development of Relationships to Predict Poisson's Ratio for Paving Materials," *Report for NCHRP 1-37A*, University of Maryland, College Park, MD, 1999.

[14] Dopravoprojekt, *Katalóg Tuhých a Netuhých Vozoviek Pozemných Komunikácií*, Dopravoprojekt Bratislava, Bratislava, Slovak Republic, 1984.

[15] Yoder, E. J. and Witczak, M. W., *Principles of Pavement Design*, 2nd ed., Wiley, New York, 1975.

[16] Nunn, M. E., *Characterisation of Bituminous Macadams by Indirect Tensile Stiffness Modulus*, Thomas Telford, London, 1999.

[17] Žák, J., Stastna, J., Zanzotto, L., and Daryl, M., "Laboratory Testing of Paving Mixes – Dynamic Material Functions and Wheel Tracking Tests," *Int. J. Pavement Res. Technol.*, Vol. 2013, No. 6, 2013, pp. 147–154.

[18] Underwood, B. S., Yun, T., and Kim, Y. R., "Experimental Investigations of the Viscoelastic and Damage Behaviors of Hot-Mix Asphalt in Compression," *J. Mater. Civ. Eng.*, Vol. 23, No. 4, 2011, pp. 459–466.

[19] CSN EN 13108-1: Bituminous Mixtures—Material Specification—Part 1: Asphalt Concrete, Czech Office for Standards, Metrology and Testing, Prague, Czech Republic, 2008.

[20] CSN EN 12591: Bitumen and Bituminous Binders—Specifications for Paving Grade Bitumens, Czech Office for Standards, Metrology and Testing, Prague, Czech Republic, 2009.

[21] Tschoegl, N. W., *The Phenomenological Theory of Linear Viscoelastic Behavior: An Introduction*, Springer–Verlag, Berlin, Germany, 1989.

[22] Kästner, S. and Pohl, G., "Ein Beitrag zur Frage der vollstÄndigen Erfassung des Mechanischen Relaxationsverhaltens der Polymeren," *Kolloid-Z. Z. Für Polym.*, Vol. 191, No. 2, 1963, pp. 114–123.

[23] AASHTO T342-11: Standard Method of Test for Determining Dynamic Modulus of Hot Mix Asphalt (HMA), American Association of State Highway and Transportation Officials, Washington, D.C., 2009.

[24] Ferry, J. D., *Viscoelastic Properties of Polymers*, 3rd ed., Wiley, New York, 1980.

[25] Dealy J. M. and Wissbrun, K. F., *Melt Rheology and its Role in Plastics Processing: Theory and Applications*, Springer, New York, 1999.

[26] Winter, H. and Mours, M., "IRIS Version 2011; Inovative Rheological Interface Software," IRIS Development LLC, Amherst, MA, 2011.

[27] Žák, J., "IRIS Rheo-Hub, Program Description," CVUT, FSv, Department of Road Structures, Prague, Czech Republic, 2012.

Journal of Testing and Evaluation

doi:10.1520/JTE20140085 / Vol. 43 / No. 2 / March 2015 / available online at www.astm.org

Wen-Cheng Liao[1] and Shih-Ho Chao[2]

Crack Opening Evaluation and Sustainability Potential of Highly Flowable Strain-Hardening, Fiber-Reinforced Concrete (HF-SHFRC)

Reference

Liao, Wen-Cheng and Chao, Shih-Ho, "Crack Opening Evaluation and Sustainability Potential of Highly Flowable Strain-Hardening, Fiber-Reinforced Concrete (HF-SHFRC)," *Journal of Testing and Evaluation*, Vol. 43, No. 2, 2015, pp. 326–335, doi:10.1520/JTE20140085. ISSN 0090-3973

ABSTRACT

Highly flowable, strain-hardening fiber-reinforced concrete (HF-SHFRC) has good workability in the fresh state, and it exhibits the strain-hardening and multiple-cracking characteristics of high-performance, fiber-reinforced cementitious composites in the hardened state. HF-SHFRC can be easily manufactured and delivered by ready-mix trucks for cast-on-the-job sites. Structural large-scale test results from several research programs also showed that HF-SHFRC is effective in increasing shear strength, displacement capacity, and damage tolerance in members subjected to large inelastic deformations. The results of two tests, a long prismatic tensile test with continuous reinforcement and an in-plane pure shear panel test, are summarized in this paper. Relative to conventional concrete, HF-SHFRC not only demonstrates much better mechanical performance, but also presents reduced crack potential and excellent crack width control. These characteristics of HF-SHFRC can further diminish the need for repairs, rehabilitation, and maintenance after extreme loading events and give infrastructure a longer service life, which will eventually lower the life-cycle cost.

Keywords

SCC, FRC, HPFRCC, strain hardening, sustainability, crack opening

Introduction

Highly flowable strain-hardening fiber-reinforced concrete (HF-SHFRC) combines the self-compacting property of self-consolidating concrete (SCC) in its fresh state with the strain-hardening and multiple-cracking characteristics of high-performance fiber-reinforced cement

Manuscript received February 28, 2014; accepted for publication June 24, 2014; published online October 7, 2014.

[1] Assistant Professor, Dept. of Civil Engineering, National Taiwan Univ., Taipei 10617, Taiwan.

[2] Associate Professor, Dept. of Civil Engineering, Univ. of Texas at Arlington, Arlington, TX 76019, United States of America.

composites (HPFRCCs) in their hardened state. SCC has high flowability and moderate viscosity, and there is no blocking by the reinforcement during flow. With proper use of a superplasticizer (SP) and viscosity-modifying agents (VMAs), SCC can achieve higher flowability and higher slump without segregation. SCC also maintains better slump retention, which makes the concrete more durable as a result of its lower water-to-binder ratio, thereby reducing sulfate attack and salt penetration. In addition to containing the fresh-state characteristics of SCC, HF-SHFRC also has the same excellent mechanical properties as HPFRCC. HPFRCC shows a tensile strain-hardening response that can lead to multiple cracks, unlike the tensile strain-softening response of conventional fiber-reinforced concrete (FRC), as shown in **Fig. 1** [1].

Several HF-SHFRC compositions have been developed for different compressive strength demands (30, 40, 50, and 60 MPa) through modification of SCC mixtures as recommended in previous studies and use of available local materials, including 30-mm-long high-strength steel-hooked fibers in volume fractions of 1.5 % [2]. It is also worth mentioning that a substantial amount of the cement was replaced with fly ash in the mix design, which must be factored in when considering cost, durability, and sustainability.

Two tests—the long prismatic tensile test with continuous reinforcement and the in-plane pure shear panel test—were also carried out to verify the resistance to crack openings in HF-SHFRC. The results showed that relative to conventional concrete, HF-SHFRC not only had much better mechanical performance, but also exhibited lower crack potential and excellent crack width control.

Concrete and Sustainability

Concrete is an environmentally sound building material; however, it is not deemed green because of its high consumption of natural resources, high life cycle cost caused by related repair and maintenance, and fairly large carbon footprint caused by the energy used to produce cement, which is the main component of concrete. Cement production is a highly energy-intensive production process, and the energy consumption of cement is almost 5 % of the total global industrial energy consumption, according to the World Energy Council [3]. The World Business Council for Sustainable Development also approximates that the manufacture of cement produces about 0.9 lb of carbon dioxide (CO_2) for every pound of cement and manufacturing a cubic yard of concrete (about 3900 lb) and is

FIG. 1

Stress-strain responses of conventional FRC and HPFRCC.

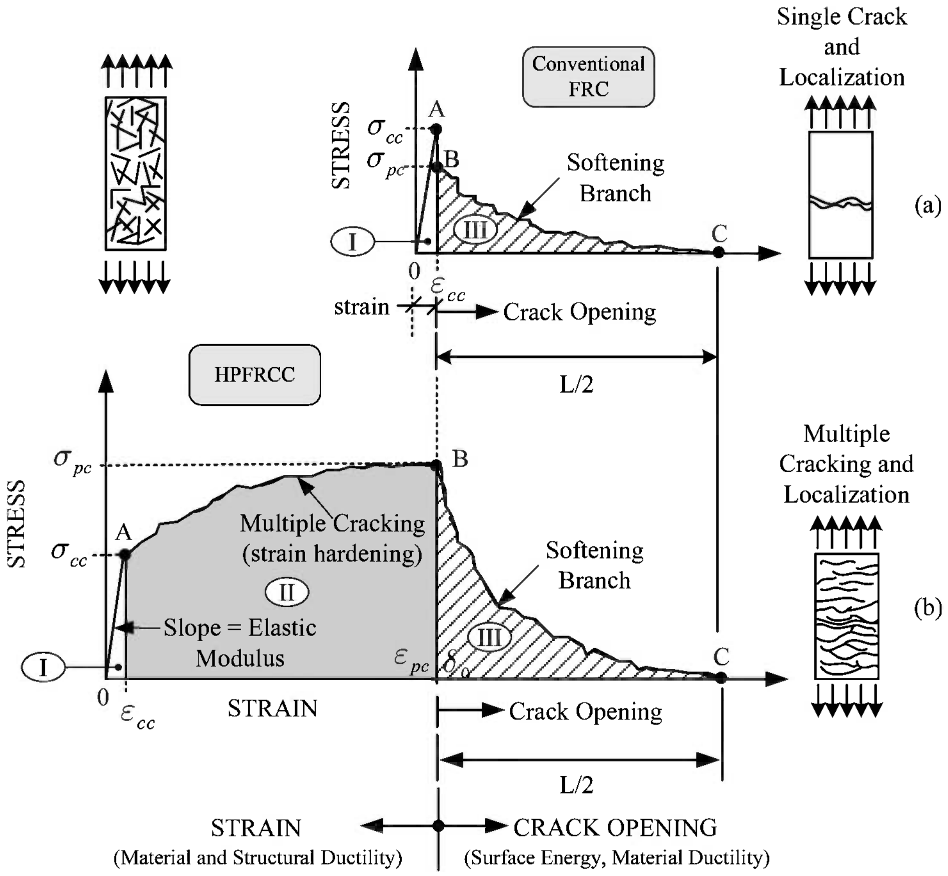

responsible for emitting about 400 lb of CO_2 [3]. Further CO_2 emission occurs during construction, repair, and maintenance of concrete infrastructure, as well as energy consumption. The use of HF-SHFRC will lead to less repair and a longer life for concrete structures, thereby reducing the carbon footprint and lessening the impact on the world's energy crisis.

Durability issues have long been the main cause of unsustainability in concrete structures in view of life-cycle costs. The durability of concrete is defined as the ability of concrete to resist weathering action, chemical attack, and abrasion while maintaining its desired mechanical properties. Because of the higher water/cement ratio in conventional concrete, as voids interconnect with propagating cracks under environmental actions and loadings, gradual losses of watertightness can trigger or worsen durability problems, including sulfate attack, alkali–silica reaction, and corrosion of steel reinforcements. Therefore, concrete deterioration leads to an increase in repair and replacement costs, as well as the consumption of more natural resources.

In recent years, considerable efforts have been made to enhance the sustainability of concrete by using recycled materials or sustainable construction materials such as fly ash, slag, and silica fume to replace cement and to upgrade the mechanical properties of concrete to prevent deterioration. HF-SHFRC improves sustainability without compromising performance.

Mix Design Concept

It is generally agreed that adding fibers can expand the applications of SCC; however, a reduction in workability due to fiber addition may become a barrier to its application in practice. Through modification of SCC mixtures recommended in previous studies and the use of locally available materials, HF-SHFRC mixtures for different strength demands can be easily manufactured and delivered by ready-mix trucks for cast-in-place applications.

Although adding fibers can significantly enhance the mechanical properties—particularly the tensile behavior—of SCC, a reduction in workability due to fiber addition may become a handicap in practice. Thus, the mix design of SCC must be further adjusted if fibers are added. Numerous commercial laboratories have been involved in the development of SCC with fibers and are continuously improving their performance. Following is a summary of key findings based on their studies [4,5]:

(1) The coarse-to-fine aggregate ratio in the mix needs to be reduced so that individual coarse aggregate particles are fully surrounded by a layer of mortar. Furthermore, it was recommended by Johnston [6] that the volume of coarse aggregates be reduced by at least 10 % relative to plain concrete to facilitate pumping.
(2) Before the addition of fibers, the slump flow of SCC must be relatively high. The slump flow criterion of qualified SCC is 600 mm for a 300-mm-high cone.
(3) Everything else being equal, the addition of fibers reduces the slump flow of SCC; a higher fiber volume and higher aspect ratio of fibers reduces the slump flow of SCC as well, leading to a greater possibility of blocking and segregation.

Experimental Program

MATERIALS AND MIX PROPORTIONS

The cementitious materials used in this study were ASTM Type I Portland cement and class C fly ash. The coarse aggregate had a maximum size of 12.7 mm and consisted of solid crushed limestone from a local source with a density of about 2.70 g/cm^3. The fine aggregate was #16 flint silica sand. Polycarboxylate-based SP was used to achieve the desired workability. In addition to the SP, a VMA was also used to enhance the viscosity and avoid fiber segregation. This mixture had a 1.5 % volume fraction of hooked steel fiber with a circular cross-section used with a tensile strength of 2300 MPa and an aspect ratio of 79 (diameter = 0.38 mm and length = 30 mm). The average 28-day compressive strength of concrete based on 100 mm by 200 mm cylinders was approximately 40 MPa. Details of the matrix composition are given in **Table 1**.

DIRECT TENSILE TEST

A direct tensile test was needed to ascertain whether the developed HF-SHFRC could give a strain-hardening response in tension after first cracking. Dog-bone-shaped tensile specimens were prepared and tested for the HF-SHFRC mixture. The specimen had a cross-sectional dimension of 25.4 mm by 50.8 mm as shown in **Fig. 2**.

The applied load was monitored by the load cell of the testing machine, and the elongation was recorded by a pair of linear variable differential transformers (LVDTs) attached to the specimen (**Fig. 3**) with a gauge length of about 178 mm. It is noted that compared to the fiber length, the relatively smaller cross-section led to a somewhat two-dimensional distribution of fibers.

LONG PRISMATIC REINFORCED TENSILE TEST

It has been established that the presence of continuous reinforcement helps concrete carry tension between cracks through

TABLE 1 Relative composition of HF-SHFRC mixture by weight.

Cement	Fly Ash	Sand	Coarse Aggregate	SP	Water	VMA	Steel Fiber
1.00	0.88	2.20	1.2	0.005	0.8	0.038	0.32

FIG. 2 Geometry and dimensions of direct tensile test specimen.

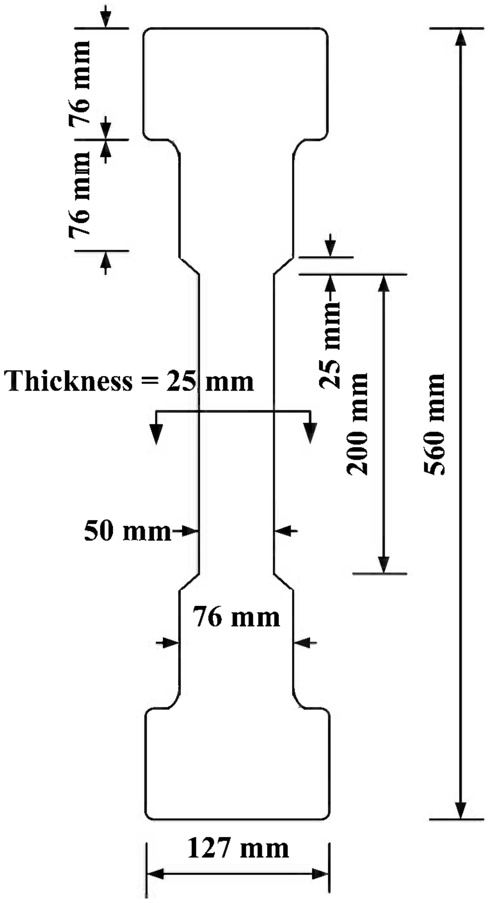

FIG. 3 Direct tensile test setup.

the transfer of bond forces. This in turn results in better control of member stiffness, deformation, and crack widths in reinforced concrete (RC) members than in plain concrete members. In this study, an unstressed prestressing steel strand was placed at the center of the specimen to simulate the presence of reinforcing steel in HF-SHFRC. The advantage of using a prestressing steel tendon is that a strain as high as 0.9 % can be applied while the tendon remains linear elastic; this allows a stable environment for loading–unloading and for measurements of crack width and spacing at every loading step. Moreover, tests conducted by Chao et al. [5] have shown that HPFRCCs lead to a much higher bond strength between a seven-wire strand and surrounding matrix than plain concrete (as much as three times greater), thus ensuring the tension stiffening effect in test specimens.

Details of the specimen geometry, test setup, and instrumentation are shown in **Fig. 4**. The long prismatic specimen had cross-sectional dimensions of 64 mm by 76 mm. The specimen was placed in a prestressing bed and supported by a few steel strips that allowed the specimen to move easily on its bed support during tension. The strand going through the specimen was attached at each end by a prestressing chuck. The tensile load was applied monotonically to the strand through a hydraulic jack and recorded by a pair of load cells at both ends of the prestressing bed as shown in **Fig. 4(*a*)**. Five zones in the middle of the specimen were selected to record the strains in the concrete through the use of LVDTs, as shown in **Fig. 4(*b*)** (zones 1 through 5). The gauge length of each zone was 250 mm. Elongation of the entire specimen was also monitored by two LVDTs attached to the ends of the specimen. Strains in the strand (inside the matrix) were measured by strain gauges attached at predesignated locations corresponding to the middle points of the five zones (zones 1 through 5) mentioned above. Strain gauges were also mounted on the strand outside the matrix [**Fig. 4(*b*)**] in order to obtain the stress-strain curve of the bare strand.

The stress in the fiber concrete for the long prismatic reinforced tensile test was calculated by

$$\sigma_c = \frac{F - E_s\varepsilon_s}{A_t - A_s} \tag{1}$$

where:

σ_c = tensile stress in fiber concrete, MPa,
F = total force measured by load cell, kN,
E_s = elastic modulus of strand, MPa,
ε_s = strain in strand measured by strain gauge, mm/mm,
A_t = gross cross-sectional area of the specimen (4860 mm^2), and

A_s = nominal cross-sectional area of a 12.7-mm seven-wire strand (100 mm^2).

It was mentioned previously that a prestressing steel strand remains linear elastic when the strain reaches as much as 0.9 %. This was indeed the case in the strand used in this study, as indicated by the stress-strain relation obtained based on strain gauges mounted outside the matrix; the curve was linear with an elastic modulus of 206 GPa. Because the specimen was able to move freely during testing with minor frictional force, the force measured by the load cell (F) could be taken as constant along the specimen and used for zones 1 through 5. The force sustained by the fiber concrete was calculated as the difference between F and force in the strand, $E_s \cdot \varepsilon_s$. The average tensile stress was then calculated by dividing the force difference using the net concrete area $A_t - A_s$. The tensile strains in the fiber concrete were obtained by dividing the elongation (measured through LVDTs) by the gauge length of each zone (250 mm).

FIG. 4 (a) Geometry and dimensions of tensile test specimen. (b) Tensile test setup.

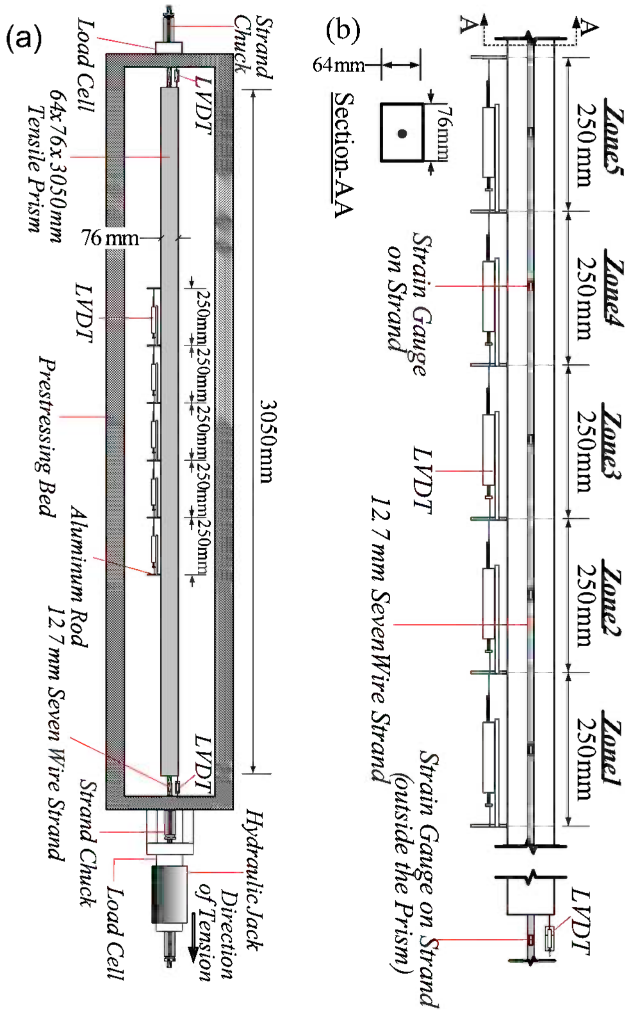

IN-PLANE PURE SHEAR PANEL TEST

An 890 mm by 890 mm by 70 mm concrete panel was fabricated for the shear panel test. **Figure 5** illustrates the geometry and reinforcement layout of the panel. In order to provide adequate post-cracking resistance of the panel, 40 D6 deformed wires were provided for x-direction reinforcement, giving a total reinforcement area of 1543 mm^2, which equated to a reinforcement ratio of 2.47 %.

This in-plane pure shear panel test was conducted using the Panel Tester Machine developed by Vecchio [7] at the University of Toronto. This machine and experimental setup were designed to apply various in-plane loading conditions to a concrete panel. The in-plane shear forces were generated by the horizontal and vertical jacks on each opposing side of the panel. There are adjustable links on the frame to prevent out-of-plane displacement and keep the panel aligned. Deformations (strains) of the panel were obtained continuously from the LVDTs and strain gauges throughout the duration of each test. **Figure 6** shows the arrangement of the LVDT setup. Additional data were also obtained from Zurich gauge readings that were taken at each load stage to verify the accuracy of the LVDTs. These data were subsequently analyzed to investigate the response characteristics of the concrete panels under in-plane pure shear loading.

Test Results

DIRECT TENSILE TEST

The stress-strain curves were recorded from the dog-bone specimens tested. Multiple cracks developed up to peak stress (post-cracking strength), at which crack localization occurred. Typical

FIG. 5 Dimensions and reinforcement layout of panel.

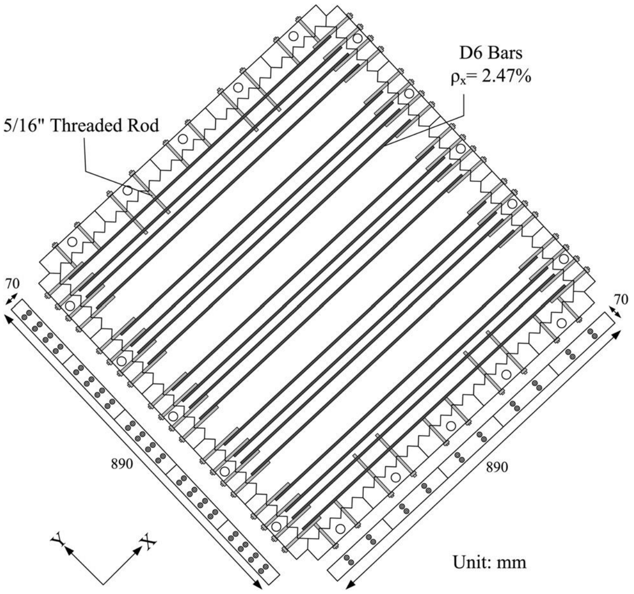

FIG. 6 LVDT setup for panel test.

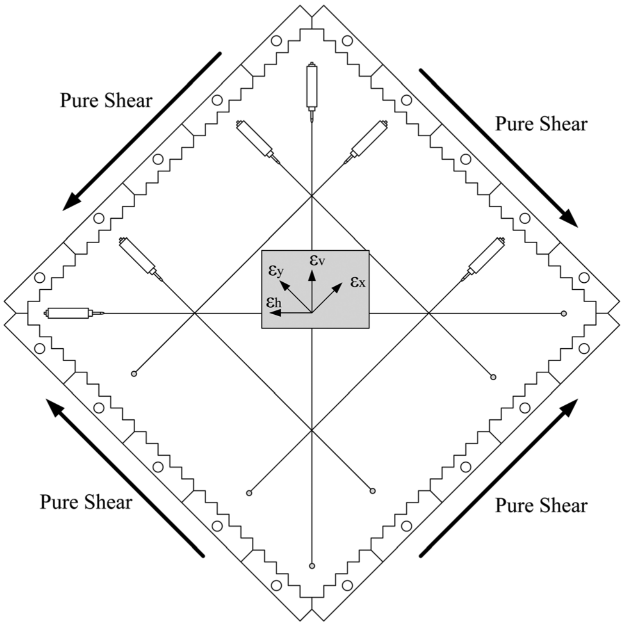

stress-strain curves are shown in **Fig. 7**. It can be observed that the tensile stress increased with an increase in strain after the first crack. Thus these mixtures all satisfied the requirements for the strain-hardening behavior of HPFRCC. Beyond the peak stress, the tensile stress dropped gradually because of fiber kinematic pullout from the matrix. Some key results are summarized in **Table 2**.

LONG PRISMATIC REINFORCED TENSILE TEST

A detailed discussion regarding the test results can be found in Ref 5. Typical tensile load-elongation responses of the composite and bare strand in zone 3 are shown in **Fig. 8**.

FIG. 7 Typical tensile stress-strain curve of HF-SHFRC.

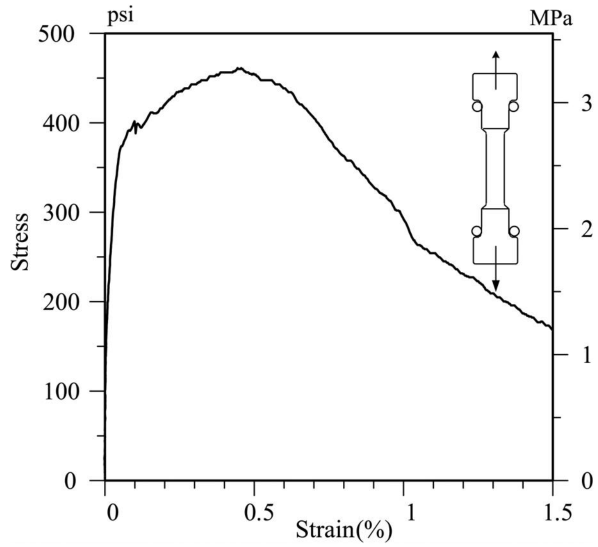

TABLE 2 Key results of HF-SHFRC direct tensile test.

Tensile Properties of HF-SHFRC	
Average post-cracking strength, MPa	3.61
Average strain at peak stress, %	0.45
Stress at apparent strain = 0.5 %	3.54
Percentage of peak stress, MPa	98 %
Average number of cracks	6
Average crack spacing, mm	25.7

The stress-strain response of the HF-SHFRC was also obtained based on Eq 1 and is plotted in **Fig. 9**, along with an envelope curve. The unloading loops were the result of softening caused by the hydraulic jack during crack measurement and photographing.

Figure 9 shows that the HF-SHFRC used in this study exhibited tensile strain-hardening behavior up to 0.7 % composite strain, along with extensive multiple cracking. The stress-strain curve was generally very stable without any sudden degradation in strength. This can be attributed to the presence of the longitudinal reinforcement, which was able to redistribute tensile stress through bonding when cracks occurred.

Figure 10 compares the tensile stress-strain responses of the direct tensile test and long prismatic reinforced tensile test specimens made of the same HF-SHFRC mixture. It is observed that the peak tensile strength of the former was greater than that of the long prismatic reinforced specimen. This can be attributed to scale effects and to the possible two-dimensional versus three-dimensional fiber orientations in the two specimens, respectively. In addition, the onset of damage localization as a result of fiber pullout at peak stress was significantly delayed in the presence of continuous reinforcement. Indeed, the tensile strain up to the peak strength in the long prismatic reinforced specimen was more than two times that of the dog-bone-shaped specimen. The smaller strain in the dog-bone-shaped specimen possibly resulted from the fact that smaller

FIG. 8 Typical tensile load-elongation of reinforced HF-SHFRC prism.

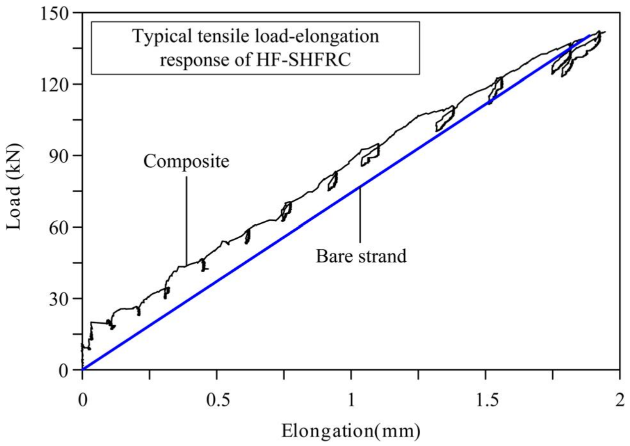

FIG. 9 Typical tensile stress-strain responses of HF-SHFRC in long prismatic reinforced tensile test.

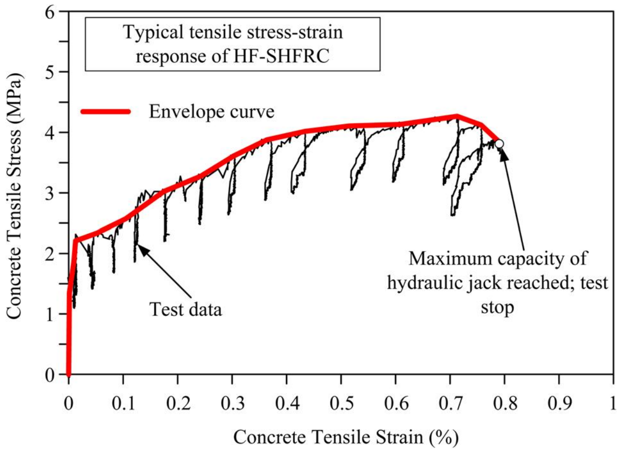

specimens are more sensitive to defects such as nonuniformly distributed fibers and coarse aggregates. Furthermore, without continuous reinforcement, crack extension is more likely to become unstable during stressing.

IN-PLANE PURE SHEAR PANEL TEST

The shear stress–shear strain response of an HF-SHFRC panel is plotted in **Fig.** 11. The behavior remained linear up to first cracking at a shear stress of 1.5 MPa. The panel failure occurred at a maximum shear stress of 4.3 MPa and a corresponding shear strain of 6.20×10^{-3}. At the onset of panel failure, the applied load gradually declined, and the major cracks opened up slowly. The failure of the panel was dictated by an aggregate interlock failure, as there was no indication of concrete crushing or reinforcement rupture.

A comparison of principal tensile stress-strain behaviors of HF-SHFRC and control panels is shown in **Fig.** 12. The test data for the control panel were adopted from Susetyo's previous work [8]. It is noted that the control panel ($f'_c = 50$ MPa), which was made of conventional concrete, had higher reinforcement ratios (x-direction: reinforcement area of 2061 mm^2, $\rho_x = 3.31$ %; y-direction: reinforcement area of 260 mm^2, $\rho_y = 0.42$ %) than the HF-SHFRC panel. The principal tensile stress-strain relationships of HF-SHFRC and conventional concrete were converted from the shear stress-strain relation based on Mohr's circle method. Because of the higher compressive strength of conventional concrete, the maximum principal tensile stress of conventional concrete was higher than that of HF-SHFRC, as expected. However, in contrast to the strain-softening behavior of conventional concrete, HF-SHFRC exhibited tensile strain hardening until failure occurred, at which point the principal tensile strain reached 4.1×10^{-3}. This proved that strain-hardening behavior can be achieved with the addition of fibers and that fiber addition can significantly improve the tension-carrying capacity of the concrete.

FIG. 10 Comparison between stress-strain responses of dog-bone and long prismatic reinforced specimens made of HF-SHFRC mixture.

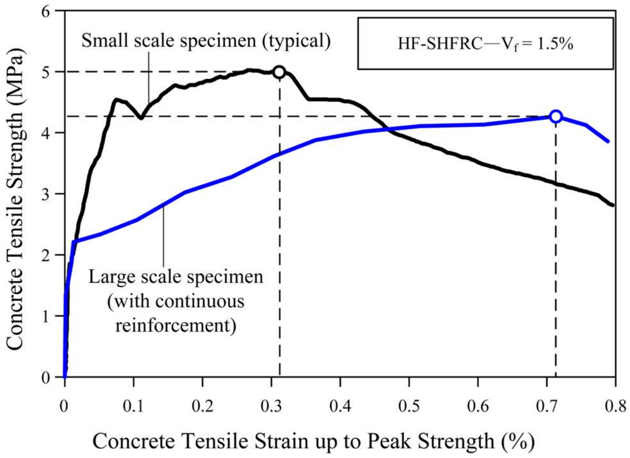

FIG. 11 Shear stress–shear strain response of HF-SHFRC panel.

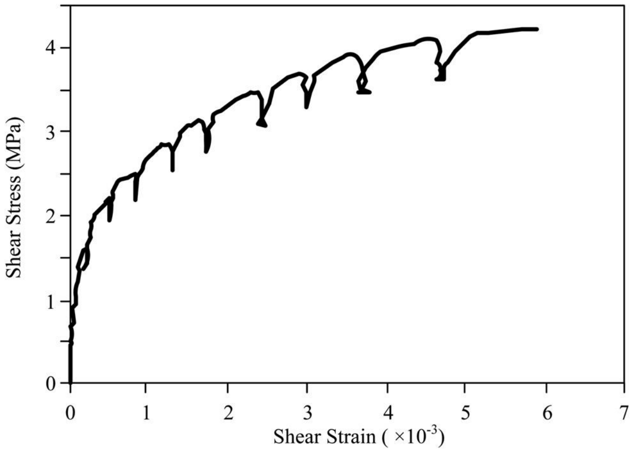

FIG. 12 The principal tensile stress-strain relationships of HF-SHFRC and conventional concrete.

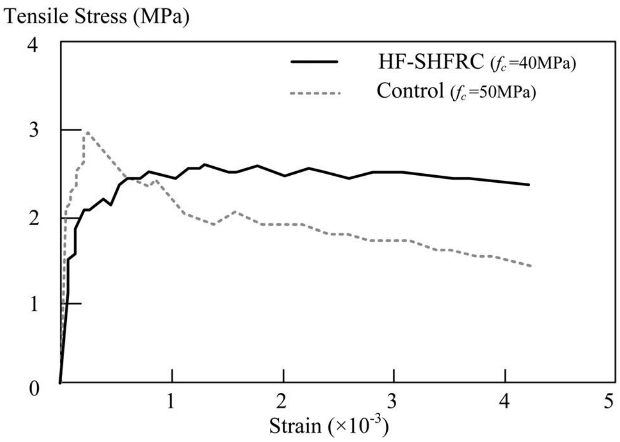

Crack Opening Evaluation

Adding fibers into concrete can enhance its performance in many aspects. Cracking width control is also one of the most important advantages of adding fibers. Fiber addition can control and minimize not only plastic shrinkage cracking but also other volumetric expansions caused by alkali–silica reaction, as well as cyclic loading and tensile forces [9]. The resistance to crack opening of HF-SHFRC under tensile and shear forces is discussed in the following sections.

LONG PRISMATIC REINFORCED TENSILE TEST

Figure 13 shows HF-SHFRC exhibiting multiple cracking at the conclusion of testing. Compared to the crack localization of conventional concrete, more extensive, well-distributed multiple cracks can be observed in the HF-SHFRC specimen.

The test results also showed that no primary crack opening localization occurred, and additional secondary cracks were still able to develop with an average crack width of less than 50 μm under concrete tensile strains of up to 0.7 %, as illustrated in **Fig. 14**.

The tensile tests showed the behavior of HF-SHFRC concrete to be significantly improved. The comparison of HF-SHFRC crack patterns and control panels at failure is shown in **Fig. 15**. It was observed that the failure of the HF-SHFRC panel was caused by the inability of the concrete to transmit the load across the cracks (coarse aggregate interlock failure), instead of the yielding or fracture of the transverse reinforcement in the conventional concrete panel. The cracks in the HF-SHFRC panel were significantly finer and well-distributed across the face of the panel, with crack spacing smaller than that observed in the control panel.

IN-PLANE PURE SHEAR PANEL TEST

An important property of HF-SHFRC is its ability to control crack propagation through the addition of fibers. In conventional RC, crack control is provided by the bonded steel reinforcement; without it, the concrete exhibits brittle behavior. In HF-SHFRC, the intrinsic fibers act as crack controllers. Maximum crack opening widths at different shear stress levels of HF-SHFRC and conventional concrete were also recorded as seen in **Fig. 16**. It can be observed that even without the presence of transverse reinforcement, HF-SHFRC exhibited smaller crack opening widths at the same shear stress level, representing about 40 % improvement over conventional concrete. This signifies the ability of fibers to control crack propagation.

FIG. 13 Crack distributions in HF-SHFRC after long prismatic reinforced tensile test.

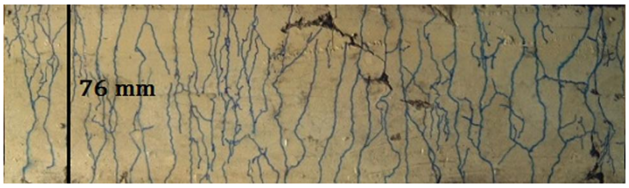

FIG. 14 Average crack widths (zones 1 through 5) in HF-SHFRC versus tensile strain.

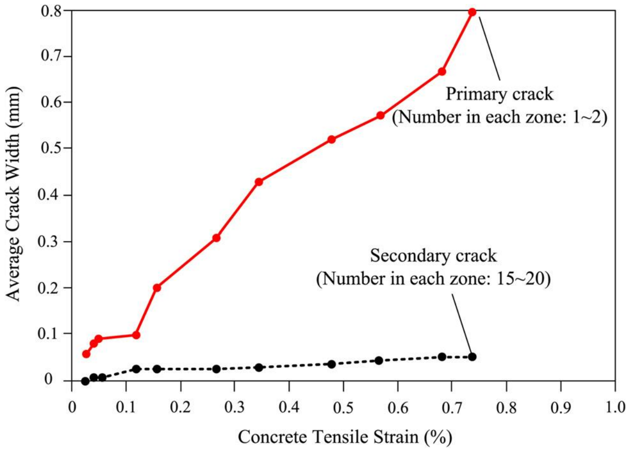

Sustainability Potential of Highly Flowable Strain-Hardening Fiber-Reinforced Concrete

As mentioned earlier, HF-SHFRC can enhance sustainability without compromising mechanical performance. This is mainly due to its mix composition and the addition of fibers. It is noteworthy that the water/binder material ratio of HF-SHFRC is relatively low, thus providing good watertightness and durability. Considerable amounts of fly ash and slag are also used in HF-SHFRC as the main replacement for cement. Moreover, the excellent workability and mechanical properties of HF-SHFRC offer opportunities to reduce labor costs and simplify structural member design to further eliminate steel reinforcement. All these sustainable characteristics of HF-SHFRC are briefly summarized in the following subsections.

LOW WATER/BINDER RATIO

Too much mixing water can be the main cause of concrete's durability problems. The permeability of concrete in the hardened state is directly affected by the amount of water added to fresh concrete. Water or environmental solvents can easily pass through under the high permeability of concrete. Concrete mixes with low water/binder ratios produce few interconnected capillaries and therefore enhance the durability of concrete. A water/binder material ratio of 0.45 or less is considered as an essential requirement for highly durable concrete. With the use of SP and VMAs, HF-SHFRC can still achieve self-consolidating rheological properties with water/binder ratios of 0.30 to 0.42.

FIG. 15 Crack pattern at failure stage of HF-SHFRC and conventional concrete.

SUSTAINABLE CONSTRUCTION MATERIAL

Sustainable construction materials are industrial byproducts, such as fly ash, blast furnace slag, silica fume, or other pozzolanic materials. The use of sustainable construction materials as substitutes for considerable amounts of cement not only significantly reduces energy consumption, carbon footprint, and emissions of CO_2 due to the cement manufacturing process, but also improves the durability of concrete by leading to further reactions with carbon hydroxide ($Ca(OH)_2$). In compositions of HF-SHFRC, it can be observed that there is 50 % replacement of cement by fly ash in the HF-SHFRC mix design. Owen [10] also found that the fine particle size and spherical shape of fly ash allow it to act as a water reducer to help cement particles disperse and reduce friction between particles. Therefore, the water-reducing property of fly ash can further reduce the drying shrinkage of concrete to improve volume stability. In addition, a substantial substitution of cement by fly ash can significantly lower the hydration heat during the early stage of production to prevent thermal cracking. To sum up, a combination of reduction of water content, pozzolanic reaction, particle advantage, and low heat of hydration ensures the durability of concrete.

FIG. 16 Comparisons of maximum crack opening widths in HF-SHFRC and conventional concrete.

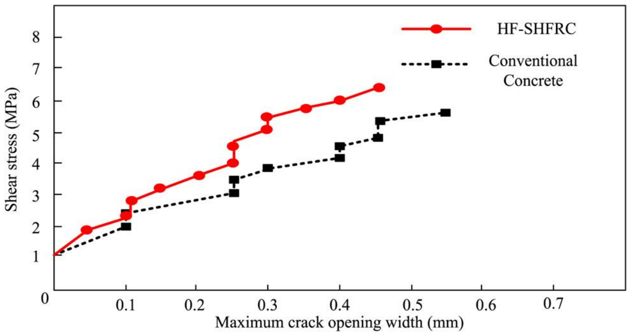

ADDITION OF FIBER

Adding fibers into concrete can enhance its durability in many aspects. Grubb et al. [11] found that the potential for corrosion of steel reinforcing bars can be decreased by the formation of passive confinement due to fibers. Cracking width control is also one of the most important advantages of adding fibers. Plastic shrinkage cracking, other volumetric expansions caused by alkali–silica reaction, and cyclic loading or tensile forces can also be effectively controlled and minimized [12].

EXCELLENT MECHANICAL PROPERTIES

Structural member sizes can be further reduced owing to the greater strength of HF-SHFRC. Moreover, in terms of reinforcement layouts, the excellent mechanical properties of HF-SHFRC also offer the opportunity to significantly simplify the design and construction of structural members while ensuring adequate strength, ductility, and damage tolerance. Lequesne et al. [13] proposed a simplified design using coupling beams and found that HF-SHFRC can be relied on to provide sufficient confinement of diagonal reinforcement even without heavy steel confinement reinforcement. The significant field placement difficulties, labor, and costs can be efficiently eliminated. Li et al. [14] applied engineered cementitious composites (ECCs), which are considered as one type of HPFRCC, to link slabs of jointless bridge decks to replace mechanical expansion joints and estimated the life-cycle cost based on a 60-year lifetime. The estimation showed that the ECC system provides a 15 % cost advantage over the traditional system because of the ultra-high ductility of ECC. The excellent mechanical properties provide advantages in terms of life-cycle costs, including those due to maintenance and rehabilitation of deteriorated structures.

Conclusions

(1) It is generally agreed that adding fibers can expand the applications of SCC; however, a reduction in workability

due to fiber addition may become a barrier for its application in practice. By modifying SCC mixtures recommended in previous studies and using locally available materials, one can easily manufacture HF-SHFRC mixtures for different strength demands.

(2) In terms of the tensile behaviors of HF-SHFRC, the peak tensile strength obtained from dog-bone-shaped specimens was generally higher than that of long prismatic reinforced specimens. The tensile strain at the onset of damage localization in the long prismatic reinforced specimens was about twice that observed in the dog-bone-shaped specimens in which no reinforcement was used. The presence of continuous reinforcement leads to a significantly better crack development, as well as a significant increase in energy absorption capacity.

(3) This paper also presents in-plane pure shear panel test results for HF-SHFRC, including shear stress–shear strain responses and principal tensile stress-strain behavior. Noticeable tensile strain hardening was observed in HF-SHFRC. In terms of failure mode and crack patterns, HF-SHFRC showed fine and well-distributed cracks with much smaller crack spacing than observed in the conventional concrete panel. HF-SHFRC exhibited smaller crack opening widths at the same shear stress level, with an improvement of about 40 % over conventional concrete. This signified the ability of fibers to control crack propagation.

(4) HF-SHFRC permits the incorporation of substitute sustainable construction materials and a high volume fraction of steel fibers while allowing good workability, guaranteeing excellent mechanical performance and high damage tolerance. All these advantages have served rather well relative to conventional concrete; thus, it is believed that HF-SHFRC will achieve higher levels of performance, safety, and economy, including with regard to life cycle costs.

ACKNOWLEDGMENTS

The research described herein was sponsored by the National Science Foundation under Grant Nos. CMS 0530383 and CMS 0754505, the University of Michigan, and the University of Toronto. Their support is gratefully acknowledged. In addition, the guidance and instruction of Dr. Antoine E. Naaman at the University of Michigan and Dr. Gustavo Parra-montesinos at the University of Wisconsin-Madison are highly appreciated. The opinions expressed in this paper are those of the authors and do not necessarily reflect the views of the sponsors.

References

[1] Naaman, A. E., "Strain Hardening and Deflection Hardening Fiber Reinforced Cement Composites," *High Performance Fiber Reinforced Cement Composites 4, Proceedings of the Fourth International RILEM Workshop*, Ann Arbor, MI, June 15–18, RILEM, France, 2003, pp. 95–113.

[2] Liao, W.-C., Chao, S.-H., and Naaman, A. E., "Experience with Self-consolidating High Performance Fiber Reinforced Mortar and Concrete," *ACI Special Publication No. 247: Fiber Reinforced Self-Consolidating Concrete—Research and Applications*, American Concrete Institute, Farmington Hills, MI, 2010, pp. 79–94.

[3] Eliasson, B., Riemer, P., and Wokaun, A., *Greenhouse Gas Control Technologies*, Elsevier, New York, 1999.

[4] Bui, V. K., Geiker, M. R., and Shah, S. P., "Rheology of Fiber-Reinforced Cementitious Materials," *RILEM PRO30 High Performance Fibre Reinforced Composites HPFRCC4*, Ann Arbor, MI, June 15–18, RILEM, France, 2003, pp. 221–232.

[5] Chao, S.-H., Liao, W.-C., and Naaman, A. E., "Large Scale Tensile Tests of High Performance Fiber Reinforced Cement Composites," *RILEM PRO53 High Performance Fibre Reinforced Composites HPFRCC5*, Mainz, Germany, July 10–13, 2007, RILEM, France, pp. 77–86.

[6] Johnston, C. D., "Proportioning, Mixing and Placement of Fibre-Reinforced Cements and Concretes," Bartos, Marrs, and Cleland, Eds., *Production Methods and Workability of Concrete*, E&FN Spon, London, 1996, pp. 155–179.

[7] Vecchio, F. J., 1979, "Shear Rig Design," M.Eng. thesis, University of Toronto, Toronto, ON, Canada.

[8] Susetyo, J., 2009, "Fiber Reinforcement for Shrinkage Crack Control in Prestressed, Precast Segmental Bridges," Ph.D. thesis, University of Toronto, Toronto, ON, Canada.

[9] Bektas, F., Turanli, L., and Ostertag, C. P., "New Approach in Mitigating Damage Caused by Alkali-Silica Reaction," *J. Mater. Sci.*, Vol. 41, 2006, pp. 5760–5763.

[10] Owen, P. L., "Fly Ash and Its Usage in Concrete," *J. Concr. Soc.*, Vol. 13(7), 1979, pp. 21–26.

[11] Grubb, J. A., Blunt, J., Ostertag, C. P., and Devine, T. M., "Effect of Steel Microfibers on Corrosion of Steel Reinforcing Bars," *Cem. Concr. Res.*, Vol. 37, 2007, pp. 1115–1126.

[12] Bektas, F., Turanli, L., and Ostertag, C. P., "New Approach in Mitigating Damage Caused by Alkali-Silica Reaction," *J. Mater. Sci.*, Vol. 41, 2006, pp. 5760–5763.

[13] Lequesne, R., Setkit, M., Parra-montesinos, G. J., and Wight, J. K., "Seismic Detailing and Behavior of Coupling Beams with High-performance Fiber Reinforced Concrete," *Antoine E. Naaman Symposium—Four Decades of Progress in Prestressed Concrete, Fiber Reinforced Concrete, and Thin Laminate Composites*, Los Angeles, CA, March 30–April 3, ACI, Farmington Hills, MI, 2009.

[14] Li, V. C., Lepech, M., Wang, S., Weimann, M., and Keoleian, G., "Development of Green ECC for Sustainable Infrastructure Systems," *Proceedings of the International Workshop on Sustainable Development and Concrete Technology, Beijing, China*, K. Wang, Ed., Iowa State University, Beijing, China, May 20–21, 2004, pp. 181–192.

Journal of Testing and Evaluation

doi:10.1520/JTE20140025 / Vol. 43 / No. 2 / March 2015 / available online at www.astm.org

Xinzhuang Cui,[2] Jiong Zhang,[1] Fei Hou,[2] Zhijun Gao,[2] Zengtang Wang,[3] and Wei Sui[2]

Experimental Study of the Effect of RCC Specimen Size and Crack Depth Ratio on Double-K Fracture Parameters

Reference

Cui, Xinzhuang, Zhang, Jiong, Hou, Fei, Gao, Zhijun, Wang, Zengtang, and Sui, Wei, “Experimental Study of the Effect of RCC Specimen Size and Crack Depth Ratio on Double-K Fracture Parameters,” *Journal of Testing and Evaluation*, Vol. 43, No. 2, 2015, pp. 336–343, doi:10.1520/JTE20140025. ISSN 0090-3973

Manuscript received January 22, 2014; accepted for publication November 4, 2014; published online December 12, 2014.

[1] School of Civil Engineering, Shandong University, 17922 Jingshi Road, Jinan, Shandong 250061, China (Corresponding author).

[2] School of Civil Engineering, Shandong University, 17922 Jingshi Road, Jinan, Shandong 250061, China.

[3] Weifang Highway Bureau of Luqiao Construction, Engineering Development Center, Weifang, Shandong 261031, People’s Republic of China, China.

ABSTRACT

When the height of roller compacted concrete (RCC) specimen is less than 400 mm, the specimen size and crack depth ratio will affect the double-K fracture parameters. In this paper, two groups of RCC specimens with different specimen size and crack depth ratio were investigated and the wedge splitting method was employed. Double-K fracture parameters were calculated employing the double-K fracture theory of concrete. It is indicated that when the crack depth ratio, α, increased from 0.4 to 0.6, the unstable fracture toughness, K_{IC}^{un}, increases, while the initial fracture toughness, K_{IC}^{ini}, decreases. The crack depth ratio, α, has a continuous effect on K_{IC}^{ini}, however the effect on K_{IC}^{un} decreases with the increase of α. When the height of the specimen, h, is less than 300 mm, the effect of specimen size on K_{IC}^{un} is significant, but it decreases when h is greater than 300 mm and less than 500 mm.

Keywords

wedge splitting test, specimen size, crack depth ratios, double-K fracture parameters

Introduction

Unlike conventional concrete (CC), roller compacted concrete (RCC) is a drier mix, stiff enough to be compacted with vibratory rollers. Typically, RCC is constructed without joints and needs neither forms nor finishing, nor does it contain dowels or steel reinforcing. These characteristics make RCC a simple, fast, and economical mix, and as such, more and more countries have begun to use RCC as an effective pavement solution [1]. Due to its advantages as a comparatively low cost, durable paving material, RCC has been used widely in urban street reconstruction, residential subdivision roads, and some heavy traffic pavements. However, like CC, cracking is a serious problem for RCC.

Traditional strength theory provides a criterion for judging the failure of concrete. Shihata [2] conducted an experimental program to study the effect of compaction on the strength of RCC specimens. However, the traditional theory ignores the effect of specimen size on load-carrying capacity. By analyzing the stress and strain fields at the crack tip, fracture mechanisms introduced the concept of fracture toughness to reflect the ability to resist crack propagation in concrete materials [3]. It is used widely to analyze the failure of concrete structure because it can be employed to estimate the response of structure more accurately by reasonably explaining the size effect. Ramsamooj [4] presented an approximate analytical model for the fatigue crack propagation rate in concrete; the model considers fatigue cracking at all stress levels up to the modulus of rupture. Nguyen et al. [5] studied various fatigue criteria with indirect tensile mode of loading. A new approach was proposed to identify the fatigue failure based on a crack-length criterion. In plastic limit analysis or elasticity with strength limit, the nominal strength of concrete is size independent; this phenomenon is called the size effect. Bazant and Kazemi [6] proposed the size effect model and studied the fracture and size effect in concrete [7]. Several studies have been done on crack development and fracture mechanisms of the RCC. Nallathambi and Karihaloo [8] studied the effects of the specimen and crack sizes upon fracture toughness of concrete. Pittman and McCullough [9] carried out experiments to study the crack development of RCC pavement. Based on toughness and fracture tests, Albuquerque et al. [10] studied the fracture characterization of RCC and determined the crack extension resistance curve of the concrete mixtures. In order to avoid the non-ordered cracks, induced cracks are adopted in the RCC. Based on the characteristics of the induced cracks, Liu and Song [11] employed a fictitious crack model and linear elastic fracture mechanics to study equivalent strength of induced cracks. Results indicated that equivalent strength could be used as the fracture criterion for induced cracks. Zhang et al. [12] evaluated the fracture parameters and the critical crack length of RCC and provided a calculation method for the initial fracture and development of induced cracks.

Xu and Zhao [13] put forward the double-K (the initial fracture toughness, K_{IC}^{ini}, and the unstable fracture toughness, K_{IC}^{un}) fracture theory and gave a simple and practical crack fracture criterion. The use of three point bending beam test and wedge-splitting test (WST) to determine the double-K fracture parameters of concrete is recommended by the Chinese norm for fracture test of hydraulic concrete [14]. However, the specimen size and crack depth ratio will affect the double-K fracture parameters. Moreover, minimal research has been done in this area. In this paper, WST is employed to study the effect of specimen size and crack depth ratio on double-K fracture parameters.

Double-K Fracture Theory of Concrete

Based on the stress intensity factor of concrete and the concept of virtual cracks that reflect the softening properties of concrete, the double-K fracture theory is a more complete theory used to describe the fracture of concrete. The double-K criterion can predict the different stages of crack propagation during the fracture process in quasi-brittle materials. According to this criterion, the two size independent parameters, K_{IC}^{ini} and K_{IC}^{un}, can be used to describe the fracture process of concrete [15].

Double-K fracture theory of concrete can be described as follows: comparing with K_{IC}^{ini} and K_{IC}^{un}, if the crack tip stress intensity factor, K, is less than K_{IC}^{ini}, the concrete structure has no cracks. When K is greater than K_{IC}^{ini} but less than K_{IC}^{un}, cracks occur and begin to extend steadily. If K is greater than K_{IC}^{un}, the cracks of the structure start to extend unsteadily.

For the concrete structures in any shape, K can be calculated by many numerical methods. In practical application, $K = K_{IC}^{ini}$ is the judgment criterion of the crack propagation in main structure. $K_{IC}^{ini} < K < K_{IC}^{un}$ can be used as the security alert of the unstable propagation of the main structure. $K > K_{IC}^{un}$ is the judgment criterion of the general structure.

Preparation of RCC Specimens

When the height of specimens is greater than 400 mm, the double-K fracture parameters are approximately constant [16]. So in this study, the sizes of the specimens were ~400 mm. The specimens were prepared according to the Chinese Test Methods of Cement and Concrete for Highway Engineering [17]. All the RCC specimens were made by the same batch, which had the same mix proportions of concrete, the materials, and the compressive strength of the RCC specimens as shown in **Table 1**. The cement was P.O32.5R silicate cement, the river sand with grain size <5 mm was used as the fine aggregate, and the coarse aggregate was the crushed stone with grain size <20 mm. All the materials were mixed and fully stirred, then the mixture was

TABLE 1 The materials and the compressive strength of RCC.

Water (%)	Cement (%)	Fly Ash (%)	Fine Aggregates (%)	Coarse Aggregates (%)	Additive (%)	f_{cu} (MPa)
5.33	5.40	3.69	32.35	52.48	0.75	37.87

TABLE 2 The sizes and crack depth ratios of the two groups of specimens.

Group	l by h by t (mm by mm by mm)	α	a (mm)	m (mm)
Group1	150 by 150 by 150	0.4	60	3
	150 by 150 by 150	0.5	75	3
	150 by 150 by 150	0.6	90	3
Group2	300 by 300 by 150	0.4	120	3
	400 by 400 by 150	0.4	160	3
	500 by 500 by 150	0.4	200	3

placed into the molds, and a vibrating hammer was used to produce specimens with two layers. After casting, the specimens were covered with plastic film until the next day when they were de-molded. The specimens were then stored in water, with a temperature of 21 ± 2°C, until the time of testing that in most cases took place 28 days after casting.

A total of 18 specimens were prepared. Three types of specimens were included in group 1 and group 2. There were 3 RCC specimens in each type, as shown in **Table 2**. The specimen is equipped with two blocks of marble (for applying the splitting force), and the shape and size of the RCC specimen is shown in **Fig. 1**, and the real RCC specimen is shown in **Fig. 2**. In **Table 2** and **Fig. 1**, l, h, t are the length, height and thickness of the specimens, respectively, α is the crack depth ratio, a is the length of the crack, and m is the thickness of the crack.

Wedge Splitting Test (WST)

In this paper, WST was employed. The WST method, originally proposed by Linsbauer and Tschegg [18] and later developed by Brühwiler and Wittmann [19], is a simple method since it does not require sophisticated test equipment and the result is stable. The WST method has been proved successful for the determination of fracture properties of concrete [20,21].

FIG. 1 Shape and size of RCC specimen.

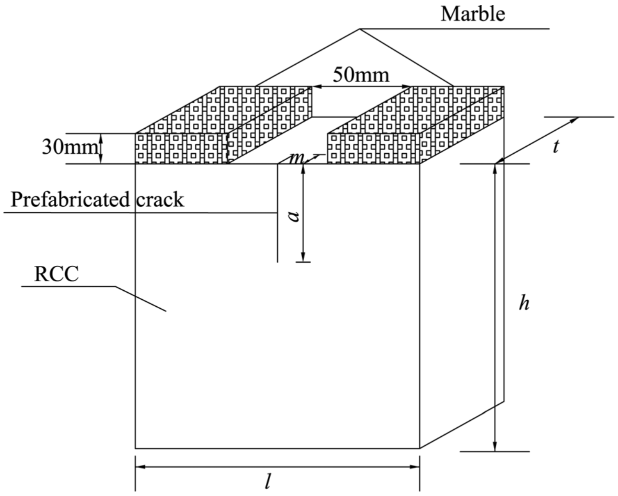

FIG. 2 RCC specimen.

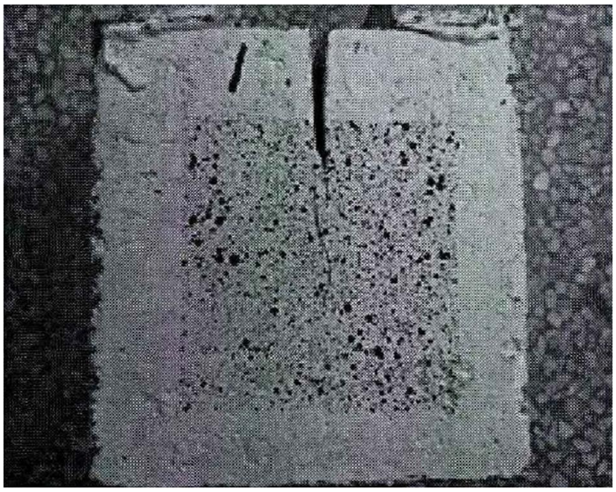

A schematic of the testing equipment is clarified in **Fig. 3**, and the real testing picture shown in **Fig. 4**. Two steel plates with roller bearings and the wedge-shaped frame are placed partly on top of the specimen and partly into the groove that is between the two blocks of marble. On the surface of the upper platen, there is a reservation groove, through which the clip-on extensometer can be installed on the surface of the RCC specimen. During the test, the force on the specimen (F) and the crack mouth opening displacement ($CMOD$) can be measured by the force sensor and the clip-on extensometer, respectively. Through the signal acquisition instrument, the data can be acquired and sent to the computer, then F and $CMOD$ obtained. The typical F-$CMOD$ curve is shown in **Fig. 5**. The $CMOD_c$ is $CMOD$ corresponding to $F_{\max}$.

Calculation Methods of Double-K Fracture Parameters

For specimens with different sizes, the calculation methods of the double-K fracture parameters are different. For the specimen with the size of 150 by 150 by 150 mm, according to the Chinese specification of norm for fracture test of hydraulic concrete (DL/T5332-2005), the double-K fracture parameters can be calculated as follows:

Unstable fracture toughness, K_{IC}^{un}, is determined by Eq 1:

$$K_{IC}^{un} = \frac{F_{H\max} \times 10^{-3}}{h\sqrt{t}} \times f(\alpha) \qquad (1)$$

where:

$F_{H\max}$ = the maximum horizontal force, determined by Eq 2,

t and h = the thickness and height of specimen, as shown in **Fig. 1**, $f(\alpha) = (3.675[1 - 0.12(\alpha - 0.45)])/(1 - \alpha)^{3/2}$, $\alpha = (a_c/h)$, and

FIG. 3

Schematic of the equipment.

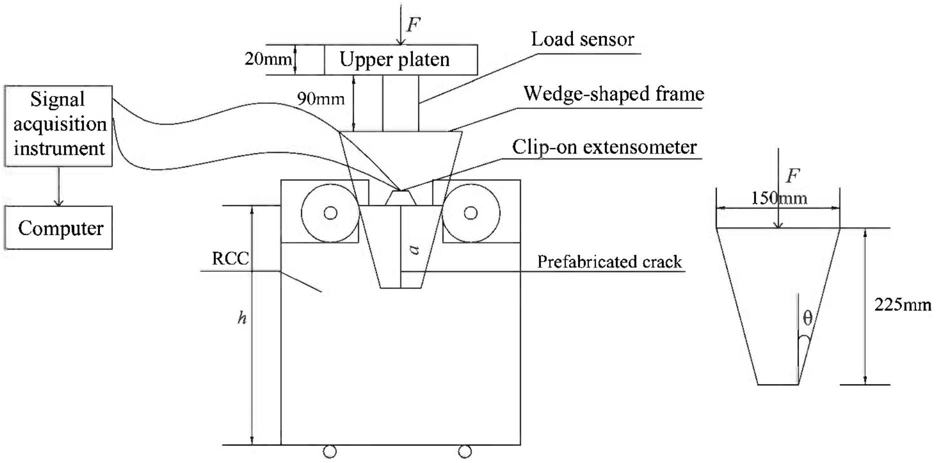

a_c = effective crack length, determined by Eq 3.

$$F_{H\max} = \frac{F_{\max} + mg \times 10^{-2}}{2\tan\theta} \tag{2}$$

where:

$F_{\max}$ = the maximum force, as shown in **Fig. 5**,

m = the mass of the wedge loading frame,

g = the acceleration due to gravity, and

θ = the angle between wedge loading frame wedge surface and the longitudinal axis, as shown in **Fig. 3**.

$$a_c = (h + h_0)\left[1 - \left(\frac{13.18F_{H\max}}{tECMOD_c} + 9.16\right)^{1/2}\right] - h_0 \tag{3}$$

where:

h_0 = the thickness of the steel plate in clip-on extensometer,

$CMOD_c$ = the critical crack mouth opening displacement, as shown in **Fig. 5**, and

FIG. 4 Real testing picture.

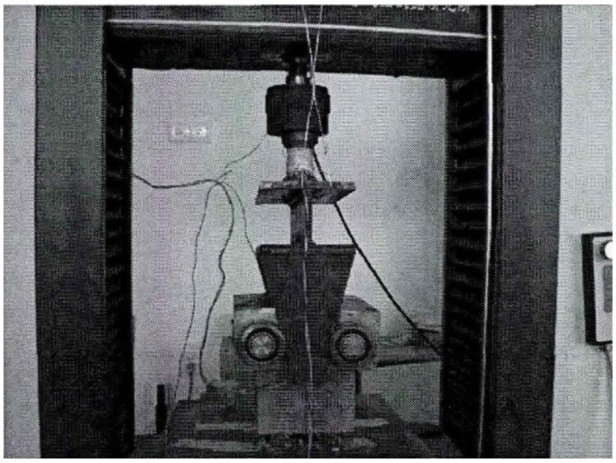

E = the calculated elastic modulus (GPa), determined by the following equation:

$$E = \frac{1}{tc_i}\left[13.18\left(1 - \frac{a_0 + h_0}{h + h_0}\right)^{-2} - 9.16\right] \tag{4}$$

where:

c_i = the initial value of $CMOD/F$,

$CMOD$ = the crack mouth opening displacement, as shown in **Fig. 5**,

F = the force on the specimen, as shown in **Fig. 3**, and

a_0 = the initial crack length.

Initial fracture toughness K_{IC}^{ini} is determined by Eq 5:

$$K_{IC}^{ini} = \frac{F_{HQ} \times 10^{-3} \times f(\alpha)}{t\sqrt{h}} \tag{5}$$

where F_{HQ} is the crack initiation horizontal load, determined by Eq 6:

$$F_{HQ} = \frac{F_Q + mg \times 10^{-2}}{2\tan\theta} \tag{6}$$

where F_Q is the crack initiation load.

FIG. 5 Typical F-CMOD curve.

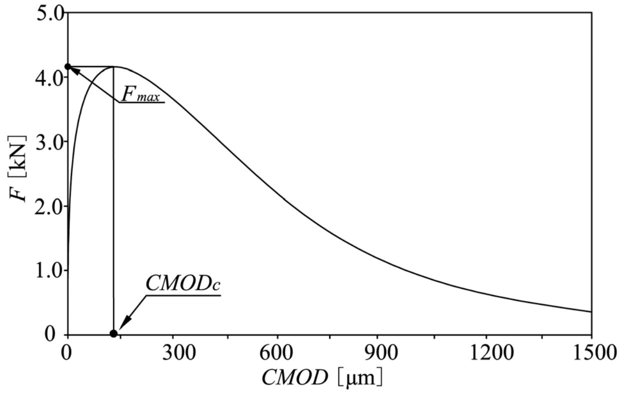

FIG. 6

Force conditions and equivalent force analysis of RCC specimen.

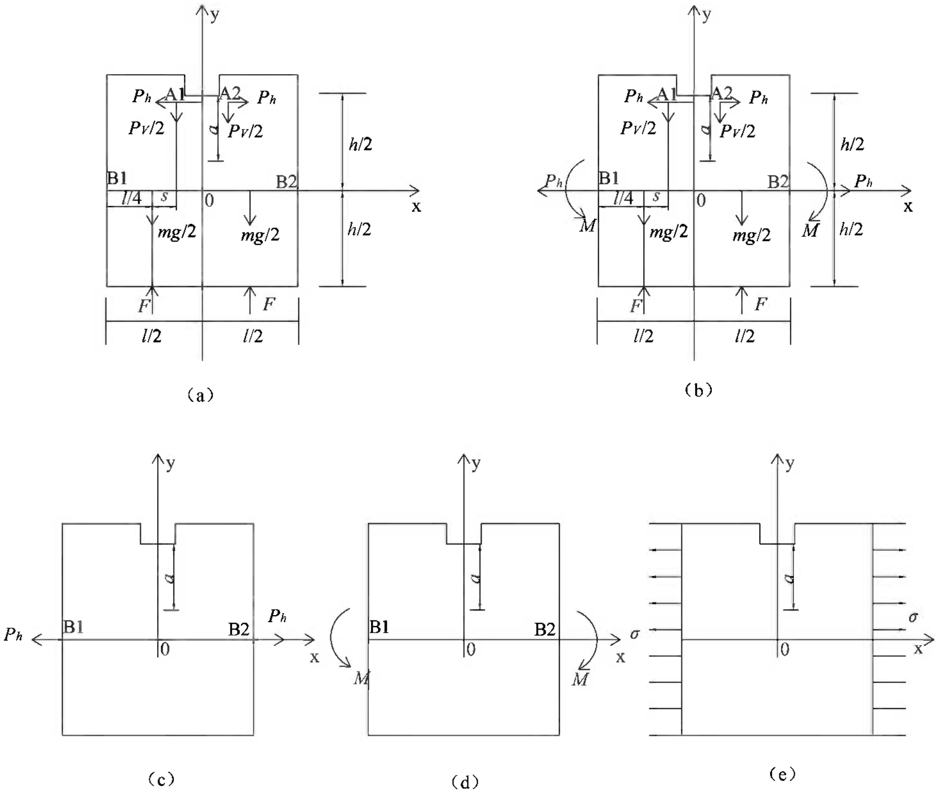

For the specimen with sizes larger than 150 by 150 by 150 mm, the coordinate system with the center of specimen as the origin is drawn as in **Fig. 6(*a*)**, where A1 and A2 is force points of the wedge loading frame; P_h is the horizontal force and P_v is the vertical force from the wedge loading frame; F is the support force. According to the balance of force, $F = \frac{1}{2}mg + \frac{1}{2}F_v$, when the symmetrical force of both side moved to B1 and B2 (as shown in **Fig. 6(*a*)**), the stress system of **Fig. 6(*a*)** is equivalent to **Fig. 6(*b*)**, where M is the equivalent bending moment. According to the superposition principle of intensity factor [22], **Fig. 6(*b*)** can be decomposed into the **Fig. 6(*c*)** and **Fig. 6(*d*)**, and **Fig. 6(*c*)** is equivalent to **Fig. 6(*e*)**. Then the stress condition of the specimen turns into the sum of uniaxial tension and pure bending moment.

So the unstable fracture toughness, K_{IC}^{un}, can be expressed as Eq 7:

$$K_{IC}^{un} = K_1 + K_2 \tag{7}$$

K_1 is the unstable fracture toughness for the specimen under uniaxial tension, determined by Eq 8:

$$K_1 = \sigma(\pi a_c)^{\frac{1}{2}} \times f\left(\frac{a_c}{h}\right) \tag{8}$$

where $f(a_c/h) = 1.122 - 0.231(a_c/h) + 1.055(a_c/h)^2 - 21.71(a_c/h)^3 + 30.382(a_c/h)^4$; $\sigma = P_h/th$.

K_2 is the unstable fracture toughness for the specimen under pure bending moment, determined by Eq 9:

$$K_2 = \frac{6M}{th^2}(\pi a_c)^{\frac{1}{2}} \times g\left(\frac{a_c}{h}\right) \tag{9}$$

where $g(a_c/h) = 1.122 - 1.40(a_c/h) + 7.33(a_c/h)^2 - 13.08(a_c/h)^3 + 14.0(a_c/h)^4$; $M = (1/2)P_h - (1/2)sP_v$.

Results and Analyses

The crack in the RCC specimen during the test is shown in **Fig. 7**.

In **Fig. 7**, the subcritical effective crack can be clearly seen; the crack develops roughly. This phenomenon is caused by the aggregate in the RCC specimen, when the crack meets the aggregates, it will then bypass.

EFFECT OF CRACK DEPTH RATIO ON DOUBLE-K FRACTURE PARAMETERS

The relationships of $CMOD_c$, $F_{H\max}$, a_c, K_{IC}^{ini}, and K_{IC}^{un} with the crack depth ratio α can be obtained from tests with specimens of group 1. The results are shown in **Figs. 8–12**.

The relation curves of $CMOD_c$–α, $F_{H\max}$–α, and a_c–α all can be well fitted by exponential function, whereas K_{IC}^{ini}–α can be fitted by Boltzmann function. For the K_{IC}^{un}–α, the linear

FIG. 7 Crack propagation of RCC specimen.

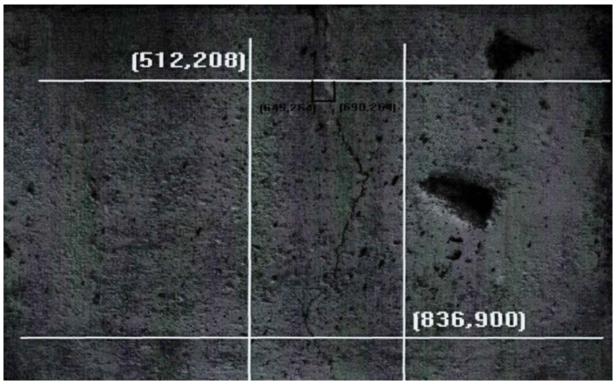

function is appropriate to fit the relation curve. All the fitting equations are shown in the corresponding figures above, where R is the correlation coefficient. It can be found that $CMOD_c$ and a_c increase with the increase of α, whereas $F_{H\,\max}$ decreases.

The effect of α on K_{IC}^{ini} is different from K_{IC}^{un}, α has a negative influence on K_{IC}^{ini}, i.e., K_{IC}^{ini} decreases with the increase of α. The effect of α on K_{IC}^{un} is positive, i.e., K_{IC}^{un} increases with the increase of α. In the range of 0.4 ~ 0.6, α has a continuous effect on K_{IC}^{ini}; however, the effect on K_{IC}^{un} decreases with the increase of α.

EFFECT OF SPECIMEN SIZE ON THE UNSTABLE FRACTURE TOUGHNESS K_{IC}^{un}

The relationships of $CMOD_c$, $F_{H\,\max}$, a_c, and K_{IC}^{un} with h can be obtained from tests with specimens of group 2. The results are shown in **Figs.** 13–16, respectively.

The relation curves of $CMOD_c$–h, a_c–h can be fitted by a linear function, while $F_{H\,\max}$–h can be fitted by Gauss function. For the K_{IC}^{un}–h, the exponential function is appropriate to fit the relation curve. All the fitting curves are shown in the

FIG. 8 $CMOD_c$–α curve.

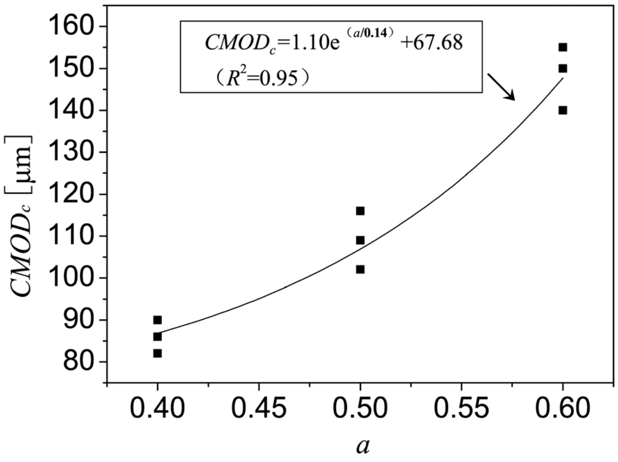

FIG. 9 $F_{H\,\max}$–α curve.

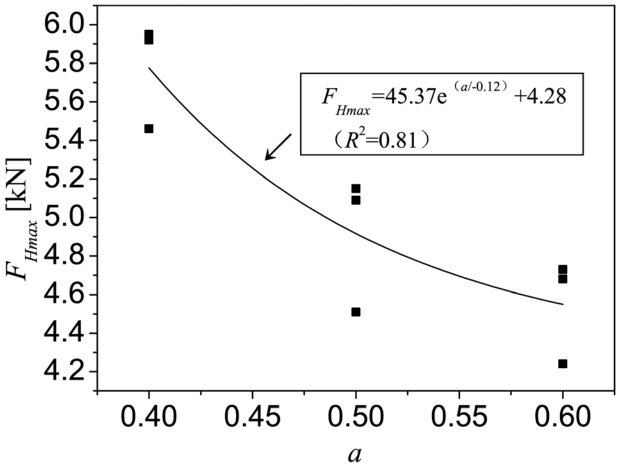

FIG. 10 a_c–α curve.

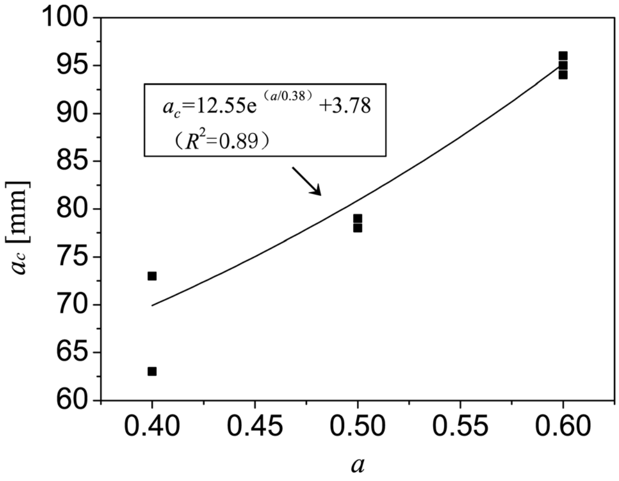

FIG. 11 K_{IC}^{ini}–α curve.

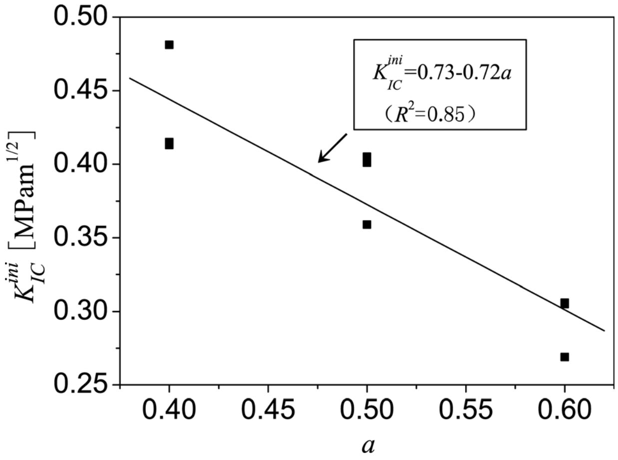

FIG. 12 K_{IC}^{un}–α curve.

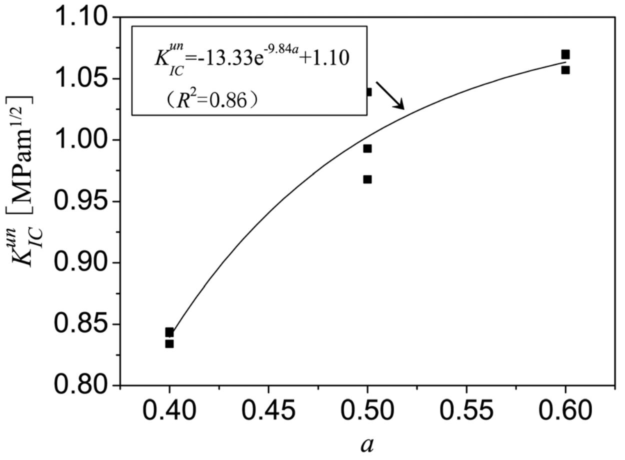

FIG. 13 $CMOD_c$–h curve.

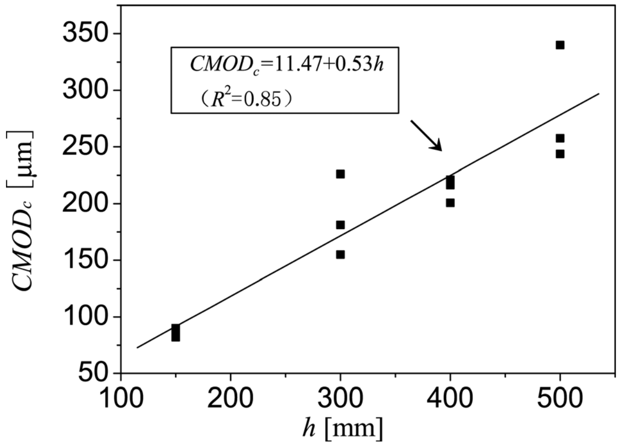

FIG. 14 $F_{H\max}$–h curve.

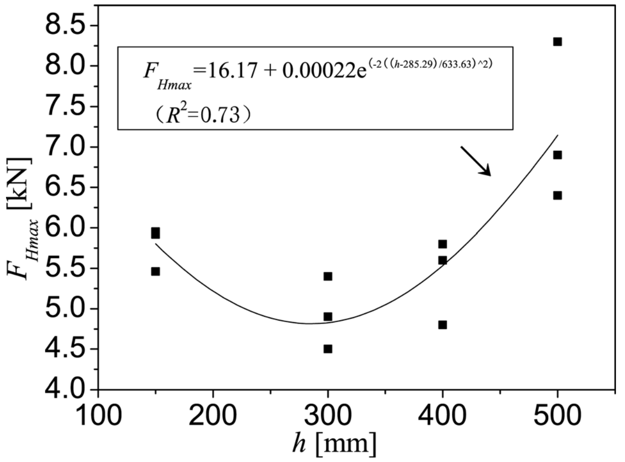

FIG. 15 a_c–h curve.

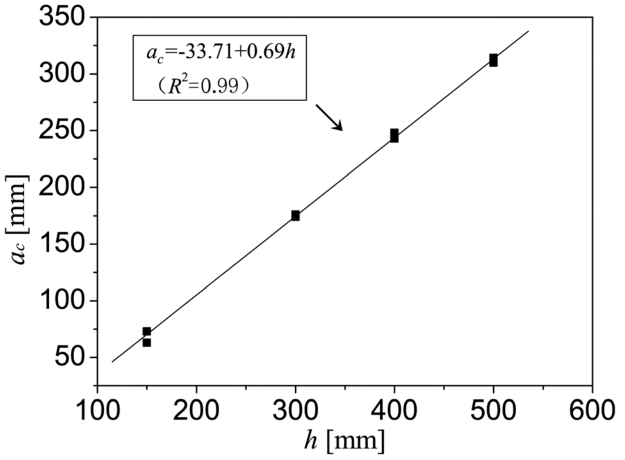

corresponding figures above. It implied that $CMOD_c$ and a_c increase with the increase of h. $F_{H\max}$ reaches the minimum when h is 300 mm.

For α is 0.4 and h is <500 mm, the results above indicated that K_{IC}^{un} increase with the increase of h. When h is <300 mm, K_{IC}^{un} grows rapidly; however, it tends to be stable when h is >300 mm. It implied that when h is <300 mm, the effect of specimen size on K_{IC}^{un} is significant, but it decreases when h is >300 mm.

Conclusions

Two groups of RCC specimens with different specimen size and crack depth ratio were investigated by wedge splitting method to study the effects of different specimen sizes and different crack depth ratios of roller compacted concrete on double-K fracture model parameters. Double-K fracture parameters were

FIG. 16 K_{IC}^{un}–h curve.

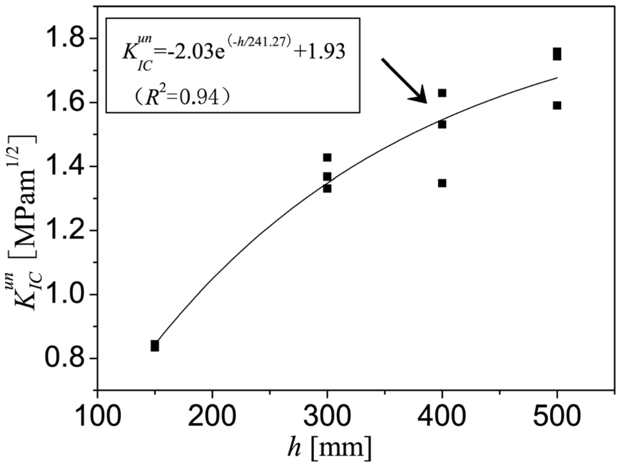

calculated by the Double-K fracture theory of concrete. The following conclusions can be drawn:

1. When the crack depth ratio α increased from 0.4 to 0.6, the unstable fracture toughness K_{IC}^{un} increases, whereas the initial fracture toughness K_{IC}^{ini} decreases. α has a continuous effect on K_{IC}^{ini}; however, the effect on K_{IC}^{un} reduces with the increase of α.
2. For α is 0.4 and h is <500 mm, K_{IC}^{un} increases with the increase of h. When h is <300 mm, K_{IC}^{un} grows rapidly; however, it tends to be stable when h is >300 mm. It implied that when h is <500 mm, the specimen size will affect K_{IC}^{un}, so if double-K fracture theory is employed as the practical crack fracture criterion, the height of the specimen should be >500 mm.

ACKNOWLEDGMENTS

This work was supported by the Natural Science Foundations of China (Nos. 51279094, 51078222, 51308324, and 51379115), the Fundamental Research Funds of Shandong University (Nos. 2014YQ013 and 2012HW003), the Natural Science Foundations of Shandong Province of China (Nos. ZR2011EEM012 and ZR2013EEQ025), and the Program for New Century Excellent Talents in University of Ministry of Education of China (NCET-13-0340).

References

[1] Pittman, D. W. and White, T. D., "Roller-Compacted Concrete Pavements," *Proceedings of the Third International Conference on Concrete Pavement Design and Rehabilitation*, Purdue University, West Lafayette, IN, April 23–25, 1985, pp. 107–112.

[2] Shihata, S. A., "Strength and Density of Laboratory-Prepared RCC Specimens: Effect of Compaction Procedure," *ASTM Cem., Concr. and Aggr.*, Vol. 22, No. 1, 2000, pp. 1–9.

[3] Jenq, Y. S. and Shah, S. P., "A Fracture Toughness Criterion for Concrete," *Eng. Fract. Mech.*, Vol. 21, No. 5, 1985, pp. 1055–1069.

[4] Ramsamooj, D. V., "Analytical Model for Fatigue Crack Propagation in Concrete," *J. Test. Eval.*, Vol. 30, No. 4, 2002, pp. 340–349.

[5] Nguyen, M. T., Lee, H. J., and Baek, J., "Fatigue Analysis of Asphalt Concrete Under Indirect Tensile Mode of Loading Using Crack Images," *J. Test. Eval.*, Vol. 41, No. 1, 2013, pp. 148–152.

[6] Bazant, Z. P. and Kazemi, M. T., "Determination of Fracture Energy, Process Zone Length and Brittleness Number From Size Effect, With Application to the Rock and Concrete," *Int. J. Fract.*, Vol. 44, No. 2, 1990, pp. 111–131.

[7] Bazant, Z. P. and Planas, J., *Fracture and Size Effect in Concrete and Other Quasi-Brittle Materials*, CRC Press, Boca Raton, FL, 1998.

[8] Nallathambi, P. and Karihaloo, B. L., "Effect of Specimen Crack Sizes, Water/Cement Ratio and Coarse Aggregate Texture Upon Fracture Toughness of Concrete," *Mag. Concr. Res.*, Vol. 129, No. 36, 1984, pp. 227–236.

[9] Pittman, D. W. and McCullough, B. F., "Development of a Roller-Compacted Concrete Pavement Crack and Joint Spacing Model," *J. Transp. Res. Board*, Vol. 1568, No. 7, 1997, pp. 52–64.

[10] Albuquerque, M. C. F., Balbo, J. T., Sansone, E. C., and Pinto P. C., "Fracture Characterization of Roller Compacted Concrete Mixtures With Blast Furnace Slag and Industrial Sand," *Int. J. Pave. Res. Technol.*, Vol. 4, No. 4, 2011, pp. 244–251.

[11] Liu, H. C., Song, Y. P., Yao, G. J., and Wu, Z. M., "Study of Cracking for Induced Joints of Shapai RCC Arch Dam," *J.Dalian Univ. Technol.*, Vol. 44, No. 1, 2004, pp. 104–109 (in Chinese).

[12] Zhang, X. G., Song, Y. P., and Wu, Z. M., "Calculation Model of Equivalent Strength for Induced Crack Based on Double-K Fracture Theory and its Optimizing Setting in RCC Arch Dam," *Trans. Tian jin Univ.*, Vol. 11, No. 1, 2005, pp. 59–65 (in Chinese).

[13] Xu, S. L. and Zhao, G. F., "Determination of Double–K Criterion for Crack Propagation in Quasi-Brittle Fracture, Part I: Experimental Investigation of Crack Propagation," *Int. J. Fract.*, Vol. 98, No. 2, 2005, pp. 111–149.

[14] DL/T5332-2005: Norm for Fracture Test of Hydraulic Concrete, Electrical Power Standard of People's Republic of China, Beijing.

[15] Kumar, S. and Barai, S. V., "Determining the Double-K Fracture Parameters for Three-Point Bending Notched Concrete Beams Using Weight Function," *Fatigue Fract. Eng. Mater. Struct.*, Vol. 33, No. 10, 2010, pp. 645–660.

[16] Zhang, X. F., Xu, S. L., and Zheng, S., "Experimental Measurement of Double-K Fracture Parameters of Concrete With Small-Size Aggregates," *J. Hydraul. Eng.*, Vol. 37, No. 5, 2006, pp. 543–553 (in Chinese).

[17] JTG E30-2005: Test Methods of Cement and Concrete for Highway Engineering, Industry Standard of People's Republic of China, Beijing.

[18] Linsbauer, H. N. and Tschegg, E. K., "Fracture Energy Determination of Concrete With Cube Shaped Specimens," *Z. Beton*, Vol. 31, 1986, pp. 38–40.

[19] Brühwiler, E. and Wittmann, F. H., "The Wedge Splitting Test, A New Method of Performing Stable Fracture Mechanics Test," *Eng. Fract. Mech.*, Vol. 35, No. 1/2/3, 1990, pp. 117–125.

[20] Østergaard, L., 2003, "Early-Age Fracture Mechanics and Cracking of Concrete—Experiments and Modeling," Ph.D. thesis, University of Denmark, Lyngby, Denmark.

[21] De Place Hansen, E. J., Hansen, E. A., Hassanzadeh, M., and Stang, H., "Determination of the Fracture Energy of Concrete: A Comparison of the Three-Point Bend Test on Notched Beam and the Wedge–Splitting Test," *NORDTEST Project 1998 No. 1327-97*, Nordtest, Taastrup, Denmark, 1997.

[22] Zhang, X. F., Xu, S. L., and Gao, H. B., "Superposition Calculation of Double-K Fracture Parameters of Concrete Using Wedge Splitting Geometry and Boundary Effect," *J. Dalian Univ. Technol.*, Vol. 46, No. 6, 2006, pp. 867–874 (in Chinese).

Journal of Testing and Evaluation

doi:10.1520/JTE20140059 / Vol. 43 / No. 2 / March 2015 / available online at www.astm.org

Zhanyong Yao,[1] Xiaomeng Zhang,[2] Zhi Ge,[1] Zhuang Jin,[1] Jie Han,[3] and Xianghong Pan[1]

Mix Proportion Design and Mechanical Properties of Recycled PET Concrete

Reference

Yao, Zhanyong, Zhang, Xiaomeng, Ge, Zhi, Jin, Zhuang, Han, Jie, and Pan, Xianghong, "Mix Proportion Design and Mechanical Properties of Recycled PET Concrete," *Journal of Testing and Evaluation*, Vol. 43, No. 2, 2015, pp. 344–352, doi:10.1520/JTE20140059. ISSN 0090-3973

ABSTRACT

The mix proportion and mechanical properties of polyethylene terephthalate (PET) concrete were studied by orthogonal test. PET concrete was produced by mixing melted PET with aggregate and mineral admixtures. The effects of several factors on the properties of PET concrete were investigated. These factors included: (1) coarse aggregate type, (2) mineral materials, (3) PET and mineral/aggregate (PETAM/AG) ratio, (4) sand ratio, (5) PET/mineral (PET/MA) ratio, and (6) maximum particle size of coarse aggregate. The results showed that the most important factor was PETAM/AG, followed by sand ratio and PET/MA. Samples with 10 mm coarse aggregate had the highest compressive strength of 36 MPa. The compressive strength decreased 8.6 and 37 % as the coarse aggregate maximum particle sizes changed from 10 to 4.75 and 13 mm, respectively. There was no significant difference in flexural strength when the sand ratio changed from 35 to 68 %. The strength of PET concrete with basalt was higher than that of concrete with limestone. The concrete containing fly ash and 5 % talc had the highest strength followed by concrete with fly ash, Portland cement (PC), fly ash with 5 % asphalt, without any mineral. The best mix proportion of PET concrete was PETAM/AG of 1:3, sand ratio of 35 % and PET/fly ash of 2:1.

Keywords

PET concrete, mix proportion, compressive strength, flexural strength, orthogonal test

Manuscript received February 26, 2014; accepted for publication July 8, 2014; published online October 7, 2014.

[1] School of Civil Engineering, Shandong Univ., 17922 Jingshi Road, Jinan 250061, People's Republic of China.

[2] School of Civil Engineering, Shandong Univ., 17922 Jingshi Road, Jinan 250061, People's Republic of China (Corresponding author), e-mail: 13969011305@126.com

[3] China Railway Siyuan Survey and Design Group Co., Ltd., 745 Heping Dadao, Wuhan 430063, People's Republic of China.

Introduction

Polyethylene terephthalate (PET), a semi-crystalline polymer, is the first linear thermoplastic polymer which was industrialized. The tensile modulus and flexural modulus is 2.9 and 2.4 GPa, respectively. Its melting point is 260°C and its density is $1.3\sim1.4\ \text{g/cm}^3$ [1].

PET is widely employed as a raw material to produce products such as bottles for soft-drinks and containers for the packaging of food and other consumer goods. PET bottles have already replaced the glass bottles to transport and store soft drinks because of their advantages, including light quality, easy production, and storage. Now, it is reported that the world's annual consumption of PET bottles is approximately 20×10^6 tons. This number grows up to about 15 % every year. However, the number of recycled bottles is very low [1]. The waste PET (WPET) recycled method has great influence on the ecological environment because PET cannot be biodegraded [2]. One of the recycling methods is using PET in civil engineering. This is because PET has some advantages such as high toughness, good durability, and light weight [3].

Recently, recycled PET has been used to produce concrete. This method not only provides an effective way of recycling PET [4,5], but also saving raw mineral resources and reducing the environmental pollution caused by cement production [6,7]. Three ways to use waste PET in concrete: (1) waste PET is depolymerized for unsaturated polyester resin (UPR) as binder and produces polyester concrete, (2) waste PET as a raw material is produces fiber reinforced concrete, and (3) waste PET as a fine aggregate produces lightweight aggregate concrete.

Used UPR as binder to produce polyester concrete has higher compressive strength and flexural strength than Portland cement concrete. The daily strength could reach 80 % of the final strength [8,9]. However, the concrete is sensitive to temperature [10,11]. Mahdi [12] depolymerized the recycled PET through glycolysis to produce unsaturated polyester resin (UPR) and used UPR to produce polymer mortar (PM) and polymer concrete (PC). The flexural strength of UPR polyester concrete was higher than Portland cement concrete. However, the depolymerization of recycled waste PET has shortcomings, including high cost and a complex process. Ge [9] used waste PET as binder to produce plastic mortar. The effects of PET to sand ratio, curing time, and the addition of asphalt on physical and mechanical properties of plastic mortar were investigated. The results showed plastic mortar had the characteristics of low water absorption and fast strength development. As the sand content increased, the compressive and flexural strength of plastic mortar increased. Under room temperature, plastic mortar could attain over 90 % of its ultimate compressive strength within 3 h. Moreover, adding a small amount of asphalt could improve the plastic mortar's flexural strength. Lei [13–15] analyzed the influence of calcium carbonate ($CaCO_3$) and talcum powder to PET crystallization. Mixing 5 % of talcum powder (by weight) could improve the tensile strength and flexural modulus of PET obviously.

The second way is using waste PET to produce fibers and fiber-reinforced concrete [16]. PET fiber reinforced concrete can restrain concrete cracks effectively [17]. However, the characteristics and low surface energy of plastic materials result in a poor mechanical bond with the cement-based composite [18–20]. In addition, PET fibers only contained 0.3 to 1.5 % in the fiber reinforced concrete by volume. In this case, compared with the first recycling method, only a small amount of waste PET is reused [21,22].

The third way is using waste PET as fine aggregate to produce lightweight aggregate concrete [23,24]. Choi [25] used waste PET as lightweight aggregate in partial substitution of river sand in concrete. The concrete compressive strength decreased 6 % and splitting tensile strength decreased 19 %. Choi [26] heated waste PET to 250°C and mixed it with river sand as lightweight aggregate (WPLA) to produce mortar. The compressive strength of mortar tended to decrease as the mixture proportion of WPLA increased. Akçaözoğlu [27] found WPET mortar decreasing the structure weight and keeping the strength. Albano [28] analyzed the mechanical behavior of concrete contained 10 and 20 % weight of WPET. The compressive strength, flexural strength, and elastic modulus of WPET concrete decreased as the weight and particle size of WPET increased. Naik [29] used high-density polyethylene (HDPE) as fine aggregate to produce concrete. The HDPE were washed by water, bleach, or bleach with sodium hydroxide caustic soda (NaOH). The compressive strength of concrete decreased as the amount of HDPE above 0.5 %. The highest compressive strength of concrete was washed by bleach with NaOH. Liu [30–32] mixed recycle ABS/PC plastic particles into concrete to produce plastic concrete and test the strength.

Limited studies showed that it was possible to use melted waste PET as binder to produce concrete. However, the factors that influence properties of PET concrete were not studied. This paper investigated mix design and the major factors that could affect the mechanical properties of PET concrete.

Experimental

MATERIALS

Two types of waste PET were investigated. One was recycled PET bottles. The PET flakes produced from waste PET bottles were shown in **Fig. 1**. Another was the PET particles produced by the recycle PET bottles (**Fig. 2**). The density of the PET

FIG. 1 PET flakes produced from waste bottles.

FIG. 2 PET particles.

particles was 1.35 g/cm^3, melting point was 260°C, the maximum particle size was 4 mm, and minimum particle size was 2 mm.

Figure 3 showed the infrared spectrum of waste PET bottles and PET particles. The band at 1712 cm^{-1} was assigned to carbonyl C=O stretching; 1411 cm^{-1} was assigned to aromatic skeletal stretching; 1240 cm^{-1} was assigned to C(O)–O stretching of the ester group; 872 and 726 cm^{-1} were assigned to the coupled vibrations of the aromatic out-of-plane C–H bending mode and the out-of-plane O=C–O bending mode. Two lines almost coincided in crest and trough of the band. The results clearly indicated that the two kinds of PET material had similar characters. Since the producing flake with PET bottle was labor intensive, PET particles were used in the experiment because to save time and labor.

TABLE 1 Main chemical compositions of cement and fly ash.

Chemical Composition	CaO	SiO_2	Al_2O_3	Fe_2O_3	MgO	Na_2O	LOI
Cement	60.69	21.31	6.87	2.73	4.15	1.12	2.43
Fly ash	3.88	45.66	31.51	9.70	0.89	3.02	0.37

The fine aggregate was local river sand with a fineness modulus of 2.87. Water absorption was 2.2 % and specific gravity was 2.6. Two types of coarse aggregate, washed local limestone and basalt, were employed. The maximum particle sizes were 13, 10, and 4.75 mm, respectively. Both aggregates meet the requirements of the Fuller grading curves.

The admixtures used include fly ash (FA), limestone dust, Portland cement (PC), talc, and asphalt. These materials were used to partially replace PET to reduce the amount of PET and improve the concrete strength.

The cement used was ordinary Portland cement with a 28-day compressive strength of 42.5 MPa. According to Chinese GT/B 1596, the fly ash was Class I fly ash. The main chemical compositions of cement and fly ash are provided in **Table 1**.

EXPERIMENT PROGRAM

Since there were many factors affecting the properties of PET concrete, the experiment was carried out in two stages. In the first stage, the effects of three factors: (A) PET/minerals (PET/MA) ratio, (B) PET and mineral/aggregate (PETAM/AG) ratio, (C) sand ratio were investigated. Each factor had three different levels (**Table 2**). Since the full factorial design required 27 mixes, the orthogonal experimental design was adopted to reduce the number of mixes. According to the orthogonal experimental design table of L9(3^3), a total of 9 mixes were tested. The orthogonal experimental design was shown in **Table 2**. In this

FIG. 3

Infrared spectrum of waste PET bottles and PET particles.

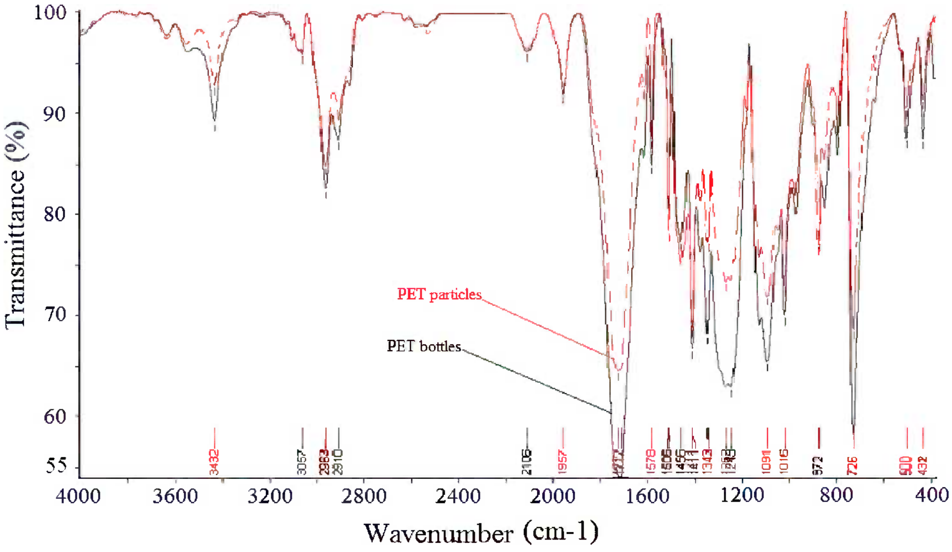

TABLE 2 Orthogonal test of PET concrete mix proportion.

	Level		
Mix	Sand Ratio (%)	PETAM/AG	PET/MA
1	30	1:1	4:1
2	30	1:2	2:1
3	30	1:3	1:1
4	35	1:1	2:1
5	35	1:2	1:1
6	35	1:3	4:1
7	40	1:1	1:1
8	40	1:2	4:1
9	40	1:3	2:1

stage, the effect of coarse aggregate and mineral admixture were fixed. Limestone with the maximum particle size of 10 mm was used as coarse aggregate. The limestone dust was used as mineral admixture. In stage two, the PET/MA ratio, PETAM/AG ratio, and sand ratio were fixed based on the orthogonal experimental results. The effects of aggregate and mineral mixtures were studied. Variables were divided into five groups: (1) maximum particle size of coarse aggregate (Series I), (2) coarse aggregate type (Series II), (3) mineral materials type (Series III), (4) PET to Fly ash ratio (Series IV), (5) sand ratio (Series V). The experiment design was shown in **Table 3**. For coarse aggregate's maximum particle size, three sizes (13, 10, and 4.75 mm) were employed. Two types of coarse aggregate, limestone and basalt, were used. Four mineral materials were used as admixture to produce PET concrete, including fly ash, Portland cement, fly ash and 5 % talc, fly ash and 5 % asphalt. The PET to fly ash ratio used in the Series IV was 1:0, 4:1, 3:1, 2:1, and 1:1; 35 and 68 % sand ratio were used in series V.

FIG. 4 PET concrete cube.

SPECIMEN PREPARATION

PET particles were first mixed with mineral for 3 min and then heated to 260°C∼285°C. At the same time, the aggregate was also heated to the same temperature. When PET particles were completely melted, melted PET was mixed with aggregate for

TABLE 3 Experiment design for the study of different factors.

		PETAM/AG	Sand Ratio (%)	PET/MA	Coarse Aggregate Material	Maximum Particle Size (mm)	Mineral
Series I							
	1	1:3	35	1:1	Limestone	13	Fly ash
	2	1:3	35	1:1	Limestone	10	Fly ash
	3	1:3	35	1:1	Limestone	4.75	Fly ash
Series II							
	1	1:3	35	1:1	Limestone	10	Fly ash
	2	1:3	35	1:1	Basalt	10	Fly ash
Series III							
	1	1:3	35	1:0	Limestone	10	none
	2	1:3	35	1:1	Limestone	10	FA + 5 % asphalt
	3	1:3	35	1:1	Limestone	10	FA
	4	1:3	35	1:1	Limestone	10	PC
	5	1:3	35	1:1	Limestone	10	FA + 5 % talc
Series IV							
	1	1:3	35	1:0	Limestone	10	Fly ash
	2	1:3	35	4:1	Limestone	10	Fly ash
	3	1:3	35	3:1	Limestone	10	Fly ash
	4	1:3	35	2:1	Limestone	10	Fly ash
	5	1:3	35	1:1	Limestone	10	Fly ash
Series V							
	1	1:3	35	2:1	Limestone	10	Fly ash
	2	1:3	68	2:1	Limestone	10	Fly ash

TABLE 4 Range of PET concrete mix proportion orthogonal test.

	Level			
Mix	Sand Ratio (%)	PETAM/ AG	PET/ MA	Compressive Strength (MPa)
1	30	1:1	4:1	24.21
2	30	1:2	2:1	19.73
3	30	1:3	1:1	18.10
4	35	1:1	2:1	13.13
5	35	1:2	1:1	32.73
6	35	1:3	4:1	25.23
7	40	1:1	1:1	16.60
8	40	1:2	4:1	15.75
9	40	1:3	2:1	27.00
K_1	62.04	53.94	65.19	
K_2	71.09	68.21	59.86	
K_3	59.35	70.33	67.43	
R	11.74	16.39	7.57	

2 min. After that, PET concrete was put into the mold and compacted for 1 min at room temperature. After compaction, specimens were cured in preheated 180°C oven for 1 h and then put in the room until test (**Fig. 4**).

TEST METHODS

Infrared Spectrum Analysis was conducted to measure the main functional groups and the amount of crystal. The tests were conducted using VERTEX-70 FT-IR spectrometers (BRUKER OPTICS). The powder of PET was ground with potassium bromide, and then pressed into a thin film. The scanned absorption bands ranged from 400 to 4000 cm^{-1}.

Bulk density and water absorption were tested according to JTJ 052-2000 [33]. The compressive and flexural strengths of the PET concrete were measured according to JTG E30-2005 [34]. The size of specimens for the compressive strength test was 100 by 100 by 100 mm. The tests were carried out by using the Microcomputer Controlled Electronic Universal Testing Machine under force control at the rate of 0.5 kN/s until its failure.

Prisms of 100 by 100 by 400 mm were cast for the flexural strength test. The flexural strength tests were performed on the prismatic specimens by the three points loading test under force controlled at the rate of 0.04 kN/s until its failure. **Figure 4** shows the specimens for compressive strength tests.

All strength was obtained from three samples. The variation of three samples could not exceed more than 15 %. The average of these three samples is presented and discussed in the next section.

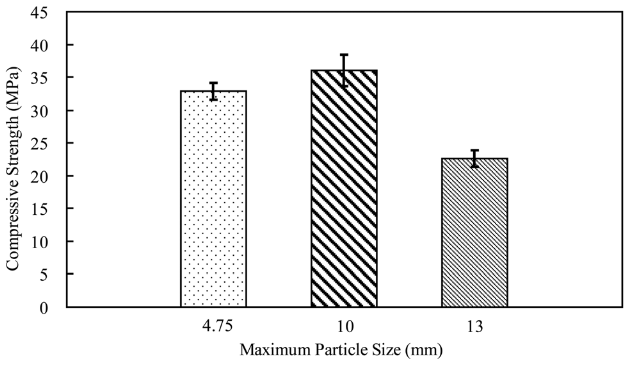

FIG. 5 Compressive strength of concrete with different coarse aggregate max particle size.

Results and Discussion

RESULTS OF ORTHOGONAL TEST

The orthogonal experimental analysis was employed to obtain the optimal concrete mix. The analysis process is as follows [35]:

1. Select the suitable mix proportion based on the experimental results.
2. Conduct the range analysis to evaluate the significance levels of all the influencing factors and select the optimal level of each factor. For range analysis, the K value, k value, and range value (R) were calculated. The K value for each level of a parameter was the sum of three values of samples with the same level. For example, for concrete compressive strength, the K_1 for sand ratio was the sum of concrete compressive strength of samples with sand ratio of 30 % (**Table 4**). The range value for each factor was the difference between the maximal and minimal values of the three levels. The most significant factor has the highest R value. The mix proportion was selected based on the range analysis.
3. According to the nine selected mix designs and the order of significance levels, the optimal concrete mix design can be found.
4. The sum of squares, degree of freedom, and F value were summarized and compared to determine the significance level of all factors. With the orthogonal experimental design form $L9(3^3)$, a table was set in the orthogonal table for error estimation. F value was used to test the significance of various factors. Then the optimal concrete mix design can be confirmed.

TABLE 5 Variance of PET concrete mix proportion orthogonal test.

Source	Square Sum	Degree of Freedom	Mean-Square Deviation	F	F_a	Significance Level
Sand ratio	25.22	2	12.61	6.41	$F_{0.05}(2,8) = 4.46$	*
PETAM/AG	52.97	2	26.49	13.46	$F_{0.01}(2,8) = 8.65$	**

FIG. 6 Specimen after compressive strength test.

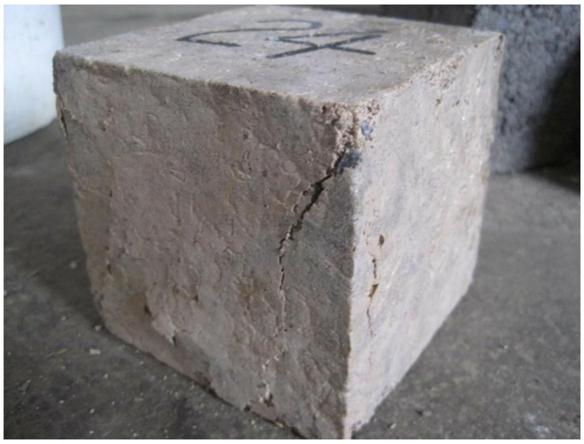

In **Table 4**, the R of PETAM/AG ratio was the highest, followed by sand ratio. The R of PET/MA ratio was the lowest. The result showed that PETAM/AG was the most significant factor for the PET concrete mix proportion. In **Table 5**, F value showed that PETAM/AG and sand ratio were significant. However, PETAM/AG was more important than sand ratio. According to **Table 4** and **Table 5**, the optimal mix proportion was PETAM/AG of 1:3, sand ratio of 35 % and PET/MA of 1:1.

COMPRESSIVE STRENGTH ANALYSIS

The Compressive Strength of Concrete With Different Coarse Aggregate Maximum Particle Size

Figure 5 showed that the maximum size of coarse aggregate had a significant effect on PET concrete compressive strength. As the maximum particle size increased, compressive strength first increased and then decreased. When the maximum particle size was 10 mm, PET concrete had the highest compressive strength of 36 MPa. The compressive strength was 32.9 and 22.68 MPa for concrete with a 4.75 and 13 mm aggregate, respectively. Compared with concrete with a 10 mm aggregate, compressive strength decreased 8.6 and 37 %, respectively. This could be caused by the bond conditions between the aggregate and PET. Further investigations were needed. **Figure 6** and **Fig. 7** indicated that the failure mode of PET concrete was similar to normal cement concrete.

FIG. 7 PET concrete's cross section after test.

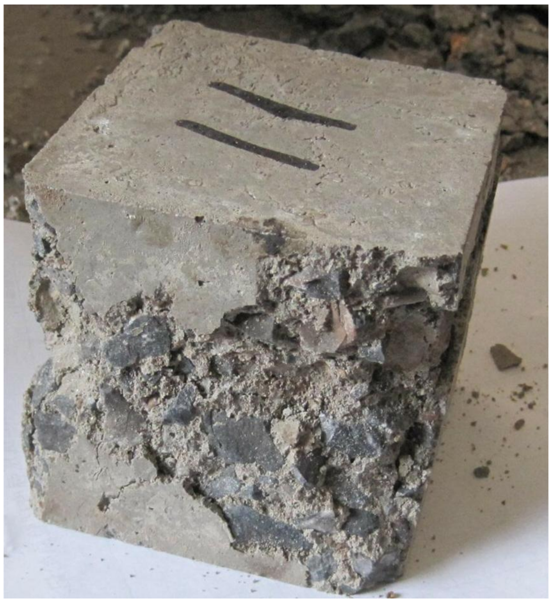

FIG. 8 Compressive strength of concrete with different coarse aggregate materials.

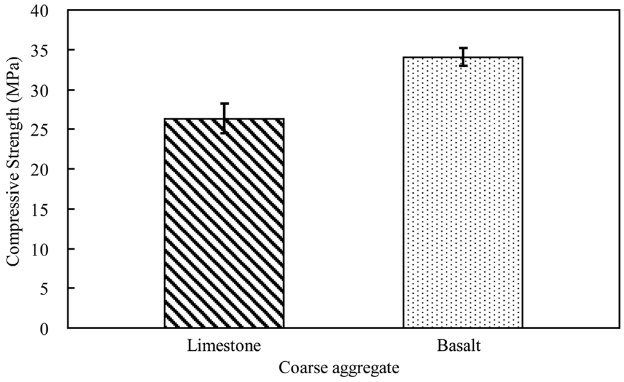

The Compressive Strength of Concrete With Different Coarse Aggregate Materials

In **Fig. 8**, compressive strength of PET concrete used basalt was 34.04 MPa, which was 29.2 % higher than the strength of concrete with limestone. This could be caused by the strength of aggregate. The broken sample showed that most limestone aggregate was fractured. However, less basalt aggregate was fractured due to basalt's high strength. Therefore, the strength of PET concrete with basalt was more controlled by the bonding between aggregate and PET. However, the price of basalt was higher than limestone. The limestone was employed as coarse aggregate for the following study.

FIG. 9 Compressive strength of concrete with different minerald.

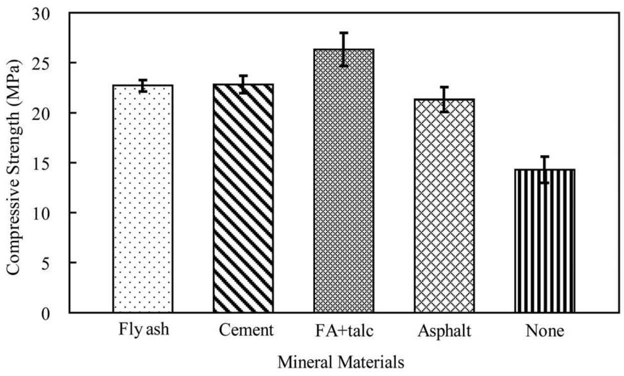

FIG. 10 Compressive strength of concrete with different PET to FA ratio.

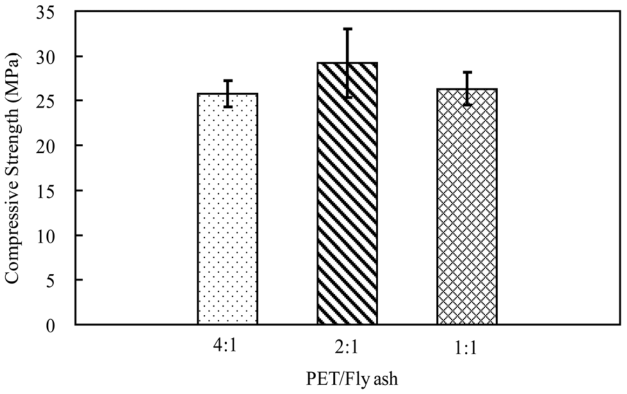

The Compressive Strength of Concrete with Different Mineral Materials

In **Fig. 9**, samples with different mineral materials had different compressive strength. The compressive strength of PET concrete without any mineral was only 14.28 MPa. The compressive strength of PET concrete with fly ash and 5 % asphalt was 21.34 MPa. It was decreased 5.9 % compared with the PET concrete only with fly ash. The compressive strength was 22.68 and 22.84 MPa for samples with fly ash and Portland cement, respectively, which were 60 % higher than that of PET concrete without mineral. Because fly ash particles were spherical, it could be easily mixed with melted PET and improve the workability. If the fly ash was mixed with 5 % quality talc, the compressive strength was 26.34 MPa and increased 16.1 % compared with PET concrete only with fly ash and PC.

The results indicated that proper mineral was beneficial for compressive strength of PET concrete. Fly ash and PC had significantly improvement of compressive strength. The 5 % talc could promote the crystallization of PET [13–15] and increase PET concrete compressive strength effectively. However, the price of fly ash was lower than PC, so it was recommended to use fly ash with talc or only fly ash as mineral admixture.

FIG. 11 Flexural strength of concrete with different PET to FA ratio.

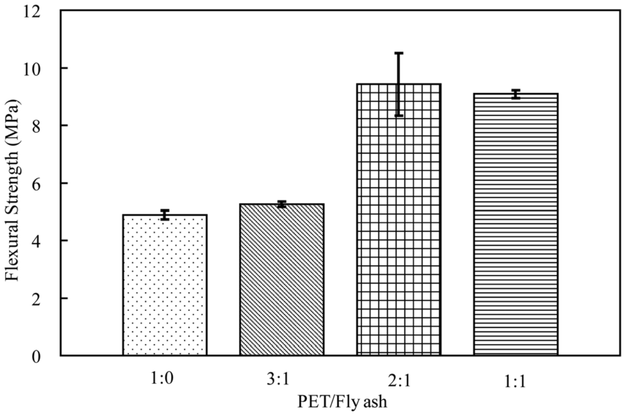

FIG. 12 Flexural strength of concrete with different coarse aggregate materials.

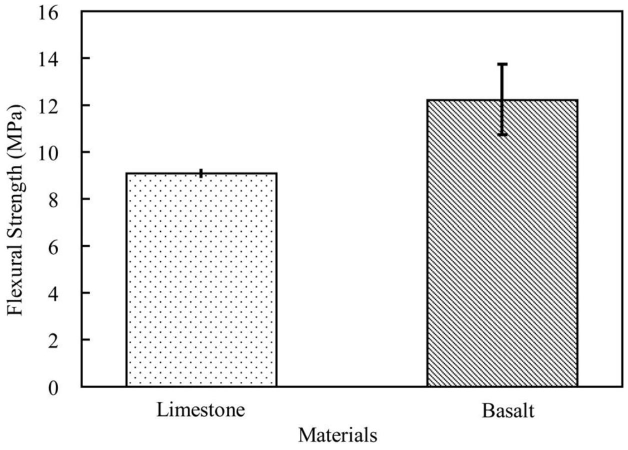

The Compressive Strength of Concrete With Different PET to Fly Ash Ratio

In **Fig. 10**, the compressive strength of specimens with PET/FA of 4:1, 2:1, and 1:1 were 25.8, 29.2, and 26.54 MPa, respectively. The sample with PET/FA of 2:1 had the highest compressive strength. It was increased about 13.2 % compared with PET/FA of 4:1. As PET/FA of 1:1, the compressive strength only decreased 9.1 % compared with PET/FA of 2:1. Considering the cost of materials, the best PET/FA ratios were 2:1 or 1:1.

FLEXURAL STRENGTH ANALYSIS

The Flexural Strength of Concrete With Different PET to Fly Ash Ratio

In **Fig. 11**, the flexural strength was increased as the fly ash increased. The flexural strength of PET concrete without fly ash

FIG. 13 Flexural strength of concrete with different sand ratio.

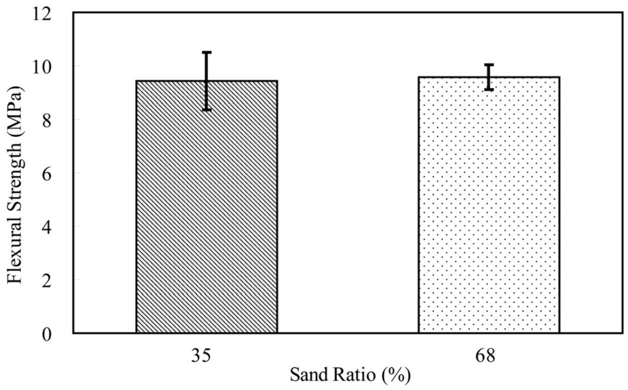

TABLE 6 Statistical analysis of compressive strength results.

Source	Sum of Squares	df	Mean Square	F	P
Maximum particle size	291.481	2	145.74	49.225	0.000
Coarse aggregate material	88.935	1	88.935	37.912	0.004
Mineral material	236.303	4	59.076	41.314	0.000
PET/FA	20.031	2	10.016	1.482	0.300

was 4.88 MPa. The flexural strength was 5.25 and 9.42 MPa as PET/FA of 3:1 and 2:1, respectively, which increased 7.6 and 93 % compared with PET concrete without fly ash. As PET/FA of 1:1, the flexural strength was decreased 3.5 % compared with PET/FA of 2:1. The PET concrete flexural strength increased prominent by adding fly ash. The PET/FA of 2:1 and 1:1 had good performance on flexural strength.

The Flexural Strength of Concrete With Different Coarse Aggregate Materials

In **Fig. 12**, the flexural strength with limestone was 9.09 MPa and basalt was 12.23 MPa. Compared with limestone, the flexural strength of basalt increased remarkably by 34.5 %. This trend was consistent with that of compressive strength.

According to the results of compressive strength and flexural strength, PET concrete with basalt had great strength and could be applied to the structures which required high strength.

The Flexural Strength of Concrete With Different Sand Ratio

In **Fig. 13**, as the sand ratio was 35 and 68 %, the flexural strength of PET concrete was 9.42 and 9.56 MPa, respectively. Specimens had similar flexural strength. The sand ratio showed the negligible effects on PET concrete's flexural strength.

STATISTICAL ANALYSIS

Statistical analysis was performed for the compressive strength and flexural strength. The results were shown in **Tables 6** and **7**. According to the F and P values, the maximum particle size was the most significant factor for the compressive strength, followed by coarse aggregate and mineral material. The *P* value for PET/FA ratio was 0.3, which indicates that PET/FA ratio was not significant for compressive strength. Different from compressive strength, the PET/FA ratio was the most significant factor for flexural strength (**Table 7**). Besides PET/FA ratio, the coarse aggregate material was also significant. However, the sand ratio was not significant for flexural strength.

TABLE 7 Statistical analysis of flexural strength results.

Source	Sum of Squares	df	Mean Square	F	P
PET/FA	53.037	3	17.679	58.126	0.000
Coarse aggregate material	14.789	1	14.789	13.033	0.023
Sand ratio	0.029	1	0.029	0.042	0.847

Conclusions

(1) The PETAM/AG effected on PET concrete compressive strength significantly, followed by sand ratio and PET/MA. The optimal mix proportion in orthogonal test was PETAM/AG of 1:3, sand ratio of 35 %, and PET/MA of 1:1.
(2) As the maximum particle size of coarse aggregate was 10 mm, the compressive strength of PET concrete was the highest. The strength was 8.6 and 37 % higher than that of concrete with 4.75 and 13 mm aggregate, respectively.
(3) As the coarse aggregate was basalt, the PET concrete compressive strength and flexural strength increased 29.2 and 34.5 % compared with the limestone. However, the flexural strength of PET concrete with limestone aggregate could easily reach 9 MPa.
(4) As the PET/MA of 1:1, fly ash with 5 % talc could provide the highest compressive strength. The second was only mixed fly ash and PC, and then fly ash with 5 % asphalt. The fourth was without mineral.
(5) As PET/FA of 2:1, the PET concrete compressive strength was the highest, 29.2 MPa. Then, for the PET/FA of 2:1, the compressive strength was 26.54 MPa. The lowest was PET/FA of 4:1, 25.8 MPa. As the concrete without any fly ash, the flexural strength was only 4.88 MPa. As the PET/FA of 3:1, the flexural strength was increased 7.6 %. As PET/FA of 2:1, the flexural strength was increased 93 % up to 9.42 MPa. As PET/FA of 1:1, the flexural strength was decreased 3.5 % compared with PET/FA of 2:1, and it was 9.09 MPa.
(6) The best mix proportion was PETAM/AG of 1:3, sand ratio of 35 %, and PET/fly ash of 2:1.

Based on the research, PET concrete could be used for the following purposes: (1) fast repairing material for the bridge expansion joint and pavement distresses, (2) a prefabricated highway and bridge safety barrier, and (3) enhanced anti-seismic ability of concrete construction.

ACKNOWLEDGMENTS

This study is supported by National Natural Science Foundation of China (51108247) and Shandong Province Transportation Science and Technology Innovation Project (22). Sincere acknowledgements are also given to Zhiqin Zhao and Heng Cui for their great help in the lab.

References

[1] Mariaenrica, F., "Recycling of PET Bottles as Fine Aggregate in Concrete," *J. Waste Manage.*, Vol. 30, 2010, pp. 1101–1106.
[2] Korean Institute of Resources Recycling, "The Korea Institute of Resources Recycling," *Recycling Handbook*, Korean Institute of Resources Recycling, Seoul, Korea, 1999, pp. 206–215.

[3] de Mello, D., Pezzin, S. H., and Amico S. C., "The Effect of Post-Consumer PET Particles on the Performance of Flexible Polyurethane Foams," *J. Polym. Test.*, Vol. 28, 2009, pp. 702–708.

[4] Mobasher, B. and Li, C. Y., "Effect of Interfacial Properties on the Crack Propagation in Cement Based Composites," *J. Adv. Cem. Based Mater.*, Vol. 4, 1996, pp. 93–105.

[5] Pezzi, L., De Luca, P., Vuono, D., Chiappetta, F., and Nastro, A., "Concrete Products With Waste's Plastic Material (Bottle, Glass, Plate)," *J. Mater. Sci. Forum*, Vols. 514–516, 2006, pp. 514–516.

[6] Tam, W. Y. V., Tam, C. M., and Wang, Y., "Optimization on Proportion for Recycled Aggregate in Concrete Using Two-Stage Mixing Approach," *J. Constr. Build. Mater.*, Vol. 21, No. 10, 2007, pp. 1928–1939.

[7] Fernando, P. T., Castro Gomes, J. P., and Said, J., "Adhesion Characterization of Tungsten Mine Waste Geopolymeric Binder," *J. Constr. Build. Mater.*, Vol. 22, No. 3, 2008, pp. 154–161.

[8] Siddique, R., Khatib, J., and Kaur, I., "Use of Recycled Plastic in Concrete: A Review," *J. Waste Manage.*, Vol. 28, 2008, pp. 1835–1852.

[9] Ge, Z., Wang, H., Zhang, K., and Li, P. C., "Investigation on the Properties of Plastic Mortar," *J. Shandong Univ. (Eng. Sci.)*, Vol. 1, 2012, pp. 1–3.

[10] Rebeiz, K. S., "Precast Use of Polymer Concrete Using Unsaturated Polyester Resin Based on Recycled PET Waste," *J. Constr. Build. Mater.*, Vol. 10, No. 3, 1996, pp. 215–220.

[11] Sam T. D. and Tam, M. N., "Polymer Concrete Based on Recycled Polyethylene Terephthalate (PET)," *Proceedings of the Vietnam International Conference on Non-Conventional Material and Technologies 2002*, Hanoi, Vietnam, Mar. 12–13, 2002, pp. 226–228.

[12] Mahdi, F., Abbas, H., and Khan, A. A., "Strength Characteristics of Polymer Mortar and Concrete Using Different Compositions of Resins Derived From Post-Consumer PET Bottles," *J. Constr. Build. Mater.*, Vol. 24, 2010, pp. 25–36.

[13] Lei, M. and Yu, Z. Z., "Effect of Nucleating Agents on Crystallization, Mechanical and Rheological Behavior of Polyethylene Terephthalate," *J. Polym. Mater. Sci. Eng.*, Vol. 17, No. 2, 2001, pp. 105–108.

[14] Chen, H. Z. and Liu, Q. F., "Effects of Modified Clay on the Crystallization Property of PET Clay Nanocomposites," *J. China Univ. Min. Technol.*, Vol. 36, No. 2, 2007, pp. 701–706.

[15] Zhang, G. Y., Yi, G. Z., and Wu, L.H., "Synthesis and Properties of PET-Clay Nano-Composite," *J. Acta Polym. Sin.*, Vol. 3, 1999, pp. 309–314.

[16] Bentur, A. and Mindess, S., *Fibre Reinforced Cementitious Composites*, Elsevier, Amsterdam, the Netherlands, 1990.

[17] Won, J. P. and Park, C. G., "Shrinkage Cracking and Durability Characteristics of Polypropylene Fibre Reinforced Concrete," *J. KSCE*, Vol. 15, No. 5, 1999, pp. 783–790.

[18] Sehaj, S., Arun, S., and Richard, B., "Pullout Behavior of Polypropylene Fibers From Cementitious Matrix," *J. Cem. Concr. Res.*, Vol. 34, No. 10, 2004, pp. 1919–1925.

[19] Silva, D. A., Betioli, A. M., Gleize, P. J. P., Roman, H. R., Gomez, L. A., and Ribeiro, J. L. D., "Degradation of Recycled PET Fibers in Portland Cement-Based Materials," *J. Cem. Concr. Res.*, Vol. 35, 2005, pp. 1741–1746.

[20] Wang, K., Shah, S. P., and Pariya, P., "Plastic Shrinkage Cracking in Concrete Materials: Influence of Fly Ash and Fibers," *J. ACI Mater.*, Vol. 96, No. 6, 2001, pp. 458–464.

[21] Kim, S. B., Yi, N. H., and Kim, H.Y., "Material and Structural Performance Evaluation of Recycled PET Fiber Reinforced Concrete," *J. Cem. Concr. Compos.*, Vol. 32, 2009, pp. 232–240.

[22] Ochi, T., Okubo, S., and Fukui, K., "Development of Recycled PET Fiber and its Application as Concrete-Reinforcing Fiber," *J. Cem. Concr. Compos.*, Vol. 29, 2007, pp. 448–455.

[23] Koide, H., Tomon, M., and Sasaki, T., "Investigation of the Use of Waste Plastic as an Aggregate for Lightweight Concrete," *J. Sustain. Concr. Constr.*, Vol. 1, No. 7, 2002, pp. 177–186.

[24] Ismail Z. Z. and Al-Hashmi, E. A., "Use of Waste Plastic in Concrete Mixture as Aggregate Replacement," *J. Waste Manage.*, Vol. 28, 2008, pp. 2041–2047.

[25] Choi, Y. W., Moon, D. J., Chung, J. S., and Cho, S. K., "Effects of Waste PET Bottles Aggregate on the Properties of Concrete," *J. Cem. Concr. Res.*, Vol. 35, No. 4, 2005, pp. 776–781.

[26] Choi, Y. W., Moon, D. J., Kim, Y. J., and Lachemi, M., "Characteristics of Mortar and Concrete Containing Fine Aggregate Manufactured From Recycled Waste Polyethylene Terephthalate Bottles," *J. Constr. Build. Mater.*, Vol. 23, 2009, pp. 2829–2835.

[27] Akçaözoğlu, S., Atiş, C. D., and Akçaözoğlu, K., "An Investigation on the Use of Shredded Waste PET Bottles as Aggregate in Lightweight Concrete," *J. Waste Manage.*, Vol. 30, No. 2, 2010, pp. 285–290.

[28] Albano, C., Camacho, N., Hernandez, M., Matheus, A., and Gutierrez, A., "Influence of Content and Particle Size of Waste Pet Bottles on Concrete Behavior at Different w/c Ratios," *J. Waste Manage.*, Vol. 29, 2009, pp. 2707–2716.

[29] Naik, T. R., Singh, S. S., Huber, C. O., and Brodersen, B. S., "Use of Post-Consumer Waste Plastics in Cement-Based Composites," *J. Cem. Concr. Res.*, Vol. 26, No. 10, 1996, pp. 1489–1492.

[30] Liu, F., Huang, H. B., and Xia, X. Z., "Mechanical Test on Modified Concrete With Recycled Plastic Particles and its Numerical Simulation," *J. Build. Mater.*, Vol. 4, 2011, pp. 173–179.

[31] Liu, F., Pan, D. P., and Li, L. J., "Numerical Simulation on Micro-Level of Stress and Strength in Crumb Rubber Concrete," *J. Build. Mater.*, Vol. 11, No. 2, 2008, pp. 144–151.

[32] Huang, H. B., Liu, F., and Li, L. J., "Reutilization of Plastic and Application of Recycled Plastic in Construction Materials," *J. Eng. Plast. Appl.*, Vol. 37, No. 7, 2009, pp. 56–59.

[33] JTJ 052-2000: Standard Test Methods of Bitumen and Bituminous Mixtures for Highway Engineering, China Ministry of Transport, Beijing, China, 2000.

[34] JTG E30-2005: Test Methods of Cement and Concrete for Highway Engineering, China Ministry of Transport, Beijing, China, 2005.

[35] Liu, S. H. and Leng, F. G., *Mathematic Skills Applied to Experimental Researches for Building Materials*, China Architecture & Building Press, Beijing, China, 2006.

Journal of Testing and Evaluation

doi:10.1520/JTE20130341 / Vol. 43 / No. 2 / March 2015 / available online at www.astm.org

Wenjie Ge,[1] Jiwen Zhang,[2] Dafu Cao,[3] Biyuan Wang,[4] and Linglong Pan[5]

Experimental Study on the Seismic Behaviors of HRBF400 RC Columns

Reference

Ge, Wenjie, Zhang, Jiwen, Cao, Dafu, Wang, Biyuan, and Pan, Linglong, "Experimental Study on the Seismic Behaviors of HRBF400 RC Columns," *Journal of Testing and Evaluation*, Vol. 43, No. 2, 2015, pp. 353–362, doi:10.1520/JTE20130341. ISSN 0090-3973

ABSTRACT

In order to investigate the seismic behaviors of RC columns reinforced with HRBF400 steel bar (HRBF-high strength hot rolled bars of fine grains), four rectangle cross-section HRBF400 RC columns' bending low-cycle reversed loading experiments were made. Influences of reinforcement ratio, axial compression ratio, and stirrup ratio on the seismic behaviors of HRBF400 RC columns were analyzed. Characteristic of hysteretic curve and skeleton curve are studied, and characteristic value and displacement ductility of each specimen was calculated. The results show HRBF400 RC columns have good seismic behavior. Yield load, peak load, and ductility improve with the increasing of reinforcement ratio. Columns of high compression ratio have high peak load and yield load, but their skeleton curves decrease quickly after peak load and have low ductility. Columns of low compression ratio have low peak load and yield load, but decrease gentlly after peak load and also have good ductility. Seismic behaviors and ductility of RC columns improve with the increasing of stirrup ratio.

Keywords

seismic behavior, concrete column, HRBF400

Introduction

In order to conserve resources and build a sustainable society, the People's Republic of China began to popularize 400 MPa grade steel bar in engineering construction, and current code for design of concrete structures [1] had been recommending 400 MPa grade steel bar as RC structure's dominated reinforcement. Moreover, certain numbers of RC structures reinforced with 400 MPa grade steel bar were made. Although a 400 MPa grade steel bar has the same elastic

Manuscript received December 30, 2013; accepted for publication July 7, 2014; published online October 7, 2014.

[1] Lecturer, College of Civil Science and Engineering, Yangzhou Univ., Huayang Xilu 198, YangZhou, Jiangsu, China 225127, e-mail: gewj@yzu.edu.cn

[2] Professor, Key Laboratory of C&RC Structures, Ministry of Education, Southeast Univ., Nanjing 210096, China, e-mail: jshagwj@163.com

[3] Director, College of Civil Science and Engineering, Yangzhou Univ., Huayang Xilu 198, YangZhou, Jiangsu, China 225127 (Corresponding author), e-mail: dfcao@yzu.edu.cn

[4] Postgraduate, College of Civil Science and Engineering, Yangzhou Univ., Huayang Xilu 198, YangZhou, Jiangsu, China 225127, e-mail: wbyronaldo@sina.com

[5] Postgraduate, College of Civil Science and Engineering, Yangzhou Univ., Huayang Xilu 198, YangZhou, Jiangsu, China 225127, e-mail: xiaopan1009@163.com

FIG. 1 Mechanical testing of HRBF400.

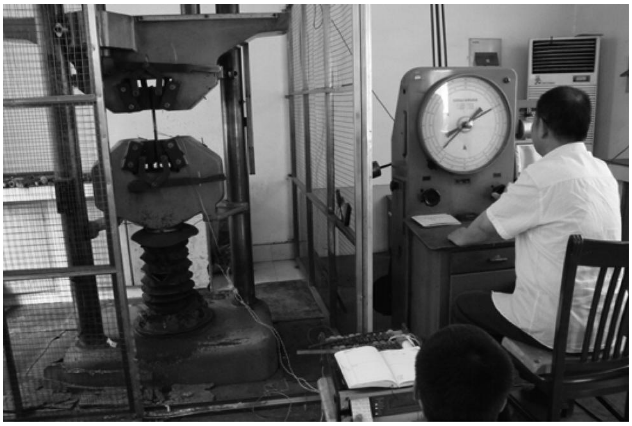

modulus with 335 MPa grade steel bar, its yield strain and yield deformation of RC columns reinforced with 400 MPa steel bar increases significantly. Ultimate deformation of 400 MPa RC columns are larger than RC columns reinforced with 335 MPa grade steel bar, and its displacement ductility factor is smaller than RC columns reinforced with low strength steel bar. Thus, it is necessary to study the seismic behaviors of RC columns reinforced with a 400 MPa high strength steel bar.

Li [2] studied five full-scale square cross-section high strength concrete columns' seismic behaviors. Azizinamini [3] studied the ductility and flexural capacity of high strength RC columns under proposed experimental earthquake force. Shamin [4] performed an experimental test of large proportion high concrete grade reinforced columns ($f_c = 55.5$ MPa) with cube base. Hou [5] conducted an experimental study on the seismic behavior of high strength reinforced high-strength concrete compression-bending members. Guan [6] performed an experimental study on the ductility of high-strength concrete columns, which take cold-rolled ribbed steel bars as its stirrups. Li [7] studied the seismic behaviors of concrete frame columns reinforced with high-strength steel bars. Xiao [8] studied six inverted T-shaped specimen in a fixed axial load and horizontal cyclic loading experiment. Liu [9] performed a six 500 MPa fine grain high strength reinforced concrete columns compression-bending low cyclic loading experiment. Zhang [10] made a cyclic loading experiment of a four concrete-beam cross-shaped joint with different reinforcement ratio (reinforced with fine grain high strength steel bars). Wang [11] simulated an analysis of the seismic performance of RC columns reinforced with HRB500.

FIG. 2 Fractured specimen of HRBF400 ($D = 16$ mm).

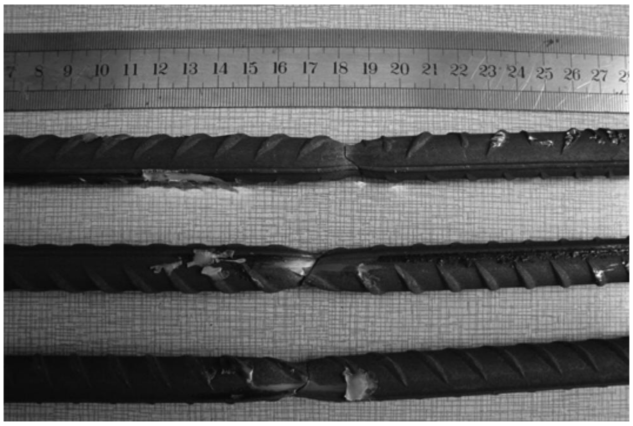

FIG. 3 Stress–strain curves of HRBF400.

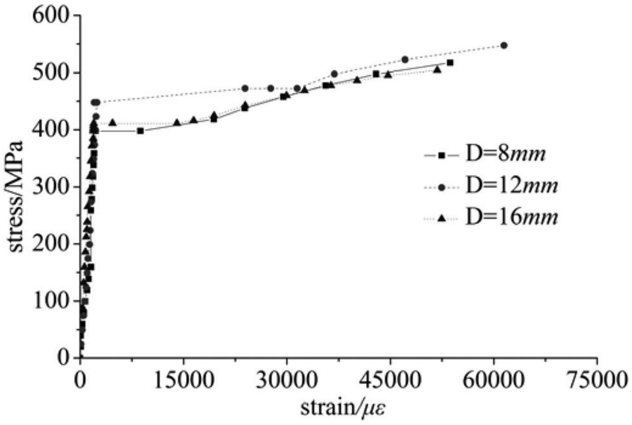

Current studies regarding seismic behaviors of concrete columns reinforced with fine grain high strength steel bars are still lacking. As such, it is necessary to undertake a depth study to provide a theoretical basis of fine grain high-strength steel bars for its application in engineering construction.

Experiment Design

400 MPa grade fine grain high strength steel bars produced by the Jiangsu Yonggang group were used as longitudinal reinforcement and stirrups. Mechanical properties of HRBF400 were tested in the building materials central laboratory of Southeast University (**Fig. 1**) [12]. Before the test, strain gauges were affixed on the surface of test samples to measure the strain during the test, and the surface of test samples were marked to measure elongation (**Fig. 2**). Stress–strain curves of HRBF400 are shown in **Fig. 3**, and mechanical properties of HRBF400 are listed in **Table 1**.

TABLE 1 Mechanical properties of HRBF400.

D/mm	f_y/MPa	f_u/MPa	f_u/f_y	E_s/GPa	δ/%
8	404	579	1.38	185	31.7
12	405	558	1.38	185	32.2
16	452	603	1.33	185	29.6

Note: D, diameter of HRBF400; f_y, yield strength of HRBF400; E_s, elastic modulus of HRBF400; δ, elongation of HRBF400.

TABLE 2 Experimental parameters.

Number	h/mm	b/mm	H/mm	A_s	ρ_s/%	Stirrups	ρ_{sv}/%	n	Vertical Load/kN
CE4A	250	250	1175	2Φ^{F}12	0.42	Φ^{F}8@100	1.00	0.3	521
CE4B	250	250	1175	2Φ^{F}12	0.42	Φ^{F}8@100	1.00	0.45	782
CE4C	250	250	1175	2Φ^{F}16	0.74	Φ^{F}8@100	1.00	0.3	521
CE4D	250	250	1175	2Φ^{F}16	0.74	Φ^{F}8@75	1.34	0.3	521

Note: h, section height; b, section width; H, columns height; f_y, yield strength of steel bars; ρ_s, longitudinal reinforcement ratio; n, Axial compression ratio; Φ^{F}, HRBF400 steel bar; ρ_{sv}, stirrups volume ratio.

Symmetrical reinforcement was adopted. The concrete cover thickness of longitudinal reinforcement was 25 mm. Specimens parameters are listed in **Table 2**, where the diameter of longitudinal reinforcement is 12 and 16 mm and the diameter of the stirrup is 8 mm. Concrete compressive strength was made at the same time with a component test and its value was 27.8 MPa. The test device is shown in **Fig. 4** and its schematic diagram is shown in **Fig. 5**.

Firstly, vertical load was applied to the specimen by hydraulic jack and kept constant; then horizontal load was applied by electro-hydraulic servo actuator. The load-displacement mixed control loading method was adopted (**Fig. 6**): (1) force control before steel bars yield, sub-three loaded once per stage reciprocating cycle; (2) displacement control after steel bars yield, each level in increments of displacement corresponding reinforcement yielding, reciprocating cycle three times per level; (3) stop loading when horizontal load drops to 85 % of the maximum load.

Experimental Phenomenon

In specimen CE4A, when loaded to +40 kN, horizontal cracks occur at the east side of concrete, 15 mm in height from the root of the column. When loaded to −40 kN, horizontal cracks occur at the west side of concrete, a 25.0 mm height from the root of the column. When loaded to $+4\Delta'$ (+, indicate forward loading; Δ, displacement corresponding reinforcement yielding; $'$, first cycle), vertical cracks appear at the west side of the concrete column. The specimen failure mode is shown in **Fig. 7**.

For specimen CE4B, when loaded to +40 kN, horizontal cracks occur at the east side of concrete, a 20.0 mm height from the root of the column. When loaded to −40 kN, horizontal cracks occur at the west side of concrete, a 17.5 mm height from the root of column. When loaded to $+3\Delta'$, vertical cracks appear at the east side of the concrete column. However, when loaded to $-3\Delta'$, vertical cracks appear at the west side of the concrete column. When loaded to $-4\Delta'$, the east side concrete crushed. The specimen failure mode is shown in **Fig. 8**.

For specimen CE4C, when loaded to +40 kN, horizontal cracks occur at the east side of concrete, 15.0 and 30.0 mm in height from the root of the column. When loaded to −40 kN, horizontal cracks occur at the west side of concrete, 6.3 mm in height from the root of the column. When loaded to +60 kN, horizontal cracks occur at the east side of the concrete, 25.5 and 44.5 mm in height from the root of the column; 15.0 mm crack (occurred at +40 kN) began downwards. When loaded to −60 kN, horizontal cracks occur at the west side of the concrete, 17.5, 22.5, 35.5, and 44.0 mm in height from the root of the column. When loaded to $+4\Delta'$, vertical cracks appear at the west

FIG. 4 Loading device.

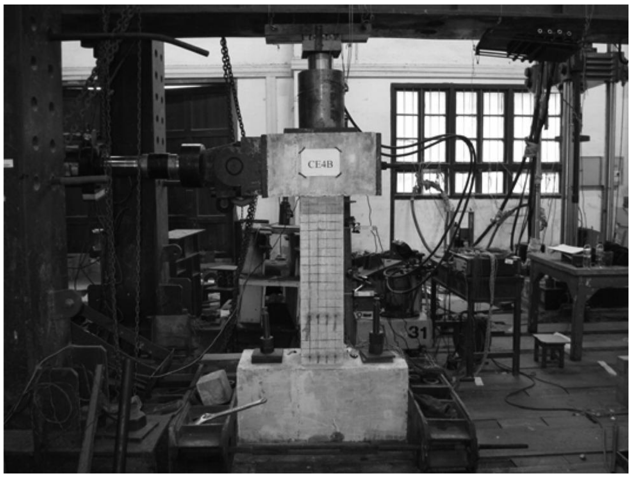

FIG. 5 Schematic diagram of Loading device and measuring points.

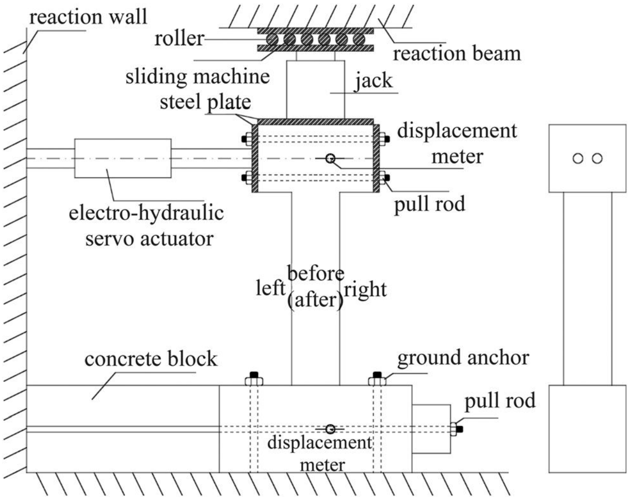

FIG. 6 Loading procedure.

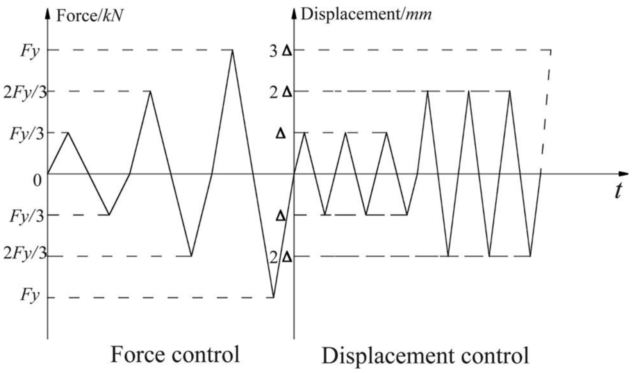

side of the concrete column; when loaded to −4Δ′, vertical cracks appear at the east side of the concrete column. However, when loaded to +4Δ″, the west side concrete crushed. The specimen failure mode is shown in **Fig.** 9.

For specimen CE4D, when loaded to +40 kN, horizontal cracks occur at the east side of the concrete, 13.0 mm in height from the root of the column. When loaded to −40 kN, horizontal cracks occur at the west side of the concrete, 4.5 mm in height from the root of the column. When loaded to +60 kN, horizontal cracks occur at the east side of the concrete, 19.0, 26.0, 32.5, and 41.0 mm height from the root of the column; an original 13.0 mm crack began downwards. When loaded to −60 kN, horizontal cracks occur at the west side of the concrete, 23.0 and 26.0 mm in height from the root of the column. When loaded to −Δ′, horizontal cracks occur at the west side of the concrete, 42.0 mm in height from the root of the column. When loaded to +4Δ′, vertical cracks appear at the west side of the concrete column. When loaded to −4Δ′, vertical cracks appear at the east side of the concrete column. When loaded to +4Δ′, the west side concrete crushed. The specimen failure mode is shown in **Fig.** 10.

FIG. 7 Failure mode of CE4A.

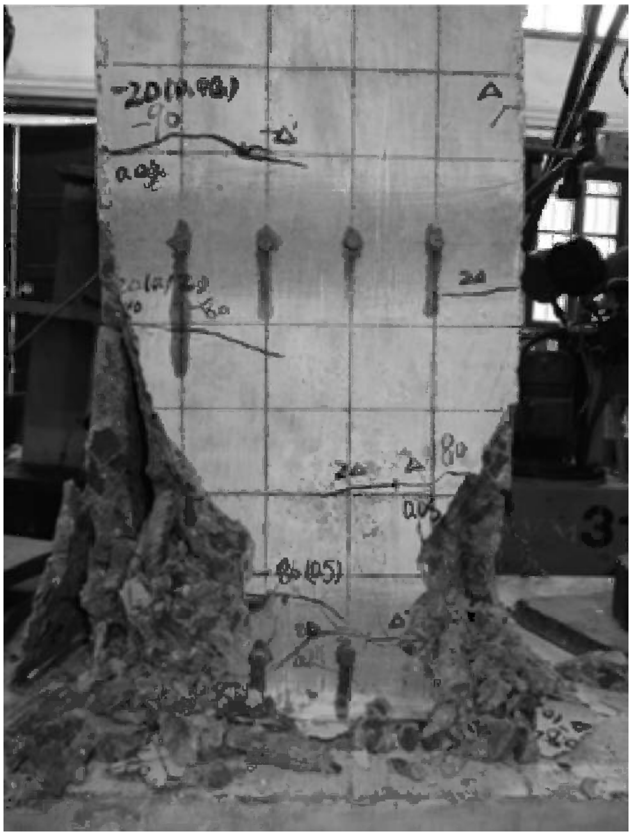

FIG. 8 Failure mode of CE4B.

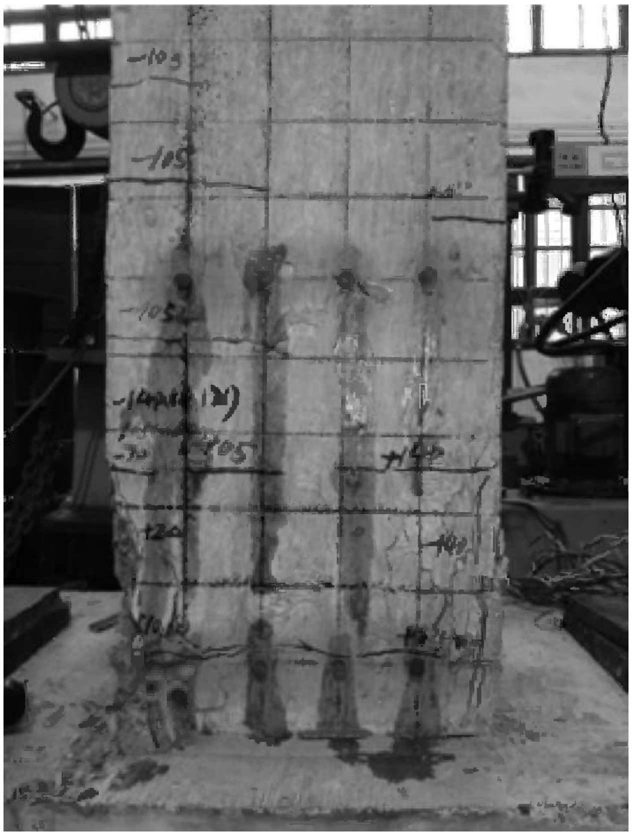

HYSTERESIS CURVE

At each loading–unloading–reverse loading–unloading cyclic loads, relationship curves of the specimen's repeated load and displacement will form a ring, which was called the hysteresis loop. Repeat cyclic loading forms a series of hysteresis loops that constitute a specimen hysteresis curve. The hysteresis curve is a specimen under a cyclic loading force–displacement curve; it is not only a comprehensive reflection of seismic performance, but also the foundation to study the seismic performance. Each specimen hysteresis curve is shown in **Figs.** 11–14.

As can be seen from **Figs.** 11–14, the HRBF400 RC columns' hysteresis curves have the same regulation with normal RC

FIG. 9 Failure mode of CE4C.

FIG. 10 Failure mode of CE4D.

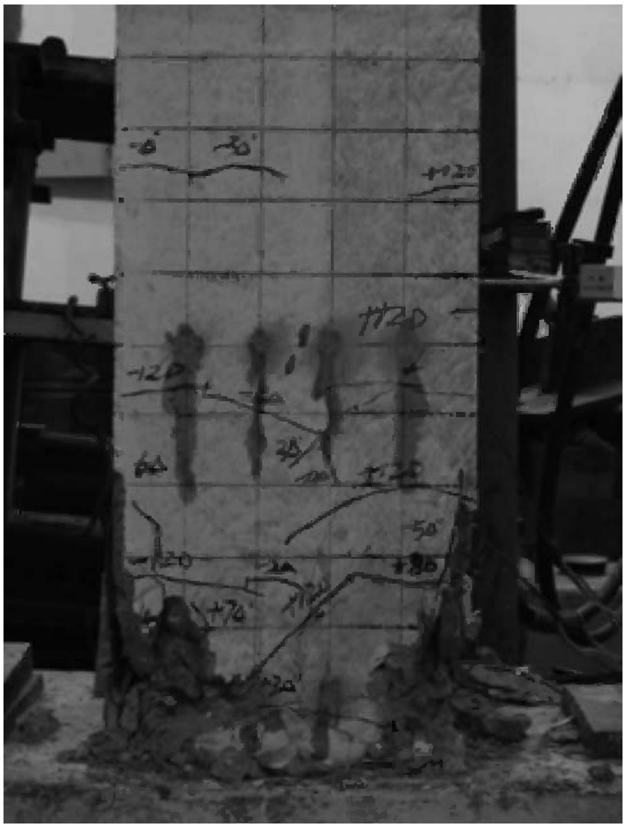

columns. The components of curved destruction have a full hysteresis curve and no pinching phenomenon occurs. Its hysteresis loop appears in spindle form and has a bigger surrounding area; the components show good seismic performance and energy performance. Hysteretic curve of specimen CE4A was fuller than CE4C; this indicated that the specimen with large longitudinal reinforcement ratio have a large energy consumption capacity. Hysteretic curve of specimen CE4D was fuller than CE4C. This indicated that the specimen with small stirrup spacing (big stirrup ratio) has a large energy consumption capacity. Hysteretic curve of specimen CE4A was fuller than CE4B, which indicated that the specimen with a small axial compression ratio has a large energy consumption capacity.

SKELETON CURVES

Linking all the peaks of load-displacement hysteresis curve of each cycle would form the skeleton curve, which is also the maximum peak point movement of each cycle load-displacement curve; the peak point could not cross skeleton curve at any time. The skeleton curve was called the restoring force curve, which is an important parameter for studying inelastic seismic response. The skeleton shape of a curve, in general, is the same as the monotonic loading curve, while its ultimate load is slightly lower and could be used to reflect strength, deformation, and the ductility of components' seismic performance. Skeleton curves of specimen are shown in **Fig. 15**.

As can be seem from **Fig. 15**, the HRBF400 RC columns' skeleton curves have the same regulation with normal RC columns. Skeleton curves are relatively symmetric about the origin, and each curve has three stages: elasticity, yield, and ultimate. Yield and peak load increase with the increasing of reinforcement ratio. The column with big axial compression ratio (CE4B) has a greater peak load, but decreases faster after peak load and has lower ductility. The column with small axial compression ratio (CE4A) has lower peak load, but decreases slower

FIG. 11 Hysteretic curve of CE4A.

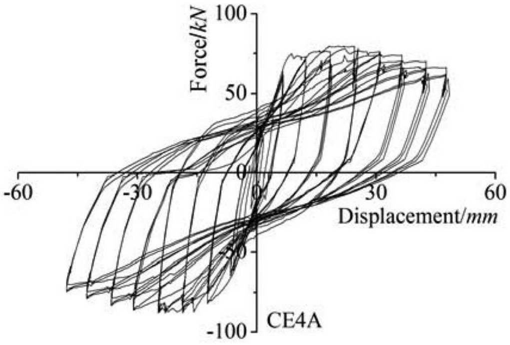

FIG. 12 Hysteretic curve of CE4B.

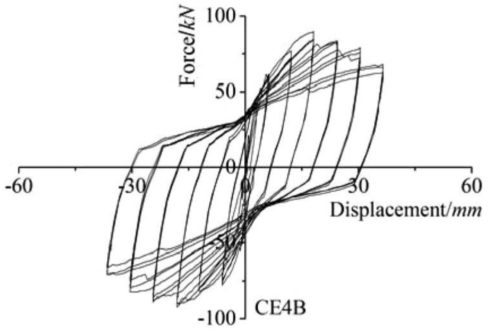

FIG. 13 Hysteretic curve of CE4C.

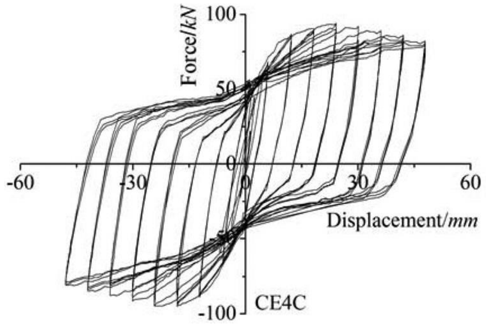

FIG. 14 Hysteretic curve of CE4D.

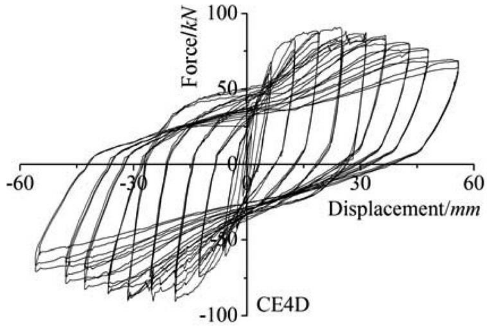

FIG. 15 Components' skeleton curve.

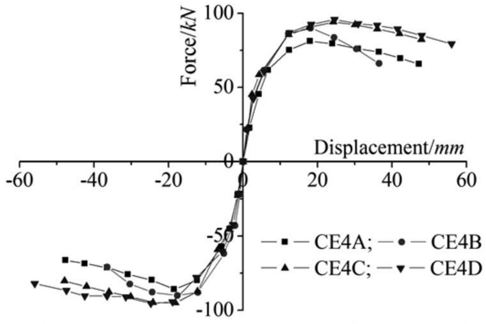

after peak load and has better ductility. Components' ductility increases with the increasing of stirrup ratio.

Analysis of Test Results

DUCTILITY FACTOR

Ductility is the non-elastic deformation capacity of structure, components, and materials while bearing capacity has no significant drop before failure [13]. Traditional ductility factor is built on the base of steel or RC structure, and it is defined as the ratio of ultimate deformation to yield deformation; it can be divided into curvature ductility factor u_φ, rotation ductility factor u_θ, and displacement ductility factor u_Δ. Curvature ductility factor only reflects the section ductility, while displacement ductility factor not only considered the size of the plastic hinge length and curvature, but also the length of components; thus, displacement ductility factor u_Δ was used to describe ductility properties frequently.

$$u_\Delta = \Delta_u/\Delta_y \tag{1}$$

where:

$\Delta_y =$ component's yield displacement, and

$\Delta_u =$ component's ultimate displacement.

The equal energy method was adopted to determine the equivalent yield point. Ultimate load F_u was defined as the largest capacity $F_{\max}$ decreased by 15 %, that is $F_u = 0.85F_{\max}$. Yield displacement Δ_y, ultimate displacement Δ_u, and ductility factor u obtained by the above method are listed in **Table 3**, where Δ_u is the horizontal displacement corresponding to F_u.

As can be seen from **Table 3**, all specimens' displacement ductility factors are larger than 3.0, and so HRBF400 RC columns have good ductility. HRBF400 RC columns' yield load and peak load increase with the increasing of axial compression ratio, while displacement ductility decreases. HRBF400 RC columns' yield load and peak load are almost invariant with the increase of stirrup spacing, while its displacement ductility factor decreased.

ENERGY DISSIPATION CAPACITY

RC structures' equivalent viscous damping coefficient h_e proposed by Jacobson [14] was used to evaluate HRBF RC columns' energy dissipation capacity, structural nonlinear absorption, and energy dissipation could be reflected from the shaded area shown in **Fig. 16**.

$$h_e = \frac{1}{2\pi}\frac{S_1}{S_{OAB} + S_{OCD}} \tag{2}$$

where:

$S_1 =$ shade areas enclosed by hysteresis loop,

$S_{OAB} =$ areas of triangle OBA, and

$S_{OCD} =$ areas of triangle OCD.

TABLE 3 Components' characteristic value and displacement ductility.

Number	F_y/kN	Δ_y/mm	$h_{e,y}$	$F_{\max}$	$\Delta_{\max}$/mm	$h_{e,\max}$	F_u/kN	Δ_u/mm	$h_{e,u}$	u_Δ
CE4A	69.2	9.3	0.19	82.3	24.3	0.25	70.0	45.0	0.29	4.86
CE4B	72.8	9.0	0.2	90.1	17.9	0.25	75.6	32.5	0.29	3.61
CE4C	80.1	9.3	0.19	94.6	24.2	0.26	80.4	49.5	0.3	5.32
CE4D	79.1	9.5	0.23	95.7	24.7	0.29	81.3	55.0	0.35	5.82

The specimen's equivalent viscous damping h_e under yield load, peak load, and ultimate load are compared and listed in **Table 3**. As can be seen from the table, the specimens' equivalent viscous damping under yield load, peak load, and ultimate load are almost the same. This indicates that their energy performance was similar. Equivalent viscous damping h_e under yield load, peak load, and ultimate load of specimens with higher stirrup ratio (CE4D) were slightly higher than specimens with lower stirrup ratio (CE4C). The specimen's equivalent viscous damping coefficient under peak load and ultimate load were larger than the values under yield load, indicating that the specimen has better energy performance.

STIFFNESS DEGRADATION

Under the conditions of the same displacement, with the increasing of the numbers of horizontal loading cycles, structural stiffness degraded to some extent. Stiffness degradation could be express as ring stiffness K [14].

$$K = \sum F_{j,i} \Big/ \sum \Delta_{j,i} \tag{3}$$

where:

$F_{j,i}$ = the peak point of the ith cycle load value while the j-level displacement is loaded, and

$\Delta_{j,i}$ = the ith cycle peak point displacement while the j-level displacement is loaded.

In this paper, relative stiffness is used to describe specimen stiffness degradation. Relative stiffness $\alpha = K/K_y$, K_y is the specimen yielding stiffness. Relative stiffness degradation curve of each specimen is shown in **Fig. 17**.

FIG. 16 Equivalent viscous damping β calculate schematic diagram.

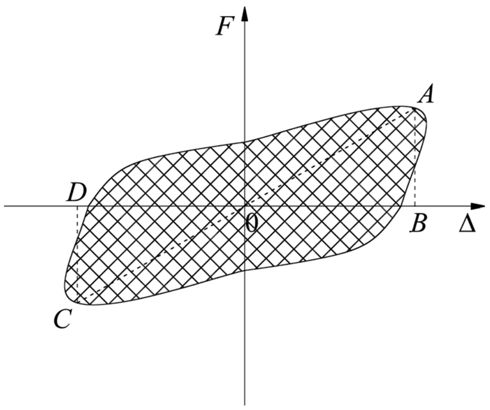

As can be seen from **Fig. 17**, relative stiffness of HRBF RC columns decrease with the increasing of displacement. Specimen with bigger axial compression ratio (CE4B) has larger initial stiffness whereas its stiffness degraded faster. Specimen with bigger volumetric tie ratio (CE4D) could be conducive to slow stiffness degradation and also improve component deformation capacity and seismic performance.

Restoring Force Model

SIMPLIFIED THEORETICAL SKELETON CURVE

The theoretical skeleton curve is shown in **Fig. 18**. Solving the following five parameters is the key point to establish a theoretical skeleton curve: yield load F_y and corresponding displacement Δ_y, peak load $F_{\max}$ and corresponding displacement Δ_P, and degradation of stiffness K_d.

YIELD LOAD AND CORRESPONDING DISPLACEMENT

The yield condition of reinforced concrete compression-bending members is defined as the end-section tensile reinforcement yield or the outer edge of the concrete that reached the limits of compressive strain. To shear type columns, the interlayer shear yield force F_y and section yield moment M_y has the following relationship:

$$F_y = M_y/H \tag{4}$$

FIG. 17 Components' stiffness degradation curves.

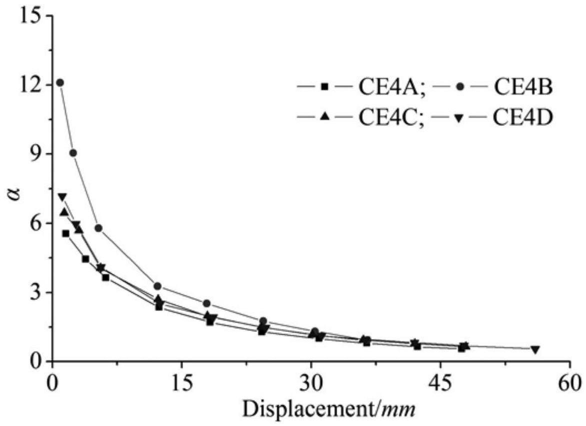

FIG. 18 Theory skeleton curve model.

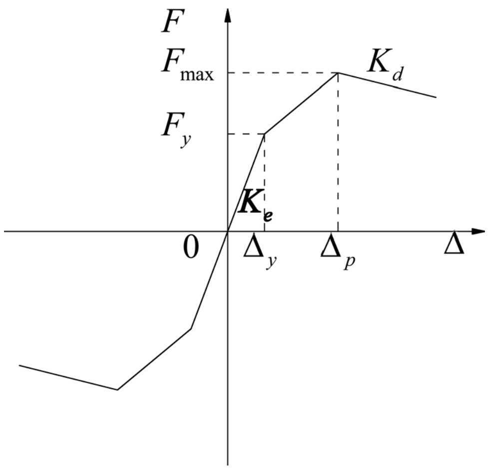

where H represents the height of the column, the vertical distance from horizontal loading to column's root. Column root section yield moment M_y could be obtained by the definition of yield and plane-section assumption [15,16].

$$M_y = f_y A_s(h_0 - a_s) + nbh_0 f_c(h/2 - a_s) - 0.5\eta bh_0 f_c'(\eta h_0/3 - a_s) \tag{5}$$

where:

f_y = yield strength of steel bars,

f_c = concrete compressive strength,

n = axis compression ratio,

h_0 = effective height of cross-section,

b, h = the width and height of cross-section,

A_s = the cross-section area of tensile reinforcement,

a_s = the distance of the centerline of reinforcement to concrete tensile edge, and

f_c' = concrete cross-section yielding maximum compressive stress and could calculate as the following formula.

$$f_c' = \frac{\eta}{1-\eta}\cdot\frac{f_y}{a_E} \tag{6}$$

where:

$a_E = E_s/E_c$,

E_s, E_c = elastic modulus of steel and concrete, and

η = the height coefficient of the concrete compression zone and could be calculate as the following formula.

$$\eta = \left\{\left(\rho_t + \frac{n}{a_f}\right)^2 a_E^2 + \left[\rho_t\left(1+\frac{a}{h_0}\right) + \frac{2n}{a_f}\right]a_E\right\}^{1/2} - \left(\rho_t + \frac{n}{a_f}\right)a_E \tag{7}$$

where:

$a_f = f_y/f_c$, and

ρ_t = reinforcement ratio of tensile steel bars.

Specimen were considered as elasticity before yield and yield displacement theoretical value could be obtained by the definition of yield and plane-section assumption.

$$\Delta_y = \frac{f_y H^2}{3h_0(1-\eta)E_s} \tag{8}$$

PEAK LOAD POINT F_{max} AND Δ_p

According to the statistical analysis of reinforced concrete compression-bending members test results [16,17], the peak load F_{max} and yield load F_y has the following relationship:

$$F_{max} = (1.24 - 0.775\rho_t a_f - 0.5n)F_y \tag{9}$$

$$\Delta_p = u_u \Delta_y \tag{10}$$

u_u, specimen ductility factor [18,19],

$$u_u = \frac{\sqrt{1 + 6a_w\lambda_w}}{0.045 + 1.75n} \tag{11}$$

where:

$\lambda_w = \rho_w a_f$,

a_w = coefficient related to the stirrups form, and

a_w = 1.0, 2.05, and 3.0 to normal, spiral, and composite stirrups, respectively.

ULTIMATE LOAD POINT F_u AND Δ_u

Ultimate load is defined as the maximum load decreased by 15 %; that is, $F_u = 0.85F_{max}$.

When ultimate load decreased 10 %, ductility factor can be determined as follows [19]:

$$u'_{cu} = \frac{\sqrt{1 + 30a_w\lambda_w}}{0.045 + 1.75n} \tag{12}$$

The following formula can be obtained after geometric conversion

$$u_{cu} = 1.5u'_{cu} - 0.5u_u \tag{13}$$

COMPARISON OF EXPERIMENTAL AND THEORETICAL VALUES

A comparison of the theory value of the specimen skeleton curve characteristic calculated by Eqs 4–13 and experimental values is listed in **Table 4**.

As can be seen from **Table 4**, the average ratio of experimental value to theoretical value of yield load, yield displacement ratio are 1.20, 1.15, and discrete coefficients are 0.09, 0.06. The average ratio of experimental value to theory value of peak load, peak displacement ratio are 1.35, 1.27, and discrete coefficients are 0.05, 0.09. The average ratio of experimental value to theory value of ultimate load, ultimate displacement ratio are

TABLE 4 Comparison of skeleton curve characteristic parameters.

Number		CE4A	CE4B	CE4C	CE4D
Experimental Values V_e	F_y/kN	69.22	72.76	80.05	79.09
	Δ_y/mm	9.27	9.00	9.30	9.45
	F_{max}/kN	82.29	90.08	94.55	95.68
	Δ_{max}/mm	24.28	17.92	24.19	24.70
	F_u/kN	70.00	75.57	80.37	81.33
	Δ_u/mm	45.02	32.47	49.50	54.96
Theory Value V_t	F_y/kN	52.29	68.55	66.31	66.31
	Δ_y/mm	7.48	8.26	8.33	8.33
	F_{max}/kN	56.79	69.31	71.75	71.75
	Δ_{max}/mm	17.65	13.35	20.17	21.72
	F_u/kN	48.27	58.91	60.99	60.99
	Δ_u/mm	35.41	26.79	41.47	47.32
V_e/V_t	F_y	1.32	1.06	1.21	1.19
	Δ_y	1.24	1.09	1.12	1.14
	F_{max}	1.45	1.30	1.32	1.33
	Δ_{max}	1.38	1.34	1.20	1.14
	F_u	1.45	1.28	1.32	1.33
	Δ_u	1.27	1.21	1.19	1.16

1.35, 1.21, and discrete coefficients are 0.05, 0.04. Theoretical values seem to agree well with experimental results.

Conclusions

An experimental study was conducted on four HRBF400 RC columns' compression-bending cyclic loading influence of reinforcement strength, concrete strength, axial compression ratio, and volumetric stirrup ratio to examine the seismic performance and ductility of HRBF400 RC columns. The results were as follows:

1. HRBF400 RC columns' hysteresis curves have the same regulation with normal RC columns, and have good seismic performance and energy dissipation capacity according to experimental results.
2. Yield load and peak load increase with the increasing of reinforcement ratio, and columns' ductility increase correspondingly. A column with a big axial compression ratio has greater peak load, but decreases faster after peak load and has lower ductility. A column with small axial compression ratio has lower peak load, but decreases slower after peak load and has better ductility. The components' ductility increases with the increasing of stirrup ratio.
3. Theoretical value of a characteristic parameter calculated by a restoring force model agrees well with experimental results. This indicated that the given model could be applied to engineering practice.

ACKNOWLEDGMENTS

The writers appreciate the support of the National Natural Science Foundation of China (51308490), the Natural Science Foundation of Jiangsu Province, China (BK20130450), the Science and Technology Projects of Ministry of Housing and Urban-Rural Development (2013-K4-17), and the Natural Science Foundation for Colleges and Universities in Jiangsu Province (13KJB560015), The Science and Technology Projects Fund of Yangzhou City (2012149), and the Open Foundation of Southeast University, Key Laboratory of Concrete and Pre-Stressed Concrete Structure of Ministry of Education.

References

[1] GB50010-2010: Code for Design of Concrete Structures, China Academy of Building Research, Beijing, China.

[2] Li, B., "Strength and Ductility of Reinforced Concrete and Frames Constructed Using High-Strength Concretes," University of Canterbury, Christchurch, New Zealand, 1994.

[3] Azizinamini, A., Kuska, S. S. B., Brungardt, P., and Hatfield, E., "Seismic Behaviors of Square High-Strength Concrete Columns," *ACI J. Struct.*, Vol. 91, No. 3, 1994, pp. 336–345.

[4] Sheikh, A. S., Shah, D. V., and Khoury, S. S., "Confinement of High-Strength Concrete Columns," *ACI J. Struct.*, Vol. 91, No. 1, 1994, pp.100–111.

[5] Hou, C. X., 1993, "Experimental Study on the Seismic Behavior of Compression-Bending Member Reinforced With High Strength Steel Bars," M.S. thesis, Tsinghua University, Beijing, China.

[6] Guan, P. and Wang, Q. X., "Effect of Ductility of High-Strength Concrete Columns With Cold-Rolled Ribbed Wires Hoping," *J. Dalian Univ.*, Vol. 20, No. 4, 1999, pp. 56–58.

[7] Li, L. R., Zhi, Y. F., Chen, Y. Q., and Zhang, X. M., "Research on Anti-Seismic Ability of Hoop Reinforced High Strength Concrete Frame Column," *J. Chongqing Jianzhu Univ.*, Vol. 24, No. 5, 2002, pp. 38–45.

[8] Yan, S., Xiao, X., Kan, L. X., and Meng, Q. G., "Resilience Model of High Strength Reinforcement and High Strength Concrete Columns," *J. Shenyang Jianzhu Univ.*, Vol. 21, No. 2, 2005, pp. 81–85.

[9] Liu, J. S., Su, X. Z. and Zhao, Y., "Experiment on Concrete Columns Reinforced With 500 MPa Fine-Grained Rebar Under Low Cycle Reversed Loading," *Struct. Eng.*, Vol. 25, No. 3, 2009, pp. 135–140.

[10] Zhang, J. W. and Jiang, C. W., "Experimental Study on a Seismatic Performance of Concrete Beam-Column Assemblies Reinforced With Fine Grained High Strength Steel Bars," *Indust. Constr.*, Vol. 39, No. 11, 2009, pp. 33–39.

[11] Wang, X. F., Fu, J. P., Zhu, A. M., Liu, C. W., and Deng, Y. Q., "Numerical Simulation of Seismic Behavior of RC Columns Reinforced With HRB500 Steel Bars," *J. Build. Struct.*, Vol. 32, No. 8, 2011, pp. 99–105.

[12] GB/T228.1-2010: Metallic Materials-Tensile Testing-Method of Test at Room Temperature, General Administration of Quality Supervision, Inspection and Quarantine of the People's Republic of China, Beijing, China.

[13] Maaman, A. E., Harajli, M. H., and Wight, J. K., "Analysis of Ductility in Partially Prestressed Concrete Flexural Members," *PCI J.*, Vol. 31, No. 3, 1986, pp. 64–87.

[14] Tang, J. R., *Seismic Behavior of Reinforced Concrete Frame Joints*, Southeast University Press, Nanjing, China, 1989.

[15] He, Z., "Nonlinear Analysis of RC Structures and Seismic Damage Performance Control Design," Harbin Institute of Technology, Harbin, China, 2000.

[16] Wang, X., 2003, "Research of Seismic Performance and Hysteretic Mode of Corroded Reinforced Concrete Members," M.S. thesis, Xian University of Architecture and Technology, Xi'an, China.

[17] Park, Y. J. and Ang, A. H. S., "Seismic Damage Analysis of Reinforced Concrete Buildings," *J. Struct. Eng.*, Vol. 111, No. 4, 1985, pp. 740–757.

[18] Weng, Y. J., Shen, J. M. and Ma, B. M., "Improvement of Ductility of Reinforced Concrete Columns With Different Types of Stirrups," J. Build. Struct., Vol. 6, No. 4, 1985, pp. 41–47.

[19] Wen, Y. J. and Feng, S. P., *Seismic Design of Building Structure*, Seismological Press, Albany, CA, 1990.

Journal of Testing and Evaluation

doi:10.1520/JTE20140080 / Vol. 43 / No. 2 / March 2015 / available online at www.astm.org

Xueliang Zhao,[1] Jian Xu,[2] Baogang Mu,[3] and Bing Li[4]

Macro- and Meso-Scale Mechanical Behavior of Caissons During Sinking

Reference

Zhao, Xueliang, Xu, Jian, Mu, Baogang, and Li, Bing, "Macro- and Meso-Scale Mechanical Behavior of Caissons During Sinking," *Journal of Testing and Evaluation*, Vol. 43, No. 2, 2015, pp. 363–375, doi:10.1520/JTE20140080. ISSN 0090-3973

Manuscript received February 28, 2014; accepted for publication October 9, 2014; published online November 5, 2014.

[1] Ph.D., Associate Professor, School of Civil Engineering, Southeast Univ., Nanjing, China 210096 (Corresponding author), e-mail: zhaoxl@seu.edu.cn

[2] School of Civil Engineering, Southeast Univ., Nanjing, China 210096, e-mail: xujian19881024@163.com

[3] Ph.D., Associate Professor, School of Civil Engineering, Southeast Univ., Nanjing, China 210096, e-mail: mubaogang@seu.edu.cn

[4] Ph.D., Associate Professor, School of Civil Engineering, Southeast Univ., Nanjing, China 210096, e-mail: lbershui@seu.edu.cn

ABSTRACT

Caissons are often used as the foundation of important structures. The sinking process of a caisson has a significant effect on its serviceability. In this study, laboratory experiments and numerical simulations were performed to study the macro- and meso-scale mechanical behaviors of caissons during sinking. Earth pressures near the toe of the caisson during sinking were measured. Particle movements and coordinate numbers were investigated to explain the distribution of earth pressure on the caisson from the meso-scale viewpoint. The region affected by the sinking process was fitted by a parabolic function. Soil arching and rotation of principal stress were found to be the important mechanisms affecting the mechanical behaviors of caissons during sinking. A numerical solution is proposed and is shown to offer a good approximation of the earth pressure on a caisson. The results of this paper are supposed to be useful for the design and construction of caissons in practice.

Keywords

caisson, sinking, macro- and meso-scale, earth pressure

Introduction

A caisson is an underground structure and a type of deep foundation in geotechnical engineering. Because of their stiffness, high structural strength, and good integrity, caissons are widely used as foundations for large bridges. In recent years, several large bridges such as the Taizhou Bridge and the Nanjing Forth Yangtze River Bridge have been constructed in China. Most of these large bridges have caissons as the foundation of the main pier in suspension bridges or as the foundation of the anchorage system in cable-stayed bridges. The sinking or construction process of a caisson can have a significant effect on the mechanical behavior of the completed caisson, which will consequently influence the serviceability of the caisson as the foundation of a bridge. It is important to investigate the mechanical behavior of the caisson and its interaction with the soil during the process of sinking.

In order to design and control the sinking of caissons in practice, a lot of work has been done to study the mechanisms and the mechanical behavior of caissons during sinking. Different methods including field measurement, laboratory experiments, and numerical simulation methods have been employed by some researchers. In terms of field work, Chen et al. [1] performed whole-process monitoring of a caisson during sinking. The magnitude and distribution of the resistance force on the caisson were investigated. Feng et al. [2] measured the resistance force on the bottom of a caisson, the earth pressure on the side of the caisson, and the structural stress of the caisson in the anchorage foundation of the Taizhou Bridge. Zhu et al. [3,4] utilized systematic measurement and monitoring of the caissons in the Nanjing Forth Yangtze River Bridge and the Ma'anshan Yangtze River Bridge to study the distribution of the resistance force on caissons during sinking. Most of these field works indicated that the earth pressure on the side of a caisson was much more complex than and quite different from the result calculated using classical earth pressure theory. In terms of laboratory work, most of the research has focused on the suction caisson rather than the common caisson. Hogervorst [5] performed an experiment on a full-size suction caisson to study the axial force and the side friction. Tjelta et al. [6] simulated the sinking of a caisson using penetration experiments. Dyvik et al. [7] investigated the stress of a caisson under static load and cyclic load. Wang [8] explored the resistance force on a caisson using a micro-penetrometer. Wang found that the development of side friction had three stages during the sinking of the caisson. In the first stage, the side friction increased linearly with increasing sinkage depth. In the second stage, the side friction continued to increase, but the rate of increase slowed; at some depth, it reached a maximum value. In the third stage, the side friction decreased with increasing sinkage depth. Some researchers simulated the behaviors of caissons using numerical methods [9–11], but most of these numerical methods were applied to suction caissons.

Although a lot of practical experiences have been achieved, theoretical analysis has lagged behind practice. Some very simple methods are still used to design caissons. For example, the side friction of a caisson is an important factor in controlling the sinking of the caisson, but it is very difficult to predict it accurately during sinking. Because of the complexity, classical earth pressure theory is often used to calculate the side friction for simplification in practical design. This often results in a significant difference between the predicted value and the value measured on site. This is one of the main reasons for some engineering problems such as sudden sinking and the difficulty of sinking at the site.

In this study, laboratory experiments were carried out and numerical simulations were performed to study the macro- and meso-scale mechanical behaviors of caissons during sinking. The influence region of the caisson during sinking was investigated. The earth pressure on the side of the caisson was analyzed. The earth pressure at the toe of the caisson was measured. The macro-scale behaviors are revealed and explained from the meso-scale viewpoint according to the particle displacement and the coordination number of the particles. A new numerical solution to calculate the earth pressure on the side of a caisson is proposed and shown to be able to give a better result than the classical method.

Laboratory Experiment

EXPERIMENT METHOD

Considering the structural symmetry of a caisson under symmetric load, a half-model was used in this study to facilitate the observation of the behaviors of the caisson and the surrounding soils. The half-model was designed to be 0.36 m in length, 0.07 m in width, and 0.48 m in height. The caisson was made of Plexiglas. A picture of the caisson model is shown in **Fig. 1**.

Taking the boundary effect in the experiment into consideration, the size of the test box was 1 m in length, 0.5 m in width, and 0.9 m in height, such that the distance from the caisson to the test box was larger than the half-size of the model.

FIG. 1 Caisson in the experiment.

FIG. 2 Test box with the caisson.

The front face of the box was made of transparent Plexiglas of 2-cm thickness with a marked grid to facilitate monitoring of the displacements of the caisson and the soils. The other three sides of the box were made of steel plate with a thickness of 1 cm. A picture of the test box is shown in **Fig. 2**.

Standard test sand from Fujian Pingtan was used in this work. The physical characteristics of the sand are listed in **Table 1**. In the test, the box was filled with sand layer by layer. In the concerned part, 6-cm-thick layers of common sand were separated by 2-cm-thick layers of colored sand in order to mark the deformation of the soil around the caisson. Each layer of sand was weighted first and tamped to a given thickness to ensure a specific void ratio.

During the sinking of the caisson, the earth pressure on the wall of the caisson was measured using a mini strain earth pressure cell with a measuring range of 0.1 MPa. The setup of the pressure cells is shown in **Fig. 3**. Because it is difficult to sink a caisson using only its self-weight, a vacuum method was used to excavate the soil from the inside of the caisson to help the caisson sink (simulating the soil excavation inside caissons in the field). The vacuum was a small household vacuum cleaner (type Secline-3201) with a power of 350 W. After each 2 cm of sinking, the sand was left to rest for 10 min, and the earth pressure was recorded after it became stable.

TABLE 1 Physical characteristics of Pingtan sand.

d_{50}, mm	C_u	C_c	G_s	$\rho_{\max}$, kg/m^3	$\rho_{\min}$, kg/m^3	$e_{\max}$	$e_{\min}$
0.34	1.542	1.104	2.643	1749	1430	0.848	0.519

FIG. 3 Setup of the earth pressure cells on the caisson.

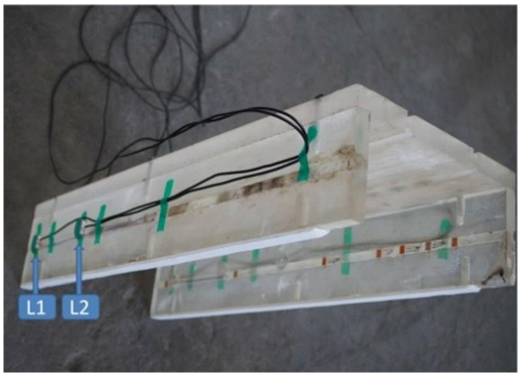

ANALYSIS OF THE EXPERIMENT RESULTS

A picture of the experimental setup after the caisson had finished sinking is shown in **Fig. 4**. The deformation of the soil around the caisson can be observed through the colored sand. It indicates that the soils around the caisson moved downward in the shape of a funnel and flowed into the caisson from the toe during the sinking of the caisson. The friction between the caisson and the soil and the consequent drag force on the adjacent soil particles might have been the reason for the downward movement of the particles outside the caisson, and the excavation of the soil inside the caisson and the consequent pressure difference between the outside and inside of the caisson might have been the reason for the flow of the particles at the toe of the caisson during sinking.

Earth pressures near the toe of the caisson at different sinkage depths of the caisson were measured. The data from two pressure cells (L1 and L2 in **Fig. 3**) are shown in **Fig. 5**. They show that the earth pressure increased first, reached a peak value at a sinkage depth of about 2/3 the height of the caisson, and then started to decrease with increasing sinkage depth. What are the reasons for this change in earth pressure near the toe of the caisson during sinking? In the early stage of sinking, the earth pressure near the toe of a caisson is mainly dependent on the self-weight of the soil, which is linear with the depth. With further sinking, there is a pressure difference at the toe of the caisson caused by the excavation of soil inside the caisson. The soil particles tend to flow from the outside to the inside of the caisson. This flow of soil particles results in a loosened region near the toe of the caisson. It is the loosened region that causes the decrease in earth pressure near the toe. When the sinkage depth is small, the mobility of soils above the toe of the caisson is relatively large. The downward movement of the soil particles compensates for the decrease in earth pressure in the loosened region. When the sinkage depth is less than 2/3 the

FIG. 4

Picture after the sinking of the caisson.

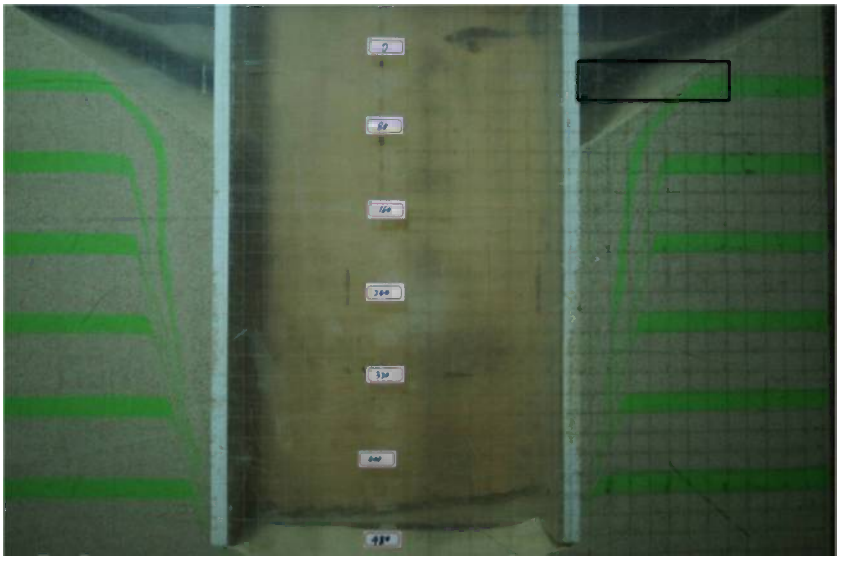

height of the caisson, the earth pressure near the toe of the caisson is mainly dependent on the depth of the soil. When the caisson sinks more, the soil in the region above the toe goes into a self-hold state because of the friction between the caisson and the soil. Some researchers have considered this as soil arching [12]. The mobility of the soil decreases, and the compensation of the earth pressure from the downward movement of the soil is weakened by the effect of the soil arching. At this stage, the flow and the loosening effect of the soil near the toe play more of a role, which causes decrement of the earth pressure. So, the earth pressure near the toe of the caisson has different mechanisms at different sinkage depths, and the behaviors of the soil particles are the underlying physical cause of the change in the earth pressure at the toe of the caisson.

FIG. 5 Earth pressure near the toe of the caisson during sinking.

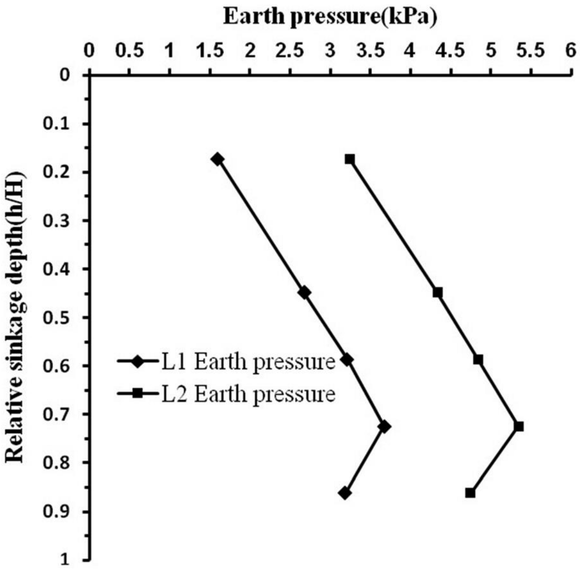

Numerical Simulation

NUMERICAL MODELING

In order to explore the behaviors of the soil around the caisson and the interaction between the caisson and the soil on a meso-scale at the level of soil particle size, we used the discrete element method (DEM) in this study to simulate the sinking process of the caisson. The DEM is a numerical method that is more suitable for discontinuous materials and large deformation problems than numerical methods based on continuous methods such as the finite element method and the finite difference method. Using the DEM, the behaviors of the soil around a caisson can be captured and the behavior of the caisson can be revealed through the interaction of the caisson and the soil at the meso-scale level. The specific implementation of the DEM used here was "Particle Flow Code in Three Dimensions" (PFC3D). Two types of objects may be used in particle flow code, "balls" and "walls." Balls are used to simulate the soil particles, and walls are used to simulate the caisson. As in the laboratory experiment, the size of the half-model was 0.36 m by 0.07 m by 0.48 m. Taking advantage of the symmetry of the caisson, we included only one-quarter of the caisson and the soil in the numerical model to save computing time. In the main affected region, the field of the soil was set to be 0.3 m by 0.3 m by 0.6 m. The average radius of the particles was 5 mm, and there were about 60 000 particles in total.

To minimize the effect of the boundaries, fast Lagrangian analysis of continua in three dimensions (FLAC3D), based on the finite difference method, was used to simulate the soils in

FIG. 6 Numerical model coupled with PFC3D and FLAC3D.

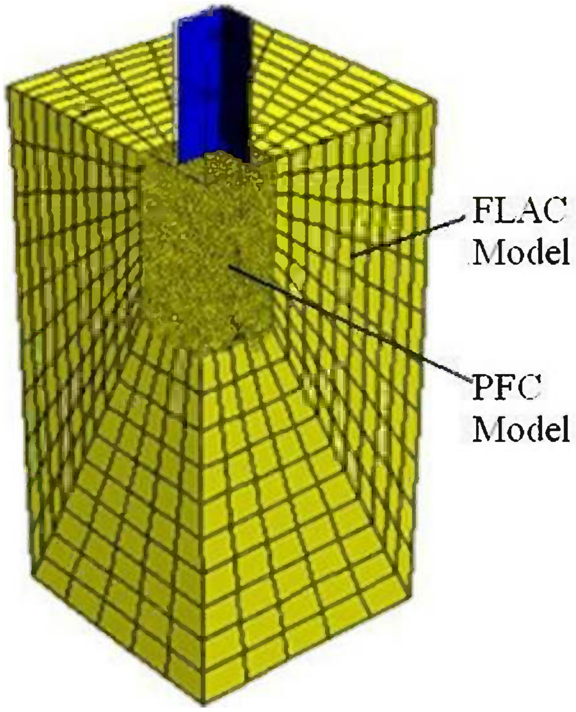

the larger field around the soils in the DEM region. Beyond the region of 0.3 m by 0.3 m by 0.6 m of particles, a finite difference grid of 1 m by 1 m by 2 m was used to simulate the extended soils around the caisson. In this way the effect of the boundary was thought to be minimized. At the interface of the PFC3D and FLAC3D regions on the plane where $x = 0.3$ m, $y = 0.3$ m, and $z = -0.6$ m, Socket I/O was used to couple the two codes. The coupled model with PFC3D and FLAC3D is shown in **Fig. 6**.

In the coupled numerical model, linear contact mode was used for PFC3D, and Mohr–Coulomb mode was used for FLAC3D. The microscale parameters in PFC3D and the macroscale parameters in FLAC3D were carefully selected to make sure the particle and finite difference grids in the two codes could be coupled well as the same material. The main parameters used in the coupled model are listed in **Table 2**. Before we simulated the sinking of the caisson, the model was initialed first to stabilize the coupling between PFC3D and FLAC3D and reach an initial equilibrium state.

MOVEMENTS OF THE SOIL PARTICLES

The behaviors of soil and the interaction between the soil and a caisson are significantly related to the mechanical characteristics of the caisson. Problems such as the resistance force and the affected area of the caisson during sinking can be revealed through meso-scale analysis at the particle level. Contours of the soil particle displacement at different sinkage depths of the caisson are shown in **Fig. 7**.

It can be seen from **Fig. 7** that the soil movements occurred mainly in the regions near the wall of the caisson, at the toe of the caisson, and under the bottom of the caisson. During sinking, the caisson moved downward relative to the surrounding soil. Friction existed between the soil and the wall, and consequently the soil particles adjacent to the caisson were dragged downward. At the toe and bottom of the caisson, because of the excavation of the soil inside the caisson, there was a stress difference between the inside and outside of the caisson. This stress difference caused the flow of soil particles from the outside to the inside. At the same time, heaving of the soil occurred at the bottom of the caisson because of the unloading by excavation. The area of the affected region grew with increasing sinkage depth. At some sinkage depth, the affected region at the ground surface would become almost constant.

For the magnitude of the displacement of the soil particles, in the horizontal direction, the closer the particle is to the caisson, the larger the particle displacement is. In the vertical direction, the particle displacement decreases with increasing depth from the ground. The vectors of the soil particle displacements are shown in **Fig. 8**. Notice that the vectors in the figure are to show the directions and relative magnitudes of the particle movements. The length of the vector is only a relative magnitude, rather than the absolute magnitude of the particle displacement. The caisson is considered to be a rigid body, and the particle can never penetrate the caisson.

Figure 8 shows that according to the magnitude of the displacement, the particle movements mainly occur within some region. This region can be considered as the region affected by the sinking process of the caisson. A curve like a sliding surface in a retaining wall can be drawn to delineate the affected region according to the magnitude and the direction of the particle movements. After comparison with some functions such as the exponential function and the polynomial function, the parabolic function was found to fit the curve better. The parabolic function can be given as follows:

TABLE 2 Micro- and macro-scale parameters in the coupled model.

PFC3D	d, mm	K_n, kN/m	K_s, kN/m	Porosity	Density, kg/m^3	φ, deg
	10	5×10^3	6.25×10^2	0.41	2000	27
FLAC3D	c	K, MPa	G, MPa	Porosity	Density, kg/m^3	φ, deg
	0	9.11	4.2	0.41	2000	27

FIG. 7

Contours of the soil particle displacement at different sinkage depths.

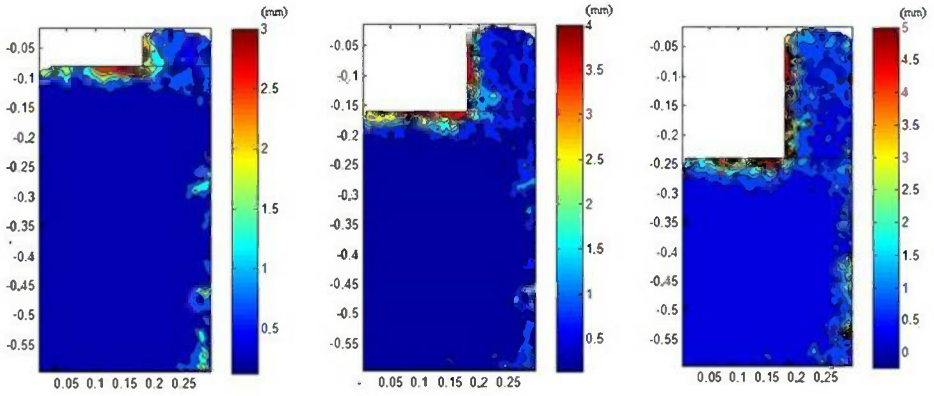

(a) Sinkage depth of 0.08m (b) Sinkage depth of 0.16m (c) Sinkage depth of 0.24m

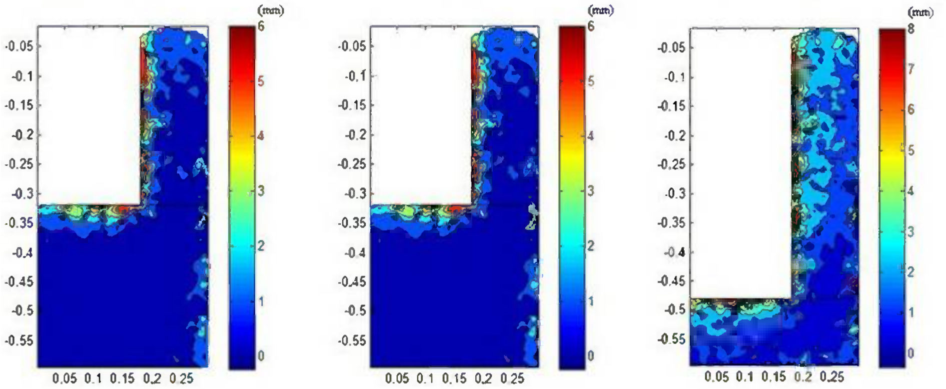

(d) Sinkage depth of 0.32m (e) Sinkage depth of 0.4m (f) Sinkage depth of 0.48m

$$x = f(y) = \lambda \cot \beta \sqrt{H^2 - Hy} \tag{1}$$

where:

x = horizontal distance from the caisson,
y = depth from ground level,
H = sinkage depth,
$\beta = 45° + \varphi/2$,
φ = internal friction angle of the soil, and
λ = attenuation coefficient.
λ can be calculated as

$$\lambda = \exp(-\alpha H/B) \tag{2}$$

where:

α = fitting coefficient, and
B = width of the caisson.

From Eqs 1 and 2, it can be seen that the affected region is mainly a function of the caisson width, the sinkage depth, and the internal friction angle of the soil. According to Eq 1, $x = 0$ when $y = H$, and $x = \lambda H \cot \beta$ when $y = 0$. For a specific caisson and soil, the values of B and β are given. The value of x, which means the region that is affected by the sinking of the caisson at some depth, is a function of λ. In order to calculate λ, one needs to determine the value of α first. If the x values at $y = 0$ for different sinkage depths (H) are known, the value of α can be back-calculated. Based on the results of our numerical simulation, the x values at $y = 0$ (denoted by x_0) for different H values were measured. The value of α was calculated based on **Table 3** and **Fig. 9**. From the fitting line in **Fig. 9**, the α value was calculated as 0.763. The fitting line has a correlation coefficient as high as 0.972. By putting the value of α into Eq 1, we could determine the boundary of the affected region.

The contours of the particle displacements with the fitting curves according to Eq 1 at different sinkage depths are shown in **Fig. 10**. The figure shows that the fitting curves approximate the boundaries of affected regions well. This verifies the validity of the proposed Eq 1. The evolution of the affected region can be revealed if the curves are put in the same plot (**Fig. 11**).

When the sinkage depth is small, the value of H/B is small. The attenuation coefficient λ approaches 1. The affected area at the ground level is approximately $H\cot \beta$. The boundary of the affected region approximates a straight line. This agrees well with the sliding surface according to classical Rankine's earth pressure theory. At this stage, although friction between the caisson and the soil exists, the movements of the soil particles

FIG. 8 Vectors of the soil particle displacement.

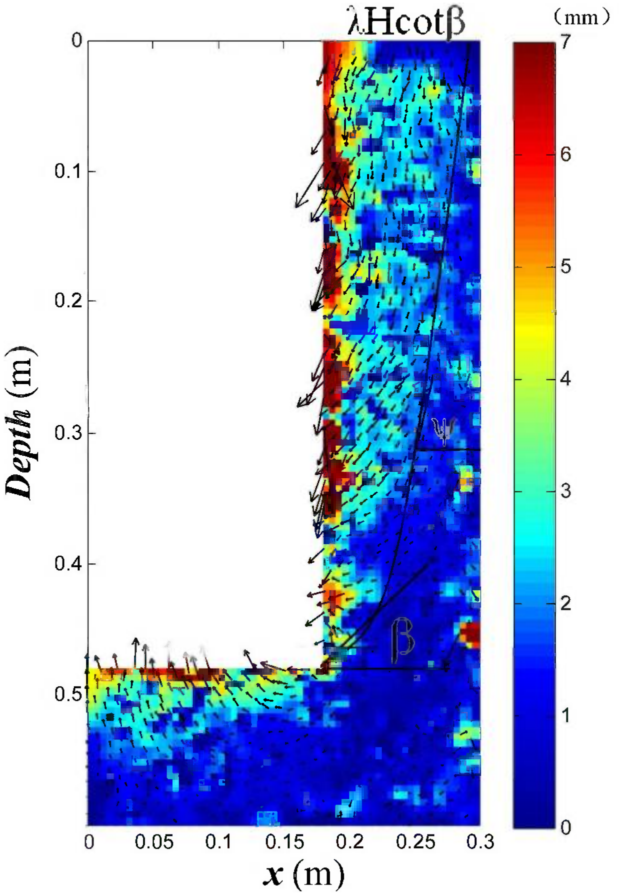

are mainly influenced by the flow of the soil from the outside to the inside of the caisson. The flow of the soil particles weakens the friction force on the soil particles. With increasing sinkage depth, the values of H/B and λ become smaller. The rate of increase of the affected region at ground level decreases. It is almost the same as when the sinkage depth is large. At this stage, the friction between the soil and the caisson plays more of a role in the movement of the particles.

EARTH PRESSURE ON THE CAISSON DURING SINKING

The earth pressures at the toe of the caisson at different sinkage depths were obtained from the numerical simulation as shown in **Fig. 12**. Compared with **Fig. 5**, **Fig. 12** indicates that the trends of the earth pressure from the numerical simulation and laboratory experiment were similar. That is, the earth pressure increased with increasing sinkage depth first. At a sinkage depth of about 2/3 the height of the caisson, the earth pressure at the toe reached the maximum value, and it started to decrease with further sinking.

TABLE 3 Parameters for calculating α.

H, m	cotβ	Hcotβ, m	H/B	x_0, m	λ	$\alpha H/B$
0.08	0.612	0.049	0.222	0.041	0.920	0.084
0.16	0.612	0.098	0.444	0.070	0.746	0.293
0.24	0.612	0.147	0.667	0.088	0.593	0.523
0.32	0.612	0.196	0.889	0.099	0.475	0.744
0.40	0.612	0.245	1.111	0.105	0.417	0.875
0.48	0.612	0.294	1.333	0.106	0.378	0.973

FIG. 9 Fitting line for α.

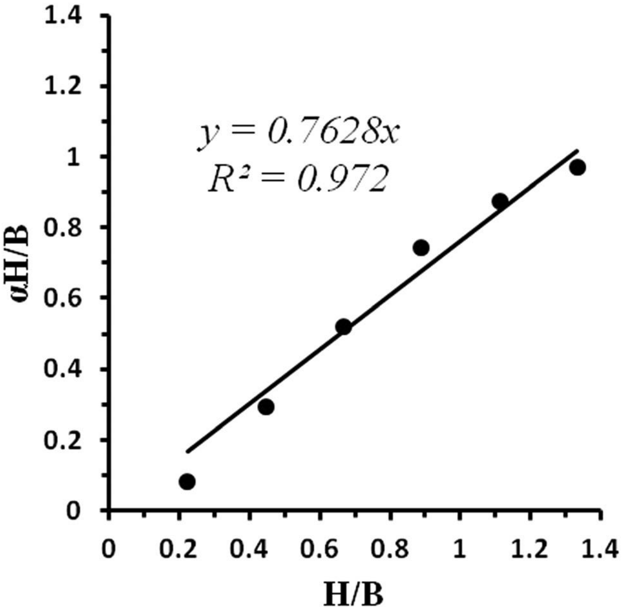

For the distribution of the earth pressure on the caisson after the completion of sinking, the pressures on the different positions of the wall from the numerical simulation are shown in **Fig. 13**. The figure indicates that the earth pressure increased with increasing depth of the caisson. At some point, it reached a maximum value and started to decrease with increasing depth. Liu [13] performed in situ measurements of the earth pressure on the walls of two caissons in a drainage work. The measured earth pressures on the walls are shown in **Fig. 14**. It can be seen that the trend of the earth pressure from the current numerical simulation approximates that from the data measured in situ. This indicates that the numerical simulation in this study is valid and can be used to investigate the sinking process of a caisson properly.

In order to investigate the mechanical characteristics of the soil around the caisson during sinking, coordination numbers of the surrounding soils were examined, and the contours are shown in **Fig. 15**. The figure shows that the coordination numbers of the particles near the caisson decreased obviously with the sinkage of the caisson. In the early stage of sinking, the excavation of soil inside the caisson caused a flow of soil particles from outside. This resulted in a loosened region near the caisson and consequently a smaller coordinate number in this region. The coordination number of the particles below the bottom of the caisson also decreased. This was due to the heave of the bottom because of the unloading with excavation. With further sinking, the coordination number of particles near the upper

FIG. 10
Affected regions with fitted curves at different sinkage depths.

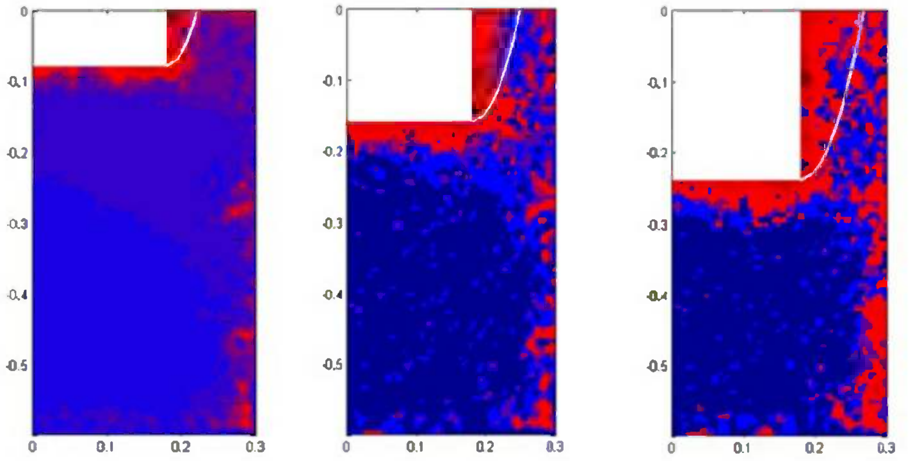

(a) Sinkage depth of 0.08m (b) Sinkage depth of 0.16m (c) Sinkage depth of 0.24m

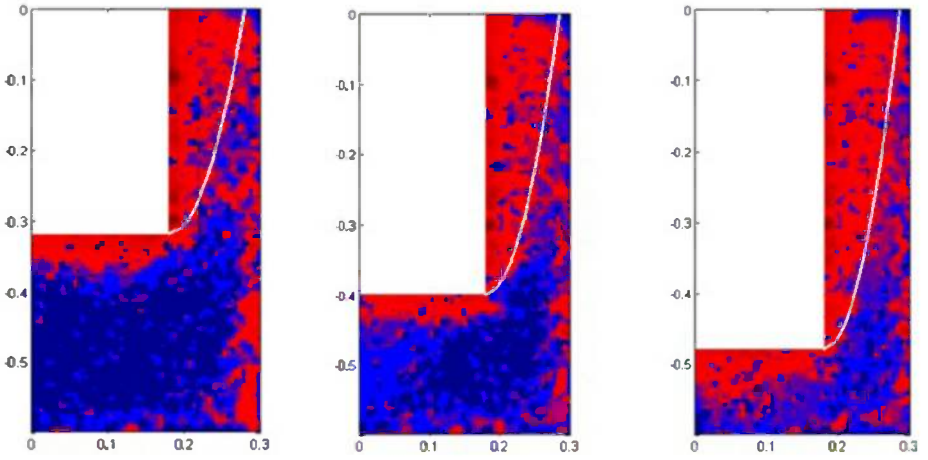

(d) Sinkage depth of 0.32m (e) Sinkage depth of 0.4m (f) Sinkage depth of 0.48m

part of the caisson increased gradually. This might have been due to the downward movement of the particles around the caisson. These movements filled some voids because of the flow of the particles. At the same time, because of the friction between the soil and the caisson, the particles adjacent to the caisson were dragged downward, but the particles far from the caisson moved much less. The particles near the caisson pushed the neighboring particles outward, which compacted the soils and resulted in an increase in the coordinate number. This reveals the phenomenon of soil arching [12].

According to the distribution of the coordinate numbers around the caisson, the distribution of the earth pressure on the caisson can be explained from a meso-scale perspective. Firstly, the decrease in the coordinate number near the toe indicates the flow of particles from outside to inside the caisson. This results in a loosened region. The earth pressure in this region is less than the earth pressure at rest, and maybe even less than active earth pressure. Secondly, because of the effect of the soil arching, there is a rotation of the major principal stress. As a result, the earth pressure at the shallow part is greater than the active earth pressure. Finally, with increasing depth, the effect of soil arching decreases. At a depth of about 2/3 the height of the caisson, the effect of soil arching becomes insignificant. The earth pressure decreases and tends toward the active earth pressure. At the toe of the caisson, because of the flow of the particles, the earth pressure might even be less than the active earth pressure.

NUMERICAL SOLUTION TO THE EARTH PRESSURE ON THE CAISSON

Earth pressure is a typical problem in retaining walls. Coulomb's theory and Rankine's theory are the classical methods. Terzaghi [14] conducted some experiments on large-scale retaining walls and investigated the relationship between the critical state of the soil and the movement of the retaining wall. He confirmed that only when the movement of soil was big

FIG. 11 Evolution of the affected regions.

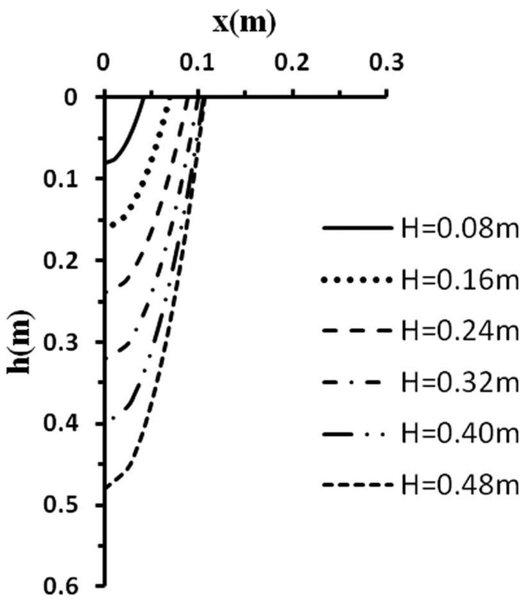

enough and when shear failure occurred did the earth pressure on the retaining wall approximate the value calculated according to Coulomb's or Rankine's theory. Afterward, a lot of researchers [15–17] did a lot of work on the distribution of earth pressure on retaining walls. It is generally known that the distribution of the earth pressure is different with different movements of the retaining wall. For earth pressure on caissons, some researchers concluded that the earth pressure distribution is very similar to that on retaining walls according to the data from in situ measurements of some large caissons. In the opinion of the authors, the common thing between retaining walls and caissons is that there is friction between the wall and the soil. This friction will result in a rotation of the major principal stresses (deviating from the vertical and horizontal directions). Furthermore, the interaction between the soil and the caisson is much more complex near the toe of the caisson.

FIG. 12 Earth pressures near the toe of the caisson at different sinkage depths.

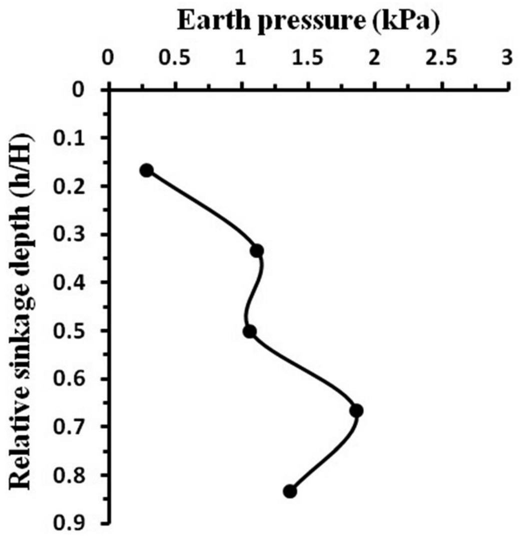

FIG. 13 Earth pressures at different positions of the caisson.

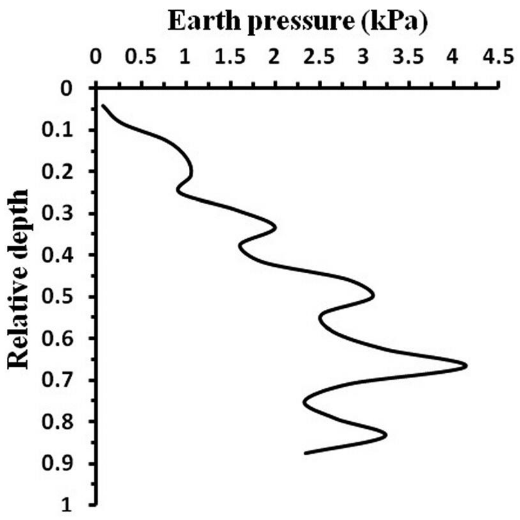

COEFFICIENT OF EARTH PRESSURE

Handy [12] studied the redistribution of earth pressure due to the rotation of the principal stress because of the friction between a wall and soil. He considered this phenomenon as soil arching. Two stages of the development of the arching were proposed. The first one is the rotation of the principal stresses, and the second is the decrease of the horizontal and vertical stresses near the toe of the wall. Similarly, here, during the sinking of the caisson, the soil exerted a friction force upward on the caisson, and the caisson imposed a downward force on the soil in reaction. This friction force resulted in the rotation of the principal stresses and soil arching (**Fig. 16**).

FIG. 14 Measured earth pressures on the caissons from Liu [13].

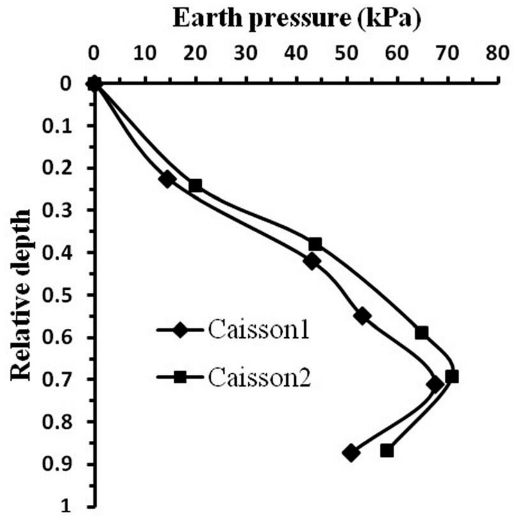

FIG. 15 Contours of the coordination number at different sinkage depths.

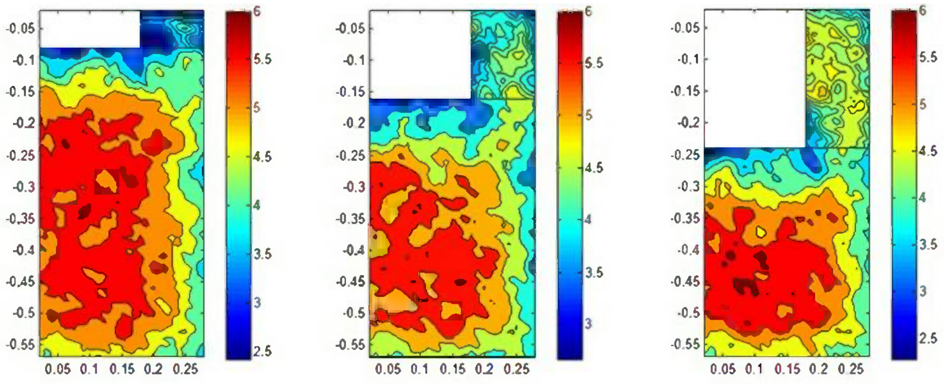

(a) Sinkage depth of 0.08m

(b) Sinkage depth of 0.16m

(c) Sinkage depth of 0.24m

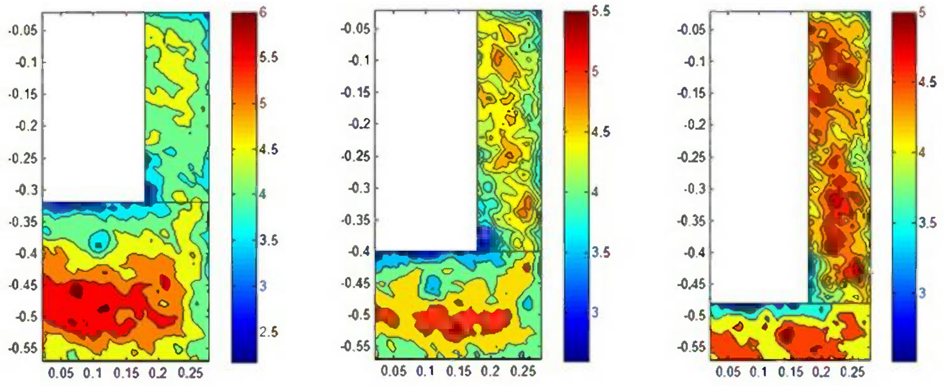

(d) Sinkage depth of 0.32m

(e) Sinkage depth of 0.4m

(f) Sinkage depth of 0.48m

Assuming the soil adjacent to the caisson reaches a state of critical equilibrium, because of the friction force between the caisson and the soil, the trajectory of the minor principal stress will be an arch, which is termed the arch of minor principal stress (see **Fig. 16**). From the Mohr circle of stress [18] (**Fig. 17**), the stresses on the caisson (τ, σ_h) can be calculated using the following equations:

$$\tau = (\sigma_1 - \sigma_3)\sin\theta\cos\theta \tag{3}$$

$$\sigma_h = \tau\cot\theta + \sigma_3 \tag{4}$$

where:

$\theta = 45° + \delta/2$, and

δ = friction angle between the caisson and the soil.

Substituting Eq 3 into Eq 4 gives

$$\sigma_h = \sigma_1\cos^2\theta + \sigma_3\sin^2\theta \tag{5}$$

If K_a is defined as the principal stress ratio (σ_3/σ_1), the ratio of the horizontal stress and the major principal stress can be obtained from Eq 5.

$$K = \frac{\sigma_h}{\sigma_1} = \cos^2\theta + K_a\sin^2\theta \tag{6}$$

Then, the ratio of the stresses in the horizontal and vertical directions K_w (called the nominal earth pressure coefficient) can be calculated as

$$K_w = \frac{\sigma_h}{\sigma_{av}} = \frac{1}{\frac{\sigma_{av}}{\sigma_1}}K \tag{7}$$

FIG. 16 Rotation of the principal stresses and soil arching.

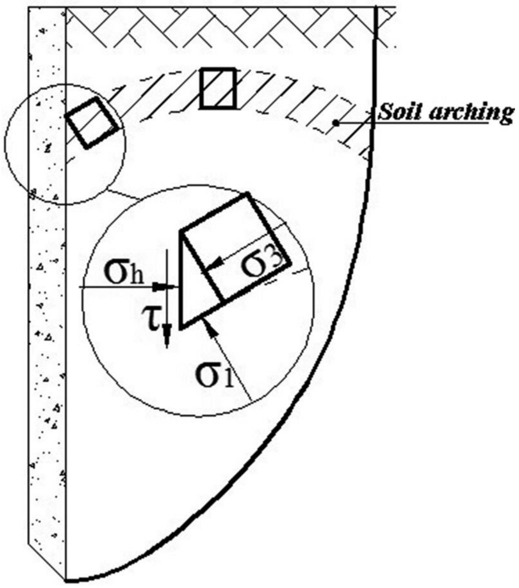

FIG. 17 The Mohr circle of stress with friction force.

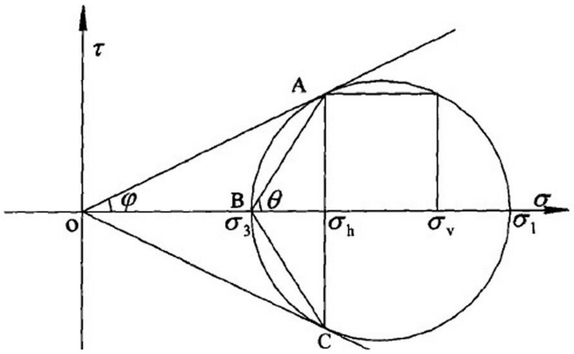

σ_{av} is the average vertical stress and can be calculated as

$$\sigma_{av} = \Delta\frac{W}{L} = \gamma\Delta\frac{h}{L} \tag{8}$$

in which L is the horizontal distance from the boundary of the affected region to the caisson.

According to Handy [12], if the friction angle between the caisson and the soil (δ) is thought to be the same as the internal friction angle of the soil (φ, which is usually between 10° and 40°), σ_{av}/σ_1 is usually 0.94 to 0.95. Then K_w can be approximately calculated as

$$K_w = \frac{\sigma_h}{\sigma_{av}} = 1.06K = 1.06(\cos^2\theta + K_a\sin^2\theta) \tag{9}$$

NUMERICAL SOLUTION TO THE EARTH PRESSURE

According to the results from the numerical simulation and in situ measurement (**Figs. 13** and **14**), the distribution of the earth pressure on the caisson was quite different from that according to the classical theory. The earth pressure was less at the toe of the caisson, and it was greater than the active earth pressure near the top. To capture these characteristics and give a better approximation, a numerical solution to calculate the earth pressure on the caisson was proposed based on the meso-scale analysis of the soil around the caisson. Two assumptions are important for the given method: (1) the boundary of the affected region is in the parabolic function in the form of Eq 1 derived previously, and (2) soil arching due to the friction between caisson and soil is the main reason for this problem.

Figure 18 is a force analysis of a slice element of the soil near the caisson. We took a slice with a thickness of dy at depth of y from the ground surface. In **Fig. 18**, σ_{av} is the average vertical stress on the top of the slice, $\sigma_{av} + d\sigma_{av}$ is the average vertical stress on the bottom, σ_h is the horizontal stress on the slice, τ_1 is the friction between the caisson and the slice, r is the reaction force perpendicular to the boundary of the affected region, τ_2 is the friction between the sliding soil slice and the stable soil, and dW is the gravity of the soil slice.

FIG. 18 Force analysis of a soil slice near the caisson.

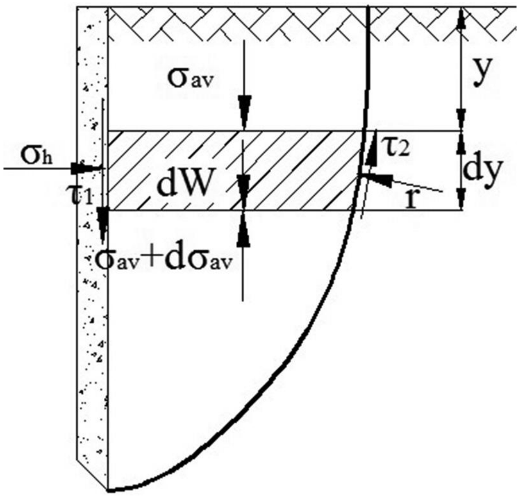

According to **Fig. 18**, the static equilibrium of the force in the horizontal and vertical directions can be calculated as

$$\sigma_h + \tau_2\cot\psi dy - rdy = 0 \tag{10}$$

$$\sigma_{av}x + dW - (\sigma_{av} + d\sigma_{av})(x + dx) + \tau_1 dy - \tau_2 dy - rdy\cot\psi = 0 \tag{11}$$

where:

$dW = \gamma x dy$,

$\sigma_h = K_w\sigma_{av}$,

$\tau_1 = \sigma_h\tan\delta$,

δ = friction angle between the caisson and soil that is approximated to the soil internal friction angle (φ),

$\tau_2 = r\tan\psi$,

ψ = angle between the boundary of the affected region and the horizontal line, and

$\cot\psi = f'(y)$ if the boundary of the affected region is assumed to follow Eq 1.

If we combine Eqs 10 and 11 and neglect the second order terms,

$$\frac{d\sigma_{av}}{dy} = \gamma + \frac{\sigma_{av}}{f(y)}\left[-f'(y) + K_w\tan\delta - \frac{K_w\tan\varphi}{1+\tan\varphi f'(y)} + \frac{f'(y)K_w}{1+\tan\varphi f'(y)}\right] \tag{12}$$

Equation 12 is a complex differential equation. The modified Euler equation was used in this study to get the numerical solution for σ_{av}. Then, the earth pressure on the caisson could be calculated as

$$\sigma_h = K_w\sigma_{av} \tag{13}$$

The distribution of the earth pressure on the caisson calculated according to Eq 13 was compared with the results from the numerical simulation and from the calculation according to the classical earth pressure theories as shown in **Fig. 19**.

FIG. 19

Earth pressure on the caisson with different methods.

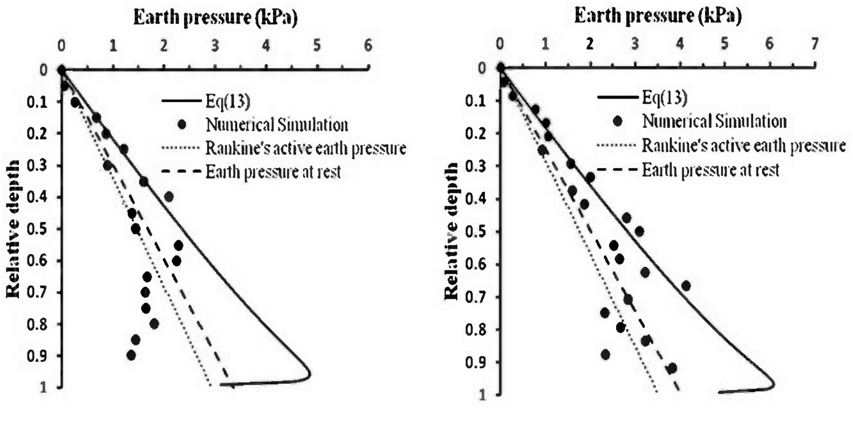

(a)H=0.4m

(b) H=0.48m

Figure 19 shows that when the relative depth (the ratio of the depth to the height of the caisson) was less than 0.6, the earth pressure on the caisson increased with increasing depth. The values from both the numerical simulation and Eq 13 are greater than the earth pressure at rest and the active earth pressure from Rankine's theory, and the numerical solution from Eq 13 is closer to the numerical simulation results. This indicates that the numerical solution offers a better approximation of the earth pressure on the caisson.

When the relative depth was more than 0.6, there was an inflexion point, and the earth pressure started to decrease with increasing relative depth. The values started to deviate from the numerical solution value from Eq 13 and tend toward the active earth pressure and values even less than that. The flow of the particles near the toe and the loosening effect in this region discussed previously might be the main reasons for the complexity of the stress state around the toe. This indicates that the numerical solution from Eq 13 is proper when the relative depth is less than 0.6 but is invalid when it is more because of the complex state near the toe of the caisson.

The earth pressure on the caisson is closely related to the resistance force on the caisson during its construction and its workability in its service state. So, a reasonable and accurate calculation of the earth pressure is important for the design and construction of the caisson.

Conclusions and Discussion

Laboratory experiments and numerical simulations were performed to study the sinking process of a caisson. Macro- and meso-scale mechanical behaviors of the caisson and the surrounding soils were investigated. The main conclusions are as follows.

Deformation and flow of the soil around the caisson were revealed in the laboratory experiment. The earth pressures near the toe of the caisson during sinking were measured and found to increase with sinking depth, but they started to decrease at the inflexion point at a relative sinkage depth of about 2/3 of the caisson height. The flow of the soil particles from outside to inside the caisson and the resulting loosened region near the toe are thought to have had a dominant effect on the distribution of the earth pressure on the caisson during sinking.

The discrete element method (DEM), coupled with the finite differential method, was used to simulate the sinking process of the caisson. Particle movements of the soil around the caisson were investigated and compared with the results from the experiment. The function of the boundary of the affected region was proposed based on the movements of the soil particles. The earth pressures on the caisson were obtained from the numerical simulation and compared with the data from the laboratory experiment and the in situ measurements reported in the literature. The evolution of the coordinate number of the soil particles around the caisson was explored. The phenomenon of soil arching was revealed and used to explain the distribution of the earth pressure on the caisson.

The friction between the caisson and the soil and the consequent rotation of principal stress were used to explain the phenomenon of soil arching. A numerical solution to calculate the earth pressure on the caisson based on the function of the affected region boundary and soil arching theory was proposed. The results were compared with those from the numerical simulation and the classical theory. It was shown that the numerical solution offers a better approximation of the earth pressure on the caisson. This is useful for the design and construction of caissons in practice.

ACKNOWLEDGMENTS

This work was financially supported in part by the National Nature Science Foundation of China (Grant No. 51079030) and was part of a project funded by the Priority Academic Program

Development of Jiangsu Higher Education Institutions (Grant No. CE01-2-08). The writers express appreciation to the editor and anonymous reviewers for their valuable comments and suggestions.

References

[1] Chen, X. R., Qian, P. Y., and Zhang, Z. Y., "Study on Penetration Resistance Distribution Characteristic of Sunk Shaft Foundation," *Chin. J. Geotech. Eng.*, Vol. 27, No. 2, 2005, pp. 148–152.

[2] Feng, Z. X., Wang, J. G., and Wang, J., "Security Monitoring Technology of the Caisson Foundation of Anchorage in Construction," *Chin. J. Eng. Sci.*, Vol. 12, No. 4, 2010, pp. 68–72.

[3] Zhu, J. M., Gong, W. M., and Mu, B. G., "Sinking Safety Monitoring Research on North Anchorage Caisson of the Forth Nanjing Yangtze-River Bridge," *Chin. J. Build. Struct.*, Vol. 31, No. 8, 2010, pp. 112–117.

[4] Zhu, J. M., Gong, W. M., and Mu, B. G., "Stress Monitoring of Bottom Steel Plate of the South Anchorage Caisson, Ma'anshan Changjiang-River Bridge," *Chin. J. Lanzhou Univ. Nat. Sci.*, Vol. 47, 2011, pp. 255–258.

[5] Hogervorst, J. R., "Field Trials With Large Diameter Suction Piles," *Proceedings of the 12th Annual Off-Shore Technology Conference*, Houston, TX, May 5th, Program Committee of the Offshore Technology Conference of the Coasts, Oceans, Ports, and Rivers Institute of ASCE, Reston, VA, 1986, pp. 201–212.

[6] Tjelta, T. I., Guttormsen, T. R., and Hermstad, J., "Large Penetration Test at a Deepwater Site," *Proceedings of the 18th Annual Off-Shore Technology Conference*, Houston, TX, May 5–8, 1986, pp. 201–212.

[7] Dyvik, R., Anderson, K. H., and Hansen, S. B., "Field Tests on Anchors in Clay," *J. Geotech. Eng.*, Vol. 119, No. 10, 1993, pp. 1515–1531.

[8] Wang, Y., 2011, "Study on Distribution Pattern of Load in Process of Large Caisson Sinking," M.Sc. thesis, Southeast University, Nanjing, China.

[9] Handayanu, Swamidas, A. S. J., and Booton, M., "Behavior of Tension Foundation for Offshore Structures Under Extreme Pull-out Loads," *Proceedings of the 18th International Conference on Offshore Mechanics and Arctic Engineering*, St. Johns, NF, Canada, Jul. 11–16, OMAE99, 1999, pp. 635–641.

[10] Sukumaran, B., McCarron, W. O., Jeanjean, P., and Abouseeda, H., "Efficient Finite Element Techniques for Limit Analysis of Suction Caissons Under Lateral Loads," *Comput. Geotech.*, Vol. 24, 1999, pp. 89–107.

[11] Cao, J., Phillips, R., Popescu, R., Audibert, J. M. E., and Al-Khafaji, Z., "Numerical Analysis of the Behavior of Suction Caissons in Clay," International Journal of Offshore and Polar Engineering, 2003, Vol. 13, No. 2, pp. 154–159.

[12] Handy, R. L., "The Arch in Soil Arching," *J. Geotech. Eng.*, Vol. 111, No. 3, 1985, pp. 302–318.

[13] Liu, Q., 2010, "Study for the Lateral Earth Pressure of Open Caisson Structure," M.Sc. thesis, Xi'an University of Architecture & Technology, Xi'an, China.

[14] Terzaghi, K., "A Fundamental Fallacy in Earth Pressure Computations," *Boston Soc. Civ. Eng. J.*, Vol. 23, No. 2, 1936, pp. 71–88.

[15] Fang, Y., Chen, T., and Wu, B., "Passive Earth Pressures With Various Wall Movements," *J. Geotech. Eng.*, Vol. 120, No. 8, 1994, pp. 1307–1323.

[16] Zhang, J. G., 2002, "Centrifugal Model Test Study on the Soil Pressure and Deformation of Retaining Wall With Equilibrator," M.Sc. thesis, Southwest Jiaotong University, Chendu, China.

[17] Yuan, J., Gu, R. G., and Fang, Y. G., "Model Test Research on Earth Pressure of Underground Retaining Wall of Conventional Island in a Nuclear Power Station," *Chin. J. Rock Mech. Eng.*, Vol. 31, No. 1, 2012, pp. 3370–3376.

[18] Jiang, B., 2005, "Studies on Soil Arching Effect and Earth Pressure for Retaining Structure," Ph.D. Sc. thesis, Zhejiang University, Hangzhou, China.

Journal of Testing and Evaluation

doi:10.1520/JTE20140039 / Vol. 43 / No. 2 / March 2015 / available online at www.astm.org

Changjie Xu,[1,2] Qizhi Chen,[3] and Qingsong Feng[4]

Bearing Capacity Estimation of Soil Under a Constructed Building by Rayleigh Wave Method

Reference

Xu, Changjie, Chen, Qizhi, and Feng, Qingsong, "Bearing Capacity Estimation of Soil Under a Constructed Building by Rayleigh Wave Method," *Journal of Testing and Evaluation*, Vol. 43, No. 2, 2015, pp. 376–384, doi:10.1520/JTE20140039. ISSN 0090-3973

Manuscript received January 31, 2014; accepted for publication April 28, 2014; published online August 11, 2014.

[1] Professor, School of Civil Engineering and Architecture Departments, East China Jiaotong Univ., Nanchang, Jiangxi, 330013, People's Republic of China, e-mail: xucj@zju.edu.cn

[2] Professor, Research Center of Coastal and Urban Geotechnical Engineering, Zhejiang Univ., Hangzhou, Zhejiang, 310058, People's Republic of China.

[3] Graduate Student, Research Center of Coastal and Urban Geotechnical Engineering, Zhejiang Univ., Hangzhou, Zhejiang, 310058, People's Republic of China, e-mail: chenqizhi@zju.edu.cn

[4] Professor, School of Civil Engineering and Architecture Departments, East China Jiaotong Univ., Nanchang, Jiangxi, 330013, People's Republic of China (Corresponding author), e-mail: fqshdjtdx@aliyun.com

ABSTRACT

It is always difficult to test the bearing capacity of soil under constructed buildings. Thus, the adoption of the Rayleigh wave method to address this problem is investigated in this study. The fundamental of the Rayleigh wave velocity method in geological engineering is initially presented. The in situ shear wave velocity can be obtained by Rayleigh wave method. Rayleigh wave velocity and soils static load tests are conducted on several different kinds of soil. Thus, the fitting formula between shear wave velocity and soil bearing capacity under specific soil conditions is determined. A reconstruction engineering project that uses the Rayleigh wave velocity method to test the bearing capacity of soil under a constructed building is then studied. Rayleigh wave velocity tests are conducted based on this fitting formula to analyze the soil bearing capacity. The reconstruction is proven to be successful by settlement observation. The fitting formula between shear wave velocity and soil bearing capacity are probably different for various kinds of soil. Therefore, the application of the wave velocity test method in detecting the soil bearing capacity of a constructed building has to be studied before it can be popularized.

Keywords

soil bearing capacity, Rayleigh wave method, constructed building, nondestructive examination

Introduction

The bearing capacity determination of a soil layer under a foundation is of vital importance in geotechnical engineering. In practice, the static load test is always conducted to test the bearing capacity of foundation soils. However, this approach is time consuming and costly. As such, in situ determination of shear wave velocity can be an alternative in the characterization of bearing capacity of foundation soil.

The in situ shear wave velocity (V_S) can be measured directly by placing two sensors in separate bore holes (cross hole method) or in a single bore hole with one of them being buried at depth and the other at the ground surface (down hole method). The shear wave velocity can also be evaluated by Rayleigh wave method. The velocity of Rayleigh wave has been used for a long time to provide information on the elastic properties of soils and pavements, since the measurements are made at the ground surface without the need of borings or intrusion in the soil. Thus, Rayleigh wave method is a nondestructive in situ testing method. One important feature of Rayleigh wave method is the predominance of the Rayleigh wave at the surface when generated by a vertical source.

The Rayleigh wave was first predicted in 1885 by John William Scott (Lord Rayleigh) [1]. Later on, the propagation characteristic of the Rayleigh wave in elastic half-space media was revealed [2–5]. Rayleigh waves are surface waves that travel along a free surface, such as the earth–air interface or the earth–water interface, and are usually characterized by relatively low velocity, low frequency, and high amplitude [6]. In the 20th century, particularly during the 1950s, the dispersion of the Rayleigh wave was determined by several scientists. Nazarian and Stokoe [7] studied the Rayleigh wave signal measured during a field test and formulated the spectral analysis of surface waves (SASW) method. Near-surface shear wave velocity can be obtained by inversing Rayleigh wave phase velocity. In China, Wu and his colleagues [8–12] conducted many researches on the SASW method, and Wu wrote a book in Chinese entitled *Wave in the Soil Medium* in 1996 [13]. In this book, several problems concerning Rayleigh wave exploration were solved. The SASW method has been applied in numerous engineering projects. At present, the SASW method is applied underwater [14]. In 1999, Xia et al. [15] developed a new Rayleigh wave inversion method for estimating shear wave velocity near the surface, which is an effective improvement of the SASW method. According to his research in 2002 and 2012 [16,17], quality factors of near-surface materials can also be obtained by using constrained inversion of attenuation coefficients of high-frequency Rayleigh waves.

In the present work, the fundamentals of Rayleigh wave method are described. A relationship exists between foundation soil bearing capacity and shear wave velocity depending on several field tests; thus, the soil bearing capacity of constructed buildings can be determined by wave velocity.

Fundamentals of the Rayleigh Wave Method

The Rayleigh wave method is a wave velocity test method. The traditional wave velocity test method requires drilling holes in the ground, which causes damage to the foundation, particularly in constructed buildings. Therefore, the application of the traditional method is limited. The Rayleigh wave method is a nondestructive testing method that can be used on constructed buildings.

Body waves (compression and shear waves) and surface waves (Rayleigh and Love waves) will be generated in soil when the surface of a uniform half space elastic soil system is subjected to a vertical load excitation. Rayleigh wave is the most important wave of the surface waves.

Most of the surface wave energy exists within one wavelength of depth. In layered media, the propagation velocity of surface wave depends on the frequency (or wavelength) of the wave because waves of different wave lengths sample different parts of the layered medium. For example, high-frequency (short wavelength) waves propagate only in the near-surface layers and low-frequency waves with longer wavelengths propagate through deeper layers as well as the near-surface layers. Therefore, by using surface waves over a wide range of frequencies, one can effectively sample different portions of the material profile.

If a disturbance occurs on the surface of an elastic semi-infinite body, then vertical ground displacements caused by the Rayleigh wave are significantly larger than displacements caused by compression and shear waves. The disturbance amplitude decreases with the increasing distance. If sensors are located appropriately from the source and the magnification of the test system is reduced, then the signal from the equipment will primarily be a Rayleigh wave signal when the ground under a vertical pulse loads. The SASW testing procedure was designed to minimize the contribution of higher modes and thus assumes that the Rayleigh waves which propagate at the surface belong only to the fundamental mode.

The Rayleigh wave method consists of three steps; field testing, evaluation of dispersion curve by phase unwrapping method, and determination of shear wave velocity profile by inversion process. The first two steps are straightforward tasks which have been to a great extent automated.

The principle diagram of the Rayleigh wave method is shown in **Fig. 1**. Sensors 1 and 2 receive the vertical component of the wave signal when the ground is subjected to a vertical load excitation. The auto-power spectra of signals 1 and 2 are obtained from the vertical component of the wave signal via

FIG. 1 The schematic of the spectral analysis of surface waves method.

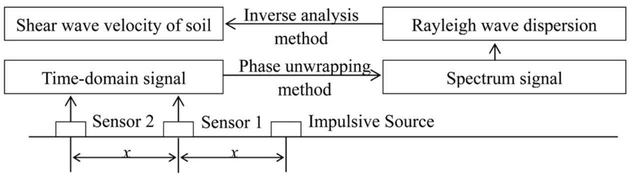

spectral analysis. The cross-power spectrum, transfer function, and coherence function between signals 1 and 2 are also obtained in the same manner. If the linear spectrum of signal 1 is $S_x(f)$ and the linear spectrum of signal 2 is $S_y(f)$, then the auto-power spectra are as follows:

$$G_{xx}(f) = S_x(f)S_x^{'}(f) \tag{1}$$

$$G_{yy}(f) = S_y(f)S_y^{'}(f) \tag{2}$$

where $S_x^{'}(f)$ and $S_y^{'}(f)$ are the conjugate complex numbers of $S_x(f)$ and $S_y(f)$. The cross-power spectrum between signals 1 and 2 is given as follows:

$$G_{yx}(f) = S_y(f)S_x^{'}(f) \tag{3}$$

The phase of $G_{yx}(f)$ indicates the phase difference caused by the time lag during wave propagation. According to vibration theory, the corresponding time when the phase turns 360° is termed T. The time spent by the Rayleigh wave spreading from sensor 1 to sensor 2 is calculated by phase difference ϕ, as follows:

$$t = \frac{\phi}{360}T \tag{4}$$

or

$$t = \frac{\phi}{360f} \tag{5}$$

The distance between the two sensors is known as x. The wave propagation path along the two sensors is a straight line. Therefore, the Rayleigh wave velocity can be expressed as follows:

$$V_R = \frac{360f}{\phi}\cdot x \tag{6}$$

A relationship also exists among wave velocity, wavelength, and frequency in an elastic medium, as follows:

$$L_R = \frac{V_R}{f} \tag{7}$$

By substituting Eq 6 into Eq 7, we obtain Eq 8.

$$L_R = \frac{x\cdot 360}{\phi} \tag{8}$$

The dispersion of surface wave will not occur in the homogeneous elastic half space. The equation of Rayleigh wave velocity can be written as follows:

$$\left(\frac{V_R}{V_S}\right)^6 - 8\left(\frac{V_R}{V_S}\right)^4 + \left(24 - 16\frac{V_S^2}{V_P^2}\right)\left(\frac{V_R}{V_S}\right)^2 - 16\left(1 - \frac{V_S^2}{V_P^2}\right) = 0 \tag{9}$$

The velocity of compression wave and the velocity of shear wave have following relations:

$$\frac{V_P}{V_S} = \sqrt{\frac{\lambda + 2G}{G}} = \sqrt{\frac{2(1-\mu)}{1-2\mu}} \tag{10}$$

Substitute Eq 10 into Eq 9:

$$\left(\frac{V_R^2}{V_S^2}\right)^3 - 8\left(\frac{V_R^2}{V_S^2}\right)^2 + 8\frac{2-\mu}{1-\mu}\frac{V_R^2}{V_S^2} - \frac{8}{1-\mu} = 0 \tag{11}$$

The solution of this cubic equation depends on the Poisson's ratio of the material. Rayleigh wave velocity V_R is related to shear wave velocity V_S of the material by Poisson's ratio μ. The approximate equation is shown as flows:

$$V_R \approx \frac{0.862 + 1.14\mu}{1+\mu}V_S \tag{12}$$

where μ is Poisson ratio.

Therefore, if the V_R of a uniform layer of soil has been measured, the shear wave velocity V_S can be easily determined. For a non-uniform or layered soil system, dispersion of surface wave will occurs. Dispersion means Rayleigh wave velocity varies with frequency *f*; which forms the theoretical basis of the SASW test method. The overall objective of SASW test is to measure Rayleigh wave dispersion curve. Rayleigh wave dispersion curve can be determined from Eqs 6 and 8. Moreover, shear wave velocity profile is then obtained through inversion of dispersion curve. Inversion of the Rayleigh wave dispersion curve of a site provides information on the variation of shear wave velocity with depth. A lot of studies developed many different inversion methods for estimating shear wave velocity [8,9,11,15]. The detailed description of the inversion method will not be listed in this passage.

Elastic dynamics theory states that the shear wave velocity in a solid medium is a function of the density and elastic constant of the medium. The dynamic shear modulus in an elastic isotropy infinite medium is given as follows:

$$G = \rho V_S^2 \tag{13}$$

where ρ is the medium density.

We conclude from the preceding formula that a relationship exists between shear wave velocity and the mechanical properties of the medium. Medium mechanical properties are calculated by determining the shear wave velocity.

Several field tests are carried out by many researchers over the world to find out the relationship between shear wave velocity and the mechanical properties of soil. According to a Japanese book entitled *Soil Survey Method* [18], a relationship between blow count of SPT and shear wave velocity is given as follows:

$$V_S = AN_{63.5}^{B} \quad (14)$$

where A and B are dependent on the soil properties.

In this passage, a comparative study is carried out on the field test. The static load test and the Rayleigh wave method are conducted on several different kinds of soil to find the relationship between the foundation soil bearing capacity and the shear wave velocity. A fitting formula is given depending on the results of field tests.

Engineering Project Background

A four-story flat had been constructed for three years. A natural shallow foundation is used for this building. The foundation investigation report states that the characteristic value of the foundation bearing capacity is 120 kPa. The soil below this building can be divided into miscellaneous fill and gravelly soil. The thickness of miscellaneous fill is about 1 m. The thickness of gravelly soil is between 7 and 17 ms. Grain diameter of gravel soil is among 10 and 70 mm. The compression modulus of gravel soil is 16.2 MPa.

An additional two floors are requested for this building. Therefore, according to calculation, the characteristic value of the foundation bearing capacity should be 150 kPa or higher. The foundation of the constructed building is difficult to reinforce because it is a shallow foundation. Reconstruction can proceed depending on the reappraisal of the characteristic value of the foundation bearing capacity. In order to determine the value of foundation bearing capacity, a comparative study is carried out on field tests.

Comparative Study on Field Tests

The static load tests and the Rayleigh wave method are conducted on the undisturbed soil near the constructed building to determine the statistical law between shear wave velocity and foundation soil bearing capacity.

Twenty eight groups (S1# to S28#) of contrast tests are performed. S1# to S28# are different measured points of Rayleigh wave method near the building. The arrangement plan is shown in **Fig. 2**. The measured points are arranged in line 20 ms away from the constructed building. The distance between each measured point in the line is 4 ms.

Static load test is time-consuming and costly. Only ten groups of static load tests are conducted. Theses ten measured points are pointed out in **Fig. 2**.

The settlement of three of these points is shown in **Fig. 3** and **Table 1**. They are S9#, S11# and S25#. The settlement results of other points are not listed in this passage. The area of the test board is 1.0 m^2. The length of each side of the test board is 1 m.

FIG. 2 Arrangement plan of measured points.

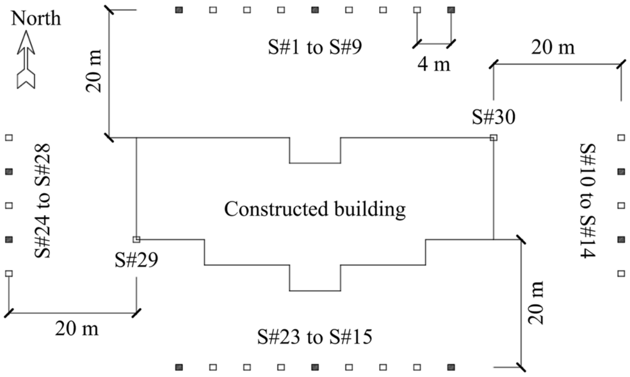

The maximum load of the static load test is 300 kPa. The results indicate that the ultimate bearing capacity of each measured point is no less than it. The settlements of each measured point are 22.12, 18.32, and 12.45 mm, respectively, when the load is 300 kPa. Too much settlement or differential settlement will be harmful to a constructed building. So in this passage, the characteristic value of the soil bearing capacity is defined as the value of the load when the settlement is 12 mm. Therefore, the characteristic value of the soil bearing capacity of S9#, S11#, and S25# are 170, 194, and 291 kPa, respectively. The characteristic values of the soil bearing capacity of the other measured points are obtained in a similar manner. The characteristic values of the soil bearing capacity of the unmeasured points are obtained by interpolation method. Their data are provided in **Table 2**.

The Rayleigh wave method is then applied to the measured points, and the dispersion curve of the Rayleigh wave is obtained from the test. The dispersion curve of the Rayleigh wave is shown in **Fig. 4**. The inverse analysis method is then applied to determine the shear wave velocity. The average shear

FIG. 3 Settlements of the static load test (S9#, S11#, S25#).

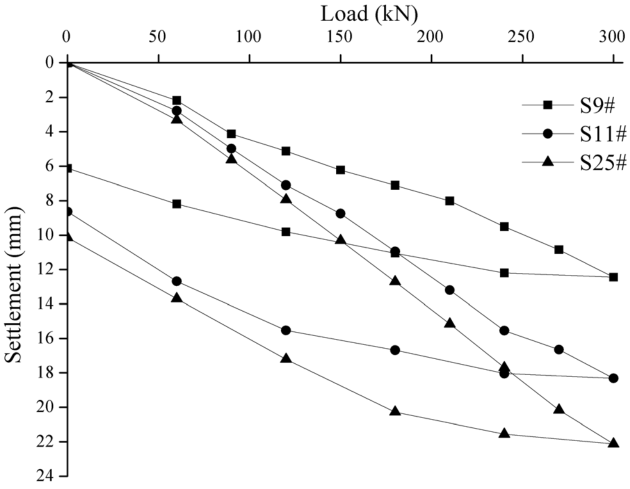

TABLE 1 Settlement of static load tests (S9#, S11#, S25#).

			The Corresponding Settlement (mm)			The Cumulative Settlement (mm)		
Load (kN)	Duration (min)	The Cumulative Duration (min)	S9#	S11#	S25#	S9#	S11#	S25#
0	0	0	0.00	0.00	0.00	0.00	0.00	0.00
60	60	60	2.78	3.31	2.18	2.78	3.31	2.18
90	60	120	2.20	2.32	1.95	4.98	5.63	4.13
120	60	180	2.12	2.31	1.00	7.10	7.94	5.13
150	60	240	1.62	2.37	1.10	8.75	10.31	6.23
180	60	300	2.20	2.40	0.88	10.95	12.71	7.11
210	60	360	2.25	2.44	0.90	13.20	15.15	8.01
240	60	420	2.34	2.54	1.50	15.54	17.69	9.51
270	60	480	1.11	2.49	1.34	16.65	20.16	10.85
300	60	540	1.67	1.96	1.60	18.32	22.12	12.45
240	30	570	−0.28	−0.57	−0.25	18.04	21.55	12.2
180	30	600	−1.36	−1.28	−1.15	16.68	20.58	11.05
120	30	630	−1.15	−3.07	−1.24	15.53	17.21	9.81
60	30	660	−2.84	−3.51	−1.62	12.69	13.7	8.19
0	60	720	−4.06	−3.56	−2.06	8.63	10.14	6.13

wave velocity is obtained according to **Fig. 5**. This value only considers a depth of within 4 m because the influence depth of the static load test is always within this range. The average velocities of S9#, S11#, and S25# are 308.45, 360.96, and 388.12 m/s, respectively. The shear wave velocities of the other measured points are obtained in a similar manner. Their data are provided in **Table 2**.

The curve of shear wave velocity squared and soil bearing capacity is shown in **Fig. 6**. It is obviously a linear relation between $V_S{}^2$ and P. The statistical law between shear wave velocity and bearing capacity is then obtained from the results of S1# to S27#. The fit curve is shown in **Fig. 6**, and the fitting formula is given as follows:

$$P = AV_S^2 + B \tag{15}$$

Factor A and B can be obtained by least square method.

$$A = \frac{\sum V_{Si}^2 P_i - \left(\sum V_{Si}^2\right)\left(\sum P_i\right)/n}{\sum V_{Si}^4 - \left(\sum V_{Si}^2\right)^2/n} \tag{16}$$

$$B = \overline{P} - A\overline{V_S^2} = \frac{1}{n}\sum P_i - \left(\frac{1}{n}\sum V_{Si}^2\right)A \tag{17}$$

The data listed in **Table 2** are submitted into Eqs 16 and 17 to calculate A and B. A is 0.00282 and B is −146.480. The standard error of A is 1.611×10^{-4} and the standard error of B is 22.283, which means the fitting formula may be suitable for this kind of soil.

$$P = 0.00282V_S^2 - 146.480 \tag{18}$$

TABLE 2 Results of field tests (S1# to S28#).

Measure Point	Soil Bearing Capacity (kPa)	Shear Wave Velocity (m/s)	Measure Point	Soil Bearing Capacity (kPa)	Shear Wave Velocity (m/s)
S1#	287	395.39	S15#	237	364.52
S2#	269	382.42	S16#	242	367.32
S3#	251	370.42	S17#	246	375.43
S4#	233	369.65	S18#	251	379.39
S5#	215	362.36	S19#	255	372.74
S6#	204	343.34	S20#	259	374.59
S7#	193	357.35	S21#	262	379.79
S8#	181	346.84	S22#	266	382.12
S9#	170	332.56	S23#	269	386.95
S10#	168	333.42	S24#	303	402.36
S11#	194	360.96	S25#	291	388.12
S12#	220	362.24	S26#	279	387.32
S13#	246	369.93	S27#	267	379.98
S14#	272	384.23	S28#	255	378.43

FIG. 4 The dispersion curve of the Rayleigh wave (S9#, S11#, S25#).

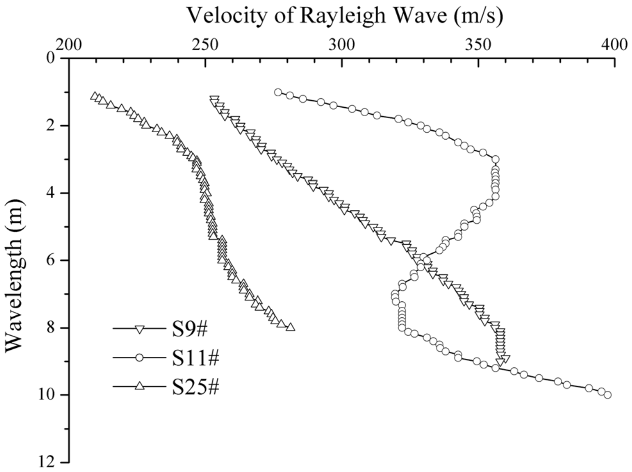

The data from S28# is substituted into this fitting formula Eq 18 to check the veracity. The calculated result is 257 kPa, which is very close to the measured data of 255 kPa.

Then, several similar field tests are carried out on different fields where the soil is different from the previous one. These field tests are constructed to test the correctness of Eq 15 and to find the relationship between soils properties and the factor *A* and *B*.

Twelve groups (C1# to C12#) of contrast tests are performed in Western of Hangzhou, China. The soils in this area can be divided into clay and silty clay. According to the geological survey report, the compression modulus of clay and silty clay are 4.3 and 6.1 MPa, respectively.

Another twelve groups (F1# to F12#) of contrast tests are performed in Eastern of Hangzhou, China. The soils in this area are mainly floury soil. The geological survey report shows that the compression modulus of floury soil is 8.5 MPa.

FIG. 5 The variations of shear wave velocities with respect to depth (S9#, S11#, S25#).

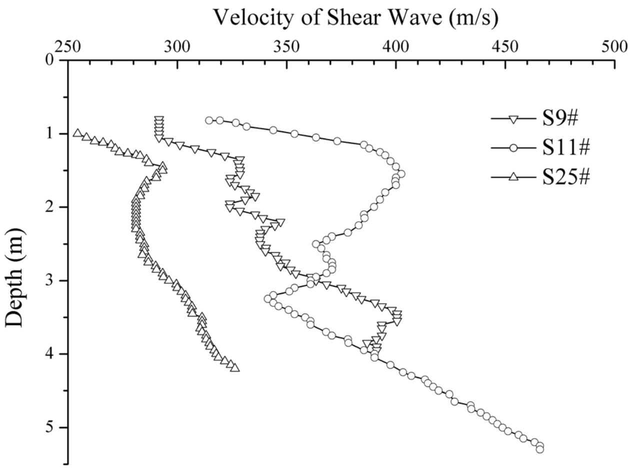

FIG. 6 The fit curve of shear wave velocity squared and bearing capacity of gravelly soil.

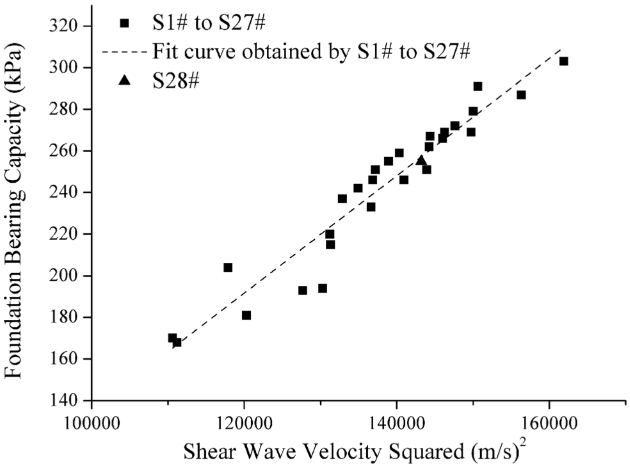

The characteristic value of the soil bearing capacity and the shear wave velocities of these measured points are obtained in a similar manner as previous one. Their data are provided in **Tables 3** and **4**.

The curve of the results of field tests (C1# to C12#) is shown in **Fig. 7**. Obviously a linear relation also exists in this kind of soil. Then the results of field tests are submitted into Eqs 16 and 17 to get *A* and *B*. *A* is 0.00118 and *B* is 46.560. The fit curve is shown in **Fig. 7**, and the fitting formula is given as follows:

$$P = 0.0118V_S^2 + 46.560 \tag{19}$$

The standard error of *A* is 5.492×10^{-5} and the standard error of *B* is 2.569, which means fitting formula Eq 19 may be suitable for this kind of soil.

Then the process is repeated with the results of field tests (F1# to F12#). A linear relation also exists in floury soil (see **Fig. 8**). The fitting formula is given as follows:

$$P = 0.0157V_S^2 + 78.713 \tag{20}$$

The value of *A* in Eq 20 is 0.0157, whose standard error is 1.164×10^{-4}. The value of *B* in Eq 20 is 78.713, whose standard error is 8.687. The formula obtained from the results of field tests (F1# to F12#) is capable for predicting the bearing capacity of this kind of soil.

Thus, a conclusion can be drawn that Eq 15 is a good fitting formula between soil bearing capacity and shear wave velocity. Factor *A* and *B* which depended on the soil condition can be obtained by field tests. The factor *A* and *B* is certain in a specific kind of soil.

When taking Eqs 18, 19, and 20 into account, we can draw a conclusion that factor *A* is concerned with the bearing capacity. The value of Factor *A* in gravelly soil is much more than the value of floury soil and clay. The soil bearing capacity increases faster in gravelly soil when shear wave velocity

TABLE 3 Results of field tests of clay and silty clay (C1# to C12#).

Measure Point	Soil Bearing Capacity (kPa)	Shear Wave Velocity (m/s)	Measure Point	Soil Bearing Capacity (kPa)	Shear Wave Velocity (m/s)
C1#	95	205.84	C7#	125	259.60
C2#	83	181.29	C8#	94	203.22
C3#	72	141.43	C9#	118	244.25
C4#	136	272.31	C10#	79	157.49
C5#	82	168.59	C11#	96	209.48
C6#	114	228.48	C12#	89	199.86

TABLE 4 Results of field tests (F1# to F12#).

Measure Point	Soil Bearing Capacity (kN)	Shear Wave Velocity (m/s)	Measure Point	Soil Bearing Capacity (kN)	Shear Wave Velocity (m/s)
F1#	212	309.12	F7#	278	343.56
F2#	153	200.26	F8#	206	294.61
F3#	252	327.54	F9#	143	185.53
F4#	133	194.59	F10#	212	278.43
F5#	168	254.93	F11#	162	232.13
F6#	191	265.42	F12#	149	219.87

increases. Factor *A* may also be related to the compression modulus. A positive correlation existed between the value of factor *A* and the compression modulus. A reasonable explanation is that the shear wave velocity has a closely correlation with the mechanical properties of the soil.

From the test results of three different kinds of soil, several conclusions can be drawn:

1. Shear wave velocity generally increases with the increasing of depth.
2. Shear wave velocity is mainly governed by soil skeleton, so it is closely related to the bearing capacity of soil. Shear wave velocity of gravelly soil is much higher than the velocity of floury soil and clay on the same depth. Obviously, the bearing capacity of gravelly soil is much more than the others. A positive correlation existed between shear wave velocity and foundation bearing capacity.
3. The correlation between shear wave velocity and soil bearing capacity can be obtained for different kinds of soils. A fitting formula is given in Eq 15. The factor *A* and *B* are different for different kinds of soils.

FIG. 7 The fit curve of shear wave velocity squared and bearing capacity of clay and silty clay.

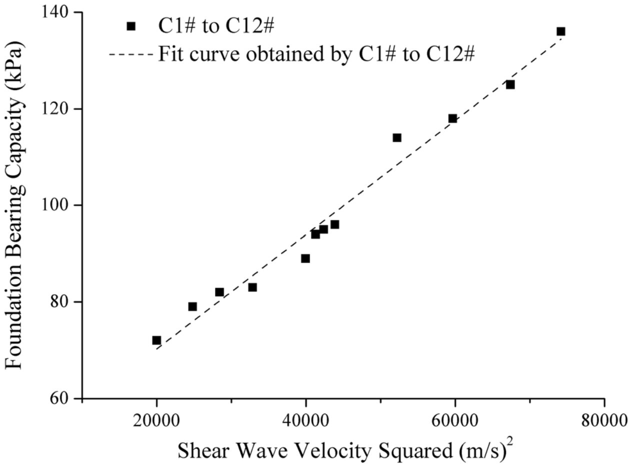

Constructed Building Wave Velocity Tests

The Rayleigh wave method is then applied to the constructed building. The measured points considered are S29# and S30# which are shown in **Fig. 2**. S29# is on the southwest corner of the building and S30# is on the northeast corner.

The dispersion curve of the Rayleigh wave is shown in **Fig. 9**, whereas the relation curve of shear wave velocity and depth is shown in **Fig. 10**.

FIG. 8 The fit curve of shear wave velocity squared and bearing capacity of floury soil.

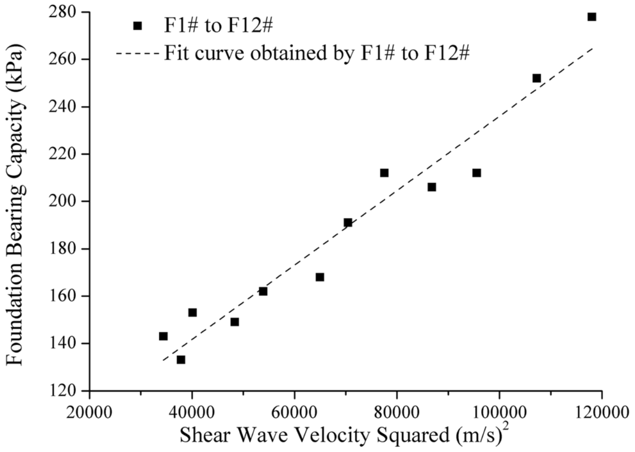

FIG. 9 The dispersion curve of the Rayleigh wave (S29#, S30#) in constructed site.

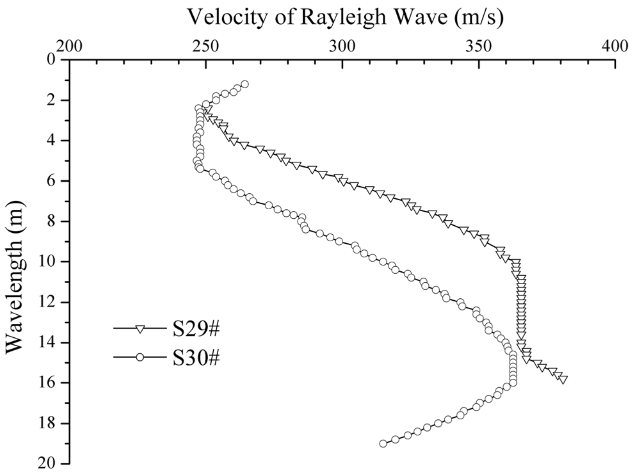

FIG. 10 The relation curve of shear wave velocity and depth (S29#, S30#) in constructed site.

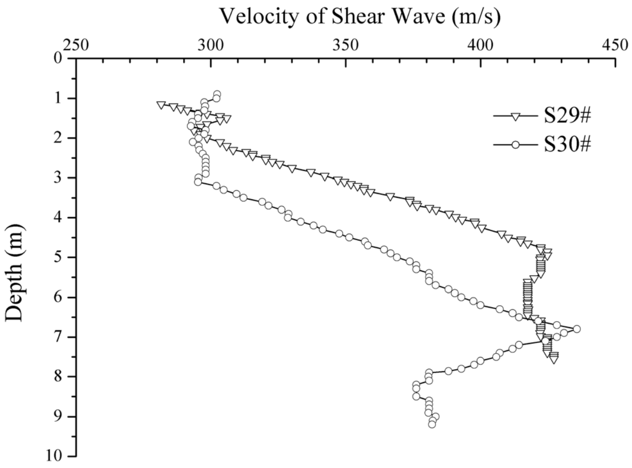

FIG. 11 Sketch map of settlement observation of the constructed building.

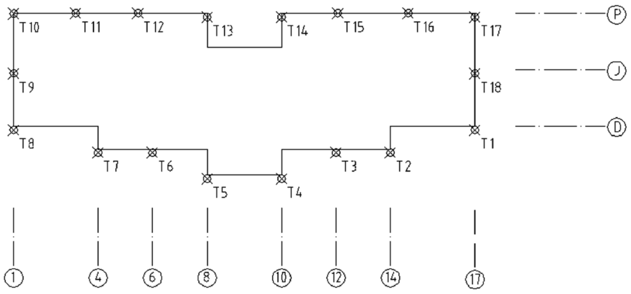

TABLE 5 Observation time and construction status.

	1st	2nd	3rd	4th
Time	December 2002	January 2003	March 2003	May 2003
Status	Reconstruction began	Construction	Top off	Decoration
	5th	6th	7th	8th
Time	July 2003	November 2003	April 2004	August 2004
Status	Opened for occupancy	Service	Service	Service

The average shear wave velocity is obtained according to **Fig. 10**. The average velocities of S29# and S30# are 369.38 and 327.58 m/s, respectively. The bearing capacities of S29# and S30# are estimated using Eq 18, and the results are 238 and 156 kPa, respectively.

Therefore, adding two more floors to the constructed building is safe because the characteristic value of the foundation bearing capacity is higher than 150 kPa. Then reconstruction stared at Dec. 15, 2002.

Settlement Observation

Settlement observation is applied to this building when the reconstruction began. Eighteen measure points are decorated around the building as shown in **Fig. 11**.

Settlement observation is performed on the aforementioned building. Observations are performed eight times during the construction and service stages from Dec. 15, 2002 to Aug. 2, 2004. The time of observation is shown in **Table 5**.

The settlement of a portion of the measured point is shown in **Fig. 12**. An obvious conclusion can be obtained that the settlement increases with time. Settlement grows rapidly at first and then becomes stable during service stage. The results show that the maximum settlement is 13.3 mm and the minimum settlement is 7.5 mm, which is acceptable and thus proves

FIG 12 Results of settlement observation for a portion of the measured point of the constructed building.

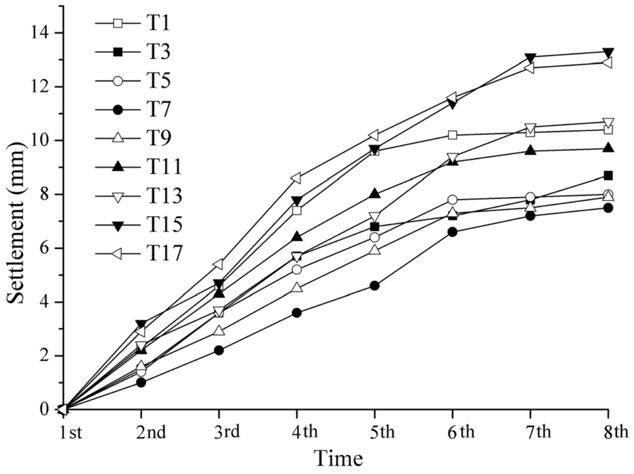

that the reconstruction is successful. The maximum differential settlement is 5.8 mm, which will not cause crevices.

According to the results of constructed building wave velocity tests, the soil bearing capacity on the southwest corner of the building is much higher than on the northeast corner. The results of settlement observation show nearly the same tendency. The settlement values of T15 and T17 are much higher than T7 and T8. On the other hand, the results of constructed building wave velocity tests are proved to be correct by settlement observation.

Conclusions

The classical static load test for soil bearing capacity approach is not only costly but also time consuming. The Rayleigh wave method is a fast, economic, and effective method in bearing capacity test comparing with conventional test method such as static load test. Rayleigh wave method has many advantages in testing the bearing capacity of soil especially under a constructed building. The most significant advantage of Rayleigh wave method is that it costs no damage to the soil and the structure. In other words, Rayleigh wave method is a nondestructive in situ testing method.

A typical engineering project is introduced in this paper. Several comparative field tests are conducted using the static load test and the Rayleigh wave method. The relationship between shear wave velocity and soil bearing capacity is determined. The result of the aforementioned measurements concludes that the Rayleigh wave method can be used in testing the bearing capacity of soil under constructed buildings, and the engineering project has validated this conclusion.

The statistical laws between shear wave velocity and foundation bearing capacity are probably different for various kinds of soil in different area. Therefore, the application of the Rayleigh wave velocity test method in detecting constructed building foundation soil bearing capacity needs to be further studied before it can be popularized.

ACKNOWLEDGMENTS

Many people and organizations contributed to the success of this project. And this research is supported by the National Natural Science Foundation of China (NSFC Grant No. 51278449, NSFC Grant No. 51238009 and NSFC Grant No. 51338009).

References

[1] Rayleigh, L., “On Waves Propagated along the Plane Surface of an Elastic Solid,” *Proc. Lond. Math. Soc.*, Vol. 17, No. 253, 1885, pp. 4–11.

[2] Thomson, W. T., “Transmission of Elastic Waves Through a Stratified Solid Medium,” *J. Appl. Phys.*, Vol. 21, 1950, pp. 89–93.

[3] Haskell, N. A., *The Dispersion of Surface Waves on Multilayered Media*, Vol. 30, American Geophysical Union, Washington, DC, 1990.

[4] Rosenbaum, J. H., “A Note on the Computation of Rayleigh Wave Dispersion Curves for Layered Elastic Media,” *Bull. Seismol. Soc. Am.*, Vol. 54, No. 3, 1964, pp. 1013–1019.

[5] Thrower, E. N., “The Computation of the Dispersion of Elastic Waves in Layered Media,” *J. Sound Vib.*, Vol. 2, No. 3, 1965, pp. 210–226.

[6] Sheriff, R. E., *Encyclopedic Dictionary of Exploration Geophysics*, Vol. 1. Society of Exploration Geophysicists, Tulsa, OK, 1973.

[7] Nazarian, S., Stokoe, I. I., and Hudson, W. R., “Use of Spectral Analysis of Surface Waves Method for Determination of Moduli and Thicknesses of Pavement Systems,” *Transp. Res. Rec.*, Vol. 930, 1983, pp. 38–45.

[8] Wu, S., Zeng, G. X., Chen, Y. M., and Geng, G. R., “Research on Testing Soil Velocity Using SASW Method,” *Chin. J. Earthquake Eng. Eng. Vib.*, Vol. 8, No. 4, 1988, pp. 27–32.

[9] Xia, T., Chen, Y. M., and Wu, S. M., “Research on Parameter Inversion of Foundation Using the Dispersion Characteristics of Rayleigh Wave,” *Chin. J. Earthquake Eng. Eng. Vib.*, Vol. 4, No. 4, 1991, pp. 31–37.

[10] Zhang, Z., Wei, Y. Y., Chen, Y. M., and Wu, S. M., “Transient Surface Wave Test and its Application on Evaluation of Foundation Treatment,” *Chin. J. Geophys. Geochem. Expl.*, Vol. 16, No. 1, 1992, pp. 48–55.

[11] Chen, Y., Wu, S. M., and Zeng, G. X., “Surface Wave Spectrum Analysis Method and its Application,” *Chin. J. Geotech. Eng.*, Vol. 14, No. 3, 1992, pp. 61–65.

[12] Yang, X. and Wu, S. M., “SASW Method Considering Neglected Modes,” *J. Zhejiang Univ. (Eng. Sci.)*, Vol. 30, No. 2, 1996, pp. 149–156.

[13] Wu, S., *Wave in the Soil Medium*, Science Press, Beijing, China, 1997.

[14] Luke, B. A. and Stokoe, K. H., II, “Application of SASW Method Underwater,” *J. Geotech. Geoenviron. Eng.*, Vol. 124, No. 6, 1998, pp. 523–531.

[15] Xia, J., Miller, R. D., and Park, C. B., “Estimation of Near-Surface Shear-Wave Velocity by Inversion of Rayleigh Waves,” *Geophysics*, Vol. 64, No. 3, 1999, pp. 691–700.

[16] Xia, J., Miller, R. D., Park, C. B., and Tian, G., “Determining Q of Near-Surface Materials From Rayleigh Waves,” *J. Appl. Geophys.*, Vol. 51, No. 2, 2002, pp. 121–129.

[17] Xia, J., Xu, Y., Miller, R. D., and Ivanov, J., “Estimation of Near-Surface Quality Factors by Constrained Inversion of Rayleigh-Wave Attenuation Coefficients,” *J. Appl. Geophys.*, Vol. 82, 2012, pp. 137–144.

[18] Japanese Society of Soil Mechanics and Foundation Engineering, *Soil Survey Method*, Japanese Society of Soil Mechanics and Foundation Engineering, Tokyo, Japan, 1979.

Journal of Testing and Evaluation

doi:10.1520/JTE20140052 / Vol. 43 / No. 2 / March 2015 / available online at www.astm.org

Mingwu Wang,[1] Peng Xu,[2] Jian Li,[3] and Shuai Qin[4]

Microstructure and Unsaturated Geotechnical Properties of Net-like Red Soils in Xuancheng, China

Reference

Wang, Mingwu, Xu, Peng, Li, Jian, and Qin, Shuai, "Microstructure and Unsaturated Geotechnical Properties of Net-like Red Soils in Xuancheng, China," *Journal of Testing and Evaluation*, Vol. 43, No. 2, 2015, pp. 385–397, doi:10.1520/JTE20140052. ISSN 0090-3973

ABSTRACT

This study aimed at proper characterization of the microstructure and unsaturated properties of undisturbed red soil with white net-like veins from the Chenshan laterite section in Xuancheng City, China. The chemical composition and micromorphology of the white veins and red matrix were studied using a scanning electron microscope, an energy dispersive spectrometer, and digital image processing. Then a series of soil–water characteristic curves (SWCCs) and shear strength experiments were performed on undisturbed net-like red soils using triaxial stress path testing, and empirical expressions commonly adopted for geotechnical engineering applications were used to represent measured SWCCs. A detailed comparison of microstructures in undisturbed soils and on failure planes was undertaken. The results showed that the white veins and red matrix clearly appeared as distinct features at both macro and micro levels. More quartz amassed in the white vein, and more intense depletion of Fe oxide occurred in the red matrix. Measured SWCCs at drying and wetting behaved with hydraulic hysteresis. Change in the axial strain did not match that in the volumetric strain. The stress-strain curve obtained from the unsaturated triaxial shearing test showed the characteristic of strain softening; the peak deviator stress increased with increments of the confining pressure and suction. Pores less than 5 μm^2 in size were much more common on the shear failure plane than in the undisturbed soil, whereas pores larger than 50 μm^2 were fewer. The major axial angle of soil pores showed a dominant orientation after shearing. In addition, the roundness and fractal dimension of pore outlines on the shear failure plane were greater than those in the undisturbed soil. These results reveal that microstructure and suction play important roles in the unsaturated mechanical behaviors of net-like red soil.

Keywords

unsaturated soil, microstructure, soil–water characteristic curve, triaxial shear test, net-like red soil, geotechnical property

Manuscript received February 12, 2014; accepted for publication August 26, 2014; published online October 10, 2014.

[1] Professor, School of Civil and Hydraulic Engineering, Hefei Univ. of Technology, Hefei 230009, People's Republic of China (Corresponding author), e-mail: wanglab307@foxmail.com

[2] Master Student, School of Civil Engineering and Hydraulic Engineering, Hefei Univ. of Technology, Hefei 230009, People's Republic of China, e-mail: swu1989@126.com

[3] Master Student, School of Civil Engineering and Hydraulic Engineering, Hefei Univ. of Technology, Hefei 230009, People's Republic of China, e-mail: lj20073495@163.com

[4] Master Student, School of Civil Engineering and Hydraulic Engineering, Hefei Univ. of Technology, Hefei 230009, People's Republic of China, e-mail: shuaiqin87@126.com

Introduction

The Quaternary net-like red soil that is found widely in southern China is also known as lateritic red earth, reticulate red clay [1], or vermiculated red soil [2,3] and is characterized by mottled or net-like white veins. It is a red paleosol and is usually considered as a stratigraphic marker for its easy identification in the field. Among red soil profiles, the Chenshan red soil sequence located in Xuancheng City, Anhui Province, east China, is famous because it is in a Paleolithic site of the early humans. The profile is also a standard red earth profile and a record of environmental change in the middle-late Pleistocene in mid-lower reaches of the Yangtze River. However, previous research on the profile focused mainly on particle size [4,5], stratigraphy, age [6], and climate significance [7,8], and rarely on microstructure and unsaturated mechanical behaviors. In addition, to date, the original process of net-like red soils is controversial [9–11]. In particular, the mechanism causing differences in composition and weathering degrees of the net-like vein and the red matrix is still not known [12,13]. At the same time, engineers are more willing to pay attention to unsaturated engineering properties of net-like red soils on-site. Unfortunately, there are few reports on the hydraulic and unsaturated behaviors of net-like red soils. In order to develop suitable design and construction methods and ensure the safety of buildings founded on net-like red soils, it is important to estimate properly the hydraulic and mechanical properties associated with their microstructure characteristics.

Geotechnical properties of unsaturated soil are related not only to the mineral composition, stress state, and compactness [14–16], but also to the soil–water characteristic curve (SWCC) and micro-level texture and structure [17–23]. Some researchers have attempted to set up empirical formulas based on testing [24,25] to describe the stress-strain relation of unsaturated soil. Whalley et al. [26] examined the effects of altered matric potentials and confining pressures on the shear wave velocities of loamy sand and sandy clay. Hoyos et al. [27] introduced a servo-controlled true triaxial apparatus to realize a wide range of stress paths for unsaturated soils in a controlled-suction manner. Kim et al. [28] examined the shear behaviors of saturated and unsaturated soils via direct shear tests under a constant volume condition. Meanwhile, some reports show that soil macroscopic properties are related to microstructures [29–31]. However, so far there have been few reports on the mechanical and hydraulic behaviors of reticulate red clay from the unsaturated view. Although many studies have focused on the spatial variability of red soil strength, few have attempted to find out the microstructure's effects on the unsaturated mechanical behavior. This limits the understanding of microstructure evolution and hydraulic properties and the applications of net-like red soils in engineering practice. Obviously, quantification of micromorphology is important for a thorough understanding of the hydraulic properties and moisture transfer of unsaturated net-like red soil. Previous studies have pointed out that digital image processing (DIP) is a powerful tool for the characterization of pore structure and microcracks [32,33], but few applications have been made regarding the pore characterization of unsaturated net-like red soil via DIP on thin sections.

As mentioned above, soil scientists have paid much attention to the climate and environmental significance of net-like red soil, but not to microstructure and unsaturated behaviors. Additionally, the previous macro-mechanical research on net-like red soil was performed mostly on saturated soils with triaxial tests or direct shearing tests. Unluckily, it is hard to understand fully the engineering properties of unsaturated net-like red soil using only saturated testing methods at the macro scale.

The objective of this study was to examine the microstructure and unsaturated mechanical behaviors of undisturbed net-like red soils using scanning electron microscopy (SEM), energy dispersive spectrometry (EDS), DIP, SWCCs, and triaxial tests. This work will throw more light on macro–micro interactions of hydraulic-mechanical properties and soil microstructures for the justification of ground treatments.

Materials and Methods

TESTED MATERIALS

The soil samples were taken from the Chenshan laterite section (118°51′50″E, 30°52′24″N) adjacent to the Zhaojiabian village and located at the foot of northeast Chenshan Hill with an elevation of 45 m and a relative height of 25 m. The red net-like soil occurs mainly on the second terrace of the Shuiyang River, a branch of the mid-lower reaches of the Yangtze River. The area lies in a subtropical monsoon climatic zone with a mean annual precipitation of 1000 to 1600 mm and a mean annual temperature of 15°C to 18°C. The Chenshan soil profile clearly displays a layered structure with distinct color and texture as shown in **Fig. 1(*a*)**. The Chenshan section is composed of three layers from top to bottom: yellow-brown soil, uniform red clay without any white veins, and net-like red soil [**Fig. 1(*a*)**]. Better developed net-like veins occur from 1.0 m under the ground to the profile bottom. The net-like red soil, in which white veins taking different shapes are distributed randomly in the red matrix in all directions [**Fig. 1(*b*)**], is a main body of the Quaternary red soil. The soil is mainly composed of illite, kaolinite, illite-smectite mixed-layer clay, and minor chlorite [9]. In addition, the net-like red soil is a typical unsaturated soil, as it often occurs above the water level in the field.

TESTING MATERIAL PREPARATION

The thin-section specimens used in SEM tests were prepared via a natural air-drying method.

The preparation procedures for specimens for SWCCs and shear strength tests were as follows.

FIG. 1 Images of net-like red soils: (*a*) and (*b*) in the field; (*c*) specimen.

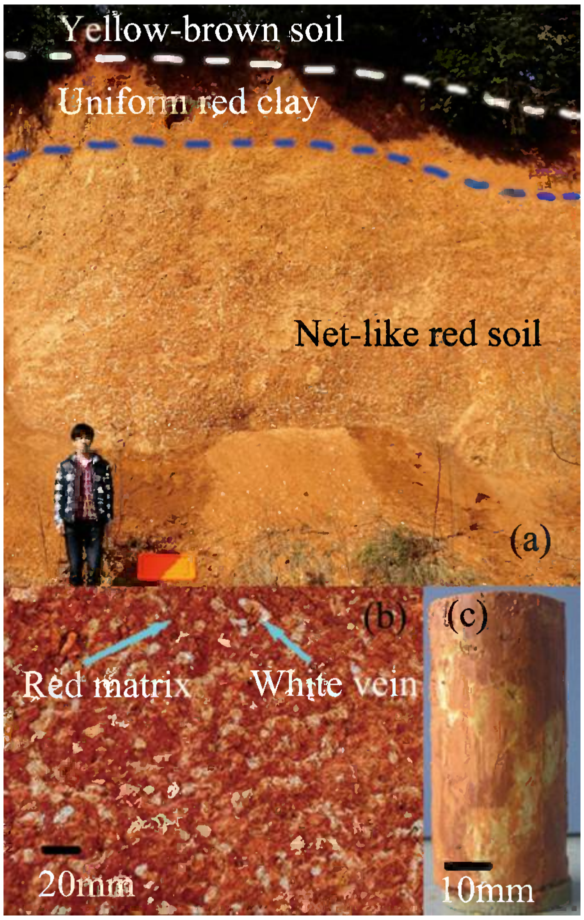

First, a bulk undisturbed soil block with dimensions of 500 (W) by 400 (L) by 400 mm (H) was excavated and sealed in the field and then taken back to the lab and cut into portions with a wire saw and a spatula in a site with constant temperature and humidity.

Then, cylindrical specimens 38 mm in diameter and 80 mm in height [**Fig. 1(*c*)**] were trimmed from the small soil block with a soil lathe and a knife.

Finally, specimens were de-aired and put into cylindrical split molds for 10 days.

AN ANALYSIS OF BASIC PROPERTIES OF TESTED SOIL

All basic properties of the soil were tested according to Chinese National Standard GB/T50123-1999 [34].

SCANNING ELECTRON MICROSCOPY-ENERGY DISPERSIVE SPECTROMETRY TEST

Soil micromorphology is helpful for understanding the mechanical characteristics of paleosols; for instance, textural features are useful in the analysis of micro–macro interactions [25]. As we know, a SEM system equipped with EDS is a powerful analytical tool for the rapid, nondestructive, sensitive, multi-elemental, low-cost analysis of micromorphology. The microstructure was analyzed here in thin sections extracted from the undisturbed soil and on the failure plane after shearing. Composition analysis focused on the local regions in the thin sections and was performed on the red matrix and the white vein via EDS incorporated in the JSM-6490LV SEM system.

QUANTIFICATION OF MICROMORPHOLOGY WITH DIGITAL IMAGE PROCESSING TECHNIQUE

Quantitative analysis of the fabric is essential for the successful interpretation of soil behaviors. In a soil SEM image, pores are likely at a lower or darker gray level in contrast to the background, so pores can be discriminated by different gray levels after the gray-level SEM image is transformed into a binary image [35,36]. The DIP technique is a computerized technique for quantifying SEM images and can save time in numbering pores relative to manual counting [37–39]. Here, Image-pro Plus software, produced by Media Cybernetics, was adopted for the DIP analysis. DIP analysis with Image-pro Plus consists of four steps: spatial calibration of the digital image, image segmentation, counting and sizing on the basis of measured parameters, and data output and statistical analysis. Concrete steps are depicted below.

First, a calibration unit of measurement is used to fix the number of pixels representing 10 μm in horizontal and vertical directions for the SEM image.

Then, the SEM image is converted into a black-and-white binary image for convenience in analysis. Attained binary images can be used to further identify pores and calculate relevant parameters in the geometry and morphology of the pores. Segmentation of the grayscale data is a crucial step for extracting objects including minerals, pores, and clay aggregates from the binary image [36,40]. In general, segmentation involves two main steps: set thresholds for gray level and pore area, and then add or delete objects if needed. The image threshold, by which interesting objects can be distinguished well from the background, is searched in terms of object gray levels. The Image-pro Plus software can recognize interesting objects almost automatically according to the proper threshold. Also, those useful objects wrongly discarded in segmentation can be recovered, and false objects resulting from gray errors in the SEM image can also be removed through the use of an area of interest.

Next, select measured parameters for the software to process their values.

Finally, the measured results are output to Excel for statistical analyses and are graphically plotted in histograms.

SOIL-WATER CHARACTERISTIC CURVE TEST

The SWCC is the most fundamental and important property in unsaturated soil mechanics. The SWCC is often revealed on the basis of direct measurement and mathematical analysis. There are numerous indoor methods for the determination of the

SWCC, such as the volumetric pressure plate extractor method, the temple instrument method, the filter paper method, and so on. All of them have strengths and weaknesses. In addition, methods of moisture content determination based on frequency domain reflectometry [41], time-domain reflectometry [42], and neutron technology were put forward by scholars to gain the SWCC indirectly. However, most previous research focused on the SWCC of a remolded sample and did not take account of the effects of volumetric strain and stress state on the SWCC. Herein, to account for those effects on unsaturated net-like red soil, the geotechnical digital system (GDS) developed by Ng et al. [43] was adopted to conduct the SWCC test. The procedure for testing is as follows.

Step 1: Specimen installation. Place the specimen vertically in a 0.2-mm thick rubber membrane that is sealed against the pedestal and the top cap with two rubber O-rings on the base plate with a high air-entry disk using a split-part mold. Then mount a coarse porous disc and a top cap on the upper end of the specimen. Add de-aired water to the inner chamber and after the reference tube, check its leakage and eliminate air bubbles from the testing system. Prior to the next stage, calibrate transducers to zero and check the sealability of the measuring equipment under a 30-kPa cell pressure after mounting the outer chamber.

Step 2: Suction balance in cycles of drying or wetting. A desired suction in the unsaturated specimen can be built up in drying and wetting cycles through the application of a pressure difference between the pore water pressure and the pore air pressure. The suction balance will be reached when the change in the back volume is less than 50 mm^3 within 24 h (**Fig. 2**).

Step 3: Processing of measured data with Excel software. The volumetric water content of the specimen with the corresponding amount of suction can be calculated from the water content at the final cycle measured via the oven-drying method.

Tests involving wetting and drying processes were carried out to obtain SWCCs of the net-like red soil under 510-kPa axial pressure and 505-kPa radial pressure. The parameters of test models are listed in **Table 1**.

PREDICTING SOIL-WATER CHARACTERISTIC CURVES

Generally, direct measurements on actual testing of soil hydraulics are preferred in engineering practice. However, the high cost, long duration, and complexity of SWCC tests impede the analysis of unsaturated soil mechanics in designs [44]. In addition, the number of measurements achieved for a given site is often too few to capture the spatial variability of soil properties. So, mathematical approaches have been employed to predict SWCCs in recent years because they are cheap to perform, convenient to use, and beneficial for further awareness of hydraulic characteristics. It is significant and necessary to build forecasting formulas for analyzing the suction phenomenon and further understand the SWCC characteristic of the reticulate red soil. Specially, three empirical formulas by Gardner, Van Genuchten, and Fredlund [45] were utilized to represent the first drying cycle of measured SWCCs. The calculated equation is written as

FIG. 2 Histories of pore water pressure, pore air pressure (*a*), axial stress, and radial stress (*b*).

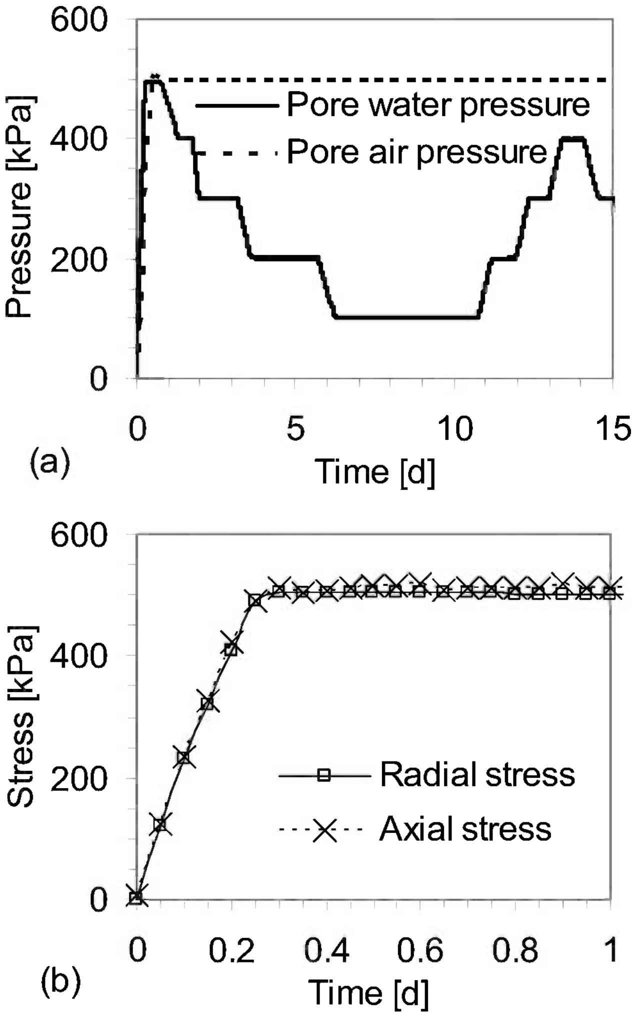

$$\theta_w = \begin{cases} \theta_r + \dfrac{\theta_s - \theta_r}{1 + a\psi^{b}} & \text{For Gardner model} \\[2ex] \theta_r + \dfrac{\theta_s - \theta_r}{[1 + a\psi^{b}]^{c}} & \text{For Van Genuchten model} \\[2ex] \theta_r + \dfrac{\theta_s - \theta_r}{\left\{ \ln\left[e + \left(\dfrac{\psi}{a}\right)^{b} \right] \right\}^{c}} & \text{For Fredlund model} \end{cases} \tag{1}$$

where:

θ_w = volumetric water content ($\theta_w \in (\theta_r, \theta_s]$),

θ_r and θ_s = residual and saturated volumetric water contents, respectively,

TABLE 1 Suction balance conditions of SWCC tests.

Test Step	Pore Air Pressure, kPa	Pore Water Pressure, kPa	Suction, kPa	Test Process
1	0	0	0	Saturated process
2	500	495	5	First drying cycle
3	500	400	100	
4	500	300	200	
5	500	200	300	
6	500	100	400	Wetting cycle
7	500	200	300	
8	500	300	200	
9	500	400	100	Second drying cycle
10	500	300	200	

ψ = matric suction ($\psi \in (0,\psi_r]$),

ψ_r = corresponding matric suction with $\theta_w = \theta_r$,

a = shape parameter associated with the air-entry value,

b = shape parameter related to the drying rate when the matric suction is greater than the air-entry value, and

c = shape parameter related to the residual water content.

UNSATURATED STRENGTH TEST

The GDS for unsaturated soils was also adopted to discuss the evolution of unsaturated shear strength with the variation of suction. Confining pressures of 205 kPa and 305 kPa and suctions of 50 kPa, 100 kPa, and 200 kPa were implemented for shear tests. Detailed experimental schemes are listed in **Table 2**. The test process consisted of four steps: saturation, suction equilibrium, consolidation, and shear.

Results and Discussion

BASIC SOIL PROPERTIES

Basic physical properties of tested soils are presented in **Table 3**. The values in **Table 3** are averaged values from all specimens. The net-like red soil had a moisture content of 23.3 % to 24.1 % with a maximum dry density of 1.79 g/cm^3 to 1.83 g/cm^3. The liquid limit, plastic limit, and plasticity index ranged from 46.7 % to 49.4 %, 26.9 % to 29.3 %, and 19.5 to 21.6, respectively. The optimum moisture content was 17.9 %. The unconfined compressive strength of remolded soil lay in the range of 1067.5 kPa to 4648.7 kPa.

FABRIC FEATURES AND MINERAL COMPOSITION

SEM images of undisturbed samples and specimens after shearing are shown in **Figs. 3** and **4**, respectively.

The white vein and the red matrix showed radically different microstructures, as shown in **Fig. 3**. Textures of micro-pores and micro-particles in the white vein presented features of a granular structure, but mineral grains without a prevailing orientation can be clearly differentiated in the SEM image [**Fig. 3(*a*)**]. Soil particle sizes varied, and some particle diameters were greater than 20 μm. However, the red matrix exhibited aggregate textures of layered structures and pores [**Fig. 3(*b*)**]. Microscopy observation showed that particle orientations were predominantly edge-to-face and face-to-face in the undisturbed soil prior to the shear test but face-to-face in the soil after shearing. Additionally, micro-pores were embedded in the macro- and skeleton-pores. Quartz crystals with a subrounded shape and approximately 10 -μm diameter occurred more richly in the white vein than in the red matrix. It is seen that the microstructure of the red soils obviously behaved anisotropically because of the difference between the white vein and the red matrix. The Fe oxide was depleted usually along fissures between the white veins and the red matrix.

From **Fig. 4**, it is seen that particles on the shear failure plane were smaller and denser than those in the undisturbed sample. This might have been due to processes of consolidation and shearing. Slickensides on the shear failure plane can be clearly observed in **Fig. 4(*c*)**.

The chemical element content was separately analyzed via EDS for the white vein and red matrix. EDS mapping showed Al (K line), Si (K line), K (K line), Ca (K line), Mg (K line), Fe (K line), and Ti (K line) as listed in **Table 4**.

EDS analyses revealed that the tested soil was high in kaolin and mainly made up of O, Si, Al, and Fe elements. This shows that formation of the soil occurred in an acidic and strongly

TABLE 2 Experimental schemes for shear tests.

Case	Initial Moisture Content of Specimen During Shear Test, %	Cell Pressure, kPa	Pore Air Pressure, kPa	Pore Water Pressure, kPa	Suction, kPa
A	24.05	305	300	250	50
B	23.63	305	300	200	100
C	23.53	305	300	100	200
D	22.33	305	105	5	100
E	24.14	305	205	105	100
F	24.56	305	255	155	100
G	23.18	205	155	55	100
H	23.82	205	200	100	100

TABLE 3 Physical properties of tested soils.

Maximum Dry Density, g/cm^3	Moisture Content, %	Liquid Limit, %	Plastic Limit, %	Plasticity Index	Optimum Moisture Content, %	Unconfined Compressive Strength, kPa
1.81	23.6	48.5	28.2	20.0	17.9	3246.9

weathered environment with the leaching of mobile elements Ca and Mg and the accumulation of immobile elements Fe and Al. Quartz accumulated much more in the white vein than in the red matrix, but the vein's clay mineral content was less than that of the red matrix. The better developed the white vein was, the more intensely the Fe oxide was depleted. However, Ti is a stable chemical component in net-like red soils. Sometimes the percentage of Fe was lower in the white vein than in the red matrix. Al_2O_3 in the white vein presented uncertainty; for instance, Al_2O_3 in case E was significantly leached, whereas that in case G was accumulated. This might be the result of pH differences in the soil. We found that differential depletion and accumulation contributed to the chemical composition of the white vein.

FIG. 3 SEM images of undisturbed net-like red soils: (*a*) white vein; (*b*) red matrix.

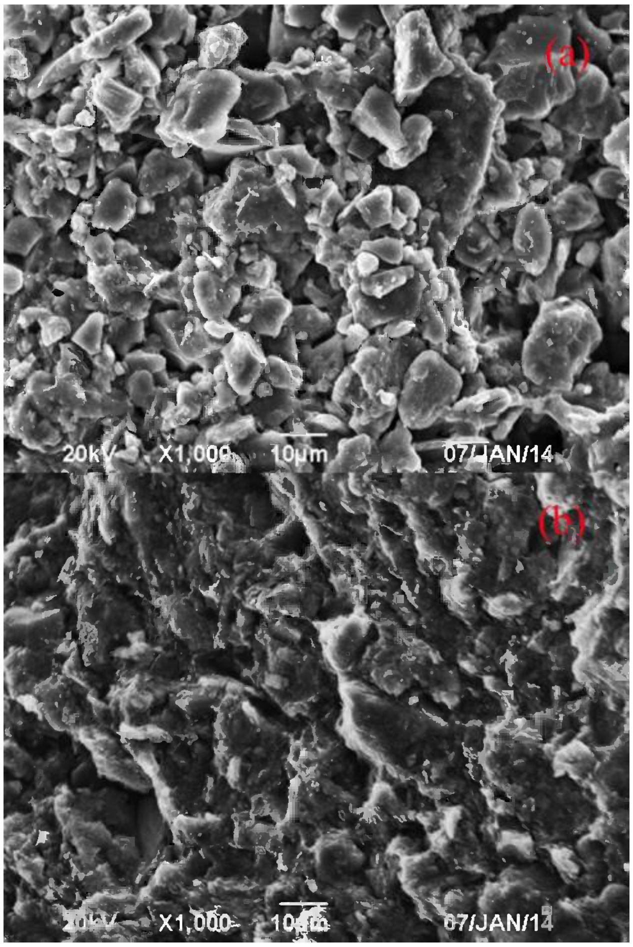

SOIL-WATER CHARACTERISTIC CURVE

The axial strain, volumetric strain, total volume, and back volume behaviors from the SWCC test are presented in **Fig. 5**. It is observed in **Fig. 5** that the total volume and volumetric strain increased with the test. The growth rate of the SWCC in the drying cycle was greater than that in the wetting cycle, but the axial strain barely changed in both cycles.

FIG. 4 SEM images of case F after the triaxial shearing test: (*a*) white vein; (*b*) red matrix; (*c*) slickensides on the shear failure plane.

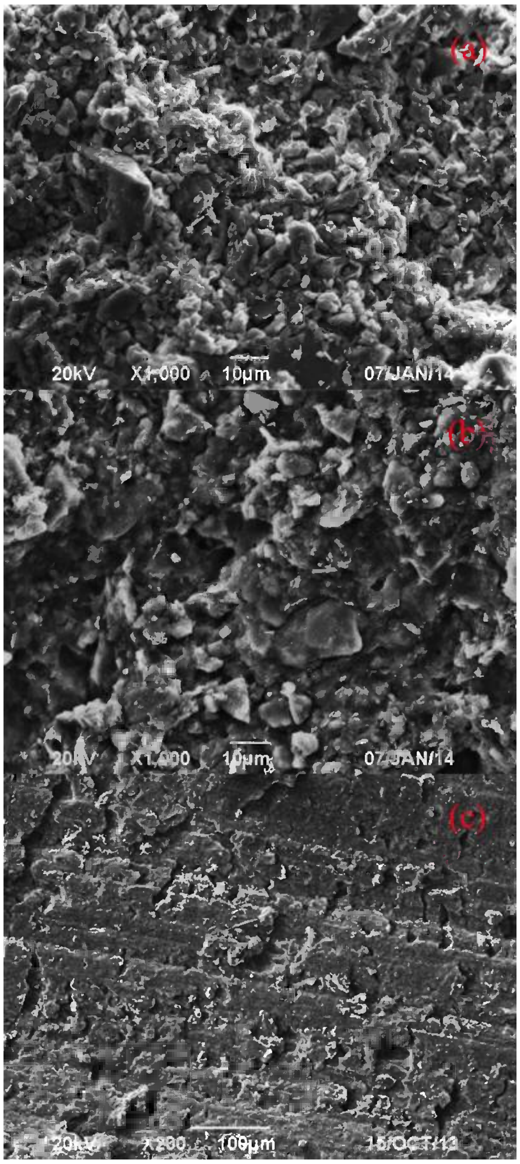

TABLE 4 EDS findings for atomic percentages of Al, Si, Ca, Mg, Fe, and Ti.

Case	O	Al	Si	K	Ca	Mg	Fe	Ti
White vein in undisturbed soil	56.19	3.77	39.11	0.93	—	—	—	—
Red matrix in undisturbed soil	61.25	5.85	26.3	0.55	—	—	2.65	0.44
Red matrix in case D	57.95	5.62	33.75	0.56	—	—	2.12	—
White vein in case E	62.13	6.00	28.32	0.66	0.19	0.67	1.78	0.24
White vein in case G	62.75	10.09	25.08	1.08	—	—	1.00	—
Red matrix in case H	55.11	11.36	30.10	1.12	0.32	—	1.68	0.31

Figure 6(*a*) shows that the measured volumetric water content in the dehydration process was greater than that in the adsorption process under the same matric suction. The SWCC of the second dehydration process was not consistent with that of the first process. Specifically, the change in the volumetric water content in the subsequent drying cycle was smaller than that in the first drying cycle under the same suction. Obviously, the hydraulic feature of net-like red soil demonstrates hysteresis.

FIG. 5 Time histories of axial and volumetric strains, back and total volumes.

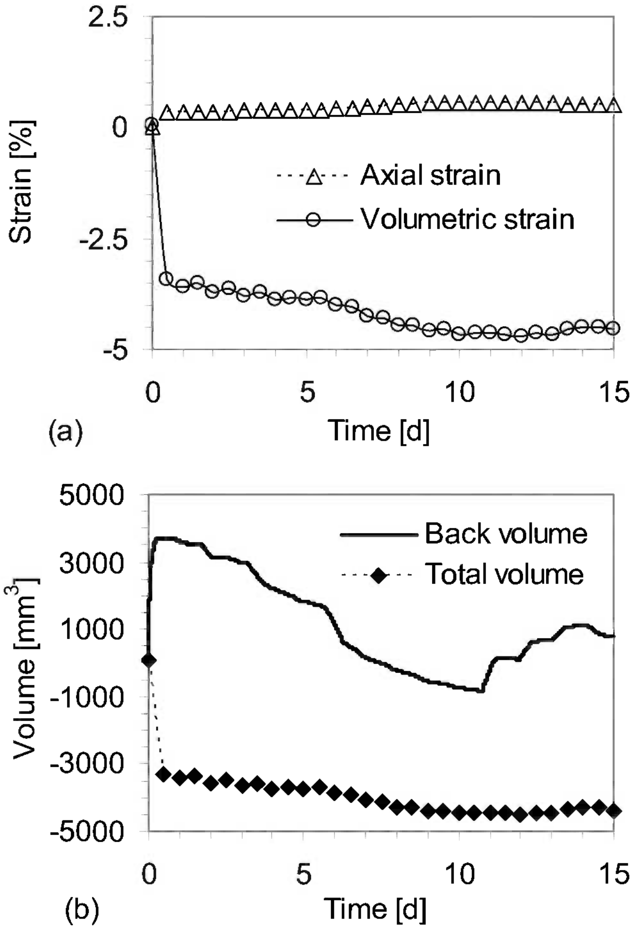

FIG. 6 Measured and computed SWCCs: (*a*) measured; (*b*) computed.

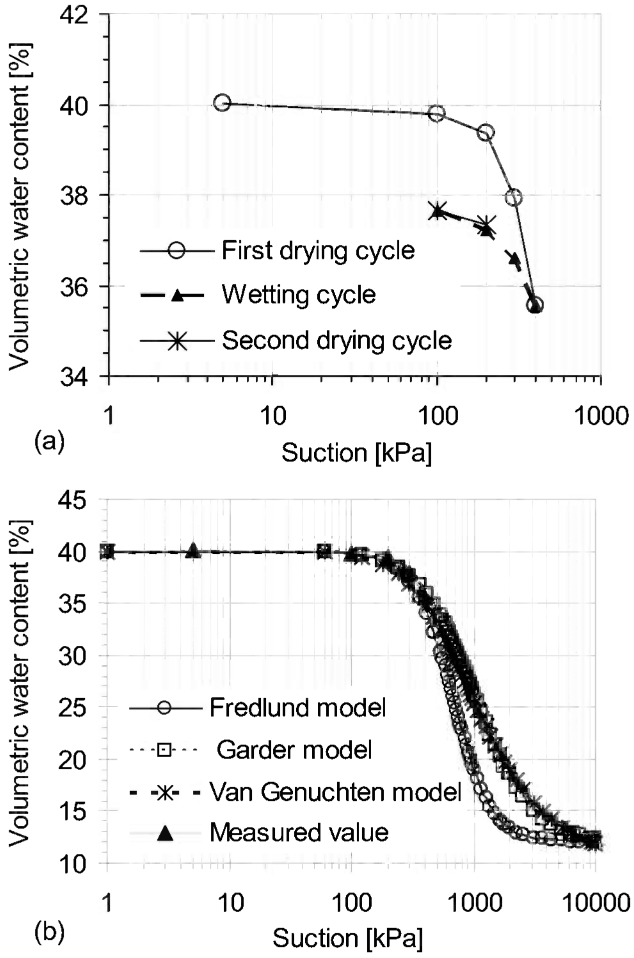

Predicted results are illustrated in **Fig. 6(*b*)** and **Table 5**. The error square sum R^2 was used to further estimate inverse analysis results via Eq 1. The calculated formula of the error square sum R^2 is

$$R^2 = 1 - \frac{\Sigma(\theta - \theta_2)^2}{\Sigma(\theta - \theta_1)^2} \tag{2}$$

where θ, θ_1, and θ_2 are the volumetric water content and mean value from laboratory tests and the calculated value from empirical mathematical models, respectively. More detailed information on the analytical model can be found in Ref 16. The closer R^2 is to 1, the better the inversion is. Results show that calculated suctions from the Fredlund

TABLE 5 Simulation parameters and correlation coefficients.

Parameters	Fredlund Model	Van Genuchten Model	Gardner Model
a	810.86	2.64×10^{-6}	1.85×10^{-6}
b	2.52	2.0	1.94
c	3.30	0.5	—
R^2	0.957	0.916	0.884

model had good agreement with measured ones. The GDS for unsaturated soils [43] measures the suction via an axis translation technique. For a specimen 38 mm in diameter, suction from 0 to 500 kPa can be monitored with an ordinary high-air-entry disk. To ensure equipment safety, the maximum suction is often set at 450 kPa. Therefore, the volumetric water content discussed here was inside a partial range. Additional testing with a ceramic plate of high pressure is required in order to clarify the details of hydraulic behavior under a full range of suctions in the future.

UNSATURATED STRENGTH

The measured strengths of unsaturated net-like red soils are shown in **Figs. 7**, **8**, and **9** and in **Table 6**. Measured deviator stress-strain curves under desired suctions are presented in **Fig. 7**. The stress-strain relations obtained from the experiments performed with 305-kPa confining pressure and 100-kPa suction at desired net confining pressures are shown in **Fig. 8**. Deviator stress-strain relations under constant suction and net confining pressure but different confining pressures are compared in **Fig. 9**. From the measured results, we can see that axial strains tended to be stable when they reached 12 %. Thus, here the deviator stress at the axial strain of 12 % is used to denote residual deviator stress, and the corresponding shear strength is referred to as the residual shear strength.

Suctions for cases A, B, and C under a cell pressure of 305 kPa were 50 kPa, 100 kPa, and 200 kPa, respectively (**Fig. 7**). The tested condition for case H was 100-kPa suction and 205-kPa confining pressure. For cases A, B, and C, it is seen that the maximum deviator stress, residual shear strength, and axial strain at the maximum shear stress increased with the increment of suction. For cases H and B with the same suction of 100 kPa, the effect of pore water pressure on the residual strength was small, but the peak shear strength depended on the pore water pressure.

FIG. 7 Measured deviator stress–axial strain curves for cases A, B, C, and H.

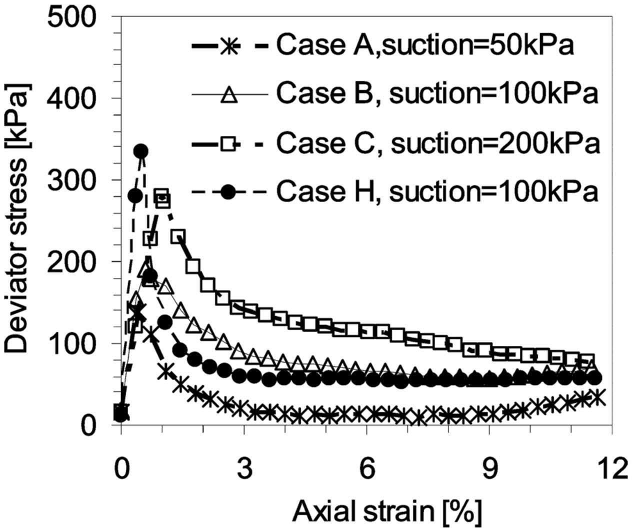

It can be seen from **Fig. 8** that the amounts of deviator stress, residual shear strength, and axial strain at the peak deviator stress increased with increments of the net confining pressure. The ratio of the maximum deviator stress to the residual deviator stress decreased with increasing net confining pressure. The maximum deviator stress in case D was 267.32 % greater than that in case B. This suggests that net confining pressure and air phase in soils play important roles in the shear strength of unsaturated net-like red soil. We can see in **Fig. 9** that confining pressure had an effect on the residual shear strength, but not on the peak deviator stress.

FIG. 8 Measured curves of deviator stress versus axial strain for cases B, D, E, and F.

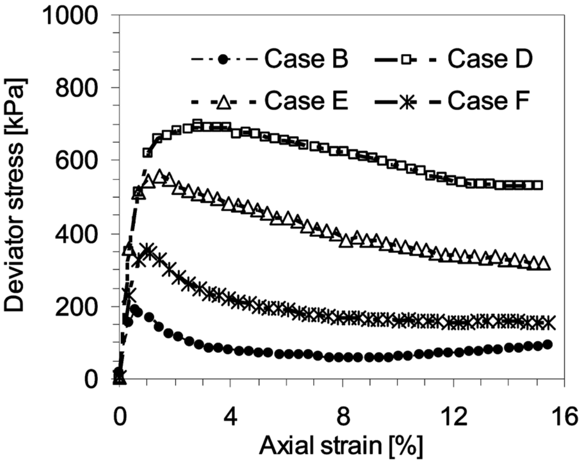

FIG. 9 Measured curves of deviator stress versus axial strain for cases F and G.

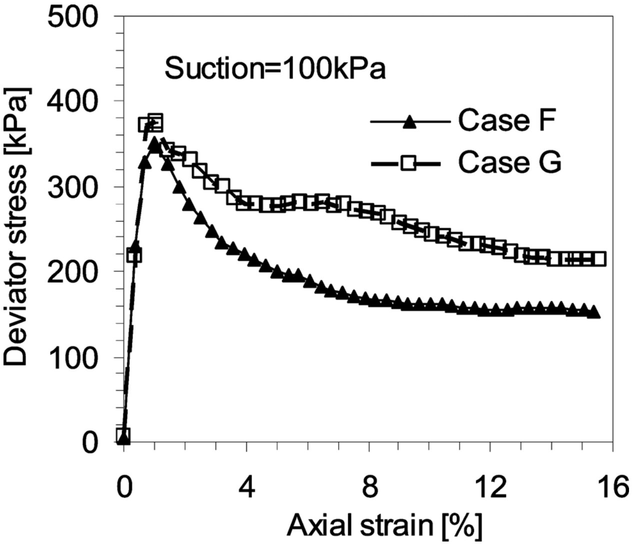

TABLE 6 Results of unsaturated shear strength tests.

Case	Peak Deviator Stress, kPa	Axial Strain at Maximum Shear Stress, %	Deviator Stress at 5 % Axial Strain, kPa	Residual Deviator Stress, kPa	Ratio of Maximum Deviator Stress to Residual Deviator Stress
A	138.95	0.70	12.55	34.34	4.05
B	190.13	1.06	74.35	68.37	2.78
C	279.91	1.62	125.17	77.61	3.61
D	698.38	3.66	681.34	561.31	1.24
E	557.63	2.07	478.17	351.42	1.59
F	352.29	1.51	213.59	157.72	2.23
G	376.07	1.44	275.34	230.21	1.63
H	334.02	0.84	55.90	57.44	5.82

Thus, it is concluded that deviator stress gradually decreased after it arrived at the peak value in cases with a cell pressure of 305 kPa. However, for specimens under a cell pressure of 205 kPa, the attenuation rate of the deviator stress was faster. All axial strains at peak shear strengths were below 1.5 %. All stress-strain curves exhibited strain softening. Deviator stress and peak shear strength decreased with increasing moisture content. In samples under constant suction and net confining pressure, pore water pressure contributed to the axial strain at peak strength and the residual shear strength in a way.

DEFORMATION FEATURES

Measured shear deformations of unsaturated net-like red soils are illustrated in **Figs.** 10, 11, and 12. **Figure** 10 shows volumetric strains plotted against time for specimens with suctions of 50 kPa, 100 kPa, and 200 kPa, respectively. A comparison of volumetric strain versus time is presented in **Fig.** 11 for net confining pressures from 5 kPa to 200 kPa under constant suction of 100 kPa. The effect of confining pressure on the volumetric strain is depicted in **Fig.** 12.

The difference in the volumetric strain generation between low and high suctions is noticeable after prolonged shearing, as shown in **Fig.** 10. Larger amounts of volumetric strain are found in specimens with higher suction despite constant confining pressure. The volumetric strain at 15 % axial strain in case C with 200-kPa suction was 94.73 % greater than that in case A with 50-kPa suction. With a suction of 100 kPa, the volumetric strain in case B under 305-kPa cell pressure was smaller than that in case H under 205-kPa cell pressure. These behaviors agree with the effects of suction on the shear strength.

It can be seen in **Fig.** 11 that the volumetric strain was altered with the magnitude of the net confining pressure. For cases D and E, with net confining pressures of 200 kPa and 100 kPa, respectively, the curves started out with a contraction pattern of decreasing rate followed by dilation during a specific period. But their volumetric strains increased more gradually and smoothly than that in case F with a net cell pressure of

FIG. 10 Time histories of volumetric strain for cases A, B, C, and H.

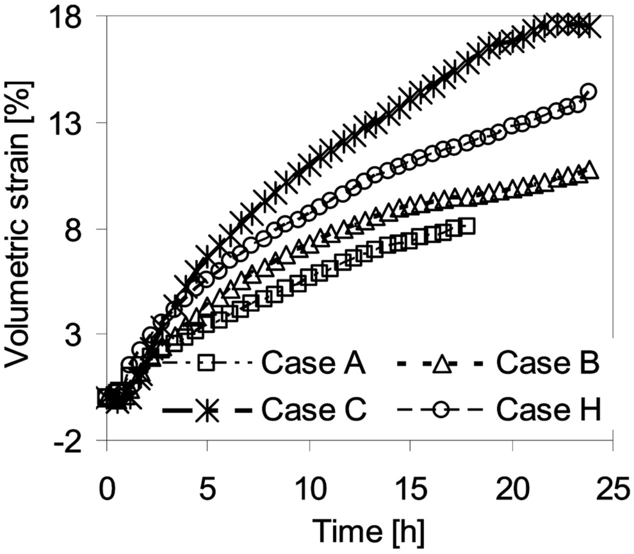

FIG. 11 Comparison of volumetric strains among cases B, D, E, and F.

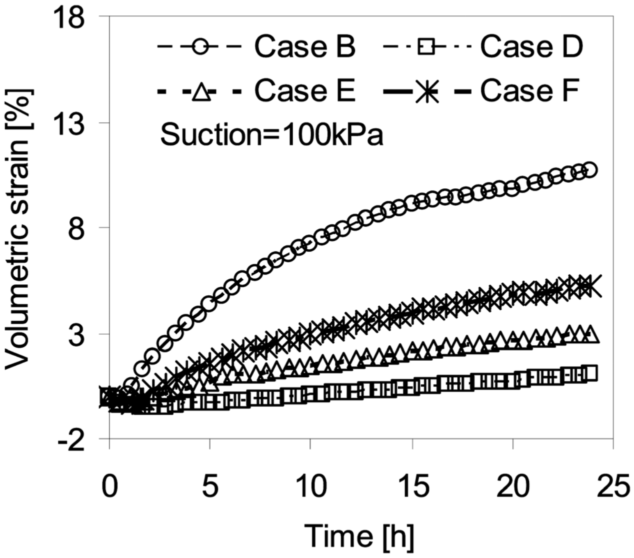

FIG. 12 Time histories of volumetric strain for cases F and G.

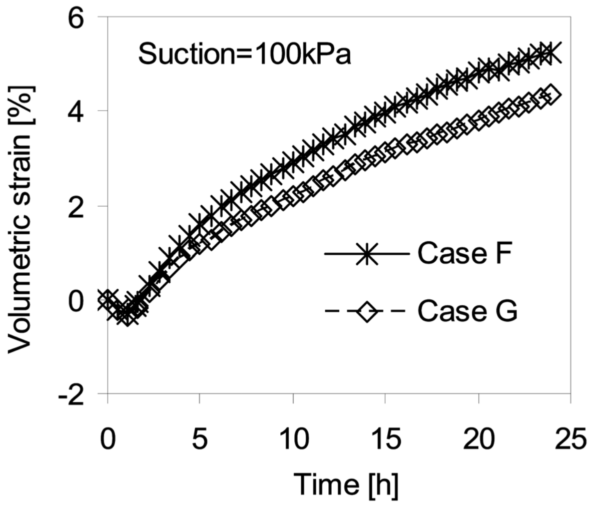

50 kPa. The final volumetric strain in case B under a net confining pressure of 5 kPa was nearly nine times that in case D under a net confining pressure of 200 kPa. This indicates that net confining pressure plays a role in soil deformation.

It can be seen from **Fig. 12** that the initial volumetric strain in case F was very similar to that in case G. The volumetric strain at 15 % axial strain in case F was 5.24 %, whereas it was 4.33 % in case G. The growth rate of the volumetric strain in case F was faster than that in case G. Initial water contents in cases G and F prior to the shear process were 23.18 % and 24.56 %, respectively. So these phenomena might be caused by differences in the moisture content and the pore water pressure.

MICROSCOPIC AND QUANTITATIVE FEATURES OF SOIL ON THE SHEAR FAILURE PLANE

Changes in shear strength associated with microstructure were also further explored via SEM, EDS, and DIP analysis approaches. Cases F and G under the same net cell pressure and suction were chosen for the analysis. As noted above, threshold specification is a crucial step in the segmentation process. A global threshold method [36,46] was adopted here to identify the threshold. The range of gray-level thresholds

FIG. 13 Images of specimens after shear test: (*a*) case F; (*b*) case G.

FIG. 14 SEM images of microstructures on the shear failure plane: (*a*) and (*b*) case F; (*c*) and (*d*) case G.

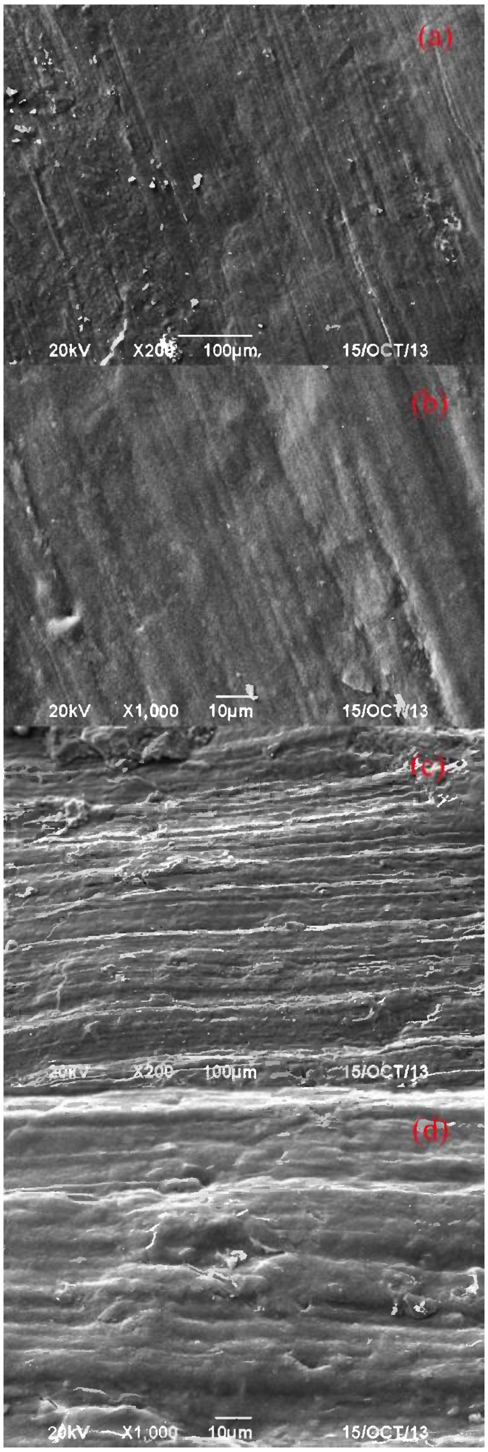

TABLE 7 Statistical characteristics of pores in undisturbed soils and on shear failure planes.

Case	Roundness	Porosity, %	Angle, deg	Diameter, μm	Area, μm^2	Perimeter, μm	Fractal Dimension
Undisturbed white vein	2.46	15.9	86.15	2.65	7.84	13.76	1.18
Undisturbed red matrix	3.20	19.4	102.55	2.71	8.41	16.71	1.23
White vein on the shear failure plane	2.27	10.14	86.37	2.01	3.86	9.79	1.20
Red matrix on the shear failure plane	2.73	12.7	83.09	2.26	5.28	12.34	1.23

obtained for tested sections was 60 to 80. The segmentation process was performed several times and by several individuals to reduce subjective errors. The characteristic of shear failure at the macro scale can be observed in **Fig. 13**. SEM images of thin sections extracted from the failure planes are illustrated in **Fig. 14**. Quantitative features of pores in the net-like red soil from DIP analyses are presented in **Table 7** and **Fig. 15**.

From **Fig. 14**, it is seen that microstructures on the failure plane in cases F and G were different. Micro-slickenside was smoother, straighter, and more intensive in cases under high confining pressures than in cases under low confining pressures. In addition, micro-steps were observed in cases with high confining pressures.

Porosity and pore size are essential properties of soil mass because they govern the transport of water, solutes, and gas. The parameters in **Table 7**, used to describe the complexity and variation of pores, are mean values. It is clear that the shear process resulted in the major axial angle of pores from disorder to order. The fractal dimension of the pore outline increased; in contrast, the perimeter, area, diameter, and roundness of the pore decreased.

Statistical characteristics of pores before and after shearing are shown in **Fig. 15**. The figure indicates that pore areas in the undisturbed soil generally ranged from 1 to 5 μm^2, and the proportion of 5- to 10-μm^2 pores in the white vein was less than that in the red matrix. Moreover, fewer pores larger than 50 μm^2 and more pores 0.6 to 5 μm^2 in size appeared on the failure plane. This might be due to the compactness of 10- to 50-μm^2 pores and grain crushing during consolidation and shear processes. In addition, micro-pore sizes on the failure plane decreased with the increment of confining pressure. It is concluded that shear dilatancy is not induced by changes in micro-pores and might be due to cracking of the soil mass. Pore sizes tended to be smaller after shearing. These results agree well with macro-mechanical observations. It is also proposed that the DIP technique might be an effective alternative for quantitative analysis of the effects of particle crushing and rearrangement on geotechnical properties of net-like red soils.

Conclusions

The net-like red soil at the Chenshan profile in Xuancheng City is a red paleosol with extraordinary textures. To date, few

FIG. 15

Statistical characteristics of micro-pore area in the undisturbed soil and on the shear failure plane.

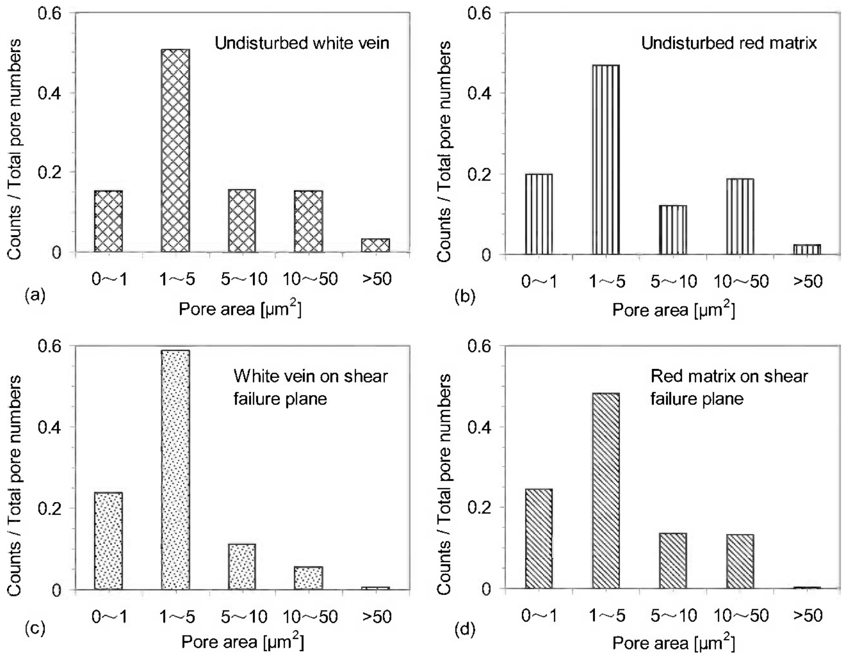

studies have focused on its microstructure and unsaturated behaviors. This study examined the hydraulic-mechanical behaviors and microstructure features at the macro- and microscales via SEM, EDS, SWCCs, unsaturated triaxial shear tests, and a DIP analysis approach. The roles of mineral composition and microstructure in the evolution of the unsaturated mechanical behaviors of the net-like red soil were further discussed. Some conclusions are drawn as follows.

1. The white vein and red matrix in tested soils presented significant differences in color, microstructure, and chemical components. More quartz and fewer clay minerals were present in the white vein than in the red matrix. The better the white vein is developed, the more intensely the Fe oxide is depleted.
2. Measured SWCCs in drying and wetting cycles behaved with hydraulic hysteresis. The curve of the second drying cycle clearly lay below that of the initial drying cycle under the same test conditions. The back volume changed with the magnitude of the suction, but there was much more variation in the drying cycle than in the wetting cycle. The SWCC test showed that changes in the axial strain did not correspond with those in the volumetric strain.
3. Net-like red soils from the Chenshan profile exhibited strain softening and brittle failure features during the unsaturated shear process. Axial strains at the peak shear strength were less than 1.5 %. For cases under constant suction, the higher the confining pressure, the greater the shear strength. The shear strength of a specimen increases with increasing suction under constant confining pressure.
4. DIP analysis of a SEM image was found to be a useful tool in the characterization of microscopic changes. More intensive micro-slickensides and micro-steps occurred in the specimens under higher confining pressure. The composition of pores in the undisturbed soil and on the failure plane was different. There were a high percentage of pores larger than 10 μm^2 and a low percentage of pores smaller than 5 μm^2 in the undisturbed soil, but pore sizes on the failure plane exhibited opposite characteristics. The major axial angle of pores tended toward one orientation. Changes in microstructure and differences in suction might be critical factors contributing to the variations in unsaturated mechanical behaviors of net-like red soils. This serves as a bridge between the macroscopic mechanical behavior and the microscopic structure characteristic. It will enable us to provide a more comprehensive background for the characterization of unsaturated behaviors and explore appropriate treatment methods for net-like red soils. However, further investigations will still be in progress with a rational threshold algorithm to quantify the effects of wetting and drying cycles on the unsaturated geotechnical properties.

ACKNOWLEDGMENTS

Financial support provided by the National Natural Sciences Foundation, China (Grant No. 41172274), is gratefully acknowledged. The writers also express their sincere thanks to the reviewers for their thorough reviews and useful suggestions.

References

[1] Hu, X. F., Zhu, Y., and Shen, M. N., "Grain-size Evidence for Multiple Origins of the Reticulate Red Clay in Southern China," *Chin. Sci. Bull.*, Vol. 50, No. 9, 2005, pp. 910–918.

[2] Liu, C. C., Deng, C. L., and Liu, Q. S., "Mineral Magnetic Studies of the Vermiculated Red Soils in Southeast China and Their Paleoclimatic Significance," *Palaeogeogr. Palaeoclimatol. Palaeoecol.*, Vol. 329, 2012, pp. 173–183.

[3] Yin, K., Hong, H. L., Churchman, G. J., Li, R. B., Li, Z. H., Wang, C. W., and Han, W., "Hydroxy-Interlayered Vermiculite Genesis in Jiujiang Late-Pleistocene Red Earth Sediments and Significance to Climate," *Appl. Clay Sci.*, Vol. 74, 2013, pp. 20–27.

[4] Li, X. S., Yang, D. Y., Lu, H. Y., and Han, H. Y., "The Grain-size Features of Quaternary Aeolian-dust Deposition Sequence in South Anhui and Their Significance," *Marine Geol. Quaternary Geol.*, Vol. 17, 1997, pp. 73–81 (in Chinese).

[5] Hu, X. F., Yuan, G. D., and Gong, Z. T., "Origin of Quaternary Red Clay of Southern Anhui Province," *Pedosphere*, Vol. 8, No. 3, 1998, pp. 267–272.

[6] Hu, X. F., Wei, J., Xu, L. F., Zhang, G. L., and Zhang, W. G., "Magnetic Susceptibility of the Quaternary Red Clay in Subtropical China and Its Paleoenvironmental Implications," *Palaeogeogr. Palaeoclimatol. Palaeoecol.*, Vol. 279, No. 3, 2009, pp. 216–232.

[7] Xiong, S. F., Sun, D. H., and Ding, Z. L., "Aeolian Origin of the Red Earth in Southeast China," *J. Quaternary Sci.*, Vol. 17, No. 2, 2002, pp. 181–191.

[8] Hu, X. F., Wei, J., Du, Y., Xu, L. F., Wang, H. B., Zhang, G. L., Ye, W., and Zhu, L. D., "Regional Distribution of the Quaternary Red Clay With Aeolian Dust Characteristics in Subtropical China and Its Paleoclimatic Implications," *Geoderma*, Vol. 159, No. 3, 2010, pp. 317–334.

[9] Hong, H. L., Gu, Y. S., Yin, K., Zhang, K. X., and Li, Z. H., "Red Soils With White Net-like Veins and Their Climate Significance in South China," *Geoderma*, Vol. 160, No. 2, 2010, pp. 197–207.

[10] Hong, H. L., Churchman, G. J., Gu, Y. S., Yin, K., and Wang, C. W., "Kaolinite–Smectite Mixed Layer Clays in the Jiujiang Red Soils and Their Climate Significance," *Geoderma*, Vol. 173, 2012, pp. 75–83.

[11] Hong, H. L., Wang, C. W., Zeng, K. F., Gu, Y. S., Wu, Y. B., Yin, K., and Li, Z. H., "Geochemical Constraints on Provenance of the Mid-Pleistocene Red Earth Sediments in Subtropical China," *Sediment. Geol.*, Vol. 290, 2013, pp. 97–108.

[12] Yin, Q. Z. and Guo, Z. T., "Mid-Pleistocene Vermiculated Red Soils in Southern China as an Indication of Unusually Strengthened East Asian Monsoon," *Chin. Sci. Bull.*, Vol. 51, No. 2, 2006, pp. 213–220.

[13] Hong, H. L., Li, Z., Yang, M. Z., Xiao, P., and Xue, H. J., "Kaolin in the Net-like Horizon of Laterite in Hubei, South China," *Clay Min.*, Vol. 44, No. 1, 2009, pp. 51–66 (in Chinese).

[14] Fredlund, D. G., Xing, A., Fredlund, M. D., and Barbour, S. L., "The Relationship of the Unsaturated Soil Shear Strength to the Soil-Water Characteristic Curve," *Can. Geotech. J.*, Vol. 33, No. 3, 1996, pp. 440–448.

[15] Wang, M. W. and Chen, G. Y., "A Novel Coupling Model for Risk Analysis of Swell and Shrinkage of Expansive Soils," *Comput. Math. Applicat.*, Vol. 62, No. 7, 2011, pp. 2854–2861.

[16] Wang, M. W., Li, J., Ge, S., and Li, S., "Moisture Migration Tests on Unsaturated Expansive Clays in Hefei, China," *Appl. Clay Sci.*, Vol. 79, 2013, pp. 30–35.

[17] Lim, T. T., Rahardjo, H., Chang, M. F., and Fredlund, D. G., "Effect of Rainfall on Matric Suction in a Residual Soil Slope," *Can. Geotech. J.*, Vol. 33, No. 4, 1996, pp. 618–628.

[18] Leong, E. C. and Rahardjo, H., "Review of Soil-Water Characteristic Curve Equations," *J. Geotech. Geoenviron. Eng.*, Vol. 123, No. 12, 1997, pp. 1106–1117.

[19] Melinda, F., Rahardjo, H., Han, K. K., and Leong, E. C., "Shear Strength of Compacted Soil Under Infiltration Condition," *J. Geotech. Geoenviron. Eng.*, Vol. 130, No. 8, 2004, pp. 807–817.

[20] Puppala, A. J. and Punthutaecha, V. S. K., "Soil-Water Characteristic Curves of Stabilized Expansive Soils," *J. Geotech. Geoenviron. Eng.*, Vol. 132, No. 6, 2006, pp. 736–751.

[21] Al-Mukhtar, M., Khattab, S., and Alcover, J. F., "Microstructure and Geotechnical Properties of Lime-Treated Expansive Clayey Soil," *Eng. Geol.*, Vol. 139, 2012, pp. 17–27.

[22] Hunt, A. G., Ghanbarian, B., and Saville, K. C., "Unsaturated Hydraulic Conductivity Modeling for Porous Media With Two Fractal Regimes," *Geoderma*, Vol. 207, 2013, pp. 268–278.

[23] Schnellmann, R., Rahardjo, H., and Schneider, H. R., "Unsaturated Shear Strength of a Silty Sand," *Eng. Geol.*, Vol. 162, 2013, pp. 88–96.

[24] Wheeler, S. J., Sharma, R. S., and Buisson, M. S., "Coupling of Hydraulic Hysteresis and Stress-Strain Behaviour in Unsaturated Soils," *Geotechnique*, Vol. 53, No. 1, 2003, pp. 41–54.

[25] Alonso, E. E., Pereira, J. M., Vaunat, J., and Olivella, S., "A Microstructurally Based Effective Stress for Unsaturated Soils," *Geotechnique*, Vol. 60, No. 12, 2010, pp. 913–925.

[26] Whalley, W. R., Jenkins, M., and Attenborough, K., "The Velocity of Shear Waves in Unsaturated Soil," *Soil Till. Res.*, Vol. 125, 2012, pp. 30–37.

[27] Hoyos, L. R., Pérez-Ruiz, D. D., and Puppala, A. J., "Refined True Triaxial Apparatus for Testing Unsaturated Soils Under Suction-controlled Stress Paths," *Int. J. Geomech.*, Vol. 12, No. 3, 2011, pp. 281–291.

[28] Kim, B. S., Shibuya, S., Park, S. W., and Kato, S., "Suction Stress and Its Application on Unsaturated Direct Shear Test Under Constant Volume Condition," *Eng. Geol.*, Vol. 155, 2013, pp. 10–18.

[29] Sivakumar, V., Doran, I. G., and Graham, J., "Particle Orientation and Its Influence on the Mechanical Behaviour of Isotropically Consolidated Reconstituted Clay," *Eng. Geol.*, Vol. 66, No. 3, 2002, pp. 197–209.

[30] Ye, W. M., Huang, Y., Cui, Y. J., Tang, Y. Q., and Delage, P., "Microstructural Changing Characteristics of Densely Compacted Bentonite With Suction Under Unconfined Hydrating Conditions," *Chin. J. Rock Mech. Eng.*, Vol. 24, No. 24, 2005, pp. 4570–4575.

[31] Or, D. and Ghezzehei, T. A., "Modeling Post-tillage Soil Structural Dynamics: A Review," *Soil Till. Res.*, Vol. 64, No. 1, 2002, pp. 41–59.

[32] O'Donnell, T. K., Goyne, K. W., Miles, R. J., Anderson, S. H., and Sudduth, K. A., "Identification and Quantification of Soil Redoximorphic Features by Digital Image Processing," *Geoderma*, Vol. 157, No. 3, 2010, pp. 86–96.

[33] Marinoni, N., Pavese, A., Foi, M., and Trombino, L., "Characterisation of Mortar Morphology in Thin Sections by Digital Image Processing," *Cem. Concr. Res.*, Vol. 35, 2005, pp. 1613–1619.

[34] GB/T50123, 1999, "Standard for Soil Test Method," China Planning Press, Beijing (in Chinese).

[35] Dathe, A., Eins, S., Niemeyer, J., and Gerold, G., "The Surface Fractal Dimension of the Soil–Pore Interface as Measured by Image Analysis," *Geoderma*, Vol. 103, No. 1, 2001, pp. 203–229.

[36] Liu, C., Shi, B., Zhou, J., and Tang, C., "Quantification and Characterization of Microporosity by Image Processing, Geometric Measurement and Statistical Methods: Application on SEM Images of Clay Materials," *Appl. Clay Sci.*, Vol. 54, No. 1, 2011, pp. 97–106.

[37] Vogel, H. J. and Kretzschmar, A., "Topological Characterization of Pore Space in Soil-sample Preparation and Digital Image-processing," *Geoderma*, Vol. 73, No. 1, 1996, pp. 23–38.

[38] Martínez-Nistal, A., Veniale, F., Setti, M., and Cotecchia, F., "A Scanning Electron Microscopy Image Processing Method for Quantifying Fabric Orientation of Clay Geomaterials," *Appl. Clay Sci.*, Vol. 14, No. 4, 1999, pp. 235–243.

[39] Aydemir, S., Keskin, S., and Drees, L. R., "Quantification of Soil Features Using Digital Image Processing (DIP) Techniques," *Geoderma*, Vol. 119, No. 1, 2004, pp. 1–8.

[40] Liu, Z., Shi, B., Inyang, H. I., and Cai, Y., "Magnification Effects on the Interpretation of SEM Images of Expansive Soils," *Eng. Geol.*, Vol. 78, No. 1, 2005, pp. 89–94.

[41] Gao, L., Shi, B., Tang, C. S., Wang, B. J., Gu, K., and Gan, Y. K., "Experimental Study of Temperature Effect on FDR Measured Soil Volumetric Water Content," *J. Glaciol. Geocryol.*, Vol. 32, No. 5, 2010, pp. 964–969.

[42] Chen, Y., Chen, Y. M., and Zhou, Q. J., "Measurement of Water Content of Multiple Geomaterials by Time-Domain Reflectometry Technique," *J. Southwest Jiaotong Univ.*, Vol. 46, No. 1, 2011, pp. 42–48 (in Chinese).

[43] Ng, C. W. W., Zhan, L. T., and Cui, Y. J., "A New Simple System for Measuring Volume Changes in Unsaturated Soils," *Can. Geotech. J.*, Vol. 39, No. 3, 2002, pp. 757–764.

[44] Satyanaga, A., Rahardjo, H., Leong, E. C., and Wang, J. Y., "Water Characteristic Curve of Soil With Bimodal Grain-size Distribution," *Comput. Geotech.*, Vol. 48, 2013, pp. 51–61.

[45] Fredlund, D. G., Xing, A., Fredlund, M. D., and Barbour, S. L., "The Relationship of the Unsaturated Soil Shear Strength to the Soil-Water Characteristic Curve," *Can. Geotech. J.*, Vol. 33, No. 3, 1996, pp. 440–448.

[46] Prakongkep, N., Suddhiprakarn, A., Kheoruenromne, I., and Gilkes, R. J., "SEM Image Analysis for Characterization of Sand Grains in Thai Paddy Soils," *Geoderma*, Vol. 156, No. 1, 2010, pp. 20–31.

Journal of Testing and Evaluation

doi:10.1520/JTE20140125 / Vol. 43 / No. 2 / March 2015 / available online at www.astm.org

James C. Ni[1] and Wen-Chieh Cheng[2]

Field Response of High Speed Rail Box Tunnel During Horizontal Grouting

Reference

Ni, James C. and Cheng, Wen-Chieh, "Field Response of High Speed Rail Box Tunnel During Horizontal Grouting," *Journal of Testing and Evaluation*, Vol. 43, No. 2, 2015, pp. 398–413, doi:10.1520/JTE20140125. ISSN 0090-3973

Manuscript received March 20, 2014; accepted for publication October 27, 2014; published online December 12, 2014.

[1] Professor, Department of Civil Engineering, National Taipei Univ. of Technology (Taipei Tech), Taipei, 10608, Taiwan, e-mail: ckni@ntut.edu.tw

[2] Research Associate, College of Engineering, National Taipei Univ. of Technology (Taipei Tech), Taipei, 10608, Taiwan, (Corresponding author), e-mail: s2428030@gmail.com

ABSTRACT

The construction of two bored tunnels passing underneath an existing high speed rail (HSR) box tunnel needed to traverse obliquely through the diaphragm wall originally used for excavation and lateral support during construction of the HSR box tunnel. An access lift shaft was constructed adjacent to the HSR box tunnel diaphragm wall to provide access for the horizontal grouting equipment used to modify the surrounding soil to have sufficient water tightness and shear strength for safe tunnel eye creation and removal of steel H-beams left within the soil mixing wall. The grout block behind the tunnel eye was constructed first, followed by a long distance (up to 52 m) horizontal grouting (LDHG) program to form the other grout block around the steel H-beams. Since the grouted area was confined by a box tunnel on top and diaphragm walls on both sides, inappropriate grouting pressure could cause significant vertical movement of the HSR box tunnel above and potentially endanger the safety of the HSR service within. The grouting program was adjusted in accordance to real time box tunnel motion as detected by electronic beam sensors along the side walls of the box tunnel. Our strategies for overcoming the challenges associated with long distance horizontal wash boring through diaphragm walls, scattered with steel H-beams, and accompanying grouting strategy will be presented in this paper. The vertical movement of the HSR box tunnel during the LDHG program was well controlled to less than 4 mm, while the maximum lateral displacement of the shaft diaphragm wall was maintained below 9 mm.

Keywords

long distance horizontal grouting, high speed rail box tunnel, sleeve pipe grouting, diaphragm wall deflection, dual tube grouting

Introduction

The construction of a new tunnel adjacent to a pre-existing tunnel can cause impacts to the surrounding soil structures significant enough to induce stress changes in the tunnel lining and produce angular distortion of the existing tunnel. These distortions can exceed the existing tunnel's safety and serviceability limits and therefore must be accounted for during the planning and design stages of the new tunnel. This is of particular importance when the expected tunnel is to be constructed less than one tunnel diameter distance away from an existing tunnel [1–3]. Compensation grouting has been utilized to effectively reduce the settling of an overlying structure by injecting grout through sleeve pipes, known as tubes à manchettes (TAM), into the foundation soil of an overlying structure when a newly excavated tunnel is created underneath [4].

However, it is not always possible to construct these grouting holes from the ground surface or from the inside of a tunnel due to active tunnel traffic. Therefore, our solution utilized the construction of an adjacent lift shaft to provide sufficient access to place a series of horizontal grouting holes through the HSR box diaphragm wall to modify the soil's water tightness and strength, facilitating the removal of the underground H-beams within the expected path of the shield machine. The horizontal grouting can be conducted through either sleeve pipe with low pressure (TAM grouting) or through nozzle with high pressure (jet grouting). Horizontal jet grouting has been used to create an umbrella of canopy providing the pre-confinement ahead of the tunnel face for a subsequent safe boring environment with New Austrian Tunneling Method (NATM) [5–8]. The application of horizontal jet-grouting is difficulties for several reasons, including the back flow of excessive jet-grouting fluid to the excavation face resulting in settlement and excessive high jetting pressure causing heave to adjacent structures. Preventer valves and retainers at the mouth of the bore hole can control the outflow of solid or liquid spoils from drilling when the ground soil is sandy and susceptible to "piping" [5]. However, limiting the backflow may induce heaving and/or blow-ups, making proper control of flow volume critical in balancing the effects of settlement and heave, while undertaking horizontal jet grouting [5,9,10]. There are very few field observations on the behavior of adjacent underground structures in response to horizontal boring and grouting activities. The horizontal sleeve pipe grouting with low pressure providing easier control and less adverse effect was selected in this project. This paper presents the observed response of an active HSR box tunnel and nearby access shaft during the construction of a series of horizontal boreholes and grouting works.

Site Description

GEOLOGICAL CONDITIONS

As shown in **Fig. 1**, the site consists of a Holocene basin sediment (the Sungshan formation) of alternately silty clay and silty sand layers, of which six have been studied by many investigators [11,12] and a Pleistocene basin sediment (the Chingmei gravel formation). Piezometric level in Sungshan V fluctuated between 2.7 and 4.7 m below the ground surface. Since the water content of the silty clay soil in Sungshan II is near the liquid limit, it is sufficient for the clay to flow as a liquid. Piezometric level in the underlying gravel formation is 9.4 m below the surface.

DESIGN AND CONSTRUCTION

As diagramed in **Fig. 1**, the soil mixing walls (SMWs) containing randomly scattered steel H-beams left behind during the wall's construction were installed on both sides of the normal speed rail (NSR) box tunnel to provide lateral support during the tunnel's excavation. The HSR box tunnel is located between the NSR box tunnel SMW and a diaphragm wall measuring 36-m deep and 0.8-m thick. Two new 6.1-m diameter tunnels for the Sungshan Line of the Taipei Rapid Transit System (TRTS) were to be bored by the earth pressure balance (EPB) shield machine at a depth ranging from 26 to 28 m. They were planned to pass underneath the existing HSR and NSR tunnels and pass through the NSR SMW and the HSR diaphragm wall at an angle of 60°. To remove the steel H-beams within the SMW and allow for unimpeded shield tunneling, the strength and permeability of the surrounding soil required augmentation to facilitate H-beam removal.

Boring and installing TAM grouting tubes from the ground surface or from within the box tunnel were not possible due to existing traffic. As seen in **Figs. 1** and **2**, a vertical shaft next to the HSR box tunnel diaphragm wall was constructed to provide access to form grout block B and block C in order to create the tunnel eyes and remove the steel H-beams within the SMW before shield machine passing through from north.

Prior to the construction of the grout blocks B and C, a series of soilcrete columns were jetted to form a 4-m thick grout slab below the final excavation level to reduce the diaphragm wall deflection and possible side effects to the HSR box tunnel. As the shaft diaphragm walls were not embedded into impermeable layer, a 7-m thick grout plug at the elevation ranging from 59.4 to 52.4 m was constructed to provide sufficient weight against buoyancy force during excavation from within the shaft.

On the other hand, as the shield machine would resume its drilling again from south, block A (**Figs. 1** and **2**) was utilized to prevent water ingress while breaking down the tunnel eye.

MONITORING INSTRUMENTS

Tunnel movement was monitored in real time with 101 beam sensors installed on both side walls of the HSR box tunnel [13] in conjunction with optical prisms and tiltmeters during the construction of the access shaft, excavation from within, and the horizontal wash boring and grouting works. During the excavation from within the access shaft, inclinometers inside

FIG. 1

Geological profile view with relative locations of the HSR and NSR box tunnels and grout blocks.

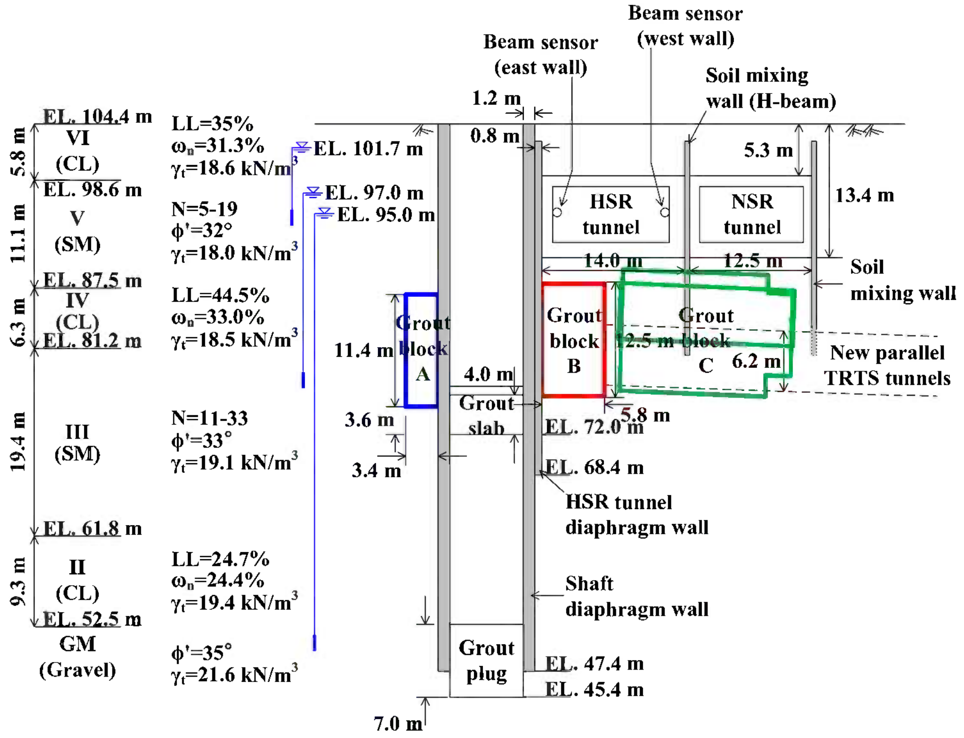

the diaphragm wall and vibrating wire strainmeters attached to struts were utilized to monitor wall deflections and strut forces. The layout of instruments is shown in **Fig. 2**.

Grouting Works

SLAB GROUTING

After installation of the shaft diaphragm wall (**Fig. 3(*a*)**), a double-fluid jet grouting was conducted from the ground surface to construct 140 1.6-m diameter overlapped soilcrete columns, of which 71 were jetted inside the access shaft C–W and the rest inside the access shaft C–E, forming a 4-m thick grout slab at the elevation ranging from 76 to 72 m (**Figs. 1** and **3(*b*)**).

A slag cement based grout (**Table 1**) was jetted at a pressure of 60 kN/m^2 within a protective conical shroud of pressurized air jet, which prevents significant pressure drop as the grout exits the nozzle and thereby allows increased radial penetration

FIG. 2

Plan view of the site and layout of monitoring instruments.

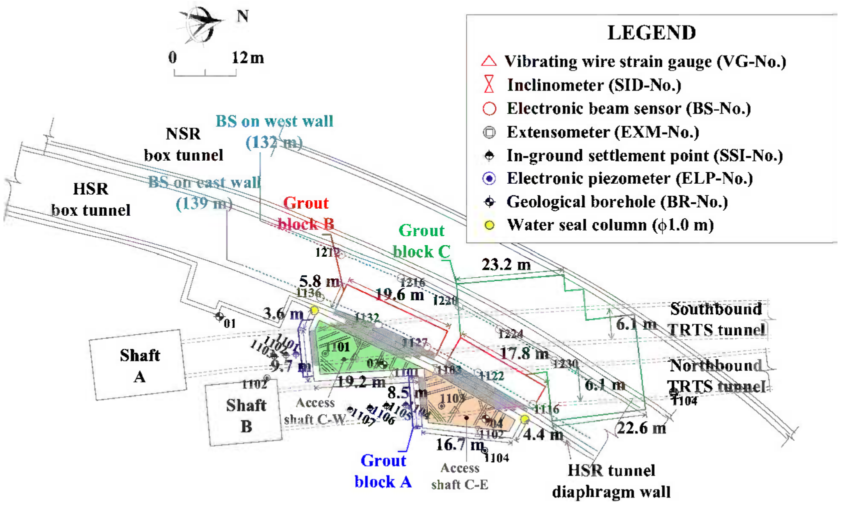

FIG. 3

Construction sequence for various grouting works inside and outside the access shaft.

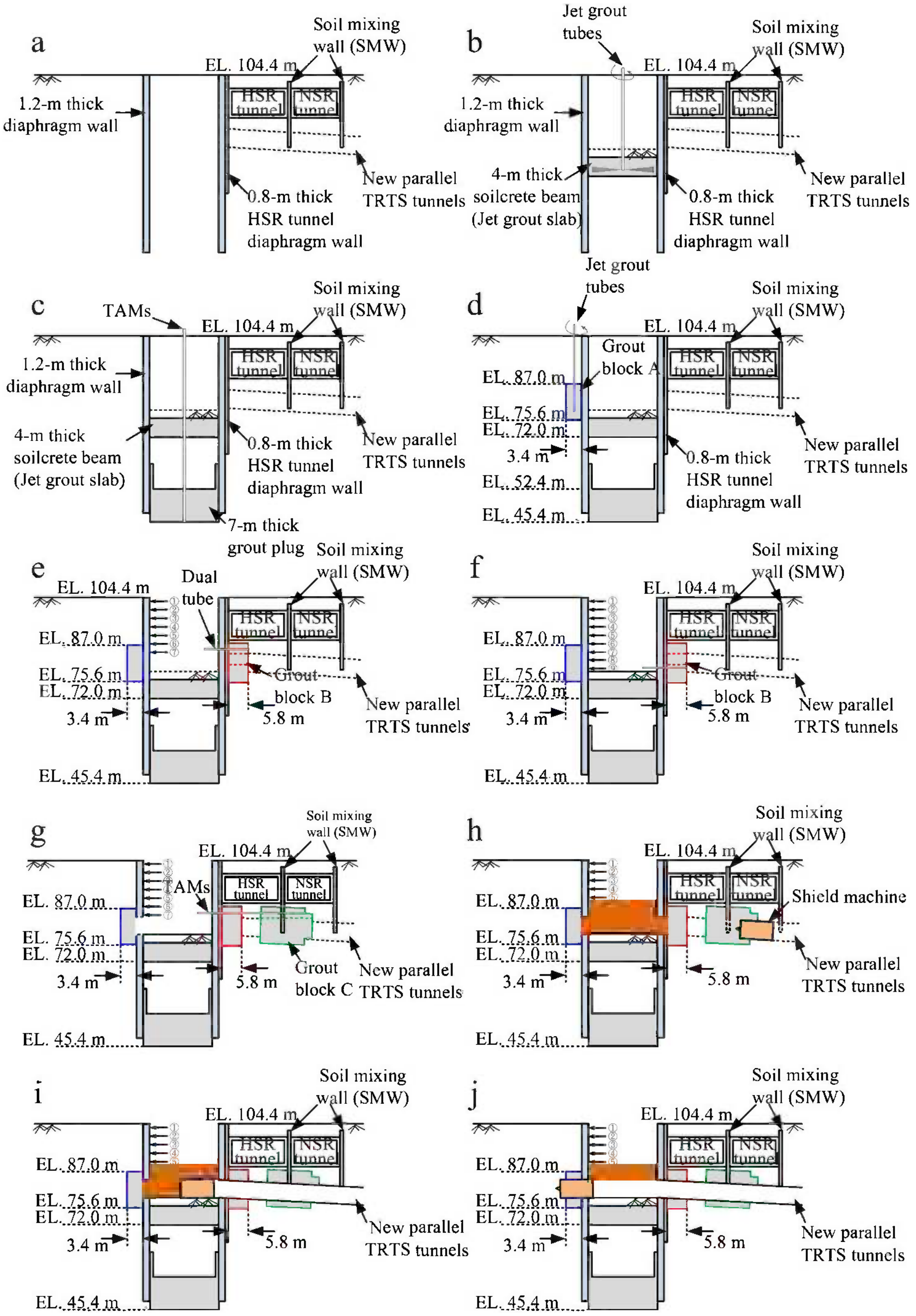

into the surrounding soil (larger column diameter). The columns were placed in a triangular arrangement with a center-to-center spacing of 1.3 m.

PLUG GROUTING

The vertical sleeve pipe grouting was then undertaken from the ground surface to construct a 7-m thick grout plug at an elevation ranging from 52.4 to 45.4 (**Figs. 1** and **3(*c*)**). The grout tube assembly consisted of a series of 33 cm long sleeve pipes. The cement-bentonite (CB) grout (**Table 2**) with injection rate of 8–15 l/min was used in the first phase to fill in large soil voids, and the silicate (SL) grout (**Table 3**) with a gel time of 60 min

TABLE 1 Mix of 6.5 h gel time grout (slab grouting) (1000 l).

	Slag Cement (154 l)	Water (846 l)
Cement (kg)	120	
JG hardener (kg)	280	

TABLE 2 Mix of CB grout (plug grouting).

Mix of CB grout (1000 l)	
Cement (kg)	150–250
Bentonite (kg)	50–80
Water (kg)	425–650

was grouted into small soil pores at a rate of 8–12 l/min in the second phase. After the grout plug construction, a pumping test confirmed the water tightness of the region within the shaft as well as between grout slab and grout plug.

"BLOCK A" GROUTING

A triple-fluid jet grouting, known as Rodin Jet Pile (RJP), was conducted from the ground surface to construct 19 2.3-m diameter jet grout columns, forming two soilcrete blocks (grout block A in **Figs. 1**, **2** and **3(*d*)**) at an elevation ranging from 87 to 75.6 m, of which one (1.9 by 9.8 by 11.4 m) is outside the access shaft C–E and the other (1.9 by 10 by 11.4 m) outside the access shaft C–W. Triple-fluid jet grouting eroded ground soils using a pressurized water jet of 19.6 MN/m^2 through a nozzle within a conical air jet shroud, and the spoils were then replaced by cement grout (**Table 4**) jetted with a pressure of 39.2 MN/m^2 through another nozzle to produce jet grout columns. To prevent any possibility of water leakage through either an untreated area in the soilcrete block or within cleavages formed between the soilcrete block and the diaphragm wall from diaphragm wall deflection during excavation, dual tube grouting was undertaken in the perimeter of the jetted columns to provide additional water sealing effect. **Table 5** shows the grout mix. Unconfined compressive strengths of the cored samples cured for 28 days from grout block A were in a range of 2.5–6.2 MN/m^2. Hydraulic conductivity in the grout block was less than 6.7×10^{-6} cm/s.

"BLOCK B" GROUTING

As seen in **Figs. 1** and **2**, grout block B is confined by the HSR box tunnel on the top and diaphragm walls on both sides, improper grouting protocol may cause impacts to the overlying structure and have an adverse influence on the normal operation of the HSR box tunnel.

Grouting was undertaken by injecting quick-setting grout first and slow-setting grout next for each of stage grouting with dual tube, which was drilled horizontally through the shaft and existing diaphragm walls to a distance of 5.8 m, as shown in **Fig. 3(*e*)**. If water ingress from grout hole exceeded 0.1 l/min during boring, the SL grout (**Table 3**) was injected to minimize ground loss.

TABLE 3 Mix of 1 h gel time SL grout (grout block C).

Mix of SL Grout (1000 l)	
Water glass (l)	250
SL actor (l)	40–60
Water (l)	690–710

TABLE 4 Mix of 7.8 h gel time grout (grout block A) (1000 l).

Slag Cement (205 l)		Water (795 l)
Cement (kg)	180	
JG hardener (kg)	420	

Whenever grout take reached estimated grout volume or a threshold grouting pressure was reached, grouting ceased, the dual tube was pulled back 25 cm for the next grouting stage. The threshold grouting pressure was set as system initial pressure plus 490 kN/m^2. During dual tube grouting, the supply line for grout A and grout B is shown in **Fig. 4**. By manipulating the on/off valve of grout B, the dual tube can provide either quick set grouting or slow set grouting. **Table 5** shows the grout mix.

The layout of grouting holes on the diaphragm wall at tunnel eyes is shown in **Fig. 5**. The block B grouting worked its way from the upper portion (after eighth stage of excavations) then the middle portion (after ninth stage of excavations), followed by the lower portion (after final excavation, as shown in **Fig. 3(*f*)**). The permeability in grout block B was verified by measuring water leakage from the leakage check holes of 2-m in length shown in **Fig. 5**.

LONG-DISTANCE HORIZONTAL GROUTING ("BLOCK C" GROUTING)

Both ground penetrating radar (GPR) and electrical resistivity tomography (ERT) surveys failed to localize the steel H-beams left in the SMW between the HSR and NSR box tunnels along the course of the planned tunnels. Therefore, long distance horizontal grouting (LDHG) was utilized to locate the H-beams and simultaneously augment the surrounding soil to facilitate their future removal, as shown in **Figs. 1**, **2**, and **3(*g*)**. After grout Block C was completed, the reinforced concrete at tunnel eyes

TABLE 5 Characteristics of the chemical grouts (grout block A and B).

RMG S2 (Gel Time: 5–10 s) (1500 l)			
A Liquid (1000 l)		B Liquid (500 l)	
Water glass (l)	250	Water glass (l)	125
NGA (l)	20–23	Water (l)	375
GS (l)	27–30		
Water (l)	700		
RMG L3 (Gel Time: 20–60 min) (A Liquid) (1000 l)			
Water glass (l)	250		
NGA (l)	20–23		
GS (l)	27–30		
Water (l)	700		

FIG. 4

Dual tube grouting system.

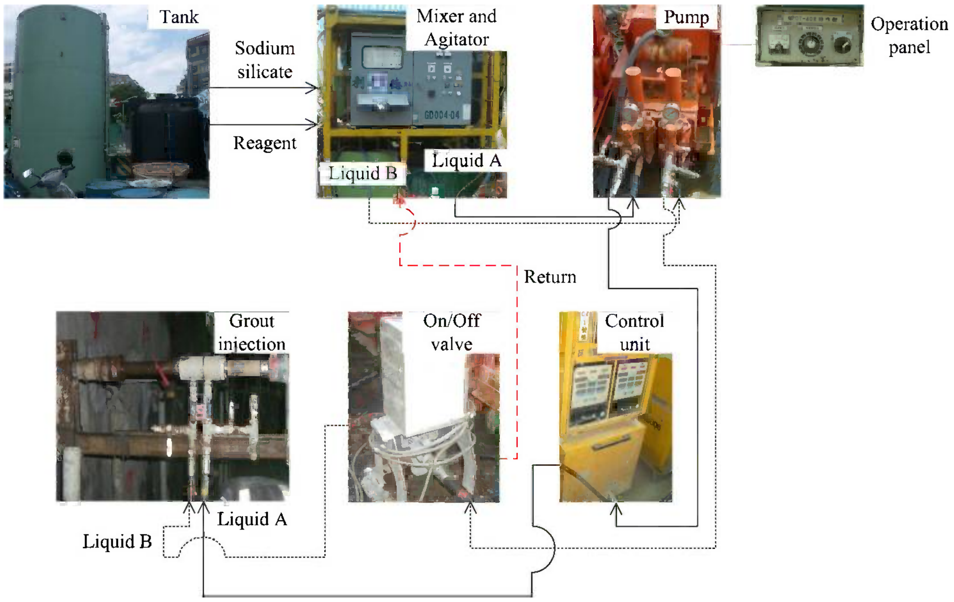

was removed as shown in **Fig.** 3(*h*). Then the backfill in the access shaft and the breakthrough of the shield machine are demonstrated in **Figs.** 3(*i*) and 3(*j*), respectively.

The drill pipes are required to both be able to maintain the borehole along its length and of sufficient stiffness to drill through a steel H-beam in order to install horizontal grouting sleeve pipes. One large size of boring casing with diameter of 196 mm, three drill pipes with diameters of 152, 118, and 89 mm, and associated hardware such as three packers and two one-way valves were used. The construction sequence of the horizontal grouting hole is illustrated with six schematic diagrams as shown in **Fig.** 6 and is further detailed below.

Figure 6(*a*) shows that a 196-mm diameter guiding bore casing is first inserted into the borehole, drilling through the diaphragm wall to facilitate the subsequent long distance drilling and set up a valve for the cuttings and drilling fluids to return. Next, a 152-mm diameter drill pipe is drilled 27 m into soil up to the steel H-beam. A one-way valve at the tip of 152-mm diameter drill pipe and a rubber packer are used to force the drilling fluids and cuttings to drain through the annular space between 196-mm casing and 152-mm diameter drill pipe. **Figure** 6(*b*) illustrates a 118-mm diameter drill pipe equipped with a cutter bit at the tip is utilized to drill through both the 152-mm pipe one-way valve and steel H-beam as well

FIG. 5

Schematic illustration showing the layout of horizontal grouting holes for Block B and corresponding geological profile.

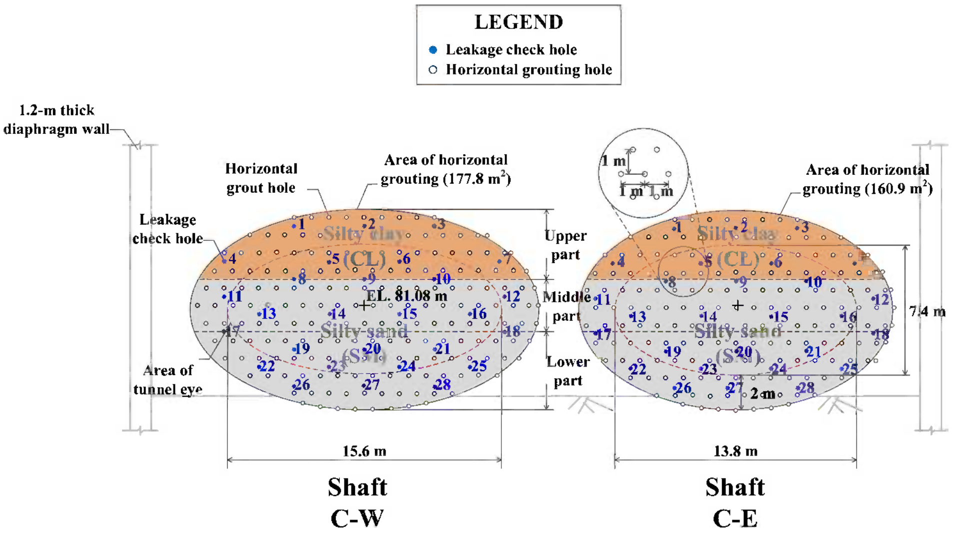

FIG. 6

Construction sequence of a horizontal grouting hole: (*a*) install 196-mm diameter guiding casing and drill 152-mm diameter drill pipe up to H-beam, (*b*) advance drill bit affixed to 118-mm diameter drill pipe through H-beam to obtain samples, (*c*) replace drill bit on 118-mm diameter drill pipe with a one-way valve at to continue boring in soil, (*d*) drill an 89-mm drill pipe through one-way valve of 118-mm diameter drill pipe, (*e*) install TAMs with spring hook at the tip, and (*f*) recover boring casing, drill pipes and rubber packers.

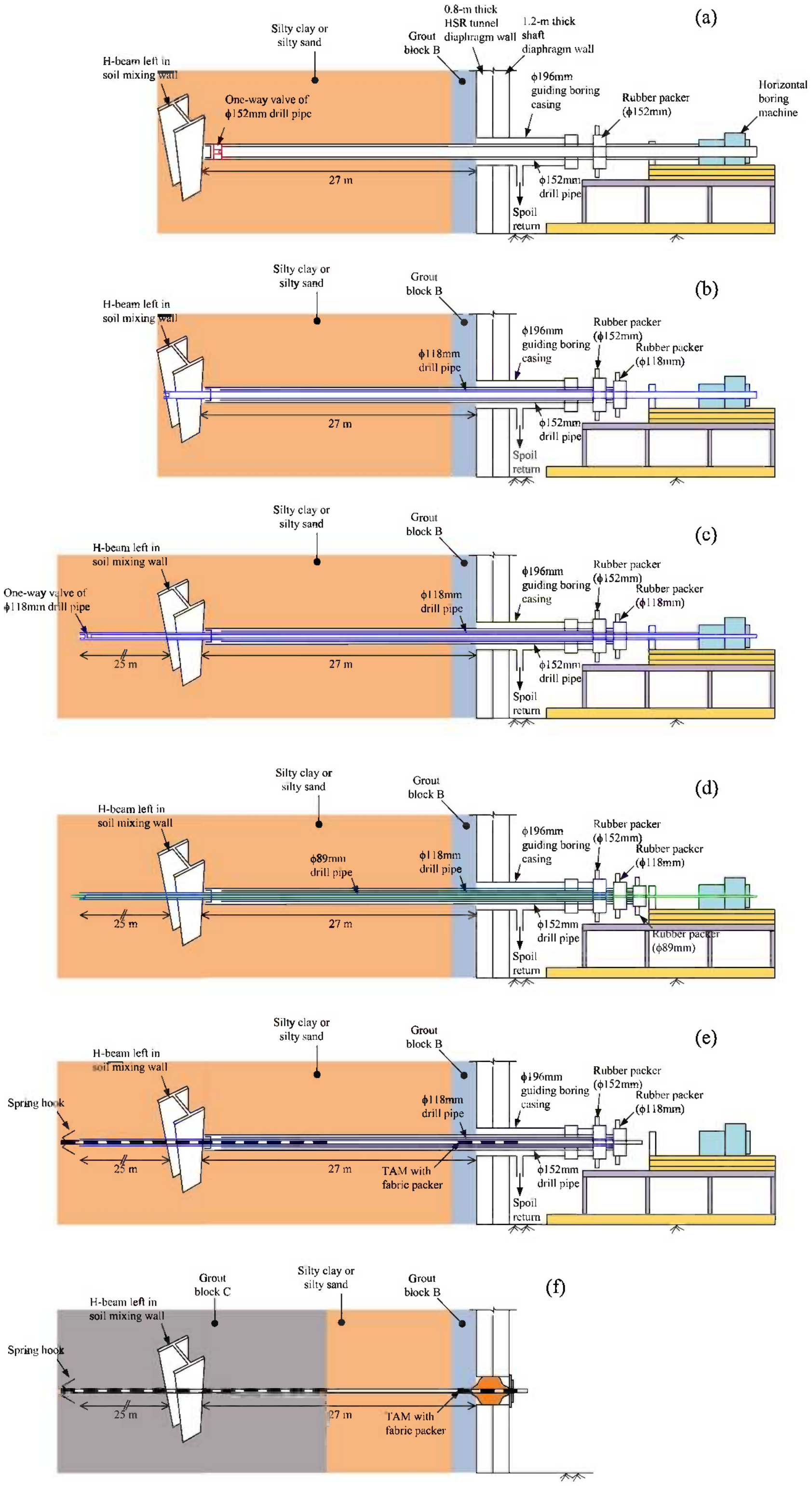

as collect core samples. **Figures 7(*a*)** and **7(*b*)** show fragments of the steel H-beams recovered from the extracted soil samples. **Figure 6(*c*)** illustrates the replacement of the 118-mm pipe cutter bit with a one-way valve for the remainder of the boring.

Figure 6(*d*) shows the 89-mm diameter drill pipe boring through the one-way valve of the 118-mm diameter drill pipe and exchanged for a customized TAM sleeve pipe. **Figure 6(*e*)** displays the customized TAM sleeve pipe with a spring hook at the

FIG. 7

(*a*) and (*b*), core samples containing H-beam fragments (refer to **Fig. 8** for the numbering system); (*c*) and (*d*) removing H-beam in grout block ahead of cutting disc (the numbering indicates the beam removal sequence).

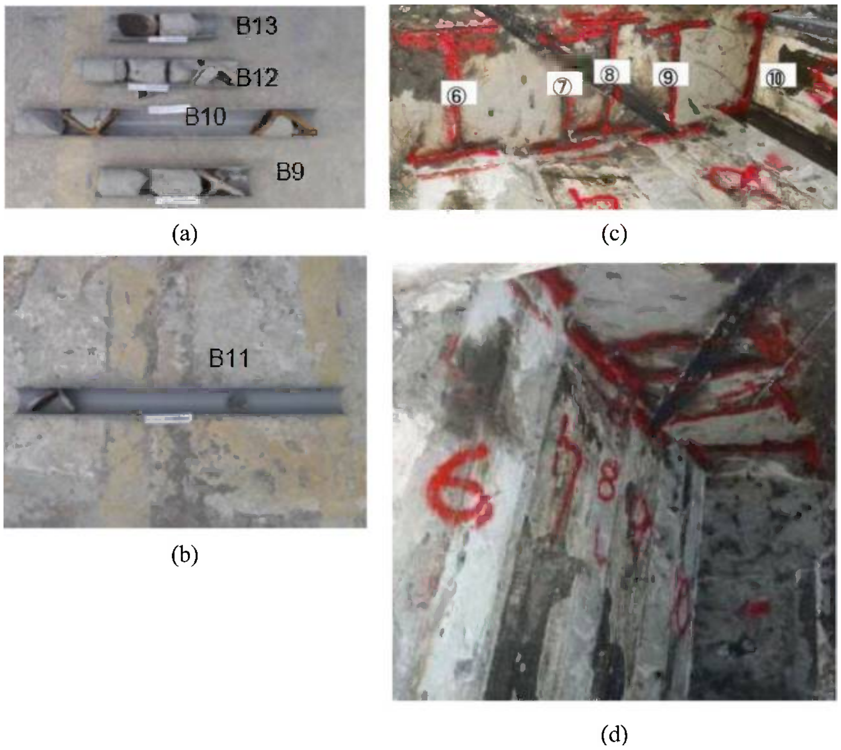

tip is inserted inside the 118-mm diameter drill pipe, then the annular space between TAM and ground soil is backfilled first with CB grout (**Table 6**) and then SL grout (**Table 3**) after the two drill pipes (ϕ)118 and ϕ152 mm and the outer casing (ϕ196 mm) are sequentially recovered. The fabric packer shown in **Fig. 6(*f*)** is utilized to seal the annular space between TAM and diaphragm wall to prevent grout from seeping around the TAM sleeve pipe while grouting block C. **Figure 8** shows the layout of the LDHG holes.

To avoid causing substantial heave to the overlying HSR box tunnel while performing grouting at a constant injection rate in such a confined space [14,15], grouting of the current stage would cease and move onto the next grouting stage as the following criteria were achieved:

(1) The measured grout take achieves the designed grout take.

(2) The grouting pressure exceeds the system initial pressure plus 98–196 kN/m^2.

(3) The grouting pressure reaches the threshold of 2.5 MN/m^2.

TABLE 6 Mix of CB grout (grout block C).

Mix of CB Grout (1000 l)	
Cement (kg)	100–250
Bentonite (kg)	50–80
Water (kg)	890–950

The hydraulic conductivity of core samples from Block B and C was tested and did not exceed 1×10^{-5} cm/s, with an average 28-day unconfined compressive strength of 0.4 MN/m^2.

Results and Discussion

HSR TUNNEL RESPONSE DUE TO THE CONSTRUCTION OF ACCESS LIFT SHAFT DIAPHRAGM WALL

A total of 23 1.2-m thick, 57-m deep diaphragm wall panels are installed next to the diaphragm wall of HSR box tunnel. It can be seen from **Fig. 9** that the maximum settlement of 4.7 mm at the east wall of HSR box tunnel is larger than the west wall's settlement of 2.1 mm. From this, it can be considered that either the skin friction on one side of the diaphragm wall of HSR box tunnel decreased or that the surrounding soil next to the HSR box tunnel diaphragm wall might have been disturbed during the construction of the diaphragm wall of access shaft. The length of the tunnel, exceeding 130 m, was affected by the differential settling resulting from the construction of the diaphragm wall, as shown in **Fig. 9**.

HSR TUNNEL RESPONSE TO SLAB GROUTING

Slab grouting within the access shaft generated excess porewater pressure in surrounding soil, which resulted in the diaphragm

FIG. 8

Layout of long distance horizontal grouting holes for Block C.

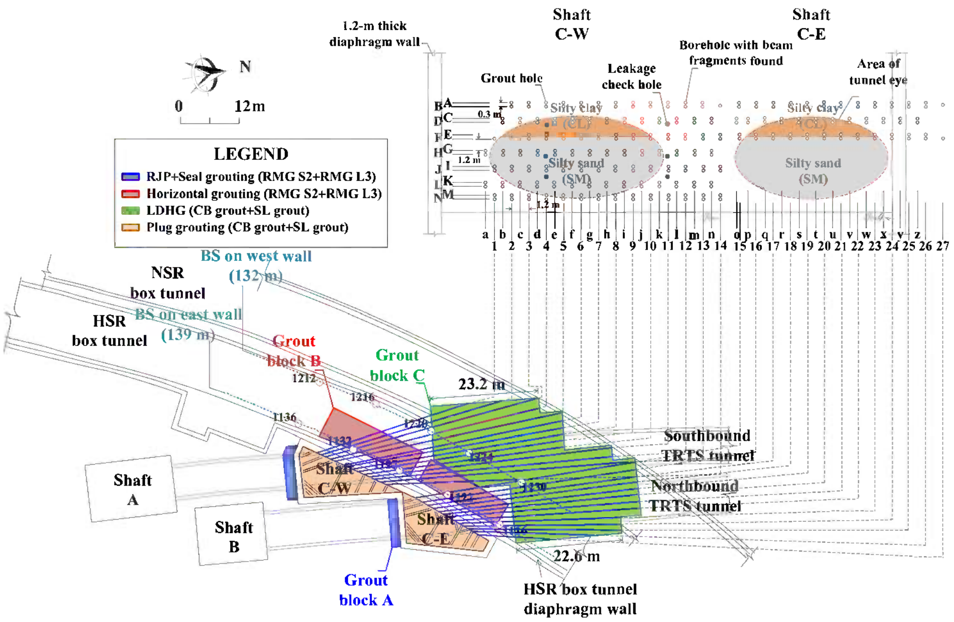

FIG. 9

Observed HSR tunnel settlement profiles during diaphragm wall construction and various grouting works; (*a*) HSR tunnel settlement profiles from beam sensors on west wall and (*b*) HSR tunnel settlement profiles from beam sensors on east wall.

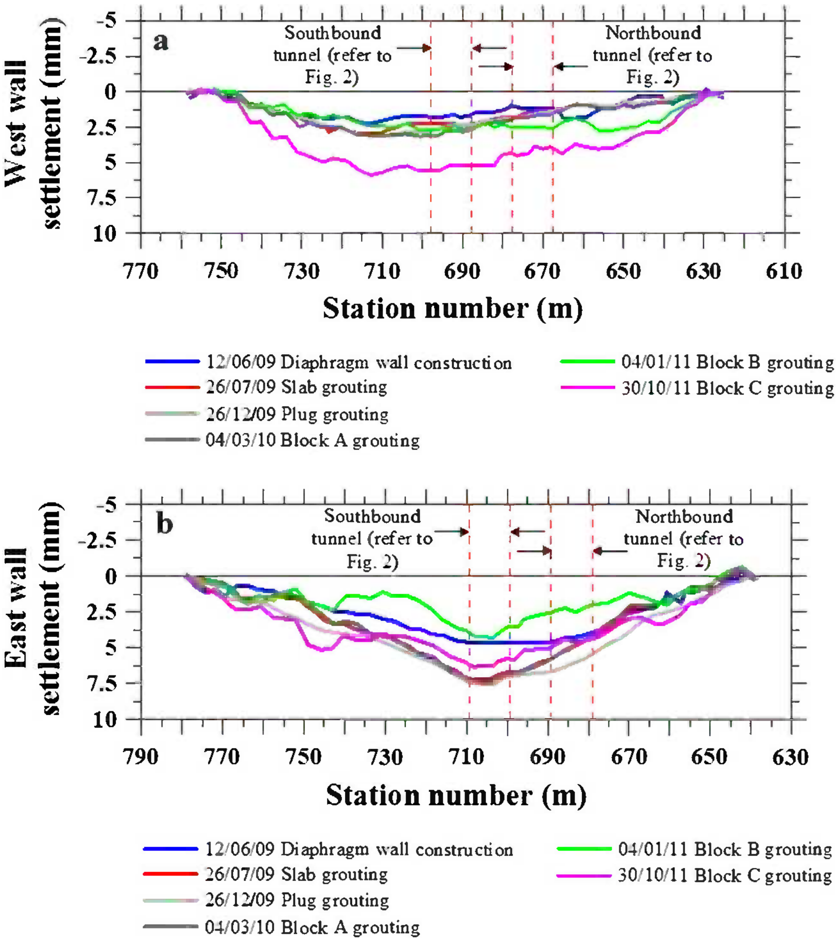

FIG. 10

Observed diaphragm wall deflection at inclinometer SID-1101 and SID-1103 before and after the slab grouting.

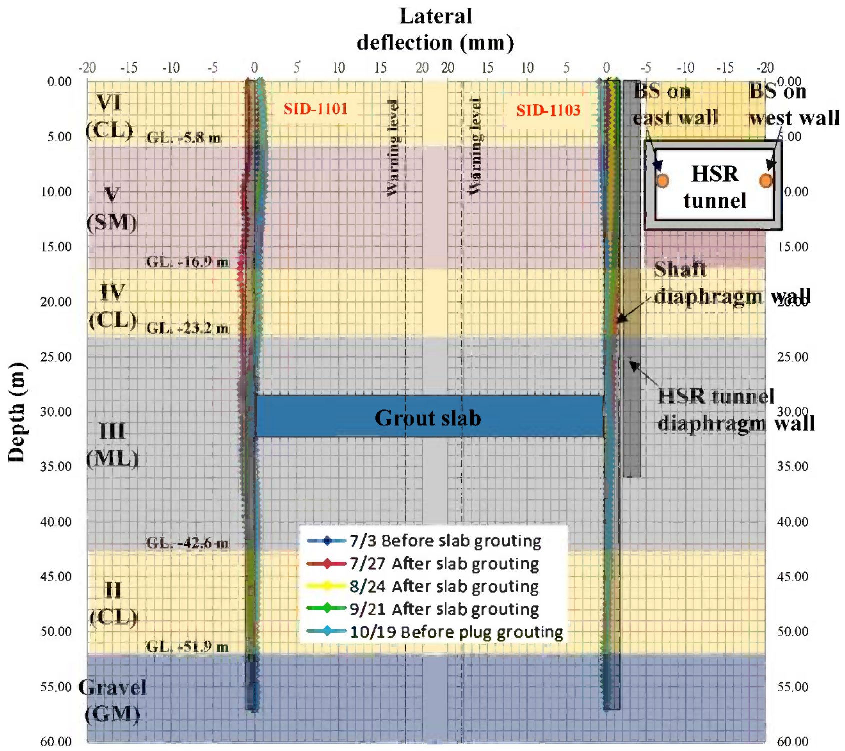

wall deflection. **Figure 10** shows that the largest outward deflection of the first wall furthest away from tunnel (SID-1101) is 2 mm, while the second wall closer to tunnel (SID-1103) moved an insignificant amount. This is due to the fact that the second wall had additional support from the adjacent diaphragm wall of the box tunnel to resist deflection from the grouting pressure. Therefore, it can be concluded that the slab grouting in access shaft should not have a significant impact on the box tunnel.

However, **Fig. 9** shows that the largest vertical movement at the west wall of the box tunnel increased from 2.1 to 3.4 mm and the east wall increased from 4.7 to 7 mm. The discrepancy from above can be explained by the construction of the shaft diaphragm wall, for which the water content of the founding soil, silty clay soil in Sungshan II, is very close to liquid limit, so that it can easily get softened once disturbed or even washed away as subjected to large hydraulic gradients. Then excess porewater pressure generated because of external excitation will dissipate gradually, resulting in consolidation and settlement in a later stage [16–20].

HSR TUNNEL RESPONSE TO PLUG GROUTING

As seen in **Fig. 11**, the maximum wall deflection, recorded as a result of the plug grouting, was 5 mm at the depth of 46 m, which was located in the soft silty clay layer of Sungshan II. It is believed that this very soft silty clay layer cannot provide the diaphragm wall with sufficient passive force to resist grouting pressure, resulting in the largest deflection but at a point 6 m away from the grouting plug. **Figure 11** also discloses one interesting fact that the wall deflection becomes smaller and smaller over time after cessation of the plug grouting. The outward deflection of the diaphragm during grouting is the result of excess porewater water pressure, and the subsequent reversal of the diaphragm wall deflection back to baseline is the result of the dissipation of that excess porewater pressure after cessation of grouting activities [13,19]. This can be confirmed by the observed settlement profiles of box tunnel showing no significant change before and after plug grouting as shown in **Fig. 9**.

HSR TUNNEL RESPONSE TO "BLOCK A" GROUTING

As displayed in **Fig. 12**, SID-1103 deflects 3 mm toward the box tunnel after block A grouting, whereas SID-1101 undergoes a greater deflection of 6 mm at a 20 m of depth in the same direction. Again, the wall nearest the tunnel receives additional support from the adjacent diaphragm wall of box tunnel to resist deformation from the grouting pressure. Therefore, block A grouting should not cause any significant change to the behavior of box tunnel. In addition, the influence on porewater pressure from the previous construction of shaft diaphragm wall dissipates with time before block A grouting starts. This explains why the settlement profile of the HSR box tunnel is nearly unchanged before and after block A grouting, as shown in **Fig. 9**.

FIG. 11

Observed diaphragm wall deflection at inclinometer SID-1101 and SID-1103 before and after the plug grouting.

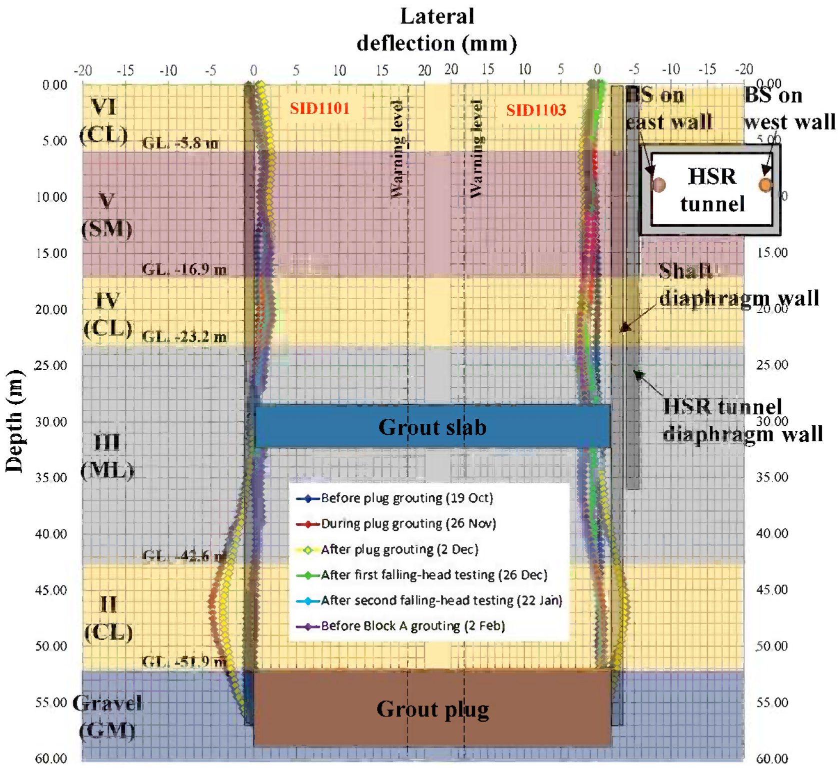

FIG. 12

Observed diaphragm wall deflection at inclinometer SID-1101 and SID-1103 before and after the Block A grouting.

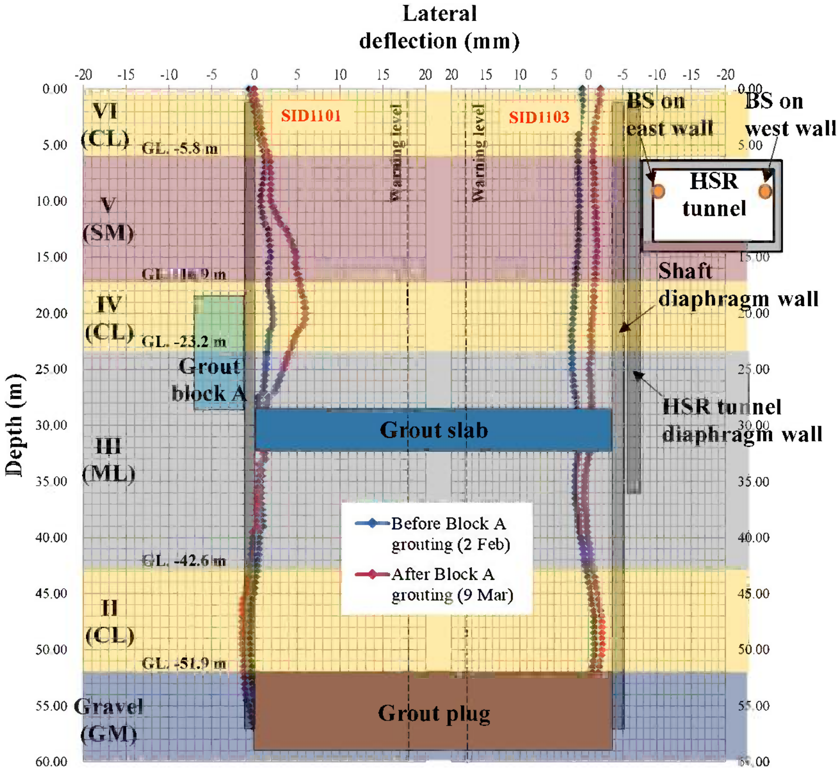

HSR TUNNEL RESPONSE TO "BLOCK B" GROUTING

The first seven alternating stages of excavation and shoring processes in the access shaft were conducted first (**Fig. 3(*e*)**), and from that point forward, each subsequent stage of excavation and shoring activities was followed by both boring and grouting to construct grout block B until the final stage. **Figure 13** shows the variations of HSR tunnel vertical movement, wall deflection at SID-1103, and strut force during excavating, shoring, boring, and grouting works. The wall deflection varies up and down, relating to excavation and shoring activities, respectively, but in an increasing trend from stage one to stage seven. In general, the HSR box tunnel tended to settle slightly at the east wall, while remaining nearly unchanged at the west wall and moving upward in response to strut preloading. This is due to the diaphragm wall deflection relieving the in situ stress of adjacent soil underneath the box tunnel, resulting in its settlement.

During the excavation of stage eight, the dual tube grouting assembly was located next to the invert of the box tunnel, as shown in **Fig. 3(*e*)**. It can be seen from **Fig. 13** that the boring process relieved the local soil stress resulting settlement, whereas the grouting process increased local soil pressure, thereby inducing heave to the box tunnel above. The box tunnel displacement is larger at the east wall than the west wall because block B grouting is undertaken near the east wall, resulting in larger porewater pressure acting on the eastern part of the box tunnel foundation due to grouting pressure. The settlement profile shown in **Fig. 9** confirms that this grouting pressure actually caused substantial heave to the tunnel east wall above than the west wall. We noted the distance of boring and grouting from the box tunnel is important, as the subsequent boring and grouting located deeper and further from the box tunnel invert resulted in smaller box tunnel displacement than the eighth stage. In general, strut force increases in the subsequent excavating process and decreases after the next level strut is preloaded during the seven alternating excavating and shoring processes. The horizontal dual tube boring process has no influence on existing strut force, but the grouting process at grout holes between the ninth and tenth stages of excavations does increase the existing strut force significantly (**Fig. 13**). It is considered that the grout block B is adjacent to the seventh, eighth, and

FIG. 13

Variation of HSR tunnel vertical movement, wall deflection at SID-1103, and strut force during shaft excavation and various grouting works.

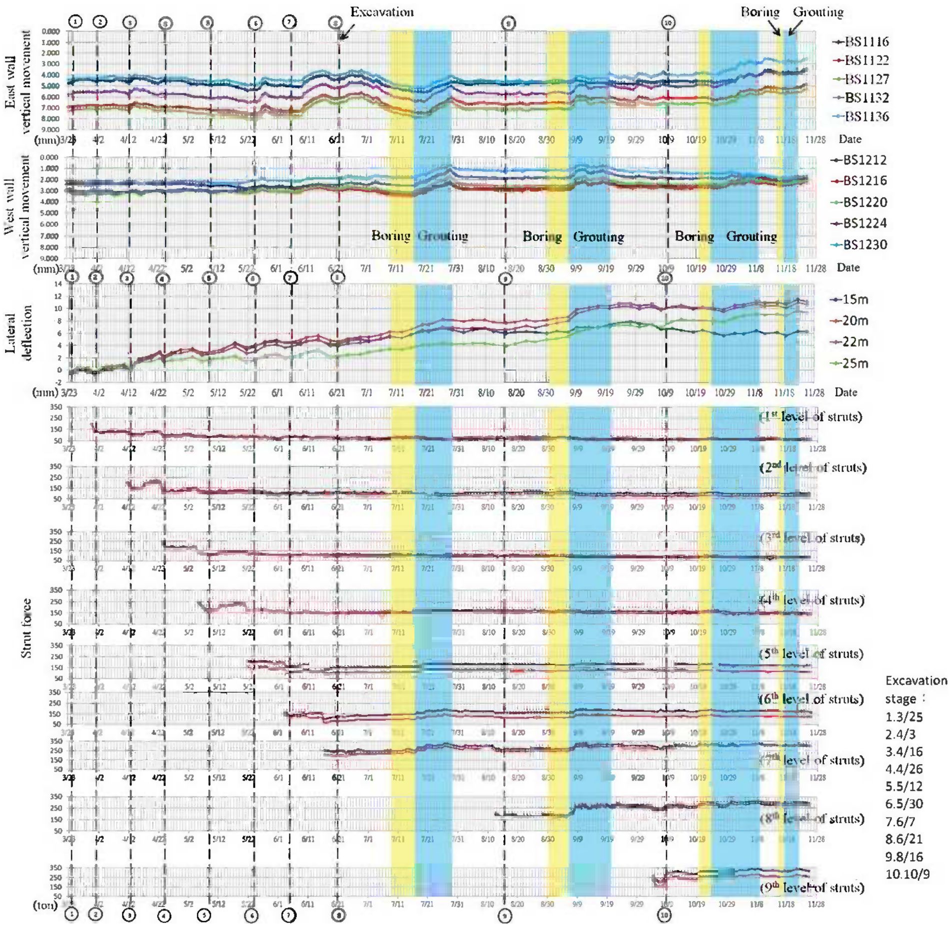

FIG. 14

Relationship between HSR tunnel vertical movement and grout take (*top*) due to nine TAMs grouting (*bottom*).

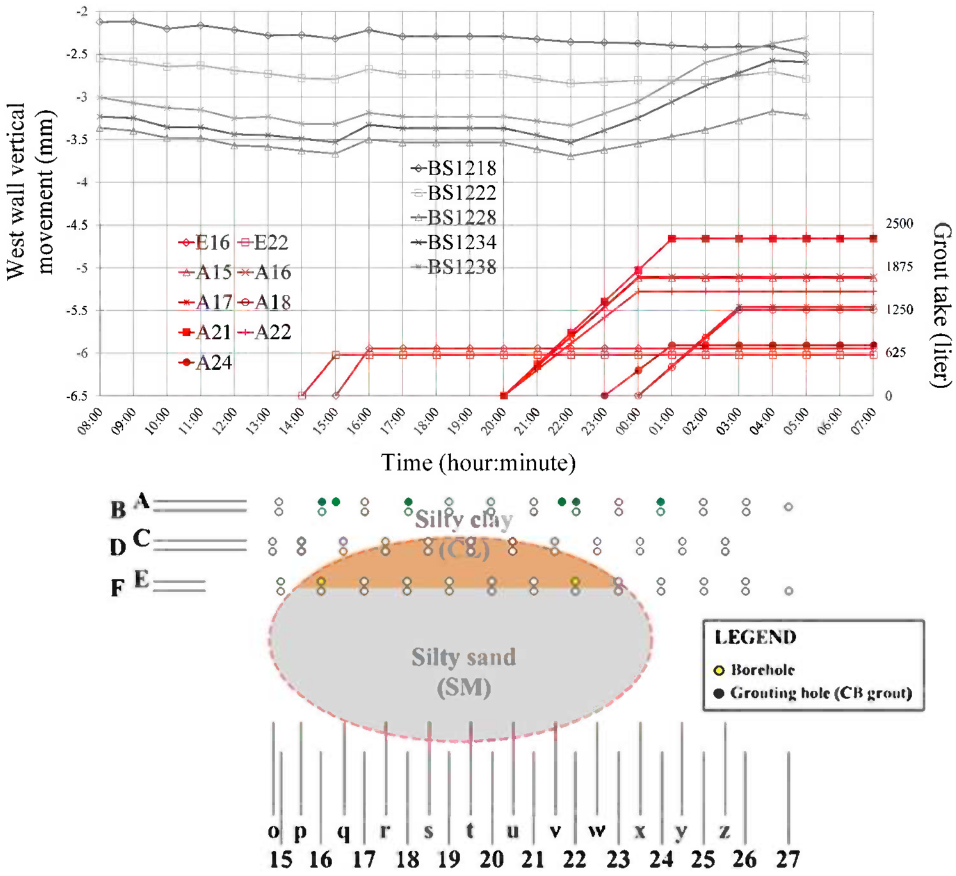

ninth level of struts (**Figs. 3(*e*)** and **3(*f*)**), and grouting pressure deflects the diaphragm wall and increases the strut force accordingly [21].

HSR TUNNEL RESPONSE TO "BLOCK C" GROUTING

Figure 16 shows the observed vertical displacements at the box tunnel's east wall and west wall as well as diaphragm wall deflection at SID-1103 during long distance boring and sleeve pipe grouting (**Fig. 8**) under both the HSR and NSR box tunnels. Since grout block C is located underneath the west wall of the HSR box tunnel, any boring and grouting activities should have direct influence on HSR box tunnel west wall above more than east wall. It can be observed from **Fig. 16** that SID-1103 undergoes a largest deflection of 8.8 mm at a depth of 22 m toward excavation side. The observed largest vertical movement change of 3.4 mm in **Fig. 16** at the west wall moving upward due to grouting and downward due to boring, rather than a change of 1 mm at the east wall, confirms the speculation above. In addition, the variation of vertical movement at the west wall is smaller when boring or grouting is conducted in the silty sand deposit rather than in the silty clay deposit (**Fig. 16**). This fact can be contributed by two factors. One is that the grouting pressure in clay will induce the same amount of excess porewater pressure as in an undrained condition, resulting in larger upward thrust force to tunnel box [5,19]. The other is that the grouting area in this silty clay deposit is closer to the box tunnel foundation than the sand deposit, resulting in larger grouting pressure and upward movement. In order to analyze this behavior precisely, the careful selection of field observation data to exclude the coupled effect between boring and grouting is necessary. The following describes two case studies highlighting the differential response of the overlying HSR box tunnel in silty clay versus in silty sand deposits.

In the first case, two horizontal boreholes in the soft silty clay deposit were constructed for six daytime hours and then grouting was conducted sequentially in nine grout holes, as shown in **Fig. 14**. Since the boring started, the HSR box tunnel west wall had experienced gradual and steady settlement of 0.3 mm 1 h after the end of boring activities, as shown in **Fig. 14**. The boring was followed by horizontal grouting for 7 night-time hours. Over 10 000 l of the CB grout were injected during that time and resulted in 1 mm of upward displacement of the box tunnel.

In the second case, one horizontal borehole in loose silty sand deposit was constructed during 6 daytime hours and then followed by 7 night-time hours of grouting conducted

FIG. 15

Relationship between HSR tunnel vertical movement and grout take (*top*) due to eight TAMs grouting (*bottom*).

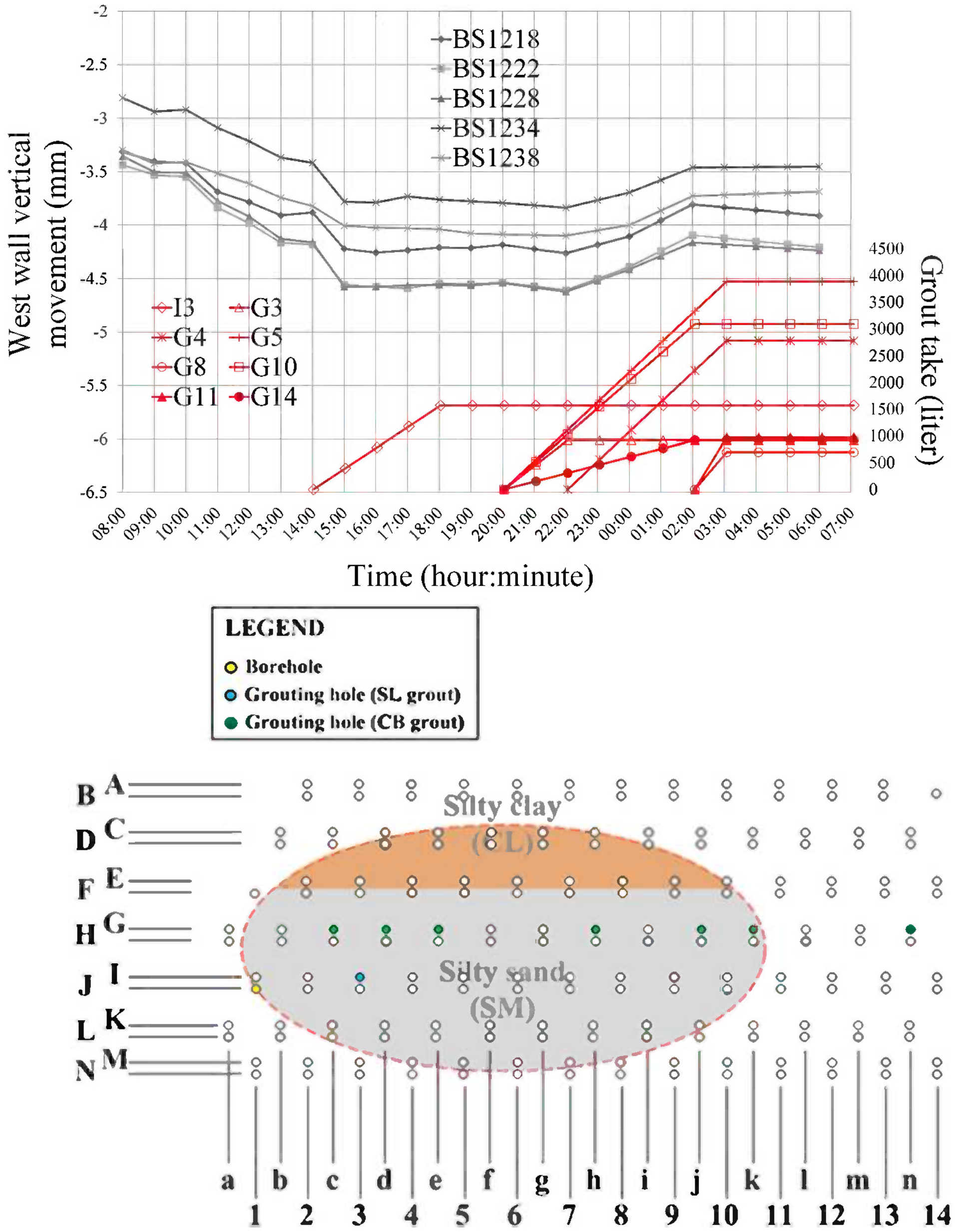

sequentially through adjacent eight grout holes as shown in **Fig. 15**. Similarly, the HSR box tunnel west wall gradually and steadily settled 1.3 mm since the boring commenced, as shown in **Fig. 15**. No further settlement was observed prior to the commencement of the horizontal grouting, which injected 15 000 l of the SL grout and resulted in 0.5 mm of upward displacement of the box tunnel, as shown in **Fig. 15**.

As observed, two holes boring in clayey soil resulted in a 0.3-mm settlement of the box tunnel, whereas a single hole boring in sandy soil caused 1.3 mm settlement. This is because the wash boring process in sandy soil causes washout and an associated larger settlement that is different from that in clayey soil. It is also observed that the 10 000 l grout take in the clayey soil is less than 15 000 l in the sandy soil, and the 1 mm heave of the box tunnel in clayey soil is larger than 0.5 mm in sandy soil. It is logical to say that the void in soil created by washout during the boring process will be backfilled with the same amount of grout during the subsequent grouting process. However, the grouting in silty clay receiving less grout results in a larger heave of the box tunnel than in silty sand receiving more grout. Because grouting pressure can induce the same amount of excess porewater pressure in saturated silty clay due to its very low permeability, grouting pressure can be transmitted a longer distance with less dissipation, resulting in greater vertical box tunnel displacement than in the sandy soil with high permeability [19,20].

FIG. 16

Observed vertical movements of east and west wall and diaphragm wall deflection at inclinometer SID-1103 during the Block C grouting.

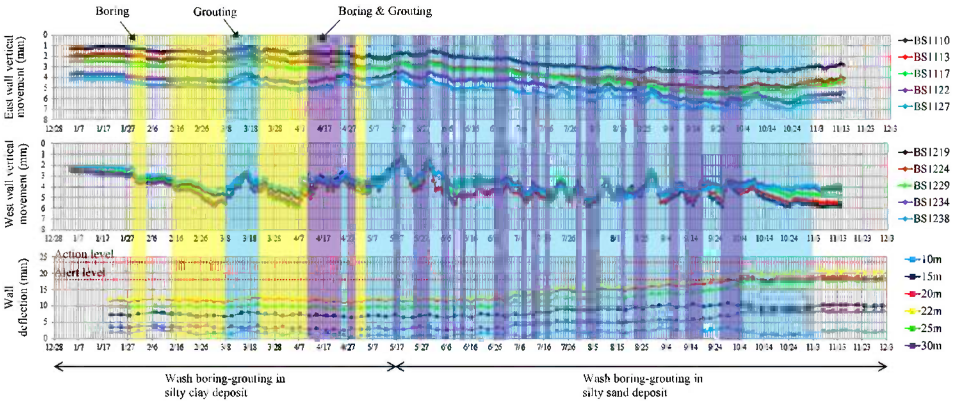

The designated sleeve pipe grouting for grout block C improves soil's strength and permeability by forcing grout fracturing or permeating to mix with in situ soil. However, the greater amount of grout injected, the larger the noted heaving to overlying structures. Therefore, the grouting strategy utilized the washout during boring to create sufficient space to subsequent grouting in order to minimize overhead heaving from exceeding safety tolerances. For instance, if one grout hole is under boring process, then the selected adjacent grout holes are subject to injection to neutralize the settlement from previous boring based on the real time monitoring results. At the end of this grouting project, the cumulative maximum vertical movement of the HSR box tunnel is effectively limited to 6.3 mm at the west wall and 7.5 mm at the east wall. It is the author's opinion that if high pressure horizontal jet grouting had been considered instead of low pressure grouting as the method to construct grout blocks B and C, it would have facilitated easier soil improvement by replacing in situ soil with cement based grout, and as a result minimizing vertical movement of the overlying box tunnel provided that the back-flow during drilling and grouting is properly controlled.

Summary and Conclusions

Based on the above discussion and data about the interaction between various grouting activities and the effect upon the overlying box tunnel, the following conclusions can be drawn:

1. The monitored results upon the overlying box tunnel were within the specified safety tolerance limit during the construction of an access lift shaft adjacent to an existing box tunnel diaphragm wall, horizontal grouting to build grout block B and C, creation of tunnel eyes, and the removal of the H-beams left within the soil mixing wall.
2. The use of a large diameter 196-mm guide casing with three concentric drill pipes measuring 152, 118, and 89 mm with the use of associated hardware such as three packers and 2 one-way valves successfully permitted long distance horizontal wash boring through diaphragm walls and steel H-beams and facilitated the grouting afterwards.
3. The grouting strategy utilized for grout block C of injecting a borehole adjacent to an area undergoing active boring allows the individual effect of either process alone to cancel each other out or minimize the heave and settlement of adjacent structures according to real time measurements.
4. The use of dual tube grouting on block B allowed an easy and effective method to inject either quick set grout or slow set grout through a computer controlled valve.
5. Wash boring process in sandy soil causes more soil washout and larger settlement than in clayey soil. In saturated clayey soil, the grouting pressure can induce the same amount of excess porewater pressure due to very low permeability of the soil, so the grouting pressure can be transmitted over a larger distance without dissipation than in sandy soil. This can cause transmission of boring pressure upon the adjacent box tunnel more than in the sandy soil with high permeability.
6. The process of injection for soil improvement or excavation of a diaphragm wall in very soft clayey soil can generate excessive porewater pressures that dissipate gradually, resulting in eventual consolidation and settlement.
7. The effectiveness of the proposed grouting strategy was verified by limiting the movement of the HSR box tunnel to 6.3 mm at the west wall and 7.5 mm at the east wall. All of these changes were within the elastic limit of the box tunnel.

ACKNOWLEDGMENTS

The writers would like to express their gratitude to the contribution of Mr. Yan-Lin Lin and Mr. Lamin Jatta in completion of the work. They also thank the Central District Project Office of Rapid Transit Systems Taipei City Government and the Sanshin

Corporation Taipei Branch for technically supporting this research. Last but not least, the proofreading provided by Jake Ni, M.D. is deeply appreciated.

References

[1] Pan, J. K. L., Plumbridge, G., Storry, R. B., and Martin, O., "Back Analysis of Cut and Cover Tunnels in Close Proximity to an Operating Railway in Hong Kong," *Tunnell. Undergr. Space Technol.*, Vol. 21, Nos. 3–4, 2006, pp. 453–454.

[2] Liao, S. M., Liu, J. H., Wang, R. L., and Li, Z. M., "Shield Tunneling and Environment Protection in Shanghai Soft Ground," *Tunnell. Undergr. Space Technol.*, Vol. 24, No. 4, 2009, pp. 454–465.

[3] Li, X. G. and Yuan, D. J., "Response of a Double-Decked Metro Tunnel to Shield Driving of Twin Closely Under-Crossing Tunnels," *Tunnell. Undergr. Space Technol.*, Vol. 28, 2012, pp. 18–30.

[4] Harris, D. I., Mair, R. J., Love, J. P., Taylor, R. N., and Henderson, T. O., "Observations of Ground and Structure Movements for Compensation Grouting During Tunnel Construction at Waterloo Station," *Geotechnique*, Vol. 44, No. 4, 1994, pp. 691–713.

[5] Tonon, F., "ADECO Full–Face Tunnel Excavation of Two 260 m^2 Tubes in Clays With Sub-Horizontal Jet-Grouting Under Minimal Urban Cover," *Tunnell. Undergr. Space Technol.*, Vol. 26, No. 2, 2011, pp. 253–266.

[6] Guatteri, G., Koshima, A., Lopes, J. R., Ravaglia, A., Pieroni, R. M., Rocha, P. and Castanheira, M., "Test Tunnel in Barcelona (Spain) for the Feasibility of a 360 Horizontal Jet Grouting and Frontal Septum," *Proceedings of the ITA–AITES World Tunnel Congress 2009 and the 35th ITA–AITES General Assembly*, Minister of Transport, Telecommunication and Energy, The Lord Mayor of the Capital City Budapest, Budapest, Hungary, May 23–28, 2009, pp. 1–8.

[7] Flora, A., Lignola, G. P., and Manfredi, G., "A Semi-Probabilistic Approach to the Design of Jet Grouted Umbrellas in Tunnelling," *Proc. Inst. Civ. Eng. Ground Improv.*, Vol. 11, No. 4, 2007, pp. 207–217.

[8] Davia, A., Marotta, M., and Peach, G., "High Pressure jet Grouting for a Collapsed Tunnel—A Case Study," *Proceedings of the International Conference and Exhibition on Tunnelling and Trenchless Technology*, The Institution of Engineers, Malaysia Tunnelling and Underground Space Technical Division, Selangor, Malaysia, March 7–9, 2006, pp. 143–155.

[9] Shen, S. L., Wang, Z. F., Sun, W. J., Wang, L. B., and Horpibulsuk, S., "A Field Trial of Horizontal Jet Grouting Using the Composite-Pipe Method in the Soft Deposits of Shanghai," *Tunnell. Undergr. Space Technol.*, Vol. 35, 2013, pp. 142–151.

[10] Koshima, A. and Guatteri, G., "Experiences of Ground Improvement for Urban Tunnels in Difficult Conditions," *Proceedings of the International Seminar on Underground Works*, Lisbon, Portugal, June 29–30, 2006, pp. 1–13.

[11] Huang, C. T., Lin, Y. K., Kao, T. C., and Moh, Z. C., "Geotechnical Engineering Mapping of the Taipei City," *Proceedings of the 9th Southeast Asian Geotechnical Conference*, Bangkok, Thailand, Dec 7–11, 1987, pp. 3-109–3-120.

[12] Woo, S. M. and Moh, Z. C., "Geotechnical Characteristics of Soils in Taipei Basin," *Proceedings of the 10th Southeast Asian Geotechnical Conference*, Taipei, Taiwan, April 16–20, 1990, pp. 51–65.

[13] Boone, S., Heenan, D., and Pennington, B., "Monitoring Systems for Control of Compensation Grouting," Grouting Committee of the Geo-Institute of ASCE (Geo–Logan), Logan, UT, 1997, pp. 101–117.

[14] Ni, J. C. and Cheng, W. C., "Quality Control for Grouting Under Rigid Pavement," *ASCE Geotechnical Special Publication No. 212*, ASCE, Reston, VA, 2011, pp. 183–191.

[15] Ni, J. C. and Cheng, W. C., "Trial Grouting Under Rigid Pavement: A Case History in Magong Airport, Penghu," *J. Test. Eval.*, Vol. 40, No. 1, 2012, pp. 107–118.

[16] Ni, J. C. and Cheng, W. C., "The Grout Efficiency of Leveling Building on Very Soft Clay," *ASCE Geotechnical Special Publication No. 194*, ASCE, Reston, VA, 2009, pp. 1–8.

[17] Ni, J. C. and Cheng, W. C., "Fracture Grouting to Lift Structure in Clayey Sand," *ASCE Special Publication No. 198*, ASCE, Reston, VA, 2010, pp. 470–485.

[18] Ni, J. C. and Cheng, W. C., "Using Fracture Grouting to Lift Structure in Clayey Sand," *J. Zhejiang Univ. Sci. A*, Vol. 11, No. 11, 2010, pp. 879–886.

[19] Soga, K., Au, S. K. A., Jafari, M. R., and Bolton, M. D., "Laboratory Investigation of Multiple Grout Injections Into Clay," *Géotechnique*, Vol. 54, No. 2, 2004, pp. 81–90.

[20] Au, S. K. A., Soga, K., Jafari, M. R., Bolton, M. D., and Komiya, K., "Factors Affecting Long-Term Efficiency of Compensation Grouting in Clays," *J. Geotech. Geoenviron. Eng.*, Vol. 129, No. 3, 2003, pp. 254–262.

[21] Ni, J. C. and Cheng, W. C., "Characterising the Failure Pattern of a Station Box of Taipei Rapid Transit System (TRTS) and its Rehabilitation," *Tunnell. Undergr. Space Technol.*, Vol. 32, 2012, pp. 260–272.

Journal of Testing and Evaluation

doi:10.1520/JTE20130296 / Vol. 43 / No. 2 / March 2015 / available online at www.astm.org

Courtney L. Busch,[1] Catherine T. Aimone-Martin,[2] and Rafiqul A. Tarefder[3]

Experimental Evaluation of Cratering and Ground Vibration in Clay Soils Subjected to Explosive Airblast Loading

Reference

Busch, Courtney L., Aimone-Martin, Catherine T., and Tarefder, Rafiqul A., "Experimental Evaluation of Cratering and Ground Vibration in Clay Soils Subjected to Explosive Airblast Loading," *Journal of Testing and Evaluation*, Vol. 43, No. 2, 2015, pp. 414–424, doi:10.1520/JTE20130296. ISSN 0090-3973

Manuscript received November 17, 2013; accepted for publication December 22, 2014; published online January 22, 2015.

[1] Ph.D. Candidate, Department of Civil Engineering, Univ. of New Mexico, MSC01 1070, NM 87131, e-mail: vallejo@unm.edu

[2] President, Aimone-Martin Associates, LLC, 1005 Bullock Avenue, Socorro, NM 87801, e-mail: cathy@aimonemartin.com

[3] Associate Professor, Department of Civil Engineering, Univ. of New Mexico, MSC01 1070, NM 87131, e-mail: tarefder@unm.edu

ABSTRACT

This study focused on the ground response of clay soils in confined conditions subjected to explosive airblast loading through small-scale field experiments. Laboratory testing was also performed to characterize the soils used during field testing and obtain material properties for future work. A total of 33 suspended explosive blasts were conducted with explosive masses ranging from 0.9 to 100.9 g and two heights of suspension of 2.5–7.6 cm above the clay surface. The field instrumentation consisted of subsurface triaxial geophones and surface airblast sensors. Results of the study included surface crater geometry measurements, ground vibration data, and air overpressure data. Crater diameters ranged from 3.8 to 22.9 cm, while crater depth ranged from 0.8 to 8.4 cm. Crater volumes ranged from 32.1 to 1720.6 cm^3. Peak particle velocity (PPV) decreased with depth and ranged from 1.0 to 40.2 cm/s. The results of the experiment provided a data set that could be used to predict the effects of airblast loads on clay soils.

Keywords

explosive airblast, cratering, ground vibration, clay soil, small scale blasts

Introduction

Airblast events from explosive detonations near earthen materials result in a high-stress, dynamic loading that may make many earthen structures, such as slopes and walls, susceptible to failure. Such a situation may occur with the detonation of explosives contained within a vehicle. A high yield blast event of this nature could induce large scale ground surface deformations and potentially result in structural failure. It is therefore of interest to investigate the effects of airblast loading on earthen materials.

Previous studies of explosive blast loading on soils have generally included empirically derived relationships to relate explosive quantity to the dimensions of a crater formed by the detonation. In addition, studies that involve blast loading of soil structures have generally been performed by government organizations and the results are not open source information. Data for elevated explosive blasts on soils are sparse. Studies typically group results from many different soil types without extensive laboratory tests to characterize the soils.

Most published airblast data is presented in terms of scaled distance. A common method of scaling the effects of open air detonations is the Hopkinson–Cranz scaling law [1] as shown in Eq 1. This relationship states that a similar explosive energy is generated when two different explosive masses with identical geometry are detonated in the same atmospheric conditions, allowing the distance from an explosive charge mass to be expressed in terms of a scaled distance. The method provides a useful way to compare blast energy from explosive events with varying explosive charge weight and distances.

$$SD_h = h/W^{1/3} \tag{1}$$

where:

SD = the scaled distance above the ground surface (m/kg$^{1/3}$),

h = the blast height above the ground surface (m), and

W = the equivalent mass of TNT (kg).

During an airblast event, soils are subjected to air-induced ground shock, which compresses the ground surface and sends a pressure pulse into the subsurface soils. Ground motions are generally downward, with maximum motion at the ground surface and attenuating with depth [2]. Ground motions from a blast event are affected by distance from the blast source and the explosive charge mass. Extensive empirical site studies have been performed for mining applications to determine a predictive relationship between these factors. This relationship, termed the "Propagation Law," was developed by the U.S. Bureau of Mines [3] by plotting vibration data versus scaled distance on log–log coordinates and determining an attenuation data fit by least squares methods as shown in Eq 2. The maximum ground motion for numerous blast events was described through the peak particle velocity (PPV) in the vertical direction, which is the maximum vertical ground motion perpendicular to the horizontal ground surface. The attenuation of air overpressures is similarly described by Eq 2. PPV values are commonly used in construction vibration standards to prevent damage to structures by specifying allowable blast and construction-induced vibration limits [4].

$$PPV = K(SD)^{-b} \tag{2}$$

FIG. 1 Crater geometry from an explosive event [6].

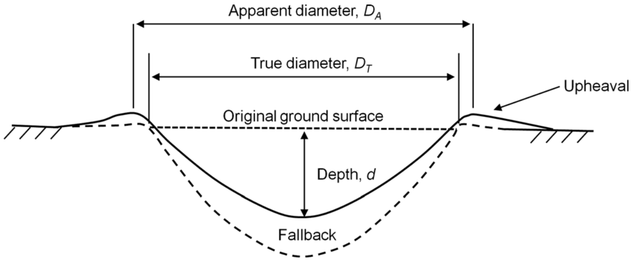

where:

PPV = the peak particle velocity in the vertical direction (cm/s),

SD = the scaled distance from blast (m/kg$^{1/3}$),

K = the K-factor, and

b = the attenuation exponent.

The K-factor describes the relative magnitude of explosive energy coupled into the ground at the blast site and is defined as the intercept of the attenuation trendline at an SD value of 1. The K-factor is highly dependent on site geology and must be experimentally derived for a specific site through the measurement of blast-induced ground vibrations [3]. The slope term, b, describes the rate of decay in PPV with distance from the blast. Large values of b result in a steep slope and indicate that the energy from the blast is absorbed quickly and that blast vibrations do not attenuate to far distances. A slope approaching zero indicates far-attenuating blast energy.

A schematic of the crater geometry from an explosive event is shown in **Fig. 1**. An explosion generates a large amount of energy (in the form of a shock wave and generation of gaseous products) in a very short period of time [5]. The explosion first generates an initial shock that scours and compacts the soil, resulting in plastic flow and the formation of an initial, "true" crater [6]. Detonation gases are infused into the ground and eject soil (termed "ejecta") into the air as they expand. The direction of the soil particle velocity reverses as a rarefaction wave travels into the compressed material and forms more ejecta [7]. Some of the ejecta are deposited back into the true crater as fallback, and the resulting crater geometry after this event is termed as the apparent crater [6].

Relationships have been suggested that correlate crater depth (d), diameter (D), and volume (V) of displaced materials with charge mass (W). A well-known study of air-blast explosions on soils was performed by Kinney and Graham [1], who compiled the results of 200 accidental, large magnitude surface explosions on soils and developed an empirically derived equation that predicted an apparent crater diameter to be equal to 80 % of the cubed root of the explosive charge mass.

Ambrosini et al. [8] performed a series of small scale field explosions with spherical charges on in situ, clay, and silt soils with varying material properties with depth. An empirical relationship incorporating explosive mass, height of burst, and crater diameter was developed based on the experimental results. The relationship showed an increase in crater diameter with increasing explosive mass and decreasing blast height. Numerical studies have also been used by Ambrosini and Luccioni [9] to form predictive relationships of crater diameters from spherical surface blasts.

Various empirical relationships were proposed to relate the ratio of crater diameter to depth for surface blasts. Kinney and Graham [1] suggested that the crater depth is approximately one quarter of the diameter for surface blasts. Vortman [10] compiled results from surface high explosive blasts in soils and developed a relationship between the ratio of apparent crater radius to depth versus explosion energy. The ratio increased with increasing explosive energy and was found to vary based on site soil conditions.

Objective and Scope

The objective of the present study was to obtain ground response data in terms of crater dimensions and ground vibrations of clay soils in confined conditions subjected to explosive airblast loading through small-scale field experiments. The field tests were performed on a horizontal surface of soil of uniform compaction and moisture content. Crater geometry results were obtained after each blast and vibration data was obtained from velocity transducers embedded into the clay soils at varying depths below the test site. Laboratory tests were conducted to characterize the soil properties for use in material models for future finite element simulations.

Experimental Methodology

The study comprised two parts: first, laboratory testing was conducted to characterize the soils utilized in the experiments and second, small-scale explosive blasts were conducted on low-plasticity clay soils. The soil used in the experiments was commercialized clay manufactured from claystone brick dust mixed with a small amount of fine sand. The clay was manufactured as relatively homogeneous blocks with a consistent density, moisture and fine sand content.

LABORATORY TESTING

The laboratory tests consisted of geotechnical identification tests and triaxial compression tests performed in accordance with ASTM standards. The tests were conducted to characterize the clay-rich soils used in the explosive blast experiments. The results of the laboratory tests will be used as input values for material models in future finite element simulations of earthen materials under blast loading. Geotechnical characteristics corresponding to average values for the clay soil are shown in **Table 1**. The laboratory tests indicated that the tested clay-rich soil was classified as Lean Clay (noted CL) with trace fine sand content based on the ASTM D2487-11 [11].

TABLE 1 Geotechnical properties of clayey soils used in experiment.

Parameter	ASTM Standard	Result
Dry density	ASTM D2487-11 [12]	1.5 g/cm^3
Saturation	ASTM D2487-11 [12]	98.0 %
Moisture content, A and C blast series	ASTM D2216-10 [13]	28.8 %
Moisture content, B blast series	ASTM D2216-10 [13]	36.6 %
Liquid limit (LL)	ASTM D4318-10e1 [14]	35
Plasticity index (PI)	ASTM D4318-10e1 [14]	15
$C_{0.075\ \mathrm{mm}}$ (% passing 0.075 mm)	ASTM D1140-00(2006) [15]	92 %

The undrained shear strength is generally used to characterize the response of soils subjected to explosive blast loading because drainage does not occur during the abrupt shock loading event [16]. Studies have shown that even drained soil specimens remain in an undrained condition during rapid transient loading because there is not enough time for drainage to occur [17]. The unconsolidated-undrained (UU) triaxial test is an appropriate method to capture the response of soil to explosive loading as it can be used to obtain undrained shear strength parameters [18]. In UU triaxial tests, drainage is not permitted, pore pressures do not dissipate, and consolidation of the soil does not occur.

Unconsolidated-undrained triaxial tests were performed on the clay-rich soils used in the explosive blast experiments in accordance with ASTM D2850-03a(2007) [19]. The Mohr–Coulomb shear strength envelope obtained from testing is shown in **Fig. 2**. The triaxial tests were performed on three soil samples with saturation levels ranging 96.1 %–98.9 %. Confining pressures of 11.7, 23.5, and 28.7 kPa were used to represent the range of overburden stress on the clay soils during the experiments as described later in this report. An axial strain rate of 1 % per minute was used for the tests, and the failure of the soil was defined as the maximum stress difference observed during testing or the deviator stress at 15 % axial strain, whichever was obtained first, based on ASTM D2850 [19]. This resulted in a cohesion value, c, of 23 kPa. The partially-saturated conditions and the trace sand content of the soil resulted in a friction angle, φ, of 4°.

EXPLOSIVE BLAST TESTING

A total of 33 explosive blasts were conducted on the homogeneous and low-plasticity clayey soil previously characterized to record airblast measurements. Of these, 24 tests in three series were performed to measure ground motions and record crater dimensions. The experimental configuration of the explosive blast tests is shown in **Fig. 3**. A pit was excavated in situ in a silty sand with gravel soil (characterized according to Ref. [11] as

FIG. 2

Shear strength envelope obtained from triaxial compression testing.

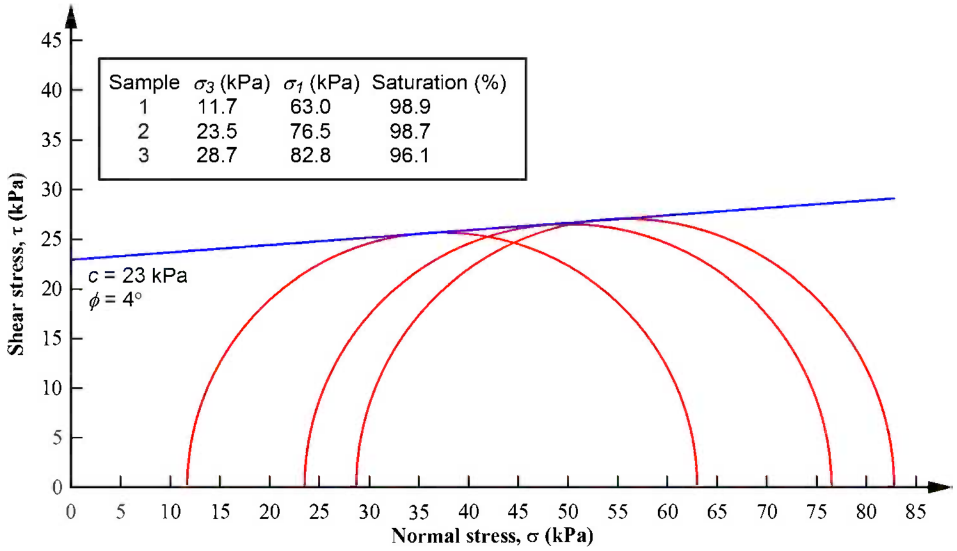

Sample	σ_3 (kPa)	σ_1 (kPa)	Saturation (%)
1	11.7	63.0	98.9
2	23.5	76.5	98.7
3	28.7	82.8	96.1

SM) to a depth of 1.5 m below the ground surface (bgs). The pit was filled with 15 cm of loosely compacted site soil.

A cylindrical cardboard form with a 30 cm diameter and length of 1.2 m was placed in the excavation and backfilled with clay. The form was lined with plastic sheeting to avoid moisture loss in the clay. The clay was backfilled in small lifts and gently tamped with a tamping rod to mold to the shape of the form and maintain a consistent density. This process was continued until the form was entirely filled with clay. The form was left in the ground during the experiments and was not removed due to the impracticality of extraction after it was filled with clay. It was assumed that the cardboard form would have a minimum impact on the experiment results from vibration reflections due to its low density.

Five triaxial geophones (**Fig. 4**) were placed in a vertical array within the clay column during the backfill process at depths of 0.2, 0.5, 0.8, 1.1, and 1.2 m bgs. The geophones had a frequency response between 2 and 250 Hz. A surface array of

FIG. 3

Experimental configuration of explosive blast tests.

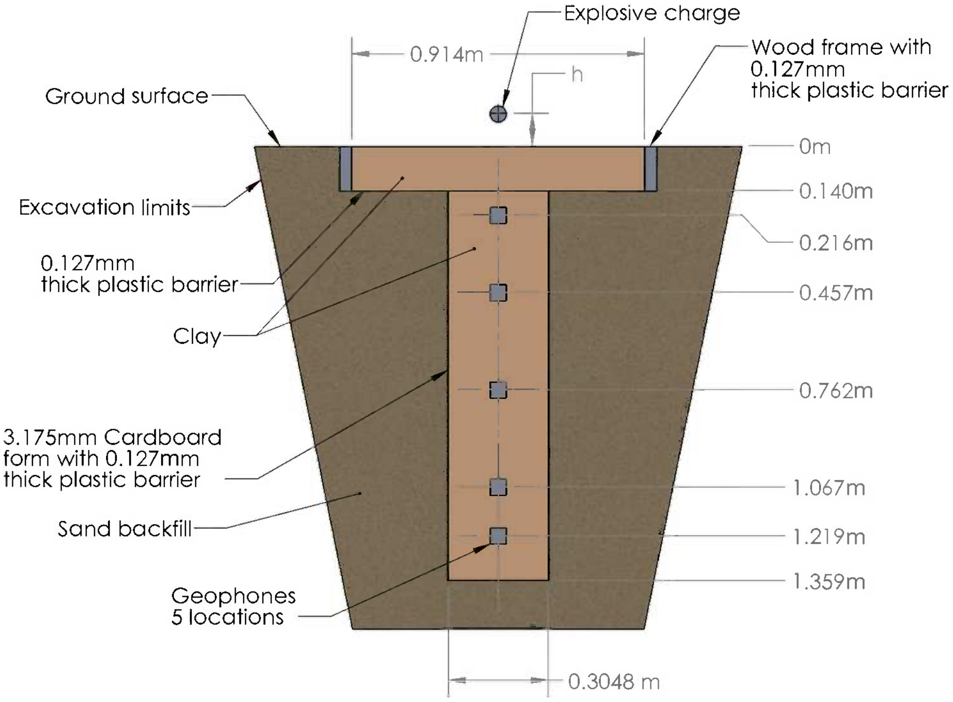

FIG. 4 Triaxial geophone installation in clay column.

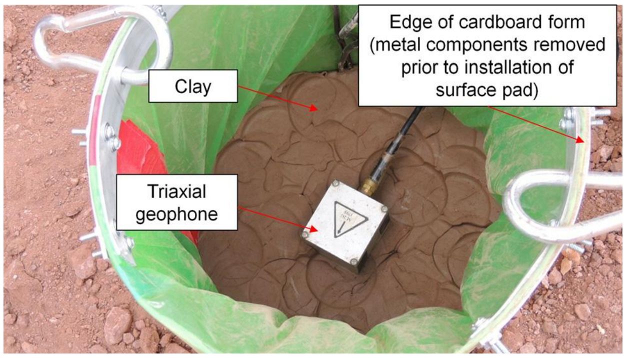

airblast sensors (**Fig. 5**) was placed on the ground surface to measure air overpressure from the blasts. The distance of the airblast sensors ranged from 1.6 to 7.8 m from the blast source. Seismographs were connected to the geophones and airblast sensors to record ground vibration and air overpressure.

The annular space between the cardboard form and the excavated pit walls was backfilled with the sandy soil from the site placed in a loosely compacted condition with an average total density of 1.6 g/cm^3 to minimize vibration reflections back into the clay column. A 0.9 by 0.9 by 14 cm wooden frame was placed on top of the clay column and backfill sand and filled with clay to create a superficial clayey pad large enough to capture blast-induced crater geometries. The base of the clayey pad was lined with plastic sheeting where it came into contact with the dry sandy soil to avoid moisture loss of the clay.

Spherical charges of a two-part binary explosive consisting of solid ammonium nitrate oxidizer and flammable liquid nitromethane [20] were utilized in the experiments. The explosive had an approximate 85 % TNT equivalence. The two components were mixed together, placed into plastic bags, hand-molded into a spherical shape, and detonated with an electric detonator containing 0.9 g of explosive.

FIG. 5 Surface airblast sensor.

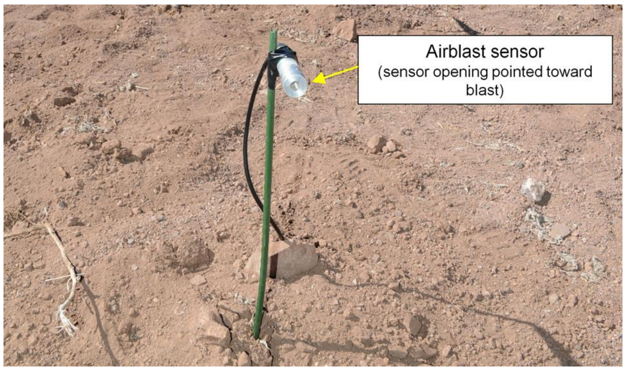

FIG. 6 Explosive charge suspended over the clay surface (a view of approximately 20° to the surface of the clay).

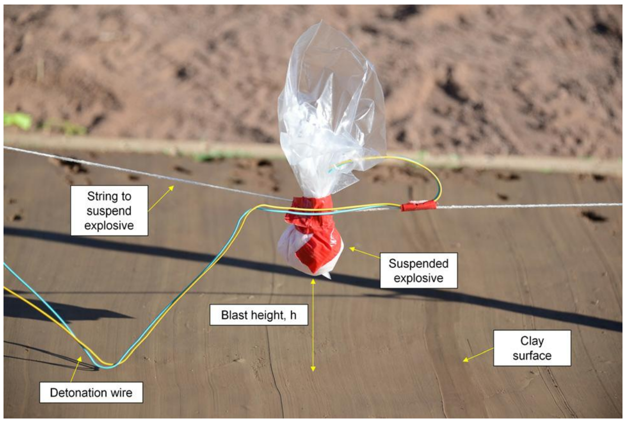

The explosive charges were suspended above the clay surface using PVC rods and string as shown in **Fig. 6**. The suspension of the charges was configured so that the explosive remained stationary if breezy weather conditions arose. Two suspension heights of the explosive above the ground surface were used for the tests and were selected to be within a general range that replicated a scaled version of the energy of an equivalent TNT explosive mass, *W* of 2270 kg (5000 lbs) and a blast height, *h* of 0.8 m (2.5 ft). This information was used to calculate a blast height that was scaled down to the explosive masses used in the experiments. A target scaled distance, *SD* value of 0.06 m/kg$^{1/3}$ was therefore calculated using Eq 1 for the experiments in this study.

Table 2 presents the test matrix for the blasts conducted in the study with two constant blast offset heights, *h*, of 2.5 and 7.6 cm and explosive mass, *W*, ranging from 0.9 to 100.9 g to obtain scaled distances, *SD*, from 0.07 to 0.28 m/kg$^{1/3}$. It was not possible to conduct experiments with *SD* values smaller than 0.07 m/kg$^{1/3}$ since this would have required a larger explosive mass that could have damaged the shallowest geophone buried within the clay column. The experiments were conducted over the course of three separate days. The blasts were conducted in three series according to blast height and moisture conditions:

- Blast series A were performed with $h = 7.6$ cm, dry weather, and a relatively stable clay moisture content of 28.8 %.
- Blast series B and C were performed with $h = 2.5$ cm. The B blast series were performed on under rainy and snowy weather conditions. While the clay did not freeze during the tests, the moisture content of the upper surface of the clay pad increased to 36.6 %. Therefore, a new series of tests designated as the C blast series were performed during dry weather so that the soil moisture conditions were the same as the A series tests and results could be directly compared.

TABLE 2 Test matrix for experimental blasts (h = the blast height, W = the explosive mass, SD = the scaled distance, w = the soil moisture content).

Blast Series	h (cm)	Blast Number	W^a (g)	SD (m/kg$^{1/3}$)	w (%)
A	7.6	A-1	5.9	0.422	28.8
		A-2	20.9	0.277	
		A-3	25.9	0.258	
		A-4	30.9	0.243	
		A-5	38.9	0.225	
		A-6	45.9	0.213	
		A-7	50.9	0.206	
		A-8	65.9	0.189	
		A-9	80.9	0.176	
		A-10	90.9	0.169	
		A-11	100.9	0.164	
B	2.5	B-1	0.9	0.265	36.6 (wet clay)
		B-2	5.9	0.141	
		B-3	10.9	0.115	
		B-4	20.9	0.092	
		B-5	30.9	0.081	
		B-6	40.9	0.074	
		B-7	50.9	0.069	
C	2.5	C-1	0.9	0.265	28.8
		C-2	10.9	0.115	
		C-3	20.9	0.092	
		C-4	30.9	0.081	
		C-5	40.9	0.074	
		C-6	50.9	0.069	

[a] The explosive mass includes an additional 0.9 g of explosive for the detonator.

The explosive blasts displaced the clay surface pad and formed craters as shown in **Fig. 7*(a)***. The crater dimensions were measured after each blast as shown in **Fig. 7*(b)*** using a profiling tool that was placed inside the crater to capture the true diameter, D_T, apparent diameter, D_A, and depth, d. Diameter measurements were taken in two perpendicular directions (North to South and East to West) across the crater and traced onto cardboard to capture the profile shape. Profiles for some of the larger blasts were not fully captured because the depth of the crater exceeded the physical dimensions of the profiler. However, the diameters and depths were still measured for these craters and the profile shape was estimated from these measurements and crater photos.

After each blast, new clay was placed back into the crater, remolded to the approximate original density, and smoothed to a flat surface. The surface of the clayey pad was covered with plastic sheeting until immediately prior to the start of each experiment and intermittently sprayed with a water mist to maintain the moisture content.

The two-dimensional crater profiles measured with the profiler tool during testing were digitized into an electronic format using a computer aided drafting software [21] and rotationally swept in the software to form a three-dimensional crater shape. The crater volume was calculated along the true diameter and depth using the three-dimensional shape. An example of a crater profile and volume is shown in **Fig. 8**.

Results and Discussion

CRATER GEOMETRY RESULTS

The average dimensions of the craters across the perpendicular profiles are presented in **Table 3**. The table includes true diameter (D_T), apparent diameter (D_A), crater depth (d), crater volume (V), and an empirical crater volume parameter (V_C). The empirical crater volume parameter relates the ratio of true diameter and depth to explosive mass, similar to the approaches of Kinney and Graham [1] and Vortman [10]. The volume parameter scales the crater dimensions to explosive energy and is useful because diameter and depth measurements (as opposed to volume) are easily attainted during field experiments. The volume parameter was calculated with Eq 3 and the results are presented in **Table 3**.

$$V_c = D_T/(d \cdot W) \tag{3}$$

FIG. 7

(a) Plan view of crater formed on the clay surface after an explosive blast and *(b)* Post-blast crater profile measurement.

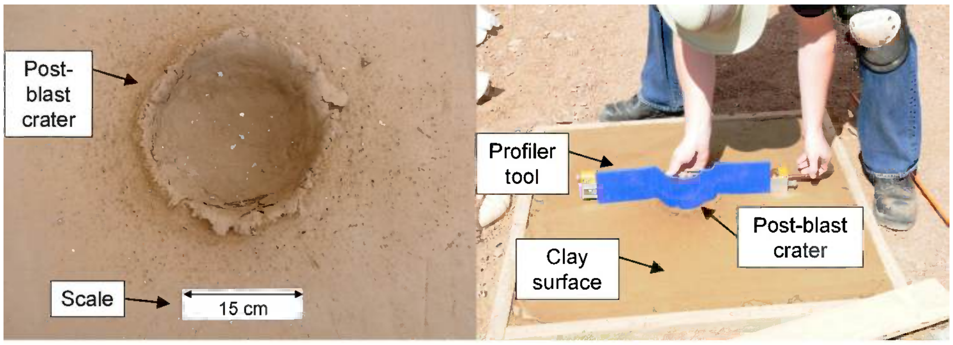

(*a*) (*b*)

FIG. 8 Crater profile and volume for Blast C-3.

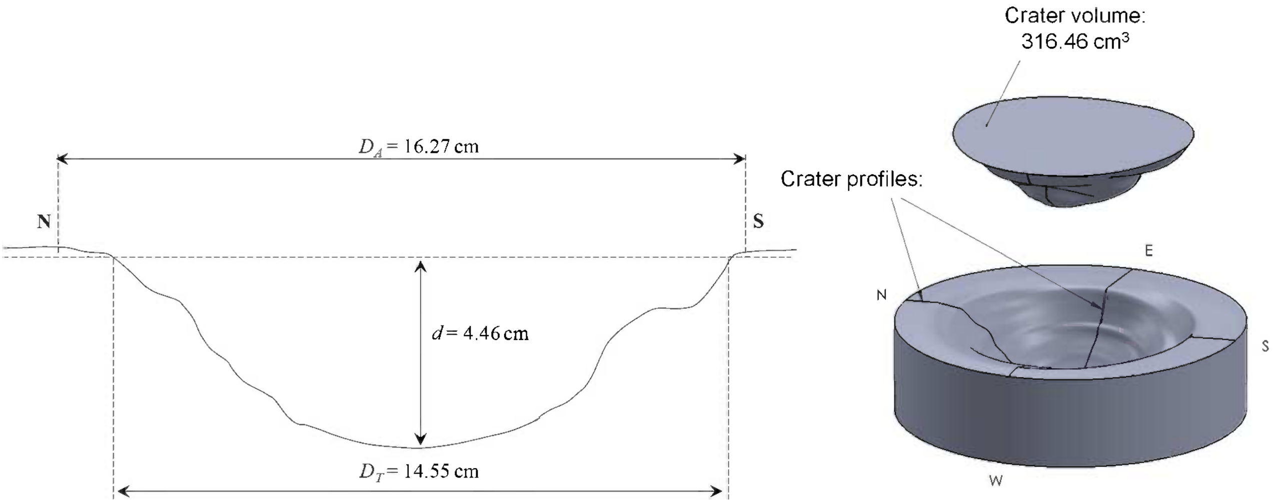

where:

V_c = the crater volume parameter (kg^{-1}),
D_T = the true crater diameter (cm),
d = the crater depth (cm), and
W = the explosive mass (kg).

TABLE 3 Crater geometries from experimental blasts (D_T = the true diameter, D_A = the apparent diameter, d = the depth, V = the volume, V_c = the volume parameter).

Blast Number	D_T (cm)	D_A (cm)	d (cm)	V (cm^3)	V_c (kg^{-1})
A-1			*No crater created*		
A-2	11.8	13.8	0.8	32.1	753.9
A-3	3.8	4.4	1.9	*Not calculated*[a]	*Not calculated*[a]
A-4	14.7	15.6	1.3	90.0	361.5
A-5	15.6	19.4	1.5	137.8	267.6
A-6	18.2	19.4	1.6	169.8	241.8
A-7	20.5	22.3	1.8	186.0	222.1
A-8	18.5	19.8	3.3	346.6	84.1
A-9	22.9	24.2	2.6	468.0	110.5
A-10	22.3	25.4	5.7	921.1	42.8
A-11	22.8	25.5	4.3	930.1	52.0
B-1	6.1	7.3	2.8	54.2	2432.2
B-2	8.1	8.7	2.1	57.7	667.2
B-3	10.3	10.8	1.6	51.1	586.7
B-4	12.8	14.3	4.0	328.1	152.3
B-5	14.3	15.5	2.8	307.3	156.1
B-6	22.4	24.6	6.9	1452.6	79.8
B-7	21.6	23.2	7.5	1564.0	56.4
C-1	6.7	8.4	3.1	64.2	2425.9
C-2	9.1	11.2	2.8	83.1	297.6
C-3	14.4	15.9	4.5	316.4	154.1
C-4	16.3	17.9	6.3	801.3	83.6
C-5	20.7	25.5	7.6	1452.6	66.7
C-6	20.9	24.4	8.4	1720.6	48.9

[a] Blast A-3 crater volume was not calculated due to irregular crater shape.

The true crater diameters, D_T, ranged from 3.8 to 22.9 cm, while apparent crater diameters ranged from 4.4 to 25.5 cm. Crater depth, d, ranged from 0.8 to 8.4 cm and volume, V from 32.1 to 1720.6 cm^3. True crater diameter to depth ratios varied widely for the A blast series, with crater diameters approximately 2–16 times the crater depth. Diameter to depth ratios were more consistent for the B and C blast series, with some diameters of 2–6 times the crater depth for the B blast series and 2–3 times the depth for the C blast series.

The blast test A-1, with an explosive mass of 5.9 g, did not create a crater. The blast test A-3 created a double crater shape with a significant spall lip and was considered to be an outlier to the experimental results. Because of the irregular shape of the A-3 crater, it was not included in the analyses and the volume could not be calculated.

Figure 9 contains various plots of crater dimensions scaled with charge weight. The relationships between the crater geometry, the charge mass, W, and blast height, h, were investigated by plotting the volumes generated from the crater profiles versus the scaled distance, SD as shown in **Fig. 9(*a*)**. The data are separated by blast series with power trendlines. The R^2 value shown in the figure is the correlation coefficient and describes how well the equation fits the data, with an R^2 value of 1.0 indicating an exact fit. The data exhibited strong trends as shown by R^2 values ranging from 0.95 for the B blast series to 0.99 for C blast series. Each blast series exhibited a trend of increasing crater volume with explosive mass. The B and C blast series with $h = 2.5$ cm exhibited larger crater volumes, V, than the A blast series with $h = 7.6$ cm, showing the larger amount of energy deposited into the ground surface with the blast charge located closer to the ground.

A plot of V_C versus SD is presented in **Fig. 9(*b*)**. The B and C blast series resulted in larger crater volume parameters than the A blast series. This was especially evident with larger values

FIG. 9

(*a*) Crater volume versus scaled distance, (*b*) Crater volume parameter versus scaled distance and (*c*) Crater diameter to blast height ratio versus scaled explosive mass.

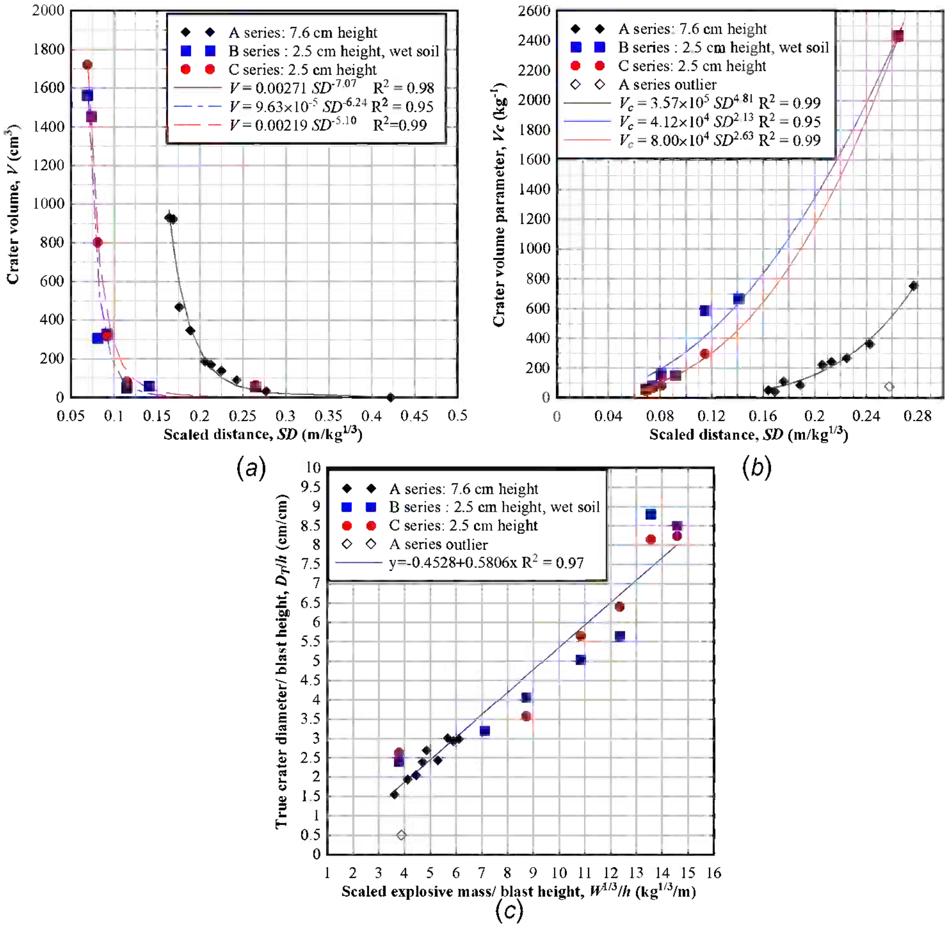

of scaled distance, where volume parameters for the B and C blast series were more than three times larger than the A blast series. The power trendlines in **Fig. 9(*b*)** exhibited a slight variation between the B and C blast series, indicating that the increased moisture content on the soil surface affected the resulting crater geometries. The wet soil present in the B blast series resulted in larger crater volumes and somewhat more data scatter than the C blast series. Volume parameters for both series were similar for $SD = 0.1\ \mathrm{m/kg^{1/3}}$ or less, but diverged at $SD \approx 0.12$ to $0.14\ \mathrm{m/kg^{1/3}}$.

The true crater diameters, D_T, and scaled explosive mass, W, were normalized by blast height, h, to obtain a predictive relationship as shown in **Fig. 9(*c*)**. A linear trendline (Eq 4) was fit to the data with an R^2 value of 0.97. This equation provides an empirical relationship between crater dimensions and scaled explosive mass for clay soils. This approach is similar to the empirical relationship developed by Kinney and Graham [1] and incorporates the blast height into the function based on the approach of Ambrosini et al. [8]. The blast test A-3 was considered an outlier and was not used in the data fit. Crater diameters increased with increasing explosive mass, W, and also increased with decreasing blast offset height, h, with the largest crater diameters corresponding to the B and C test series with $h = 2.5$ cm.

$$D_T/h = -0.4528 + 0.5806W^{1/3}/h \quad R^2 = 0.97 \tag{4}$$

where:

D_T = the true crater diameter (cm),
h = blast height (cm), and
W = the explosive mass (kg).

VIBRATION AND AIRBLAST RESULTS

Airblast time histories were constructed from peak air overpressure data obtained from the surface airblast sensors and the velocity time histories were constructed from ground motion data recorded by the subsurface geophones. An example of the PPV obtained from a velocity time history record from a subsurface geophone is shown in **Fig. 10(*a*)**. The PPV value is the maximum ground motion observed during the time history. Several of the blasts with larger explosive masses generated maximum ground motion that exceeded the capacity of the near surface geophones. PPV values were still obtained from the ground motion histories for some of these instances by

FIG. 10 (*a*) Example of peak particle velocity (PPV) obtained from velocity time history and (*b*) extrapolated PPV value obtained from exceeded capacity geophone data.

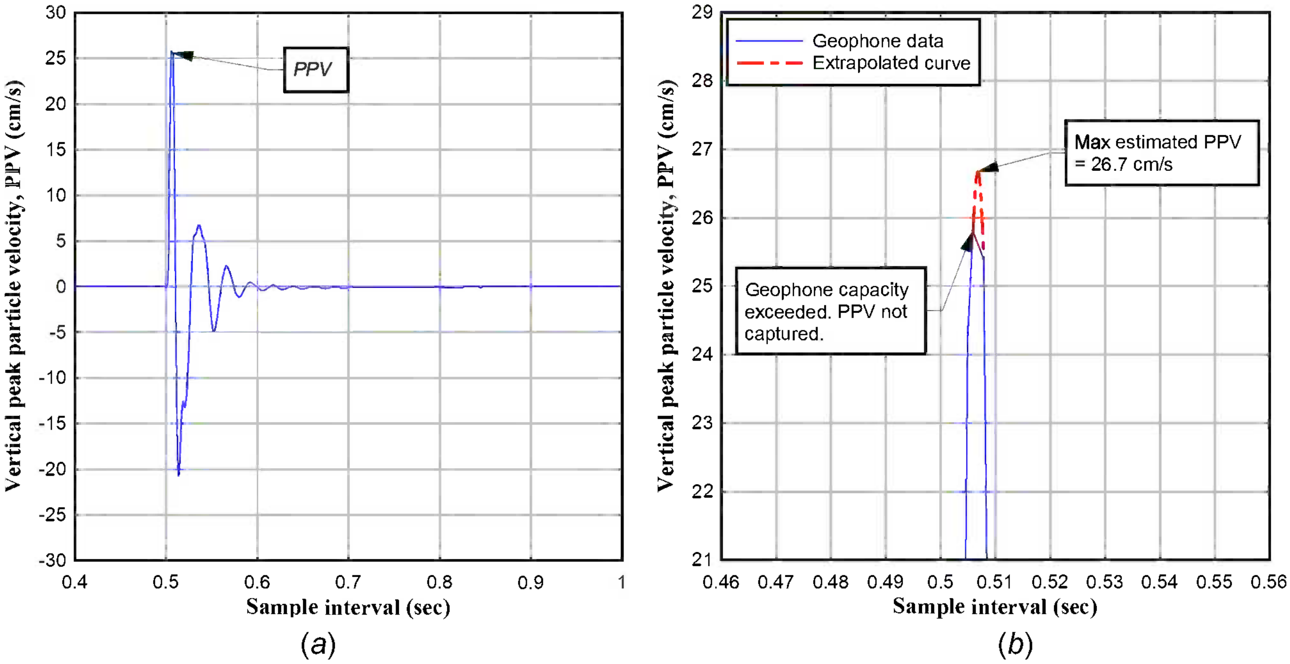

extrapolating the data curve to estimate the peak ground motion as shown in **Fig. 10(*b*)**. This method was performed on data curves that had a clear shape and were not overly distorted from excessive ground motions.

Ground vibration attenuation curves were created by plotting PPV obtained at each geophone location against the scaled distance, *SD* (computed using Eq 1 and changing *h* by *D*, the distance of the geophone to the blast source) as shown in **Fig. 11(*a*)**. Attenuation trend lines (described by Eq 2) were fit to the ground vibration data to quantify vibration attenuation and to indicate the amount of energy generated by the blast.

FIG. 11 (*a*) Vertical PPV versus scaled distance SD for subsurface sensors and (*b*) the air overpressure AOP versus scaled distance SD.

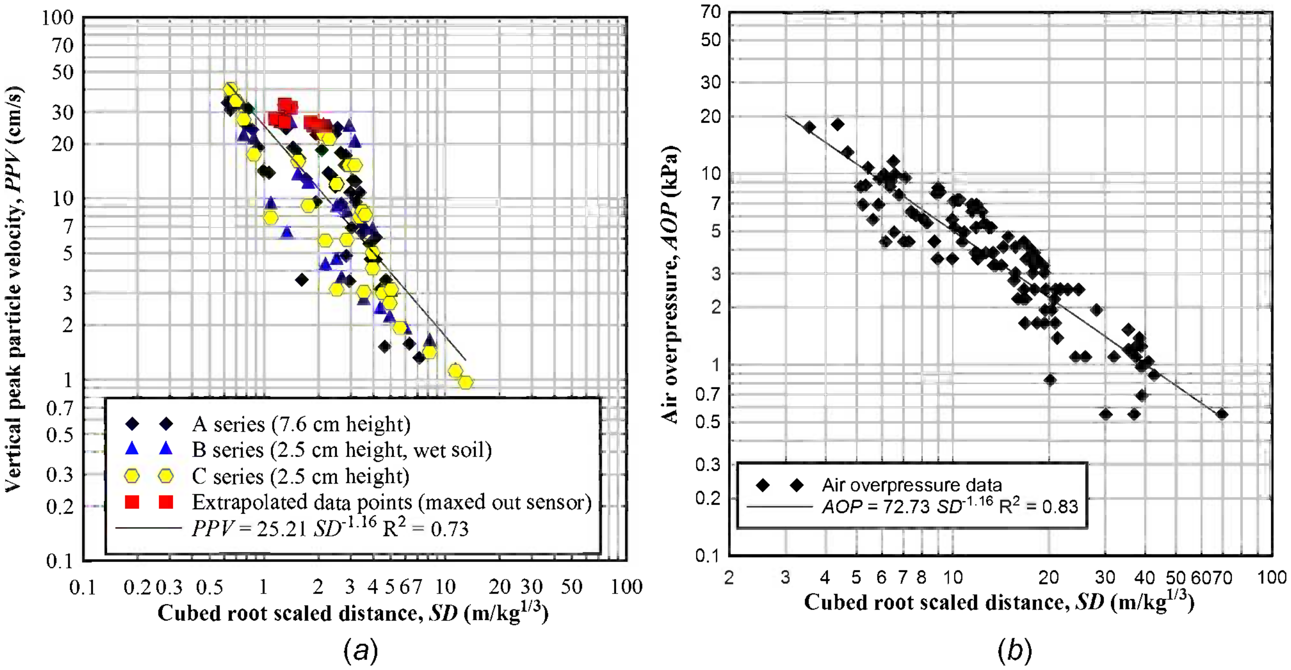

The PPV values shown in **Fig. 11(*a*)** ranged from 1.0 to 40.2 cm/s and decreased with depth as indicated by the attenuation trend line. The energy generated by the blasts as described by the K-factor was 25.21. The data exhibited a moderate amount of scatter with an R^2 value of 0.73. The data points presented in the figure did not exhibit a trend based on the different blast series, which had two different blast heights. This indicated that the scaled distance (explosive mass scaled by distance from the blast to the geophone) is a representative parameter to describe the ground vibration attenuation. PPV results also did not appear to be impacted by the moisture conditions of the clay on the ground surface for the B blast series, indicating that the additional moisture added to the topsoil by the wet weather conditions did not permeate the clay column where the geophones were embedded.

Figure 11(*b*) shows a plot of air overpressure, AOP, versus scaled distance, SD, obtained from the airblast sensors for the blasts performed in this study. The air overpressures ranged from 0.6 to 18.2 kPa and decreased with distance from the blast. The data was fit by the power Eq 5. While there was some scatter to the airblast data as shown in the figure, a relatively good data fit was obtained with an R^2 value of 0.83.

$$AOP = 72.73SD^{-1.16} \quad R^2 = 0.83 \tag{5}$$

where:

AOP = the air overpressure (kPa), and
SD = the scaled distance from blast (m/kg$^{1/3}$).

Conclusions

This study examined the effects of small scale airblast experiments on clay soils to obtain relationships for ground vibration attenuation and crater geometry with explosive mass and offset height. Thirty-three small scale blasts were conducted to record airblast measurements. Of these, 24 tests were performed to measure ground motions and record crater dimensions with offset heights of 2.5 and 7.6 cm above the ground surface and explosive masses ranging from 0.9 to 100.9 g. The experiment results provided a data set with which to predict the results of small airblast loads on clay soils.

Vibration attenuation trend lines were fit to vertical PPV versus scaled distance from the blast source. PPV decreased with depth and ranged from 1.0 to 40.2 cm/s. The energy generated by the blasts as described by the K-factor was 25.21. True crater diameters ranged from 3.8 to 22.9 cm, whereas apparent crater diameters ranged from 4.4 to 25.5 cm. Crater depth ranged from 0.8 to 8.4 cm and volume from 32.1 to 1720.6 cm^3.

Plots of crater volume, V, and volume parameter, V_c, versus scaled distance, SD, were constructed with power trendlines fit through the data. Crater volume increased with explosive mass and was larger for blasts located closer to the ground surface when more energy was coupled into the ground. Increased moisture content in the clay soils resulted in slightly larger V_c values and more data scatter. Crater diameters and scaled explosive mass were normalized by blast height to obtain a predictive relationship for crater geometry with known blast height and explosive mass. Crater diameters increased with decreasing blast offset height, h, when more energy was coupled into the soil.

Recommendations for future work include comparison of experimental results with numerical solutions obtained through finite element simulations. The objective of the future work will be to validate soil material models within a numerical framework.

References

[1] Kinney, G. F. and Graham, K. J., *Explosive Shocks in Air*, 2nd ed., Springer Verlag, Berlin, Germany, 1985.

[2] United States Army, "Structures to Resist the Effects of Accidental Explosions," *TM5-1300/NAVFAC P-397/AFR 88-22*, Joint Departments of the U.S. Army, Navy and Air Force, Washington, D.C., 1990.

[3] Nicholls, H. R., Johnson, C. F., and Duvall, W. I., "Blasting Vibrations and Their Effects on Structures," *United States Department of the Interior, Bureau of Mines Bulletin 656*, Department of the Interior, Washington, D.C., 1971.

[4] Ozcan, D. M., Bayraktar, A., and Altunisik, A. C., "Comparison of Damage Criteria for Structures to Near-Field Blast-Induced Ground Motions," *J. Test. Eval.*, Vol. 40, No. 1, 2012, pp. 148–157.

[5] Helwany, S. M. B. and Chowdhury, A., "Laboratory Impulse Tests for Soil-Underground Structure Interactions," *J. Test. Eval.*, Vol. 32, No. 4, 2004, pp. 262–273.

[6] De, A., Zimmie, T. F., Abdoun, T., and Tessari, A., "Physical Modeling of Explosive Effects on Tunnels," presented at the *Fourth International Symposium on Tunnel Safety and Security*, Frankfurt, Germany, March 17–19, 2010, SP Technical Research Institute of Sweden, Borås, Sweden, pp. 159–168.

[7] Cooper, P. W., *Explosives Engineering*, Wiley-VCH Publications, New York, 1996.

[8] Ambrosini, R. D., Luccioni, B. M., Danesi, R. F., Riera, J. D., and Rocha, M. M., "Size of Craters Produced by Explosive Charges On or Above the Ground Surface," *Shock Waves*, Vol. 12, No. 1, 2002, pp. 69–78.

[9] Ambrosini, R. D. and Luccioni, B. M., "Craters Produced by Explosions on the Soil Surface," *Trans. ASME*, Vol. 73, No. 6, 2006, pp. 890–900.

[10] Vortman, L. J., "Craters From Surface Explosions and Energy Dependence—A Retrospective View," *Impact and Explosion Cratering*, D. J. Roddy, R. O. Pepin, and R. B. Merrill, Eds., Pergamon Press, New York, 1977, pp. 1215–1229.

[11] ASTM D2487-11, Standard Practice for Classification of Soils for Engineering Purposes (Unified Soil Classification System), ASTM International, West Conshohocken, PA, 2011, www.astm.org.

[12] ASTM D7263-09, Standard Test Methods for Laboratory Determination of Density (Unit Weight) of Soil

Specimens, ASTM International, West Conshohocken, PA, 2009, www.astm.org.

[13] ASTM D2216-10, Standard Test Methods for Laboratory Determination of Water (Moisture) Content of Soil and Rock by Mass, ASTM International, West Conshohocken, PA, 2010, www.astm.org.

[14] ASTM D4318-10e1, Standard Test Methods for Liquid Limit, Plastic Limit, and Plasticity Index of Soils, ASTM International, West Conshohocken, PA, 2010, www.astm.org.

[15] ASTM D1140-00, Standard Test Methods for Amount of Material in Soils Finer than No. 200 (75-μm) Sieve, ASTM International, West Conshohocken, PA, 2006, www.astm.org.

[16] Gui, M. W. and Chien, M. C., "Taipei Shongsan Airport—A Parametric Study," *Geotech. Geol. Eng.*, Vol. 24, No. 2, 2006, pp. 227–248.

[17] Omidvar, M., Iskander, M., and Bless, S., "Stress–Strain Behavior of Sand at High Strain Rates," *Int. J. Impact Eng.*, Vol. 49, 2012, pp. 192–213.

[18] Fiserova, D., 2006, "Numerical Analyses of Buried Mine Explosions With Emphasis on Effect of Soil Properties on Loading," Ph.D. thesis, Cranfield Univ., Cranfield, Bedfordshire, UK.

[19] ASTM D2850-03a, Standard Test Method for Unconsolidated-Undrained Triaxial Compression Test on Cohesive Soils, ASTM International, West Conshohocken, PA, 2007, www.astm.org.

[20] Hallowell Manufacturing, *Kinepak Technical Data Sheet*, Hallowell Manufacturing, L. L. C., Columbus, KS, 2009.

[21] Dassault Systèmes, *SolidWorks Student Edition*, Dassault Systèmes SolidWorks Corporation, Vélizy-Villacoublay, France, 2013.

Journal of Testing and Evaluation

doi:10.1520/JTE20140123 / Vol. 43 / No. 2 / March 2015 / available online at www.astm.org

J. F. Wang,[1] J. P. Lin,[2] and X. L. Fan[3]

Evaluation of Long Multi-Span Steel U-Shaped Girder During Incremental Launching Construction

Reference

Wang, J. F., Lin, J. P., and Fan, X. L., "Evaluation of Long Multi-Span Steel U-Shaped Girder During Incremental Launching Construction," *Journal of Testing and Evaluation*, Vol. 43, No. 2, 2015, pp. 425–433, doi:10.1520/JTE20140123. ISSN 0090-3973

Manuscript received March 19, 2014; accepted for publication June 10, 2014; published online October 7, 2014.

[1] Associate Professor, Department of Civil Engineering, Zhejiang Univ., Hangzhou 310058, People's Republic of China (corresponding author), e-mail: wangjinfeng@zju.edu.cn

[2] Ph.D. Student, Department of Civil Engineering, Zhejiang Univ., Hangzhou 310058, People's Republic of China, e-mail: ljp8104@163.com

[3] Lecturer, School of Civil Engineering and Architecture, Zhejiang Univ. of Technology, Hangzhou 310014, People's Republic of China, e-mail: xinglangfan@outlook.com

ABSTRACT

Due to the low stiffness of the steel U-shaped girders of composite structure during incremental launching construction, special measures should be taken before the installation of the concrete deck. In this paper, the structural performance of steel U-shaped girder during launching construction was evaluated. The geometric configuration of the steel U-shaped girder was analyzed via transfer matrix method firstly. Then a local stress controlling strategy was developed based on a comprehensive finite element analysis of local stress characteristics. The comparison between predictions and in situ measurements of a large bridge project indicated the validity and accuracy of the proposed method.

Keywords

incremental launching construction, geometric configuration, composite structures, transfer matrix method

Introduction

Due to the high stiffness, superior strength, and low self-weight, steel-concrete composite box girders provide an economical solution for both straight and curved continuous bridges [1,2]. The steel girder and concrete deck cooperate with each other through the shear studs welded to the top flanges of the girders. Nowadays, the number of steel-concrete composite box girder bridges has been gradually increasing in several countries, especially in China for medium span bridges.

During the construction of steel-concrete composite box girders in a bridge, the incremental launching method is usually adopted. The incremental launching method was first successfully introduced by Loenardt in 1961 [3]. Based on the in-suit construction experiences, the multi-point incremental launching method in the form of wedge type [4] and draw type [5] is normally

FIG. 1 Relationship of four geometric configuration states.

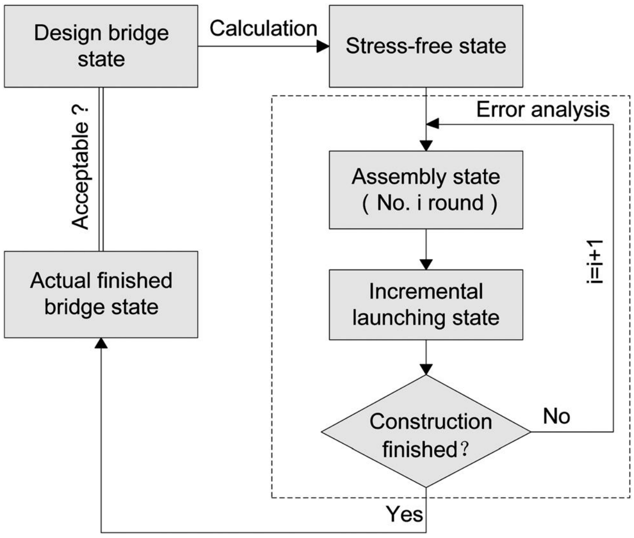

recommended. This technology requires no huge lifting equipment and little framing work, thus greatly reducing the site workload [6]. In the case of a steel-concrete composite box girder, the incremental launching method is a favorable choice for the following reasons: first, the girder can be either initially installed as a platform for further in-suit deck casting or installed simultaneously when the deck is assembling in the factory, both of which can increase the construction speed. Secondly, the light weight and low stiffness of the girder ensure a safe and quick self-tolerance in incremental launching. Therefore, the incremental launching method is expected for a composite bridge because of technical and economic benefits.

For steel-concrete composite box girder, the steel girder is an open U-shaped section with very low stiffness before installation of the concrete deck during launching construction. The flexural stiffness of the steel girder is smaller than that of the completed girder section, which results in a large deflection of the steel girder. With these peculiar features, the structural performance of steel-concrete composite box girder during construction should be well understood. The evaluation of geometric configuration, deformation, and stress of the steel U-shaped girder under construction load is needed to ensure the construction safety. Meanwhile, due to the small thickness of the bottom flange of the steel U-shaped girder, some measures should be taken to prevent local yielding.

FIG. 2 Pre-assembly angle of steel U-shaped girder segment.

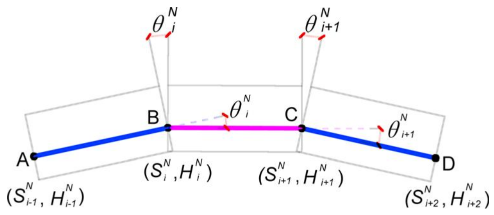

FIG. 3 Adjustment of slope angle of the final segment of launched girder.

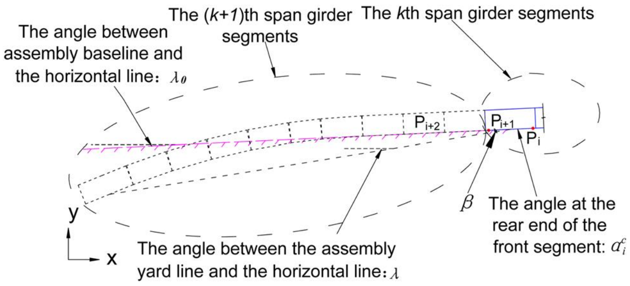

In this paper, the structural performance of the steel U-shaped girder during incremental launching construction is evaluated. First, four kinds of construction states during incremental launching are briefly introduced. Then the transfer matrix method is employed to conduct the geometric configuration analysis, and a detailed local stress analysis is performed to check the stability of bottom flange of box girder. Finally, the displacement and stresses measured in the field are compared with the computed results from analyses.

Construction States of Steel U-Shaped Girder During Incremental Launching

During the launching of steel-concrete composite girder, the construction states of the steel girder can be categories into four kinds. The first state is the design state, which is supposed to occur when launching is finished. The second state is the stress-free state where the girder is stress-free. Both of the above-mentioned states are unlikely met in real practice. The other two states, named the assembly state and launching state, refer to the construction state when the girder is under assembly and launching, respectively. The assembly state and launching state are the possible construction states during construction. The relationship between those four states is illustrated in **Fig. 1**. It is shown that the stress-free state, which the analysis of the assembly state and launching state is based on, can be back-analyzed

FIG. 4 Finite element model.

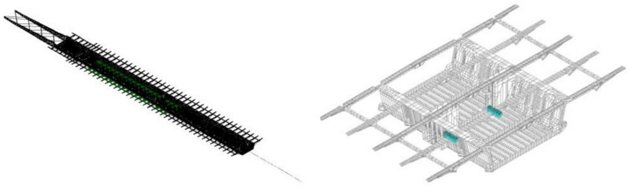

(a) Overall FEM model

(b) Local view

FIG. 5 Results of different contact boundary types.

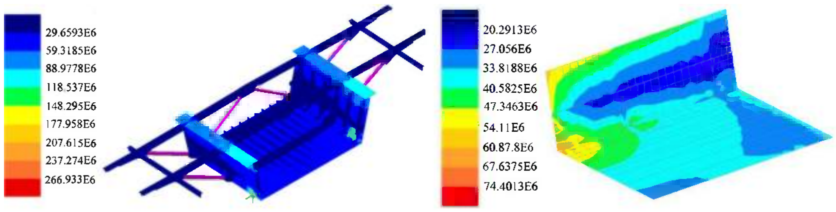

(a) Point contact (b) Line contact

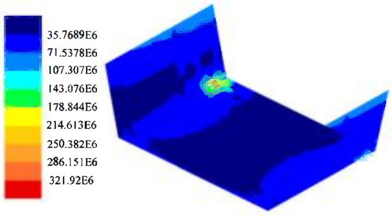

(c) Surface contact

from the design state. Therefore, the four states are closely related to each other.

Geometric Configuration

For the completed structures, the geometric configuration of the girder should match the design shape within a certain limit. Therefore, the geometric configuration of the bridge needs to be characterized beforehand as early as in the assembly state. For this purpose, the controlling parameters, the pre-assembly angle θ as shown in **Fig. 2**, and the angle at the rear end of the front girder segment α_i^c as shown in **Fig. 3**, should be identified first.

In order to improve the construction efficiency, the straight girder units are assembled in the planned curve shape, as shown in **Fig. 2**. The pre-assembly angle θ is a parameter to characterize angular discontinuities at each splices.

FIG. 6 Arrangement of the transition pad.

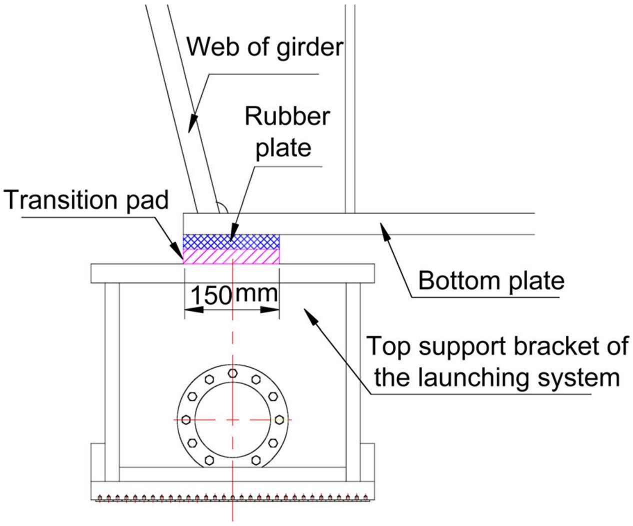

Suppose the value of pre-assemble angle is positive when the right section rotating clockwise relative to the left section. The pre-assembly angle θ_i at any control point can be calculated using the following equation:

$$\theta_i = \arctan\left(\frac{\mathrm{H}_i^N - \mathrm{H}_{i-1}^N}{\mathrm{S}_i^N - \mathrm{S}_{i-1}^N}\right) - \arctan\left(\frac{\mathrm{H}_{i+1}^N - \mathrm{H}_i^N}{\mathrm{S}_{i+1}^N - \mathrm{S}_i^N}\right) \tag{1}$$

where S_i^N and H_i^N represents mileage and elevation of the control point i under stress-free state, respectively. The pre-assembly angle is relevant to the degree of bending of the unstressed geometry and is independent of the coordinate system selected. With the aid of θ_i, the sizing of the girder is determined.

Another parameter, the angle at the rear end of the front segment α_i^c as shown in **Fig. 3**, is introduced to determine the specific position of each segment when assembling. As shown in

FIG. 7 Launching equipment.

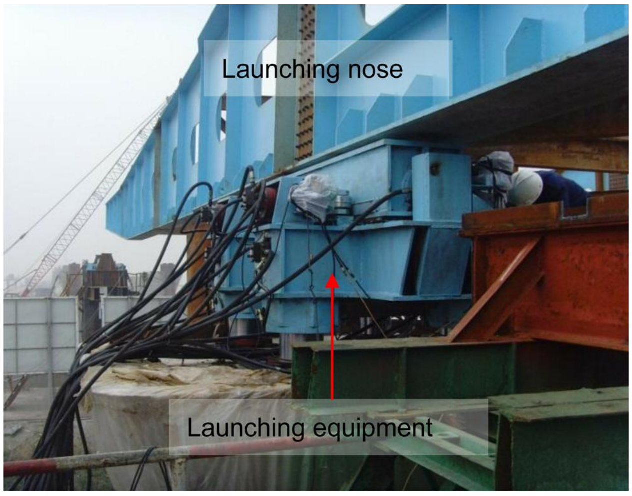

FIG. 8

Span layout of the southern approach to Jiubao Bridge (m).

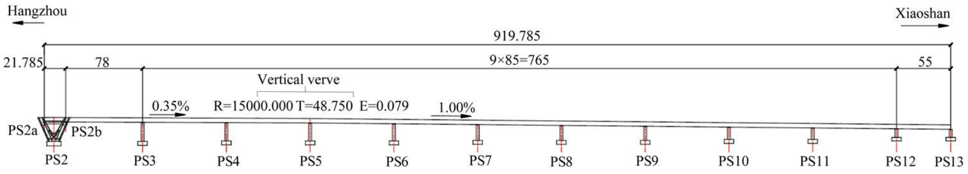

FIG. 9 Standard section of the southern approach to Jiubao Bridge (unit: cm).

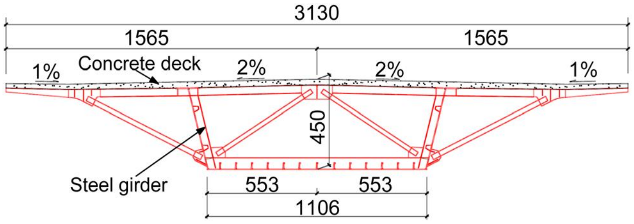

Fig. 3, the front segment of the *k*th span on the platform is the *i*th segment. When the $(k+1)$th span is a vertical curve, α_i^c can be calculated as follows:

$$\lambda = \alpha_i^c + \beta \tag{2}$$

where:

$\lambda =$ the angle between assembly baseline and the horizontal line, and

$\beta =$ the angle between assembly baseline and assembly yard line.

As shown in Fig. 3, in which λ_0 represents the angle between the assembly yard line and the horizontal line, the difference between λ_0 and λ should not exceed a certain tolerance range. This can be accomplished by adjusting α_i^c to a reasonable range: $\left(\lambda_0 + \beta + [\delta]^- / L_{k+1}, \lambda_0 + \beta + [\delta]^+ / L_{k+1}\right)$, where $[\delta]^-$ and $[\delta]^+$ refer to lower and upper tolerance displacement of the front girder segment, and L_{k+1} denotes the length of the $(k+1)$th span.

After determination of the controlling parameters, the transfer matrix method was selected for the geometric configuration analysis. The transfer matrix method has been successfully used in structural analysis and the modern control field [7–10].

FIG. 11 Finite element model of the incremental launching bridge.

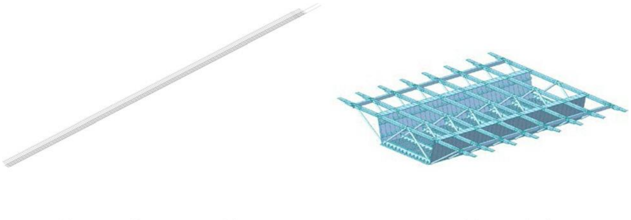
(a) Overall FEM model (b) Local view

FIG. 12 Stresses envelope diagram of bottom flange.

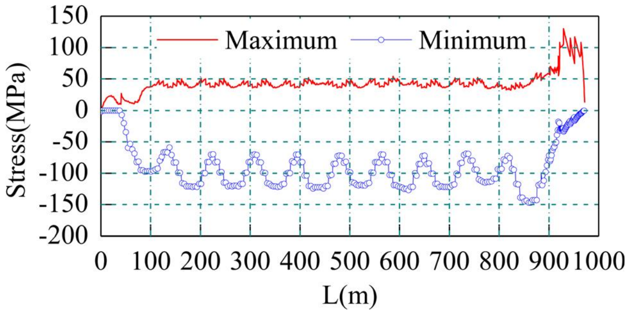

The geometric configuration of one girder segment at each cross section can be described by a state vector $\mathbf{\Phi} = [S\ H\ I]^T$, where S and H refer to mileage and elevation of one section, respectively, and a value of 1 was used to supplement the construction of transfer matrix. Then each geometric configuration in four states of the launching can be represented by $\mathbf{\Phi}^D$(design state), $\mathbf{\Phi}^N$(stress-free state), $\mathbf{\Phi}^C$(assembly state), or $\mathbf{\Phi}^L$(launching state). The stress-free state $\mathbf{\Phi}^N$ can be derived as

$$\mathbf{\Phi}^N = \mathbf{\Phi}^D + [\mathbf{0} \quad \mathbf{\Delta} \quad \mathbf{0}]^{\mathrm{T}} \tag{3}$$

FIG. 10

Incremental launching construction site.

FIG. 13 Stresses envelope diagram of top flange.

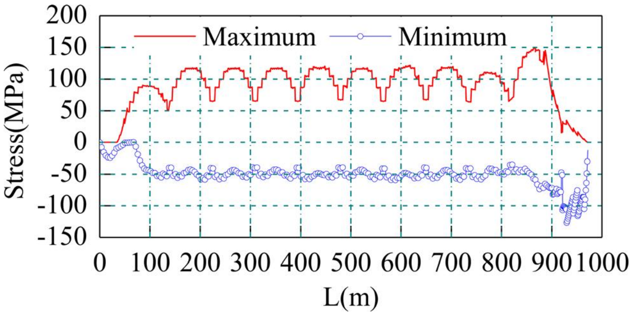

where $\boldsymbol{\Delta}$ is the camber. The value of $\boldsymbol{\Delta}$ can be adjusted according to the error identification results recorded during the construction process.

With the help of α_i^c of the front segment and the coordinate between section $i+1$ and i under stress-free state, the space state of the $(i+1)$th girder segment can be obtained by the following transfer matrix equation:

$$\boldsymbol{\Phi}_{i+2}^{C} = \mathbf{T}_{i+1}\boldsymbol{\Phi}_{i+1}^{C} + \boldsymbol{\Phi}_{i+1}^{\delta} \tag{4}$$

where $\mathbf{T}_{i+1}$ denotes the state transfer matrix and can be written as:

$$\mathbf{T}_{i+1} = \begin{bmatrix} 1 & 0 & l_{i+1}\cos(\alpha_i^C - \theta_{i+1}) \\ 0 & 1 & l_{i+1}\sin(\alpha_i^C - \theta_{i+1}) \\ 0 & 0 & 1 \end{bmatrix} \tag{5}$$

where $l_{i+1} = \sqrt{(S_{i+1}^N - S_i^N)^2 + (H_{i+1}^N - H_i^N)^2}$, $\theta_{i+1} = \arctan((H_{i+1}^N - H_i^N/S_{i+1}^N - S_i^N)) - \arctan((H_{i+2}^N - H_{i+1}^N/S_{i+2}^N - S_{i+1}^N))$, $\alpha_i^C = \arctan((H_{i+1}^C - H_i^C/S_{i+1}^C - S_i^C))$, $\boldsymbol{\Phi}_{i+1}^{\delta}$ is the state correction matrix caused by the variation of temperature which can be expressed as follows:

$$\boldsymbol{\Phi}_{i+1}^{\delta} = [\mu(T-T_0)l_{i+1} + Nw_0)]\left[\cos(\alpha_i^C - \theta_{i+1})\ \sin(\alpha_i^C - \theta_{i+1})\ 0\right]^T \tag{6}$$

where:

T = the field temperature,

T_0 = the reference temperature,

μ = the expansion coefficient of the girder,

w_0 = the shrinkage of the welding seam, and

N = the number of girder segments whose position is fixed but not welded during installation of the current segment.

The state vector of the girder segments $\boldsymbol{\Phi}^L$ can be predicted by using Eq 4 after the axial deformation caused by prestress is taken into account. Suppose that the number of girder segments that have been launched is m, and the state vector at the ith section $\boldsymbol{\Phi}_i^L$ of the front segment of launched girder on the platform is known; hence the state vector at the (i -1)th section $\boldsymbol{\Phi}_{i-1}^L$ can be predicted by the following transfer matrix equation:

$$\boldsymbol{\Phi}_{i-1}^{L} = \mathbf{U}_i\boldsymbol{\Phi}_i^{L} + \boldsymbol{\Phi}_i^{f} \tag{7}$$

where

$$\mathbf{U}_i = \begin{bmatrix} 1 & 0 & -l_i\cos\left(\alpha_i^P + \theta_i\right) \\ 0 & 1 & -l_i\sin\left(\alpha_i^P + \theta_i\right) \\ 0 & 0 & 1 \end{bmatrix} \tag{8}$$

in which

$$\alpha_i^P = \begin{cases} \arctan\left(\dfrac{H_{i+1}^C - H_i^C}{S_{i+1}^C - S_i^C}\right) & i = m \\ \arctan\left(\dfrac{H_{i+1}^N - H_i^N}{S_{i+1}^N - S_i^N}\right) & i < m \end{cases} \tag{9}$$

$\boldsymbol{\Phi}_i^f$ is the relative displacement caused by self-weight and forced displacement at the fulcrums, which is calculated according to the boundary and loading conditions on site.

Local Stress Features

Stress in the contact regions between launching bearings and bottom flanges is a major concern. Since the stress can affect the safety of girder during launching, the local stress should be checked and some measures should be taken for the contact region. Two requirements for the contact regions should be emphasized. First, the contact area should be close to the girder web because the vertical web stiffeners can distribute support reactions to the web to prevent local instability; secondly, the contact area should be controlled in an appropriate size to prevent bottom flanges from local yielding. Meanwhile, sufficient friction force should be provided during launching.

A detailed finite element analysis was performed to determine the optimum size of the contact surface. The finite

FIG. 14

Strain monitoring sections of the superstructure (Unit: m).

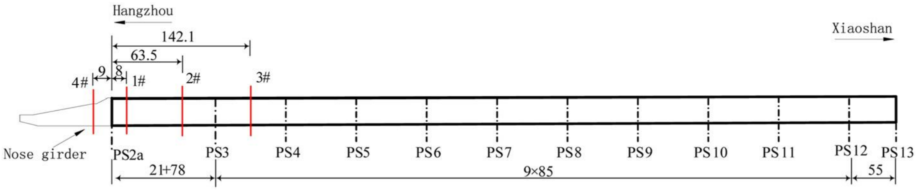

FIG. 15

Arrangement of measuring points of the steel U-shaped girder.

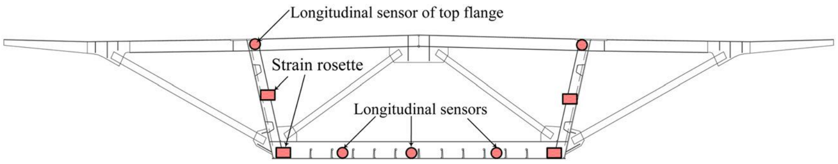

element model is shown in **Fig. 4**. Three different contact boundary conditions: (1) point contact condition, (2) line contact condition (with contact length of 1.5 m), and (3) surface contact condition (with contact area size of 1.5 m*0.5 m) were considered in order to assess the variations of the local stress. The results of the stress calculated by three contact boundary types were shown in **Fig. 5**. The maximum von Mises stress is 267, 75, and 322 MPa by point contact, line contact, and surface contact, respectively. It is demonstrated that the line contact condition is the most favorable condition.

According to the results, some measures were taken at the interface between launching equipment and the bridge girder. As shown in **Fig. 6**, a set of transition pads was placed on the top support bracket of the launching equipment. The thickness and the length of the transition pad were 0.02 and 1.6 m, respectively. The width of the contact area was 0.15 m. The thickness and the length can be adjusted during the installation according to the position of the bottom flange edge of the girder, so as to make sure that the support reaction can be applied to the web of the steel U-shaped girder. Meanwhile, a rubber plate was installed between transition pad and bottom flange to guarantee the uniform distribution of local stress. Typical launching equipment is shown in **Fig. 7**.

Structural Performance Analysis of Jiubo Bridge

PROJECT BACKGROUND

Jiubao bridge is one of the important bridges crossing the Qiantang River in Hangzhou, China. This is the first large composite bridge ever in China, with a total length of 1855 m. The main navigation span is a hybrid arch-girder structure, and the approach span is a steel-concrete box girder structure with the constant section shape. Considering the characteristics of the steel-concrete composite structure, the improved incremental launching method is adopted for the construction of the approach span. The layout of Jiubo bridge is shown in **Fig. 8**. A typical section of the steel U-shaped girder is shown in **Fig. 9**. The incremental launch construction site is shown in **Fig. 10**.

FIG. 16 Arrangement of measuring points of nose girder.

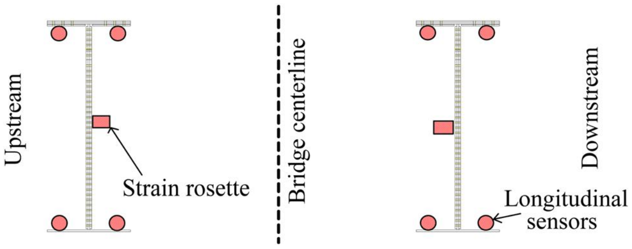

Stress Control Section Selection and Arrangement of Measuring Points

The incremental launching process was simulated by structure analysis software Midas/Civil. The superstructure was modeled as 3D beam elements, and every launching stage was modeled by altering the boundary conditions. The finite element model of the bridge is shown in **Fig. 11**. Stress envelope diagrams of the top and bottom flange of the girder are shown in **Figs. 12** and **13**, respectively. The maximum tensile and compressive stress of top flange of the steel U-shaped girder is −150 and 80 MPa, respectively. The maximum tensile and compressive stress of bottom flange of the steel U-shaped girder is −72 and 126 MPa, respectively.

According to the finite element analysis (FEA) results, the unfavorable sections of the steel U-shaped girder and the nose girder were chosen for real-time strain monitoring. These monitoring sections are shown in **Fig. 14**. The arrangement of the strain gauge in the steel U-shaped girder and nose girder are shown in **Figs. 15** and **16**, respectively.

FIG. 17 Real-time monitoring and remote transmitting system.

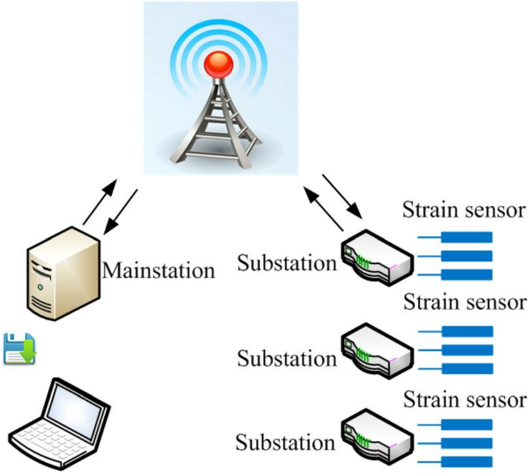

FIG. 18

Deformation after each round of incremental launching.

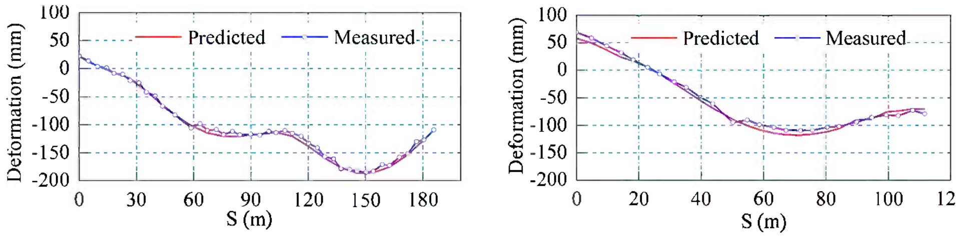

(a) Second round

(b) Third round

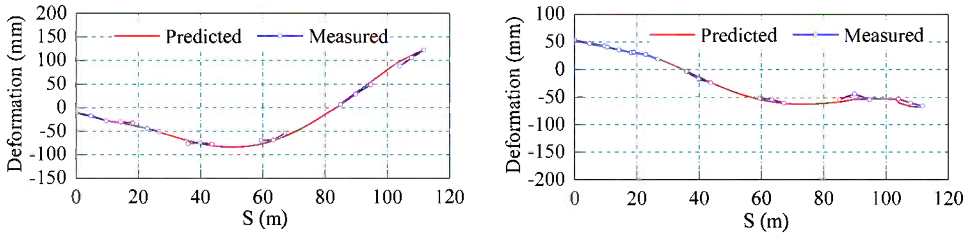

(c) Fourth round

(d) Sixth round

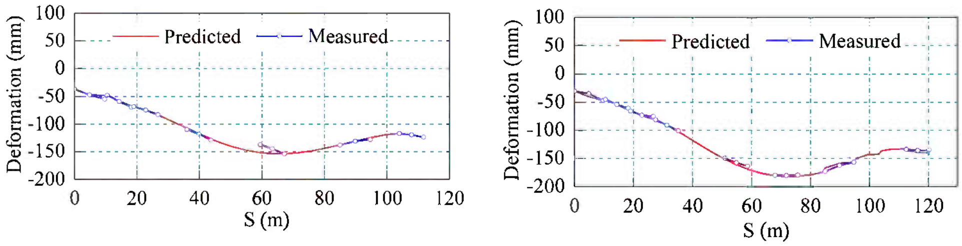

(e) Eighth round

(f) Tenth round

In order to achieve the remote real-time monitoring of the control sections, the strain of measuring points on the girder was continuously sampled. The MCU-32 type of distributed automatic measuring system was used for the strain acquisition. In order to avoid interference of the data line to the construction, GPRS instant transmission was introduced. **Figure 17** shows the corresponding real-time monitoring and remote transmitting system.

COMPARISON OF GEOMETRIC CONFIGURATION

Figure 18 shows the comparison between the measured and calculated deformation of the girders. It is found that the measurements agree reasonably well with the computed results.

The geometric configuration of the launched girder is measured and shown in **Fig. 19**. From the comparison with the computed elevation, the proposed transfer matrix method shows superiority in accuracy.

Figure 20 shows the predicted elevation of the girder unit in a vertical curved shape. Considering β is often ignored in traditional incremental launching method, the predicted elevation of the girder unit when β is assumed to be zero is also demonstrated for comparison. It can be noticed that errors, normally within 1 cm, can be as large as approximately 2.3 cm if β is ignored, which may result in the secondary stresses and is a potentially danger to the stability of the bridge.

COMPARISON OF STRESS RESULTS

Figures 21–23 show the stress of monitoring sections in construction, in which D refers to the launching distance of the

FIG. 19 Relatively elevation after completion of incremental launching.

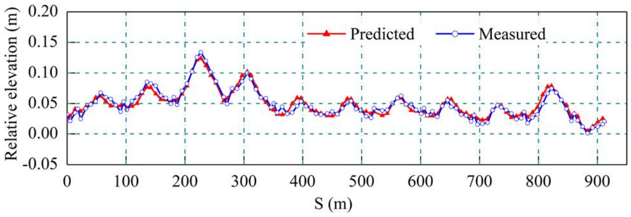

FIG. 20 Relatively elevation when angle β is ignored.

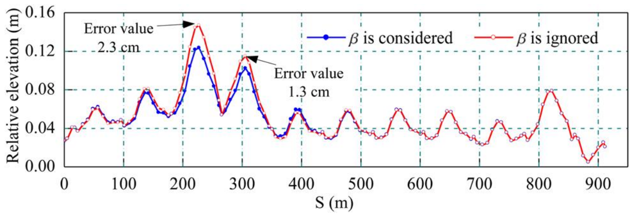

FIG. 21 Stresses in section 1.

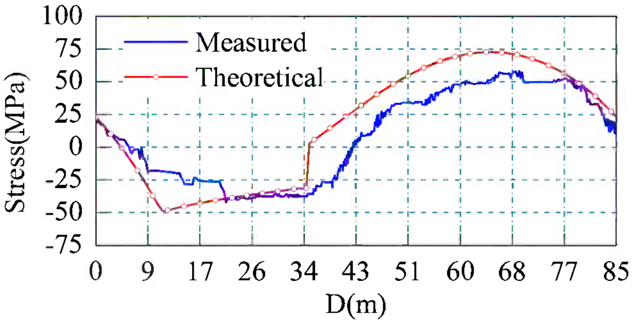

(a) Stresses in the top flange

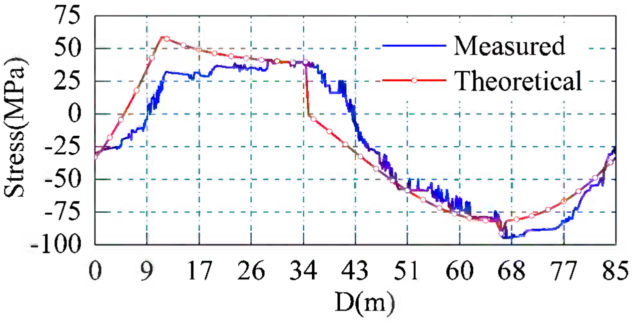

(b) Stresses in the bottom flange

FIG. 22 Stresses in mid-span section between PS2 and PS3.

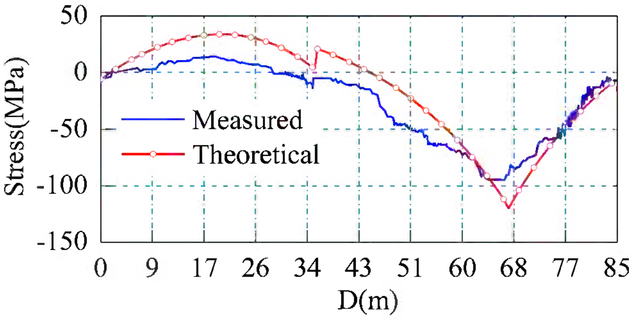

(a) Stresses in the top flange

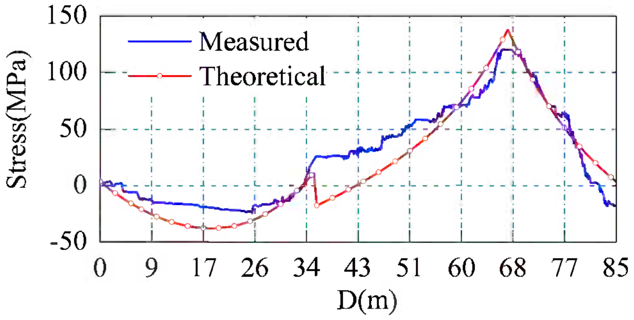

(b) Stresses in the bottom flange

FIG. 23 Stresses in mid-span section between PS3 and PS4.

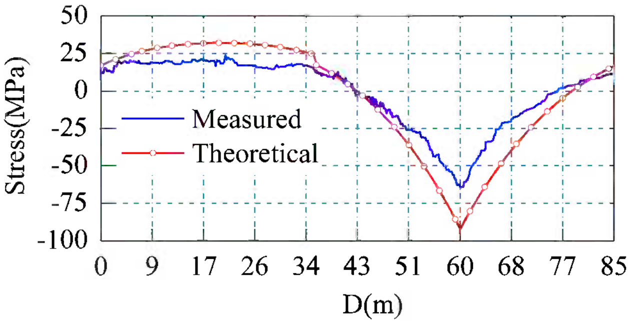

(a) Stresses in the top flange

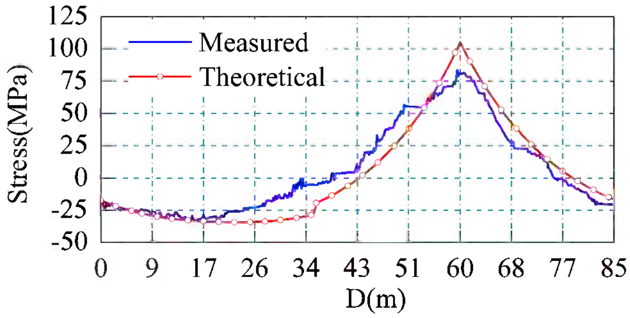

(b) Stresses in the bottom flange

FIG. 24 Stresses of monitoring section in nose girder.

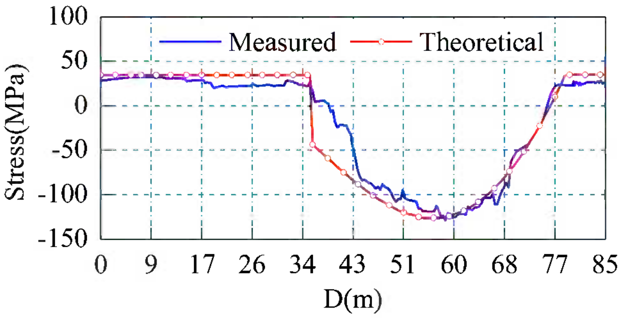

(a) Stresses in the top flange

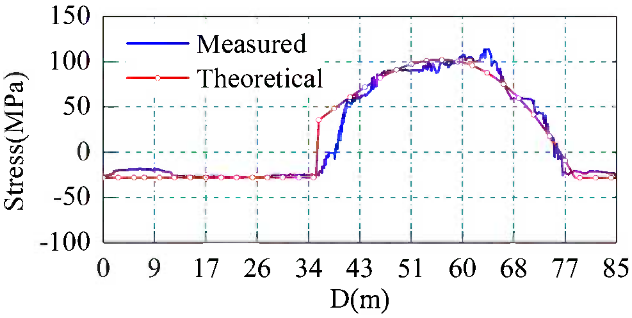

(b) Stresses in the bottom flange

corresponding construction round. It is seen from these figures that the predicted stress agrees well with the measured stress. In section 1, the stresses in the bottom flange fall into the range of −41.5 and 58.1 MPa, and the stresses in the top flange fall into the range of −94.7 and 41.2 MPa. For the mid-span section between PS2 and PS3, the stresses in the bottom flange fall into the range of −94.9 and 12.3 MPa, and the stresses in the top flange fall into the range of −24.1 and 121.2 MPa. The maximum compressive stress and tensile stress at the mid-span section between PS3 and PS4 were −64.3 and 83.5 MPa, respectively. The results show that the steel U-shaped girder can be considered as a safe structural element during the incremental launching.

The Stress of the monitoring section of the nose girder is shown in **Fig. 24**. It can be concluded from the figure that the predicted stress of the control section of the nose girder agrees well with the measured value. During launching construction, the stresses in the top flange fall into the range from −132.7 to 32.7 MPa, and the stresses in bottom flange fall into the range from −27.8 to 113.8 MPa. Both of the maximum compressive stress and tensile stress were smaller than the allowable values and the nose girder; it therefore meets the strength requirement.

Conclusions

Steel-concrete composite box girders supply a competitive solution for multi-span continuous bridges. Their structural behavior should be well understood in different construction methods. In this paper, the structural performance of the steel U-shaped girder in incremental launching construction was evaluated. The geometric configuration of the steel U-shaped girder was predicted and evaluated via transfer matrix method. The determination of the size of contact surfaces between launching equipment and bridge girder was conducted by a detailed finite element analysis. The following conclusions can be drawn:

1. The geometric configuration of the steel U-shaped girder is controlled by two parmeters, i.e., the preassembly angle and the angle α_i^c. The geometric configuration can be predicted with reasonable accuracy by the proposed transfer matrix method.
2. The size of the contact region is limited to a reasonable range to prevent local instability and local yielding. Stresses in the top flange and bottom flange fall into the range of allowable stress during construction.

ACKNOWLEDGMENTS

The writers would like to express sincere acknowledgment to Hangzhou Urban Infrastructure Development Corporation, which provided us the engineering background and supported this study. The writers also gratefully acknowledge the support from Zhejiang Provincial Natural Science Foundation (Grant No. Y1110181), National Natural Science Foundation Projects of China (Grant Nos. 51108411 and 11172266). Additional acknowledgements are also extended to Finite Element Analysis Ltd., which generously provided LUSAS software.

References

[1] Nie, J. and Zhu, L., "Beam-Truss Model of Steel-Concrete Composite Box-Girder Bridges," *J. Bridge Eng.*, Vol. 19, No. 7, 2014, p. 04014023.
[2] Brozzetti, J., "Design Development of Steel-Concrete Composite Bridges in France," *J. Constr. Steel Res.*, Vol. 55, No. 1, 2000, pp. 229–243.
[3] Zellner, W. and Svensson, H., "Incremental Launching of Structures," *J. Struct. Eng.*, Vol. 109, No. 2, 1983, pp. 520–537.
[4] Moreira De Sousa, H. F., Bento, J., and Figueiras, J., "Structural Monitoring of Lezíria Bridge Since its Construction," *Proceedings of the IABMAS 2010—The Fifth International Conference on Bridge Maintenance Safety*, Philadelphia, PA, July 11, 2010.
[5] Rosignoli, M., "Thrust and Guide Devices for Launched Bridges," *J. Bridge Eng.*, Vol. 5, No. 1, 2000, pp. 75–83.
[6] Rosignoli, M., *Bridge-Launching*, Thomas Telford, London, 2002.
[7] Granata, M. F., Margiotta, P., and Arici, M., "A Parametric Study of Curved Incrementally Launched Bridges," *Eng. Struct.*, Vol. 49, 2013, pp. 373–384.
[8] Sasmal, S. and Ramanjaneyulu, K., "Transfer Matrix Method for Construction Phase Analysis of Incrementally Launched Prestressed Concrete Bridges," *Eng. Struct.*, Vol. 28, No. 13, 2006, pp. 1897–1910.
[9] Tso, W. K. and Chan, P. C. K., "Static Analysis of Stepped Coupled Walls by Transfer Matrix Method," *Build. Sci.*, Vol. 8, No. 2, 1973, pp. 167–177.
[10] Pestel, E. C. and Leckie, F. A., *Matrix Methods in Elastomechanics*, McGraw-Hill, New York, 1963.

Journal of Testing and Evaluation

doi:10.1520/JTE20140030 / Vol. 43 / No. 2 / March 2015 / available online at www.astm.org

Jialiang Yao,[1] Congshi Wu,[2] Xianglong Liu,[3] and Keke Feng[4]

Effect of Different Interlayers of Cement Concrete Pavements on Vibration and Anti-Erosion of Bases

Reference

Yao, Jialiang, Wu, Congshi, Liu, Xianglong, and Feng, Keke, "Effect of Different Interlayers of Cement Concrete Pavements on Vibration and Anti-Erosion of Bases," *Journal of Testing and Evaluation*, Vol. 43, No. 2, 2015, pp. 434–442, doi:10.1520/JTE20140030. ISSN 0090-3973

ABSTRACT

This paper presents an experimental study in which laboratory tests were conducted to investigate how the different interlayers (between the pavement surface slabs and the bases) could improve the performances of vibration response and anti-erosion of the bases. In the tests for vibration response of the bases, geotextile and rubber sheet were used as the interlayers, and the micro-seismic testing system was employed to characterize the vibration response of bases of concrete pavements beneath different interlayers under impact loading. The vibration test results indicated that under the same impact loading, compared with the bases without an interlayer atop, vector sum of the maximum vibration velocity of the bases beneath a rubber sheet interlayer and two layers of geotextile interlayer decreased by 35 % and 80 %, respectively; and vector sum of their maximum vibration displacement decreased by 18 % and 26 %, respectively. In the laboratory tests for anti-erosion, the bases with geotextile or emulsified asphalt slurry seal as the interlayer atop were tested for performances of resisting water erosion via a self-made testing apparatus. The anti-erosion test results indicated that, under the same other conditions, compared with the bases without an interlayer atop, the erosion rate (after 12 min of testing) of the bases with geotextile or emulsified asphalt slurry seal as interlayers atop decreased by 99 % or 59 %, respectively. The interlayer has the effects of damping vibration and resisting water erosion on the pavement base.

Keywords

cement concrete pavement, base, interlayer, laboratory test for vibration response, laboratory test for anti-erosion

Manuscript received January 27, 2014; accepted for publication April 3, 2014; published online November 5, 2014.

[1] Professor, School of Traffic and Transportation Engineering, Changsha Univ. of Science and Technology, and Key Laboratory of Rd. Structure and Material of Ministry of Transport (Changsha), Changsha, Hunan 410014, China, e-mail: yao26402@126.com

[2] Professor, School of Civil Engineering and Architecture, Changsha Univ. of Science and Technology, Changsha, Hunan 410014, China, e-mail: wucosh@163.com

[3] Master, School of Traffic and Transportation Engineering, Changsha Univ. of Science and Technology, Changsha, Hunan 410014, China (Corresponding author), e-mail: 15116267914@163.com

[4] Master, School of Traffic and Transportation Engineering, Changsha Univ. of Science and Technology, Changsha, Hunan 410014, China, e-mail: fkk1042@163.com

Introduction

The interlayer of cement concrete pavement refers to the layer paved between the pavement surface slab and the pavement base. Up to now the materials for interlayer vary in different countries. Asphalt concrete interlayer is popularly used in the United States, whereas the use of geotextile interlayer is required to separate a concrete slab from a cement-treated base in Germany [1]. In Korea, polythene sheet is used as a friction reducer placed between the lean concrete base and the concrete pavement slab, and, in some cases, asphalt is employed as an alternative [2]. In China, the frequently used materials for interlayer may be asphalt concrete, emulsified asphalt slurry seal (EASS), geotextile, emulsion wax curing agent (EWCA), etc., as shown in **Fig. 1**.

What has almost been acknowledged universally is the necessity to lay an interlayer between the cement concrete slab and the rigid or semi-rigid base layer [3–5]. But disputes exist about issues such as the technical term for interlayer, the engineering requirements for using different interlayers, the materials for interlayer, the criteria for acceptance inspection of its construction, the option of its thickness, the long-term performances of interlayer and of pavements with interlayer, etc. For instance, Ref 4 emphasizes that the thinner the interlayer the better, whereas Ref 6 remarks that it would be more effective if a thicker flexible interlayer is used as a damper. The key to existence of the above-mentioned confusion is the uncertainty of some functions of interlayer. The possible functions played by the interlayer are still waiting for a systematic study. As a consequence, regular practice or experience has usually been employed as the guideline for design and construction of interlayer in practical pavement projects.

Up to now, the reports on functions of interlayer have universally focused on breaking the bond of the pavement slab from the base [7], reducing friction at the interface between the slab and the base [8], restraining reflected cracking [9], etc. The effect of interlayer on the performances of the pavement base has rarely been reported, if at all, the reports limited to the qualitative analysis. For example, Ref 10 reports that the interlayer can offer protection to the base when the pavement is under construction. It was identified in the Project of Upgrading Reconstruction of Qingyuan-Lianzhou Highway in Guangdong Province that the long-time exposure of base surface to traffic of construction vehicles has led to abrasion and even defects of base surface such as potholes or protrusion of the aggregate particles on the surface of the base (as shown in **Fig. 2(*a*)**). Considering the functions of interlayer such as separating surface slab from base and protecting base, solutions to the above-mentioned problems were proposed: (1) to the base (a) whose surface with poor quality, or (b) with more than 30 % of the inspected area full of defects such as potholes or protruding aggregate stones, or (c) which had to be temporarily open to traffic after reaching a certain strength after construction, 1-cm-thick EASS was placed atop those bases as the interlayer; (2) to the base with less than 30 % of the inspected area full of aforementioned defects, cement mortar, or asphalt mortar was used to patch the local defects first and then EWCA was sprayed atop the base as the interlayer (as shown in **Fig. 2(*b*)**); and (3) to

FIG. 1

(*a*) Interlayer of emulsified asphalt slurry seal after construction; (*b*) construction of interlayer of geotextile; (*c*) construction of interlayer of emulsion wax curing agent; and (*d*) the continuous film formed by emulsion wax curing agent atop the surface of base.

FIG. 2 (*a*) Aggregate particles protruding on the base surface; (*b*) local defects patched with asphalt mortar before construction of EWCA interlayer; and (*c*) cracked base surface fixed with asphalt felt before construction of EWCA interlayer.

the base surface with cracks, asphalt felt was used to cover the cracks first and then EWCA was sprayed atop the base as the interlayer (as shown in **Fig. 2(c)**).

As to the effect of interlayer on the performances of pavement base in the operation, there seems no specific laboratory study report. Therefore, this research is to investigate the effect of interlayer on the performances of base such as vibration response and anti-erosion via the laboratory tests whose design was based on the practice and the problems from some practical projects in Guangdong and Hunan Provinces. And in these practical projects, their interlayers were not constructed with the same materials, and, thus, in the two types of tests in this paper, different interlayer materials were tested. In the tests for anti-erosion, interlayer of a single layer of geotextile, interlayer of EASS, and no interlayer were tested; although the tests for vibration response tested the 5-mm-thick ordinary rubber sheet, a single layer or double layers of woven geotextile as the interlayer material did not test the EASS interlayer. But considering that the properties of the ordinary rubber sheet are similar to those of EASS, the test results of the rubber sheet may be of significance to EASS and vice versa. It is expected that the findings drawn from these tests can offer a scientific basis and test methods to selecting the optimum interlayer (such as the interlay that can effectively damp the vibration of the base or improve the anti-erosion of the base) in the pavement design or construction of practical projects.

Properties of Various Materials for Interlayer

GEOTEXTILE

The properties of geotextiles used in this research were determined according to the relevant standards such as JTJ/T 019-98 [11], JTJ E50-2006 [12], etc., with consideration of requirements of the tests conducted in this research. **Table 1** presents the properties of geotextile as interlay materials used in this research. To avoid wrinkles or folds in manual placing, geotextile was appropriately stretched and fixed with steel nails or particular fixing nails were driven into the base after being placed.

EMULSIFIED ASPHALT SLURRY SEAL (EASS)

The key properties of EASS used in this research were tested in accordance with JTG/T F40-02-2005 [13]. The quality control of EASS during construction includes six indicators: consistency, asphalt-aggregate ratio, gradation, appearance, paving thickness, and wheel abrasion loss after 1 h soaking. The standard mix proportion of slurry seal used in this research required 12 % of emulsified asphalt, 1 % of filler, and 87 % of mineral aggregate whose gradation is shown in **Table 2**. **Table 3** describes the mix proportion and the key properties of EASS, which conform to the requirements of JTG/T F40-02-2005 and this research.

RUBBER SHEET

In some practical projects (such as the Yunfu-Luoding Highway Project of Guangdong Province), a rubber sheet has been used as the interlayer at the joints of cement concrete pavements (as shown in **Fig. 3**) or the pavement sections that are vulnerable to damage caused by vehicle impact loading, such as ones at highway toll stations. Its use can ease problems such as loosening or

TABLE 1 Properties of geotextile as interlayer materials used in the tests.

Property	Measured Value
Mass per unit area (g/m^2)	312
Thickness under load (pressure) (mm)	2.45
Longitudinal tensile strength (kN/m)	9.69
Latitudinal tensile strength (kN/m)	9.62
Longitudinal tearing force (kN)	0.25
Latitudinal tearing force (kN)	0.26
CBR bursting force (kN)	1.59
Equivalent opening size (O95) (mm)	0.09
Water permeability in normal direction under load (pressure) (cm/s)	2.1×10^{-1}

TABLE 2 Aggregate gradation of emulsified asphalt slurry seal.

Sieve Size (mm)	Cumulative Percent Passing (%)	Criterion Specified by JTG/T F40-02-2005 (%) [13]
9.5	100.0	100
4.75	95.1	100-95
2.36	66.1	90-65
1.18	46.2	70-45
0.6	32.6	50-30
0.3	23.0	30-18
0.15	16.9	21-10
0.075	10.0	15-5

spalling of cement concrete, to which the sections next to joints are prone. The properties of the rubber sheet used in the tests in this paper are shown in **Table 4**.

Laboratory Test for Vibration Response

Vibration of pavement structure is likely to cause dynamic damages, which may lead to cracking and loosening of the base materials, and which in turn will shorten the life of the pavement. Thus, vibration damping is one of the important factors in the design of the pavement structure. Whereas among all physical quantities that can be used to describe the vibration intensity, the vibration velocity is the most relevant to the destruction of structures and is often used to represent the vibration intensity [14]. And vibration velocity has been considered as the failure criteria of vibration safety in many industries in China [15]. Therefore, to damp vibration of the base is to reduce the vibration velocity of the base, and to investigate the effect of the interlayer on the vibration response of the base is to test the effect of the interlayer on the vibration velocity of the base.

Impact loading from moving vehicle will lead to vibration of pavement, which is regarded as a kind of microseism in Ref 16. The interlayer of cement concrete pavement can be considered an elastic element linking the forced vibration system (i.e., the concrete surface slab) and the foundation (including the base layer and the subgrade), damping the vibration transmitted from the former to the latter. It is supposed in this paper that the interlayer may have an effect of damping vibration or reducing vibration velocity on the pavement base in several ways. First, the interlayer separates the surface slab from the base and breaks their similar vibration frequency, which will lead to the sympathetic vibration, and thus offers protection to both the surface slab and the base. Second, compared with the cement concrete, materials for the interlay are of smaller elastic modulus and better compressibility. When the cement concrete pavement is under impact loading of vehicle wheels, the vertical pressure will force the interlayer into compressive deformation, which can offer damping to impact the base and ease the effect of microseism on the base. Furthermore, the interlayer can increase the structural damping and dissipate vibration energy from the forced vibration system, and thus damp vibration of the base.

FIG. 3 Rubber sheet installed at the concrete pavement joint as interlayer.

METHODS

To obtain a regular pattern of effect of interlayer on the vibration response of base layer, the authors did the laboratory tests for impact vibration response with the testing apparatus for vibration (as shown in **Fig. 4**). The specimens simulating cement concrete pavement surface slabs were of strength C35 and size $300 \times 300 \times 50\ \text{mm}^3$. The base layer was made of C15 lean concrete $1000 \times 1000 \times 100\ \text{mm}^3$. Three different kinds of

TABLE 3 Mix proportion and key properties of EASS used in the tests.

Mix Proportion or Property	Measured Value	Criterion Specified by JTG/T F40-02-2005 (%) [13]
Emulsified asphalt content (%)	12 (58 % asphalt content)	More than 55 % asphalt content
Asphalt-aggregate ratio (%)	7	
Mix proportion	Aggregate:emulsified asphalt:water = 100:12:5	
Paving thickness (mm)	8–10	7–10 mm
Wet wheel abrasion loss after 1 h soaking (g/m^2)	702.5	No more than 800
Consistency (cm)	3	2–3
Appearance	Qualified	Uniform

TABLE 4 Properties of rubber sheet as interlayer material used in the tests.

Property	Measured Value
Thickness (mm)	5
Width (m)	0.5
Length	Determined by the length of expansion joints
Density (g/cm^3)	1.65
Tearing strength (MPa)	3.0
Elongation (%)	250
Hardness	65 ± 5

interlayer were used: 5-mm-thick ordinary rubber sheet, a layer of woven geotextile and two layers of woven geotextile. And the base layer without interlayer was tested for comparison.

During testing, the compaction hammer used in the geotechnical heavy compaction test was applied to impose the impact loading to simplify and unify the loading methods. In the light of the practice of the geotechnical heavy compaction tests in China, a 4.5-kg hammer fell a distance of 45 cm on the center of the specimen, whereas two sets of the same testing apparatus for microseism, which were respectively linked to the surface slab specimen and the base layer, collected their vibration waveform simultaneously. (The data of the vibration of the surface slab and their analyses would be reported in another paper.) Each set of testing apparatus for microseism consists of three sensors, a microseism recording device to collect vibration waveform, and a computer. Three sensors (CD-1 magnetic speed sensors with the maximum measurable displacement being ±1 mm and sensitivity being 604 microvibrations/cm/s) were adhered to the surface of the base of C15 lean concrete with 10 % cement by a liquid glue of rapid solidification. They were installed at the monitoring points that were located 2 cm away from the edge of the base layer surface. Sensor 1 was used to detect the vertical vibration wave whose direction (*Z*) is perpendicular to the base layer surface. The other two sensors were used to detect two kinds of horizontal vibration waves, which were parallel to the base layer surface and whose directions are mutually perpendicular, sensor 2 for the latitudinal direction (*Y*), and sensor 3 for the longitudinal direction (*X*). What the sensors detected were particle vibration velocity, whereas the microseism recording device recorded the waveform of particle vibration velocity. The vibration data were analyzed by the computer, including the maximum vibration velocity, the maximum displacement caused by vibration, and

FIG. 4

Schematic of testing apparatus for vibration caused by impact loading: (*a*) side view; and (*b*) top view.

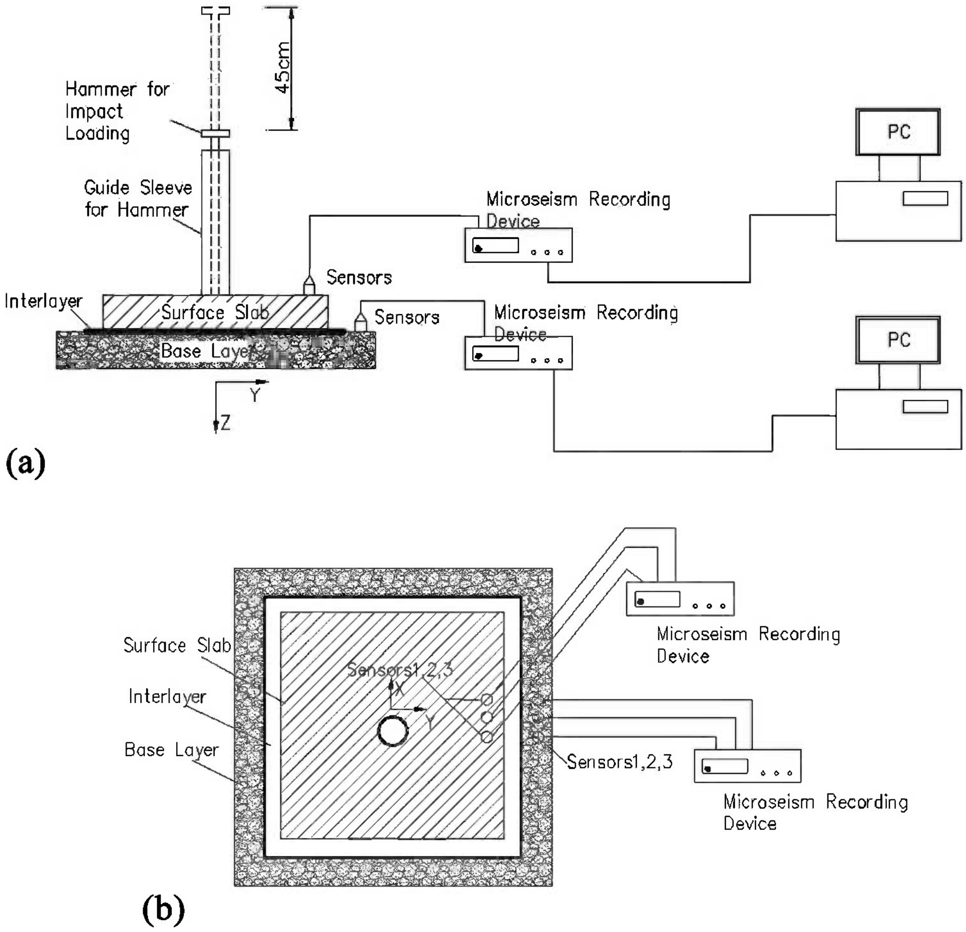

TABLE 5 Maximum vibration velocity (MVV) of bases beneath different interlayers.

Interlayer	MVV by Sensor 1 (cm/s)	MVV by Sensor 2 (cm/s)	MVV by Sensor 3 (cm/s)	Vector Sum of MVV (cm/s)	Percentage of Reduced Vector Sum of MVV (%)
No interlayer	5.86	1.86	2.92	6.81	Baseline data
Rubber sheet	3.56	2.46	0.85	4.41	35
A layer of geotextile	1.37	0.82	1.27	2.04	70
Two layers of geotextile	1.19	0.36	0.53	1.35	80

their vector sum, respectively. These maximum values were interpreted as the indicators of the damping effect of different interlayers: the smaller these maximum values, the better the damping effect. The vector sum of maximum vibration velocity or maximum displacement equals the arithmetic square root of the sum of squared vibration velocity or displacement measured by sensors 1, 2, and 3, as expressed in Eq 1.

$$d = \sqrt{(a^2 + b^2 + c^2)} \tag{1}$$

where:

d = the vector sum; and

a, b, or c = the squared vibration or displacement measured by sensor 1, sensor 2, or sensor 3, respectively.

RESULTS OF VIBRATION VELOCITY

Table 5 shows the measured vibration velocity of the base layers beneath different interlayers under the same impact loading.

Table 5 indicates that, under the same impact loading, the vector sum of maximum vibration velocity of the base layer with interlayer atop decreased thanks to the damping function played by the interlayer as well as the surface slab which increases the structural damping and dissipates vibration energy generated by the impact loading and thus damps vibration of the base. Compared with the base without an interlayer atop, the decrease was 35 % for the base with a rubber sheet as the interlayer atop, 70 % for the base with a layer of geotextile as the interlayer atop, and 80 % for the base with two layers of geotextile as the interlayer atop. The results indicate that interlayer can reduce the maximum vibration velocity of the base layer. And the better damping effect of two layers of geotextile than that of one layer may be interpreted as, for the interlayer of smaller modulus material such as geotextile (compared with rubber sheet, geotextile is of smaller modulus), the thicker the interlayer, the better the effect of vibration damping.

RESULTS OF DISPLACEMENT CAUSED BY VIBRATION

Under the same impact loading, the maximum displacement amplitude of the base layers beneath different interlayers caused by vibration is shown in **Table 6**.

Table 6 indicates that, under the same impact loading, the vector sum of maximum displacement of the base layer with interlayer atop decreased. Compared with the base without an interlayer atop, the decrease was 18 % for the base with a rubber sheet as the interlayer atop, 25 % for the base with a layer of geotextile as the interlayer atop, and 26 % for the base with two layers of geotextile as the interlayer atop. The results indicate that interlayer can reduce the displacement of the base layer caused by vibration, which helps to protect the base layer.

Laboratory Tests for Anti-Erosion

Pavement surface water is likely to enter into the base surface via the pores, joints, or cracks. If drainage of the base layer is not satisfying, especially in the rainy season and/or in low-lying areas, the free water collected on the base surface will generate considerable hydrodynamic pressure under the impact loading of moving vehicles (especially heavy-duty trucks at high speed). Reference 17 reports that the higher the vehicle speed, the greater the hydrodynamic pressure. The damage from the hydrodynamic pressure to the base layer includes punching and pumping, as shown in **Fig. 5**. In the process of punching, when the vehicle pulls into slab 1 and its wheels first press down slab 1, the water under slab 1 will spray and punch downward at a certain speed, and the strong hydrodynamic pressure will produce a huge impact and oppression on the base materials. In the process of pumping, when the wheel load pulls out from slab 1 and into slab 2, slab 2 will be pressed down, whereas slab 1 will rebound as a result of the disappearance of the load, which will lead to a huge pumping force at the interface between slab 1 and the base. With the continual vehicle load,

TABLE 6 Maximum displacement amplitude (MDA) of bases beneath different interlayers caused by vibration.

Interlayer	MDA by Sensor 1 (cm)	MDA by Sensor 2 (cm)	MDA by Sensor 3 (cm)	Vector Sum of MDA (cm)	Percentage of Reduced Vector Sum of MDA (%)
No Interlayer	0.0062	0.003	0.0025	0.0073	Baseline data
Rubber sheet	0.005	0.0023	0.0023	0.0060	18
A layer of geotextile	0.004	0.003	0.0023	0.0055	25
Two layers of geotextile	0.005	0.0017	0.0015	0.0054	26

FIG. 5 Schematic representations of production of hydrodynamic pressure from water on the base surface: (*a*) punching; and (*b*) pumping.

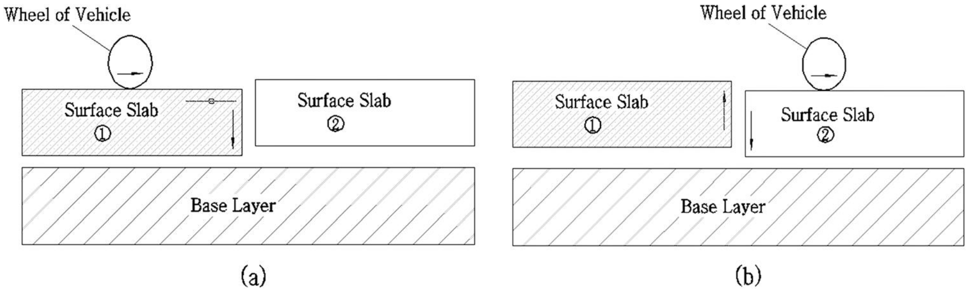

the slabs keep on rising and falling and the base keeps on being punched and pumped. As a consequence, base materials, especially fine aggregate, will lose adhesion because of the running of water and eventually will be washed away along any crevice under the hydrodynamic pressure. Reference 18 describes that the fine material within 1 mm particle size will be washed away. In this case, the fine material of base being washed away by water is referred to as water erosion of base.

METHODS

To simulate the erosion of the base caused by the hydrodynamic pressure, a testing apparatus for water erosion was made in this research, as shown in **Fig. 6**.

The testing apparatus consists of two symmetric units. Each unit is made up of a lower cylinder and an upper cylinder, respectively. Interior chambers of lower cylinder and upper cylinder can be interlinked and their sidewalls can be joined together with locking buckles and sealed. The lower cylinder is placed on a horizontally sliding track, which is fixed on a pedestal, and the lower cylinder can slide along the sliding track to join with or move away from the upper cylinder. Inside the lower cylinder, there are a lower sieve and an upper sieve, which can be fastened to the bottom and the top of the specimen, respectively. Furthermore, there is a piston in the upper cylinder; the piston is linked by a connecting rod to a lever and the other end of the lever is linked to an electric motor.

Tests were designed in this research to compare the water erosion resistance of cement-stabilized macadam bases with different interlayers—EASS, geotextile, and no interlayer. Cylinder specimens (150 mm in diameter and 150 mm in height) were shaped in the laboratory according to the field mineral aggregate gradation and with a cement content of 5 %.

In the case of EASS as the interlayer, following the practice in the field construction process, the top side of specimens for water erosion tests was first brushed with the high penetration emulsified asphalt (cationic emulsified asphalt of PC-2) whose asphalt content reached about 43.1 %, and then covered with hot asphalt of AH-90, the amount of which was at about 1.0 ± 0.2 l/m^2. Aggregates ranging from 0.6 mm to 4.75 mm were used as filler. For geotextile, it was nailed to the top side of specimens for tests as the interlayer.

In consideration of the fact that water erosion mainly has an effect on the top side of the base, the lateral sides of all specimens were wrapped with plastic film in the tests (as shown in **Fig. 7**).

The above-mentioned specimens were first bathed in water of 60°C for 24 h to shorten the time for testing, and then taken out of the water bath, wiped with a wet towel after being wrung dry, and weighed to get M_0. After that, the specimen was put

FIG. 6 Schematic of testing apparatus for water erosion: (*a*) side view; and (*b*) front view.

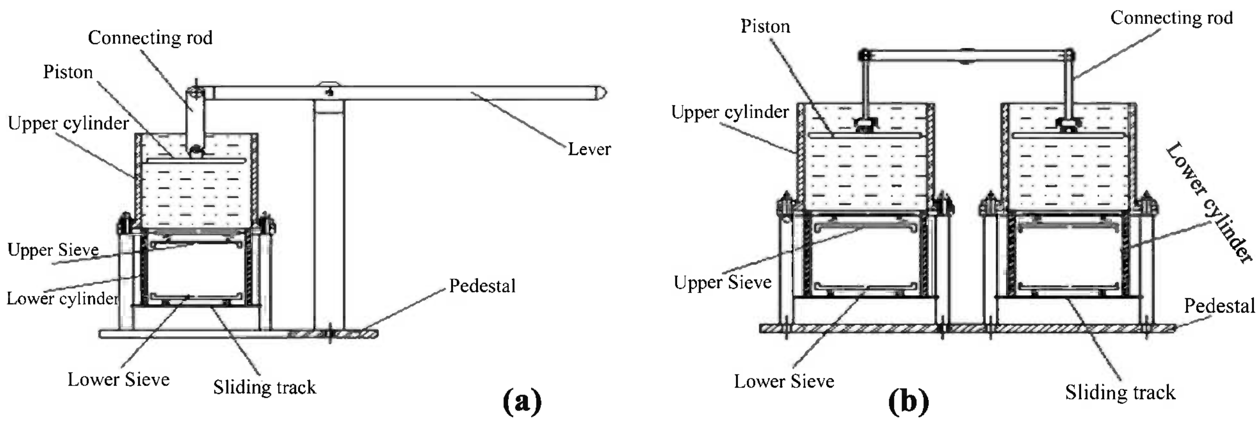

FIG. 7 Cylinder specimens with different interlayers atop for water erosion tests: (*a*) no interlayer; (*b*) geotextile as interlayer; and (*c*) EASS as interlayer.

into the lower cylinder from the side via sliding track, with the upper sieve and lower sieve fastened to the top side and the bottom side of the specimen, respectively. Water was poured into the upper cylinder until the water level reached 2 cm away from the top. Then the electric piston-driving motor was started and the piston moved up and down in the upper cylinder to simulate the water erosion of the base. The specimen was taken out after the predetermined testing time (1, 3, 6, and 12 min, respectively), and weighed again after wiping with the wet towel after being wrung dry to get M_i. The erosion rate after 1, 3, 6, and 12 min was then computed, respectively. The erosion rate after a certain period of time was defined as the lost mass of unit area per min (g/m^2 · min), which could be calculated with Eq 2.

$$\omega_i = (M_o - M_i)/(t_i \times \pi r^2) \tag{2}$$

where:

ω_i = erosion rate after a certain period of time (g/m^2 · min),
M_o = wet weight of specimen before erosion test (g),
M_i = wet weight of specimen after erosion test (g),
t_i = lasting time of test (min),
r = radius of cylinder specimen = 7.5 cm, and
πr^2 = cross-sectional area of specimen (cm^2).

RESULTS

The results from the water erosion tests are given in **Table 7**.

Table 7 describes that the erosion rate of specimens with three types of interlayer decreased with the increase of testing time. But the erosion rate of specimens without interlayer atop was the greatest at any testing time. After 1 min of testing, compared with specimens without interlayer atop, the erosion rate of specimens with geotextile as interlayer decreased by 99 %, and the erosion rate of specimens with EASS as interlayer decreased by 44 %. After 12 min of testing, compared with specimens without interlayer atop, the erosion rate of specimens with geotextile as interlayer decreased by 99 % and the erosion rate of specimens with EASS as interlayer decreased by 59 %.

TABLE 7 Erosion rate of cylinder specimens.

	Erosion Rate After Different Testing Time (g/m^2 · min)			
Interlayer	1 min	3 min	6 min	12 min
No interlayer	1612.8	976.3	709.8	552.9
300 g/m^2 geotextile	8.4	6.2	6.5	4.2
1 cm EASS	905.5	427.6	232.6	227.9

Conclusions

It has been reported that the interlayer paved between the pavement surface slab and the base plays an active role in functions such as breaking the bond of the pavement slab from the base, reducing friction at the interface between the slab and the base, restraining reflected cracking, etc. This research found that the interlayer has a satisfying effect on improving the performance of the base. The interlayer can damp vibration of the base, decrease displacement of the base caused by vibration, and improve anti-erosion of the base.

1. The finding from the tests for vibration response in this research indicated that, under the same impact loading, (a) the vector sum of maximum vibration velocity of the base layers with rubber sheet, a layer of geotextile or two layers of geotextile as interlayer atop decreased by 35 %, 70 %, and 80 %, respectively; and (b) the vector sum of maximum displacement of the base layers with rubber sheet, a layer of geotextile or two layers of geotextile as interlayer atop decreased by 18 %, 25 %, and 26 %, respectively. This means that the interlayer can significantly decrease both the maximum vibration velocity and the maximum displacement of the base layer caused by vibration. Compared with no interlayer, the interlayer of two layers of geotextile has the best vibration damping effect on the base, followed by the interlayer of a layer of geotextile and the interlayer of rubber sheet. Simultaneously, the interlayer can reduce the displacement of the base layer caused by vibration, which helps to protect the base layer.
2. The findings from the anti-erosion tests in this research indicated that, under the same conditions, compared with specimens without interlayer atop, the erosion rate (after 12 min of testing) of specimens with geotextile as interlayer atop decreased by 99 %, and the erosion rate of specimens with EASS as interlayer atop decreased by 59 %. This means that the specimen covered with

geotextile did far better than the specimen covered with EASS and the specimen without interlayer atop in resisting water erosion. It is likely that the difference in erosion resistance of specimens with different interlayers became less pronounced with the increase of eroding time, as Ref. [19] also reported. Nevertheless, it can be safely concluded that both geotextile and EASS used atop the base as the interlayer could make a significant difference in reducing water erosion damage to the base of pavement in the early stage of service.

ACKNOWLEDGMENTS

This research was performed as a part of the Research Project 51178064 funded by the National Natural Science Foundation of China.

References

[1] Hall, K., Dawood, D., Vanikar, S., Tally, R., Cackler, T., Correa, A., Deem, P., Duit, J., Geary, G., Gisi, A., Hanna, A., Kosmatka, S., Rasmussen, R., Tayabji, S., and Voigt, G., "Long-Life Concrete Pavements in Europe and Canada," *FHWA-PL-07-027*, U.S. Department of Transportation and Federal Highway Administration, Washington, D.C., 2007, p. 51.

[2] Suh, Y. C., Lee, S. W., and Kang, M. S., "Evaluation of Subbase Friction for Typical Korean Concrete Pavement," *J. Transport. Res. Rec.*, No. 1809, 2002, pp. 66–73.

[3] Okamoto, P. A., Naussbaum, P. J., Smith, K. D., Darter, M. I., Wilson, T. P., Wu, C. L., and Tayabji, S. D., "Guidelines for Timing Contraction Joint Sawing and Earliest Loading for Concrete Pavements," Vol. 1, *Final Report FHWA-RD-91-079*, Federal Highway Administration and U.S. Department of Transportation, Washington, D.C., 1994, p. 11.

[4] Yi, Z. J., Tang, B. M., and Yang, Q. G., "New Structures of Cement Concrete Pavements with Bond Breaker Mediums," *Proceedings of the 1st National Forum of Highway Scientific and Technical Innovation*, China Communications Press, Beijing, 2003, pp. 84–88 (in Chinese).

[5] Yao, J. L., Yuan, J. B., Zhang, Q. S., and Wu, X., "Characterization of Emulsion Wax Curing Agent as Bond-Breaker Medium in Jointed Concrete Pavement," *J. Perform. Constr. Facil.*, Vol. 23, 2009, pp. 447–455.

[6] Fu, Z., *Cement Concrete Pavement Construction*, Tongji University Publishing House, Shanghai, China, 2004, p. 51 (in Chinese).

[7] Rasmussen, R. O. and Garber, S. I., "Nonwoven Geotextile Interlayers for Separating Cementitious Pavement Layers: German Practice and U.S. Field Trials," Federal Highway Administration and U.S. Department of Transportation, Washington, D.C., 2009, p. 2.

[8] Ozer, H., Al-Qadi, I. L., and Zhen, L., "Fracture-Based Friction Model for Pavement Interface Characterization," *J. Transport. Res. Rec.*, No. 2057, 2008, pp. 54–63.

[9] Yao, J. L., Yuan, J. B., Zhang, Q. S., Wu, X., and Chao, D. Z., "Research on Mechanism of Using Emulsion Wax Curing Agent as Separation Layer and Its Effectiveness," *China J. Highway and Transport*, Vol. 22, 2009, pp. 47–52 (in Chinese).

[10] Yao, J. L., Yuan, J. B., and Zhang, Q. S., "Experimental Study of Emulsified Wax Curing Agent and Asphalt Slurry Seal as Bond Breaker Media in Cement Concrete Pavement," *China Civil Eng. J.*, Vol. 42, 2009, pp. 127–131 (in Chinese).

[11] JTJ/T 019-98, *Technical Specifications for Application of Geosynthetics in Highway*, China Communications Press, Beijing, 1998 (in Chinese).

[12] JTG E50-2006, *Test Methods of Geosynthetics for Highway Engineering*, China Communications Press, Beijing, 2006 (in Chinese).

[13] JTG/T F40-02-2005, *Technical Guidelines for Micro Surfacing and Slurry Seal*, China Communications Press, Beijing, 2006 (in Chinese).

[14] Shen, Y., "Study on Evaluation Index for Safety of Engineering Structures Under Environmental Vibrations," M.S. thesis, Shanghai Jiao Tong University, Shanghai, China, 2010, p. 6 (in Chinese).

[15] GB6722-2011, *Safety Regulations for Blasting*, China Standards Press, Beijing, 2012 (in Chinese).

[16] She, Y. H., Su, H. Y., and Xiao, Z. X., "Microseismic Experiment of Pavement Structure under Traffic Load," *China J. Highway Transport*, Vol. 22, 2009, pp. 40–46 (in Chinese).

[17] Wang, F. X., "Research on the Water Stability of Asphalt Mixture and Water Damage of Pavement," M.S. thesis, Zhejiang University of Technology, Zhejiang, China, 2009, p. 33 (in Chinese).

[18] Yi, Z. J., Tang, B. M., Li, Z. W., Yang, Q. G., and Wu, Z. L., "Basic Failure Types of Cement Concrete Pavement Caused by Interaction between the Surface Course and the Base Course," *J. Chongqing Jiaotong Univ.*, Vol. 20, 2001, pp. 34–38 (in Chinese).

[19] Li, L. S., "Application of Asphalt Seal Coating into Cement Concrete Pavement Structure," *Proceedings of the 3rd Session of Lu-Yue Highway and Bridge Equipment Forum*, China Highway and Transportation Society, Beijing, 2006, pp. 53–56 (in Chinese).

Journal of Testing and Evaluation

doi:10.1520/JTE20140083 / Vol. 43 / No. 2 / March 2015 / available online at www.astm.org

Kaoshan Dai,[1,2] Xuehang Song,[3] Xiaofeng Li,[4] Zhenhua Huang,[5] and Yongdong Pan[6]

Application of the Surface Wave Survey Method on Multi-Scale Engineering Problems: Laboratory and Field Testing Case Studies

Reference

Dai, Kaoshan, Song, Xuehang, Li, Xiaofeng, Huang, Zhenhua, and Pan, Yongdong, "Application of the Surface Wave Survey Method on Multi-Scale Engineering Problems: Laboratory and Field Testing Case Studies," *Journal of Testing and Evaluation*, Vol. 43, No. 2, 2015, pp. 443–451, doi:10.1520/JTE20140083. ISSN 0090-3973

Manuscript received February 28, 2014; accepted for publication October 22, 2014; published online December 5, 2014.

[1] State Key Laboratory of Disaster Reduction in Civil Engineering and College of Civil Engineering, Tongji University, 1239 Siping Road, Shanghai China 200092,
e-mail: kdai@tongji.edu.cn

[2] State Key Laboratory for GeoMechanics and Deep Underground Engineering, Xuzhou, China 221008.

[3] Shanghai Advanced Research Institute, Chinese Academy of Sciences, 99 Haike Road, Shanghai, China 201210,
e-mail: songxuehang@gmail.com

[4] College of Civil Engineering, Tongji University, 1239 Siping Road, Shanghai China 200092,
e-mail: lixiaofeng168@yeah.net

[5] Department of Engineering Technology, University of North Texas, 3940 N. Elm Street, Denton, TX 76207, USA
e-mail: zhenhua.huang@unt.edu

[6] School of Aerospace Engineering and Applied Mechanics, Tongji University, 1239 Siping Road, Shanghai China 200092 (Corresponding author),
e-mail: ypan@tongji.edu.cn

ABSTRACT

The geometric dispersion of surface waves offers the feature to infer the properties of a medium. The surface wave survey method is under continuous evolution and its applications include the noninvasive characterization of a medium at a small scale and the earthquake geotechnical survey at a large scale. Despite the significant difference in scales, these applications generally utilize the propagation of the surface waves along the boundary of a layered medium. This paper discusses standard steps involved in surface wave surveys. Two application case studies are conducted and presented in detail. In the small scale laboratory application case, a nondestructive testing (NDT) methodology is proposed for the coating investigation using laser interferometric measurements of surface waves. In the large scale field application, an accelerometer-based passive surface wave survey is designed for earthquake geotechnical engineering site characterization. Finally, recommendations for practical application of surface waves in multi-scale engineering problems are presented.

Keywords

surface wave, nondestructive testing, laser interferometer, accelerometer, site characterization, microtremor measurement

Introduction

The surface wave theory was first introduced in 1885 by Lord Rayleigh as a solution to the free vibration problem for an elastic half-space [1]. Since then, the application of surface waves has been under continuous evolution in various disciplines. Although there are great differences in scales between the problems in these fields, the practices share the same feature that they explore the geometric dispersion of surface waves to infer the medium properties through the parameter identification.

Laboratory scale surface wave techniques are mainly developed for nondestructive testing of multilayer media. The dispersion effect of surface waves provides the possibility of determining the mechanical properties of media such as thin films or coatings. Composite laminate detection [2] and coating defect investigation [3] are among the typical applications. The use of high frequency surface acoustic waves (SAWs) enables both the properties of thin layers and internal defects in the multilayer components of structures to be identified. Modern equipment enables surface acoustic waves to be generated at frequencies of the order of 1–10 GHz [4]. Due to the strong frequency-dependent attenuation of materials and the observation distance limitations, laser-based surface wave methods find their niches [3]. Laser sources can provide wavefield images with a much higher spatial resolution than conventional transducers. Laser-generated surface waves have been successfully applied to determine the thickness and elastic properties of the bonding layers of a copper-aluminum layered sample [5].

The specific characteristics of surface wave propagation in a stratified medium make them useful in the field of earthquake geotechnical engineering. Site characterization is one of the primary applications. Different field testing approaches using the surface waves have been developed, including the steady state Rayleigh method [6], the spectral analysis of surface waves (SASW) [7], the multichannel analysis of surface waves (MASW) [8], the refraction microtremor (ReMi) [9], and the passive MASW [10]. All of these methods find diverse applications in the shallow geotechnical engineering (e.g., less than 100 m). Several data processing strategies were proposed to extract geophysical information from the seismic noise (microtremor) data. These include the spatial autocorrelation (SPAC) method [11], the extended spatial autocorrelation (ESAC) method [12], the frequency-wavenumber approaches [13], and the horizontal-to-vertical spectral ratio (HVSR) method [14]. Array measurements of low frequency microtremors have been used for sedimentary exploration as deep as 1 km [15].

This paper discusses steps involved in the surface wave survey method. The applications of the surface wave survey method for engineering problems at two different scales (lab scale and full scale at field) are presented in detail as two case studies. The lab scale case is a nondestructive testing (NDT) for coating characterization of a sample specimen, and the full scale field application case deals with the geotechnical characterization of the shear-wave velocity in the field. These two cases constitute unique extremes in current surface-wave applications because of their scales in time and space. The lab case is at the level of microseconds in time and millimeters in space, whereas the field case is at the scale of milliseconds in time and meters in space. In other words, those two cases represent the time and space scale differences of 10^3.

Both cases followed a general surface wave survey procedure with specifically designed test configurations. The active MASW method and the passive MASW (SPAC) method were used for the laboratory and field scale surveys, respectively, to obtain dispersion curves. Optimization was realized and the shear wave velocity profiles were obtained for both the coating sample of the lab case and the site soil of the field case. It was demonstrated that the surface-wave survey method can be applied in a wide variety of problems to investigate one of the most critical engineering material properties related to the stiffness (i.e., shear-wave velocity).

Surface Wave Survey Method

GENERAL METHOD

A characteristic feature of surface waves is that the vibration displacement decays exponentially with depth. Most energy is contained within one wavelength from the free surface. In other words, the penetration depth of surface waves is wavelength dependent. The high frequency Rayleigh surface waves propagate in shallow zones close to the free surface, whereas the low frequency surface waves enter deeper layers. This feature of surface waves has been used to distinguish materials over a very wide range of scales. The essential differences between various scales of applications lie in the frequency range of interest and the spatial sampling.

Rayleigh waves are the most commonly used surface waves in practical applications. The equation of motion for Rayleigh waves propagating in a laterally homogeneous medium can be written with the assumption of a plane strain field. The boundary conditions of such a half-space model include no stress at the free surface and no stress and strain at the infinity. A linear differential eigenvalue problem is formed by assuming the continuity of strain and stress at layer interfaces. The displacements of the wave motion can be written as:

$$\begin{aligned} u_1 &= u_x(x,z,t) = u_x(z)e^{i(k_x x-\omega t)} \\ u_3 &= u_z(x,z,t) = u_z(z)e^{i(k_x x-\omega t)} \end{aligned} \tag{1}$$

where:

u = the displacement,

components x and z = the directions of wave propagation and depth, respectively,

t = time,

k_x = the wave number in the x direction,

ω = the angular frequency, and

i = the unit of imaginary number.

Rewriting the wave motion equation and constitutive equation by substituting Eq 1, the state vector representation of the wave propagation can be found as:

$$\frac{d\xi}{dz} = A^m(k_x, \omega)\xi \tag{2}$$

where:

$\xi = (u_1, u_3, \sigma_{13}, \sigma_{33})^T$ = a state vector,
m = the mth layer, and
A = the fundamental matrix of the state vector [16].

The characteristic equation for surface waves in a semi-infinite layered structure can be described as a function of density (ρ), compressional wave velocity (C_L), shear wave velocity (C_T), and total thickness (h) of all layers:

$$F(\rho, C_L, C_T, h) = 0 \tag{3}$$

In practice, most surface-wave applications provide a shear-wave velocity profile by a three-step strategy as shown in **Fig. 1**: (1) acquiring experimental data, (2) estimating the experimental dispersion curve through signal processing, and (3) solving an inverse problem with a reference model.

In Step 1, the data acquisition (**Fig. 1(*a*)**), the surface wave signals are usually collected by receivers deployed on the free surface of a medium. Depending on the nature of the problem, different receivers can be used, among which vibration sensors are mostly used. Excitation generation is usually required for laboratory scale experiments or some small-scale field tests; while for large scale field implementation, the passive method is mostly used in which the receivers listen to ambient "noise" directly.

The measured data are then processed to estimate the experimental dispersion curve in Step 2, as shown in **Fig. 1(*b*)**. Various signal analysis methods have been developed [17,18]. The Fourier Transform is the most commonly used data processing tool. Different frequency components of a signal are usually separated to estimate the frequency-dependent phase velocities with the consideration of the testing configuration.

The test interpretation is implemented through Step 3: solving the inverse problem theoretically (**Fig. 1(c)**). The theoretical dispersion curve can be obtained by solving the forward problem using different methods such as the Thomson–Haskell method [19,20], the reflection and transmission coefficient method [21,22], or the stiffness/compliance matrix method [23]. With an assumed model, this step compares and minimizes the difference between the experimental dispersion curve and the theoretical one. An objective function is usually established to represent the difference between experimental and theoretical data points. Either local or global search methods can then be used to find feasible model parameters that result in the theoretical dispersion curve matching the experimental data.

FIG. 1 Flow chart of the surface wave survey method.

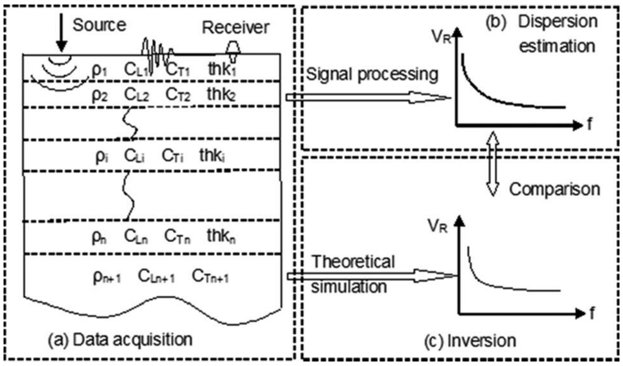

LABORATORY SCALE APPLICATION SCHEME

In laboratory, the surface wave survey method is used as one of NDT approaches. As shown in **Fig. 2**, a typical testing configuration for the laboratory scale application of the surface wave survey method includes the source, the receiver, and the motion stage. The excitation source should be wide-banded with a tiny shot spot since the thickness of a layered structure is usually among micrometers or millimeters scale. The receiver should also be wide-banded. Besides the contact transducers, laser interferometers or vibrometers are commonly used as the noncontact options in labs. The motion stage is used to adjust the distance between the source and the receiver. Either the source or the receiver can be mounted on the stage; however, to acquire weak signals with a steady focus, the receiver is usually fixed while the source is attached to the stage.

Piezoelectric transducers can generate surface wave signals during laboratory NDT experiments. However, pulsed laser sources can be used as an alternative and the laser interferometer can be simultaneously used to detect small vibrations. This technique allows both the excitation and the detection of surface waves in a range of kHz to GHz. It can be used to probe structures in a completely nondestructive manner without any contact. The broad band nature of laser techniques makes them well suited for the characterization of material systems in small scale.

FIG. 2 Diagram of the surface wave survey method in laboratory.

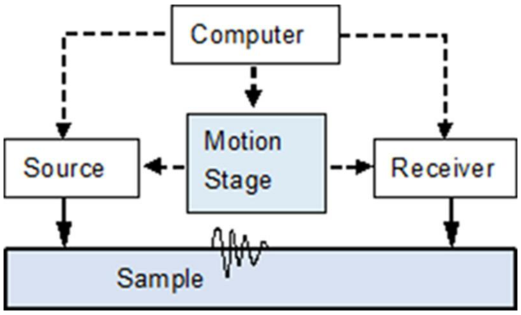

After the test data is collected, experimental dispersion curves could be extracted by many manners such as the two dimensional Fourier transform method [24] and the phase spectrum method [25]. The measured SAW dispersion can, in principle, be inverted to estimate material parameters such as the density, the thickness of the coating and the elastic properties of the tested structure. As described in the aforementioned general method, a popular procedure of obtaining the elastic properties is to compare the measured dispersion curves with the theoretical dispersion curves resulted from inversion algorithms such as the genetic algorithm, the neural network algorithm, the simulated annealing algorithm, and the least-squares fit algorithm.

FIELD TESTING APPLICATION SCHEME

Depending on the excitation features, surface wave survey methods used in earthquake geotechnical engineering are divided into active and passive techniques. A comprehensive literature review about those techniques was reported by Foti et al. [26]. Although most practical applications of surface waves in geotechnical engineering deploy conventional geophones, there has, recently, been considerable interest in exploring the use of accelerometers, which generally have flat response over a broad frequency range [27]. In field applications, sledge hammer, drop weight, or explosion are the typical excitation sources for active surface wave surveys, while the passive tests extract surface waves directly from seismic noise recordings. The array-based surface wave method as a passive technique has been used for extracting information of the subsoil structures through the estimation of the local shear wave velocity profile.

Similar to the traditional surface wave survey methods, the array-based surface wave method should be implemented in three steps. Field measurements are conducted by measuring ambient ground vibrations due to either natural events or human activities close to the testing site. The feasibility of using ambient vibration records depends on the condition whether such signals can be essentially associated to Rayleigh waves. Receivers can be deployed in a 1D or a 2D layout. The 1D linear array layout, as shown in **Fig. 3(*a*)**, is applied when the excitation source is ascertained or when the space for receiver deployment is limited. Commonly used 2D array layouts, more suitable for cases as the excitation sources cannot be clearly determined, include the triangular, circular, and "L" shape arrays shown in **Fig. 3(*b*)**. The maximum dimension of the array is usually related to the measurement depth.

Like other surface wave techniques, the array-based surface wave method processes data from the field measurement to obtain the dispersion curve. The frequency-wave number (*f*–*k*) analysis could be a straightforward data processing method with the application of the fast Fourier transform (FFT) algorithm. The SPAC and ESAC methods could also provide stable results in the low-frequency band.

FIG. 3 Receiver layout in the array-based surface wave method: (*a*) 1D; (*b*) 2D.

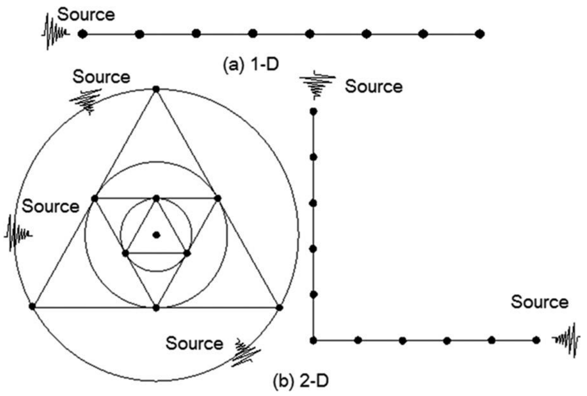

The inversion procedure is usually performed using a layered linear elastic model. To reduce the number of unknowns, some model parameters are assigned priori. Another important aspect related to the inversion is the selection of algorithm between the local search methods (LSMs) and the global search methods (GSMs).

Case Studies

LABORATORY NDT CASE

A laboratory setup was designed for the coating quality evaluation and product improvement case study, as shown in **Fig. 4**. Due to its high temporal and spatial resolutions and precision requirement, the laser ultrasonic technology [28] was used in the test system.

The experimental setup mainly consisted of the IOS AIR-1550-TWM laser interferometer inspection system, the Brilliant Nd:YAG laser, the Newport motion stage, the Tektronix digital oscilloscope, and a personal computer. The laser interferometer worked as a receiver, which has a detector with 125 MHz bandwidth. The noise equivalent surface displacement of the system was 6×10^{-7} nm $(\text{W/Hz})^{1/2}$. The laser source was a pulsed Nd:YAG laser with the wavelength of 1064 and 532 nm. The focused spot size of the laser was 14–200 μm. In this case study, the wavelength was 532 nm and its pulse duration was about 5 ns, under which the maximum pulse energy was 100 mJ/pulse and the maximum repetition rate of the Q-switched laser is 20 Hz. The motion stage was composed of a 3-Axis Motion Controller/Driver and three intelligent stepper motor linear stages with 200 mm travel range. The minimum increment motion of the stage was 0.15 μm and the uni-directional repeatability was 2 μm. The on-axis accuracy of motion is ± 5 μm and the maximum speed was 20 mm/s. A cylindrical lens and a spherical lens were used to focus the Nd:YAG laser beam for a line source and a point source, respectively. The digital oscilloscope with at

FIG. 4 The laser ultrasonic experimental system at Tongji University: test flow chart (top); experimental setup (bottom).

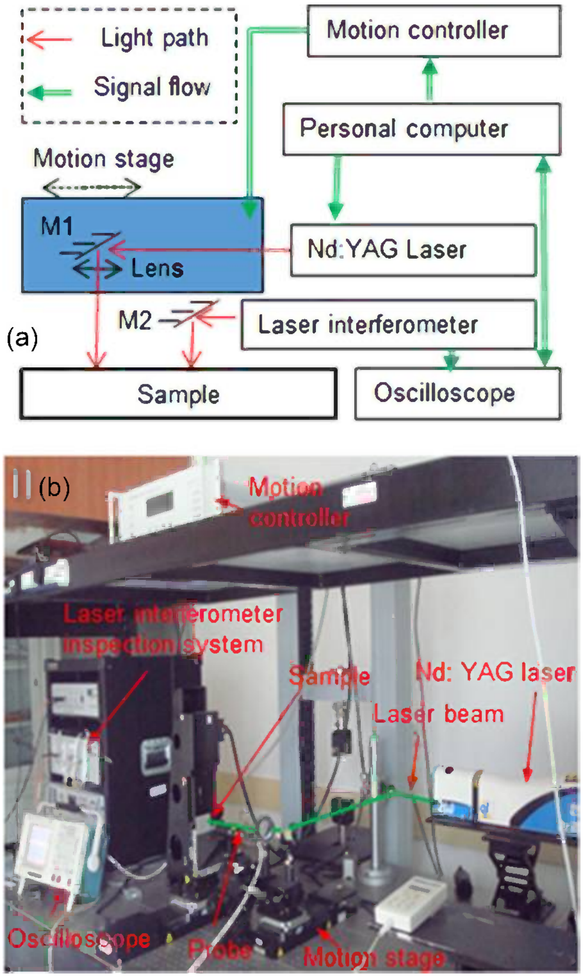

least 2 channels was used to display the reference signal and the detected waveform. To obtain the surface wave field, the source and the receiver were deployed at the same side of the specimen.

A series of signals obtained from the lab testing configuration were processed for Fourier transform displays. Two-dimensional Fourier transform was employed to obtain the frequency-wavenumber domain results. The least-squares fit algorithm was a common optimization method to find the minimum difference between the tested dispersion data and the theoretical dispersion data. The optimum material properties were estimated through this approach.

The coating specimen for this case study was made of cobalt (Co)-based tungsten carbide (WC) with the thickness of about 0.5 mm. The substrate was made of stainless steel. WC–Co materials have a wide range of industrial applications. The density, Young's modulus, and Poisson ratio for the WC–12 wt. % Co used for this study was 13.1–14.3 g/cm^3, 125–350 GPa, and 0.3–0.36, respectively [29–33]. The shear velocity of WC–Co coating media is calculated as 1792–3206 m. During the test, the ultrasonic wave field was generated by a line laser beam. 128 groups of signals were obtained at 128 points with a 0.1 mm spacing interval and 100 MHz sampling frequency as shown in **Fig. 5**. The first part of the distinct signals that had the travel time between 2 and 5 μs represents the surface wave travelled in the media. The wavefronts of these signals revealed the velocity of about 2710 m/s (Line 1 in **Fig. 5**) and 1720 m/s (Line 2 in **Fig. 5**). The second part of the signals (right to Line 3 in **Fig. 5**) that had a more than 12 μs travelling time represents the wave propagating along the interface between coating and air with the velocity of a little more than 300 m/s. As shown in **Fig. 6**, by using the two-dimensional Fourier transform, the frequency-wavenumber domain spectrum was obtained. Using the least-squares fit algorithm, theoretical dispersion curve matched relatively well with the measured data. Finally, the shear wave velocity profile was obtained: the shear wave velocity of the coating was 2300 m/s at the top surface and increased to about 3400 m/s at the interface of coating and substrate. Chivavibul et al. [32] reported that coatings made of different average WC grain sizes or different Co contents showed variations in shear wave velocity; in addition, the properties of coatings relied strongly on the spraying technique. Considering this, the shear wave velocity profile obtained from the lab experiment is compatible with the material physical parameter

FIG. 5

The coating specimen and typical collected waveforms.

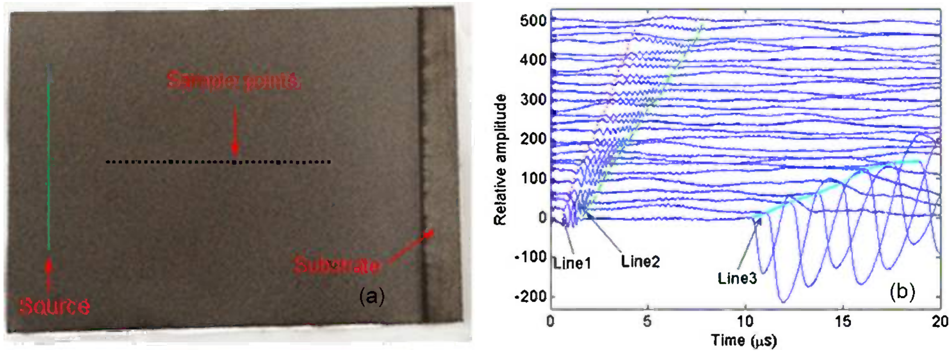

FIG. 6

Dispersion calculation results: (*a*) dispersion image in the frequency-wavenumber domain, (*b*) comparison of the test and the theoretical dispersions, and (*c*) the shear wave velocity profile.

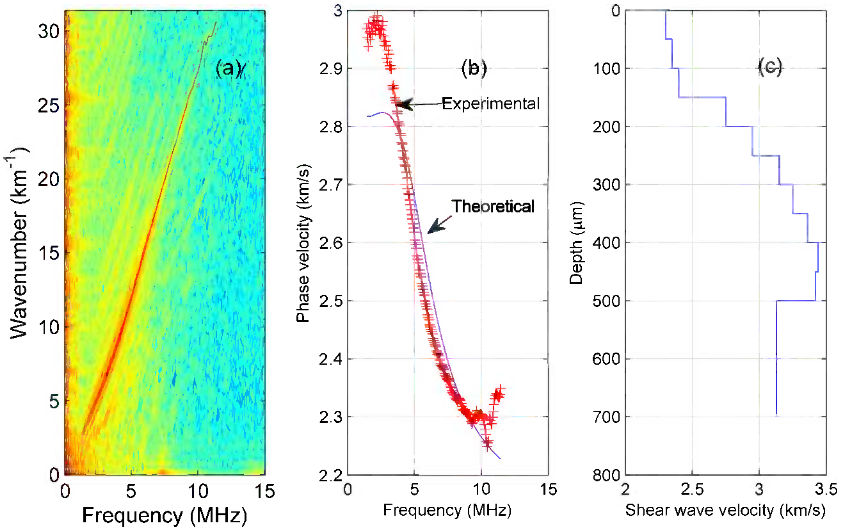

range of the specimen. Additionally, the measured waveforms in time domain matched relatively well with the theoretical ones as shown in **Fig. 7**, which validated that the tested shear wave velocity profile was acceptable.

FIELD TESTING CASE

A series of array-based surface wave surveys were conducted at an open site on the Tongji Univ. campus, where the borehole data was available. The receivers were deployed in the vertices of two equilateral triangles as well as the center of the triangles, as shown in **Fig. 8**. These receivers were uniaxial low-frequency accelerometers, which combined a piezoelectric sensing unit and a built-in micro amplifying circuit. They had a broad frequency band from 0.05 to 500 Hz. The amplitude range and the sensitivity of those accelerometers were ±0.1 g and 44 V/g, representatively. Due to the limited number of available accelerometers, a roaming strategy was used during the field test: step 1—four sensors were deployed first at Points 1–4 to collect ground motions simultaneously; step 2—after the completion of the test with the step-1 lay-out, three receivers at the Points 2–4 were relocated from Points 5 to 7, respectively, for another ground motions collection. Field tests of this case study were conducted during late afternoons. The typical vertical ground vibration acceleration signals are shown in **Fig. 9**. Ten sets of measurement data were collected for each “triangle” sensor array layout (four data acquisition channels). Each measurement was five minutes long with 200 samples per second.

With the assumption that surface waves at different propagation directions and with different frequencies that are statistically independent, a spatial correlation function can be

FIG. 7 Waveform comparison of surface waves: experimental data (solid), theoretical (dot) results.

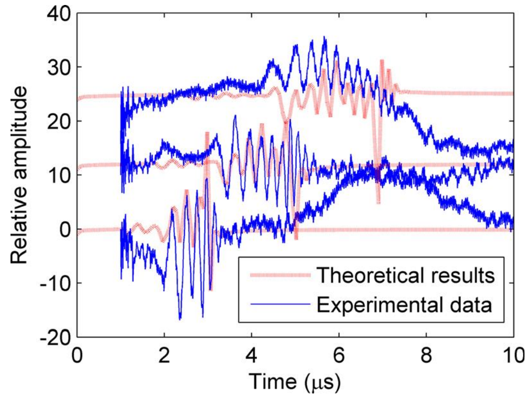

FIG. 8 Sensor array design.

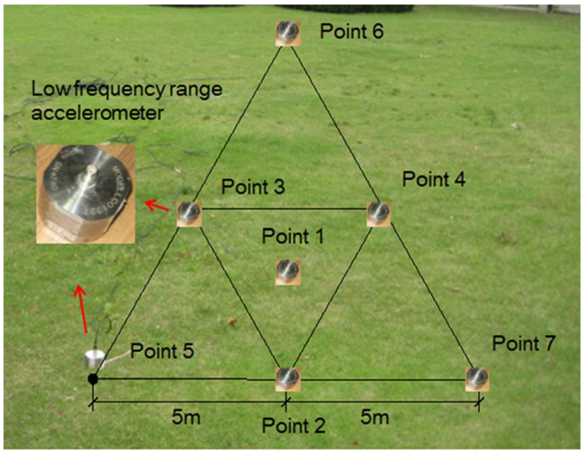

FIG. 9

Typical ground vibration signal.

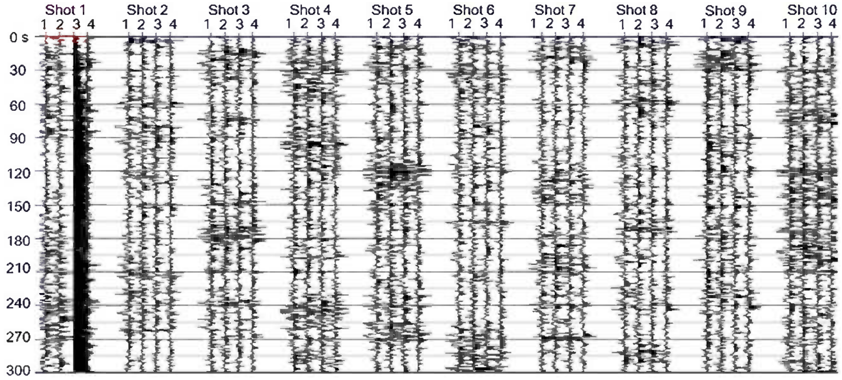

established. Aki [11] proposed a spatial cross correlation coefficient based on this function as:

$$\rho(r,\omega) = J_0\left[\frac{\omega r}{c(\omega)}\right] \tag{4}$$

where:

$c(\omega)$ = the phase velocity, and

J_0 = the first kind and zero-order Bessel function for a given inter-receiver distance r and angular frequency ω.

By fitting the azimuthally averaged spatial correlation function obtained from measured data to the Bessel function, the phase velocity $c(\omega)$ can be calculated.

During the analysis, all the collected vertical ground motion data were first stacked. Then the dispersion image as shown in **Fig. 10(*a*)** was obtained following the SPAC method by setting the inter-receiver distance r as 3.5 m and 7.0 m for the two different arrays, respectively. Next, the dispersion curves were extracted from the dispersion image. The shear wave velocity profile was then obtained through the inversion analysis of the dispersion curve. The genetic algorithm (GA), one of GSM approaches, was used for the inversion analysis. The inversion parameters for the GA include: 60 iterations, 0.9 crossover probability, and 0.02 mutation probability. **Figure 10(*b*)** demonstrates the result shear wave profile of this case study, in which the blue line represents the initial shear wave velocity used in the GA inversion processing and the red line is the inverted shear wave velocity profile.

The elastic properties of the near surface soils are important for earthquake geotechnical engineers and civil engineers. According to the International Building Code (IBC) [34], the site classification for seismic design is determined by the equivalent shear wave velocity down to 30 ms, V_s^{30}.

FIG. 10

Dispersion calculation results: (*a*) dispersion image, (*b*) shear velocity profile, and (*c*) borehole data.

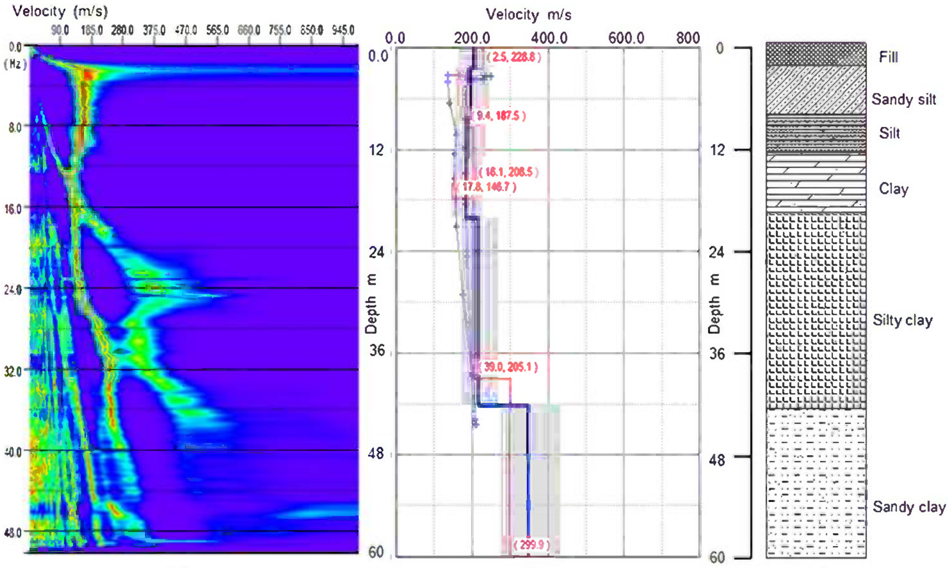

(a) (b) (c)

$$V_s^{30} = \frac{30}{\sum_{i=1}^{N} (d_i/v_i)}$$

where d_i and v_i denote the thickness (in meters) and the shear wave velocity in m/s of the ith layer soil, respectively, in a total of N layers, down to the depth of 30 m. Usually, the average V_s is considered at the uppermost 30 m (V_s^{30}). However, if rock is found within the top 30 m depth, the surface shear wave velocity of the soil from the ground surface to the rock is calculated instead.

To figure out the V_s^{30} distribution at the testing site, this study calculated the average shear velocity using Eq 5, which resulted in $V_s^{30} = 175$ m/s. Because it was smaller than 180 m/s, the near surface soil of this site was defined as soft soil and the site was classified as Site Class E according to the IBC.

The geotechnical information, shown in **Fig. 10(*c*)**, was obtained from the results of the drilled boreholes at the testing site. The shear wave velocity profile derived from the surface wave field survey was validated, at a certain degree, by this geotechnical boring log data.

Discussion and Conclusion

The surface wave survey method, taking advantage of the dispersion feature of surface waves, find its applications in various scales of engineering problems. The three-step strategy can be used in most of these applications. One of the critical considerations is the test configuration design for different scale situations. Usually, in a small-scale lab experiment, the testing system should have high temporal and spatial resolution and sensitivity and its components should be compacted; however, in a large scale field testing, the receiver deployment design should consider excitation sources in order to average the directional error. During the signal processing steps, the data processing methods developed for the forward problem and the inverse problem are valid at different scales. Therefore, theoretical advances in one discipline can be borrowed to another to promote surface wave measurement interpretation.

Based on the surface wave survey method, this paper studied two application cases with distinct scale difference. In the laboratory application case, a nondestructive testing (NDT) methodology was proposed for the coating inspection. A testing scheme based on the ultrasonic laser technique was developed. A wideband laser source was deployed to excite the short wavelength surface wave. Signals were obtained along a line at the coating surface. The data was processed by two-dimensional Fourier transform to obtain the dispersion curves and the least square fit algorithm was adopted to further solve the inverse problem. The result shear wave velocity profile of the coating matched well with the known information. According to the profile, the mechanical properties of the coating structure were evaluated.

In the field application case, an array-based passive surface wave survey was designed for earthquake geotechnical engineering site characterization. The uniaxial low-frequency accelerometers were deployed with the triangular layout to collect ambient ground vibrations. The measured data were processed with the SPAC method for the dispersion curve and the GA algorithm was adopted to solve the inverse problem. The shear wave velocity profile of the site was successfully obtained and validated with the borehole data. Based on the shear wave velocity profile, the near surface soil of this testing site was determined as soft soil and the site was classified as Class E according to the IBC.

Through the two application case studies, it is demonstrated that, with reasonable test design, the surface wave survey method can be successfully used to solve engineering problems in different scales, among various disciplines such as laser ultrasonics, nondestructive testing, geotechnical engineering, and seismology. This method offers the nonintrusive and nondestructive features, which benefit sustainable engineering practices.

ACKNOWLEDGMENTS

The writers would like to acknowledge the support from following programs: National Natural Science Foundation of China (51208382, 11090333), State Key Lab for Geomechanics and Deep Underground Engineering (SKLGDUEK1002), Shanghai Science Foundation (12ZR1433500), Specialized Research Fund for the Doctoral Program of Higher Education (20120072120001), Shanghai Pujiang Scholar (13PJ1407900), and Scientific Research Foundation for the Returned Overseas Chinese Scholars, State Education Ministry (2013-693). The writers would also like to acknowledge Mr. Dong Zhao of Geogiga Technology Corp. and Dr. Weixing Shi of Tongji University for their support. The writers appreciate the sponsorship of Zhenhua Huang from Tongji University, China, during his stay in Shanghai and Professor Zhihai Han from Xi'an Jiaotong University, China, for providing the coating specimen. The views, opinions, findings and conclusions reflected in this publication are the responsibility of the authors only and do not represent the policy or position of any agency.

References

[1] Rayleigh, L., "On Waves Propagated Along the Plane Surface of an Elastic Solid," *Proc. Lond. Math. Soc.*, Vols. 1–17, 1885, pp. 4–11.

[2] Lafond, E. and Zhang, X., "Spectral Analysis of Suface Waves Combined to Laser Ultrasonics for the Non– Destructive Testing of High Performance Materials and Composites," *AIP Conf. Proc.*, Vol. 894, No. 201, 2007, pp. 201–208.

[3] Murray, T. W., Balogun, O., Steen, T. L., Basu, S. N., and Sarin, V. K., "Inspection of Compositionally Graded Mullite Coatings Using Laser Based Ultrasonics," *Int. J. Refract. Met. H.*, Vol. 23, Nos. 4–6, 2005, pp. 322–329.

[4] Odagawa, H. and Yamanouchi, K., "10 GHz Range Extremely Low-Loss Surface Acoustic Wave Filter," *Electron. Lett.*, Vol 34, No. 9, 1998, pp. 865–866.

[5] Wu, T.T. and Liu, Y.H., "Inverse Determinations of Thickness and Elastic Properties of a Bonding Layer Using Laser-Generated Surface Waves," *Ultrasonics*, Vol. 37, No. 1, 1999, pp. 23–30.

[6] Jones, R., "In-Situ Measurement of the Dynamic Properties of Soil by Vibration Methods," *Géotechnique*, Vol. 8, 1958, pp. 1–21.

[7] Nazarian, S., Stokoe, I., and Hudson, W. R., "Use of Spectral Analysis of Surface Waves Method for Determination of Moduli and Thicknesses of Pavement Systems," T*ransport Res. Rec.*, Vol. 1983, pp. 38–45.

[8] Park, C., Miller, R., and Xia, J., "Multichannel Analysis of Surface Waves," *Geophysics*, Vol. 64, No. 3, 1999, pp. 800–808.

[9] Louie, J. N., "Faster, Better: Shear-Wave Velocity to 100 Meters Depth from Refraction Microtremor Arrays," *Bull. Seismol. Soc. Am.*, Vol. 91, No. 2, 2001, pp. 347–364.

[10] Park, C., Miller, R., Laflen, D., Neb, C., Ivanov, J., Bennett, B., and Huggins, R., "Imaging Dispersion Curves of Passive Surface Waves," *SEG Technical Program Expanded Abstracts*, SEG, Tulsa, OK, 2004, pp. 1357–1360.

[11] Aki, K., "Space and Time Spectra of Stationary Stochastic Waves With Special Reference to Microtremors," *Bull. Earthquake Res. Inst.*, Vol. 35, 1957, pp. 415–457.

[12] Okada, H. and Suto, K., *The Microtremor Survey Method, Geophysical Monograph Series*, Society of Exploration Geophysicists, Tulsa, OK, 2003.

[13] Capon, J., "High-Resolution Frequency-Wavenumber Spectrum Analysis," *Proceedings of the IEEE*, Vol. 57, 1969, pp. 1408–1418.

[14] Nogoshi, M. and Igarashi, T., "On the Amplitude Characteristics of Microtremor (Part 2)," *J. Seismol. Soc. Jpn.*, Vol. 24, 1971, pp. 26–40.

[15] Yamanaka, H., Takemura, M., Ishida, H., and Niwa, M., "Characteristics of Long-Period Microtremors and Their Applicability in Exploration of Deep Sedimentary Layers," *Bull. Seismol. Soc. Am.*, Vol. 84, 1994, pp. 1831–1841.

[16] Gilbert, F. and Backus, G., "Propagator Matrices in Elastic Wave and Vibration Problems," *Geophysics*, Vol. 31, No. 2, 1966, pp. 326–332.

[17] Zhang, H., Dai, S., and Zhang, C., "Coherent Measurement of the Dispersive Curves of an Elastic Waveguide," *Appl. Phys. Lett.*, Vol. 78, No. 2846, 2001, pp. 2846–2848.

[18] Hurley, D. H. and Spicer, J. B., "Line Source Representation for Laser-Generated Ultrasound in an Elastic Transversely Isotropic Half-Space," *J. Acoust. Soc. Am.*, Vol. 116, No. 2194, 2004, pp. 2914–2922.

[19] Thomson, W. T., "Transmission of Elastic Waves Through a Stratified Solid Medium," *J. Appl. Phys.*, Vol. 21, No. 89, 1950, pp. 89–93.

[20] Haskell, N. A., "The Dispersion of Surface Waves on Multilayered Media," *Bull. Seismol. Soc. Am.*, Vol. 43, 1953, pp. 17–34.

[21] Kennett, B. L. N. and Kerry, N. J., "Seismic Waves in a Stratified Half Space," *Geophys. J. Roy. Astron. Soc.*, Vol. 57, No. 3, 1979, pp. 557–583.

[22] Kennett, B. L. N. and Clarke, T. J., "Rapid Calculation of Surface Wave Dispersion," *Geophys. J. R. Astron. Soc.*, Vol. 72, No. 3, 1983, pp. 619–631.

[23] Wang, L. and Rokhlin, S. I., "Stable Reformulation of Transfer Matrix Method for Wave Propagation in Layered Anisotropic Media," *Ultrasonics*, Vol. 39, No. 6, 2001, pp. 413–424.

[24] Alleyne, D. and Cawley, P., "A Two-Dimensional Fourier Transform Method for the Measurement of Propagating Multimode Signals," *J. Acoust. Soc. Am.*, Vol. 89, No. 1159, 1991, pp. 1159–1168.

[25] Sachse, W. and Pao, Y., "On the Determination of Phase and Group Velocities of Dispersive Waves in Solids," *J. Appl. Phys.*, Vol. 49, No. 4320, 1978, pp. 4320–4327.

[26] Foti, S., Parolai, S., Albarello, D., and Picozzi, M., "Application of Surface-Wave Methods for Seismic Site Characterization," *Surv. Geophys.*, Vol. 32, No. 6, 2011, pp. 777–825.

[27] Mougenot, D. and Thorburn, N., "MEMS-based 3D Accelerometers for Land Seismic Acquisition: Is it Time?," *The Leading Edge*, Vol. 23, No. 3, 2004, pp. 246–250.

[28] Scruby, C. B. and Drain, L. E., *Laser Ultrasonics: Techniques and Applications*, Adam Hilger, Bristol, UK, 1990.

[29] Chivavibul, P., Watanabe, M., Kuroda, S., and Shinoda, K., "Effects of Carbide Size and Co Content on the Microstructure and Mechanical Properties of HVOF-Sprayed WC–Co Coatings," *Surf. Coat. Technol.*, Vol. 202, No. 3, 2007, pp. 509–521.

[30] Wang, H., Song, X., Wei, C., Gao, Y., and Guo, G., "Abrasion Resistance Enhancement of Ultrafine-Structured WC–Co Coating Fabricated by Using In Situ Synthesized Composite Powder," *J. Mater. Sci. Technol.*, Vol. 29, No. 11, 2013, pp. 1067–1073.

[31] Lima, M. M., Godoy, C., Modenesi, P. J., Avelar-Batista, J. C., Davison, A., and Matthews, A., "Coating Fracture Toughness Determined by Vickers Indentation: An Important Parameter in Cavitation Erosion Resistance of WC–Co Thermally Sprayed Coatings," *Surf. Coat. Technol.*, Vols. 177–178, 2004, pp. 489–496.

[32] Chivavibul, P., Watanabe, M., Kuroda, S., and Shinoda, K., "Effects of Carbide Size and Co Content on the Microstructure and Mechanical Properties of HVOF–Sprayed WC–Co Coatings," *Surf. Coat. Technol.*, Vol. 202, No. 3, 2007, pp. 509–521.

[33] Lima, R. S., Kruger, S. E., Lamouche, G., and Marple, B. R., "Elastic Modulus Measurements via Laser-Ultrasonic and Knoop Indentation Techniques in Thermally Sprayed Coatings," *J. Therm. Spray Technol.*, Vol. 14, No. 1, 2005, pp. 52–60.

[34] International Code Council, *2012 International Building Code*, ICC, Washington, D.C., 2012.

Journal of Testing and Evaluation

doi:10.1520/JTE20140087 / Vol. 43 / No. 2 / March 2015 / available online at www.astm.org

João Martins[1] and A. Gomes Correia[2]

Comparison Between Laboratory and Field Stiffness by Wave Measurements

Reference

Martins, João and Gomes Correia, A., "Comparison Between Laboratory and Field Stiffness by Wave Measurements," *Journal of Testing and Evaluation*, Vol. 43, No. 2, 2015, pp. 452–464, doi:10.1520/JTE20140087. ISSN 0090-3973

Manuscript received February 28, 2014; accepted for publication September 30, 2014; published online December 12, 2014.

[1] Univ. of Madeira, 9020-105 Funchal, Portugal (Corresponding author), e-mail: jmartins@uma.pt

[2] ISISE, University of Minho, 4804-533 Guimarães, Portugal.

ABSTRACT

The present work aims to establish a relationship between field and laboratory moduli obtained from mechanical wave measurements. Spectral analysis of surface waves was performed on a clayey sand trial layer during tests in a full-scale trial. Laboratory triaxial tests involving S-wave measurements with bender elements and accelerometers were conducted on specimens under similar conditions, and the shear modulus was determined. Both laboratory and field methodologies for the determination of the shear modulus were based on S-wave propagation through the tested material; thus they involved similar stress and strain levels. A reasonable relationship was observed between field and laboratory moduli, taking into account field conditions (moisture content and void ratio) and stress state.

Keywords

stiffness, wave measurements, SASW, bender elements, shear modulus

Introduction

The construction of transportation infrastructures—namely, earthworks—is one of the most material demanding industries, as it requires material selection and excavation, transport, spreading, and compaction to meet the final objectives and quality requirements. Avoiding deficiencies in each one of these processes promotes construction quality and performance, especially during the serviceability phase. Furthermore, the design and construction of transportation infrastructures, and therefore their performance and maintenance, rely to a great extent on the geotechnical properties of their supports, particularly subgrade, embankments, and natural ground. Therefore, proper design and quality assessment of materials used in infrastructure (specifically, subgrade soils and embankments), as well as quality control during and after construction, are required in order to achieve cost-effectiveness and sustainable infrastructures.

As far as construction quality control of transportation infrastructures is concerned, current field practice typically predicts performance based on in situ moisture and density measurements. Such quality control methods are adopted mainly because of their traditional use and relative simplicity. However, these parameters might not provide all the information necessary to ensure a high-quality product and consequently do not provide a sustainable approach [1,2]. Moreover, mechanical properties are a measure of quality, as the non-uniformity of stiffness or strength is directly related to progressive failures and life-cycle costs. As a result, current practice does not effectively indicate the values of mechanical properties, leading to a great disconnect between rational design parameters and performance evaluation. Thus the quality control/quality assurance procedures of construction should be based on a criterion that closely correlates to the performance parameters used in the design. Taking into account the aforementioned procedures, quality control/quality assurance practice based on mechanical properties determined from field and laboratory tests promotes a sustainable approach to the design and construction of transportation infrastructures [2].

In fact, there is a recent trend in the transportation geotechnics community toward improved quality assessment, including measurement of performance-related parameters of soils and structural materials [2–4]. Many tools have been developed to measure field mechanical properties, such as soil stiffness gauges, falling weight deflectometers, spectral analysis of surface waves (SASW), and the Portancemètre [5], among others. These tools permit non-destructive dynamic tests that can be performed independently or together with conventional practices to improve statistical evaluation and allow reduced variability, thereby substantially enhancing the construction quality of the entire earthwork [6] and construction sustainability. Although these tests enable determination of the mechanical properties of compacted layers, it should be highlighted that different stress–strain conditions are induced.

It is generally accepted that soil shows approximately elastic behavior at small and very small strains and non-linear behavior at medium strains [7–9]. However, it is in the range of elastic behavior that Young's modulus E_0 and the shear modulus G_0 are key parameters for both dynamic and static geotechnical problems. The small-strain shear modulus G_0 is the initial stiffness of the stress–strain curve for a given soil and is related to Young's modulus E_0 by Eq 1.

(1) $$E_0 = 2G_0(1+\nu)$$

where:

G_0 = shear modulus,
E_0 = Young's modulus, and
ν = Poisson ratio.

This modulus, if properly normalized with respect to the void ratio and effective stress, is, in practical terms, independent of the type of loading, number of loading cycles, strain rate, and stress/strain history [8]. It is therefore a fundamental parameter of the ground, considered as a benchmark value that reveals the true elastic behavior of the ground. In addition, it is used to normalize experimental curves from different types of tests in order to obtain simple mathematical stress–strain curves [10]. This is the case for the shear modulus obtained from SASW tests.

In the laboratory, the shear modulus can be evaluated throughout the very-small-strain domain (strains below 10^{-5}) by means of resonant-column tests and bender elements (BEs) or accelerometers. The soil modulus can then be computed according to Eqs 1 and 2.

(2) $$G_0 = \gamma V_s^2$$

where:

V_s = S-wave velocity, and
γ = density.

Considering that design is based on mechanical properties usually determined from laboratory tests, the relationship between field and laboratory results is of great importance [11]. In this framework, we here present a comparison between SASW test results and results from triaxial tests involving S-wave measurements with BEs and accelerometers. Field tests were performed on a clayey sand (SC) trial layer during tests in a full-scale trial, and laboratory tests were conducted on a specimen of the same material under similar conditions. Furthermore, a comparison between mechanical properties obtained from both laboratory and field tests is established.

Bender Elements

The BE technique is a non-destructive dynamic method used to obtain the small-strain shear modulus of soil. BEs are piezoelectric transducers that enable transmission and receiving of shear or compression waves (or both) [12]. The technique consists in exciting one of the transducers at one end of a specimen and receiving the shear wave that travels through the specimen in the other transducer. Both the input and output signals are registered by an oscilloscope, allowing the shear modulus to be obtained via the signal interpretation technique. As the maximum shear strain induced by this method is less than 10^{-5} [13], the shear modulus determined is the small-strain or maximum shear modulus of the soil.

Although the principle appears to be straightforward, in practice the use of BEs can lead to ambiguous and uncertain results, because signals can be distorted by near-field effects, cross-talk, and sample size effects [14–19].

A number of methods for the interpretation of BE results are commonly used, in the time or frequency domain [20–22]. Time domain techniques are generally simple and straightforward, as the travel time can be directly defined from the measurement of the time interval between characteristic points in the transmitted and received wave traces. However, the input signal is given by the function generator and might not exactly correspond to the input BE signal [18]. In addition, near-field and sample size effects contribute to the distortion of the output signal and lead to misinterpretation. Frequency domain techniques tend to be more elaborate, as they are supported by signal processing and spectrum analysis tools and enable automated data acquisition and processing. However, computed signals are not of the same nature, which also may lead to misinterpretation. Ferreira [23] found that the exclusive use of either method proved to be unreliable. Therefore, a practical framework for BE testing was recently proposed [21], combining two distinct interpretation methods, in the time and the frequency domains, as a means to effectively reduce the uncertainty and subjectivity often associated with BE testing and obtain the most reliable value for the travel time.

The aforementioned issues can be overcome if two sensors acting as receivers are used. Ferreira et al. [24] proposed the instrumentation of specimens with two accelerometers in combination with BEs. In this setup, the signal produced by the BE transmitter is acquired by the BE receiver and by the two accelerometers. The advantages of this setup are two-fold: (i) the interpretation of the acceleration measurements can be made directly in both time and frequency domains, as the signals are of the same nature, and (ii) these measurements can be used to verify the BE signals and thus minimize the subjectivity of the interpretation of BE results. This technique has proved to be reliable, and differences given by these two type of transducers were less than 7 % in the time domain and 9 % in the frequency domain.

In the present study a series of tests on unsaturated specimens was carried out using BEs and accelerometers in a Bishop–Wesley stress-path chamber where soil was allowed to consolidate under different isotropic stress levels.

Spectral Analysis of Surface Waves

SASW, proposed and developed during the 1980s, is a widely used method for in situ testing [25,26]. With this nondestructive method one can use the dispersion of Rayleigh waves to determine the shear wave velocity, modulus, and depth of each layer of a pavement profile. Elastic waves are propagated through materials at low deformation levels, in the range of 10^{-5}. At this deformation level, one can relate the deformations and mechanical characteristics of materials by using the theory of elasticity in a linear system. The shear moduli obtained with these methods are considered as maximum values of G_0.

A brief description of the SASW test is presented below. For a detailed description of the SASW test, one should refer to Refs 25–27.

SASW testing can be summed up in three steps that lead to the final result of a stiffness profile for the site: field testing, dispersion curve evaluation, and inversion process.

Field testing consists of making field measurements of the surface wave phase velocity V_R at numerous wavelengths λ_R. In order to ensure the adequate application of an SASW test, it is necessary to take the energy source and receivers into account, considering the desirable frequency range, the space between receivers, and the range of exciting frequencies for each space adopted. The energy source that generates surface waves is normally a mechanical (impact) or electromechanical (continuous) source that applies dynamic vertical loads to the surface. The receivers are placed vertically and aligned in relation to the energy source. The selection of the receiver and its spacing depends mostly on the frequency domain used in the test. In order to minimize the effects of proximity to the source, mainly related to body waves and aliasing phenomena in spectral analysis, it is necessary to impose limitations on the distance L between the energy source and receivers and on the receiver spacing d. In Ref 28 the positioning of the receivers is proposed such that

$$L > \frac{\lambda_R}{4} \tag{3}$$

$$\frac{\lambda_R}{16} \le d < \lambda_R \tag{4}$$

After the field data have been recorded, a dispersion curve is calculated. For testing with multiple receivers, receiver pairs are used to determine the dispersion curve. For each receiver pair, the time histories recorded by the two receivers are transformed into the frequency domain, and the cross-power spectrum and coherence function are calculated. The coherence function represents a signal-to-noise ratio and is often close to 1 in the range of acceptable data. The time delay between receivers as a function of frequency $t(f)$ is calculated from the phase of the cross-power spectrum. The surface wave velocity V_R is calculated using Eq 5. The corresponding wavelength of the surface wave λ_R with a given frequency f is calculated via Eq 6. Then a dispersion curve (V_R versus λ_R) is obtained.

$$V_R = \frac{d}{t(f)} \tag{5}$$

$$\lambda_R = \frac{V_R}{f} \tag{6}$$

After a dispersion curve is calculated from the field data, forward modeling is used in the laboratory to evaluate the shear wave velocity profile. Forward modeling is the process of calculating the shear wave velocity profile via trial-and-error matching of a theoretical dispersion curve with the measured field dispersion curve. The final result consists of a shear wave velocity profile, such as the one shown in **Fig. 1**, where results from cross-hole tests also performed at the site are presented [29].

FIG. 1 Shear wave velocity profiles determined from SASW and cross-hole tests at the same site [29].

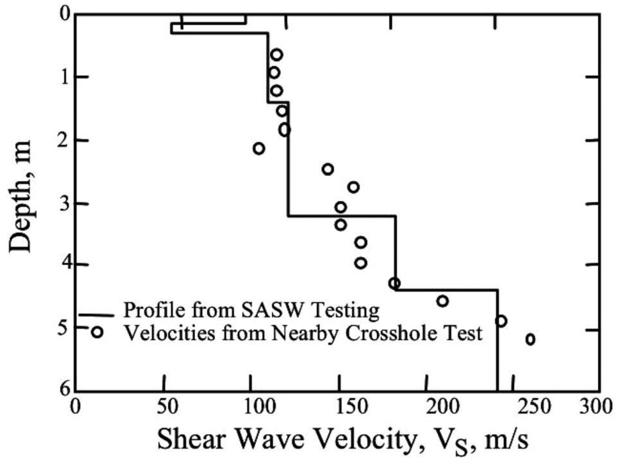

According to the theory of elasticity, the relationship between the velocity of shear waves V_S and the velocity of Rayleigh waves V_R in a uniform field is given by Eq 7.

$$V_S \leq CV_R \tag{7}$$

The constant C is dependent on the Poisson coefficient. For values of this coefficient of 0.2 and 0.5, C assumes values of 1.09 and 1.05, respectively, which means that the error in evaluating the Poisson coefficient has little effect on the value of V_S. The value of the shear modulus G_{SASW} is determined from measured values of the velocity of Rayleigh waves and the density of the material ρ via the theory of elasticity, given by Eq 2. In this way it is possible to convert the vertical profile of velocities into a profile of shear modulus values.

Laboratory Campaign

A laboratory campaign was conducted in order to evaluate the shear modulus at very small strains under the same conditions as in the field. Laboratory tests were carried out on reconstituted samples of the same material employed in a full-scale trial, with the aim of investigating the influence of compaction conditions on the mechanical behavior of this material. Physical, hydro-, and mechanical characterization was conducted in an attempt to reproduce field state conditions. For this purpose, the void ratio was fixed corresponding to 97 % of the modified Proctor value, and the moisture content was varied, corresponding to 4 % dry of optimum ($w_{\text{OPM}-4\%}$), 2 % dry of optimum ($w_{\text{OPM}-2\%}$), optimum (w_{OPM}), or 2 % wet of optimum ($w_{\text{OPM}+2\%}$). In the following sections, only results relevant to the present research are presented.

TABLE 1 Results from identification tests.

Atterberg Limits			Modified Proctor	
w_L	w_P	I_P	γ_d, kN/m^3	w, %
32	21	11	20.14	8.6

PHYSICAL CHARACTERIZATION

The grain-size distribution curve is plotted in **Fig. 2**. **Table 1** presents the index properties, namely, Atterberg limits and compaction characteristics determined using the modified Proctor test. According to the Unified Soil Classification System, the material used is classified as SC.

HYDRO-CHARACTERIZATION

In order to obtain information on the influence of the variation in moisture content on the behavior of the SC material, we performed hydro-characterization (suction–water content relationship). Specimens were compacted to 97 % of the maximum dry density of modified Proctor samples (i.e., to the same void ratio) with a vibrating hammer over the range of moisture contents employed in the full-scale trial ($w_{\text{OPM}-4\%}$, $w_{\text{OPM}-2\%}$, w_{OPM}, and $w_{\text{OPM}+2\%}$).

The filter paper technique was employed to measure the matric suction of SC specimens [30]. The initial negative pore

FIG. 2

SC grain-size distribution.

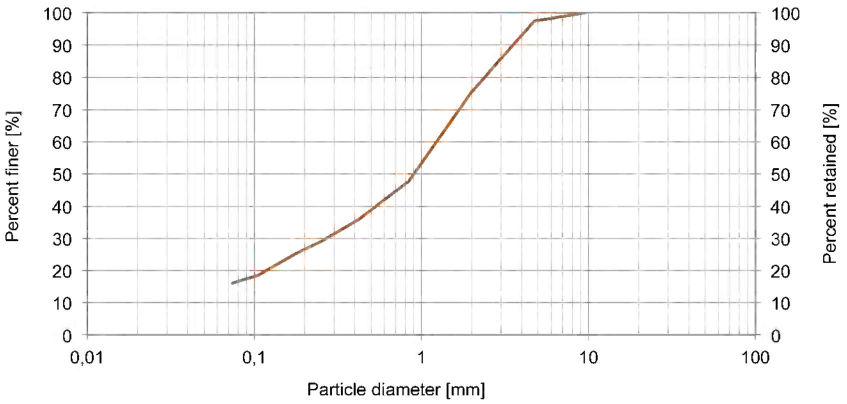

TABLE 2 Filter paper method performed on SC specimens

w, %	*e*	*S*, %
4.6	0.342	35.6
4.6	0.332	36.7
4.7	0.329	37.8
6.0	0.329	48.3
6.9	0.335	47.5
6.9	0.331	47.2
9.3	0.319	77.4
9.4	0.322	77.4
9.4	0.334	74.5
11.6	0.321	95.8
11.9	0.323	97.4
11.5	0.320	95.3

Notes: w, molding water content; *e*, void ratio; *S*, saturation degree.

water pressure (under $\sigma_3 = 0$) was controlled by means of calibrated Whatman #42 filter papers (ashless quantitative Type II) with a diameter of 9 cm. After compaction, two initially dry filter papers were placed on the top and bottom of the specimens. The outer filter papers were used for suction measurement, and the filter papers in contact with the specimen were used to protect the outer filter papers from soil fouling or contamination. To ensure good contact between the specimen and the filter papers and to make it easier to manage the set, the specimen and filter papers were sandwiched in acrylic plates and then wrapped up in a plastic foil. After that, the set was placed in an airtight plastic bag and stored inside a temperature-controlled cabin. Then, the filter papers and the soil specimen moisture content were allowed to equilibrate.

The specimen preparation procedure was the same for all samples. Each sample was mixed with the right quantity of water and placed in a sealed plastic bag for 24 h to achieve uniform moisture conditions. After equilibrium was reached, specimens were compacted with a vibrating hammer in a cylindrical mold 100 mm in diameter. During the compaction process the specimen height was controlled in order to obtain the fixed dry density. With this purpose in mind, we prepared specimens 100 mm in diameter and 25-mm high.

The period allowed for the specimens, filter paper, and air in the sealed container to reach equilibrium was at least 14 days. At the end of the equilibration period, the filter papers were removed from the soil specimen, and the wet mass of the outer filter papers was measured with a high-precision balance with 0.0001-g accuracy. The measurement process was completed within a few seconds to avoid moisture loss from the filter papers. Subsequently, filter paper and soil were oven-dried at 110°C for 24 h. The moisture content of each paper was individually determined. The equilibrium filter paper water content of the specimen was then converted to a matric suction value using the calibration curve [31].

FIG. 3 Matric suction versus saturation degree for SC specimens with approximately the same void ratio (*e* = 0.331).

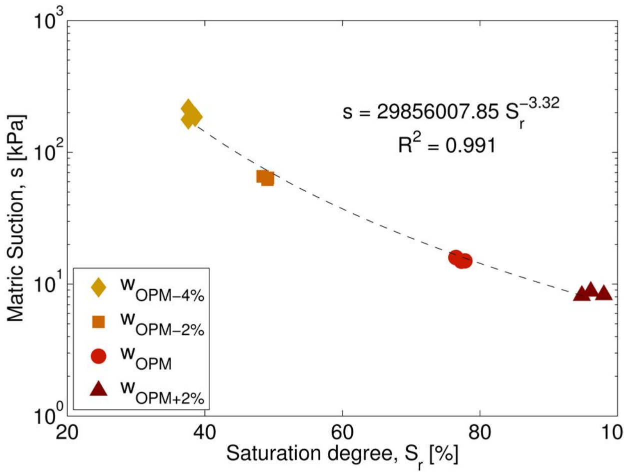

A series of tests was conducted over the range of molding water contents employed in the field investigation and at the same void ratio, corresponding to 97 % of the modified Proctor value ($e = 0.331$). For each series corresponding to a given molding water content, three tests were carried out in order to verify repeatability. The parameters of each test are given in **Table 2**. Note that although slight variation of the void ratio was observed, it was considered insignificant.

Figure 3 is a plot of the matric suction versus the saturation degree for specimens with similar void ratios (about 0.331). The following calibration equation was used [31]:

$$\log_{10}(\text{suction}) = \begin{cases} 4.842 - 0.0622 \times w & \text{if } w < 47\% \\ 6.050 - 2.48 \times \log_{10}(w) & \text{if } w > 47\% \end{cases} \tag{8}$$

where *w* is the filter paper gravimetric water content.

The matric suctions obtained for the range of molding water contents from 4 % dry of optimum to 3 % wet of optimum varied from 215 to 8 kPa, respectively. Matric suction was found to decrease with increasing saturation degree (*S*) according to the expression given in **Fig. 3**. One notes that there is a strong power relation with $R^2 = 0.991$ between matric suction and saturation degree. For the molding water contents studied (4 % and 2 % dry of optimum, optimum, and 2 % wet of optimum), the corresponding values of matric suction were approximately 170, 51, 21, and 11 kPa, considering a void ratio $e = 0.331$.

MECHANICAL CHARACTERIZATION IN THE SMALL-STRAIN DOMAIN

A series of tests using BEs and accelerometers was carried out on an unsaturated SC specimen. For this purpose, a Bishop–Wesley stress-path chamber was used and adapted to

FIG. 4

BE and accelerometer setup: (*a*) scheme; (*b*) view [24].

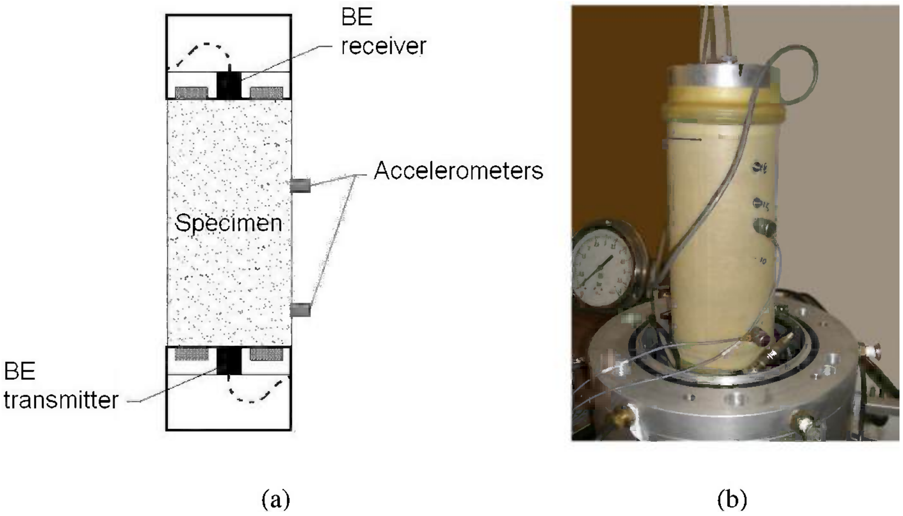

accommodate the bender–extender elements and the accelerometers [24]. The bender–extender elements used in this work were manufactured by GDS and allowed transmission of P-waves and S-waves. However, we measured only S-waves, because of the maximum limit of the acquisition frequency rate allowed by the acquisition equipment used, which did not enable the measurement of P-waves. As accelerometers, we employed two type 4513–001 piezoelectric sensors from Brüel and Kjær, with sensitivity of 100 mV/g, a measurement range of ±50 g, a frequency range between 1 and 10 kHz, dimensions of 12.7 mm in diameter and 15.65 mm in height, and a weight of approximately 9 g.

The final setup is illustrated in **Fig. 4**. The conceived testing system comprised a total of four sensors: two bender–extender elements placed on the top and bottom, and two accelerometers placed 2.5 and 17.5 cm from the bottom. The sensor located on the bottom platen was the transmitter BE that sent seismic S-waves, which traveled through the specimen and were received and recorded by the remaining transducers, the receiver BE, and the accelerometers.

The associated electronics equipment consisted of two main components: a function generator from Thurlby Thandar Instruments (model TG1010A) and a National Instruments data logger system (SCXI–1600), with 16-bit accelerometer cards (SCXI–1531), connected to a portable computer. The function generator produced the output signal to a transmitting BE with the maximum amplitude allowed by the equipment (±10 V) in order to enhance the response of the BE–soil system. Reference 15 recommends the use of a single sinusoidal input pulse because this signal has a narrower frequency spectrum and the output signal is expected to have a similar shape.

Specimens 100 mm in diameter and 200-mm high were prepared with moisture contents close to the optimum value (8.8 %). After moisture equilibrium was reached, and in order to get the best possible standard homogeneity, compaction was performed in four layers, each one with the same mass of material, in a 100-mm diameter cylindrical mold. For the first 50-mm layer, compression was performed until the desired volume was reached, corresponding to 97 % of the modified Proctor value and a void ratio of 0.331. Each of the remaining three layers was successively compacted on top of the previous one using the volume criterion. The interfaces between the different layers were carefully scarified in order to provide good bonding between the layers.

Triaxial consolidated drained isotropic tests with measurement of S-wave velocity were conducted on unsaturated SC specimens. These were submitted to isotropic stresses, namely, 25, 50, 100, 200, and 300 kPa, and consolidation was allowed. For each stage measurement of S-wave velocity was conducted. The interpretation of the BE and accelerometer data was performed in the time domain.

A critical review of the literature showed that the shear modulus of unbound granular materials at very small strains follows a power law according to Eq 9.

$$G_0 = Cp^n \tag{9}$$

where:

G_0 = maximum shear modulus,
C = constant, and
p = mean stress.

After shear modulus correction to the same void ratio via Eq 10, with the void ratio function given by Eq 11 and proposed in Ref 32, data were plotted (**Fig. 5(*a*)**) regarding the normalized moduli versus the total normal stress. Values obtained for Eq 9 are given in **Table 3**. In **Fig. 5(*b*)** we attempt to interpret

FIG. 5 Evolution of normalized shear moduli with (*a*) total normal stress and (*b*) effective normal stress obtained from measurements of S-waves on SC unsaturated specimens under isotropic stress.

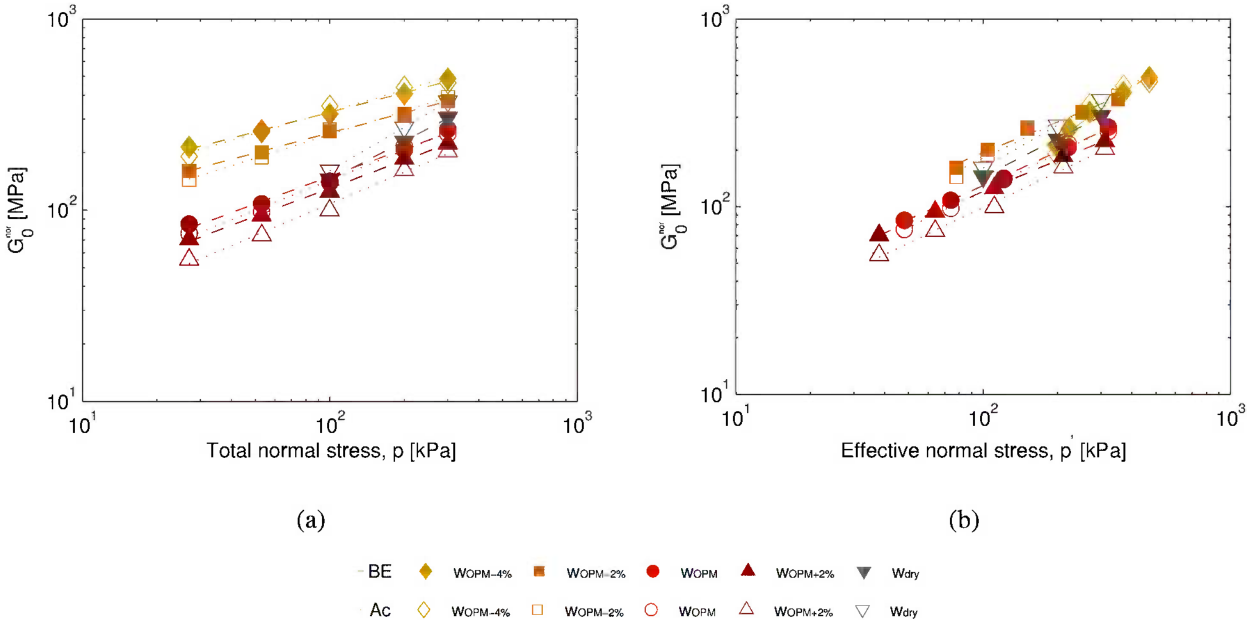

(a)

(b)

the effective normal stress by means of a simple approach consisting of adding suction, determined from **Fig. 3**, to the total normal stress. Although suction may vary during an isotropic test, it is thought that this variation is slight [33]. To some extent a trend may be observed: results from several tests seem to be aligned, as would be expected in effective stress analysis [33]. Values obtained for Eq 9 are given in **Table 4**.

$$G_0^{nor} = G_0 \frac{f(e = 0.331)}{f(e)} \tag{10}$$

$$f(e) = \frac{(2.17 - e)^2}{(1 + e)} \tag{11}$$

where:

G_0^{nor} = normalized maximum shear modulus,
$f(e)$ = void ratio function, and
e = void ratio.

TABLE 3 Values of parameters *C*, *n*, and coefficient of determination R^2 from normalized shear modulus ($e = 0.331$) regression lines at isotropic total stress state.

	Bender Elements			Accelerometers		
Specimen	C	n	R^2	C	n	R^2
$w_{OPM-4\%}$	68.0	0.340	0.994	57.5	0.378	0.978
$w_{OPM-2\%}$	50.8	0.350	0.998	37.7	0.410	0.991
w_{OPM}	16.8	0.476	0.990	13.0	0.521	0.993
$w_{OPM+2\%}$	13.8	0.486	0.997	8.6	0.550	0.990
w_{dry}	6.4	0.677	1.000	4.9	0.760	1.000

Field Campaign

A cooperation protocol has been settled on by the National Railway Network (REFER) and four national research institutions (University of Minho, National Laboratory of Civil Engineering, New University of Lisbon, and Technical University of Lisbon) to develop knowledge concerning the methodology for the construction and control of railway embankments and rail track layers for high-speed trains. The protocol was established under the framework of National Research Project POCI/ECM/61114/2004, entitled "Interaction Soil–Rail Track for High Speed Trains," financed by the Foundation for Science and Technology.

A trial embankment was constructed with the cooperation of REFER, MOTA–ENGIL, and GEOCONTROLE. This took place near the new railway line between Sines and Caia, in section Casa Branca–Évora at PK 106 + 800, about 2.5 km from

TABLE 4 Values of parameters *C*, *n*, and coefficient of determination R^2 from normalized shear modulus ($e = 0.331$) regression lines at isotropic effective stress state.

Specimen	Bender Elements			Accelerometers		
	C	n	R^2	C	n	R^2
$w_{OPM-4\%}$	1.77	0.918	0.984	1.28	0.976	0.884
$w_{OPM-2\%}$	15.59	0.547	0.982	9.54	0.639	0.968
w_{OPM}	8.14	0.601	0.999	5.96	0.655	0.995
$w_{OPM+2\%}$	9.33	0.555	0.999	5.47	0.628	0.996
w_{dry}	6.37	0.677	1.000	4.85	0.760	1.000

FIG. 6 General overview of SC trial layer.

the Monte das Flores railway station, and tests were run between October and November of 2006. An experimental program was established consisting of the employment of different materials (**Fig. 6**) and in situ evaluation of the physical and mechanical properties of embankment and sub-balast layers with different thicknesses and moisture contents, for several energy levels. For a detailed description of the experimental program, see Ref 34.

EXPERIMENTAL PROGRAM

A SC was employed in embankment trial layers with 0.30-, 0.40-, and 0.50-m thicknesses and moisture contents 2 % dry of optimum ($w_{OPM-2\%}$), optimum (w_{OPM}), and 2 % wet of optimum ($w_{OPM+2\%}$) relative to the modified Proctor value. It should be noted that poor quality superficial soils were removed before construction of the trial layers. An excavation 0.60 m deep was made within an area of approximately 2000 m^2. In order to promote homogeneity of the support of the trial embankment, a foundation 0.60 m thick was compacted in two layers, each 0.30 m thick, with the moisture content on the dry side of the modified Proctor curve (**Fig. 7(*a*)**). Each layer was compacted with an energy level corresponding to 12 passes of the vibrating roller.

Trial layers were constructed with dimensions in plant of 25 and 50 m in length and 6 m in width. A mesh was then created in order to establish locations for field tests, as illustrated in **Fig. 7(*b*)**. This consisted in dividing the width into 2-m lanes (*A*, *B*, and *C*) and the length into 5-m columns (1 to 10), resulting in grids with dimensions of $(5 \times 2)\text{m}^2$. A set of field tests was conducted in selected grids to evaluate the physical and mechanical properties of the trial layer for each energy level applied. **Figure 7(*b*)** shows the experimental plan for a trial layer 0.40 m thick with a moisture content close to optimum (0.40 m w_{OPM}) at an energy level corresponding to 12 passages of the vibrating roller.

Because the nuclear method was employed in different grids than SASW tests, the spatial distribution of state conditions was computed from in situ test results in order to estimate conditions regarding SASW tests. The void ratio and moisture content spatial distribution presented in **Fig. 8** was derived using inverse distance weight interpolation. This method takes into account the assumption that results that are close to one another are more alike than those that are farther apart.

SPECTRAL ANALYSIS OF SURFACE WAVES

For the purposes of the present work, SASW tests were conducted on an SC trial layer with 0.40-m thickness and a

FIG. 7

(*a*) Embankment profile; (*b*) trial layer mesh with field test location. NM, nuclear method.

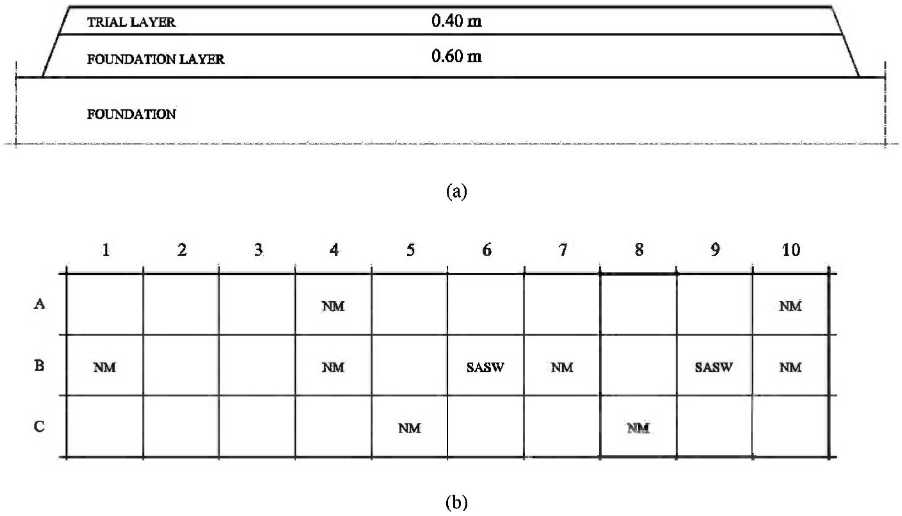

FIG. 8 State condition spatial analysis for trial layer 40 cm w_{OPM}: (*a*) void ratio; (*b*) moisture content.

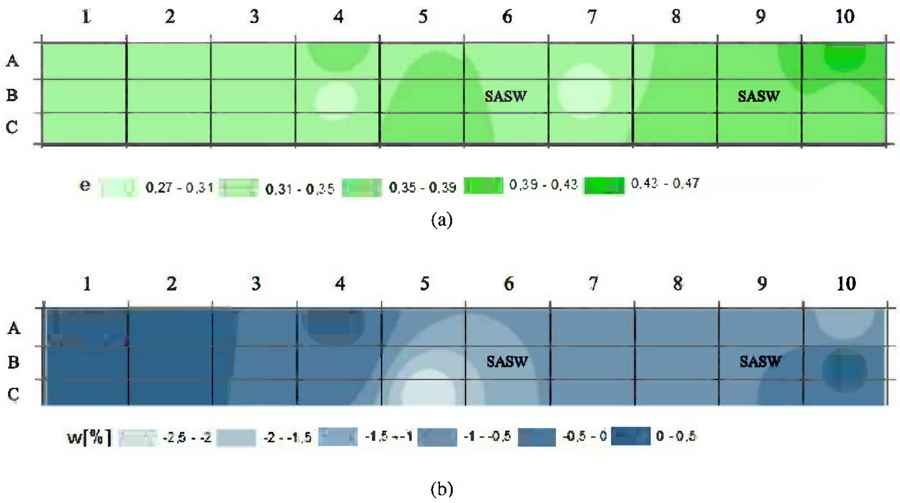

moisture content close to optimum (0.40 m w_{OPM}) inside grids B6 and B9 (**Fig. 7(*b*)**). The setup involved the instrumentation of the surface layer with accelerometers placed at equal distances, as illustrated in **Fig. 9**. Four vertical receivers (accelerometers) were placed on the ground at an equal distance from a fixed centerline. Because an upper compacted layer of about 0.40 m and a foundation layer of about 0.60 m (see **Fig. 7(*a*)**) were under consideration, 1-m receiver spacing was used in this study.

An impulsive load was applied in line with the receivers at a distance from the receiver equal to the receiver spacing. To improve the signal-to-noise ratio, we repeated the impacts several times (about 20 impacts). A reverse test was also performed with the source on the opposite side of the receiver array, in order to confirm the first test. Active Rayleigh wave data were generated using a light hammer source.

The signals picked up by the receivers were recorded by a laptop with an acquisition program developed in LabVIEW. A National Instruments SCXI 1600 acquisition system with accelerometer card 1531, with a maximum sampling rate of 200 kS/s and a resolution of 16 bits, was used to collect the signals from both the source and the receiving accelerometers. Data acquisition was performed at a frequency of 2 kHz per channel ($\Delta t = 0.0005$ s).

The software Signal Processing in Civil Engineering (SPICE) v2.0 was used for spectral analysis. For each pair of signals, one pair involving receivers Ac1 and Ac2 with 1-m spacing and another involving receivers Ac2 and Ac4 with 2-m spacing, we obtained an estimate of the dispersion curve over a certain frequency range, considering the filtering criterion and coherence between signals of 0.90. By assembling the information from the different pairs of receivers, we obtained the composite dispersion curve shown in **Fig. 10**. Because the experimental dispersion curve corresponding to the reverse test spanned a short frequency range, data were discarded. The good agreement between theoretical and experimental composite dispersion curves is verified in **Fig. 10**.

Then a shear wave profile was computed using all data available for the trial layer and foundation layer, namely, foundation and compacted layer thicknesses (0.40 and 0.60 m, respectively) and density (**Fig. 11**). For this purpose, state conditions obtained from spatial analysis at grids B6 and B9 were employed.

In order to achieve the best fit of the theoretical dispersion curve to the experimental dispersion curve, we conducted the inversion process in an iterative way, starting with three layers, until a satisfactory result was achieved. We note that because of the sensor spacing, the shear wave profile beyond the 2-m depth should be discarded. From the shear wave profile, the shear modulus can be computed according to Eq 2.

FIG. 9 Setup adopted to perform SASW on layer 0.40 w_{OPM}.

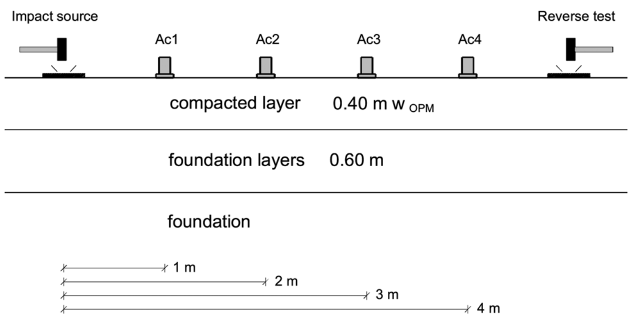

FIG. 10 Theoretical and experimental composite dispersion curve from SASW carried out on layer 0.40 m w_{OPM} inside grids (*a*) B6 and (*b*) B9.

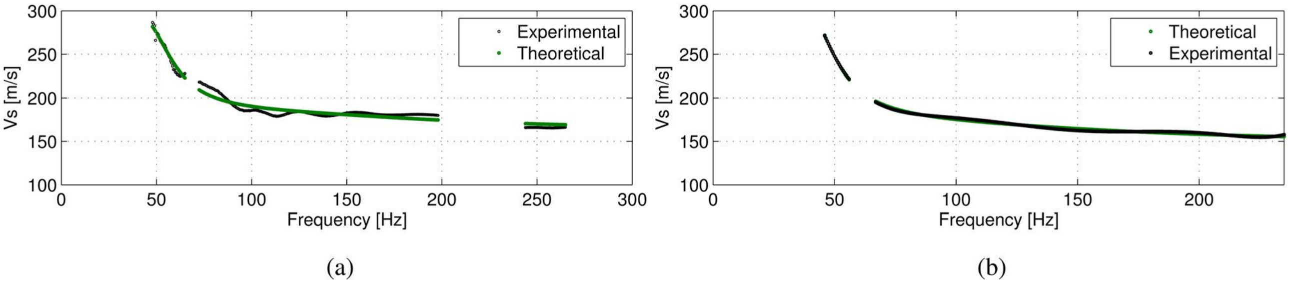

(a) (b)

Comparison between Field and Laboratory Results

Comparison between the shear modulus obtained from SASW tests carried out on 0.40 m w_{OPM} and the shear modulus computed from laboratory S-wave measurements was performed. We highlight that the methodology for the determination of moduli was based on S-wave propagation through geomaterial, and thus involved similar stress and strain levels.

The state conditions and shear moduli determined from field and laboratory tests are summarized in **Table 5**. From **Fig. 8** one can see that field tests were carried out on grids with moisture contents 1.2 % dry of optimum (grid B6) and 0.5 % dry of optimum (grid B9) and void ratios of 0.330 and 0.370, respectively. Note that these are average values. Because these data did not clearly match the state conditions from laboratory specimens, the laboratory shear modulus was corrected, taking into account the field void ratio and moisture content, according to the following approach.

First, the saturation degree was computed from field state conditions and the matric suction was determined according to the equation given in **Fig. 3**. It should be borne in mind that for grid B9, the matric suction is just an approximation, as the curve representing laboratory matric suction versus saturation degree was determined for a void ratio of 0.331, whereas the field void ratio was 0.370. In fact, hydro-characterization of static compacted specimens of the same material shows that suction at a saturation degree of about 58 % and a void ratio of 0.373 is 46 % lower than the corresponding suction value for a void ratio of 0.331 [35].

Second, the effective normal stress at the middle of the trial layer was computed. For this, a total stress of about 2.6 kPa corresponding to normal stress at the middle of the trial layer was considered. Because of the unsaturated condition, matric suction was added and an effective normal stress was obtained via Eq 9. Data are given in **Table 4**. This is considered a reasonable approximation taking into account a high saturation degree (about 60 %) [33].

FIG. 11 Shear wave profile from SASW carried out on layer 0.40 m w_{OPM} inside grids (*a*) B6 and (*b*) B9.

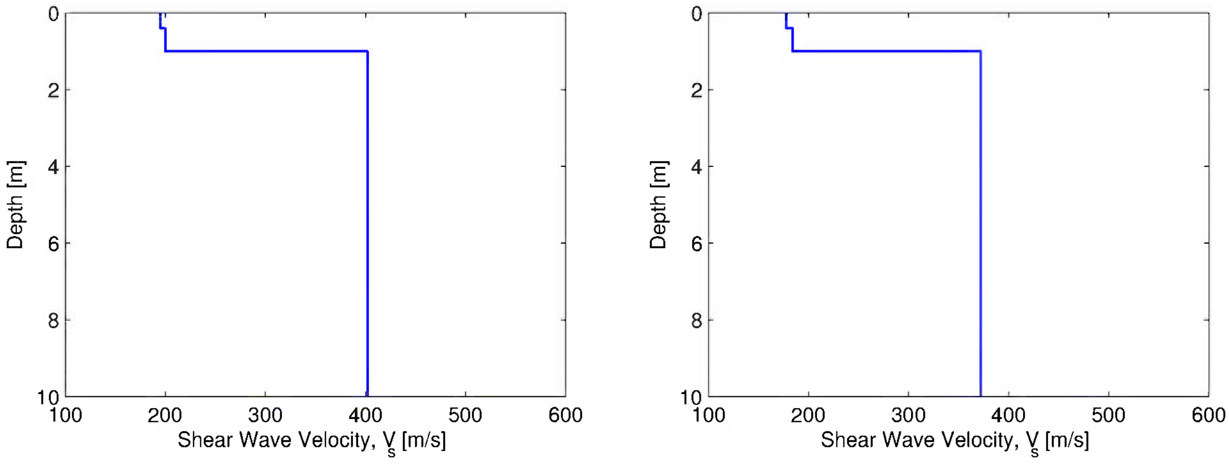

(a) (b)

TABLE 5 Field and laboratory conditions and modulus for SC geomaterial.

	Field	Laboratory		Field	Laboratory	
	Grid B6	BE	Acc	Grid B9	BE	Acc
γ, kN/m^3	20.99	21.21		20.51	21.21	
w, %	7.4	7.4		8.1	8.1	
e	0.370	0.331		0.370	0.331	
S, %	59.4			58.0		
s, kPa	38.5			41.7		
p', kPa	41.1			44.2		
V_s, m/s	195			178		
G_0, MPa	81	106	92	66	95	84
$f(e\ \text{field}), f(e\ \text{lab})$	2.55	2.54		2.36	2.54	
$G^{\text{nor}}_{0\text{field}}$, MPa	81	106	92	66	88	78

Note: Acc, accelerometer.

Third, the laboratory shear modulus was computed via interpolation between the optimum moisture content and results at 2 % dry of optimum, and finally the shear modulus was normalized for the same void ratio.

A comparison plot of field versus laboratory results is presented in **Fig.** 12. In the results of the SASW test performed inside grid B6, where the field void ratio (0.330) was similar to the laboratory void ratio (0.331), a difference of 14 % between the SASW shear modulus and the shear modulus computed from S-wave measurements with accelerometers is observed. However, the shear modulus computed from S-wave measurements with BEs was about 31 % higher. Although specimens' moisture contents were not the same as the field moisture content, a reasonable relationship between field and laboratory S-wave measurements with accelerometer results was found.

Concerning the results obtained from the SASW test performed at grid B9, where the field void ratio (0.370) was higher than the laboratory void ratio (0.331), moduli comparison showed a difference of 18 % and 34 % in the shear modulus computed from S-wave measurements with accelerometers and BEs, respectively. This greater difference is thought to be due to a field void ratio (0.337) higher than the laboratory void ratio (0.331). This was not unexpected, as it is known that a higher void ratio leads to a lower matric suction value, as long as the same saturation degree is considered. Consequently, the effective normal stress will be lower, and therefore a lower modulus will be obtained. Indeed, if the matric suction in grid B9 were reduced by 46 % [35], then the difference between field and laboratory moduli would be less than 10 %, and hence the relationship would be greatly improved.

FIG. 12 Field versus laboratory shear modulus.

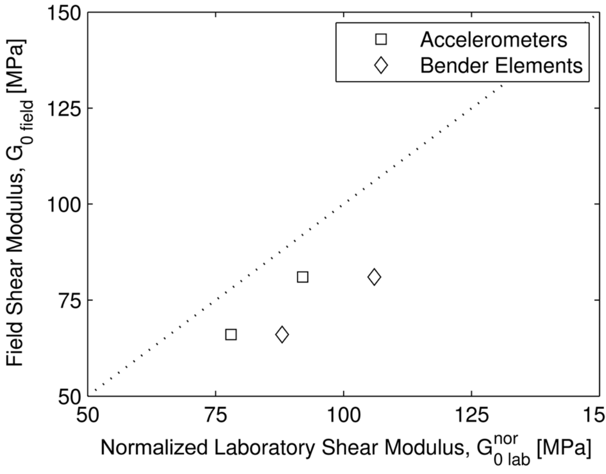

Although specimens' moisture contents were not the same as the field moisture content, a reasonable relationship between field and laboratory results was found, as long as the void ratio and saturation degree were considered. It should be pointed out that the saturation degree has a great influence on the determination of the effective normal stress; thus laboratory hydro-characterization of dynamic compacted specimens for different void ratios is required.

Conclusions

It is in the range of elastic behavior that Young's modulus *E* and the shear modulus *G* are key parameters for both dynamic and static geotechnical problems. In this scope, both laboratory and field tests assume great importance in the determination of these parameters.

In the present work, the relationship between laboratory and field shear modulus values was established. Both were determined from wave measurements and thus involved similar stress–strain conditions. Despite differences between field and laboratory moisture contents, reasonable agreement was obtained when the shear modulus was normalized for the same void ratio and effective normal stress. Considering that designs are based on mechanical properties usually determined from laboratory tests, the relationship between field and laboratory results is of great importance, because it allows a connection between rational design parameters and performance evaluation. Thus quality control/quality assurance is enhanced, promoting a sustainable approach to design and construction.

This study shows that laboratory hydro-mechanical characterization of materials to be used in compacted layers under unsaturated conditions is required with regard to field moisture content and void ratio, and a laboratory approach is described. An approach for comparison of laboratory and field shear modulus values determined under unsaturated conditions is also described, considering field conditions (void ratio and moisture content) and stress state.

These results allow us to conclude that SASW represents a powerful tool for the evaluation of mechanical behavior in the range of elastic behavior of compacted layers. Because the geometric conditions are known and the state conditions are determined through current field practice, unknown parameters in the inversion process are reduced, enabling a more reliable determination of the mechanical properties of compacted layers.

References

[1] Gomes Correia, A., "Innovations in Design and Construction of Granular Pavements and Railways. Advances in Transportation Geotechnics," E. Ellis, N. Thom, H. Yu, A. Dawson, and G. McDowell, Eds., *Proceedings of the International Conference*, Nottingham, UK, Aug 25–27, 2008, CRC Press, London, 2008, pp. 3–13.

[2] Gomes Correia, A. and Magnan, J.-P., "Trends and Challenges in Earthworks for Transportation Infrastructures," S. Miura, T. Ishikawa, N. Yoshida, Y. Hisari, and N. Abe, Eds., *Advances in Transportation Geotechnics 2*, CRC Press, London, 2012, pp. 1–12.

[3] Briaud, J. L., "Introduction to Soil Moduli," *Geotechnical News*, BiTech Publishers Ltd, Richmond, B.C., Canada, Vol. 19, No. 2, 2001, pp. 54–58.

[4] Gomes Correia, A., Martins, J., Caldeira, L., Maranha das Neves, E., and Delgado, J., "Comparison of in Situ Performance-based Tests Methods to Evaluate Moduli of Railway Embankments," *8th International Conference on the Bearing Capacity of Roads, Railways and Airfields*, Vol. 2, Tutumluer, E. and I. L. Al-Qadi, Eds., CRC Press, London, 2009, pp. 1331–1340.

[5] Quibel, A., "New in Situ Devices to Evaluate Bearing Capacity and Compaction of Unbound Granular Materials," *Unbound Granular Materials: Laboratory Testing, In-situ Testing and Modelling*, A. Gomes Correia, Ed., Technical University of Lisbon, Lisbon, Portugal, 1999, pp. 141–151.

[6] Edil, T. and Sawangsurya, A., "Earthwork Quality Control Using Soil Stiffness," *Proceedings of the 16th International Conference on Soil Mechanics and Geotechnical Engineering*, Osaka, Japan, Sept 12–16, International Society for Soil Mechanics and Geotechnical Engineering, London, 2005.

[7] Atkinson, J. H., "Non-linear Soil Stiffness in Routine Design," *Géotechnique*, Vol. 50, No. 5, 2000, pp. 487–508.

[8] Santos, J. A. and Gomes Correia, A., "Shear Modulus of Soils under Cyclic Loading at Small and Medium Strain Level," *Proceedings of the 12th World Conference on Earthquake Engineering*, Auckland, New Zealand, Jan 30–Feb 4, New Zealand National Society for Earthquake Engineering, Wellington, New Zealand, 2000.

[9] Gomes Correia, A., "Soil Mechanics in Routine and Advanced Pavement and Rail Track Rational Design," *Geotechnics for Roads, Rail Tracks and Earth Structures*, Balkema, A. Gomes Correia and H. Brandl, Eds., Balkema, Netherlands, 2001, pp. 165–187.

[10] Santos, J. A. and Gomes Correia, A., "Reference Threshold Shear Strain of Soil: Its Application to Obtain an Unique Strain-dependent Shear Modulus Curve for Soil," *Proceedings of the Fifteenth International Conference on Soil Mechanics and Geotechnical Engineering*, Istanbul, Turkey, Aug 27–31, 2001, Volumes 1–3, 2001, pp. 267–270.

[11] Schneider, J., Hoyos, L., Jr., Mayne, P., Macari, E., and Rix, G., "Field and Laboratory Measurements of Dynamic Shear Modulus of Piedmont Residual Soils," B. Edelen, Jr., P. E. Ed., *Behavioral Characteristics of Residual Soils, GSP 92*, ASCE, Reston, VA, 1999, pp. 12–25.

[12] Leong, E., Cahyadi, J., and Rahardjo, H., "Measuring Shear and Compression Wave Velocities of Soil Using Bender–Extender Elements," *Can. Geotech. J.*, Vol. 46, No. 7, 2009, pp. 792–812.

[13] Dyvik, R. and Madshus, C., "Laboratory Measurements of $G_{\max}$ Using Bender Elements," *Advances in the Art of Testing Soils under Cyclic Conditions*, Detroit, MI, Oct 24, ASCE, Reston, VA, 1985.

[14] Sánchez-Salinero, I., Roesset, J. M., and Stokoe, I. K. H., "Analytical Studies of Body Wave Propagation and Attenuation," *Technical Report No. GR86-15*, Civil Engineering Department, University of Texas, Austin, TX, 1986.

[15] Viggiani, G. and Atkinson, J., "Interpretation of Bender Element Tests," *Géotechnique*, Vol. 45, No. 1, 1995, pp. 149–154.

[16] Arroyo, M., Muir Wood, D., and Greening, P., "Source Near-field Effects and Pulse Tests in Soil Samples," *Géotechnique*, Vol. 53, No. 3, 2003, pp. 337–345.

[17] Greening, P. and Nash, D., "Frequency Domain Determination of G_0 Using Bender Elements," *Geotech. Test. J.*, Vol. 27, 2004, pp. 1–7.

[18] Lee, J. S. and Santamarina, J. C., "Bender Elements: Performance and Signal Interpretation," *J. Geotech. Geoenviron. Eng.*, Vol. 131, No. 9, 2005, pp. 1063–1070.

[19] Kuwano, R., Wicaksono, R., and Mulmi, S., "Small Strain Stiffness of Coarse Granular Materials Measured by Wave Propagation," *4th International Symposium on Deformation Characteristics of Geomaterials*, S. E. Burns, P. W. Mayne, and J. C. Santamarina, Eds., IOS Press, Amsterdam, The Netherlands, Vol. 2, 2008, pp. 749–756.

[20] Brignoli, E., Gotti, M., and Stokoe, K., "Measurement of Shear Waves in Laboratory Specimens by Means of Piezoelectric Transducers," *Geotech. Test. J.*, Vol. 19, No. 4, 1996, pp. 384–397.

[21] Viana da Fonseca, A., Ferreira, C., and Fahey, M., "A Framework for Interpretation of Bender Element Tests, Combining Time-domain and Frequency-domain Methods," *Geotech. Test. J.*, Vol. 32, No. 2, 2009, pp. 1–17.

[22] Styler, M. and Howie, J., "Combined Time and Frequency Domain Approach to the Interpretation of Bender-element Tests on Sand," *Geotech. Test. J.*, Vol. 36, No. 5, 2013, pp. 649–659.

[23] Ferreira, C., 2008, "The Use of Seismic Wave Velocities in the Measurement of Stiffness of a Residual Soil," Ph.D. thesis, University of Porto, Porto, Portugal.

[24] Ferreira, C., Martins, J. P., and Gomes Correia, A., "Determination of the Small-strain Stiffness of Hard Soils by Means of Bender Elements and Accelerometers," *Geotech. Geol. Eng.*, 2013, pp. 1–7.

[25] Heisey, J. S., Stokoe, K. H. I., and Meyer, A., "Moduli of Pavement Systems from Spectral Analysis of Surface Waves," *Transportation Research Record. 852*, Transportation Research Board, Washington, D.C., 1982, pp. 22–31.

[26] Nazarian, S., 1984, "In Situ Determination of Elastic Moduli of Soil Deposits and Pavement Systems by

Spectral-analysis-of-surface-waves Method," Ph.D. thesis, University of Texas, Austin, TX.

[27] Stokoe, K. I., Nazarian, S., Rix, G., Sanchez-Salinero, I., Sheu, J., and Mok, Y., "In Situ Seismic Testing of Hard-to-sample Soils by Surface Wave Method," J. L. Von Thun, Ed., *Earthquake Engineering and Soil Dynamics II—Recent Advances in Ground-motion Evaluation*, ASCE, Reston, VA, 1988, pp. 264–277.

[28] Tokimatsu, F., Kuwayama, S., Tamura, S., and Miyadera, Y., "V_s Determination from Steady State Rayleigh Wave Method," *Soils Found.*, Vol. 32, No. 2, 1991, pp. 153–163.

[29] Stokoe, K., Wright, S., Bay, J., and Roesset, J., "Characterization of Geotechnical Sites by SASW Method," *Technical Review: Geophysical Characterization of Sites*, ISSMFE Technical Committee 10, R. D. Woods, Ed., Oxford Publishers, New Delhi, 1994, pp. 15–25.

[30] Bicalho, K., Marinho, F., Fleureau, J.-M., and Gomes Correia, A., "Evaluation of Filter Paper Calibrations for Indirect Determination of Soil Suctions of Unsaturated Soils," E. Alonso and A. Gens, Eds., *Unsaturated Soils*, Alonso and Gens, Eds., Taylor & Francis, London, 2011, pp. 609–613.

[31] Chandler, R. J., Crilley, M. S., and Montgomery-Smith, G., "A Low-cost Method of Assessing Clay Desiccation for Low-rise Buildings," *Proc. ICE Civ. Eng.*, Vol. 92, 1992, pp. 82–89.

[32] Hardin, B. O. and Richart, F. J., "Elastic Wave Velocities in Granular Soils," *J. Soil Mech. Found. Div.*, Vol. 89, No. SM1, 1963, pp. 33–65.

[33] Fleureau, J. M., Hadiwardoyo, S., and Gomes Correia, A., "Generalised Effective Stress Analysis of Strength and Small Strains Behavior of a Silty Sand, from Dry to Saturated State," *Soils Found.*, Vol. 43, No. 4, 2003, pp. 21–33.

[34] Martins, J., 2011, "Compaction and Its Influence on the Structural Behavior of High-speed Railways," Ph.D. thesis, University of Minho, Braga, Portugal.

[35] Gomes, E., 2012, "Influência da não saturação no comportamento mecânico de camadas de aterro [Influence of non-saturation on the mechanical behaviour of embankment layers]," M.S. thesis, University of Madeira, Funchal, Portugal (in Portuguese).

Journal of Testing and Evaluation

doi:10.1520/JTE20130291 / Vol. 43 / No. 2 / March 2015 / available online at www.astm.org

Xianhua Chen[1]

From Texture to Skid Resistance: A Multi-Scale Modeling Approach

Reference

Chen, Xianhua, "From Texture to Skid Resistance: A Multi-Scale Modeling Approach," *Journal of Testing and Evaluation*, Vol. 43, No. 2, 2015, pp. 465–471, doi:10.1520/JTE20130291. ISSN 0090-3973

Manuscript received November 13, 2013; accepted for publication December 22, 2014; published online January 22, 2015.

[1] Associate Professor, School of Transportation Engineering, Southeast Univ., 2 SiPaiLou, Nanjing 210096, People's Republic of China, e-mail: chenxh@seu.edu.cn

ABSTRACT

Real-time measurement of the tire–road friction coefficient is extremely valuable for road-maintenance operations and highway safety management. This paper presents a systematic framework to predict skid resistance of wet pavement with a non-contact method, which could be a potential approach for real-time measurements of pavement friction. The grip potential of pavement is estimated according to the measured pavement texture based on theoretical simulation of the complete hysteresis and partial adhesive effects during tire sliding on wet pavement. Such a method could be potentially used for the purpose of harmonization analysis of skid resistance and potential capability of optimization of pavement surface texture.

Keywords

skid resistance, non-contact method, pavement texture complete hysteresis effect, partial adhesive effect

Introduction

The safe passage of road traffic needs a certain amount of grip between the tires of the vehicles and the road surface. The frictional forces are necessary for vehicle maneuvers, such as acceleration, braking, or safely cornering. The level of frictional forces depends on contact geometry and topology, properties of the bulk and surface materials of the bodies, displacement and relative velocity of the bodies, and presence of lubrication.

To characterize road surfaces with respect to friction, many countries have derived their own test methods for several decades, measuring in some way the frictional force developed between a moving tire or slider and the road surface, and recording the quotient of the measured force with the applied vertical load. These are, of necessity, very much simplified to assess, specifically, the condition of the road surface. As current available standardized test methods all simplify the reality of the complex friction process in the tire–road interface during vehicle maneuvers, it is difficult to harmonize analysis between the outputs of those test methods for the purpose of global improvement on road traffic safety.

In this paper, a non-contact method to predict the skid resistance of wet pavements is proposed. The skid resistance is simulated with complete hysteretic effects and partial adhesive effects. The theoretical skid resistances predicted by the model are compared with test results of 17 specimens. It is concluded that the approach can be potentially adopted for wet grip prediction.

Schematic Framework of Non-Contact Method Prediction

TIRE AND WET PAVEMENT CONTACT IN MACRO-SCALE

As is well known, three distinct zones exist when rubber tires slide over wet pavement [1]: the hydrodynamic region I (squeeze film region in which the tire is fully floated), the viscous hydrodynamic region II (transition zone in which the tire is partially floated), and the complete dry contact region III (traction regime in which the tire attaches to the road directly) (**Figs. 1** and **2**). It is worth noting that the occurrence of individual regions depends on the water depth and the tire-sliding velocity.

ORIGINATION OF THE SKID RESISTANCE OF PAVEMENT IN MICRO-SCALE

The skid resistance of a pavement originating from the interaction between a rubber tire and pavement involves comprehensive and complex physical mechanisms, like adhesion, hysteresis, cohesion, and viscous friction, of which adhesion and hysteresis are known to be primary contributions (**Fig. 3**) [1–5].

The adhesion component arises from molecular interactions between the two surfaces during the sliding process, and can be strongly reduced because of interfacial lubricating [6]. The hysteresis component, referred to as the deformation contribution, results from the energy lost through the macroscopic dynamic deformation process of a certain volume of rubber induced by surface roughness. Also, the level of hysteresis friction is promoted with increasing surface roughness and appears to be a determining factor for tire grip performance under wet conditions. Both effects of adhesion and hysteresis depend on small relative motion between the contact partner's tire tread and the road surface of the contact area.

FIG. 1 Tire–road contact information according to Moore [1].

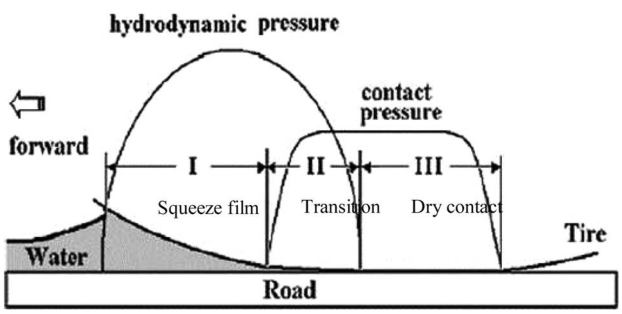

FIG. 2 Nominal slip-friction coefficient curve.

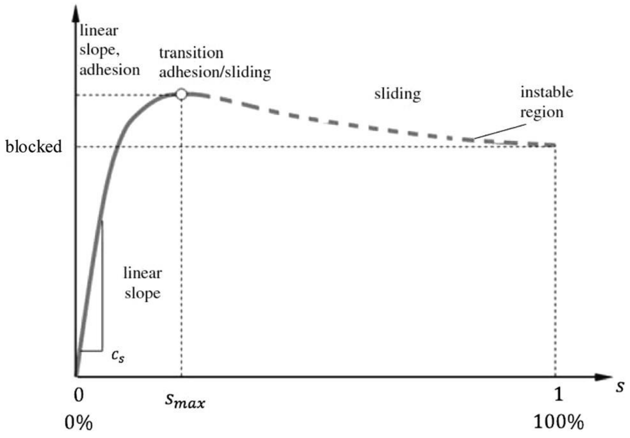

SCHEMATIC FRAMEWORK OF NON-CONTACT METHOD PREDICTION

To predict wet skid resistance five basic assumptions are adopted, and the schematic framework is illustrated in **Fig. 4**:

(1) Wet grip of pavement is allocated to complete hysteretic effects and partial adhesive effects, which can be simplified by a nominal parameter β, $\sigma_{f0} = (\mu_{hys} + \beta \cdot \mu_{adh})\sigma_0$;

(2) The hysteretic friction depends only on the complex viscoelastic modulus of the rubber and on the substrate surface roughness power spectrum according to Persson [2];

FIG. 3 Schematic representation of the main mechanisms of rubber friction at dry condition [1].

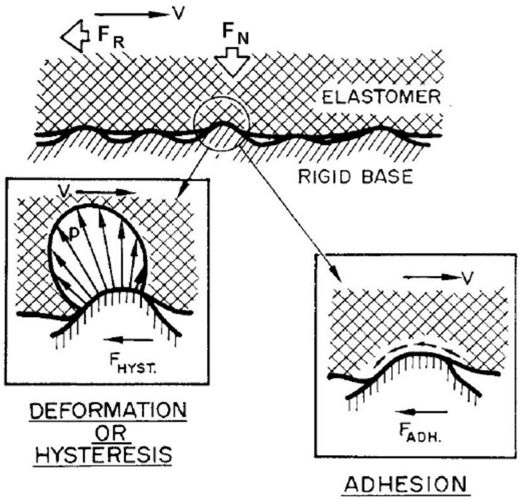

FIG. 4

Schematic framework of non-contact method prediction.

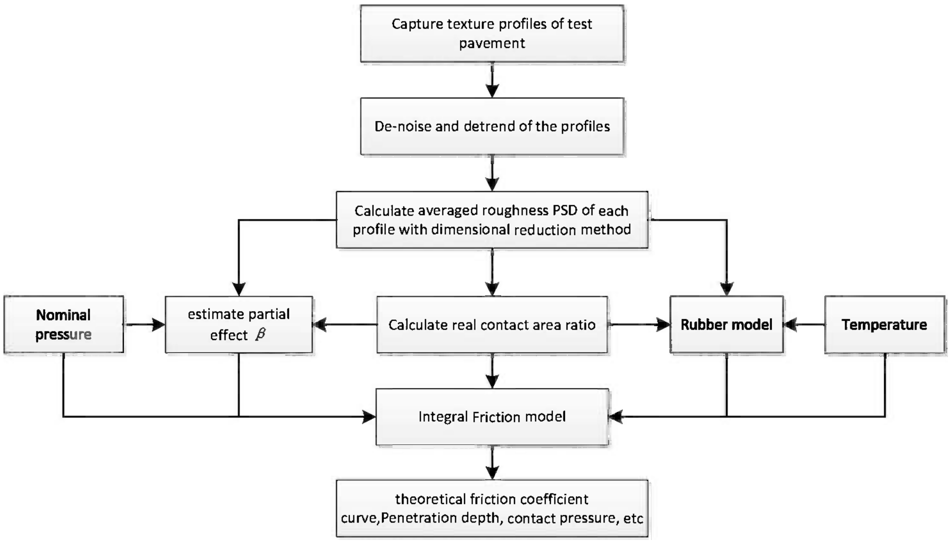

(3) The adhesive effect relies on the real area of contact combined with a velocity-dependent interfacial shear strength, which reflects the kinetics of peeling effects of rubber on the smallest length scales during the sliding process [3];

(4) Vertical displacement of the pavement under tire load can be ignored; and

(5) Statistical properties of the pavement surface are isotropic and translationally invariant within the surface plane.

Theoretical Background of the Friction Model

During the last several decades, a great deal of research has been carried out to gain a better understanding of friction and contact mechanics. Persson [2] has proposed a novel theory to predict hysteresis friction between a viscoelastic solid and a rough rigid substrate, such as the case of tire–road friction. The theory was developed for randomly rough surfaces with statistical properties that are translationally invariant and isotropic, for which the surface power spectral density (PSD) $C(q)$ depends on the wave vector q only through its module $q = |q|$, as defined in Eq 1:

$$C(q) = \frac{1}{4\pi^2}\int d^2x\langle h(X)h(0)\rangle e^{-iq\cdot X} \tag{1}$$

where:

$h(X)$ = the substrate height profile measured from the average surface plane, defined so that $\langle h(0)\rangle = 0$, and

$\langle\ldots\rangle$ = averaging over the total surface.

Figure 5 shows the surface power spectrum calculated from the height profile measured for an asphalt pavement. As illustrated in **Fig. 5**, $C(q)$ shows a power-law dependence on the wave vector q in a certain wave range, as expected for a self-affine fractal surface.

The contribution to rubber friction from the viscoelastic deformation of the rubber surface by the substrate asperities is dependent only on the complex viscoelastic modulus of the rubber and roughness spectrum of road. As the three-parameter constitutive models [3–5] are proved not suitable to characterize the real viscoelastic behaviors of the rubber tire rim over a range of temperature levels, a generalized Maxwell model is adopted, as shown in **Fig. 6**. The constants of E_i and η_i represent various spring and damper elements of the model, and the constant E_0 is referred to as the long-term or equilibrium modulus. The

FIG. 5 Roughness spectrum as a function of wave vector.

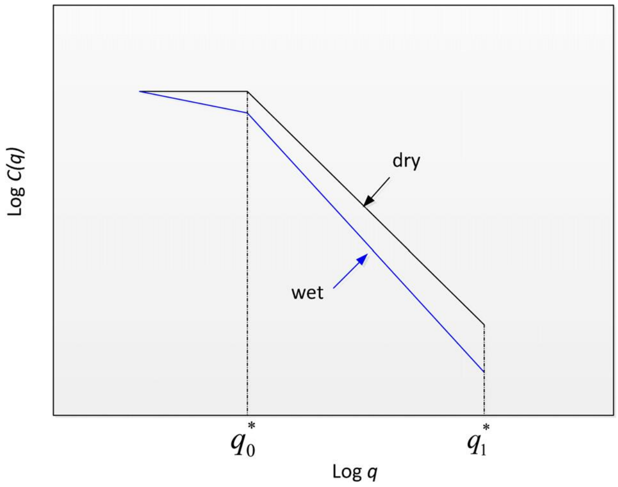

FIG. 6 Generalized model for rubber.

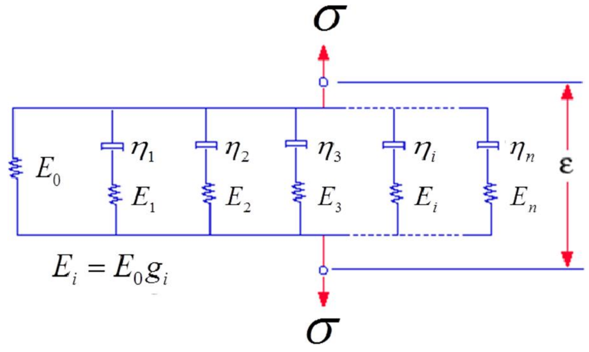

dynamic modulus of the model is expressed by the Prony series as Eq 2,

$$E(j\omega) = E_0 + \sum_{i=1}^{n} E_i \frac{(\tau_i\omega)^2}{1+(\tau_i\omega)^2} + j\sum_{i=1}^{n} \eta_i \frac{\omega}{1+(\tau_i\omega)^2} \quad (2)$$

where:

$E(j\omega)$ = the complex modulus,

$\tau_i = \eta_i/E_i$ = the characteristic periods of the viscous elements, and

ω = the circular frequency.

The temperature–frequency effects are taken into account based on the Williams–Landel–Ferry (WLF) transformation.

Hysteresis friction is characterized by the energy dissipation within the rubber tire rim, which is caused by its viscoelastic deformation while passing the road asperities on all relevant length scales, as shown in **Fig. 7** for a case where roughness occurs on two length scales.

Based on the picture shown in **Fig. 3**, a set of equations describing the friction acting on a rubber block squeezed with the stress σ_0 against a hard randomly rough surface can be derived. Neglecting the flash temperature, the nominal hysteretic friction stress $\sigma_{f0} = \mu_{\text{hys}}\sigma_0$ is determined by a sum over different length scales given by the following equations [2,4,7],

$$\mu_{\text{hys}} = \frac{1}{2}\int_{q_0^*}^{q_1^*} dq\, q^3 C(q) P(q) \times \int_0^{2\pi} d\phi \cos\phi \,\mathrm{Im}\frac{E(j\omega)}{(1-\upsilon^2)\sigma_0} \quad (3)$$

FIG. 7 The dissipated energy per unit volume of two-scale asperity contact regions [7].

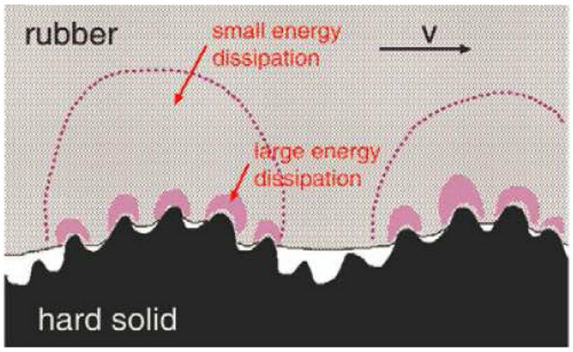

FIG. 8 Simulated hysteresis friction coefficient curves.

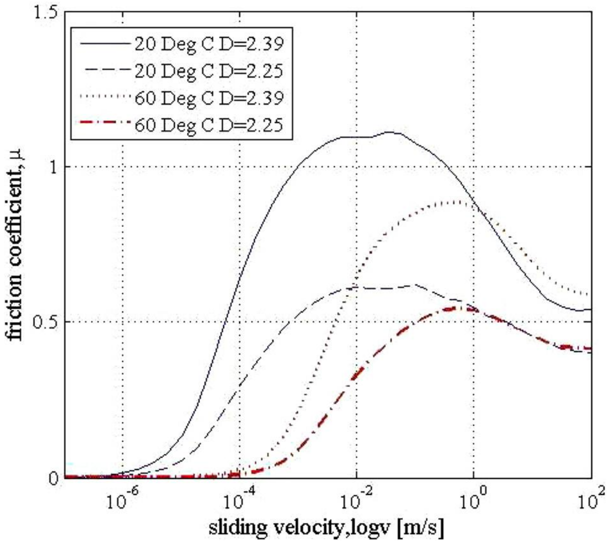

The function $P(q)$ is given by,

$$P(q) = \frac{2}{\pi}\int_0^{\infty} dx \frac{\sin x}{x} \exp[-x^2 G(q)] = \mathrm{erf}\left(\frac{1}{2\sqrt{G(q)}}\right) \quad (4)$$

with

$$G(q) = \frac{1}{8}\int_{q_0^*}^{q} dq\, q^3 C(q) \times \int_0^{2\pi} d\phi \left|\frac{E(qv\cos\phi)}{(1-\upsilon^2)\sigma_0}\right|^2 \quad (5)$$

where:

σ_0 = the averaged pressure in the nominal contact area A_0,

υ = Poisson's ratio, which equals 0.5 for rubber,

FIG. 9 Simulated interfacial shear strength curve with $\tau_{s0} = 1$. Case 1: $n = 0.75$, $v_c = 10^{-4}$ m/s, $E_\infty/E_0 = 1000$; case 2: $n = 0.3$, $v_c = 1$ m/s, $E_\infty/E_0 = 100$.

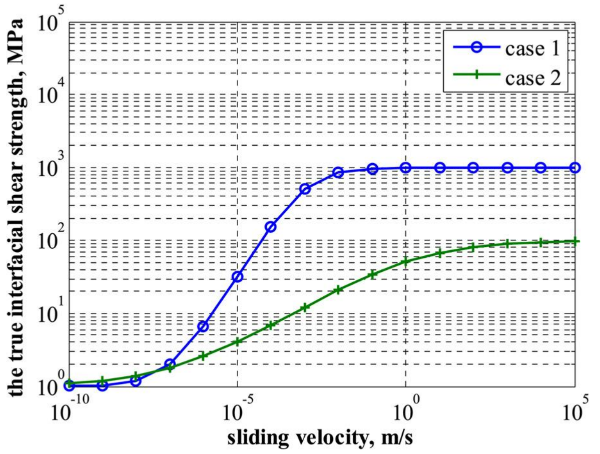

FIG. 10 Simulated adhesive friction coefficient curve.

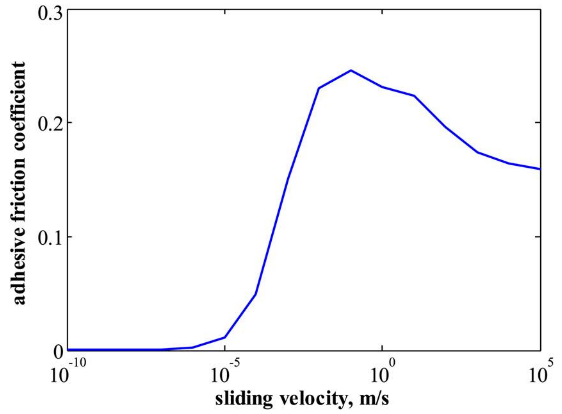

v = the sliding velocity,

q_0^* = the smallest relevant wave vector of order $2\pi/L$,

L = the diameter of the nominal contact area, and

q_1^* is the large wave vector cutoff.

The real contact area is given by $A/A_0 = P(q_1^*)$. The cutoff length $1/q_1^*$ depends, in general, on the rubber compound used and on the nature of the road surface, which are normally of the order of a few micrometers, consistent with the linear size of the smallest wear particles.

Figure 8 shows the simulated friction coefficient curve at different temperatures with regard to different pavement surfaces of varying fractal dimension. According to **Fig. 8**, both the temperature of rubber and surface roughness of the substrate have a crucial influence on rubber friction, confirming the correctness of the basic assumption (3).

As investigation has demonstrated, adhesion can even take place during rubber sliding friction on wet rough surfaces, and the presence of lubricant is a necessary, but not always a sufficient, condition for the suppression of adhesion [6]. A simple formulation of the adhesion friction given by Heinrich et al. [3] is adopted:

$$\mu_{\text{adh}} = \frac{\tau_s}{\sigma_0}\frac{A}{A_0} \tag{6}$$

where:

τ_s = the true interfacial shear strength required to break contact junctions, calculated with the empirical equation,

$$\tau_s = \tau_{s0}\left(1 + \frac{E_\infty/E_0}{\left(1 + (v_c/v)\right)^n}\right) \tag{7}$$

where:

n = a material-dependent exponent,

τ_{s0} = the interfacial shear strength in the limit of very low velocities,

v_c = the critical velocity above which the true interfacial shear strength τ_s is constant, and

E_∞/E_0 = the step height of the dynamic modulus between rubbery and glassy state.

Typical curves of the interfacial shear strength and the simulated adhesive friction coefficient are shown in **Figs. 9** and **10**.

Model Validation with Dynamic Friction Tester

To validate the system described above, a set of tests have been launched to measure the dynamic friction and surface texture. In total, 17 HMA specimens, including stone matrix asphalt (SMA-13), dense grade asphalt concrete (DAC-13), and epoxy asphalt concrete (EAC-10), made in the laboratory, have been tested.

FIG. 11

Typical dynamic friction coefficient measured by DFT.

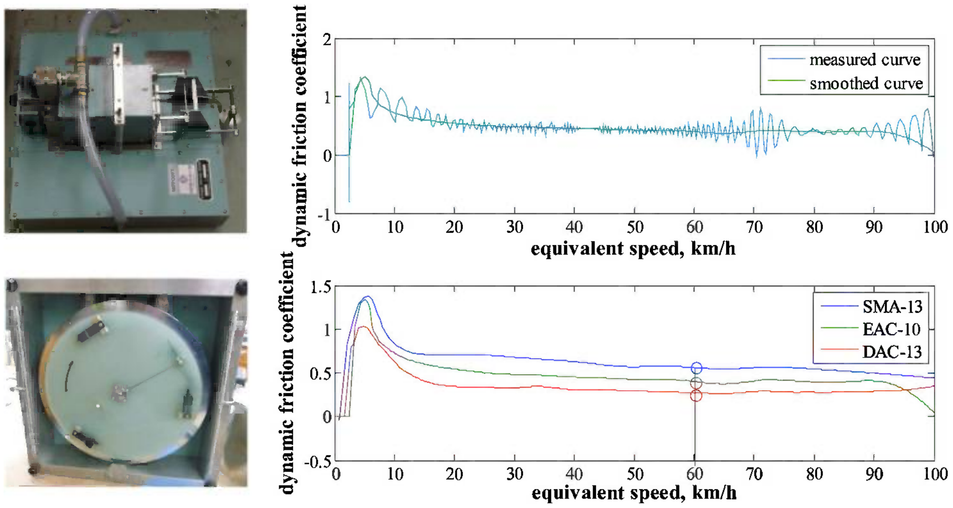

FIG. 12 The location of height profiles of specimen.

DYNAMIC FRICTION MEASUREMENTS

Dynamic friction measurements were carried out immediately after texture measurement by a dynamic friction coefficient tester (DFT), as shown in **Fig. 11**. When testing launches, the head is launched until an equivalent speed of 100 km/h is reached. When the speed reaches 90 km/h, water is projected onto the specimen surface. At 100 km/h, the motor is stopped and the disc is dropped until the rubber pads touch the specimen surface. The rotation is stopped by friction between the rubber pads and the specimen surface; the braking curve is recorded, shown in **Fig. 11**. The friction curve is smoothed and the value at 60 km/h has been included in the analysis.

TEXTURE AND HEIGHT PROFILE MEASUREMENTS

The texture and height profiles are measured combined with a non-contact, high-resolution optical metrology tool with a laser sensor. Its vertical resolution is 2 μm. Horizontal resolution is 10 μm. As the surface power spectral density can be calculated based on 1D height profiles using the dimensional reduction method [8], only 1D height profiles are measured to improve the efficiency. For each plate, texture profiles are located on the crown at three directions, and at each direction comprise at least five parallel profiles of 100 mm, spaced every 0.2 mm, with a sampling interval of 4 μm. Raw profile data were filtered and were then used to calculate the average surface power spectral density as inputs of the friction model to predict the hysteresis friction coefficient (**Fig. 12**).

The predicted friction coefficients of the specimen calculated were then compared with the dynamic friction coefficient measured by DFT by a regression analysis. As shown in **Fig. 13**, the predicted value can be fitted with the measured results with a linear model. The $R^2 = 0.78$, and most of the points lie between the boundaries of 90 % confidence, which demonstrates that the tool can be potentially used for wet grip prediction.

FIG. 13 Linear regression analysis of the prediction.

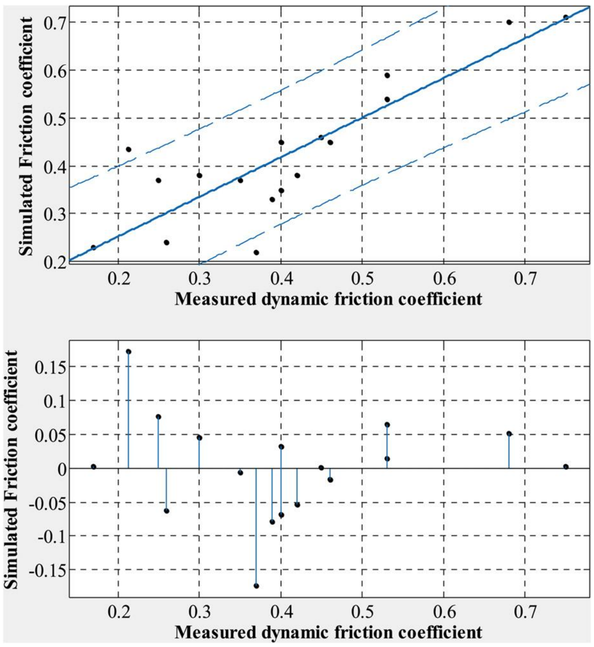

Conclusion

A non-contact method for predicting the wet grip potential of asphalt pavement has been systematically presented to include complete hysteresis friction and partial adhesive friction effect with an extended rubber material model. The predicted friction coefficients of the specimens calculated compare well with measured results from a dynamic friction tester, which demonstrates that the tool can be promisingly adopted for wet grip prediction.

ACKNOWLEDGMENTS

The writers thank the National Natural Science Foundation of China for financial support (Project No. 51478114), and they thank Dr. Andreas Ueckermann of RWTH-Aachen University for help with the rubber modeling.

References

[1] Moore, D. F., *The Friction and Lubrication of Elastomers*, Pergamon, Oxford, 1972.
[2] Persson, B. N. J., *Sliding Friction: Physical Principles and Applications*, Springer, Heidelberg, 2000.
[3] Heinrich, G., Klüppel, M., and Vilgis, T. A., "Evaluation of Self-Affine Surfaces and Their Implication for Frictional

Dynamics as Illustrated with a Rouse Material," *Comput. Theor. Polym. Sci.*, Vol. 10, Nos. 1–2, 2000, pp. 53–61.

[4] Persson, B. N. J., Albohr, O., and Tartaglino, U., Volokitin, A. I., and Tosatti, E., "On the Nature of Surface Roughness with Application to Contact Mechanics, Sealing, Rubber Friction and Adhesion," *J. Phys.: Condens. Matter*, Vol. 17, 2005, pp. R1–R62.

[5] Grosch, K. A., "Rubber Friction and Its Relation to Tire Traction," *Rubber Chem. Technol.*, Vol. 80, No. 3, 2007, pp. 379–410.

[6] Pan, X.-D., "Wet Sliding Friction of Elastomer Compounds on a Rough Surface Under Varied Lubrication Conditions," *Wear*, Vol. 262, Nos. 5–6, 2007, pp. 707–717.

[7] Lorenz, B., Persson, B. N. J., Dieluweit, S., and Tada, T., "Rubber Friction: Comparison of Theory with Experiment," *Eur. Phys. J. E.*, Vol. 34, No. 129, 2011, pp. 129–139.

[8] Geike, T. and Popov, V. L., "Mapping of Three-Dimensional Contact Problems into One Dimension," *Phys. Rev. E*, Vol. 76, 2007, p. 036710.

Journal of Testing and Evaluation

doi:10.1520/JTE20140136 / Vol. 43 / No. 2 / March 2015 / available online at www.astm.org

Shu-Rong Yang,[1] Jia-Ruey Chang,[2] Heng-Min Lin,[3] and Kun-Hu Lin[4,5]

Identification of Manholes Beneath Pavements Using RFID and AR Technologies

Manuscript received March 27, 2014; accepted for publication August 7, 2014; published online October 15, 2014.

[1] Assistant Professor, Department of Civil Engineering, National Pingtung Univ. of Science and Technology, No.1, Shuefu Rd., Neipu, Pingtung, 91201, Taiwan, e-mail: sryang@mail.npust.edu.tw

[2] Associate Professor, Department of Leisure Industry and Health Promotion, National Ilan Univ., No. 1, Sec. 1, Shen-Lung Rd., I-Lan, 26047, Taiwan (Corresponding author), e-mail: changjr@niu.edu.tw

[3] Master Student, Department of Civil Engineering, National Pingtung Univ. of Science and Technology, No.1, Shuefu Road, Neipu, Pingtung, 91201, Taiwan, e-mail: t010105@yahoo.com.tw

[4] Ph.D. Candidate, Department of Civil Engineering, National Central Univ., No. 300, Jhongda Road, Jhongli City, Taoyuan, 32001, Taiwan.

[5] Chief Secretary, New Construction Office, Public Work Department, Taipei City Government, No.1, Shifu Road, Xinyi District, Taipei, 11008, Taiwan, e-mail: cz_lkh@mail.taipei.gov.tw

Reference

Yang, Shu-Rong, Chang, Jia-Ruey, Lin, Heng-Min, and Lin, Kun-Hu, "Identification of Manholes Beneath Pavements Using RFID and AR Technologies," *Journal of Testing and Evaluation*, Vol. 43, No. 2, 2015, pp. 472–478, doi:10.1520/JTE20140136. ISSN 0090-3973

ABSTRACT

To reduce the danger due to uneven surfaces because of manholes, lowering manholes into road structures is a good approach to maintain the serviceability of the pavement. However, the vast expanse of road systems quite increases the complexity of manhole identifications when implementing maintenance and rehabilitation (M&R) activities. Hence, an emerging method for finding manholes beneath pavements is needed. In this study, radio frequency identification (RFID) technology is used to identify manholes beneath pavements. RFID tags with cement blocks were buried in dense-grade asphalt concrete at different depths in a metal mold and then were identified using RFID in the laboratory. This study developed an easy-to-use program on an RFID reader to identify RFID tags on-site. The RFID tags attached to covers of manholes beneath pavements can be easily monitored by the program. Augmented reality (AR) technology can aid users in manipulating virtual objects in real environments. This study developed a mobile manhole monitoring system (MMS) and a web-based MMS. The location and information of manholes can be transmitted from the web-based MMS through the Internet and be shown on the mobile MMS based on the AR technology. The time and costs of manhole identification can be significantly decreased and pavement maintenance activities may be implemented in a more timely fashion by using RFID and AR technologies.

Keywords

manholes, radio frequency identification (RFID), augmented reality (AR)

Introduction

A manhole on the top of pavement is used to house an access point for maintaining buried public utility and other services including sewers, telephone lines, electricity, storm drains, and gas. In

Taiwan, in most cases the top of the manhole does not match the level of the road surface, resulting in uneven surfaces. A danger to traffic, manhole covers cause numerous accidents as motorcyclists may lose control when they strike a manhole cover. Road authorities thus need to perform appropriate and timely maintenance and rehabilitation (M&R) activities.

In recent years, road authorities in Taiwan have made great efforts to level manholes in road structures so that the roads have a flat surface. For instance, the Taipei City Government has conducted the Smooth Roads Project, which calls for resurfacing all major roads in the city from 2009 to 2014. For a start, manhole covers on roads more than 8 ms wide are leveled. However, it is not easy to find the manholes from underground if it is necessary to open the manhole covers to perform maintenance. Traditionally, a handheld metal detector was used to find underground manholes, which is time-consuming. Thus, it is essential to develop a new method to find manholes beneath pavements.

Radio frequency identification (RFID) technology is a known feasible approach in manhole inspection operations. However, currently few studies have discussed the application of RFID to manhole detection. Chang et al. [1] analyzed the pros and cons of metal detection, global positioning system (GPS) location, and RFID authentication approaches as well as their restrictions. Chang et al. [2] discussed the standard deviation (S.D.) and coefficient of variation (C.V.) when using RFID to identify manholes beneath pavements. They found that with increasing reading distance, the S.D. and C.V. increase. In addition, the rapid development of wireless communications and mobile devices in recent years has greatly improved positioning services and information delivery. This has boosted augmented reality (AR) technology development. AR technology can help field road engineers complete their tasks more efficiently. Examples of such applications include car navigation, emergency services, tour planning, and yellow maps information delivery [3,4].

In this study, the performance of RFID in detecting manholes was evaluated in the laboratory, including the effect of temperature, asphalt content, burial depth, and reading distance on the RFID tags. An easy-to-use program developed on the RFID reader can be used to rapidly identify RFID tags on site. Furthermore, a mobile manhole monitoring system (MMS) (an Android app) based on AR technology and a web-based MMS were developed. Field engineers are able to use the mobile MMS to retrieve the information on neighboring manholes from the web-based MMS on site. Field engineers can dynamically browse detailed information on the neighboring manholes in real time through the AR technology in their mobile MMS.

Methods

MATERIALS

To evaluate the feasibility of manhole identification beneath pavement using RFID and AR technology, dense-grade asphalt concrete was used in this study. A dense gradation provides closer contacts among aggregate particles. Stripping-resistant aggregate with dense gradation (**Fig. 1**) and the asphalt binder with penetration grade bitumen 60/70 (AC-20) were hot mixed under controlled laboratory conditions. The gradation should be maintained on the middle between the upper and lower limits of the band. Dense-graded hot mix asphalt was designed using standard Marshall procedure to obtain the optimal asphalt content (OAC). Test results show that the optimal asphalt content (OAC) is 5.2 %, corresponding to 4 % void ratio.

RFID TECHNOLOGY

In this study, an H35B UHF RFID reader and tags whose frequency ranged from 902 to 928 MHz were used to conduct a series of tests to identify manholes beneath pavements. The H35B UHF RFID reader possesses a compact handheld computer with Microsoft Windows CE 5.0 system. In addition, the H35B uses an external antenna to scan RFID tags and incorporates a transflective LCD with touchscreen, Wi-Fi, keypad, and Bluetooth communication capabilities.

RFID is a wireless data collection technology which uses electronic tags, also called electronic labels, for storing data. The tag with 70 mm length by 30 mm width is made up of an integrated circuit chip. Even though the H35B UHF RFID reader can read tags at a distance, the performances of reading tags beneath pavements are not clear, especially the influences of properties of pavement material and burial depth on RFID signal interruption.

We use the Java programming language to develop an easy-to-use program on the RFID reader, as shown in **Fig. 2**. Clicking the "start" function on-site, the RFID reader instantly scans the neighboring RFID tags on manholes beneath pavements and displays the information about the manhole. The detailed information includes utility type, number of piles, burial time, burial depth (m), and burial company. The manhole belonging to

FIG. 1 Gradation of aggregate used in this study.

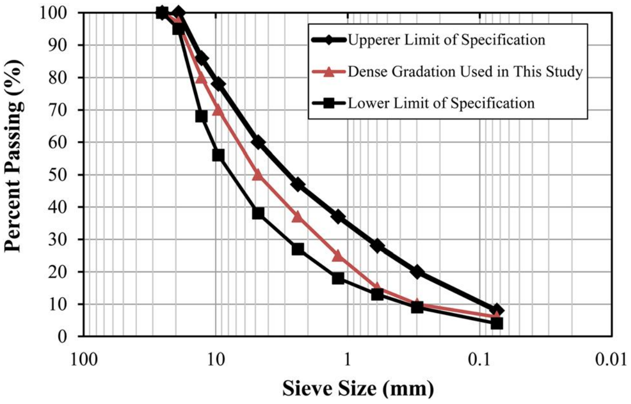

FIG. 2 The program developed on the RFID reader.

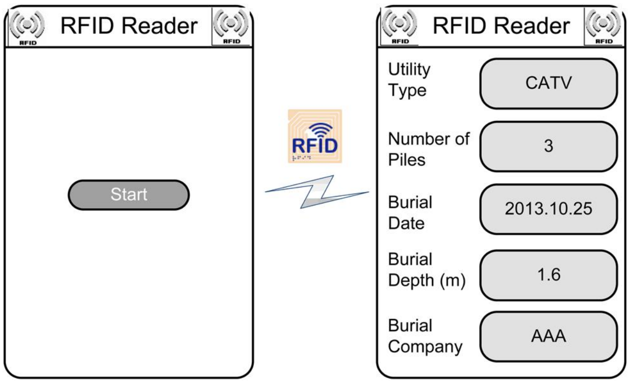

RFID Reader

Start

RFID Reader

Utility Type: CATV

Number of Piles: 3

Burial Date: 2013.10.25

Burial Depth (m): 1.6

Burial Company: AAA

cable television (CATV) is detected in **Fig. 2**. The detailed information of manholes is organized in a comprehensive database.

In this study, a RFID tag was placed at the bottom of a metal mold with diameter of 20 cm. Dense-grade asphalt concrete was then compacted into the mold and laid over the RFID tag. To evaluate the effects of the properties of pavement material and burial depth on RFID signal interruption, the specimens are compacted at optimal asphalt content (OAC), OAC-1 % and OAC +1 % at 10, 20, 30, 40, and 50 cm thickness and at dry unit weight of OAC. The test equipment is shown in **Fig. 3**. In addition, the influence of temperature on the tags was also evaluated, since asphalt pavement is paved under high temperature. The tags were detected by RFID reader at 25 and 120°C. An average of ten scans was used to evaluate the performance of underground manhole identification using RFID technology.

FIG. 3 Test equipment of manhole identification using RFID technology.

AUGMENTED REALITY TECHNOLOGY

AR is a promising technology which superimposes computer-generated information in textual or graphical format over a user's view of the real world. The user's view of the real world is augmented or enhanced beyond the normal experience [5]. Such computer-generated information is usually location-related to the user and can assist in significantly improving the performance of engineering tasks. AR is different from virtual reality (VR), a visualization technology that has been developed for several decades. VR completely submerges the user inside a synthetic or artificial environment. While submerged, the user cannot view the real world around him. By contrast, AR does not completely replace the real world. Instead, the real world is supplemented with meaningful information. Real and virtual objects thus coexist in an augmented space [6]. The advantage of AR is that the real world is viewed as a ready-made backdrop for displaying superimposed information of interest [7]. **Figure 4** shows examples of what this might look like. It shows real street scenes with several real cars and buildings from the screen of mobile phone. Inside this real street scene, the virtual icons 💡 are superimposed and indicate the location of manholes. Note that the objects are combined in 3D space, so that the virtual icons 💡 cover the real street scene. One can click the 💡 icon to further display detailed information on manholes, including utility type, number of piles, burial date, burial depth (m), and the burial company.

AR enabling technologies have been researched in a dramatically increasing number of studies in several fields of science and engineering during the recent years. For example, for entry-point guidance prior to vertebroplasty spinal surgery [8], information gathering and human navigation for situation awareness in military [9], the extent of horizontal displacements sustained by structural elements due to extreme loading conditions [10], and a computer-mediated remote collaborative design system to enhance the distributed cognition among

FIG. 4 Examples of AR technology.

remote designers [11] represent several mature applications of AR technology. There have so far been few related applications in the manhole identifications.

Results and Discussion

PERFORMANCE OF IDENTIFICATION UNDERGROUND MANHOLE USING RFID TECHNOLOGY

It is needed to consider the temperature effect on identification manhole when using RFID technology because a road is paved under high temperature using asphalt concrete. The tags were put into an oven at 25 and 120°C without laying asphalt concrete on the tags. They were detected by RFID after cooling. The data displaced on the transflective LCD of the RFID reader are the number of times detected by the RFID at the same time interval. **Table 1** shows the temperature effect on detecting the tags using RFID at 25 and 120°C. From **Table 1**, after ten measurements, the average times scanned by RFID decreased slightly with increasing temperature. In addition, the S.D. and C.V. are also slightly influenced by temperature. The tags can work well even at the high temperature of 120°C. It appears that the temperature effect on the tags is limited.

To evaluate the performance of underground manhole identification using RFID technology, a series of tests was carried out in the laboratory. First, a tag was buried in a cement block to reduce damage causing by compacting asphalt concrete. A tag with cement block was put into the bottom of round metal pail and then the dense-grade asphalt concrete with different asphalt contents (OAC-1 %, OAC, and OAC+1 %) was paved on the tag and compacted to the same density. The tag was scanned as asphalt concrete was compacted to 10, 20, 30, 40, and 50 cm thicknesses to simulate the depth of the manhole beneath the pavement. At the same time, the distance between the RFID antenna and the surface of asphalt concrete, i.e., the reading distance, was fixed at 10, 20, 30, 40, and 50 cm.

Tables 2–6 show the effects of asphalt content and reading distance on detection of RFID tags buried in asphalt concrete at 10, 20, 30, 40, and 50 cm depth, respectively. The test results show that at different reading distances and burial depths, the performance of tags identification is the better at OAC than that at OAC-1 % and OAC+1 %. With increasing reading distance, the average number of times detected by RFID exhibits an obvious decrease at OAC-1 % and OAC+1 %. However, this effect is slight at OAC. With increasing depth, the average number of times detected decreases at the same asphalt content and reading distance. The performance of tags identification is dependent on the attenuation of electromagnetic wave during propagation, which is related with the permittivity of transmission. The energy loss is low when electromagnetic wave propagates in a transmission with low permittivity. In addition, at different depths, the average number of times detected by RFID is lower than for tags without asphalt concrete. This means that the asphalt concrete has a barrier effect.

TABLE 1 Temperature effect on the tags.

	25°C	120°C
Average (Times)	30.4	29.3
S.D. (Times)	1.58	1.57
C.V. (%)	5.19	5.35

TABLE 2 Effect of asphalt content and reading distance on the tags at a depth of 10 cm.

	The Number of Times Detected by RFID				
Reading Distance (cm)	10	20	30	40	50
OAC-1 %	27.9	25.2	23.7	21.7	21.3
OAC	29.6	29.2	29.0	29.0	29
OAC+1 %	29.4	27.8	26.6	25.8	25.0

From **Tables 2–6**, it is also found that the influence of asphalt content on the performance of identification underground manholes using RFID technology is most obvious, followed by burial depth and reading distance. In addition, from the discussion above, the temperature effect is the least important. Hence, RFID technology may have limitations in identifying underground manholes. To offset this limitation, an AR technology was used to enhance management of underground manholes, as described below.

DEVELOPMENT AND IMPLEMENTATION OF THE MOBILE MANHOLE MONITORING SYSTEM (MMS) AND WEB-BASED MMS

The overall architecture of the MMS includes an on-site module and a management module, as shown in **Fig. 5**. We use Java programming language to develop the mobile MMS on mobile phones (on-site module) and the web-based MMS (management module). The application (app) for the mobile MMS is about 580 KB. The interface of the mobile MMS is designed to be simple and easy-to-use for general field engineers. Furthermore, based on the aforementioned database built by the RFID reader, the web-based MMS is developed using the concept of geographic information system (GIS) to provide data collection,

TABLE 3 Effect of asphalt content and reading distance on the tags at a depth of 20 cm.

	The Number of Times Detected by RFID				
Reading Distance (cm)	10	20	30	40	50
OAC-1 %	27.3	24.9	22.2	20.9	20.8
OAC	29.4	29.2	29.0	28.6	28.3
OAC+1 %	28.7	25.5	25.3	23.4	22.9

TABLE 4 Effect of asphalt content and reading distance on the tags at a depth of 30 cm.

	The Number of Times Detected by RFID				
Reading Distance (cm)	10	20	30	40	50
OAC-1 %	26.3	24.8	21.8	20.9	20.8
OAC	29.0	29.0	28.4	28.2	27.7
OAC+1 %	27.4	22.4	20.2	19.3	18.7

display, and post-analyses of manholes. **Figure 5** is drawn according to the actual operations in the field.

On-Site Module

After clicking the "Mobile MMS ●" function in **Fig. 5**, the field engineer is located through the built-in GPS function in the mobile phone. If the engineer is sheltered from buildings and satellites cannot be accessed, the mobile MMS will automatically activate the assisted-global positioning system (A-GPS) function. The engineer then can be located by connecting to the server through Internet. Note that the positioning accuracy of A-GPS is lower than that of GPS.

After locating the engineer, the mobile MMS browses the information of neighboring manholes in the web-based MMS database at the management module. The information is immediately transmitted from the web-based MMS to the mobile MMS and displayed on the default "Map View" interface using Google Maps. In the mobile MMS system, 👤 represents the location of the engineer and 💡 represents a manhole, as shown in **Fig. 5**. The engineer can select the "AR View" function to switch on the built-in camera in the mobile phone. In the "AR View" mode, the engineer can turn around holding the mobile phone, and view the surroundings as well as the manholes in different directions through the camera, as shown in **Fig. 5**. In addition to the superimposed 💡 icons, a summary of manholes (Utility Type) may also be displayed. AR can superimpose virtual objects (manholes) on the actual scene for display on the screen of mobile phone.

In either "Map View" or "AR View" mode, the engineer can click the 💡 icon to display detailed information on manholes, including utility type, number of piles, burial date, burial depth (m), and the burial company, as shown in **Fig. 5**. Engineers can query the manhole information through the web-based MMS at any time and any place.

TABLE 5 Effect of asphalt content and reading distance on the tags at a depth of 40 cm.

	The Number of Times Detected by RFID				
Reading Distance (cm)	10	20	30	40	50
OAC-1 %	23.6	22.5	21.3	19.8	19.2
OAC	28.3	27.4	27.1	26.8	26.4
OAC+1 %	23.8	19.5	18.4	17.0	15.5

TABLE 6 Effect of asphalt content and reading distance on the tags at a depth of 50 cm.

	The Number of Times Detected by RFID				
Reading Distance (cm)	10	20	30	40	50
OAC-1 %	22.3	20.7	19.8	18.2	17.9
OAC	27.7	26.5	26.0	24.4	24.0
OAC+1 %	20.0	18.5	17.1	15.6	14.2

Management Module

In this study, we developed a web-based MMS based on the GIS, as shown on the right side of **Fig. 5**. The manhole information stored in the database is sent to the mobile phone and displayed in Google Maps as the visual interface in real time. The web-based MMS supports browsing the manhole information from the Internet or mobile network. It enables road and/or pipeline authorities to monitor the conditions of manholes and pipelines within their jurisdiction. The management module is able to store and query the manhole information, and provide statistics for analysis and decision making.

DISCUSSION OF SYSTEM FEATURES AND BENEFITS

- Manholes are spatially scattered and location of manholes are random. Through the built-in GPS function in mobile phones, engineers can use the mobile MMS for retrieving the manhole information on-site at any time. Superimposing the neighboring manholes on Google Maps on mobile screens, engineers are able to view the manhole information related to utility type, number of piles, burial date, burial depth (m), and the burial company. Engineers can implement further pipeline work. This saves considerable time and resources, increasing the efficiency of pipeline work.
- By using AR technology, engineers can retrieve the manhole information at any time and any place and use it to make the optimal decisions for pipeline work. Using real-time information, the time lags between manhole identification and pipeline work can be greatly reduced. If manholes are incorrectly identified, this is likely to result in severe problems, including delays in pipeline work and traffic congestion caused by pipeline excavations. This would in turn increase the volume of complaints from the public. In addition, road and/or pipeline authorities can use the web-based MMS to monitor the conditions of manholes and pipeline work, ensuring that auxiliary facilities in the road system are well maintained. They can also obtain the statistics on manholes and pipelines in order to schedue road work.

FIG. 5 The mobile MMS and web-based MMS developed in this study.

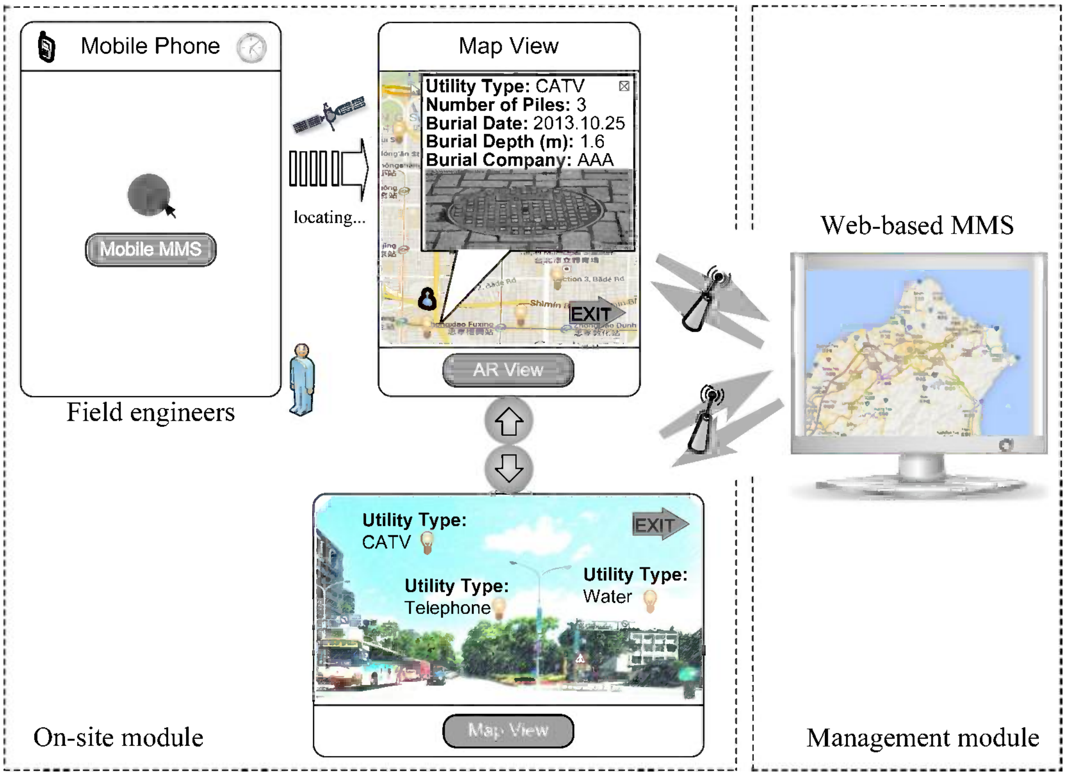

Conclusions

The effects of temperature, asphalt contents, burial depth, and reading distance on the performance of RFID tags in detecting manholes were evaluated. The dense-grade asphalt concrete with different asphalt contents (OAC-1 %, OAC, and OAC+1 %) was paved on the tags and compacted to the same density. On the basis of the results and discussions presented, we found that (1) the temperature effect on the tags is limited; (2) at different reading distances and burial depths the performance of tag identification is better at OAC than that at OAC-1 % and OAC+1 %; (3) the effects of depth and reading distance on the tags are slight at OAC; (4) with increasing depth, the average number of times detected decreases at the same asphalt content and reading distance; and (5) with increasing burial depth to 50 cm, the tags still can be detected, although the asphalt concrete has barrier effect. This study developed an easy-to-use program on RFID reader to identify RFID on-site. The RFID tags are attached to manhole covers beneath pavements can be easily monitored by the program. Field engineers can use the program to identify on-site manholes through RFID tags buried on manholes beneath pavements.

In addition, this study developed an MMS using the Java programming language, including a mobile MMS (an Android app) on the mobile phone and a web-based MMS. Field engineers can instantly retrieve detailed information on neighboring manholes from the web-based MMS. The information on manholes can be shown on a mobile phone using AR technology. By using RFID and AR technologies, the time and costs of manhole identification and pavement maintenance activities can be significantly decreased.

ACKNOWLEDGMENTS

This study was supported under projects NSC 101-2218-E-020-002 and NSC 100-2221-E-159-022 by the National Science Council of the Republic of China, Taiwan.

References

[1] Chang, A. Y., Yu, C. S., Lin, S. C., Chang, Y. Y., and Ho, P. C., "Search, Identification and Positioning of the Underground Manhole with RFID Ground Tag," *Proceedings of the 5th International Joint Conference on INC, IMS and IDC*, Aug. 25–27, 2009, Seoul, Korea, pp. 1899–1903.

[2] Chang, J. R., Yang, S. R., and Lin, K. H., "Preliminary Study of Radio Frequency Identification on Underground Manhole's Surveys," *Adv. Mater. Res.*, Vol. 723, 2013, pp. 877–884.

[3] Grejner–Brzezinska, D. A., Li, R., Haala, N., and Toth, C., "From Mobile Mapping to Telegeoinformatics: Paradigm Shift in Geospatial Data Acquisition, Processing, and Management," *Photogram. Eng. Remote Sens.*, Vol. 70, No. 2, 2004, pp. 197–210.

[4] Christian, J., and Blumer, P., "Assessment of a Portable Mapping Tool for Time–Critical Management of

Disasters," *Proceedings of the ISPRS Technical Commission II Symposium*, Vienna, Austria, July 12–14, 2006, pp. 97–102.

[5] Behzadan, A. H. and Kamat, V. R., "Visualization of Construction Graphics in Outdoor Augmented Reality," *Proceedings of the 37th Conference on Winter Simulation*, Orlando, FL, Dec. 4–7, 2005, pp. 1914–1920.

[6] Azuma, R., "A Survey of Augmented Reality," *Teleop. Virtual Environ.*, Vol. 6, No. 4, 1997, pp. 355–385.

[7] Behzadan, A. H. and Kamat, V. R., "Enabling Discovery–Based Learning in Construction Using Telepresent Augmented Reality," *Autom. Constr.*, Vol. 33, 2013, pp. 3–10.

[8] Wu, J. R., Wang, M. L., Liu, K. C., Hu, M. H., and Lee, P. Y., "Real–Time Advanced Spinal Surgery via Visible Patient Model and Augmented Reality System," *Comput. Methods Progr. Biomed.*, Vol. 113, 2014, pp. 869–881.

[9] Livingston, M. A., Rosenblum, L. J., Julier, S. J., Brown, D., Baillot, Y., Swan, I. I., J. E., Gabbard, J. L., and Hix, D., "An Augmented Reality System for Military Operations in Urban Terrain," *Proceedings of the Interservice/Industry Training, Simulation, and Education Conference (I/ITSEC'02)*, Orlando, FL, Dec. 2–5, 2002, pp. 89–96.

[10] Kamat, V. R. and El-Tawil, S., "Evaluation of Augmented Reality for Rapid Assessment of Earthquake-Induced Building Damage," *ASCE J. Comput. Civ. Eng.*, Vol. 21, No. 5, 2005, pp. 303–310.

[11] Wang, X., Love, P. E. D., Kim, M. J., and Wang, W., "Mutual Awareness in Collaborative Design: An Augmented Reality Integrated Telepresence System," *Comput. Ind.*, Vol. 65, 2014, pp. 314–324.

Journal of Testing and Evaluation

doi:10.1520/JTE20140084 / Vol. 43 / No. 2 / March 2015 / available online at www.astm.org

Albert Y. Chen,[1] Ting-Yi Yu,[2] Tsung-Yu Lu,[2] Wen-Ling Chuang,[3] Jihn-Sung Lai,[4] Chin-Hsun Yeh,[5] Yen-Jen Oyang,[6] Mathew Heui-Ming Ma,[7] and Wei-Zen Sun[8]

Ambulance Service Area Considering Disaster-Induced Disturbance on the Transportation Infrastructure

Reference

Chen, Albert Y., Yu, Ting-Yi, Lu, Tsung-Yu, Chuang, Wen-Ling, Lai, Jihn-Sung, Yeh, Chin-Hsun, Oyang, Yen-Jen, Heui-Ming Ma, Mathew, and Sun, Wei-Zen, "Ambulance Service Area Considering Disaster-Induced Disturbance on the Transportation Infrastructure," *Journal of Testing and Evaluation*, Vol. 43, No. 2, 2015, pp. 479–489, doi:10.1520/JTE20140084. ISSN 0090-3973

ABSTRACT

The effectiveness of emergency medical services (EMS) depends on the existing infrastructure and allocation of medical resources. The response time for ambulances is in general considered a critical factor to the survival of EMS patients. EMS is a challenging task due to the spatial distribution of the population and geographical layout in the urban area. The spatial configuration of ambulance fleets and hospitals should be assessed to provide an efficient service. Additionally, EMS plays a critical role in disaster situations. In this research, the effect of disasters is considered as the disturbance to the EMS system. The objective of this research is to assess the service area of EMS after a disaster. In this study, the deviation of service area before and after the disaster on the transportation infrastructure is evaluated. Multi-layer perceptron (MLP) was used to predict EMS demand in usual conditions, and a loss estimation tool is used to model the disaster triggered demand. Given the usual and disaster triggered EMS demand, location of ad hoc EMS facilities were determined using cluster analysis, and the reachability of the facilities to individual demand points were evaluated using service area analysis. The proposed approach serves as an assessment methodology and also a planning tool for the preparedness of future disaster occurrences.

Keywords

emergency medical services, transportation, geographic information system, disaster, multi-layer perceptron

Manuscript received February 28, 2014; accepted for publication August 26, 2014; published online October 10, 2014.

[1] Civil Engineering, National Taiwan Univ., Taipei 10617, Taiwan (Corresponding author), e-mail: albertchen@ntu.edu.tw

[2] Civil Engineering, National Taiwan Univ., Taipei 10617, Taiwan.

[3] Kang-Ning Junior College of Medical Care and Management, Taipei City 114, Taiwan.

[4] Center for Weather Climate and Disaster Research, National Taiwan Univ., Taipei City 10617, Taiwan.

[5] National Center for Research on Earthquake Engineering, Taipei City 106, Taiwan.

[6] Graduate Institute of Biomedical Electronics and Bioinformatics, National Taiwan Univ., Taipei 106, Taiwan.

[7] Emergency Medicine, National Taiwan Univ. Hospital, Taipei City 10048, Taiwan.

[8] Emergency Medical Service Research Center, National Taiwan Univ. Hospital, Taipei City 10048, Taiwan.

Introduction

Throughout an emergency medical action, spatial factors are critical to the performance of emergency medical services (EMS). For patients with serious conditions, the travel time between the emergency medical unit (EMU) where ambulances are located and the incident location is decisive of patients' mortality. As a result, spatial factors of emergency medical actions should be properly evaluated. On the other hand, resource distribution is important but challenging in disaster response [1]. The lack of access, standardization, coordination, and communication of basic information, such as emergency medical resources, compromise situational awareness, and decision making [2–7].

As the capacity of EMS right after a disaster in a region will not increase much, if not decreased, its performance is critical to the medical support in disaster response and to regular emergency medical demand [8,9]. As a result, this research aims to assess and provide an approach for the mission planning for post-disaster pre-hospital EMS services.

CURRENT LITERATURE

Civil infrastructure systems provide critical services to urban areas, and there is the interdependency of facilities in the systems during normal and emergency situations [10]. The efficiency of how physical infrastructures function determines the performance of critical services. Transportation networks are one of such physical infrastructures that provide critical services to facilities such as EMS in the urban area.

Pre-hospital EMS includes on-site medical treatment and transport of patients in emergency conditions [11], and EMS secures the lives of patients in such situations. For patients with severe conditions such as Out of Hospital Cardiac Arrest (OHCA) cases, the efficiency of pre-hospital EMS is critical to the patients' survival.

Limited resources must be efficiently distributed to facilitate lifesaving operations [2]. The supply of resources such as ambulances is usually not able to promptly fulfill the demand in large-scale disasters. Having investigated the relationship among critical resources, the authors in Refs. [12, 13] revealed that additional damages and causalities could be reduced with better resource preparedness to disaster incidents. As a result, efficient distribution of resources is critical in maximizing the effectiveness of disaster response efforts, such as Urban Search and Rescue (US&R).

Throughout an emergency pre-hospital medical action, which operates on the transportation infrastructure, spatial factors play important roles in its success [14]. For patients with severe conditions, the travel time between headquarters of ambulances and incident locations, and the travel time between incident locations and hospitals are both decisive of mortality. As a result, the transportation infrastructure should be taken into consideration for the assessment of EMS performance.

EMS is a specialized and unique type of intelligent transportation system for saving of human lives in normal and emergency situations [15–17]. The dispatch policies and planning of ambulances' travel routes on the transportation network have been proposed and shown to have an impact on the performance of EMS deployment [18,19]. As EMS is part of the system of systems in urban areas, assessment of its performance is nontrivial. There are various approaches to assess the performance that could improve future operations. The National Highway Traffic Safety Administration (NHTSA) [20] suggested 35 consensus-based measures that reflect EMS performance, including quality management, funding, and response operations. Although the performance of EMS has been previously evaluated in terms of patient survival rates of different response time thresholds [21], the placements of EMS facilities and the traveling of ambulances on the transportation network were not thoroughly evaluated.

A Geographic Information System (GIS) has the potential to assist the identification of less accessible areas and the planning of changes of facility relocations, for assessment of ambulance response performance [22]. By adopting an appropriate ambulance dispatch policy with GIS, the response time can be reduced [19]. Yin and Mu [23] applied a modular capacitated maximal covering location problem with GIS and optimization tools to allocate ambulances for EMS, and Bailey et al. [24] provided several candidate scenarios to improve the emergency referral system and used GIS to make the assessment and prioritization of facility upgrade. There are also risk assessment applications, which provide information of the initial response operations such as the Federal Emergency Management Agency's Methodology for Estimating Potential Losses from Disasters (HAZUS) [25] and the Taiwan Earthquake Loss Estimation System (TELES) [26]. However, these applications were not used for the location assessment and guidance of EMS deployment in disaster preparedness and response with demand estimation.

Service area is a network-based analysis to investigate regions where certain facilities provide service [27]. Service areas are usually mutually exclusive, as demands generally are allocated to a closest facility. With road network data, the service area of the facility can be determined. Rather than a circular area with the same radius, the service area takes into account the configuration of the transportation network and its traveling cost from the facility to the boundary. In the assessment of EMS, the service areas of EMUs reveal the regions where the ambulances can reach in a certain time or distance limit. Such a limit should be set to represent the golden period in which timely treatment can be provided to increase the survival rate of patients with severe conditions. Through the service area analysis, black regions that are less accessible by ambulances in the region of interest can be discovered [9].

Facilities' locations are critical to the performance of pre-hospital EMS. Emergency response systems are similar to demand responsive transit systems [28]. Adequacy of facility locations could also be assessed with cluster analysis. There have been applications in management of critical civil infrastructure systems using clustering which includes pipeline breakage indicator identification [29], optimal roadway configuration of vehicle detectors [30], and railroad track maintenance [31]. Clustering has also been applied to transportation analysis, such as for vehicle routing which helped to reduce the travel time of handicapped transportation [32] and site selection of urban transportation hubs [33]. The *k*-means method is one of the often used algorithms for clustering applications such as planning of highway transportation hub [34]. The disadvantage of using *k*-means is the determination of the number of clusters. In the literature of EMS, physical locations of facilities have not been assessed with clustering based on empirical demand together with the transportation network.

In summary, the efficiency of pre-hospital EMS is critical to the patients' survival. Efficient distribution of resources is critical in maximizing the effectiveness of disaster response efforts, such as US&R and medical treatment. When assessing the EMS performance, the transportation infrastructure should be taken into consideration. The placements of EMS facilities and the traveling of ambulances on the transportation network should be evaluated for a more efficient disaster response. Disaster risk assessment applications could be adapted for the guidance of EMS deployment in disaster preparedness and response, and the ad hoc locations for on-scene EMS could be determined using cluster analysis based on empirical and disaster triggered demand.

OBJECTIVE

The focus of this paper is to establish an approach for deployment of EMS and the assessment considering the impact of disasters such as earthquake and typhoon. The assessment should also serve as a planning tool for emergency response involving casualties.

Methodology

To achieve the objective of assessing the performance of EMS in disaster situations, we propose the following steps for the analysis. First, data from disaster simulation tools are to be acquired. The data is used to update existing transportation network data. The service area of EMS facilities could be derived based on the updated transportation network, and past EMS demand is used to calculate the coverage by the service area. Second, the number of EMS demand is to be estimated by considering two parts: demand in usual conditions and demand triggered by a disaster. The usual demand is estimated by using multi-layer perceptron (MLP) taking consideration of historical data, and the disaster triggered demand is determined based on a loss estimation tool. The two types of demands are summed together to represent a worst case scenario. Cluster analysis is performed to find potential locations for ad hoc EMS facility locations in the disaster affected zone, and a service area analysis for the ad hoc EMS facilities are carried out. The performance of the ad hoc locations of EMS is assessed based on the incident coverage (summed estimated demand) of the service area. The following paragraphs introduce Cluster Analysis and MLP in more detail.

CLUSTER ANALYSIS

To investigate how incidents are distributed and whether the locations of the ad hoc facilities of EMS are adequate, cluster analysis is conducted. We select the *k*-means method for the analysis. The incident occurrences are partitioned into *k* number of clusters. Centroids of clusters are further used as ad hoc facilities of EMS. The following is the objective function of the *k*-means method and the algorithm derivation [35,36]:

$$\text{obj} = \min \sum_{j=1}^{k} \sum_{i=1}^{n} r_{ij} \cdot \text{dist}\left(c_j, x_i\right)^2 \tag{1}$$

where $\text{dist}(c_j, x_i)$ is a distance measure between a data point x_i and cluster centroid c_j. The r_{ij} have the following definition:

$$r_{ij} = \begin{cases} 1 \text{ if } \mathrm{j} == k \\ 0 \text{ otherwise} \end{cases}$$

where

$$k = \arg\min_j \ \text{dist}(c_j, x_i) \tag{2}$$

Taking the derivative of *obj* with respect to c_j, and choosing $\text{dist}(c_j, x_i)$ to be $\left\|c_j - x_i^2\right\|$, the following is derived:

$$2\sum_{i=1}^{n} r_{ij} \cdot \left(c_j - x_i\right) = 0 \tag{3}$$

Thus c_j can be calculated with the following equation:

$$c_j = \frac{\sum_i r_{ij} \cdot x_i}{\sum_i r_{ij}} \tag{4}$$

MULTI-LAYER PERCEPTRON

Research on prediction for time series data are abundant in the literature of demand forecast. However, MLP has been proposed and shown to be effective in comparison with methods used in practice [37]. The following is a summary of the formulation and approach of MLPs [35].

For classification and regression problems, Eq 4 provides a general form using linear combination of M fixed nonlinear basis functions $\phi_j(\mathrm{x})$ with weights w_j, and $f(\cdot)$ a nonlinear activation function. Given data x and the weights w, $y(x, w)$ provides the predictive response:

$$y(x, w) = f\left(\sum_{j=1}^{M} w_j \phi_j(x)\right) \tag{5}$$

The MLP model can be described as a sequence of functional mappings. Equation 6 describes the basic unit of MLP, which produces intermediate values that are M combinations of the input data x with D dimensions. The index $j = 1, \ldots M$, and the superscript (1) indicates which layer the unit belongs to in the MLP. For the bias term $w_{j0}^{(1)}$, the corresponding $x_0 = 1$.

$$a_j = \sum_{i=0}^{D} w_{ji}^{(1)} x_i \tag{6}$$

The resulting intermediate values, a_j, are then mapped into hidden units z_j in the MLP using a nonlinear activation function $h(\cdot)$.

$$z_j = h(a_j) \tag{7}$$

The process then recurses, and the hidden units are again used to produce the K combinations of intermediate values with M dimensions. The index $k = 1, \ldots K$.

$$a_k = \sum_{i=0}^{M} w_{kj}^{(2)} z_j \tag{8}$$

The resulting intermediate values, a_k, are then mapped into another layer of hidden units y_k in the MLP using a nonlinear activation function $\sigma(\cdot)$.

$$y_k = \sigma(a_k) \tag{9}$$

The recursion could continue to form MLP with more layers. The following is the result of a 2-layer MLP based on the aforementioned derivation.

$$y_k(x, w) = \sigma\left(\sum_{j=0}^{M} w_{kj}^{(2)} h\left(\sum_{i=0}^{D} w_{ji}^{(1)} x_i\right)\right) \tag{10}$$

For the case of regression problems, the activation function in the last layer, here $\sigma(\cdot)$, is the identity. Common selections of the activation function $h(\cdot)$ in a MLP are the logistic sigmoid function and the *tanh* function.

MEASUREMENT OF PREDICTION ACCURACY

The accuracy of demand forecasts is usually evaluated by indices such as the mean average percentage error (MAPE) and the root mean square error (RMSE) [38]. The following is the definition of MAPE:

$$\text{MAPE} = \frac{1}{N}\sum_{i=1}^{N}\left|\frac{t_i - x_i}{x_i}\right| \tag{11}$$

where:

N = the total number of estimates,
x_i = the actual value, and
t_i = the estimated value.

The definition of RMSE is as follows:

$$\text{RMSE} = \sqrt{\frac{1}{N}\sum_{i=1}^{N}(x_i - t_i)^2} \tag{12}$$

where:

N = the total number of estimates,
x_i = the actual value, and
t_i = the estimated value.

CASE STUDY

The union of EMS facilities' service area is expected to cover most of the spatial extend in the region of interest. Service area reveals the potential black regions where patients cannot be served by an EMS facility in a desirable amount of time. It is crucial for patients with severe conditions to be stabilized as soon as possible. We performed an analysis to discover the problem of EMS service area in New Taipei City for the assessment [9]. **Figure 1** shows that the union of 10 km service area of the EMUs in New Taipei City is generally proper. Most of the areas not covered by the 10 km service area are located in the mountains and have a small population. Based on the preliminary results, the union service area of EMUs in normal conditions is considered to be proper.

To further assess the current infrastructure service area, we applied the same analysis to reveal the 3 and 6 km service area of the EMUs. The cutoffs—3 and 6 km—were selected manually to better visualize the service performance. This serves as a general approach to investigate the service provided considering the transportation network for pre-hospital care.

FIG. 1 Service of ambulances.

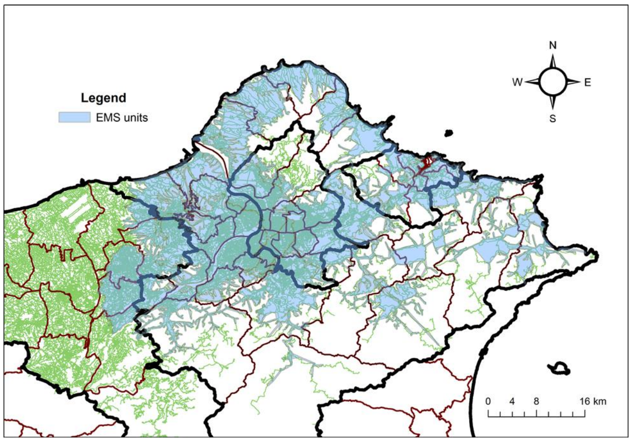

TABLE 1 EMS service area coverage.

Service Area (km)	Coverage Ratio (%)
3	93.80
6	97.81
10	99.14

Although service area reveals the spatial coverage of EMU and hospitals, investigating the percentage of EMS incidents covered by the service area provides a reasonable performance measurement. Therefore, we imported past EMS demand into the space and calculated the number of incidents covered by the service area. The number of covered incidents is then divided by the total number of incidents to form a coverage ratio. The ratios of the incidents that are covered by the different service areas are presented in **Table 1**. It is preferred that an EMU be closer to patients with severe conditions. In **Table 1**, 93.8 % of past incidents are covered by the service area of EMUs with the 3 km threshold. If better performance is preferred, adjustments are to be made, such as adding more EMU units into the system or to have ambulances dynamically allocated to places with high probability of demand occurrence.

In the case of a disaster, the transportation infrastructure will be affected. Based on the New Taipei City's regional disaster preparedness plan [39], the designed disaster scenarios could be induced by earthquake or flood. The earthquake scenario is considered due to coseismic deformation in a potential magnitude 7.6 event induced by reactivation of the Shanchiao fault located across the northwestern edge of the city [40]. On the other hand, the flood scenario is considered by inundation mapping under 500-year return-period flood with 436 mm daily precipitation.

We proposed to adopt TELES as the risk modeling tool for earthquake scenarios and use inundation hazard maps produced by the Water Resource Agency [41] as inputs for typhoon scenarios to model the effect of disasters. The scenario had been used as a disaster drill in the city in 2008, and based on the scenario, TELES provides the damage estimation on buildings and bridges.

By using the information from TELES, the transportation network is updated to represent the damage. **Figure 2** shows the changed service area of the EMUs and hospitals in New Taipei City after the earthquake. The service areas of EMUs and hospitals were reduced obviously due to the earthquake, and the reduction of service area coverage is 14.71 and 10.64 %, respectively.

Figure 3 shows the service area change of the EMUs and hospitals in New Taipei City after the 500-year return-period flood. The reduction in service area is 14.25 and 13.47 %, respectively, for the EMUs and hospitals.

In addition to the reduction of coverage area, the coverage of actual EMS demand in normal conditions by the reduced service areas is also investigated. The reduction of incident coverage of EMUs and Hospitals, respectively, are 0.83 and 3.87 % for the case of earthquake simulation and 14.03 and 15.81 % for the case for flooding.

In **Fig. 4**, individual service areas for a hospital (**Fig. 4(*a*)**) and a EMU (**Fig. 4 (*b*)**) are presented. The wider service area (in orange) is the range before the earthquake, and the narrower range (in gold) is after the earthquake. For hospitals and EMUs that reside near bridges, their service areas are greatly affected by the earthquake. However, this did not severely compromise the incident coverage rate of the union service area, as rivers are geographical borders that usually separate government jurisdictions in Taiwan. The spatial service areas produced from the analysis overlaps with adjacent entities, such as hospitals or EMUs. In other words, although the service area coverage of certain hospitals and EMUs are reduced, demand in the zone of responsibility is still reachable and can still be serviced.

FIG. 2 Service area of ambulance units (left) and hospitals (right) after the earthquake.

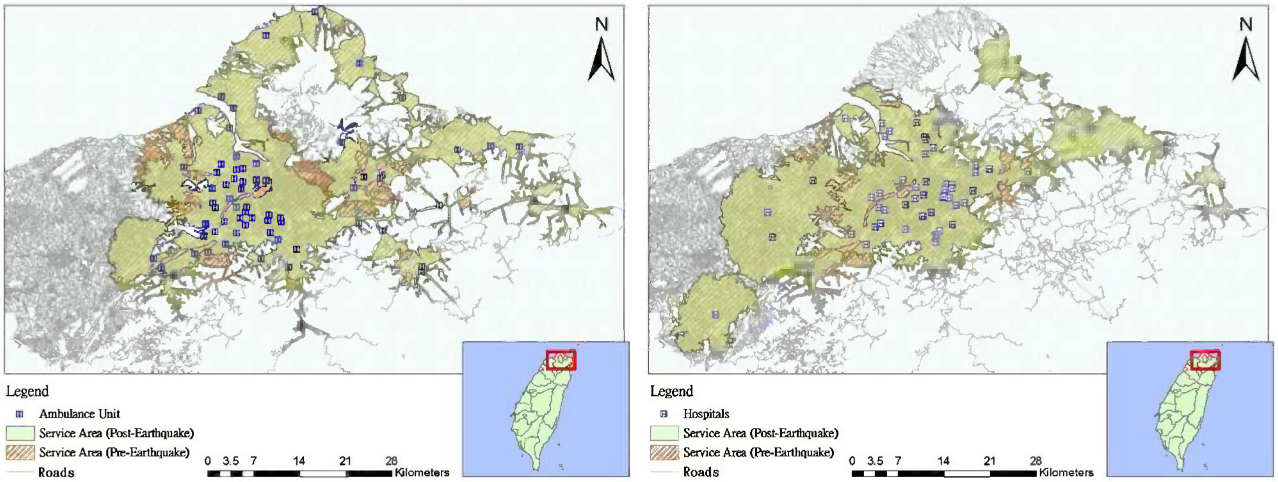

FIG. 3 Service area of ambulance units (left) and hospitals (right) after the flooding.

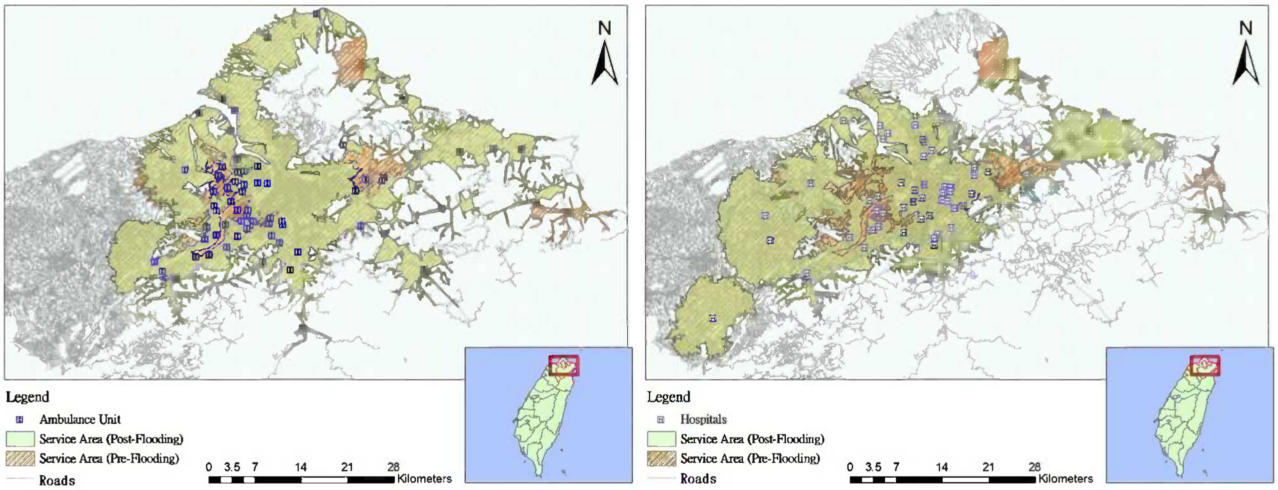

To evaluate the performance of the EMS, using post-disaster EMS demand is expected to better measure the EMS capacity and plan for emergency response in disasters. From TELES, the injured civilians triggered by the disaster are estimated and shown in **Fig. 5(*a*)**. To perform cluster analysis for seeking of ad hoc EMS facility locations on the disaster site, demand incidents are required to be in point data format. As the original estimate of the disaster triggered demand is currently in a lump sum value in districts, we assumed that the demand is uniformly distributed in the district. In each district, we generate the locations for the demand randomly while making sure that the sum of the generated points is the same as the lump sum triggered demand in each district. The generated demands are shown in **Fig. 5(*b*)**. We expect that in the future, TELES will be able to provide point data as the input to the proposed approach. As a result, in the current stage of research, the random effect of the disaggregation step in this work is not repeatedly executed for an average performance. Instead, the following results are a proof of concept with the assumption that there will be disaggregated data input from TELES.

We have collected all incidents of EMS demand for the years 2010, 2011, and 2012 that occurred in New Taipei City. Given the data of EMS demand in normal conditions, we attempted to estimate demand in future time steps using MLP. The demand data is first aggregated spatially into grids as shown in **Fig. 6(*a*)**. The three years of data are temporally aggregated into daily EMS demand for each grid to form 275 regression problems, each with time series data of 1096 temporal points. The resulting forecast for the EMS demand in usual conditions is as shown in **Fig. 6(*b*)**.

In **Fig. 7**, MAPE and RMSE are shown for the EMS demand forecast on the date same as the TELES earthquake scenario.

FIG. 4 (*a*) Service area of a single hospital (*b*) service area of a single EMU.

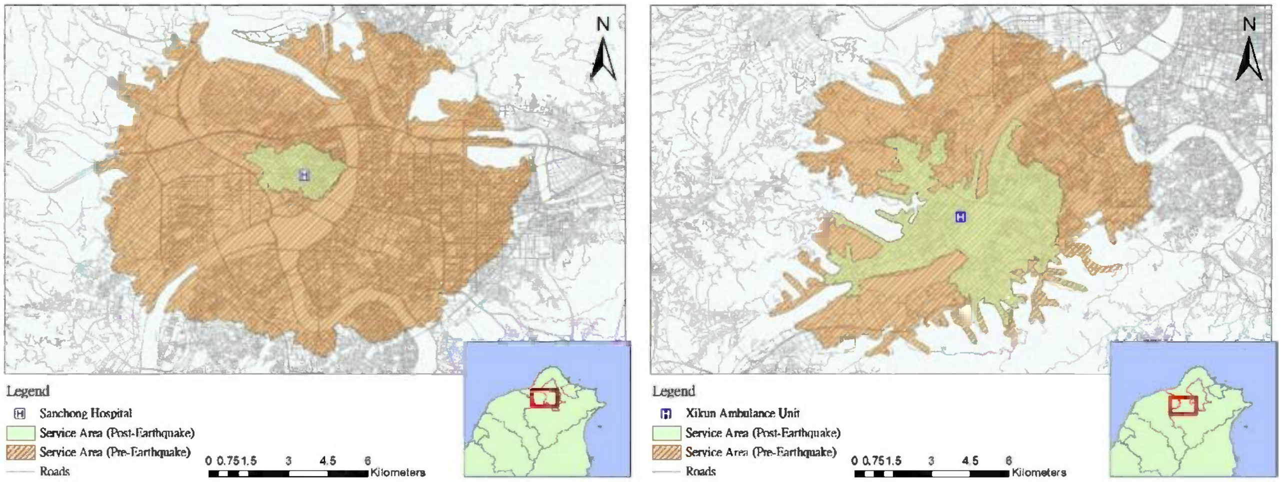

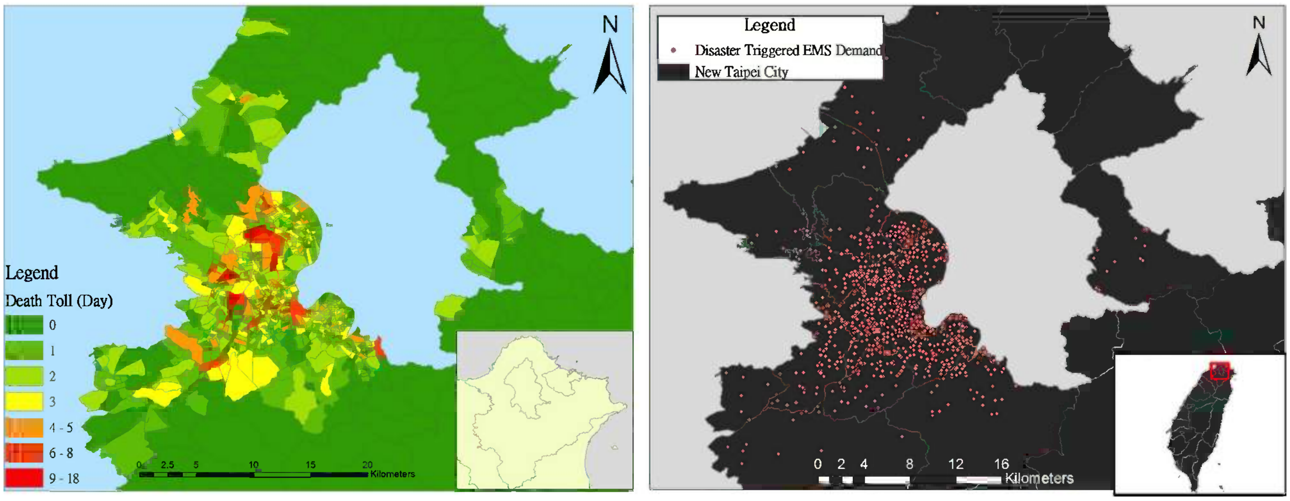

FIG. 5 (*a*) TELES output of injured civilians, (*b*) disaster triggered demand.

Figure 7(*a*) depicts the MAPE and **Fig. 7(*b*)** shows the RMSE for the demand forecast during usual conditions in the region of interest.

The MAPE value is considered with high accuracy if it has value smaller than 10 %. The estimation is considered good if the value is between 10 and 20 %, while it is acceptable for a value between 20 and 50 %. **Table 2** shows those areas in the grids (**Fig. 6(*a*)**) with greater demand amount. It can be seen that predictions of EMS demand at these areas have encouraging results; this confirms the suitability of using MLP as the forecasting model [37].

Table 3 reveals statistics on the MLP prediction for the 275 grids. The mean RMSE is 0.43 with standard deviation (STD) 1.26, and the maximum value is 11 and the minimum value is 0. The MAPE values suffer from the error definition when the actual value is 0, resulting to an infinity value. There are a total of 262 grids with non-infinity MAPE value. Among those, the mean MAPE is 11.14 with STD of 32.01. The maximum MAPE value is 200 and with a minimum value of 0. By setting the MAPE of those grids with infinity value to the maximum MAPE value of 200, the mean and STD of the MAPE becomes 20.07 and 51.30, respectively. To visually illustrate the relationship between the forecast result and the actual demand, **Fig. 8** is presented with actual demand on the horizontal axis and predicted values on the vertical axis.

By combining the EMS demand forecast in usual conditions using MLP and the estimated induced demand from TELES, a worst-case scenario of EMS demand could be modeled, and the EMS system could be assessed. **Figure 9(*a*)** shows the combined EMS demand. With this combined demand, the post-disaster incident coverage of EMUs and hospitals could be assessed. Based on this demand, cluster analysis is conducted to

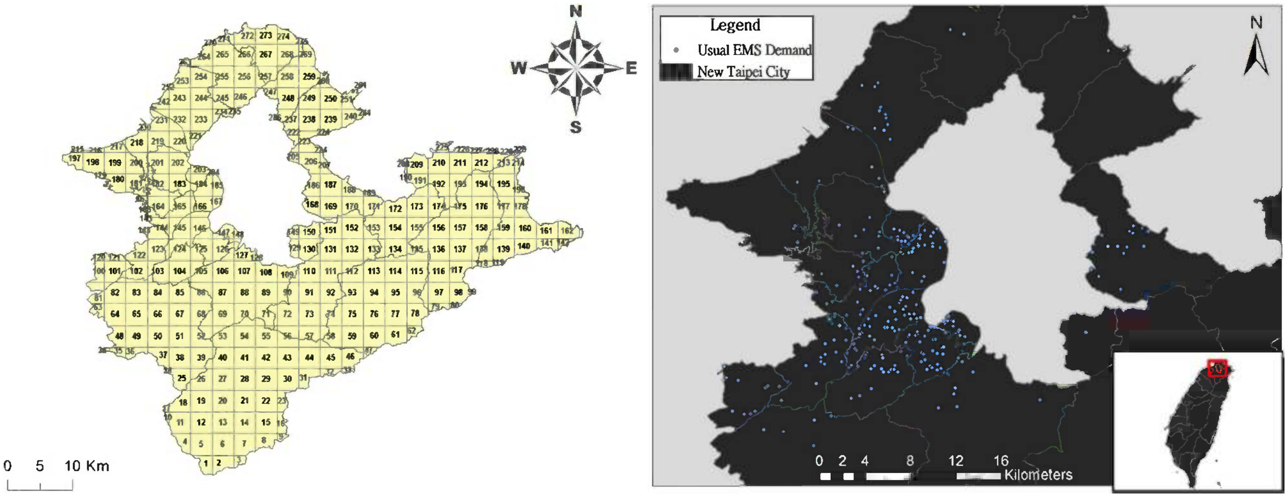

FIG. 6 (*a*) Spatial discretization using grids, (*b*) predicted usual demand.

FIG. 7 (*a*) MAPE of demand forecast, (*b*) RMSE of demand forecast.

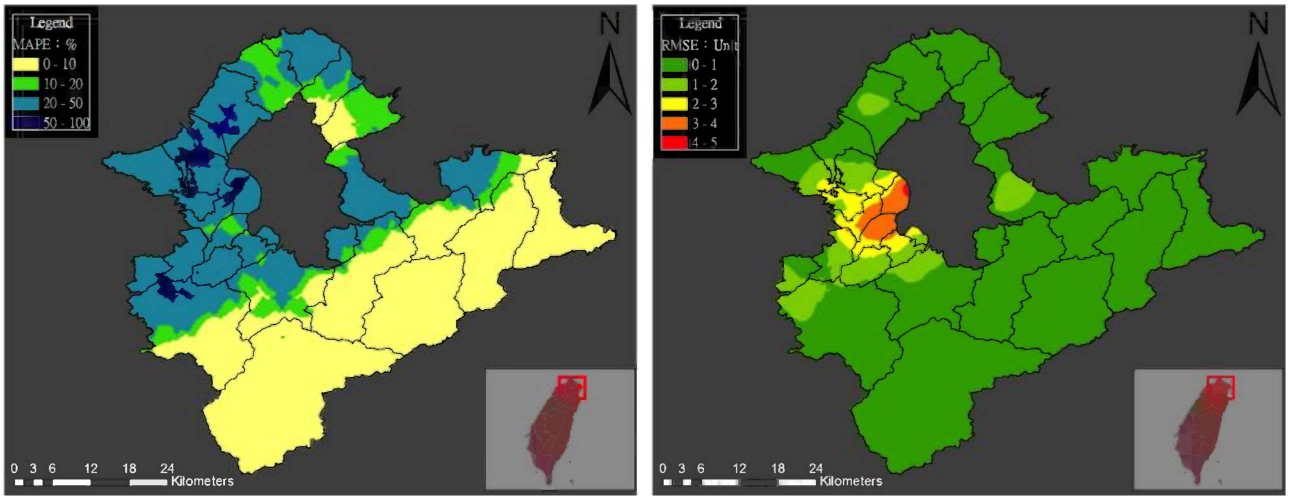

seek for suitable ad hoc facilities of EMS. **Figure 9(*b*)** depicts a result for 8 facilities and their service area. In this study, the service area is based on the road network including nearby jurisdictions such that no detour is needed if passing by other jurisdictions—such as the zone surrounded by New Taipei City—and back to New Taipei City has a shorter travel distance than strictly staying within the city.

As the number of ad hoc EMS facilities cannot be trivially determined, sensitivity analysis is performed for seven facilities to twelve facilities. **Table 4** shows the resulting coverage ratio of those facilities with an 8 km service area. As the clustering considered the Euclidian distance, while the coverage was determined with the path distance, the coverage for 11 facilities was slightly greater than that of 12 facilities.

Discussion and Future Directions

By investigating the disturbance of service area of EMUs and hospitals during disasters, the capacity of pre-hospital EMS is examined. This provides insight for decision makers to extend the capacity of EMS and efficient planning of EMS operations. Based on the best knowledge of the authors, this work is the first that attempts to combine normal EMS demand and disaster induced demand to plan for and assess a region's emergency medical disaster response.

The reduction of service area has been shown based on the two types and scenarios of disasters: earthquake and flooding.

TABLE 2 NLP prediction results.

Grid ID	Actual	Prediction	MAPE (%)	RMSE
Number 123	11	12	9.09	1
Number 124	15	17	13.33	2
Number 125	12	13	8.33	1
Number 126	19	19	0.00	0
Number 127	8	4	50.00	4
Number 144	18	11	38.89	7
Number 145	15	17	13.33	2
Number 146	40	31	22.50	9
Number 147	19	20	5.26	1
Number 148	3	2	33.33	1

TABLE 3 Statistics of prediction RMSE and MAPE.

	RMSE	MAPE[a]	MAPE[b]
Mean	0.43	11.14	20.07
STD	1.26	32.01	51.30
Max	11	200	200
Min	0	0	0

[a] Statistics excluding grids having infinity MAPE value.
[b] Statistics including grids having infinity MAPE value adjusted to max value.

FIG. 8 Actual and predicted demand.

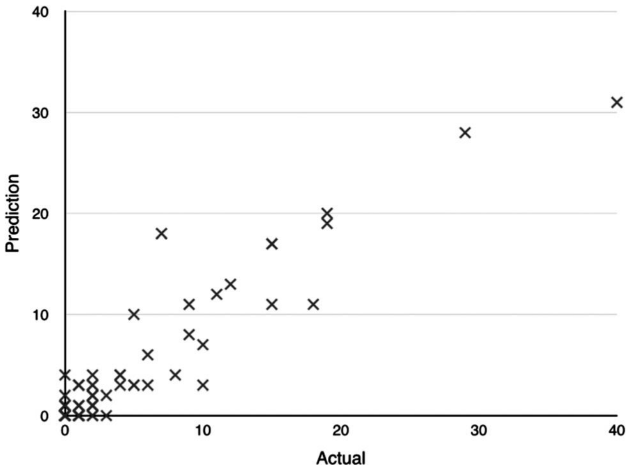

FIG. 9 (*a*) Summed demand, (*b*) clustering for 8 ad hoc EMS facilities.

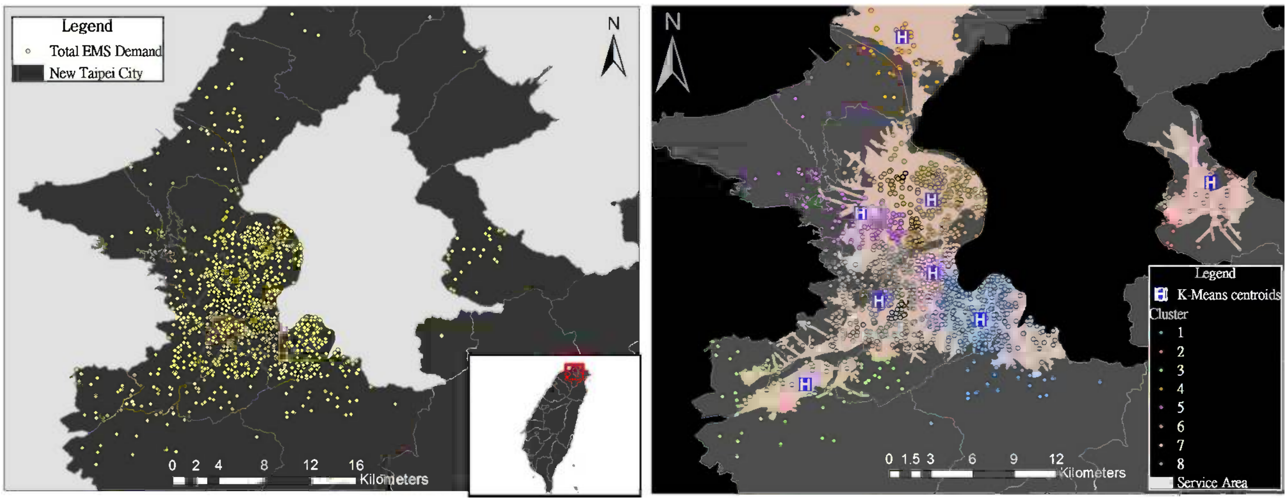

The reduction in terms of the regional coverage area and the incident coverage has been shown. The interdependency of physical infrastructure on the EMS is critical. However, in the case of earthquake, the reduction in terms of incident coverage is not significant. A potential reason for this is that TELES models the collapse of buildings and bridges. In other words, the damage of the transportation infrastructure is modeled simply based on the damage of the bridges. The blockages of road sections and the reduction in terms of traffic volume capacity are not fully taken into consideration. In addition, the responsibility region for EMUs and hospitals are often divided by landscape. Crossing a river or tunnel usually means the change of jurisdiction. Therefore, the damages to the bridges do not have significant impact on the incident coverage due to the geospatial distribution of the EMUs and hospitals.

For earthquakes, modeling of road section damage and blockage is critical and set as a future step of this study. In addition, post disaster traffic volume estimation modeling will assist in the planning of disaster response. The proposed approach could also serve as a planning tool for disaster response. Based on the available EMUs and hospitals, the post-disaster jurisdiction could be reassigned based on the demand. In addition, the service areas of EMUs and hospitals could be superimposed to show decision makers the areas where both services are inefficient, and external resources could be allocated to those areas with demand.

TABLE 4 Coverage ratio with different numbers of facilities.

EMS Facility	Coverage Ratio (%)
7	75.58
8	76.65
9	77.89
10	82.18
11	83.33
12	83.17

Different clustering methods could be adapted for further studies to consider not only the path length as the distance measure, but also hierarchical relationships and its application to the location planning of capacitated EMS on-site posts. For the grids that have high RMSE and MAPE, there is the possibility that a different learning model could better predict the demand. Noise filtering could also be considered for better regression performance.

Conclusion

We have proposed an approach to assess a region's post-disaster EMS service by investigating the interdependency of the transportation infrastructure and the EMS system. The service area analysis is adapted by incorporating post disaster disturbances to the transportation infrastructure, such as effects from flooding or damage to bridges after an earthquake. The disturbances could be from historical precipitation or earthquake, or from simulation such as TELES. In addition, the authors used the predicted casualties from TELES, together with EMS demand prediction, to evaluate the post disaster service area coverage of worst case incidents. The proposed approach could also serve as a planning tool to guide early first response deployment of the EMS on-site posts in the disaster preparedness and response phases.

ACKNOWLEDGMENTS

The writers genuinely thank the Institute of Transportation, Minister of Transportation, Taiwan for the spatial data provided, and the EMS data from the Fire Department of the New Taipei City Government. In addition, the authors appreciate the support of the Ministry of Science and Technology of Taiwan for the research grants provided (NSC 102-2219-E-002-023 and NSC 102-2627-M-002-016) for this work to be possible.

References

[1] Peña-Mora, F., Chen, A. Y., Aziz, Z., Soibelman, L., Liu, L. Y., El-Rayes, K., Arboleda, C. A., Lantz, T. S., Plans, A. P., Lakhera, S., and Mathur, S., "A Mobile Ad-Hoc Network Enabled Collaborative Framework Supporting Civil Engineering Emergency Response Operations," *ASCE J. Comput. Civ. Eng.*, Vol. 24, No. 3, 2010, pp. 302–312.

[2] Chen, A. Y., Peña–Mora, F., and Ouyang, Y., "A Collaborative GIS Framework to Support Equipment Distribution for Civil Engineering Disaster Response Operations," *Autom. Constr.*, Vol. 20, No. 5, 2011, pp. 637–648.

[3] Holguín-Veras, J., Pérez, N., Ukkusuri, S., Wachtendorf, T., and Brown, B., "Emergency Logistics Issues Affecting the Response to Katrina: A Synthesis and Preliminary Suggestions for Improvement," *Transp. Res. Rec.*, Vol. 2022, 2008, pp. 76–82.

[4] NRC, *Reducing Disaster Losses Through Better Information, Board on Natural Disasters*, NRC, Washington, D.C., 1999.

[5] Dynes, R. R., "Problems in Emergency Planning," *Energy*, Vol. 8, Nos. 8–9, 1983, pp. 653–660.

[6] Quarantelli, E. L., *Delivery of Emergency Medical Care in Disasters: Assumptions and Realities*, Irvington Publishers, New York, 1983.

[7] Fritz, J. H. and Mathewson, C. E., *Convergence Behavior in Disasters: A Problem in Social Control*, NRC, Washington, D.C., 1957.

[8] Liu, H. H. and Chen, A. Y., "Emergency Medical Dispatch: A Case Study of New Taipei City," *International Conference on Construction Applications of Virtual Reality (ConVR 2012)*, Taipei, Taiwan, Nov 1-2, National Taiwan University, Taipei City, Taiwan, 2012.

[9] Liu, H.-H., Chen, A. Y., Dai, C.-Y., and Sun, W.-Z., "Physical Infrastructure Assessment for Emergency Medical Response," *ASCE J. Comput. Civ. Eng.*, 2014 (in press).

[10] Chou, C. C. and Tseng, S. M., "Collection and Analysis of Critical Infrastructure Interdependency Relationships," *ASCE J. Comput. Civ. Eng.*, Vol. 24, No. 6, 2010, pp. 539–547.

[11] Laws & Regulation Database of The Republic of China, (Laws, Regulations DB of ROC), 2007, "Emergency Medical Services Act," http://law.moj.gov.tw/Eng/LawClass/LawAll.aspx?PCode=L0020045 (Last accessed 9 Sept 2014).

[12] Gentes, S., "Rescue Operations and Demolition Works: Automating the Pneumatic Removal of Small Pieces of Rubble and Combination of Suction Plants With Demolition Machines," *Bull. Earthq. Eng.*, Vol. 4, No. 2, 2006, pp. 193–205.

[13] Bissell, R. A., Pinet, L., Nelson, M., and Levy, M., "Evidence of the Effectiveness of Health Sector Preparedness in Disaster Response," *Fam. Commun. Health*, Vol. 27, 2004, pp. 193–203.

[14] Ko, C. I., 2008, "Spatial Distribution and Influence Factors of Cross–District Transports Among Major Trauma in Emergency Medical Services System," Ph.D. thesis, National Taiwan University, Taipei, Taiwan.

[15] Kuwata, Y. and Takada, S., "Effective Emergency Transportation for Saving Human Lives," *Nat. Haz.*, Vol. 33, 2004, pp. 23–46.

[16] Pradhan, A., Laefer, D., and Rasdorf, W., "Infrastructure Management Information System Framework Requirements for Disasters," *ASCE J. Comput. Civ. Eng.*, Vol. 21, No. 2, 2007, pp. 90–101.

[17] Levick, N., "Emergency Medical Services: Unique Transportation Safety Challenge," *Proceedings of the Transportation Research Board 87th Annual Meeting*, Washington, D.C., Jan 13–17, 2008.

[18] Cao, Z., Wang, W., Ma, D., Su, J., Gao, Z., and Han, Y., "Optimum Path Analysis of Post–Earthquake Transportation Considering Multi-Objective Based on GIS," *Proceedings of the International Conference on Transportation Engineering*, Chengdu, China, July 25–27, 2009, pp. 1104–1109.

[19] Lim, C. S., Mamat, R., and Braunl, T., "Impact of Ambulance Dispatch Policies on Performance of Emergency Medical Services," *IEEE Trans. Intell. Transp. Syst.*, Vol. 12, 2011, pp. 624–632.

[20] National Highway Traffic Safety Administration, "EMS Performance Measures: Recommended Attributes and Indicators for System and Service Performance," National Highway Traffic Safety Administration, Washington, D.C., 2009.

[21] McLay, L. A. and Mayorga, M. E., "Evaluating Emergency Medical Service Performance Measures," *Health Care Manage. Sci.*, Vol. 13, 2010, pp. 124–136.

[22] Higgs, G., "A Literature Review of the Use of GIS–Based Measures of Access to Health Care Services," *Health Serv. Outcomes Res. Methodol.*, Vol. 5, 2004, pp. 119–139.

[23] Yin, P. and Mu, L., "Modular Capacitated Maximal Covering Location Problem for the Optimal Siting of Emergency Vehicles," *Appl. Geogr.*, Vol. 34, 2012, pp. 247–254.

[24] Bailey, P. E., Keyes, E. B., Parker, C., Abdullah, M., Kebede, H., and Freedman, L., "Using a GIS to Model Interventions to Strengthen the Emergency Referral System for Maternal and Newborn Health in Ethiopia," *Int. J. Gynecol. Obstet.*, Vol. 115, 2011, pp. 300–309.

[25] HAZUS, 2013, "The Federal Emergency Management Agency's (FEMA's) Methodology for Estimating Potential Losses from Disasters," http://www.fema.gov/hazus (Last accessed 9 Sept 2014).

[26] Yeh, C.-H., Loh, C.-H., and Tsai, K. C., "Overview of Taiwan Earthquake Loss Estimation System," *Natural Hazards*, Vol. 37, No. 1-2, 2006, pp. 23–37.

[27] Upchurch, C., Kuby, M., Zoldak, M., and Barranda, A., "Using GIS to Generate Mutually Exclusive Service Areas Linking Travel on and off a Network," *J. Transp. Geogr.*, Vol. 12, 2004, pp. 23–33.

[28] Boyacı, N. and Geroliminis, B., "Facility Location Problem for Emergency and On-Demand Transportation Systems," *STRC 2012*, Urban Transport Systems Laboratory, Lausanne, Switzerland.

[29] de Oliveira, D. P., Garrett, J. H., and Soibelman, L., "A Density-Based Spatial Clustering Approach for Defining Local

Indicators of Drinking Water Distribution Pipe Breakage," *Adv. Eng. Inform.*, Vol. 25, 2011, pp. 380–389.

[30] Bartin, B. and Ozbay, K., "A Clustering Based Methodology for Determining the Optimal Roadway Configuration of Detectors for Travel Time Estimation," *Proceedings of the IEEE Intelligent Vehicles Symposium*, Istanbul, Turkey, June 13–15, 2007.

[31] Peng, F. and Ouyang, Y., "Optimal Clustering of Railroad Track Maintenance Jobs," *Comput. Civ. Infrastruct. Eng.*, Vol. 29, 2013, pp. 235–247.

[32] Ioachim, I., Desrosiers, J., Dumas, Y., Solomon, M. M., and Villeneuve, D., "A Request Clustering Algorithm for Door–to–Door Handicapped Transportation," *Transp. Sci.*, Vol. 29, No. 1, 1995, pp. 63–78.

[33] Qiu, Y., Ma, S., and Xiong, D., "Layout Planning Towards Urban Transportation Hub Based on Clustering Analysis Method," *Proceedings of the ICSSSM12*, Shanghai, China, July 2–4, 2012, pp. 706–709.

[34] Meng, Y. and Liu, X., "Application of K-Means Algorithm Based on Ant Clustering Algorithm in Macroscopic Planning of Highway Transportation Hub," *Proceedings of the 2007 First IEEE International Symposium on Information Technologies and Applications in Education*, Kunming, China, Nov 23–25, 2007.

[35] Bishop, C. M., *Pattern Recognition and Machine Learning*, Vol. 4, Spinger, New York, 2006.

[36] Tan, V., Steinebach, P. N. and Kumar, M., *Introduction to Data Mining*, Addison-Wesley, New York, 2006.

[37] Setzler, H., Saydam, C., and Park, S., "EMS Call Volume Predictions: A Comparative Study," *Comput. Oper. Res.*, Vol. 36, 2009, pp. 1843–1851.

[38] Chang, T., Chen, A. Y., Chang, C., and Chueh, C., "Traffic Speed Estimation via Data Fusion From Heterogeneous Sources for First Response Deployment," *ASCE, J. Comput. Civ. Eng.*, 2014.

[39] New Taipei City, 2013, "New Taipei City Regional Disaster Preparedness Plan," http://www.fire.ntpc.gov.tw/_file/1143/SG/24856/D.html?ctNode=248&idPath=214_221_248 (Last accessed 12 Sept 2013).

[40] Lai, J., Chiu, C., Chang, H., Hu, J., and Tan, Y., "Potential Inundation Hazards in the Taipei Basin Induced by Reactivation of the Shanchiao Fault in Northern Taiwan.," *Terr. Atmos. Ocean. Sci.*, Vol. 21, No. 3, 2010, pp. 529–542.

[41] Water Resources Agency, "Hydrological Analysis for Hazard Maps of New Taipei City," Ministry of Economic Affairs, 2013, http://fhy.wra.gov.tw/PUB_WEB_2011/Page/Frame_MenuLeft.aspx?sid=27 (Last Accessed 9 Sept 2014).

ASTM INTERNATIONAL

EDITOR-IN-CHIEF

Dr. M. R. Mitchell
Mechanics & Materials, LLC
4447 Acrete Lane
Flagstaff, AZ 86004, USA

EDITORIAL OBJECTIVES

The *Journal of Testing and Evaluation* is published in six issues per year by ASTM International, a nonprofit technical organization that develops and publishes voluntary consensus standards and related information for materials, products, systems, and services.

Some issues, in whole or in part, may be Special Issues focused on a topic of interest to our readers.

Contributions are peer reviewed prior to publication.

EDITORIAL SERVICES—SUBMISSIONS

Heather Blasco
Supervisor, Peer Review Services
Journal of Testing and Evaluation Editorial Offices
J&J Editorial Services 320 North Salem Street Apex, NC 27502, USA
Tel: (919) 267-6831
E-mail: astm@jjeditorial.com

PURPOSE AND SCOPE

The editorial objectives of the Journal of Testing and Evaluation is to serve a broad-based audience by:

- Publishing new technical information derived from the field and laboratory testing, performance, quantitative characterization, and evaluation of these materials, products, systems, and services.
- Presenting new methods and data and critical evaluations of these methods and data.
- Reporting the users' experience with test methods and the results of interlaboratory testing and analysis.
- Providing the scientific basis for both new and improved ASTM International standards.
- Stimulating new ideas in the fields of testing and evaluation.
- Including papers, technical notes, letters to the editor, discussions of previously published papers, and book reviews as contributions.

POSTMASTER: Send address change to ASTM International—JTE, 100 Barr Harbor Drive, P.O. Box C700, West Conshohocken, PA 19428-2959.

Printed in the U.S.A.

View our website: **www.astm.org**

EDITORIAL BOARD

Dr. Aziz Amoozegar
North Carolina State Univeristy
Raleigh, NC, USA
Dr. Patricia Annis
University of Georgia
Athens, GA, USA
Dr. Nemkumar Banthia
University of British Columbia
Vancouver, BC, Canada
Dr. Neal S. Berke
Tourney Consulting Group, Ltd.
Kalamazoo, MI, USA
Dr. Krishna Prapoorna Biligiri
Indian Institute of Technology
Kharagpur, West Bengal, India
Dr. Nick Birbilis
Monash University
Clayton, Australia
Dr. Laura Bix
Michigan State University
East Lansing, MI, USA
Dr. Andrew F. Braham
University of Arkansas
Fayetteville, AR, USA
Dr. Andreas Brunner
Empa, Swiss Federal Labs
Switzerland
Prof. Andrea Carpinteri
University of Parma
Parma, Italy
Dr. Wen-Ruey Chang
Liberty Mutual Research Institute for Safety
Hopkinton, MA, USA
Dr. Dar-Hao Chen
Texas Dept. Of Transportation
Austin, TX, USA
Dr. Haiqiang Chen
Xiamen University
Fujian, China
Ms. Geraldine S. Cheok
NIST
Gaithersburg, MD, USA
Dr. Richard A. Coffman
University of Arkansas
Fayetteville, AR, USA
Dr. Tong Cui
Qualcomm Packaging
San Diego, CA, USA
John S. Dick
Alpha Technologies
Akron, OH, USA
Prof. Ying Fang
Xiamen University
Xiamen, China
Dr. Yu-Ning Louis Ge
National Taiwan University
Taipei, Taiwan
Dr. T. Russell Gentry
Georgia Institute of Technology
Atlanta, GA, USA
Dr. Markus Heinimann
Alcoa Technical Center
Alcoa Center, PA, USA
Mr. Hui-Min Huang
NIST
Gaithersburg, MD, USA
Dr. Shin-Che Huang
Western Research Institute
Laramie, WY, USA
Dr. Jiancheng Jiang
University of North Carolina, Charlotte
Charlotte, NC, USA
Dr. Tao Jiang
University of Connecticut Health Center
Farmington, CT, USA
Dr. Thomas Jones
Alcoa Howmet Corp.
Whitehall, MI, USA
Dr. Sreeramesh Kalluri
Ohio Aerospace Institute
Brook Park, OH, USA
Dr. Sivakumar Kandasami
L&T Construction
Chennai, India
Dr. Vistasp M. Karbhari
University of Texas at Arlington
Arlington, TX, USA
Dr. Edward J. Kikta, Jr.
FMC Corporation
Ewing, NJ, USA
Dr. Yong-Rak Kim
University of Nebraska-Lincoln
Lincoln, NE, USA
Dr. Govindaraju Kondaswamy
Massey University
Palmerston, North New Zealand
Dr. Chaker Larabi
University of Poitiers
Poitiers, France
Dr. Robert J. Leichti
Simpson Strong-Tie Company Inc.
Pleasanton, CA, USA
Dr. Gang Li
Xi'an Jiaotong University
Shaanxi Province, China
Dr. William Luecke
National Institute of Standards and Technology
Gaithersburg, MD, USA
Mr. Thomas F. O'Connor
Milan, MI, USA
Dr. Khim Chye Gary Ong
National University of Singapore
Singapore
Dr. William T. Riddell
Rowan University
Haddonfield, NJ, USA
Mr. John Riegel, III
R3 Technology, Inc.
Springfield, VA, USA
Dr. Roberto Sabatini
RMIT University
Melbourne, VIC, Australia
Dr. Rajarshi Saha
Georgia Institute of Technology
Atlanta, GA, USA
Dr. Christopher G. Scott
Lubrizol Corporation
Wickliffe, OH, USA
Dr. Steven J. Shaffer
Bruker Nano Surfaces Division
Campbell, CA, USA
Dr. Ranganath K. Shastri
Plastics Solutions
Midland, MI, USA
Dr. Sabrina Vantadori
University of Parma
Parma, Italy
Dr. Punith Veeralinga Shivaprasad
Clemson University
Clemson, SC, USA
Dr. Cy (Chor-yiu) Sin
National Tsing Hua University
Hsinchu, Taiwan, R.O.C.
Dr. Stein Sture
University of Colorado
Boulder, CO, USA
Dr. Hao Wang
Rutgers, The State University of New Jersey
Piscataway, NJ, USA
Dr. Xuexin Wang
Xiamen University
Xiamen, China
Dr. Shaopeng Wu
Wuhan University of Technology
Wuhan, China
Dr. Feipeng Xiao
Clemson University
Clemson, SC, USA
Dr. Ming Xiao
The Pennsylvania State University
University Park, PA, USA
Dr. Xiong (Bill) Yu
Case Western Reserve University
Cleveland, OH, USA
Prof. Menglan Zeng
Hunan University
Changsha, Hunan, China
Dr. Xibin (Bill) Zhang
Monash University, Caulfield East
Victoria, Australia

Copyright by ASTM Int'l (all rights reserved); Tue Mar 24 09:08:34 EDT 2015
Downloaded/printed by
David Dammon (Dammon Engineering) pursuant to License Agreement. No further reproductions authorized.

March 2015
Journal of Testing and Evaluation
Volume 43, Number 2